THE UNIVERSITY OF HULL

Application of a new Ultrasonic Sing Around System to the Study of Magnetoelastic Effects in some Heavy Rare Earths

being a Thesis submitted for the Degree of

Doctor of Philosophy

in the University of Hull

by

David Collingwood Jiles, M.Sc. (Birmingham)

October 1979

Summary of Thesis submitted for Ph.D. degree

by David Collingwood Jiles

on

Application of a new Ultrasonic Sing Around System to the Study of Magnetoelastic Effects in some Heavy Rare Earths

---

The development of a new ultrasonic sing around system has been described. The equipment has been used to investigate the behaviour of the second order eleastic moduli of single crystal specimens of Gadolinium, Terbium, Dysprosium and Erbium under conditions of varying temperature, pressure and magnetic field.

From the results some indication of the performance of the new system has been obtained. The behaviour of the elastic properties as a function of magnetic field has allowed critical fields to be determined, and the variation of the elastic moduli with pressure have allowed the Grüneisen parameters and third order elastic constants to be calculated. Results have been compared where possible with earlier published findings.

Acknowledgements

I would like to take this opportunity to express my gratitude to the many people who have been involved in the project. In particular my supervisor Dr. S. B. Palmer and also Dr. R. D. Greenough for their guidance throughout the whole of the work. I would also like to thank Mr. D. G. Whitehead of the Department of Electronic Engineering for assistance in the development of the equipment and Mr. R. Walker for advice on practical electronics.

I am also indebted to Dr. C. Isci for the many hours of help which he gave me at the beginning of the project and also to Dr. D. Masters and the members of the Computer Centre for their assistance and patience. Thanks should also go to the members of the Mechanical Workshop for their efforts and especially Mr. E. Farr for his outstanding contribution without which many parts of the work would not have been possible.

Also I would like to thank Dr. P. C. Lanchester of the University of Southampton for allowing me the use of facilities in his laboratory and Mr. J. Penfold of Standard Telecommunications Ltd., Harlow for guidance in the use of the high hydrostatic pressure apparatus.

I am grateful to the staff of the Department of Materials Science at the University of Birmingham, in particular Dr. D. Fort for supplying single crystal specimens of the Rare Earths for our use.

My thanks also go to Mrs. G. A. Smith for her careful typing of the script and for the many hours which she has spent which were more than I could have expected. Also thanks go to Miss H. E. Graham for drawing most of the diagrams when time was very short and it would have been impossible for me to complete them soon enough.

Finally my thanks go to the many other people, too numerous to mention individually, who have contributed, however unwittingly, to this work. Their contributions have not gone unnoticed.

CONTENTS

List of Plates

Photographs produced by the University of Hull Photographic and Copying Service except Plates VII and VIII which were reproduced with the kind permission of the Photographic Department of Standard Telecommunications (ITT) Ltd., of Harlow, Essex.

CHAPTER 0

Introduction

The elements Gadolinium, Terbium, Dysprosium and Erbium belong to the 4f series, the rare earths, which lie between Lanthanum and Lutetium in the periodic table. This group of elements all have very similar chemical properties but exhibit a wide range of magnetic structures. These are due to the partially filled 4f shell which makes a significant contribution to the magnetic moment of the atoms in the solid phase, but is screened from the outside by the outer 5d and $6s^2$ electrons which are responsible for the chemical properties. Among the techniques used to obtain information about the magnetic structures of these elements are neutron diffraction, magnetisation, electrical resistivity and elastic constant measurements.

Ultrasonic techniques have been used to investigate the elastic properties of the rare earths Dysprosium and Gadolinium by Rosen [1,2], Erbium by Fisher and Dever [3] and Gadolinium, Terbium, Dysprosium, Holmium and Erbium by Palmer et al [4,5].

Direct measurements of acoustic transit times by use of an oscilloscope limits precision to about 0.1% according to Papadakis [6]. In order to obtain greater precision more sophisticated techniques are necessary and a review of these is given in chapter one. The original sing around was due to Holbrook [7] and the arrangement described in this thesis is broadly a development from the system due to Forgacs [8]. Later improvements were made by Brammer [9] and the present scheme is outlined in chapter four. Its performance will be found included in the results.

In this work measurements have been made of the single crystal elastic moduli of the heavy rare earths Terbium, Gadolinium and Erbium over the temperature range 4.2 - 300°K and in fields of 0 - 2.5 Tesla. From the location of magnetoelastic anomalies and other changes in the elastic properties the magnetic phase diagrams of Gadolinium and Terbium have been constructed and compared with those obtained by other techniques, notably by neutron diffraction. The present work is believed to be the first measurements of the elastic properties of the materials under these conditions, although some preliminary work in zero field and 2.5T was reported by Palmer and Lee [4,5].

The variation of single crystal elastic moduli of Terbium, Dysprosium and Erbium with hydrostatic pressures have also been measured over the ranges 0 - 100 bar in Hull and 0 - 5 kbar using the S.R.C. high pressure facility at S.T.L. Ltd. at Harlow. The Grüneisen parameters have been calculated from these data and compared, in the case of Erbium and Dysprosium with the earlier results of Fisher [10]. In the case of Erbium the variation of some of the second order moduli with selected uniaxial stresses along certain crystallographic directions have been measured. From these results a complete set of third order elástic moduli has been calculated according to the method outlined by Brugger [11].

In chapter four attention is drawn to the mode of operation of the new sing around system, together with other experimental methods including control of the physical environment of the specimens either at low temperature, high pressure or under applied magnetic fields. Calibration procedures for the thermocouples and strain gauges are outlined.

A brief description of the magnetic and elastic properties of the heavy rare earths is given in chapters six and seven followed by presentation of results in detail in chapters eight, nine and ten. Associated information which was either not directly relevant or too long to include in the main text will be found in the appendices.

CHAPTER 1

Ultrasonic Techniques

1.1 General Applications of Ultrasonics

Ultrasonics has been an accepted experimental technique since the work of Langevin who investigated the use of piezoelectric quartz for emission and receipt of high frequency acoustic vibrations in the early 1920's. Some of the main uses of ultrasound now include the non-destructive testing of articles for flaws, for example the detection of inhomogeneities in specimens by reflection of all or part of an incident wavefront by the defect; the investigation of elastic properties of materials from acoustic velocity measurements, and the monitoring of attenuation of ultrasound which is used in thickness gauges and level detectors. Other measurements include the estimation of grain size in specimens by the amount of acoustic scattering. It has also been used as a method of detecting obstacles on a larger scale, for example in ultrasonic radar systems.

Acoustic imaging techniques which have been available since the work of Solovev in 1934 involve a little more sophistication. However, because of the upper frequency limit the resolution of these image converters is restricted. One of the more recent developments has been the use of ultrasonic holography which contains information concerning the inside of objects including shape and size of defects or inhomogeneities. This has found an important application in medical physics.

Among the high intensity applications is the production of cavitation in liquids when rapidly fluctuating pressures are applied. This can be used to induce chemical reactions for example to produce a colloidal solution of two otherwise immiscible liquids, or in ultrasonic

cleaning baths which depend on a combination of agitation and cavitation. High intensity ultrasound is also used in fatigue testing of materials and other techniques such as the ultrasonic drill.

1.1.2 Particular Applications to Elastic Properties

The earliest reported attempts to use ultrasonic techniques to measure elastic properties of materials were reported by Pierce [1] 1925 and by Boyle and Lehman [2,3] 1926. Later attempts to measure changes in elastic moduli required more subtle techniques than direct measurement of the time between successive acoustic pulses and as a result the pulse echo overlap technique was invented by Huntingdon in 1947 [4] and an early form of sing around system by Holbrook in 1948 [5].

More recent applications of interest include the work of Crecraft [6] who used an ultrasonic sing around system to measure the differential velocity between two waves polarised along the principle stress axes of a sample and from this a knowledge of how the velocity varies with stress was gained and from the third order elastic constants the residual stress in the specimens was calculated.

1.1.3 Acoustic Methods to Investigate the Properties of Solids

Acoustic methods provide one of the three main materials testing techniques for investigating the properties of solids, the others being electromagnetic and particle methods. The use of ultrasound to determine the mechanical properties of a solid depends on measuring, however indirectly, the elastic constants of the material. Fortunately a fairly simple relationship exists between the acoustic velocity and the relevant elastic constant as indicated in section 1.3.3.

Ultrasonic frequencies are generally taken to lie between 20kHz and 500MHz. These may be further subdivided into those ranges employed in the two principle ultrasonic methods of obtaining information

concerning elastic properties. For methods involving resonance techniques the kiloherz frequencies are used, while for pulse echo methods the megaherz range frequencies are employed.

1.2 Determination of Acoustic Velocity

A short review of the main experimental methods used for the determination of acoustic velocity in solids is given. This concerns only the high frequency, megaherz, pulse-echo techniques. These fall broadly into five categories (i) Pulse Superposition, (ii) Pulse-Echo Overlap, (iii) Pulse Interferometer, (iv) Twin Specimen Interferometer and (v) Sing Around Systems.

1.2.1 Pulse Superposition Methods

Except in cases where fairly large changes in acoustic velocity are being measured, that is of the order of 0.1% or larger, which can be seen on the time base of an oscilloscope, more subtle techniques than direct measurements must be employed. The first of these methods for detecting small changes in velocity is the pulse superposition technique [7,8]. This is based on measuring accurately the time from any cycle of a given echo to the corresponding cycle of the next echo. It is therefore a very accurate method of measuring the absolute velocity of sound in a sample.

When operating, a series of pulses and corresponding echoes is observed on an oscilloscope. The frequency of the kiloherz c.w. (continuous wave) oscillator is adjusted until the initial pulse from the r.f. (megaherz) oscillator corresponds exactly with one of the echoes from the preceding pulse. This may be checked since when the two are exactly superposed the amplitude of the sum of the echoes will be a maximum.

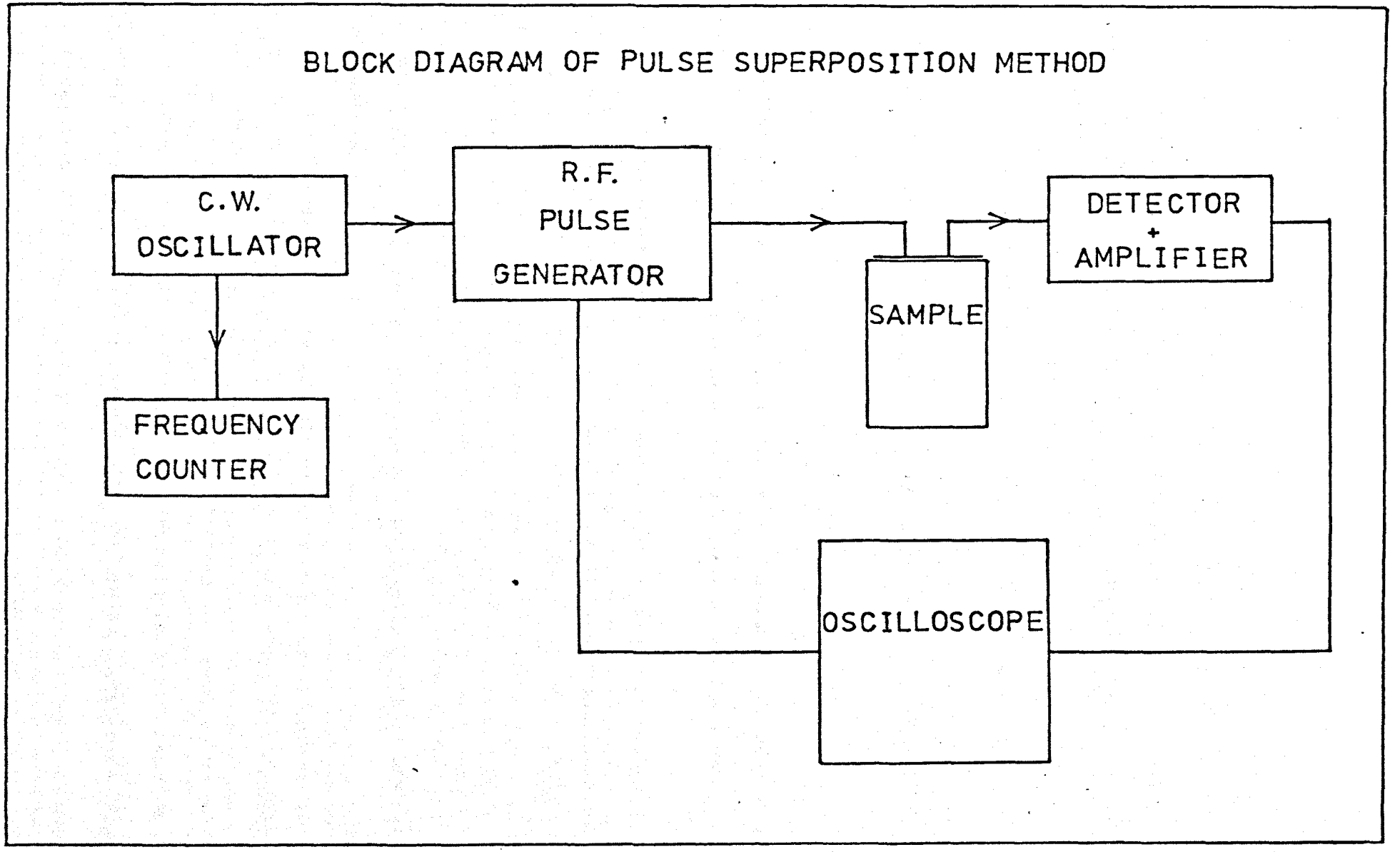
BLOCK DIAGRAM OF PULSE SUPERPOSITION METHOD
C.W.
OSCILLATOR
R.F.
PULSE
GENERATOR
SAMPLE
DETECTOR
+
AMPLIFIER
FREQUENCY
COUNTER
OSCILLOSCOPE

fig.11

If the pulse is superposed on the first echo then the radio frequency pulser fires once per round trip in the sample, and hence the reciprocal of the c.w. frequency as measured on the frequency counter gives the transit time of the acoustic pulse in the specimen. If the pulse is superposed on the second echo then the reciprocal of the c.w. frequency is twice the transit time and so on.

The actual time measured then represents the period between any point on the initial pulse and the exactly corresponding point on its nth echo. When the frequency of the c.w. oscillator is equal to the reciprocal of one transit time the superposed signal gives an interference maximum which is global because under these conditions the attenuation between the superposed pulses is a minimum. A schematic diagram of the pulse superposition method is given in fig. 1.1.

1.2.2 Precision

This method can be used for absolute velocity determination because of its capability for measuring transit times by matching cycle for cycle. Various systematic errors reduce its accuracy, such as beam spreading which causes a shift in phase of the waveform. An assessment of both the pulse superposition and pulse echo overlap methods has been given by Papadakis [9].

Concerning the precision of this method for measuring changes in transit time there will be some error due to the experimenter gauging the exact point of pulse superposition. A precision of a few parts in 10^5 is quoted for the basic system. McSkimin has made some improvements in an automated version of this method [8] and claims a precision of $\pm$ 1 part in 10^6.

1.2.3 Pulse Echo Overlap

This method is similar to the pulse superposition technique in that it measures the time between corresponding cycles of particular echoes. Hence it can also be used to measure small changes in velocity to a high precision. The absolute accuracy of the pulse echo overlap is thought to be slightly greater than the pulse superposition method according to Papadakis [9] while the precision of the pulse superposition may be better although both are quoted at a few parts in 10^5.

Some features of the pulse echo overlap (P.E.O.) [10] differ from those of the pulse superposition method. The P.E.O. can be used to measure through transmission of one transit of a sample using transducers on both ends of the specimen, acting as separate emitter and receiver. The P.E.O. does not require direct bonding, as does the pulse superposition, and thus can be operated with a buffer rod between the transducer and specimen. The most important feature is that the P.E.O. can be operated with broad band pulses so that the correct cycles may easily be overlapped. In the pulse superposition this condition is more difficult to obtain and the superposition may be an integral number of cycles out. A drawback is that the P.E.O. has not been automated in the manner in which McSkimin has automated the pulse superposition method and it is not envisaged that this will be achieved in the near future.

Operation of the P.E.O. involves the matching of a pulse and one of its succeeding echoes so that they overlap, cycle for cycle, on an oscilloscope. This condition is achieved by adjusting the frequency of the c.w. oscillator until the reciprocal of this equals the travel time between pulse and echo. The oscilloscope is operated in x-y rather than y-t mode so that by suitable choice of the c.w. frequency successive echoes will appear on successive sweeps of the trace across the screen.

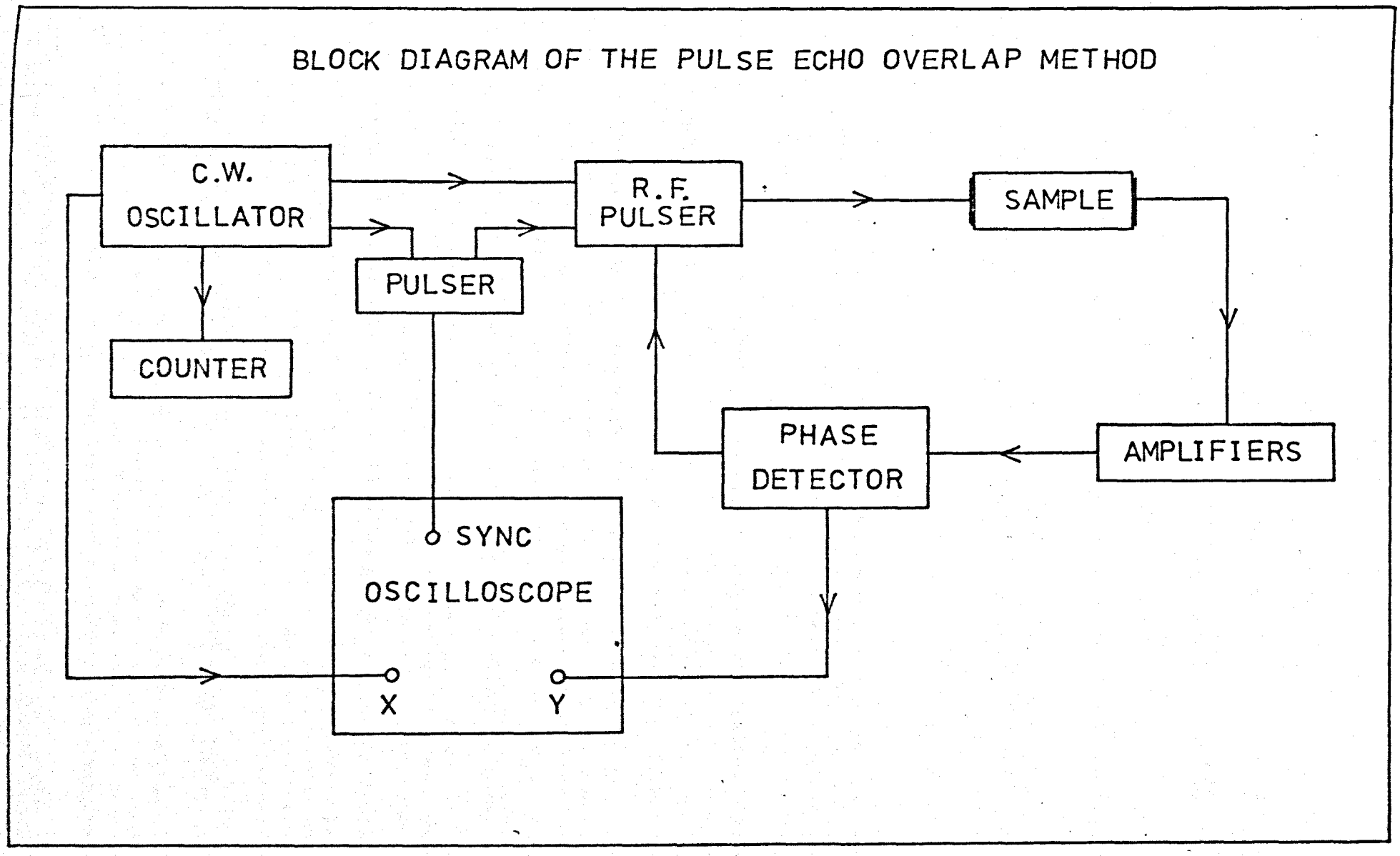
BLOCK DIAGRAM OF THE PULSE ECHO OVERLAP METHOD
C.W.
OSCILLATOR
R.F.
PULSER
SAMPLE
PULSER
COUNTER
PHASE
DETECTOR
AMPLIFIERS
SYNC
OSCILLOSCOPE
X
Y

fig. 12

Intensifier pulses are used to brighten the two echoes which are being overlapped, and others may be blacked out by turning down the intensity control on the oscilloscope. When the c.w. oscillator frequency is set correctly the pulses and echoes will all occur at the same point in the sweep on the oscilloscope screen. The reciprocal of the oscillator frequency then gives the transit time between the selected echoes. The P.E.O. system is represented schematically in fig. 1.2.

1.2.4 Precision

The same type of analysis which may be applied to the pulse superposition method also applies to the P.E.O., except that it is possible to obtain an exact overlap of the correct cycles. The precision depends mainly on the observer's ability to overlap the echoes exactly. This is taken by Papadakis to introduce errors of about 20 p.p.m. which remains the limit of precision of the system at present.

1.2.5 Pulse Interferometer (Phase Adjustment Method)

This method covers a broad category of techniques for determining velocity in which the variation of the r.f. frequency is the central theme. With these variable frequency methods it is important to note that the phase change on reflection varies with the r.f. frequency and therefore must be accounted for as the frequency is changed. The transmitting transducer is pulsed and when the first echo is received back it is pulsed again. This is achieved by using a variable delay between the two pulses, which is adjusted until the second coincides with the echo of the first pulse. Consequently all echoes are superposed in pairs except for the initial pulse.

The amplitude of the second signal is then made smaller than the first, to allow for attenuation, until both signals make equal

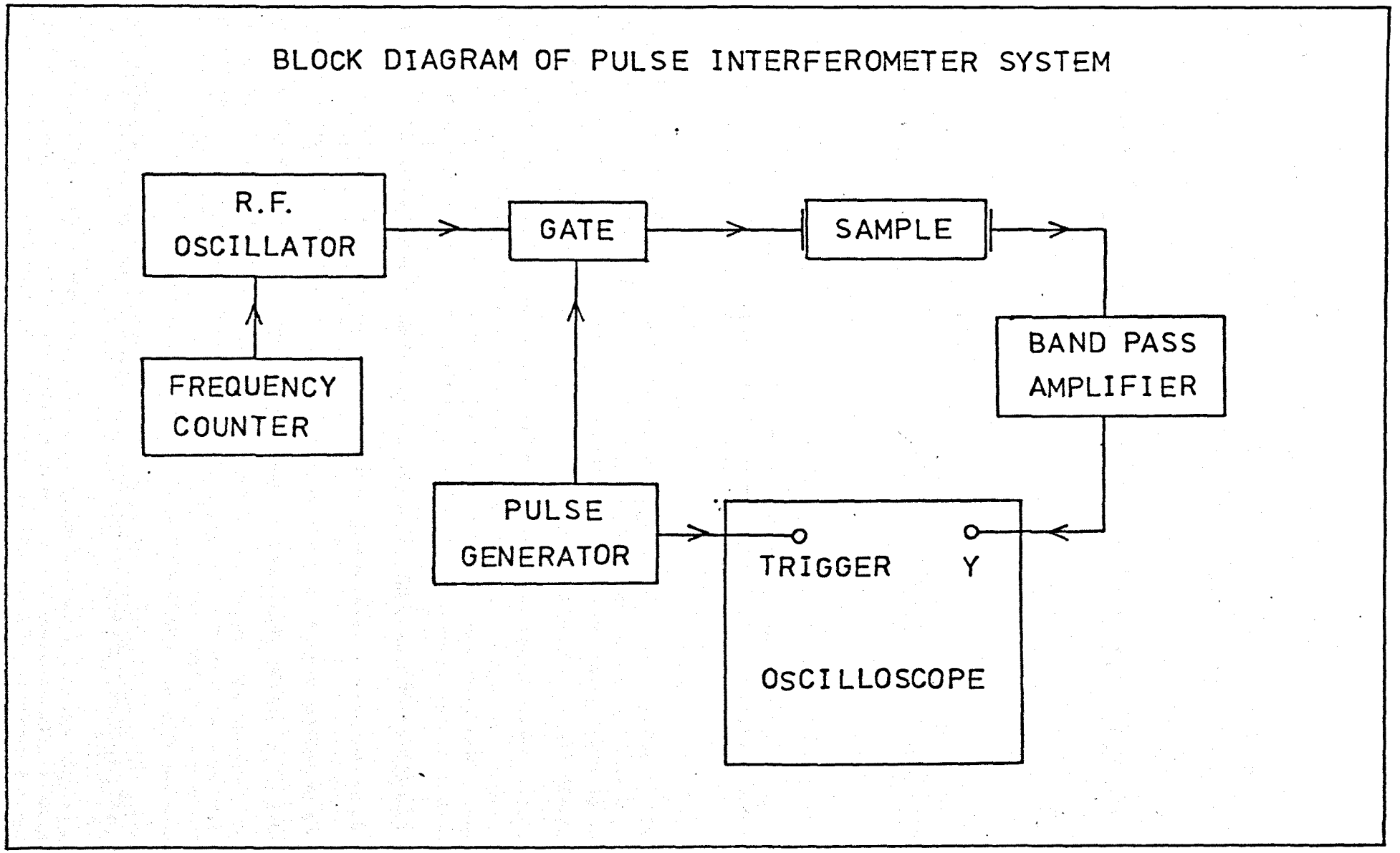
BLOCK DIAGRAM OF PULSE INTERFEROMETER SYSTEM
R.F.
OSCILLATOR
GATE
SAMPLE
BAND PASS
AMPLIFIER
FREQUENCY
COUNTER
PULSE
GENERATOR
TRIGGER
Y
OSCILLOSCOPE

fig. 1.3

contributions to the observed interference pattern. By suitable adjustment of the frequency ω the total signal may be made zero independent of time t and hence the transit time τ through the sample may be calculated as follows.

At time t the waveform of the initial pulse which will have made two round trips through the specimen and undergone two phase changes of φ will be given by

$$A_1(t) = A_1.\sin(\omega(t + 2\tau) + 2\varphi) \qquad ....1.1$$

and the waveform of the second pulse will be

$$A_2(t) = A_2.\sin\omega t \qquad ....1.2$$

The interference waveform pattern will therefore be given by

$$A_{tot} = 2.A.\sin(\omega(t-\tau)+\varphi)\cos(\omega\tau-\varphi) \qquad ....1.3$$

where both components have amplitudes A adjusted to be equal. Since by adjustment of the frequency ω the net signal may be made zero, when this occurs at ω_o the condition may only be satisfied for all t when

$$\cos(\omega_o\tau - \varphi) = 0 \qquad ....1.4$$

$$\omega_o\tau - \varphi = (2n+1)\frac{\pi}{2} \qquad ....1.5$$

where n is a positive integer. The phase angle φ may be calculated as a function of frequency and consequently the transit time calculated from the observed null frequency ω_o. A version of this method was reported by Williams and Lamb [11].

1.2.6 Twin Sample Interferometer

This is a modification of the basic pulse echo methods which is suitable for small changes ($< 0.1\%$) in acoustic velocity. Ultrasonic pulses are sent into two specimens which have the same length under the same physical conditions and the echoes from both are displayed on an oscilloscope. An interference pattern is observed by summing the two

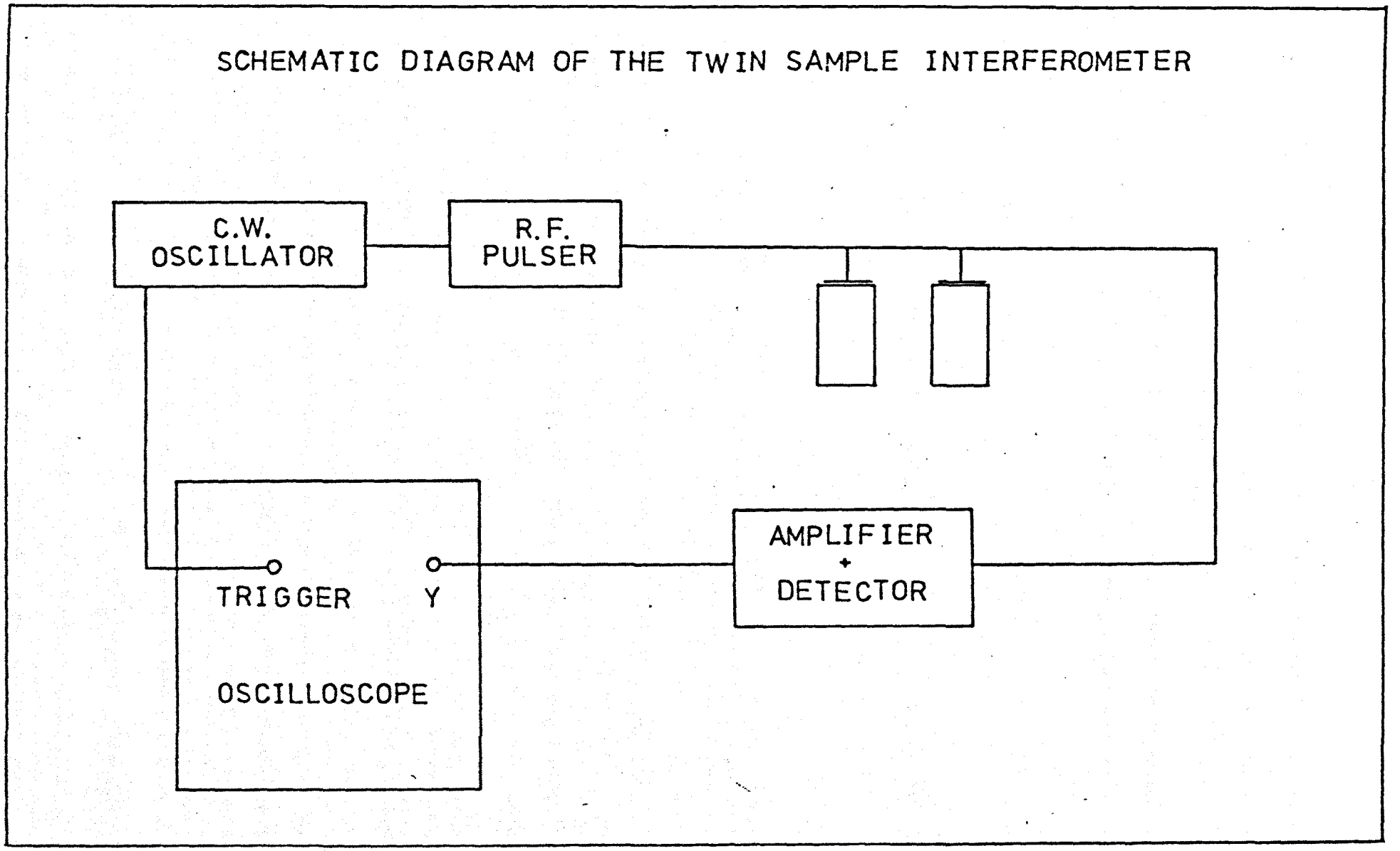
SCHEMATIC DIAGRAM OF THE TWIN SAMPLE INTERFEROMETER
C.W.
OSCILLATOR
R.F.
PULSER
AMPLIFIER
+
DETECTOR
TRIGGER
Y
OSCILLOSCOPE

fig. 1.4

signals. If the velocity in one specimen changes when its environment is modified while the other remains under its original conditions, a shift in the interference nodes occurs.

The two sets of signals will develop a progressively increasing phase difference as the velocity difference between the two samples increases. If destructive interference occurs at the nth echo, then the transit time between the two samples has changed by $\tau/2$ in n round trips, where τ is the transit time through the control sample. By this observation a precision of about 5 parts in 10^6 can be achieved. The method is described in more detail by Truell et al [12] and a block diagram of the electronics is given in fig. 1.4.

1.2.7 The Sing Around System

In this method an initial pulse from an r.f. generator is passed into the specimen by a transmitting transducer, picked up by a second receiving transducer, amplified and detected. It is then fed back to the r.f. pulser to initiate the next pulse through the specimen. This arrangement will then cycle continuously until switched off.

The travel time through the whole loop including all acoustic and electronic delays will be given by the reciprocal of the sing around repetition rate as measured by a frequency meter (see fig. 1.5). The meter measures the frequency of triggering pulses supplied to the r.f. oscillator. If the electronic delays can be accounted for or eliminated the absolute accuracy of this system would be about one part in 10^4. This is seldom practical and the system is therefore not suited to measuring absolute velocity.

The precision of the system in its simple form as shown in fig. 1.5 is quoted [9] as 2 parts in 10^5 for measuring $\Delta v/v$. However, an improved system due to Myers [13] and later Forgacs [14] employing a delay

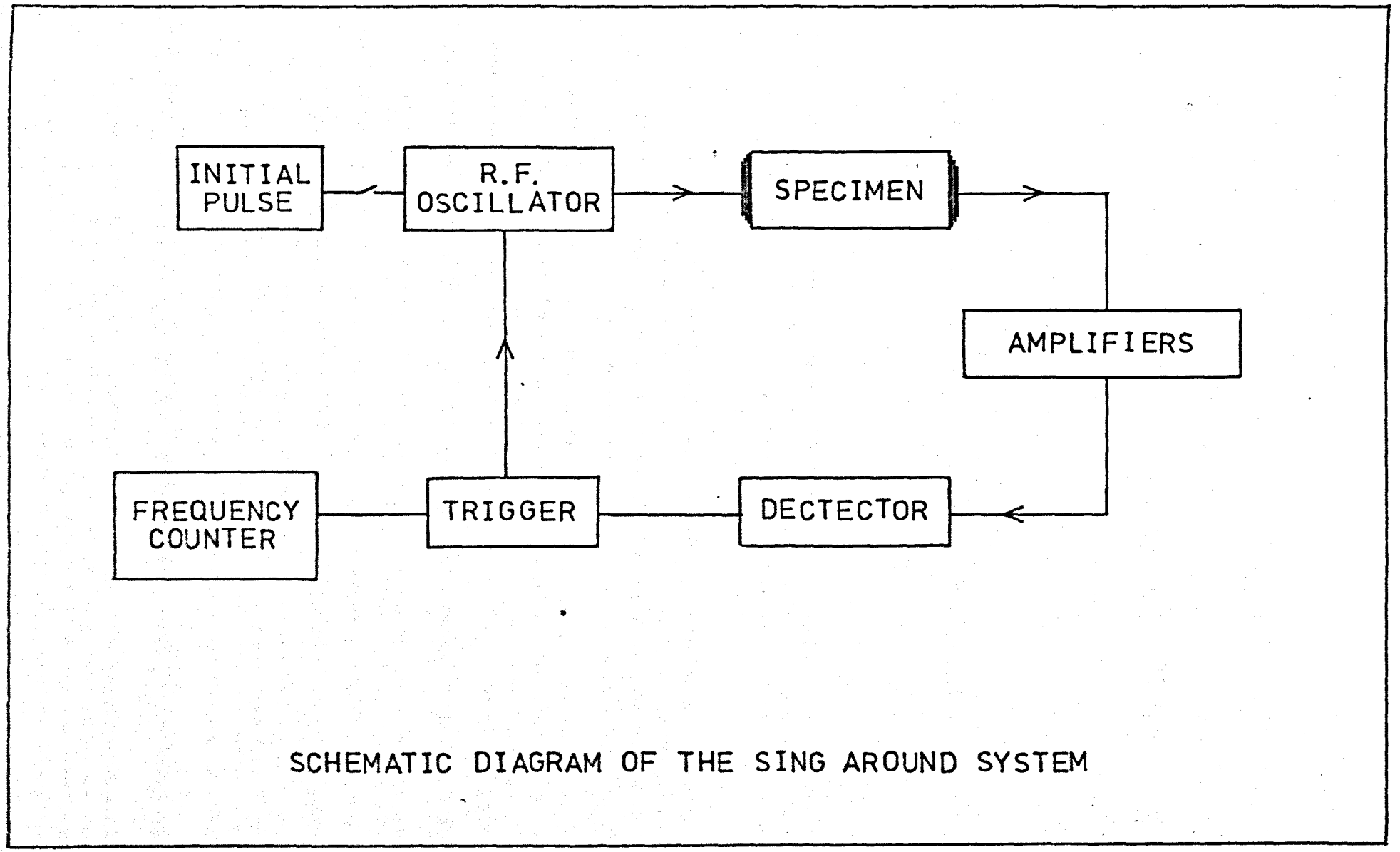

SCHEMATIC DIAGRAM OF THE SING AROUND SYSTEM

fig.1.5

gate so that the r.f. pulser was triggered not from the first echo but by one further down the echo train, was able to improve the ratio of acoustic to electronic delay and thus improve the precision. The errors in this later system were then due mainly to instability in the triggering point which was taken from the leading edge of the echo which has a slow rise time. Forgacs also introduced a 'tandem gating' idea consisting of a wide gate using a delay line like Myers to select a particular echo, and a narrow gate to select a particular cycle of that echo for triggering. The cycle select circuit then fired the trigger at a fixed point in the cycle. A precision of a few parts in 10^7 was claimed for $\Delta v/v$ for this system. This was thought to be the limiting precision since a variation of $0.001^{\circ}K$ would give rise to similar variations in $\Delta v/v$ in most materials.

1.3.1 Background to the Present Work

The precision of the sing around systems for measuring changes in acoustic velocity exceeds that of any of the other methods, although its absolute accuracy is less than the others. It is therefore the best method available to date for measurements involving location of rapid changes in elastic moduli which may be associated via magnetoelastic effects with magnetic phase transitions. It is also the best method available for the measurement of pressure derivatives of elastic moduli necessary in the determination of third order elastic constants.

The idea of an ultrasonic 'feedback' device was first used by Holbrook in 1948 [5] to study small changes in the velocity of sound in solids. Each pulse passed through the specimen was detected by a second transducer, amplified and used to trigger the system into firing another burst of ultrasound into the sample. Once started the system would therefore continue to transmit and receive acoustic pulses almost indefinitely, a mode of operation termed "sing around".

Each time the system was triggered by a detected pulse the pulse passed through a frequency counter and hence the repetition rate of the system could be measured. The change in velocity of sound through the system could then be found from the change in frequency registered by the meter. If the length of the sample can be determined to sufficient accuracy and electronic delays allowed for the absolute velocity can be measured. In practice the changes in transit time $\Delta t/t$ are found and hence changes in velocity $\Delta v/v$. Fractional changes in elastic moduli may therefore be determined to high accuracy.

It was realised that the actual delay measured between two pulses was the sum of acoustic delay in the specimen and electronic delay through the sing around detector system and triggering. The main component of electronic delay was found to be due to delays in the triggering point of the detector. Cedrone and Curran [15] developed Holbrook's ideas further using the same equipment. Their method of eliminating the electronic delay was to use two specimens which were identical except for their length, and keep both under the same experimental condition. The difference between the two delays through the specimens was the transit time through a path length equal to the difference in lengths of the specimens.

1.3.2 Previous Improvements to the Sing Around Method

Forgacs introduced some refinements to the sing around method [14] notably an improvement of the delay line employed by Myers [13] which gated out a number of received acoustic echoes allowing the system to be triggered not by the first detected pulse but by one of the later echoes. In this way the ratio of acoustic to electronic delay was maximised. The interference due to echoes continuing to reverberate inside the system when it was retriggered were also virtually eliminated.

Forgacs also preferred a different counting method using a separate counter and timer. The sing around was allowed to continue until a specified number of retriggerings had occurred, e.g. 10^3, 10^4, 10^5. The measured time interval was terminated precisely as the 10^nth sing around cycle started. This modification of the method was claimed to have a precision with a limit of ± 1 part in 10^7 for $\Delta v/v$ and on the determination of this for gold changes of the order of 5 to 15 parts in 10^6 were detected with an accuracy of about 1%. Papadakis has stated that this precision can not be improved upon under present capabilities since a change of ± 10^{-3} °C will give rise to a variation in $\Delta v/v$ which in most materials is of the order of ± 1 part in 10^7.

Later Brammer and Drabble [16,17] designed a sing around system largely along the lines of the Forgacs method but with more stable circuitry. The detector was changed to a "zero crosser" type which had previously been used in nuclear physics. The detector was not a zero crossover in the true sense in that it could not detect immediately the voltage in the receive circuit went above zero simply because there was always a finite noise level. To overcome this the detector voltage was raised to the level of the background and it triggered immediately the received voltage passed above this.

1.3.3 Determination of Elastic Constants from Acoustic Velocity Measurements

Once the velocity of sound through a sample has been determined by one of the methods outlined in section 1.2 the elastic constants can be calculated from the simple relationship which is derived below for an isotropic crystal lattice.

Consider for simplicity a one dimensional array of atoms each of mass m and at an equilibrium separation of d between nearest neighbours.

If a wave passes through the lattice causing each atom to be displaced from its equilibrium position by an amount which varies from atom to atom, then the force on the nth atom which is displaced by an amount u_n will be

$$F_n = \lambda(u_{n+1}-u_n) - \lambda(u_n-u_{n-1}) \quad \ldots.1.6$$

where λ is the force constant defined by $\partial F/\partial u = -\lambda$, and only nearest neighbour interactions have been considered. Replacing the force F_n by the product of mass and acceleration,

$$m.\frac{d^2u}{dt^2} = \lambda(u_{n+1}+u_{n-1}-2u_n) \quad \ldots.1.7$$

which is the equation of motion of the lattice under the conditions imposed. A solution of this equation will be vibrations of the form,

$$u_n = A.\exp i(knd-\omega t) \quad \ldots.1.8$$

where the ωt term has been included to indicate time dependence. Equation 1.8 in a solution of equation 1.7 provided that

$$\omega = 2\sqrt{\frac{\lambda}{m}}.\sin(\frac{k.d}{2}) \quad \ldots.1.9$$

When k and hence ω are small, that is for low frequency vibrations, in practice $<< 10^{10}$Hz, this reduces to

$$\omega = k\sqrt{\frac{\lambda.d^2}{m}} \quad \ldots.1.10$$

and hence ω is a linear function of k for these low frequency (acoustic) vibrations. Therefore because of the long wavelength of the vibrations large numbers of atoms vibrate together, and the displacement u_n may be expressed as a continuous function of the distance x in the direction of propagation. Expanding this displacement as a Taylor series gives,

$$u_{n+1} = u_n + d(\frac{\partial u_n}{\partial x}) + \frac{1}{2}d^2(\frac{\partial^2 u_n}{\partial x^2}) + \ldots \quad \ldots.1.11$$

and substituting this expression into the equation of motion 1.7 gives

$$m.\frac{d^2u_n}{dt^2} = \lambda.d^2.\frac{\partial^2 u_n}{\partial x^2} \qquad ....1.12$$

which is the equation of a wave with velocity v given by

$$v = \sqrt{\frac{\lambda.d^2}{m}} \qquad ....1.13$$

For a three dimensional solid generalising the above results, the elastic constant c would be defined by the ratio of stress to strain, so that,

$$c = \frac{dF}{dx}.\frac{d}{y.z} \qquad ....1.14$$

where y and z represent the directions orthogonal to x. The velocity may therefore be represented by

$$v = \sqrt{\frac{c}{\rho}} \qquad ....1.15$$

where ρ is the density of the solid.

This result which holds for the propagation of low frequency vibrations in a discrete lattice may be compared with an identical result obtained by considering the solid as a continuum. Such a treatment may be found for example in Champion [18].

CHAPTER 2

The Theory of Elasticity

2.1 Introduction

In the case of an isotropic or a polycrystalline solid there are only two elastic moduli which may be defined. These are the Young's modulus, E, which relates to the velocity of compressional waves through the solid, and the shear modulus, G, relating the velocity of shear waves. The results obtained in section 1.3.3 are not generally applicable in the case of an anisotropic solid like a single crystal and in the present work all results have been taken from single crystal specimens.

In this chapter a more general theory of elasticity for any three dimensional solid is expounded starting from a definition of stress and strain in section 2.1. The expression for a general deformation of a three dimensional anisotropic solid is given in section 2.2 and then the conditions of hexagonal symmetry are taken into account and the expression simplified to suit a hexagonal crystallographic group. From consideration of symmetry it is shown that there are five independent second order elastic constants (S.O.E.C.) for a hexagonal crystal, and the relation of these to particular crystal directions is illustrated.

Anharmonic effects leading to higher order elastic constants, in particular third order moduli are considered and a thermodynamic definition of elastic constants is given. Expressions for the change in path length and density of a specimen are derived in section 2.6 which allow corrections to be made to results of change of acoustic velocity as a function of temperature if necessary. Such corrections have not been made to the results reported in the present work.

Thermal expansion in the particular case of a hexagonal crystal is also described. Finally a definition of Grüneisen parameters, another manifestation of crystal anharmonicity, is given, and a method of calculation from acoustic measurements suggested.

2.1.1 Deformation of a Homogeneous Continuum

A solid body subjected to an applied force will undergo a deformation. Consider the position vector of a typical point in the undeformed body is given by $\underline{r}$ referred to a coordinate system x_i $i = 1, 2, 3$. If the point $\underline{r}$ is deformed to $\underline{r}'$ under a certain stress and the coordinate system x_i is deformed to x_i' then the transform may be represented by a tensor describing the deformation from initial to final state.

$$\underline{r}' = \underline{a}.\underline{r} \qquad \ldots.2.1$$

and the x_i' which form the basis of $\underline{r}'$ obey

$$x_i' = \sum_j a_{ij}x_j \qquad \ldots.2.2$$

The displacement vector of the typical point $\underline{r}$ due to the deformation may be represented as $\underline{u}$

$$\underline{u} = \underline{r}' - \underline{r} \qquad \ldots.2.3$$

2.1.2 The Strain Tensor

Following Landau [1] the displacement vector $\underline{u}$ whose components u_i are given by

$$u_i = x_i' - x_i \qquad \ldots.2.4$$

may be used to derive an expression for the displacement of any point in the deformed solid. Consider two points close together in the undeformed solid. If the vector joining them before deformation is $d\underline{\ell}$ with components dx_i $i = 1, 2, 3$ then the vector joining them after deformation is $d\underline{\ell}'$ with components dx_i'. Hence the initial

displacement of the points is $d\ell$ which is transformed to $d\ell'$

$$d\ell = \sqrt{(dx_1^2 + dx_2^2 + dx_3^2)} \qquad ....2.5$$

$$d\ell' = \sqrt{(dx'^2_1 + dx'^2_2 + dx'^2_3)} \qquad ....2.6$$

and from the definition of u_i given above,

$$d\ell'^2 = \sum_i (dx_i + du_i)^2$$

$$= \sum_i (dx_i^2 + 2du_i dx_i + du_i^2) \qquad ....2.7$$

Replacing du_i by $\sum_k (\frac{\partial u_i}{\partial x_k}) dx_k$ gives,

$$d\ell'^2 = d\ell^2 + 2\sum_i du_i dx_i + \sum_i du_i^2$$

$$= d\ell^2 + 2\sum_{ki}\sum (\frac{\partial u_i}{\partial x_k}) dx_k dx_i$$

$$+ \sum_{i,k,\ell} \frac{\partial u_i}{\partial x_k} \cdot \frac{\partial u_i}{\partial x_\ell} \cdot dx_k dx_\ell \qquad ....2.8$$

Interchanging suffices in the terms on the r.h.s. gives

$$d\ell'^2 = d\ell^2 + 2\sum_{ik} (\frac{\partial u_k}{\partial x_i}) dx_i dx_k$$

$$+ \sum_{i,k,\ell} \frac{\partial u_\ell}{\partial x_k} \cdot \frac{\partial u_\ell}{\partial x_i} \cdot dx_k dx_i$$

$$= d\ell^2 + \sum_{i,k} (2\frac{\partial u_k}{\partial x_i} + \sum_\ell \frac{\partial u_\ell}{\partial x_k} \cdot \frac{\partial u_\ell}{\partial x_i}) dx_i dx_k \qquad ....2.9$$

and replacing the term $\frac{\partial u_k}{\partial x_i} + \frac{1}{2}\sum_\ell \frac{\partial u_\ell}{\partial x_k} \frac{\partial u_\ell}{\partial x_i}$ by the tensor u_{ik} gives

$$d\ell'^2 = d\ell^2 + \sum_{i,k} 2\, u_{ik}\, dx_i\, dx_k \qquad ....2.10$$

where

$$u_{ik} = \frac{\partial u_k}{\partial x_i} + \tfrac{1}{2}\sum_{\ell} \frac{\partial u_\ell}{\partial x_k} \cdot \frac{\partial u_\ell}{\partial x_i} \qquad \ldots\ldots$$

This result compares with the equation given by Kittel [2], the difference being that the present expression for u_{ik} includes an extra term $\tfrac{1}{2}\sum_{\ell} \frac{\partial u_\ell}{\partial x_i} \cdot \frac{\partial u_\ell}{\partial x_k}$. The tensor u_{ik} is called the strain tensor and is symmetric, i.e. $u_{ik} = u_{ki}$. For small strains the last term in u_{ik} becomes negligible and in this case leaves the more familiar expression for u_{ik}

$$u_{ik} = \frac{1}{2}\left(\frac{\partial u_i}{\partial x_k} + \frac{\partial u_k}{\partial x_i}\right) \qquad \ldots.2.11$$

However, the extra term must be included when dealing with third order constants, and in this case Kittel's treatment is invalid.

2.1.3 Diagonalisation of Strain Tensor

The tensor u_{ik} is symmetrical and therefore it can be diagonalised at any point. That is, at any point axes can be chosen (the principal axes of the tensor) such that only the diagonal terms are non zero. This means that the strain at any point may be expressed as components of three independent strains in three mutually perpendicular directions.

2.2.1 The Stress Tensor

Consider the total force on some part of a body. The force will be equal to the sum of forces acting on the volume elements which comprise that part of the body. If F is the force per unit volume then F.dV is the force on an elemental volume dV.

The forces which cause internal stress in a solid are of very short range when compared with macroscopic distances and are typically of the order of a molecular diameter. Consequently the forces which act on a volume element can be represented as the sum of forces acting on all the surface elements surrounding it. Therefore for any elemental volume dV the components of force $\int F_i . dV$ can be transformed into an integral over the

bounding surface, by applying the divergence theorem. This states that the integral of a scalar over an arbitrary volume can be transformed into an integral over the surface if the scalar can be expressed as the divergence of a vector. That is

$$\int_V \nabla.\underline{F}\, dV = \int_s \underline{F}.d\underline{S} \qquad \ldots.2.12$$

In this particular case the scalar is an integral of a vector over a volume. Therefore it may be expressed as the divergence of a tensor of rank two. Hence the force $\underline{F}$ with components F_i can be expressed as

$$F_i = \sum_k \frac{\partial \sigma_{ik}}{\partial x_k} \qquad \ldots.2.13$$

$$\therefore \int_V F_i dV = \int_V \sum_k \frac{\partial \sigma_{ik}}{\partial x_k} .dV$$

$$= \oint_s \sum_k \sigma_{ik}.dS_k \qquad \ldots.2.14$$

where the dS_k are components of the surface element vectors $d\underline{S}$. The tensor of rank two, σ_{ik} which is obtained in this way is the stress tensor. The term $\sigma_{ik}dS_k$ is the i th component of the force on dS_k, that is the force in the i direction due to an incident stress in the k direction.

To prevent turning forces and hence to maintain equilibrium σ_{ik} must be symmetric. That is

$$\sigma_{ik} = \sigma_{ki} \qquad \ldots.2.15$$

2.2.2 Hooke's Law

This states that for sufficiently small deformations the strain is directly proportional to stress. Hence the stress may be expressed as a linear sum of the strains.

$$\sigma_{ik} = \sum_j c_{ik,j} u_j \qquad \ldots.2.16$$

where the u_j represent the strain tensor in Voigt notation and not the

displacement vector (Voigt transformation of indices is defined as follows: $11 \rightarrow 1$, $22 \rightarrow 2$, $33 \rightarrow 3$, $23 \rightarrow 4$, $31 \rightarrow 5$, $12 \rightarrow 6$). The terms $C_{ik,j}$ represent the various S.O.E.C.

2.2.3 Hydrostatic Compression

In a study of third order elastic constants measurements under hydrostatic compression are necessary. If a body is subjected to uniform compression from all sides the stress tensor will have a particularly simple form since there are no shear stresses. If the pressure is P then a force of $P.dS_i$ acts on an element of volume dS_i of the surface. By reference to equation 2.14 this force must also be equal to $\sigma_{ik}.dS_k$

$$\therefore \quad \sum_k \sigma_{ik}.dS_k = P.dS_i \qquad \ldots.2.17$$

and, in order to satisfy this condition,

$$P.dS_i = \sum_k P.\delta_{ik}.dS_k \qquad \ldots.2.18$$

where δ_{ik} is the Kronecker delta.

$$\therefore \quad P.\delta_{ik} = \sigma_{ik} \qquad \ldots.2.19$$

and therefore the stress tensor has the form,

$$\underline{\sigma} = \begin{pmatrix} P & o & o \\ o & P & o \\ o & o & P \end{pmatrix}$$

2.2.4 Dilation

The change of volume of a body due to a deformation may be found from the matrix describing the deformation. Consider a deformation represented by the tensor $\underline{a} = a_{ij}$. Any position vector $\underline{r}$ of a point in the body is transformed to $\underline{r}'$ such that according to equation 2.1

$$\underline{r}' = \underline{a} \,.\, \underline{r}$$

and in matrix form,

$$\begin{pmatrix} x'_1 \\ x'_2 \\ x'_3 \end{pmatrix} = \begin{pmatrix} a_{11} & a_{12} & a_{13} \\ a_{21} & a_{22} & a_{23} \\ a_{31} & a_{32} & a_{33} \end{pmatrix} \begin{pmatrix} x_1 \\ x_2 \\ x_3 \end{pmatrix}$$

The ratio of final to initial volume is given by the determinant of the transformation matrix

$$\frac{V'}{V} = \det \underline{a} = 1 + u_{11} + u_{22} + u_{33} \quad \ldots.2.20$$

where V' is the final volume, V is the initial volume and the u_{ij} are as defined in equations 2.10 or 2.11. The fractional change in volume $\Delta V/V$ is thus given by

$$\frac{\Delta V}{V} = u_{11} + u_{22} + u_{33} \quad \ldots.2.21$$

2.2.5 General Deformation

In the case of a general deformation the non diagonal components of the stress tensor will also be non zero. Under conditions of equilibrium the internal stresses in every volume element must balance.

$$(F_i)_{net} = 0 \quad \ldots.2.22$$

$$\therefore \sum_k \frac{\partial \sigma_{ik}}{\partial x_k} = 0 \quad \ldots.2.23$$

The external forces which act only on the surface must balance the internal stresses. If P is the external force per unit area on the surface dS, with components dS_k

$$P_i . dS = \sum_k \sigma_{ik} . dS_k \quad \ldots.2.24$$

The components of dS in the kth direction dS_k are related to dS by

$$dS_k = d\underline{S} . \underline{n}_k \quad \ldots.2.25$$

where $\underline{n}$ is a unit vector normal to the surface and n_i are its components. Therefore substituting 2.25 into 2.24,

$$\sum_k \sigma_{ik} \cdot n_k = P_i \qquad \ldots.2.26$$

So that the component of the external force in the i th direction is equal to the sum of contributions in the i th direction from all the stress components.

2.2.6 Mean Value of the Stress Tensor

It has already been shown in equation 2.23 above that under equilibrium conditions

$$\sum_k \frac{\partial \sigma_{ik}}{\partial x_k} = 0$$

multiplying through by x_k and integrating over the whole volume gives

$$\iint \sum_\ell \frac{\partial \sigma_{i\ell}}{\partial x_\ell} \cdot x_k \cdot dV = \iint \sum_\ell \frac{\partial}{\partial x_\ell} (\sigma_{i\ell} \cdot x_k) dV - \iint \sum_\ell \sigma_{i\ell} \cdot \frac{\partial x_k}{\partial x_\ell} \cdot dV \qquad \ldots.2.27$$

and both sides are zero. The first integral on the r.h.s. may be transformed into a surface integral

$$= \iint_{s\ell} \sum \sigma_{i\ell} \cdot x_k \, dS_\ell - \iint \sum_\ell \sigma_{i\ell} \cdot \delta_{k\ell} \cdot dV$$

$$= \oint_s \sum_\ell \sigma_{i\ell} \cdot x_k \, dS_\ell - \int \sigma_{ik} \cdot dV = 0 \qquad \ldots.2.28$$

From equation 2.26, $\sum_k \sigma_{ik} n_k = P_i$ and substituting this gives

$$\oint_s P_i \cdot x_k \cdot dS = \oint \sum_\ell \sigma_{i\ell} \cdot x_k \cdot dS_\ell \qquad \ldots.2.29$$

and hence that,

$$\int \sigma_{ik} \cdot dV = \int_s P_i \cdot x_k \, dS = V \cdot \overline{\sigma}_{ik} \qquad \ldots.2.30$$

where $\overline{\sigma}_{ik}$ is the mean value of σ_{ik}. By symmetry this gives

$$\overline{\sigma}_{ik} = \frac{1}{2V} \oint_s (P_i \cdot x_k + P_k \cdot x_i) dS \qquad \ldots.2.31$$

which allows the stress tensor component's mean value to be calculated simply from the prevailing macroscopic conditions.

2.3.1 Elastic Moduli of Hexagonal Crystals

The potential function ϕ of a crystal [3,4] may be used to represent either the internal energy in adiabatic processes or the free energy in isothermal processes. Expanding ϕ as a Taylor series [5] where u is the strain

$$\phi(u) = \phi_o + u \cdot \frac{d\phi}{du} + \frac{u^2}{2} \cdot \frac{d^2\phi}{du^2} + \ldots \qquad \ldots.2.32$$

and using $\frac{d\phi}{du} = \sum_i \frac{\partial \phi}{\partial u_i}$ where the u_i are components of u

$$\phi = \phi_o + \sum_{\alpha,\beta} \sigma_{\alpha\beta} u_{\alpha\beta} + \tfrac{1}{2} \sum_{ik\ell m} C_{ik\ell m} \cdot u_{ik} \cdot u_{\ell m} \qquad \ldots.2.33$$

where terms of higher order have been neglected. Since only the variation of ϕ is of interest the arbitrary constant ϕ_o may be set to zero

$$\phi = \sum_{\alpha,\beta} \sigma_{\alpha\beta} \cdot u_{\alpha\beta} + \tfrac{1}{2} \sum_{ik\ell m} C_{ik\ell m}\, u_{ik}\, u_{\ell m} \qquad \ldots.2.34$$

and the $C_{ik\ell m}$ represent the elastic moduli of the crystal since $C_{ik\ell m}$ has been shown to be

$$C_{ik\ell m} = \frac{\partial^2 \phi}{\partial u_{ik}\, \partial u_{\ell m}} \qquad \ldots.2.35$$

2.3.2 Symmetry Considerations

By the symmetry of the strain tensor, the value of the product $u_{ik}\, u_{\ell m}$ is invariant when i,k or ℓ,m are interchanged. Applying similar arguments it will be seen that

$$C_{ik\ell m} = C_{ki\ell m} = C_{ik m\ell} = C_{\ell mik}$$

which immediately limits the number of possible independent elastic moduli to 21, for the class of lowest symmetry.

For hexagonal crystals the number of possible elastic moduli may be further reduced. Let x,y and z be the coordinate axes of the system with z the six-fold axis. Define transformations to a new coordinate system ξ, η, z by

$$\xi = x + iy \qquad \ldots.2.36$$

$$\eta = x - iy \qquad \ldots.2.37$$

such a system must have invariance under a rotation through $\pi/3$ about the z axis. Applying such a rotation sends ξ and η to the following coordinates

$$\xi \rightarrow \xi e^{i\pi/3} = \xi(\cos\pi/3 + i \sin\pi/3)$$

$$\eta \rightarrow \eta e^{-i\pi/3} = \eta(\cos\pi/3 - i \sin\pi/3)$$

and in order to maintain invariance under such a transform, only those $C_{ik\ell m}$ which contain the same number of suffices of ξ and η can be non zero.

2.3.3 Independent Moduli

Replacing ξ by a and η by b and z by c gives the three principal axes of the hexagonal system. Applying the conditions on the moduli given above this reduces the number of independent moduli to C_{cccc}, C_{abab}, C_{aabb}, C_{abcc}, C_{acbc}.

The compressional constants C_{33} and C_{11} relate to longitudinal waves propagated along the c axis and in the basal plane respectively. The shear modulus C_{44} is obtained by propagating a shear wave along the c axis which is polarised in the basal plane. The shear modulus $C_{66} = \frac{1}{2}(C_{11} - C_{12})$ is found by propagating a shear wave along one axis in the base plane and polarising at right angles, along the other axis in the base plane.

The cross coupling coefficient C_{13} is related indirectly to shear and longitudinal wave propagated at 45^{o} to the c axis. All of these directions and the equations relating acoustic velocities along certain crystallographic directions to the principal elastic moduli will be found in reference six.

2.4.1 Definition of Third Order Elastic Constants

Consider a body subjected to a stress represented by the tensor σ_{jk}, and let the potential function ϕ be given by 2.34

$$\phi = \sum_{\alpha\beta} C_{\alpha\beta} u_{\alpha\beta} + \sum_{\alpha\beta\gamma\delta} C_{\alpha\beta\gamma\delta}\, u_{\alpha\beta} u_{\gamma\delta} + \ldots$$

In the above expression the terms $C_{\alpha\beta\gamma\delta}$ represent the second order elastic constants, normally referred to as elastic constant, for example in Hooke's Law

$$C_{\alpha\beta} = \frac{\partial\phi}{\partial u_{\alpha\beta}} = \sigma_{\alpha\beta} \qquad \ldots.2.38$$

$$C_{\alpha\beta\gamma\delta} = \frac{\partial^2\phi}{\partial u_{\alpha\beta}\,\partial u_{\gamma\delta}} = \frac{\partial\sigma_{\alpha\beta}}{\partial u_{\gamma\delta}} \qquad \ldots.2.39$$

The next order term in the series expansion is $C_{\alpha\beta\gamma\delta\varepsilon\zeta}$ which is the third order elastic constant term which gives deviations from Hooke's Law [5,7]

$$C_{\alpha\beta\gamma\delta\varepsilon\zeta} = \frac{\partial^3\phi}{\partial u_{\alpha\beta}\,\partial u_{\gamma\delta}\,\partial u_{\varepsilon\zeta}} \qquad \ldots.2.40$$

This gives the required definition of second and third order elastic constants. Higher order elastic constants may be easily defined by repeated differentiation of ϕ.

2.4.2 Thermodynamic Derivation of Higher Order Elastic Constants

The thermodynamic energy equations for conservative (non dissipative) media are [8]

$$dU = T.dS + dW$$
$$dF = dU - d(TS) \qquad \ldots.2.41$$

Consequently if σ_{jk} is the stress tensor and u_{jk} the strain tensor the two above expressions may be represented by

$$dU = T.dS + \sum_{jk} \sigma_{jk}\, dU_{jk} \qquad \ldots.2.42$$

$$dF = -S.dT + \sum_{jk} \sigma_{jk}\, dU_{jk} \qquad \ldots.2.43$$

The thermodynamic potential used in equation 2.34 will be the free energy F under isothermal conditions and the internal energy U under adiabatic conditions.

Therefore the equations 2.42 and 2.43 may be modified under conditions of adiabatic or isothermal processes respectively

$$\text{Adiabatic} \quad dU = \sum_{jk} \sigma_{jk} dU_{jk} \qquad \ldots.2.44$$

$$\text{Isothermal} \quad dF = \sum_{jk} \sigma_{jk} du_{jk} \qquad \ldots.2.45$$

Under their respective conditions the internal energy and free energy become functions of strain only. The isothermal and adiabatic third order elastic constants are therefore, according to Brugger [9]

$$C^{S}_{jkpq\ell m} = \left(\frac{\partial^3 U}{\partial u_{jk} \cdot \partial u_{pq} \cdot \partial u_{\ell m}} \right)_S \qquad \ldots.2.46$$

$$C^{T}_{jkpq\ell m} = \left(\frac{\partial^3 F}{\partial u_{jk} \partial u_{pq} \partial u_{\ell m}} \right)_F \qquad \ldots.2.47$$

2.4.3 Anharmonic Vibrations

From the expression for the potential function given in equation 2.34

$$\phi = \sum_{\alpha\beta} C_{\alpha\beta} U_{\alpha\beta} + \sum_{\alpha\beta\gamma\delta} C_{\alpha\beta\gamma\delta} u_{\alpha\beta} U_{\gamma\delta} + \ldots$$

Previously only terms up to the second order had been considered, and under such conditions the components of the stress tensor are linear functions of the components of the strain tensor. This may be shown as follows.

If ϕ remains constant under either an adiabatic or isothermal change,

$$\frac{\partial \phi}{\partial u_{\alpha\beta}} = C_{\alpha\beta} + \sum_{\gamma\delta} C_{\alpha\beta\gamma\delta} U_{\gamma\delta} = 0 \qquad \ldots.2.48$$

and replacing $C_{\alpha\beta}$ by $-\sigma_{\alpha\beta}$ gives

$$\sigma_{\alpha\beta} = \sum_{\gamma\delta} C_{\alpha\beta\gamma\delta} U_{\gamma\delta} \qquad \ldots.2.49$$

which gives the required linear relationship between stress components and strain components.

If higher order terms are included then the contributions due to the additional terms are called anharmonic effects because the corresponding equations of motion are non-linear, and hence do not permit simple periodic solutions.

2.4.4 Third Order Anharmonic Effects

The cubic terms in the elastic energy expression give quadratic terms in the stress tensor in addition to the linear terms. The strain tensor must then be given by the form of equation 2.10

$$u_{ik} = \frac{1}{2}\left[\frac{\partial u_i}{\partial x_k} + \frac{\partial u_k}{\partial x_i} + \sum_{\ell} \frac{\partial u_\ell}{\partial x_i} \frac{\partial u_\ell}{\partial x_k} \right]$$

Expressing the elastic energy of a body under strain and substituting in for u_{ik} as given above,

$$\begin{aligned}\phi = {} & C_{\alpha\beta} \cdot \frac{1}{2}\left(\frac{\partial u_\alpha}{\partial x_\beta} + \frac{\partial u_\beta}{\partial x_\alpha} + \sum_{\ell} \frac{\partial u_\ell}{\partial x_\alpha} \cdot \frac{\partial u_\ell}{\partial x_\beta} \right) \\ & + C_{\alpha\beta\gamma\delta} \cdot \frac{1}{4} \prod_{\alpha\beta\gamma\delta} \left(\frac{\partial u_\alpha}{\partial x_\beta} + \frac{\partial u_\beta}{\partial x_\alpha} + \sum_{\ell} \frac{\partial u_\ell}{\partial x_\alpha} \cdot \frac{\partial u_\ell}{\partial x_\beta} \right) \\ & + C_{\alpha\beta\gamma\delta\varepsilon\zeta} \cdot \frac{1}{8} \prod_{\alpha\beta\gamma\delta\varepsilon\zeta} \left(\frac{\partial u_\alpha}{\partial x_\beta} + \frac{\partial u_\beta}{\partial x_\alpha} + \sum_{\ell} \frac{\partial u_\ell}{\partial x_\alpha} \cdot \frac{\partial u_\ell}{\partial x_\beta} \right)\end{aligned} \qquad \ldots.2.50$$

and the variation in this energy may be expressed as

$$d\phi = \sum_{i,k} \frac{\partial \phi}{\partial\left(\frac{\partial u_i}{\partial x_k}\right)} \cdot d\left(\frac{\partial u_i}{\partial x_k}\right) \qquad \ldots.2.51$$

where $\frac{\partial u_i}{\partial x_k} = u_{ik}$ as defined in equation 2.11. Therefore,

$$\frac{\partial \phi}{\partial\left(\frac{\partial u_i}{\partial x_k}\right)} = \frac{\partial \phi}{\partial u_{ik}} = \sigma_{ik} \qquad \ldots.2.52$$

$$\therefore \quad d\phi = \sum_{ik} \sigma_{ik}\, d\left(\frac{\partial u_i}{\partial x_k}\right) \qquad \ldots.2.53$$

$$= \sum_{ik} \left(\frac{\partial}{\partial x_k} (\sigma_{ik}.du_i) - du_i.\frac{\partial \sigma_{ik}}{\partial x_k} \right) \qquad \ldots.2.54$$

where the terms $\sum_k {}^{\partial \sigma_{ik}}/_{\partial x_k}$ are the components of force on the body as shown in equation 2.13. Hence although the expression for $d\phi$ is different when anharmonic effects are included the equation of motion remains the same , that is,

$$\rho_o \frac{\partial^2 u_i}{\partial t^2} = \sum_k \frac{\partial \sigma_{ik}}{\partial x_k} \qquad \ldots.2.55$$

where ρ_o is the density of the undeformed body. The components of σ_{ik} must now be given by the complete expression.

Thus even although an extra anharmonic term has been included into the stress tensor the elastic constant can still be obtained from an equation of the form given by 1.15 because the equation of motion is still of the form given by equation 1.12.

2.5.1 Variation of Acoustic Velocity with Temperature

If v is the acoustic velocity in a solid of density ρ with elastic constant c, then by equation 1.15

$$v = \sqrt{\frac{c}{\rho}} \qquad \ldots.2.56$$

then the derivative is [7]

$$\frac{\partial v}{\partial T} = \frac{1}{2v}\left(\frac{1}{\rho} \frac{\partial c}{\partial T} - \frac{c}{\rho^2} \frac{\partial \rho}{\partial T} \right) \qquad \ldots.2.57$$

The sing-around method measures a period τ or a frequency f of acoustic waves through the specimen, which is related to the wave path length through the specimen ℓ

$$f = \frac{v}{\ell} \qquad \ldots.2.58$$

The path length ℓ is temperature dependent and often it is more convenient to measure the frequency f and calculate the corresponding velocity v assuming the length of specimen ℓ remains constant, which is taken as the room temperature value ℓ_o.

Differentiation of the equation 2.58 with respect to temperature T gives,

$$\frac{\partial v}{\partial T} = \ell \frac{\partial f}{\partial T} + f \frac{\partial \ell}{\partial T} \quad \ldots.2.59$$

If the effects of temperature on both specimen length and density are ignored then the relationship between sing around frequency and elastic constant will be given by combining equations 2.59 and 2.57

$$\ell_o \cdot \frac{\partial f}{\partial T} = \frac{1}{2v\rho_o} \cdot \frac{\partial c}{\partial T} \quad \ldots.2.60$$

and rearranging gives

$$\rho_o \ell_o^2 \cdot \frac{\partial}{\partial T}(f^2) = \frac{\partial c}{\partial T} . \quad \ldots.2.61$$

where ρ_o and ℓ_o are the room temperature values of ρ and ℓ which are assumed to remain constant. Integration of 2.61 gives

$$\ell_o^2 \cdot f^2 = \frac{c}{\rho_o} \quad \ldots.2.62$$

which is analogous to equation 2.5.6.

The correct relationship between elastic constant and sing around frequency is given by

$$\ell \cdot \frac{\partial f}{\partial T} + f \cdot \frac{\partial \ell}{\partial T} = \frac{1}{2f\ell} \left(\frac{1}{\rho} \frac{\partial c}{\partial T} - \frac{c}{\rho^2} \frac{\partial \rho}{\partial T} \right) \quad \ldots.2.63$$

In order to estimate the correction necessary to the raw data consider a cube of isotropic material of side ℓ and linear thermal expansion coefficient α, although this has limited applicability to the materials under consideration which are hexagonal single crystals, because of their anisotropy.

If the length of side of the cube changes from ℓ_o to ℓ during a temperature change ΔT

$$\ell - \ell_o = \alpha.\Delta T.\ell_o \qquad \ldots.2.64$$

and similarly the volume changes by

$$V - V_o = 3\alpha.\Delta T.V_o \qquad \ldots.2.65$$

The density of the material of mass m will therefore vary by

$$\rho - \rho_o = -3.\alpha.\rho_o \qquad \ldots.2.66$$

Returning to equation 2.63 gives,

$$2 f \ell_o^2 \frac{\partial f}{\partial T} + 2 f^2 . \ell_o \frac{\partial \ell}{\partial T} = \frac{1}{\rho_o} \frac{\partial c}{\partial T} - \frac{c}{\rho_o^2} \frac{\partial \rho}{\partial T} \qquad \ldots.2.67$$

Differentiation of the equations 2.64 and 2.66 gives

$$\left(\frac{\partial \ell}{\partial T}\right)_{\ell_o} = \alpha.\ell_o \qquad \ldots.2.68$$

$$\left(\frac{\partial \rho}{\partial T}\right)_{\rho_o} = -3.\alpha.\rho_o$$

and substituting these into equation 2.67

$$\ell_o^2 \frac{\partial}{\partial T}(f^2) + 2f^2 \ell_o^2 \alpha = \frac{1}{\rho_o} \frac{\partial c}{\partial T} + \frac{3.\alpha.c}{\rho_o} \qquad \ldots.2.69$$

Integrating on both sides with respect to T and setting the limits of integration as T_o and $T_o + \Delta T$ where T_o may represent for example room temperature

$$\ell_o^2 . f^2 (1 + 2\alpha\Delta T) = \frac{c}{\rho_o} (1 + 3\alpha\Delta T) \qquad \ldots.2.70$$

and both ℓ_o and ρ_o are measured at room temperature so the required correction is

$$c = \rho_o . f^2 . \ell_o^2 \frac{(1 + 2\alpha.\Delta T)}{(1 + 3\alpha.\Delta T)} \qquad \ldots.2.71$$

2.5.2 Thermal Expansion in Hexagonal Crystals

Thermal expansion is probably the most obvious consequence of anharmonicity in lattice vibrations and can yield information on the strain dependence of forces in the solid. The linear thermal expansion coefficient in the ith direction may be defined from macroscopic considerations. If x_i' is the length of the solid at temperature T_o and x_i' is the length at temperature T, then

$$x_i' = x_i(1 + \alpha_i(T - T_o)) \qquad \ldots.2.72$$

and as in 2.1.2 the displacement $u_i = x_i' - x_i$

$$u_i = \alpha_i . x_i (T - T_o) \qquad \ldots.2.73$$

$$\therefore \frac{\partial u_i}{\partial x_i} = \alpha_i (T - T_o) \qquad \ldots.2.74$$

and the l.h.s. may be expressed as the strain component u_{ii} of the strain tensor. $\underline{u}_{ij}$

$$u_{ii} = \alpha_i (T - T_o) \qquad \ldots.2.75$$

Now if u_{ii} is replaced by η_i where the reduced (Voigt) notation is used

$$\therefore \left(\frac{\partial \eta_i}{\partial T}\right)_\sigma = \alpha_i \qquad i = 1, \ldots 6 \qquad \ldots.2.76$$

where σ denotes that all stress components are held constant.

Thermal expansion is generally described in terms of the Grüneisen functions Γ_j which are given by [10]

$$\Gamma_i = \frac{1}{C_\eta} \left(\frac{\partial S}{\partial \eta_i}\right)_{\eta', T} \qquad \ldots.2.77$$

where C_η is the specific heat capacity at constant strain and η', T denotes that strain components, other than η_i and temperature are maintained constant. This equation may then be expressed in terms of measurable quantities,

$$\Gamma_i = \sum_j \frac{V}{C_\eta} . C^T_{ij} . \alpha_j = \sum_j \frac{V}{C_\sigma} C^S_{ij} . \alpha_j \qquad ....2.78$$

and the C^T_{ij} and C^S_{ij} are the isothermal and adiabatic elastic constants, and C_η, C_σ are the heat capacity.

The thermal expansion coefficients can then be obtained from the Grüneisen functions,

$$\alpha_j = \frac{C_\eta}{V} \sum_i S^T_{ji} \Gamma_i = \frac{C_\sigma}{V} \sum_i S^S_{ji} \Gamma_i \qquad ....2.79$$

where the S^T_{ji} and S^S_{ji} are the elastic compliances.

The above three equations may be used to give the two independent Grüneisen parameters for axially symmetric crystals like hexagonal. These may be defined as $\Gamma_{//}$ and $\Gamma_\perp$ with respect to the principal symmetry axis.

$$\Gamma_\perp = \frac{1}{2C_\eta} \left(\frac{\partial S}{\partial \ell n a} \right)_{c,T} \qquad ....2.80$$

$$\Gamma_{//} = \frac{1}{C_\eta} \left(\frac{\partial S}{\partial \ell n c} \right)_{a,T}$$

where a and c are the lattice parameters of the unit cell. This may be expressed as,

$$\Gamma_\perp = \frac{V}{C_\sigma} \left((C^S_{11} + C^S_{12}) \alpha_\perp + C^S_{13} \alpha_{//} \right) \qquad ....2.82$$

$$\Gamma_{//} = \frac{V}{C_\sigma} \left(2C^S_{13} \alpha_\perp + C^S_{33} \alpha_{//} \right) \qquad ....2.83$$

and solving these equations to give $\alpha_\perp$ and $\alpha_{//}$ explicitly in terms of the Grüneisen parameters

$$\alpha_\perp = \frac{C_\sigma}{V} \cdot \frac{[C^S_{33} \Gamma_\perp - C^S_{13} \Gamma_{//}]}{C^S_{33}(C^S_{11} + C^S_{12}) - 2(C^S_{13})^2} \qquad ....2.84$$

$$\alpha_{//} = \frac{C_\sigma}{V} \cdot \frac{[(C^S_{11} + C^S_{12}) \Gamma_{//} - 2C^S_{13} \Gamma_\perp]}{C^S_{33}(C^S_{11} + C^S_{12}) - 2(C^S_{13})^2} \qquad ....2.85$$

2.5.3 Grüneisen Parameters

In studying the anharmonicity of a crystal lattice, the analysis in most cases deals primarily with the Grüneisen function Γ, which is a measure of the change of lattice frequencies with the volume of the crystal. For the cases of isotropic or cubic crystallographic solids the Grüneisen parameter Γ may be defined by

$$\Gamma = \frac{1}{C_\eta}\left(\frac{\partial S}{\partial \eta}\right)_{\eta,T} \qquad \ldots.2.86$$

$$= \frac{V}{C_V}\left(\frac{\partial S}{\partial V}\right)_{\eta,T} \qquad \ldots.2.87$$

where η is the Lagrangian strain, and C_V is the specific heat at constant volume. Functions such as $\left(\frac{\partial S}{\partial V}\right)_T$ or Γ can be calculated fairly easily from the Helmholz free energy [e.g. 10 P.518] and are therefore convenient for describing theoretical models.

For the case of an anisotropic solid, and in particular for the case of a hexagonal material, the expressions for the Grüneisen parameters must be modified to include each strain coordinate since all directions are no longer equivalent. A natural generalisation of equation 2.86 is therefore

$$\Gamma_\lambda = \frac{1}{C_V}\left(\frac{\partial S}{\partial \eta_\lambda}\right)_{\eta',T} \qquad \lambda = 1, \ldots 6 \qquad \ldots.2.88$$

as given by Barron and Munn [11, P.86] where the η',T indicate that all strains other than η are held constant and that temperature is held constant. Each independent Γ_λ may then be analysed as the single Γ is in the isotropic and cubic cases. The equation 2.86 may be obtained from 2.88 by simply allowing $\Gamma_1 = \Gamma_2 = \Gamma_3 = \Gamma$; $\Gamma_4 = \Gamma_5 = \Gamma_6 = 0$ using abbreviated Voigt notation.

The equation 2.88 may also be expressed in terms of directly measurable quantities like the elastic constants and thermal expansions in the way outlined by Munn [10]

$$\Gamma_\lambda = \frac{V}{C_V} \sum_\mu C^T_{\lambda\mu} . \alpha_\mu \qquad \ldots.2.89$$

$$= \frac{V}{C_P} \sum_\mu C^S_{\lambda\mu} . \alpha_\mu$$

where the $C^T_{\lambda\mu}$ and $C^S_{\lambda\mu}$ are the elastic stiffnesses under isothermal and adiabatic conditions and α_μ is the thermal expansion coefficient along the μth direction and the C_V and C_P are heat capacities at constant strain and constant stress.

When electronic contributions are negligible then both C_V and S will depend, to a first approximation, only upon the temperature and the normal mode frequencies ω_r, while Γ depends upon the derivative $\frac{\partial \omega_r}{\partial V}$. Expressing the specific heat capacity C_V as the sum of contributions C_r from all the available modes, gives,

$$C_V = \sum_{r=1}^{3N-6} C_r \qquad \ldots.2.91$$

where N is the number of atoms in the solid.

From the quasi-harmonic approximation all thermodynamic and elastic properties of a crystal are assumed to be determined by the harmonic lattice frequency distribution and its dependence on volume, or strain. The Γ's may be related to the strain derivatives of the normal mode frequencies by

$$\Gamma_\lambda = \frac{\sum_{r=1}^{3N-6} \gamma_r . C_r}{\sum_{r=1}^{3N-6} C_r} \qquad \ldots.2.92$$

where the γ_r's are called the mode Grüneisen parameters. These general

mode Grüneisen parameters may be defined, e.g. Elliott and Gibson [12,P80], by considering that the characteristic vibrational modes of a crystal change with volume, and in particular making the assumption that they undergo the same fractional change

$$\frac{d\omega}{\omega} = \gamma \frac{dV}{V} \qquad \ldots.2.93$$

and specifying for a wavevector $\underline{q}$ with polarisation P

$$\gamma_{q,P} = \frac{\partial \ \ell n \ \omega_{q,P}}{\partial \ \ell n \ V} \qquad \ldots.2.94$$

This last equation is the form quoted for the individual mode gammas by Collins [13,P. 325]. Replacing the frequency $\omega_{q.P}$ by

$$\omega_{q,P} = q.S_p(\theta,\phi) \qquad \ldots.2.95$$

where $q = |\underline{q}|$ and $S_p(\theta,\phi)$ is the velocity of sound of the p th branch in the direction given by the angles (θ,ϕ).

$$\gamma_{q,P} = - \frac{\partial \ \ell nq}{\partial \ \ell nV} - \frac{\partial \ \ell n \ S_p(\theta,\phi)}{\partial \ \ell n \ V} \qquad \ldots.2.96$$

This is the form of expression arrived at by Sheard [14]. Deviating from this paper and following the method of Gerlich [15] the q may be replaced by

$$q \quad \alpha \quad (L_1^2 + L_2^2 + L_3^2)^{-\frac{1}{2}} \qquad \ldots.2.97$$

where the L_i are lengths of the crystal parallel to the x, y and z crystal axes.

$$\gamma_{q,P} = - \frac{\partial (\ell n (L_1^2 + L_2^2 + L_3^2)^{-\frac{1}{2}})}{\partial \ \ell nV} - \frac{\partial \ell n S_p(\theta,\phi)}{\partial \ell nV} \qquad \ldots.2.98$$

Converting here from derivatives with respect to ℓnV to derivatives with respect to P and using

$$d\ell nV = \frac{dV}{V} = - \beta_V . dP \qquad \ldots.2.99$$

where β_V is the volume compressibility

$$\gamma_{q,P} = \frac{1}{\beta_V} \cdot \frac{\partial \left(\ell n (L_1^2+L_2^2+L_3^2)^{-\frac{1}{2}}\right)}{\partial P} + \frac{1}{\beta_V} \cdot \frac{\partial . \ell n\, S_P(\theta,\phi)}{\partial P}$$

....2.100

Differentiation of the terms on the right-hand side gives,

$$\gamma_P(q) = \frac{\ell^2\beta_{1_T} + m^2\beta_{2_T} + n^2\beta_{3_T}}{\beta_{V_T}} + \frac{1}{\beta_V} \frac{\partial}{\partial P} \left(\ell n\, S_P(\theta,\phi)\right)$$

....2.101

where the β_{i_T} are isothermal linear compressibilities along the directions of the crystallographic axes, l,m,n are direction cosines of q, and β_{V_T} is the isothermal volume compressibility.

Denoting the elastic constant associated with the mode q,P by $C_P(q)$ and using this to replace the velocity $S_P(\theta,\phi)$ gives the following

$$\frac{\partial\ \ell n\, S_P(\theta,\phi)}{\partial P} = \frac{1}{2} \frac{\partial\ \ell n\, C_P(\theta,\phi)}{\partial P} - \tfrac{1}{2}\beta_{V_T} \qquad ....2.102$$

This therefore leaves the expression as,

$$\gamma_P(\underline{q}) = \frac{\ell^2\beta_{1_T} + m^2\beta_{2_T} + n^2\beta_{3_T}}{\beta_{V_T}} - \frac{1}{2}\left[1 - \frac{1}{\beta_V} \cdot \frac{\partial\ \ell n\, C_P(\theta,\phi)}{\partial P}\right]$$

....2.103

$$\gamma_P(q) = \frac{\ell^2\beta_{1_T} + m^2\beta_{2_T} + n^2\beta_{3_T}}{\beta_{V_T}} - \frac{1}{2} + \frac{1}{2C_P(\theta,\phi).\beta_V} \left(\frac{\partial C_P(\theta,\phi)}{\partial P}\right)$$

....2.104

This last equation is then analogous to the equation used by Fisher [16] to calculate Grüneisen parameters from pressure derivatives of elastic constants.

Since ℓ, m and n are direction cosines of the wavevector $\underline{q}$ then by suitable choice of $\underline{q}$ along crystallographic directions two of these three ℓ, m, n can be made zero leaving the simplified expression

$$\gamma_P(\underline{q}) = \frac{\beta_\ell(q)_T}{\beta_{V_T}} - \frac{1}{2} + \frac{1}{2.\beta_V.C_P(\theta,\phi)} \cdot \left(\frac{\partial C_P(\theta,\phi)}{\partial P}\right)$$

....2.105

The average mode value of the Grüneisen parameter is then obtained by summation over the possible polarisations P for a particular propagation direction q

$$\Gamma_q = \frac{1}{3}\sum_{P=1}^{3}\gamma_P(q) \qquad \ldots.2.106$$

and therefore for a hexagonal crystal the Grüneisen parameters perpendicular and parallel to the unique axis may be defined by

$$\Gamma_{//} = \frac{1}{3}\sum_{P=1}^{3}\gamma_P(c) \qquad \ldots.2.107$$

$$\Gamma_{\perp} = \frac{1}{3}\sum_{P=1}^{3}\frac{1}{2}(\gamma_P(a) + \gamma_P(b)) \qquad \ldots.2.108$$

The Grüneisen parameter for the whole crystal is given by

$$\Gamma = \frac{1}{3N}\sum_{P}\sum_{q=1}^{N}\gamma_P(q) \qquad \ldots.2.109$$

The average mode Grüneisen parameters may then be compared with that determined from thermal expansion data.

CHAPTER 3

Magnetic Interactions and Phase Transitions

A brief outline of magnetic phenomena in general terms is given. Some aspects of the historical development of theoretical magnetism are discussed including the Weiss classical theory and the quantum mechanical theory. Two models for the behaviour of magnetic structures are presented, the Heisenberg model, based on quantum mechanics, and the Ising model.

The thermodynamic behaviour of magnetic materials in the proximity of magnetic phase transitions is also treated including the applicability of two models.

3.1.1 Types of Magnetic Order

The most widely recognised of magnetic phenomena is that of ferromagnetism in which the magnetic moments within a domain are all aligned parallel, although direction frequently changes from domain to domain. Neighbouring domains may be aligned by application of a magnetic field and when the field is removed the material in general retains some of its magnetisation.

In paramagnetic solids the atomic moments are randomly oriented in the absence of an applied field. By application of a magnetic field however they may be aligned in a similar manner to the ferromagnet, but when the field is removed they revert to their former random orientations.

Antiferromagnetic materials have an ordered alignment of atomic magnetic moments in such a way that the ordering produces zero bulk magnetisation in the absence of a field. Ordering of the moments in this way may be achieved by various structures the most obvious of which is that when nearest neighbour moments are aligned antiparallel to each

other. This is known as simple antiferromagnetism. Another important type of antiferromagnetic order, particularly in the rare earths, is helical antiferromagnetism in which atomic moments in a particular lattice plane of the solid are inclined at a fixed angle to the moments in the previous plane.

3.1.2 The Classical Theory of Magnetism

A non quantum mechanical explanation of the phenomenon of ferromagnetism was given by Weiss [1] in 1907. He considered that an internal or 'molecular' magnetic field existed inside the ferromagnet. This caused the moments to align parallel to the field. Unfortunately the magnitude of this field would need to be $\sim 10^3$T to explain the effects observed. It is now used only as a convenient way of considering the magnetic interactions by treating them as if they are in a mean field produced by all other magnetic moments in the solid. The mean field in a paramagnet was set arbitrarily to zero, and the same approach was later used with antiferromagnetism. The treatment leads to a simple rule known as the Curie-Weiss Law expressing the susceptibility of a ferromagnet. Analogous expressions were obtained for paramagnets and antiferromagnets.

3.2.1 Electronic Magnetic Moments

The contribution to the total magnetic moment of a solid comes in the main from electronic magnetic moments. Those atoms with partially filled inner electron shells, for example the rare earths, whose partially filled 4f shell lies inside the filled 5s, 5p and 6s states, have net magnetic moments due to these unfilled shells. This is however not the only way in which electrons can contribute to the net magnetic moment. In some metals, notably Fe, Ni, Co, the magnetic properties are thought to depend on unpaired electrons in the conduction band.

In the former case the magnetic moments are localised on the atoms and this is termed the localised moment model. It is this type of magnetism with which the present work is concerned.

3.2.2 Magnetism as a Quantum Mechanical Effect

An expression was derived by Heisenberg for the energy of two electrons whose wave functions overlapped. A term which could not be explained classically was found in the Hamiltonian and this is now known as the exchange interaction. By considering for example the case of two atoms, each with one electron, in close proximity so that the wavefunctions overlapped and the electrons were effectively shared by the two nuclei, the application of the Pauli exclusion principle was found to put a constraint on the electrons which therefore behaved as though there were an interaction energy between their spins. When the total Hamiltonian of the electrons was derived in this case the additional term H_{exch} was found to be of the form,

$$H_{exch} = -J.\ \underline{s}_i.\underline{s}_j \qquad \ldots.3.1$$

where $\underline{s}_i$ and $\underline{s}_j$ are the spin vectors of the two electrons and J is the exchange integral. This is derived mathematically in Appendix 2.

3.2.3 The Exchange Integral and the Pauli Principle

The extra term in the Hamiltonian referred to as the exchange interaction has no classical analogue and occurs in addition to a classical dipole-dipole interaction between the two electrons and their nuclei. This exchange term is derived as a direct consequence of the Pauli Exclusion Principle, and depends upon the spin vectors of the two electrons concerned and the exchange integral J, which may be positive or negative depending on the amount of overlap between the wavefunctions of the electrons.

3.2.4 Models of Ferromagnetism

The origin of the interactions which cause magnetic ordering in a solid lies in the exchange forces which were outlined in section 3.2.2. These are essentially of an electrostatic nature and lead to a contribution to the total Hamiltonian of the solid, of

$$H_{exch} = -\tfrac{1}{2} \sum_{i,j} J(\underline{R}_{ij}).\underline{s}_i.\underline{s}_j \qquad ....3.2$$

Use of this equation as the magnetic energy in the absence of an external applied magnetic field gives a semiquantitative description of the magnetic phenomena in antiferromagnets and ferrimagnets. However, ferromagnets are almost always metallic and hence the localised spin system upon which this, the Heisenberg model, depends is not always applicable, since for most of these elements the magnetic properties depend on conduction electrons.

In the case of the rare earth elements the magnetic moments are localised at the atomic sites in the lattice. However even here there is a problem because the atoms are so distant that the tightly bound 4f orbitals do not have overlapping wave functions, and hence direct exchange can not occur. The exchange between 4f electrons in this case is indirect proceding via direct exchanges between each localised 4f electron and conduction band electrons.

In the absence of an external field the vectors $\underline{s}_i$ are free to rotate so that a mode exists which has zero energy (called the zero frequency mode) and a series of low energy excited states is possible. A discussion of spin waves is given in section 3.3.3.

3.2.5 The Ising Model

The Ising model is a non quantum mechanical model of magnetic ordering having the unique distinction of being the only model of a second order phase transition which has so far given a mathematical

solution. This was achieved by Onsager [2] for a two dimensional Ising lattice.

If there is an appreciable orbital contribution to the total magnetic moment of an atom, for example if the major contribution to magnetic moment comes from tightly bound electrons localised at the lattice sites of the solid, then considerable anisotropy may occur for different directions of the moment. In the Ising model, which is the most important anisotropic model to have been given much attention so far, the moments are confined to the "z" direction with values $s^z = \pm \frac{1}{2}$ depending on whether the spin is parallel or antiparallel to this chosen "z" direction.

Consider a set of spins or magnetic moments $s_1, s_2, \ldots s_n$ associated with atoms arranged in some particular symmetry, for example on the lattice points of a particular crystallographic group. Each of the spins is allowed to have one of two possible orientations which correspond to a chosen crystallographic axis. In this case the magnetic contribution to the total Hamiltonian is,

$$H_{mag} = -\tfrac{1}{2} \sum_{i,j} J.(\underline{R}_{ij}) \underline{s}_i^z . \underline{s}_j^z \qquad \ldots.3.3$$

which may be further simplified by considering only nearest neighbours and by assuming that $J(\underline{R}_{ij})$ is the same for any pair of nearest neighbours and has the value J. This simplification allows the solution of the partition function at least in the two dimensional case, and from this all other thermodynamic function may be derived, as shown by Greene and Hurst [3].

The magnetic energy in the absence of any external applied field is then given by the expression

$$H_{mag} = -\tfrac{1}{2} . J. \sum_{\substack{i,j \\ \text{nearest} \\ \text{neighbours}}} \underline{s}_i . \underline{s}_j \qquad \ldots.3.4$$

The likely total energy may be evaluated if the partition function Z for the system can be found. The partition function has the general form,

$$Z = \sum_{\substack{\text{all configurations} \\ \text{of } s_i}} \exp\left(\frac{J}{2kT} \sum_{\substack{i,j \\ \text{nearest} \\ \text{neighbours}}} \underline{s}_i \cdot \underline{s}_j\right) \quad \ldots.3.5$$

and once this has been calculated for any particular geometrical case the thermodynamic potentials can be found.

The Ising model is therefore the only non-trivial model of order-disorder transitions for which exact solutions have been obtained. In the simplest form of the model there is exactly one atom per unit cell. (This may be shown by constructing a Wigner-Seitz cell about each lattice point). The advantage of considering such a lattice cell model is that although the number of possible configurations of spins in the solid is very large, the actual number of possible configurations of a particular cell is small. Also, on the whole, configurations of neighbouring cells will be correlated and this must be taken into consideration.

In this model there also exists an energy gap of $8.J.s^2$ between the ground state and the first excited state, which in the Ising model corresponds to the energy required to reverse one spin in the field of the others. This may be contrasted with the low energy states predicted on the Heisenberg model which give rise to spin waves as discussed in section 3.3.3.

3.3.1 Magnetic Ordering in the Heisenberg Model

In solids whose magnetic properties depend on electrons which are localised at the atomic sites the exchange mechanism is unlikely to be direct exchange between the localised electrons simply because, as explained above in section 3.2.4, their wave functions do not overlap.

Instead it is considered that the exchange between such electrons is indirect.involving electrons in the conduction band, which interact directly with bound electrons. In this way the orientation of magnetic moments of unpaired electrons on a particular atomic lattice site can influence the orientation of unpaired electrons on a neighbouring atom even though the atoms are so far apart as to prevent exchange between their electrons. An 'effective' exchange integral J may still be defined in this case and the form of the Heisenberg exchange energy retained.

The sign of the exchange integral is dependent on the interatomic or interionic spacing in the solid. It is only over a certain range that the exchange integral between nearest neighbours is positive, and hence that the minimum energy state is achieved with neighbouring spins parallel. As the interatomic spacing increases J becomes more positive while as it decreases it becomes more negative. This may be expected since the exchange energy is proportional to -J and therefore increases as the electrons come closer together.

If all the exchange integrals between electrons contributing to the magnetic moments are positive then the lowest energy state occurs when the magnetic moments are parallel and hence ferromagnetic order is favoured. If some exchange integrals are negative, however, then some spins will align antiparallel. The simplest case occurs when only the exchange integrals between nearest neighbours are significant and are negative. This gives rise to simple antiferromagnetism.

3.3.2 Helical Antiferromagnetism

Another form of magnetic ordering which also gives rise to zero total magnetisation is the helical order or helimagnetism, from which simple antiferromagnetism can be derived as a special case. If the condition for the direction of moments is

$$\mu_x : \quad g \cdot \mu_B \cdot \langle s_i^x \rangle = m.\cos(\underline{\omega}.\underline{R}_i)$$

$$\mu_y : \quad g \cdot \mu_B \cdot \langle s_i^y \rangle = m.\sin(\underline{\omega}.\underline{R}_i) \qquad ....3.6$$

$$\mu_z : \quad g \cdot \mu_B \cdot \langle s_i^z \rangle = \text{constant}$$

where μ_B is a Bohr magneton and g is the splitting factor, giving the ratio of the number of Bohr magnetons to $\hbar$.

If the constant term is set to zero then there will be no component out of the xy plane, and moments will describe a helical structure with vector along the z axis.

The total energy of such a structure may be found by using Heisenberg's expression and summing over all pairs of spins i,j

$$W = - \sum_{i,j} J(R_{ij}) \underline{s}_i . \underline{s}_j \qquad ....3.7$$

$$= - \left(\frac{m}{g.\mu_B}\right)^2 \sum_{ij} J(\underline{R}_{ij}).\cos(\underline{\omega}.\underline{R}_i - \underline{\omega}.\underline{R}_j) \qquad ....3.8$$

and replacing $\underline{R}_i - \underline{R}_j$ by $\underline{R}_{ij}$ gives

$$W = - \left(\frac{m}{g.\mu_B}\right)^2 \sum_{ij} J(\underline{R}_{ij}).\cos(\underline{\omega}.\underline{R}_{ij}) \qquad ....3.9$$

which is the total magnetic energy for such a structure. This has been employed in specific cases of helical magnetic structures, for example Dysprosium, by Enz [4] and Nicklow [5] to calculate the inter layer turn angle $\underline{\omega}$ as a function of the exchange interaction, by setting $\frac{dW}{d\omega} = 0$ at equilibrium.

3.3.3 Excited States of a Magnet: Spin Waves

At the absolute zero of temperature the magnetic moments of a magnetic solid would be perfectly ordered as governed by the exchange integrals discussed in section 3.2 and the total magnetic moment, in

the case of a ferromagnet, would reach a maximum value. As the temperature is increased, however, the moments acquire thermal energy which allows them to deviate from the perfectly ordered state.

Consider the case of a ferromagnet which in its ground state will have all its moments in a particular direction. If thermal energy is supplied then this results in low level states where all the spins precess about the original direction. If the nearest neighbour interactions only are considered and their interactions represented by the Heisenberg expression in equation 3.1

$$W = - J.\underline{s}_j \cdot \underline{s}_{j+1} \qquad ....3.10$$

and if J is the same for all nearest neighbour pairs the total energy of an N x N two dimensional lattice will be

$$W_{mag} = - J \sum_{j=1} \sum_{i=1} \underline{s}_i \cdot \underline{s}_{i+1} \qquad ....3.11$$

If one of the N magnetic moments is reversed in the field of the others then this will give a change in energy of ΔW

$$\Delta W = 8 . J . s^2 \qquad ....3.12$$

However a state of much lower energy is obtained if all the spins exhibit a precession about the original direction. The energy contribution due to the i th spin will be

$$W_i = - 2 . J . \underline{s}_i.(\underline{s}_{i-1} + \underline{s}_{i+1}) \qquad ....3.13$$

and if the magnetic moment of the i th spin is $\underline{\mu}_i$

$$\underline{\mu}_i = - g . \mu_B \cdot \underline{s}_i \qquad ....3.14$$

$$\therefore \quad W_i = \frac{2.J}{g.\mu_B} .\underline{\mu}_i \cdot (\underline{s}_{i-1} + \underline{s}_{i+1}) \qquad ....3.15$$

and replacing $\frac{2.J}{g.\mu_B} (\underline{s}_{i-1} + \underline{s}_{i+1})$ by $\underline{B}_i$, the local field which is observed by the i th spin, this gives

$$W_i = - \underline{\mu}_i.\underline{B}_i \qquad ....3.16$$

The rate of change of angular momentum $\frac{d}{dt}(\hbar.\underline{s}_i)$ is given by

$$\hbar.\frac{d}{dt}(\underline{s}_i) = \underline{\mu}_i \wedge \underline{B}_i \qquad \ldots.3.17$$

$$= \frac{2J}{\hbar}(\underline{s}_i \wedge \underline{s}_i + \underline{s}_i \wedge \underline{s}_{i+1}) \qquad \ldots.3.18$$

resolving this into components along the three orthogonal directions,

$$\frac{\partial}{\partial t}(s_i^x) = \frac{2.J}{\hbar}(s_i^y(s_{i-1}^z + s_{i+1}^z) - s_i^z(s_{i-1}^y + s_{i+1}^y)) \qquad \ldots.3.19$$

Since the excitation is assumed to be of low energy, and if the original direction of the moments was parallel to the z axis, then the x and y components would be small and therefore $s_i^z \simeq s$. The products of s_i^x and s_i^y thus become negligible.

$$\frac{\partial}{\partial t}(s_i^z) = 0$$

$$\frac{\partial}{\partial t}(s_i^x) = \frac{2.J.s}{\hbar}(2s_i^y - s_{i-1}^y - s_{i+1}^y) \qquad \ldots.3.20$$

$$\frac{\partial}{\partial t}(s_i^y) = -\frac{2.J.s}{\hbar}(2s_i^x - s_{i-1}^x - s_{i+1}^x).$$

These equations yield solutions of the form

$$s_i^x = A_x \,.\, \exp(i(nka - \omega t))$$

$$s_i^y = A_y \,.\, \exp(i(nka - \omega t)) \qquad \ldots.3.21$$

which are then satisfied when

$$\hbar\omega = 4.J.s.(1 - \cos ka) \qquad \ldots.3.22$$

which is a lower energy state than the $8Js^2$ required for reversing one of the spins. The low energy excitations in this model are therefore wave-like variations in the individual spin vectors. The excitations are known as spin waves.

3.4.1 Phase Equilibrium

Any homogeneous and physically distinguishable portion or state of a system having definite boundaries is termed a phase. The equilibrium state of a body may be determined by specifying any two thermodynamic quantities, for example pressure and temperature. However, for each pair of these values the equilibrium may not correspond to only one phase. It may happen for example that given a particular pair of values of the two variables that either or both of two phases can be in equilibrium. At such a point a phase transition occurs.

Apart from phases of a substance such as liquid, solid and gaseous states there may exist separate phases in the solid state. For example at different temperatures or pressures the solid may exhibit different crystallographic groups. The magnetic structure of a solid may also change for example the behaviour of a ferromagnet at its Curie point.

3.4.2 Phase Transitions

Phase transitions occurring at constant pressure and temperature will have the Gibbs function G continuous across the transition since the change dG is given by

$$dG = -S.dT + V.dP \qquad \ldots.3.23$$

The first derivatives of the Gibbs function are the entropy S and the volume V,

$$\left(\frac{\partial G}{\partial T}\right)_P = -S$$

$$\left(\frac{\partial G}{\partial P}\right)_T = V \qquad \ldots.3.24$$

which are discontinuous across the phase boundary in the familiar phase transitions of vaporisation fusion and sublimation. However, many phase transitions occur in which the entropy and volume remain constant at the transition point. In these cases the four parameters T, P, V, S remain constant and therefore so must the thermodynamic functions G, H, U, F.

3.4.3 Classification of Transitions

The phase transitions may be conveniently classified following Ehrenfest [6] such that the order of a transition is determined by the lowest order of differential coefficient of the Gibbs function which shows a discontinuity at the transition.

The first order transitions such as vaporisation, fusion and sublimation are accompanied by heat exchange known as latent heat because of the discontinuous change in entropy at the critical point. Second order phase transitions have the first derivative of the Gibbs function continuous and hence no latent heat is associated with these. However, changes in specific heat, expansion coefficients and compressibility occur discontinuously because these are related to the second derivatives of the Gibbs function.

According to Zemansky [7] the 'lambda' transitions may also be classified as second order transitions although they are not typical of the type. These transitions have infinite peaks of c_p, β and κ at the transition instead of a finite discontinuity. Among the many types of lambda transitions are the order-disorder type of transition in particular that of a ferromagnetic state to a paramagnetic state. This particular case is also the only physical process of its kind to have given a mathematical solution and thus been explained qualitatively, if not quantitatively, in the Ising model.

3.4.4 Transitions between Phases of Different Symmetries

Transitions between phases with different symmetries, for example between crystalline states of two different crystalline groups, or some magnetic phase transitions can not occur in the same way as transitions between for instance a liquid and a gas where the symmetries are the same. At any particular point the body has either one symmetry or the other, and therefore it is always possible to say which phase the state of the system

corresponds to. Therefore in this particular case the two states can not coexist.

Phase transitions of the order-disorder type, for example the ferro- to para-magnetic states of a solid occur in such a way that there is no discontinuous change in the parameters T, P, V, S which specify the state of the solid. That is it behaves as a second order phase transition. However, even an arbitrarily small displacement of the magnetic moments from their random symmetry positions is sufficient to give the symmetry conditions for the ferromagnetic phase. The solid can therefore only exist in one state or the other and the ferro- and para-magnetic states can not coexist. At the transition point the conditions of the two phases become identical.

The second order phase transitions are therefore less abrupt than the first order. The symmetry of the body changes continuously so that only one phase exists at any particular time.

3.4.5 Order-Disorder Transitions

At any point in the phase of a solid undergoing an order-disorder transition a parameter called the degree of ordering may be introduced which is zero in the disordered or higher symmetry phase, and finite in the ordered or lower symmetry phase. As an example from the Ising model of a ferromagnet this may be taken as,

$$\eta = \frac{P+ - P-}{P+ + P-} \qquad \ldots.3.25$$

where P+ and P- are the probabilities of any particular magnetic moment being parallel or antiparallel to a chosen direction.

When $\eta \neq 0$ this corresponds to the ferromagnetic phase (even when P- = 1) and when $\eta = 0$ this corresponds to the paramagnet when P+ = P- = 0.5. Arbitrarily small values of η, whether positive or negative, will still give the same symmetry as the ferromagnetic state.

The phase transition therefore occurs at the moment when η becomes zero. The states of the two phases are thus identical (see for example equation 3.32). The states of two phases therefore become identical at a second order phase transition when η reaches zero, and in fact the symmetries also become identical at this point.

3.4.6 Change of Symmetry

A change in the symmetry of a system by means of a second order phase transition requires that the symmetry of one of the phases is higher than the symmetry of the other. (Naturally this does not preclude the possibility of a second order phase transition occurring without change of symmetry. See for example Landau [8] and equation 3.31). In the majority of cases in which such a change of symmetry occurs it has been found that the phase of higher symmetry corresponds to the higher temperature phase. For example the paramagnetic phase is more symmetric than the ferromagnetic phase.

3.4.7 Absence of Metastable States near a Second Order Transition Point

A first order transition occurs at a point at which the Gibbs functions of the two phases $G_1(P,T)$ and $G_2(P,T)$ are equal, but it is an ordinary point for each of these two functions. Both G_1 and G_2 will correspond to some equilibrium state on both sides of the transition, although when $G_1 > G_2$ this will only correspond to a metastable state of phase one and conversely.

For a second order transition the states of the two phases become identical at the transition point, and the Gibbs functions of either phase beyond the transition point do not correspond to an equilibrium state. That is they do not correspond to local minima of G beyond the phase transition. With this latter fact is connected the impossibility of superheating or supercooling in second order transitions. Neither of the phases can exist at all beyond the transition.

3.4.8 Behaviour of the Thermodynamic Potential near the Transition Point

The parameter η has been defined in 3.4.5 such that $\eta = 0$ corresponds to the higher temperature phase and $\eta \neq 0$ to the lower temperature phase. These may now be referred to as the symmetrical and unsymmetrical phases. Considering the thermodynamic potential for a given deviation from the symmetrical phase, i.e. for a given value of η the Gibbs function may be expressed as a function of P, T and η as shown by Landau [8]. The pressure and temperature may be given arbitrary values but having done this η must be obtained on the condition that the value of G should be a minimum w.r.t. η.

In the neighbourhood of a transition G may be expanded as a function of η by a Taylor series. Using the potential ϕ to represent the Gibbs function,

$$\phi(P,T,\eta) = \phi_o + \alpha\eta + A\eta^2 + B\eta^3 + C\eta^4 + \ldots \quad \ldots.3.26$$

where α, A, B, C are functions of T and P. It can be shown (e.g. ref.8, p.439) that if the states with $\eta = 0$ and $\eta \neq 0$ have different symmetrics then α must be identically zero at all points.

3.4.9 Conditions on the Coefficients

The coefficient $A(P,T)$ of the second order term must vanish at the transition point. For the symmetrical case ϕ must have a minimum when $\eta = 0$ and this requires that $A > 0$ in that phase. Conversely in the unsymmetrical phase the minimum of ϕ must occur for non zero values of η, and therefore $A < 0$. Therefore A must vanish at the transition point.

$$A(P_c,T_c) = 0 \quad \ldots.3.27$$

For the transition itself to be a stable state so that ϕ is a minimum at $\eta = 0$ the third order term must also vanish at the transition and the fourth order term positive.

$$B(P_c,T_c) = 0 \quad \ldots.3.28$$

$$C(P_c,T_c) > 0 \quad \ldots.3.29$$

Since the coefficient C(P,T) is positive at the transition (P_C,T_C) it is also positive in a neighbourhood of (P_C,T_C). There are two possible continuations only one of which is of interest. Firstly the third order term may be identically zero, in which case there is only one condition for the transition to occur and that is,

$$A(P_C,T_C) = 0 \qquad \ldots.3.30$$

This will define P and T as functions of one another in order for a transition to occur.

The second case is when B(P,T) is not identically zero. In this case the transition is governed by the two relations

$$A(P_C,T_C) = 0$$

$$B(P_C,T_C) = 0 \qquad \ldots.3.31$$

and here the transition points will be isolated since they will be the locus of intersection of the two curves given in 3.31.

The more usual and interesting case occurs when $B(P,T) \equiv 0$ at all points, since this gives a curve in the P x T plane at which the phase transition may occur. This will be taken to refer to second order phase transitions. The expansion of the thermodynamic potential, in this case the Gibbs function, is therefore given by

$$\phi(P,T,\eta) = \phi_o + A\eta^2 + C\eta^4 \qquad \ldots.3.32$$

with the conditions $A > 0$, $C > 0$ in the symmetrical phase and $A < 0$, $C < 0$ in the unsymmetrical phase.

In the case where no change of symmetry occurs we may expect a function of the form

$$\phi(P,T,\eta) = \phi_o + \alpha.\eta + A\eta^2 + C\eta^4 \qquad \ldots.3.33$$

The general form of this last equation is identical to that of the potential function of a Riemann-Hugoniot, or Cusp, Catastrophe (see section 3.5.2).

3.5.1 Order-Disorder Transitions in an Ising Model

A mathematical treatment of the probable configuration of magnetic moments located on atomic sites in a two dimensional Ising lattice has shown [2,9] that the lattice undergoes an order-disorder transition at the Curie temperature T_C given by $J/kT_C = 0.88$ where J is the coupling energy between neighbouring spins. It has also been shown that at such a Curie point the specific heat exhibits a lambda anomaly going to infinity.

Most of the early theoretical work concerned an incompressible Ising lattice for which the above results were obtained. Later work was attempted on a compressible Ising lattice [10,11] which concluded that although a Curie point was again predicted, the lattice became unstable in the region of the Curie point, tending to collapse inwards unless a strong lattice spin coupling was invoked. This would make calculations much more difficult since the partition function could not be split into a product of contributions from the lattice and spin systems. Solutions of a three dimensional Ising lattice have not been produced.

3.5.2 Magnetic Phase Transitions as a Consequence of Catastrophe Theory

In recent years a mathematical method of describing the evaluation of forms such as the changes of state of a substance has been developed. Attempts to apply this to thermodynamic phase transitions have met with some success [e.g. 12,13, P.53] although there are still some problems to overcome [13, P.635]. Applications to other branches of physics have so far received more attention. In the appendix an attempt has been made to correlate the observed phenomena of magnetic phase transitions with the mathematical predictions of the model. It is probable that this theory, like the Ising model, will only be able to provide qualitative results.

CHAPTER 4

The Sing Around System

4.1 Development of the Present System

4.1.1 Construction of the Sing Around System

The sing around system was already available having been designed and built by Whitehead and Broadhurst [1]. It contained some modifications from the earlier systems used by Brammer [2] and by Forgacs [3,4]. It was designed as an automated device, that is it had an internal memory in which it could store its own results. The results may then be retrieved later, coded onto punched paper tape. Monitoring of the sing around frequency could be achieved by using a six digit Racal frequency meter, so that continuous sampling was maintained.

4.1.2 Automation of Velocity Measuring Systems

There are several methods available for measuring the velocity of acoustic vibrations in specimens [5,6] most of which employ the pulse-echo technique in one form or another. All employ the conversion of electrical pulses to ultrasonic pulses, using piezoelectric transducers, which then pass through the specimen, are reconverted to electrical pulses using either the same or a second, receiving transducer, amplified and passed back to the electronics. The delay due to the acoustic vibrations passing through the specimen is then measured. The methods fall into three main categories, depending on how this delay is measured; the superposition or overlap techniques, the interferometer techniques and the sing around systems. All of these have been described in detail in section 1.2.

In the overlap and superposition techniques the transit time is obtained by adding a variable delay to the waveform on the oscilloscope

until two similar points in two consecutive echoes coincide. The delay is then equal to the transit time. It is possible to automate the measurement of the transit time for such a system [7,8] by employing a cycle selection method and a timer for each of the two echoes. This could have the desired accuracy, however the two timing clocks would need to be independent and hence the amount of equipment necessary would be excessive.

A method has been found for automating the read out of measurements based on interference techniques [9] again employing delay lines and in this case also determining the phase difference between the two echoes. Consequently this is not easily achieved.

4.1.3 Automation of the Sing Around

The sing around [2,3] would appear to be the most easily automated of the three general types of technique. It does not usually require adjusting during operation since it will continue to operate during moderate changes in pulse height and shape. The gating signal can be used as a pulse to operate a frequency counter.

This system was therefore chosen for automation employing modern integrated circuits and high speed logic which had an internal memory store capable of recording 113 individual sing around periods. A frequency control and pulse width control were also incorporated.

4.1.4 Developments from Earlier Systems

In the Forgacs model the use of separate counter and timer meters had the following drawback: by measuring the number of cycles occurring over a period of ten minutes it was necessary to maintain the temperature constant over this period in order to achieve meaningful results. The present scheme employs two independent measurements of the sing around

SING AROUND SYSTEM

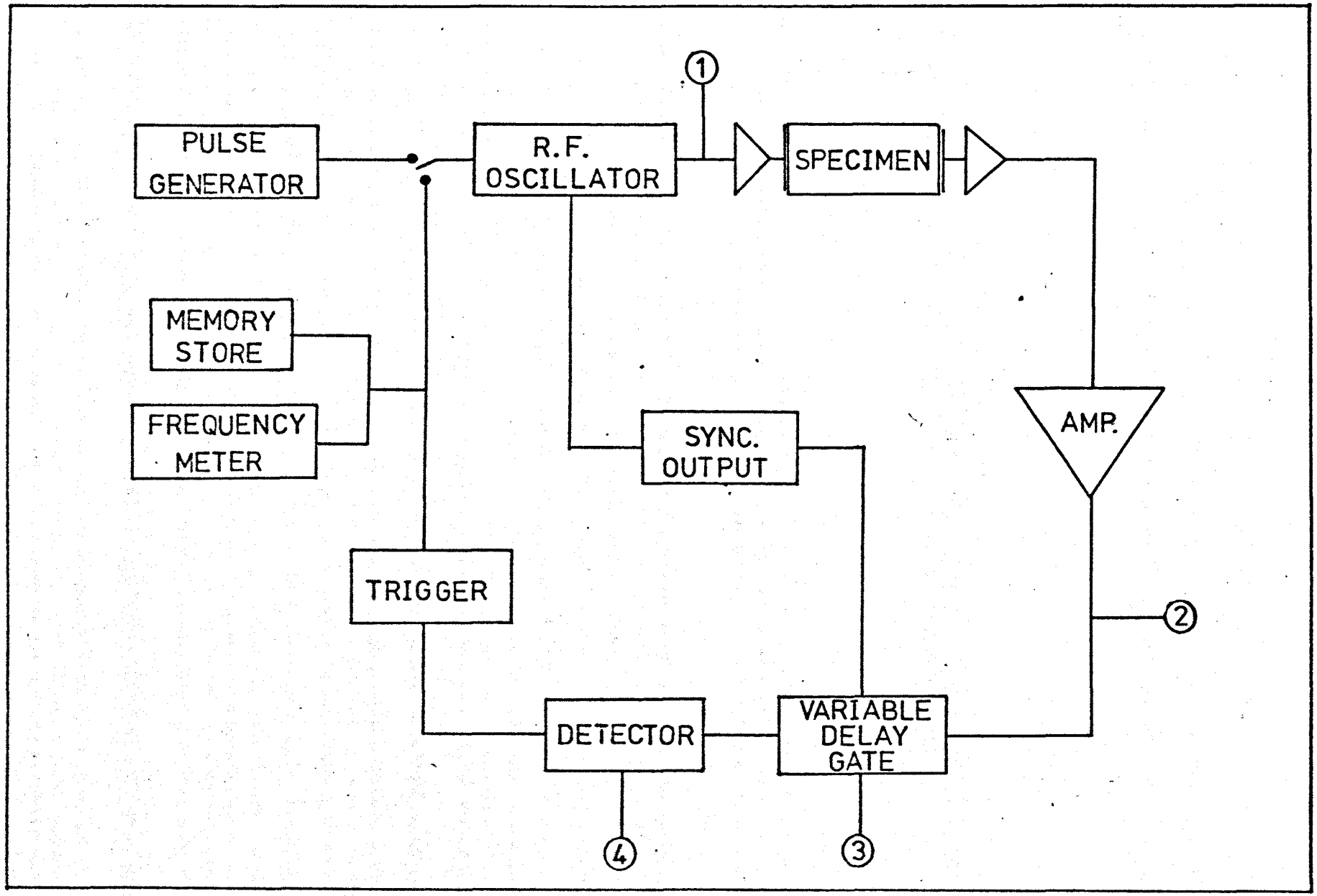

Fig. 4.1

transit time. A frequency meter with a sampling period of about a second acts in the same way as the two meters in Forgacs method. The temperature therefore only has to be maintained over an interval of a second for this. It is, of course, not as sensitive to changes in transit time as the Forgacs method because it samples fewer cycles.

The internal memory stores measurements of a single transit time through the sample which have been made over a period of ten micro-seconds. This enables meaningful results to be obtained even in materials undergoing rapid changes of thermodynamic parameters.

4.2.1 Modifications to the Electronics

In the sing around system as used by Broadhurst [1] the detector was unable to distinguish clearly between consecutive cycles of a particular echo. This caused some uncertainty in the triggering point on occasions which resulted in fluctuations in the detector and gating traces which were monitored on an oscilloscope.

The detector level had been referenced to a ramp voltage caused by integrating a received echo and setting the detector threshold to ascertain when the ramp exceeded a certain level. This was found to be unsatisfactory since it allowed a continuous change in the observed sing around period as the pulse shape changed. An improved method was devised by generating a 'spike' function as each echo was received so that the spikes coincided with the peaks of the cycles in each echo. By this method any changes in the individual transit times caused by changes in the trigger point were observed as discontinuous jumps in the data output from the internal memory store.

To reduce the occurrence of the detector jumping from one cycle to another on a given echo the threshold detector was replaced by a 'zero crossover' type as used by Brammer [2]. In this way as soon as the

amplitude of the received pulse moved above the background noise level the detector would observe it. By using this form of detector the first cycle of the echo occurring after the delay gate had opened triggered the r.f. generator. The discrete changes in the individual transit times caused by changes in the trigger point could easily be distinguished from continuous changes due to variations in elastic constants.

4.2.2 Measurement of Individual Transit Times

A particular cycle of a particular echo in the pulse-chain can be selected to retrigger the r.f. generator by a suitable choice of a preset digital delay which opens a delay gate. The zero crossover detector enables a signal to be discriminated once it moves above the noise level. The level of the detector or the amplifier gain may be adjusted so that the detector level coincides with the noise.

The time between the closing of the delay gate and the triggering of the detector is measured by reference to an internal 'clock' which is a 250MHz high-stability crystal controlled oscillator. This period is then stored in the internal memory and may be output as required. The sum of this and the preset digital delay gives the total sing around period to an accuracy of ± 3 nanoseconds. The three nanoseconds represent the limiting precision introduced because of the uncertainty in the state of the oscillator of one quarter of a cycle at the beginning of the time period and one half of a cycle at the end.

4.2.3 Accuracy of the Measurements

The sum of the preset digital delay D and the coded outputs on paper tape t_i represents the total of one sing around period as expressed in equation 4.1 below [1]

$$\tau_i = 0.128(D + 1) + \frac{t_i + 2}{1000} \qquad \ldots.4.1$$

The time is then given in microseconds. The conversion factors of 0.128 and $\frac{t_i + 2}{1000}$ are simply characteristic of the form of data output, which is not directly in microseconds, and have no physical significance.

The preset digital delay has a maximum value of ninety-nine which corresponds to a time of 12.8μsecs, although it is frequently not used at this value because attenuation of signal in the specimen makes it impossible to trigger the detector this far down the echo train.

The total error introduced into the measured period, as indicated above, is ± 3 nsecs. Taking a typical digital delay of 10μsecs the precision of the sing around period as calculated from the internal memory store is ± 3 nanoseconds in 10 microseconds which represents 3 parts in 10^4. Consequently the values of the total sing around period obtained by processing data from the internal memory store will have a precision of this magnitude.

The precision of the results measured from the frequency counter depend on the accuracy of the timer and the control of environmental conditions since the stability of the sing around circuitry is better than both of these. The Racal counter timer gives a sensitivity of about ± 1 part in 10^6 for the measurement of frequencies of the order of 500 kHz. Typical repetition rate frequencies used in the sing around are about 200 kHz which gives a sensitivity of about ± 2 parts in 10^6. This is significantly less than the sensitivity of ± 1 part in 10^7 quoted by Forgacs for his system simply because the sampling time is less.

Environmental changes may also introduce fluctuations in the sing around frequency in the specimen. According to Papadakis [5]

fluctuations of ± 0.001°K will give rise to changes in $\Delta v/v$ of about 1 part in 10^7, so that even by eliminating errors due to the stability of the electronics precision beyond 1 part in 10^7 for $\Delta v/v$ is not possible under present capabilities. The temperature stability in the present measurements was unlikely to be better than 0.1°K and therefore this would give rise to fluctuations in $\Delta v/v$ of about one part in 10^5. The sensitivity of the sing around system using the frequency meter is therefore better than the fluctuations in sing around frequency which it measures.

4.3.1 Operation in Pulse Mode

In order to operate the new sing around the waveforms at the four test-points shown in fig. 4.1 must be monitored on an oscilloscope. A Tektronix 84603N or 846 series with four beams was found to be most suitable. The traces of the waveforms at these points when in pulse mode are shown in fig. 4.2.

With the sing around switch in the 'off' position the circuit is triggered by a 27 kHz multivibrator. The output from the amplifier should be adjusted to give a large initial pulse and a series of clean echoes with a minimum of transducer 'ringing' or overlap. If the echoes are not clearly distinguishable from one another the r.f. oscillator frequency may be tuned until the optimum conditions are reached when the transducers are operating at resonance. If no echoes are visible this may be because the amplifier gain is not high enough. If having increased the gain echoes are still not visible this could be due either to attenuation of sound in the specimen or to sound not being passed into the sample due to electrical short circuits, bond-breakage or similar problems. When the cause has been rectified adjustment of the r.f. oscillator frequency should give the clean echoes desired.

TRACE WAVEFORMS AT THE FOUR TEST POINTS

WHEN IN PULSE MODE

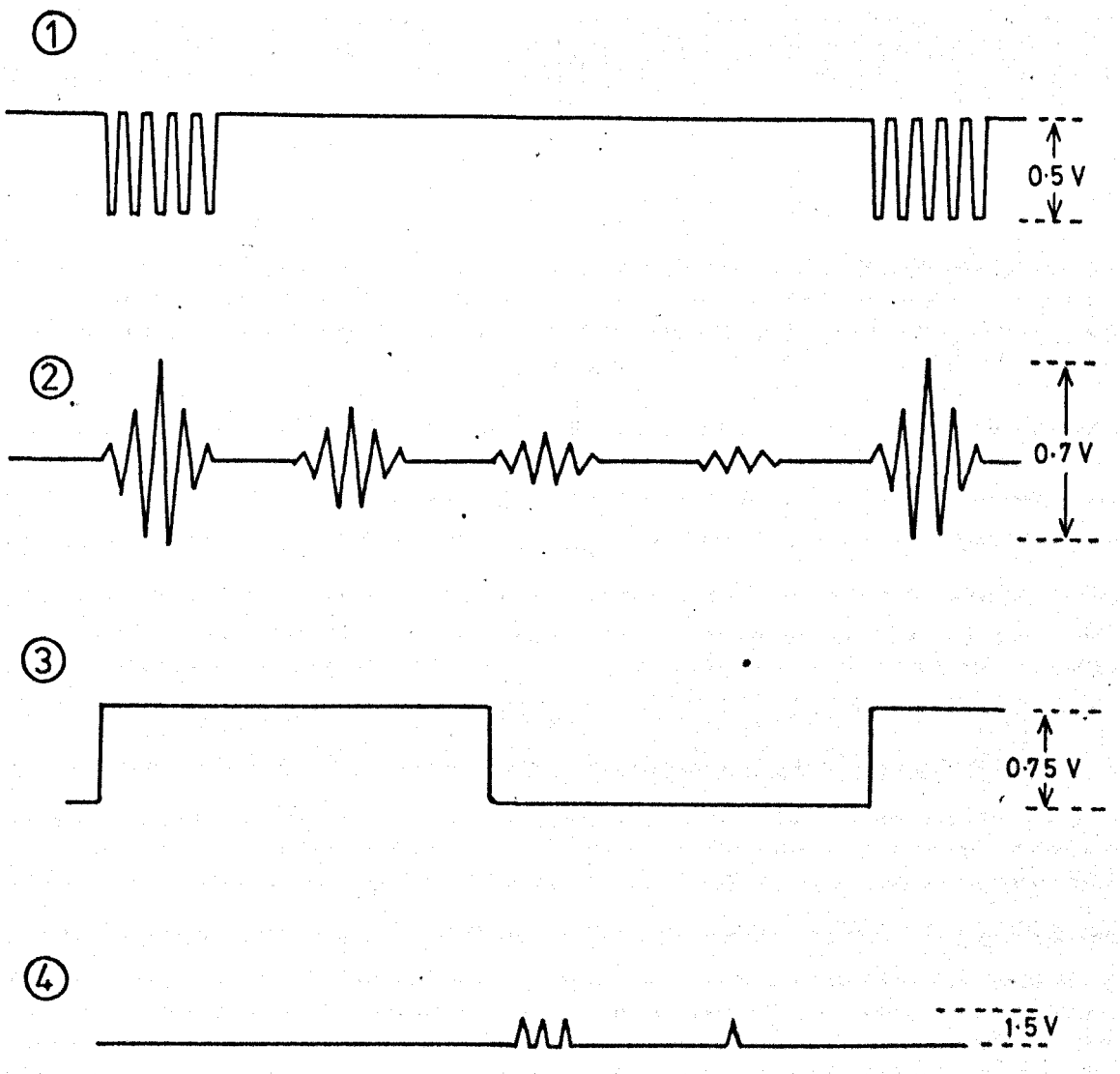

fig. 4.2

TRACE WAVEFORMS AT THE FOUR TEST POINTS

WHEN IN SING AROUND MODE

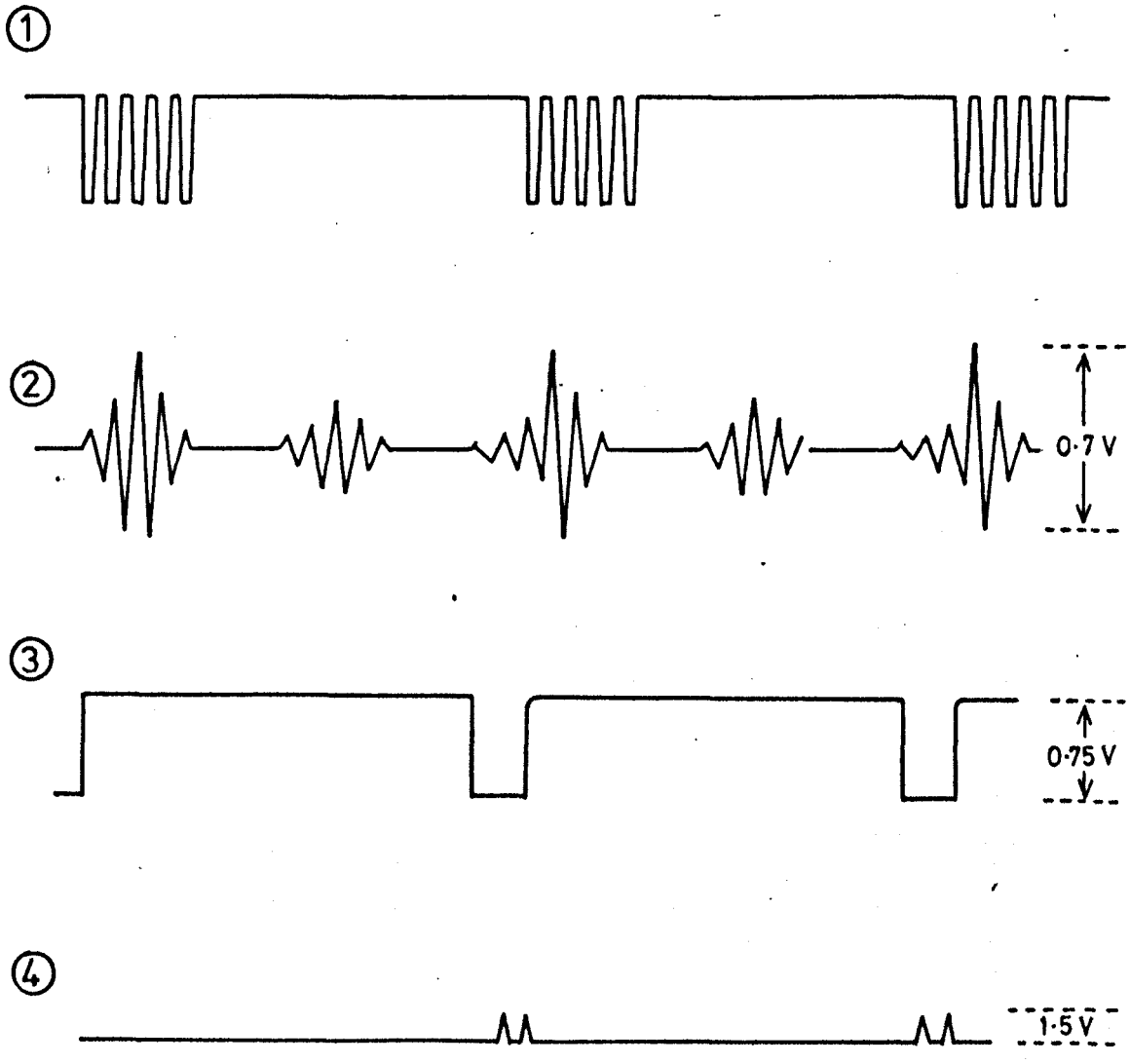

fig. 4.3

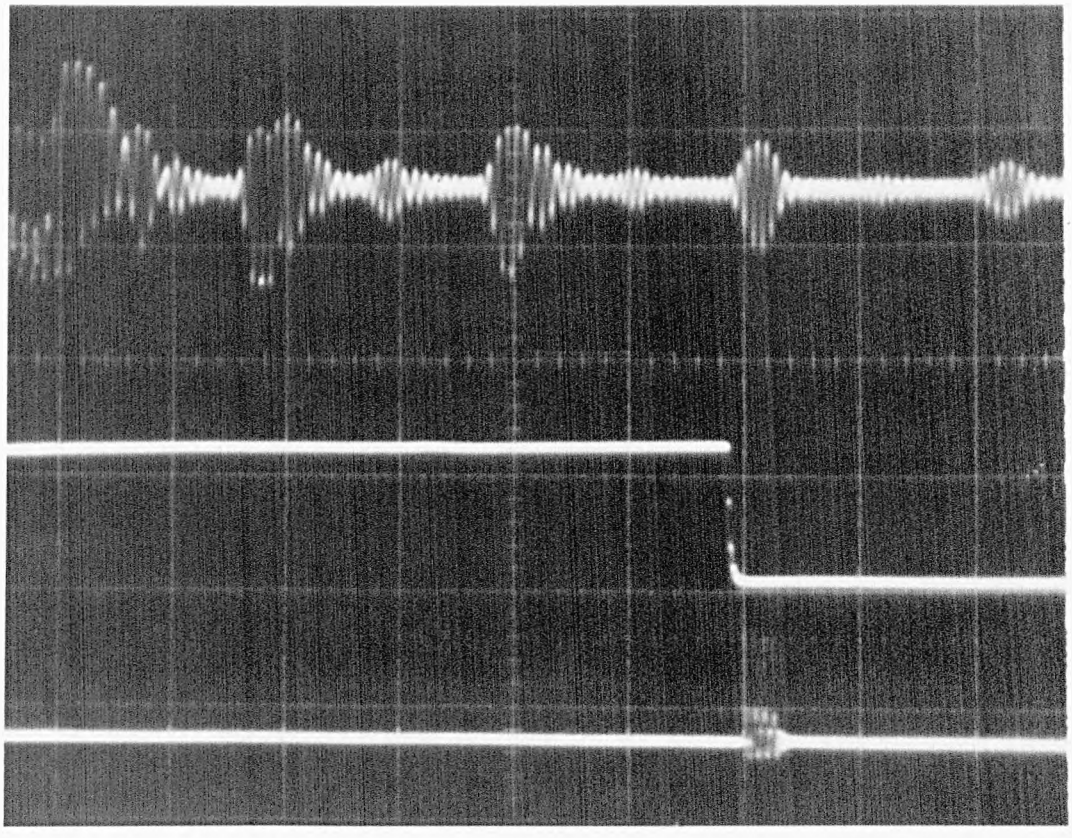

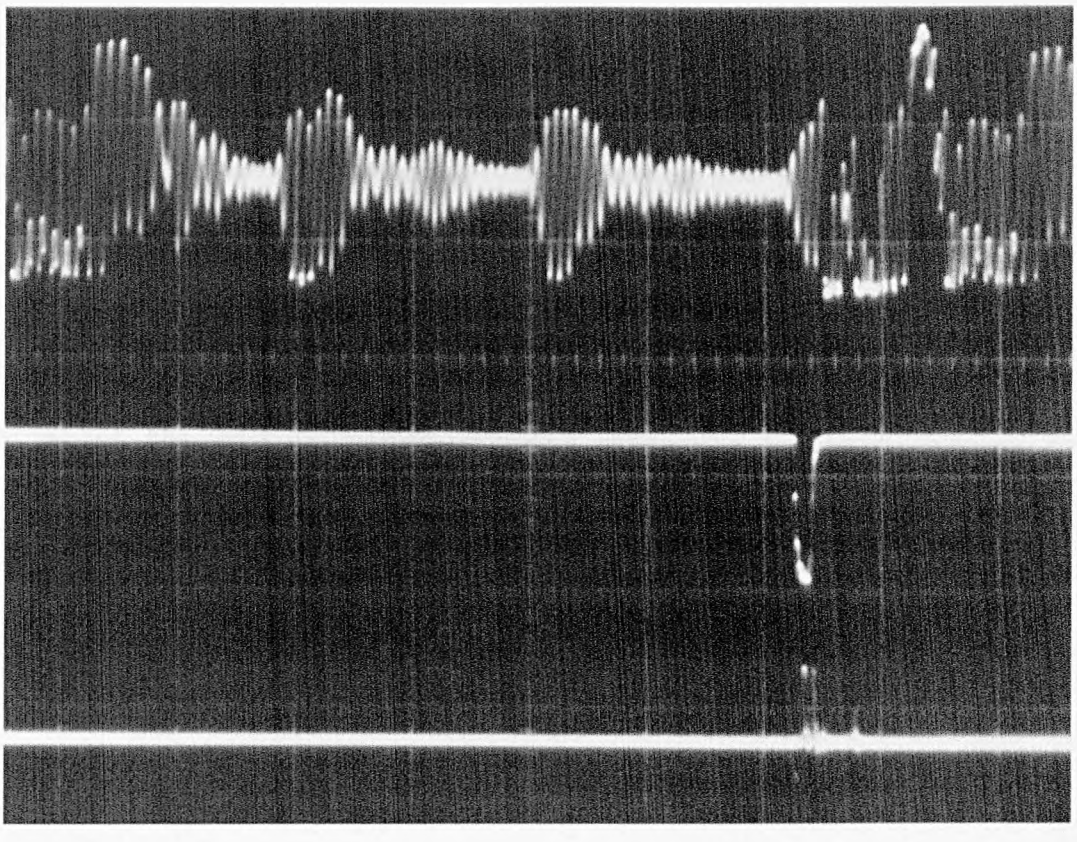

PLATE I

When the pulse echo train is in the required form the variable digital delay may be adjusted within its limits of 0 - 12.8μsecs until the gate opens within 400 nanoseconds of a suitable cycle. This may be the leading cycle or one in the middle of the echo. The detector level should then be altered until the trace from test point four has the form shown in fig. 4.2, indicating that the signal level is above the detector threshold level. It has been found that if the signal level is too far above the detector level the system will not retrigger correctly when in sing around mode. This condition may be remedied by reducing the amplifier gain. In this pulse mode the frequency meter reading should be 27 kHz, the repetition rate of the pulser.

4.3.2 Operation in Sing Around Mode

If the above set of conditions has been satisfied for the pulse mode of operation the sing around switch may be placed in the 'on' position and the multivibrator button depressed once to start the cycling. If conditions are suitable, when the multivibrator button is released the sing around will continue almost indefinitely, and the four trace waveforms will be as shown in fig. 4.3. If all procedures outlined in section 4.3.1 above have been followed and sing around does not start the problem is usually due either to too much gain or too little gain from the amplifier. Adjustment of this will give solution to the problem in most cases.

The repetition frequency of the sing around will depend on the point in the wave train chosen for retriggering. This usually lies between 100 - 500 kHz. The delay gate waveform is used to operate the frequency meter.

4.3.3 Data Output

The repetition frequency may be continuously monitored using a Racal frequency counter with a sampling rate of once per second, for measurements in which the physical parameters of the specimen were varying slowly. Under conditions in which the parameters were varying more rapidly, for example during magnetic field sweeps, the internal memory store could be used.

In order to record results in the store the 'reset and start' button should be depressed and released and the corresponding LED light switches on and remains on until the store is filled. The sample LED light will switch on each time an interval is recorded. The 'sample rate' switches select which intervals are recorded. If the thumbwheel switch is set to 'n' then one interval in every n is recorded. The multiplier switch can be used to increase this to one in every 10n or 100n. This gives a limit of one in every 900 intervals. If the multiplier switch is put into 'external trigger' mode an interval is recorded each time a suitable pulse is received at the external trigger input. A separate pulse generator is used to supply the required pulses which are of one microsecond duration negative going pulses of height 5V. The 'external trigger' input is maintained at +5V, except when induced to sample by reducing its voltage to 0V for a microsecond. The voltage must then be reset to +5V.

When the store is full the 'reset and store' LED light goes off and the sample LED light remains on. Data may then be output on the paper tape unit by pressing the 'reset and start' and 'punch' buttons simultaneously but releasing the 'punch' button first. In order to analyse the data output quickly and accurately the procedures given in Appendix 1 were used in a computer program. This converted the

recorded transit times into values of elastic constants. Final analysed output consisted of tables of the controlled physical parameters (e.g. temperature, pressure or magnetic field), the corresponding sing around frequency both new and corrected for any discontinuous jumps from cycle to cycle in the echo, and calculated elastic constant. Graphical output of elastic constant against the physical parameter was made using the Computer Centre Graph Plotter (HUGP) and is included in the results.

CHAPTER 5

Experimental Methods

5.1 Low Temperature Equipment

5.1.1 Cryostat

The cryostat used throughout the experiments was a conventional narrow tailed type suitable for use with an applied magnetic field from an electromagnet, and capable of temperatures down to liquid helium 4.2°K. A schematic diagram of the cryostat is given in fig. 5.1.

Two chambers for holding refrigerants were included. The outer one for liquid nitrogen had a volume of about 3ℓ. The inner can was used for liquid helium if temperatures down to 4.2K were required, or for liquid nitrogen again if temperatures down to only 77°K were needed. This inner chamber ran the whole length of the tail and had a volume of 50mℓ. It was screened from the outside by a copper radiation shield cooled by the refrigerant in the outer chamber. This enabled the tail to be made narrower and the magnetic field intensity, which could be achieved with this narrower tail by closing the pole pieces of the electromagnet, was therefore correspondingly higher.

Access to the chambers was by inlet and exhaust tubes as shown in the diagram. The inlet tube leading to the bottom of the can and the exhaust from the top. By this method any refrigerants or condensation could be removed from the cans by applying an overpressure via the exhaust tube. Facilities were available for a glass dewar to be used on the outside of the cryostat to reduce heat inflow when temperatures down to 4.2°K were required.

The liquid nitrogen and helium refrigerants were introduced via vacuum jacketed transfer siphons. The nitrogen was transferred by

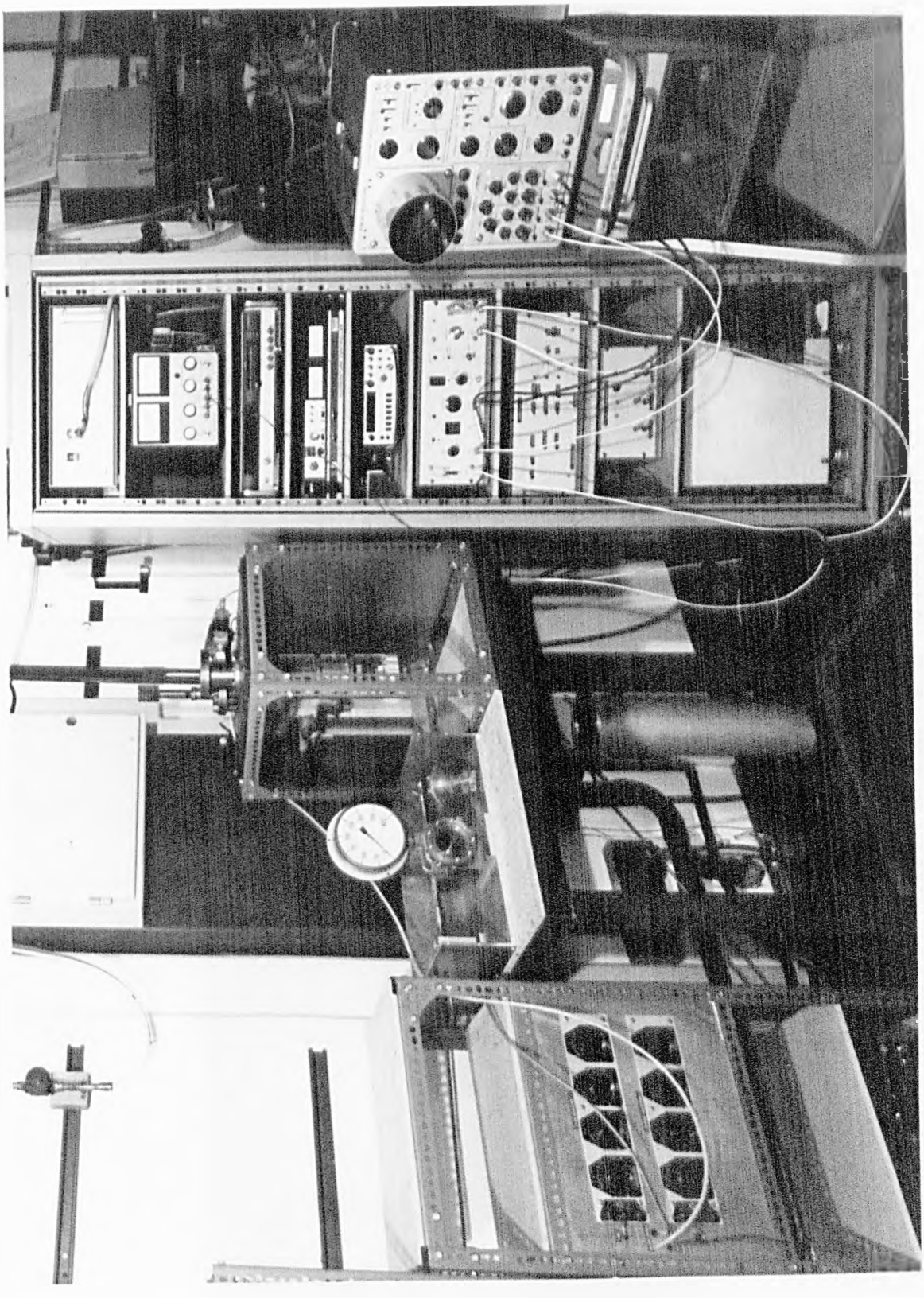

PLATE II

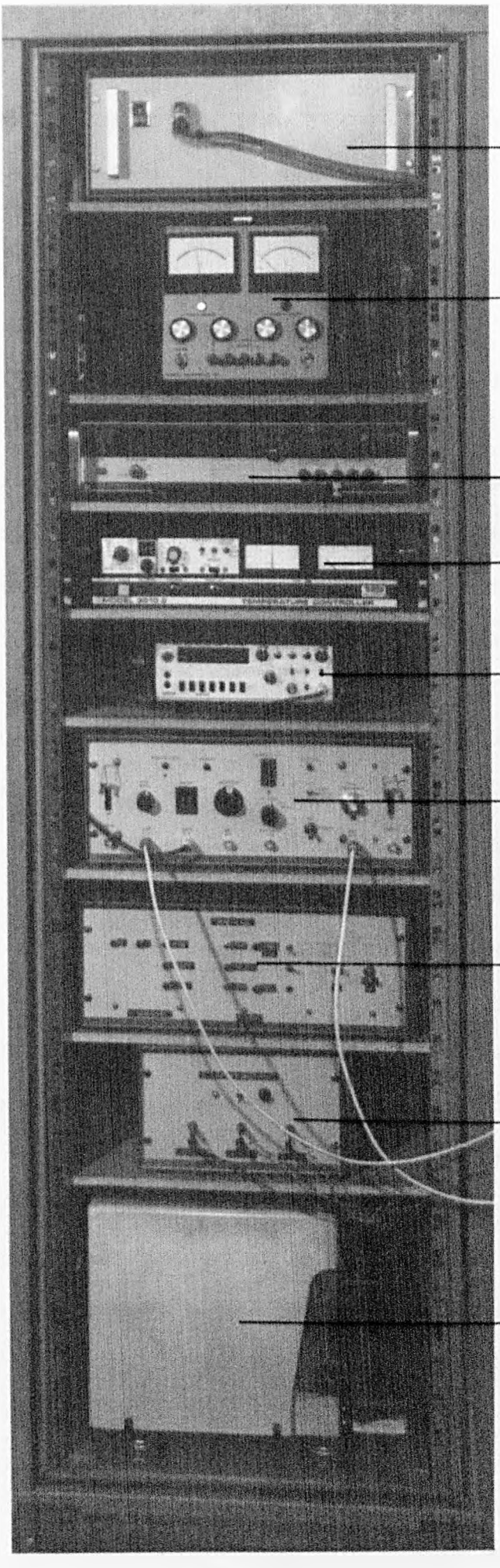
POWER SUPPLY FOR SING AROUND
POWER SUPPLY FOR AMPLIFIER
D.V.M
TEMPERATURE CONTROLLER
FREQUENCY METER
SING AROUND
PUNCH CONTROL
SUPPLY FOR PUNCH
TAPE PUNCH

PLATE III

using an overpressure of about two atmospheres of air from a pressurised air line. The liquid was allowed to boil off into the atmosphere. The helium was transferred by employing an overpressure of its own vapour and all evaporated helium was collected and recycled for liquefaction in the liquid helium plant. Condensation of air or water from the atmosphere into the two cans was reduced by employing bunsen valves on the inlet and outlet tubes.

The sample space in the cryostat was evacuated using the rotary pump of the vacuum system to obtain pressures down to 10^{-2} torr (see fig. 5.2) If exchange gas was required helium was introduced via the inlet valve. The exchange gas allowed thermal equilibrium to be reached more quickly and therefore improved temperature stability in the specimen. It was also possible to introduce exchange gas into the main vacuum space in the cryostat. This was useful for cooling down the helium can rapidly to 77^{o}K before introduction of the liquid helium. The exchange gas pressure was monitored on a Bourdon gauge close to the inlet valve (see diagram). Helium gas was contained in a bladder filled from a gas cylinder.

The main vacuum space and the vacuum jacket between the helium can and the sample space were evacuated by the high vacuum line leading to the diffusion pump. Vacuum pressures down to 10^{-5} torr were possible in the main vacuum space. Cryopumping was also utilised when liquid helium was present in the inner can to improve the vacuum. Under these conditions temperatures of 4.2^{o}K could be maintained for about 20 mins with exchange gas in the jacket or for about 1½ hours with the jacket evacuated.

THE CRYOSTAT

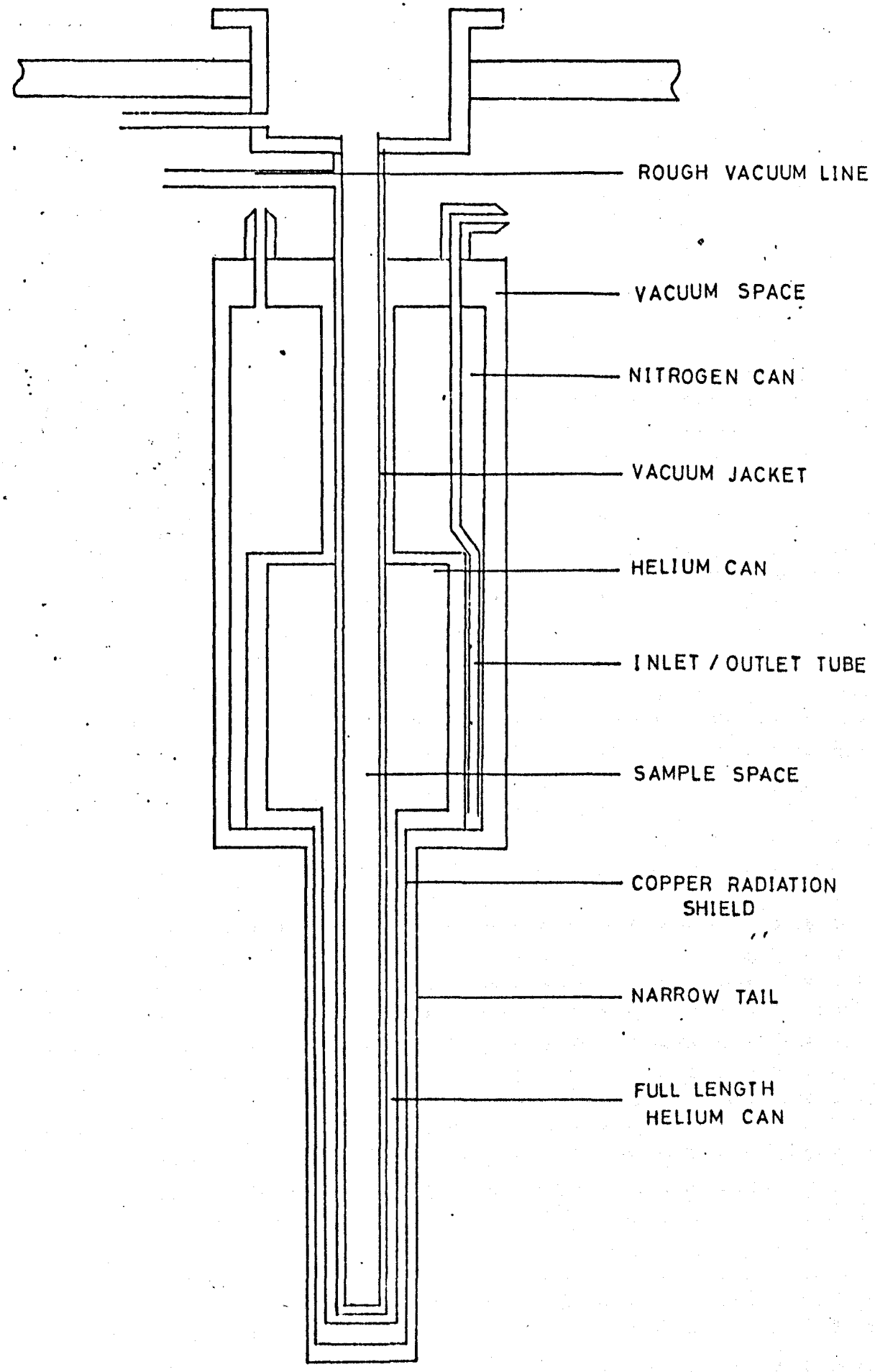

fig. 5.1

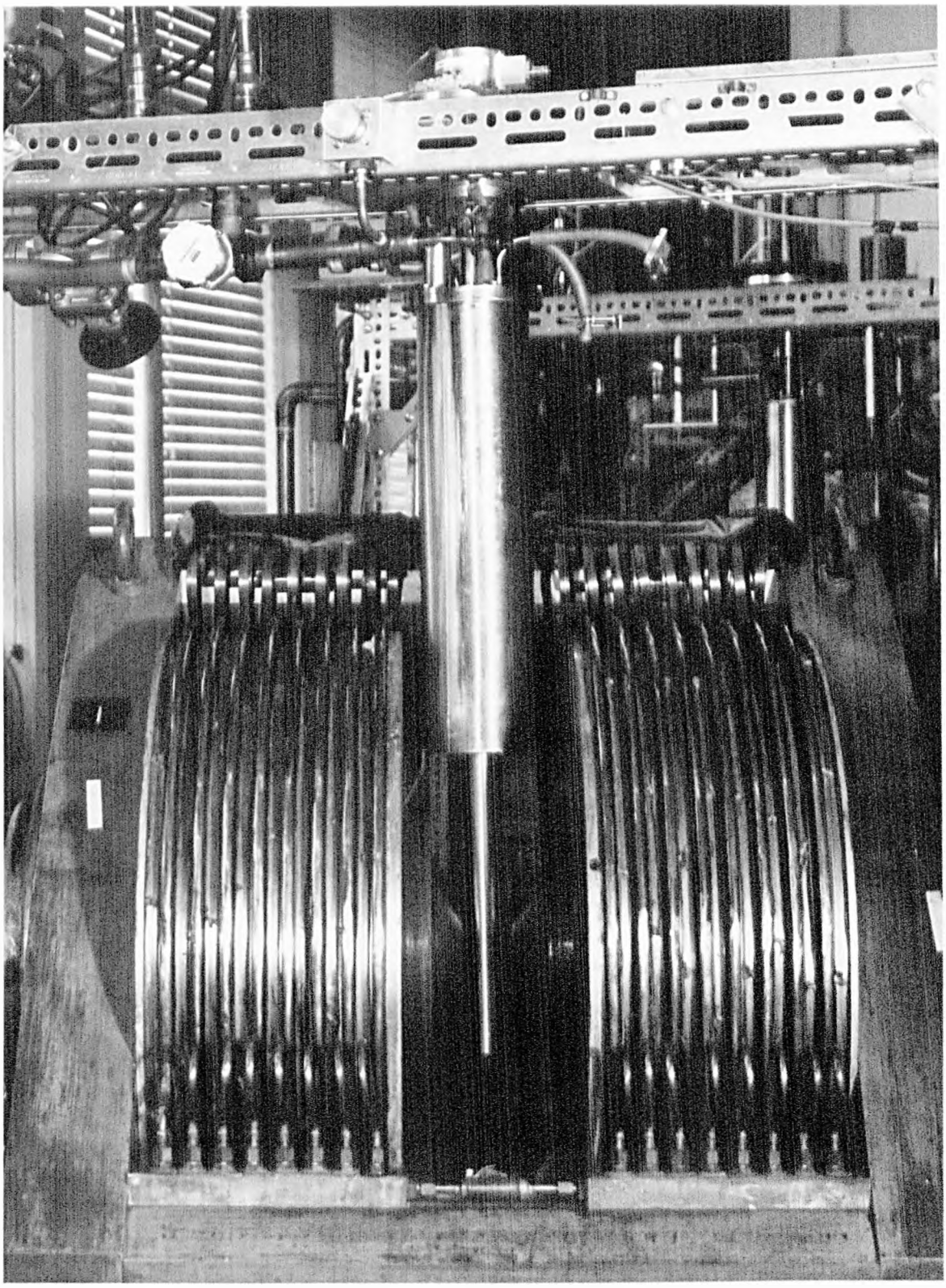

PLATE IV

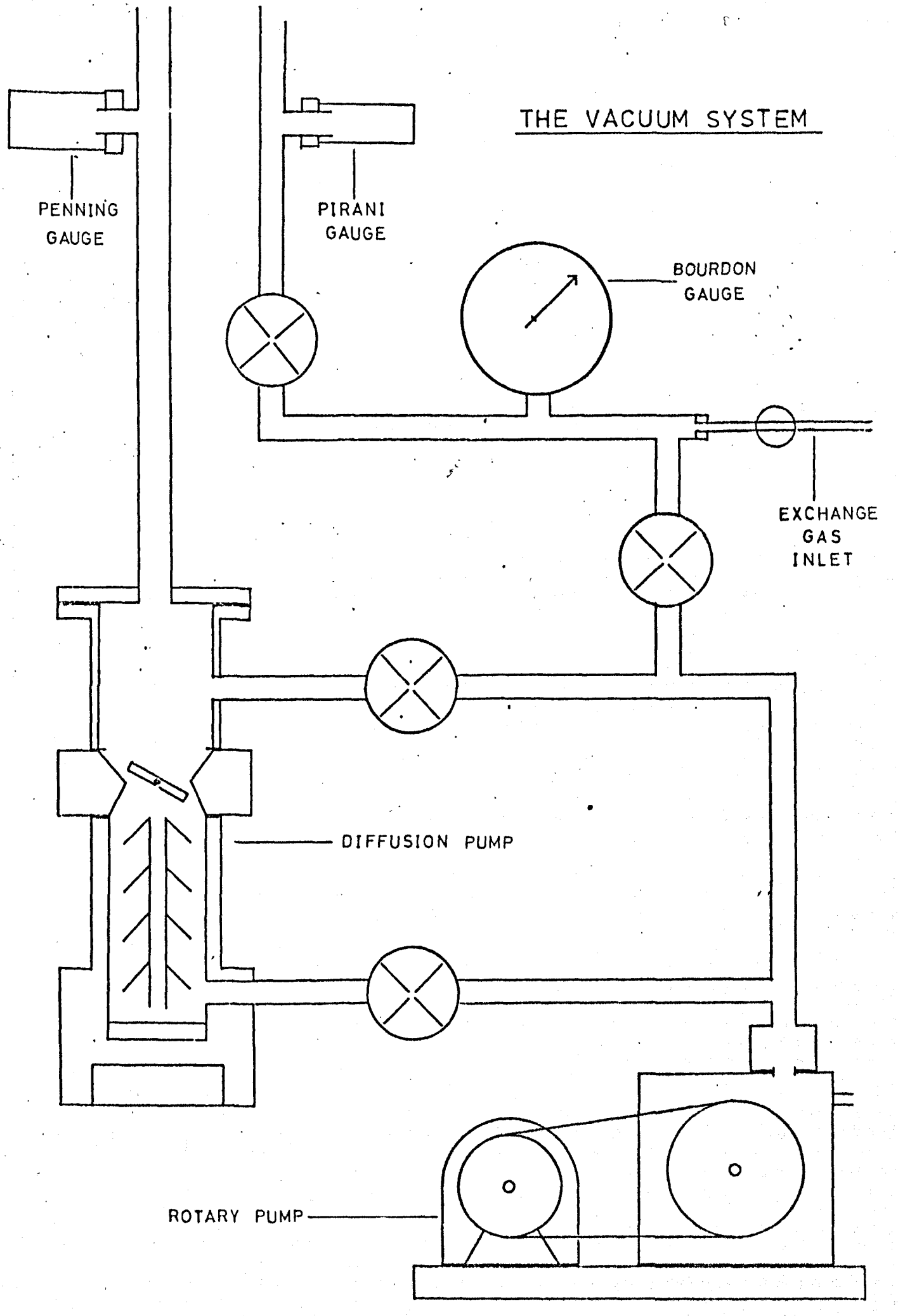
THE VACUUM SYSTEM
PENNING GAUGE
PIRANI GAUGE
BOURDON GAUGE
EXCHANGE GAS INLET
DIFFUSION PUMP
ROTARY PUMP

fig. 5.2

5.1.2 Specimen Holders

A specimen holder was designed to allow electrical contact between the input/output of the sing around system and the transducers bonded onto the specimen. The main consideration was to allow the sample temperature to be controlled and measured as accurately as possible. To facilitate this the main body of the specimen holder was made as small as possible out of good thermal conducting material, in this case copper. Heat leaks into the specimen were minimised by supporting the holder on a long hollow rod of stainless steel, which is a poor conductor.

A heater coil of 150Ω of chromel wire was wound on the main body of the specimen holder (see fig. 5.4). Two thermocouples junctions were embedded close to the specimen for temperature measurement. The supports for the two electrodes were of copper and were in good thermal contact with the main body of the sample holder. Electrodes and supports were insulated electrically from each other by thin layers of mica, which was also a good heat conductor so that thermal equilibrium was quickly achieved.

The complete specimen holder and support is shown in fig. 5.3. The sample space in the cryostat was 15mm in diameter by about 90cm in length which imposed immediate restrictions on size. Two P.T.F.E. spacers are shown on the support rod in fig. 5.3. These were designed to maintain the holder central in the sample space and prevent good thermal contact between specimen and the walls of the sample space while the temperature was being raised. A third spacer is present on the lower end of the holder.

The cap of the specimen holder was made of aluminium and when bolted into position on top of the cryostat it formed a vacuum tight

SPECIMEN HOLDER

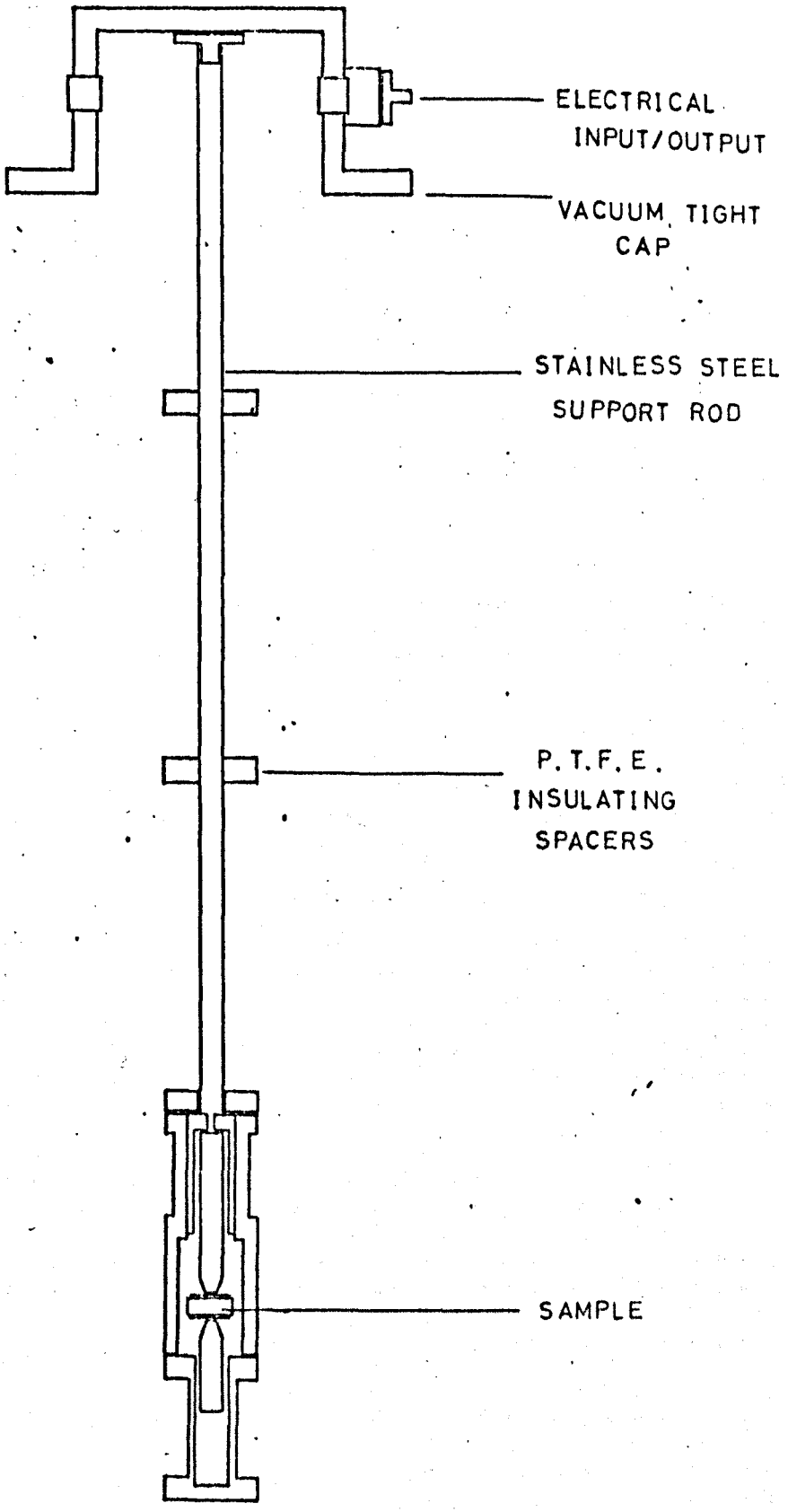

fig. 5.3

SPECIMEN HOLDER

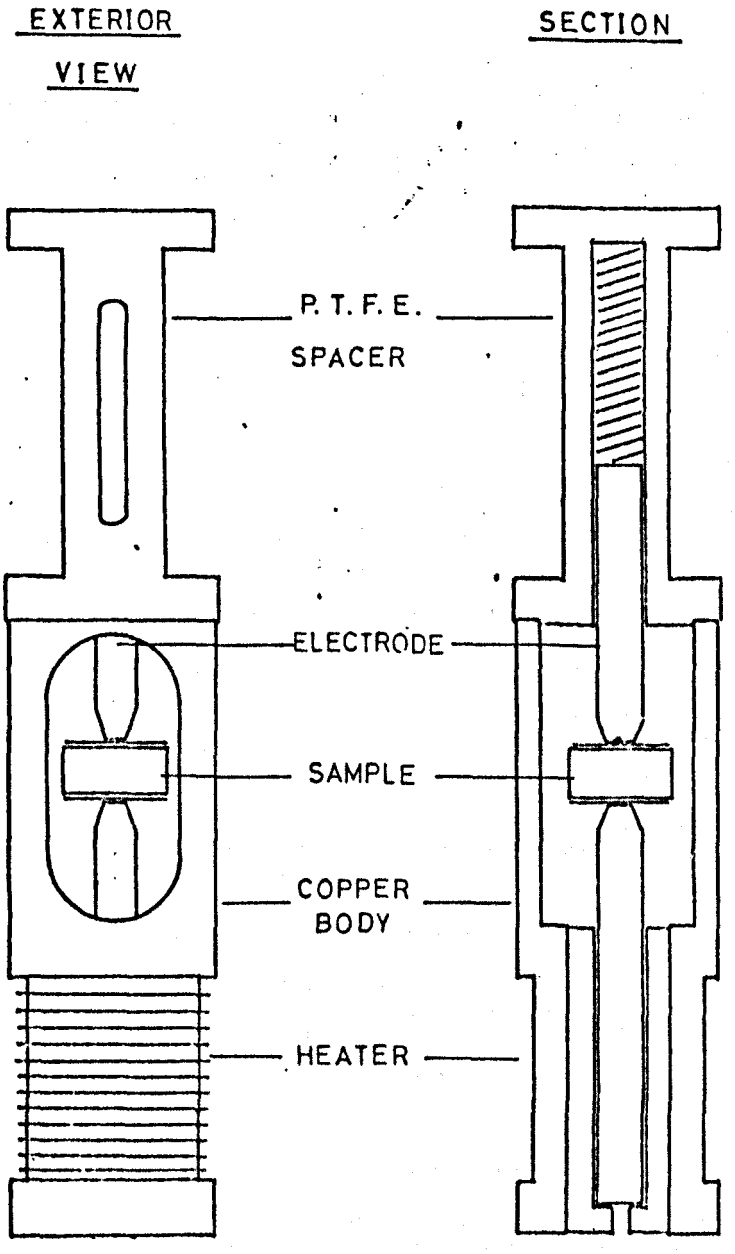

fig. 5.4

seal to the sample space, allowing it to be evacuated and exchange gas to be let in to any desired pressure.

All input/output points in the cap were glass to metal sealed vacuum lead-throughs. They could be made vacuum tight by allowing melted wax to solidify inside the 1mm diameter brass tubes of the lead through. Wires to the specimen holder were passed down the hollow centre of the stainless steel support tube.

5.1.3 Vacuum System

The vacuum system employed is shown in fig. 5.2 which used a rotary pump as backing pump to an Edwards Oil Diffusion pump enabling pressures down to 10^{-5} torr to be achieved on the high vacuum line. This was used for the main vacuum space and the vacuum jacket in the cryostat. The rough vacuum line also shown was evacuated only by the rotary pump and achieved a pressure of down to 10^{-2} torr which was used to evacuate the sample space. An exchange gas inlet is shown on the right of the diagram, the pressure of gas being registered by the Bourdon gauge.

The pressures were monitored by a Pirani gauge in the rough vacuum line and a Penning gauge in the high vacuum line. The gauge heads and measuring equipment were also supplied by Edwards.

5.2 High Pressure Apparatus

5.2.1 The Hydrostatic Pressure Cell

The purpose of this apparatus was to allow the specimens to be subjected to a controlled hydrostatic pressure in the range 1-80 kg/cm^2 (8×10^6 Pascal or 80 bar). The design of the equipment is shown in fig. 5.5. The cell was supplied by the Department of Physics at the University of Southampton.

The pressure cell was constructed of thick walled $^{3}/_{16}$" brass. At one end was the pressure inlet consisting of a P.T.F.E. sealed high pressure copper tube $^{1}/_{4}$" I.D., $^{3}/_{8}$" O.D. At the other end the sample space was closed by a brass lid sealed by nine steel bolts. An 'O' ring of neoprene which was of the "completely surrounded" type, to prevent blow outs, maintained the high pressure. Electrical input/output ports for the sing around were located in the lid and secured by P.T.F.E. seals. The specimen holder consisted of a brass plate joined to the lid which supported two spring loaded adjustable probes for maintaining electrical contact with the transducers bonded onto the specimen.

The cell was connected via high pressure copper tubing to a nitrogen gas cylinder which could supply pressures up to 180 bar. The pressure in the chamber was measured by a Bourdon gauge located close to the cell which gave readings of pressures in the range 0-80 bar with an accuracy of $\sim$ 1%. An exhaust valve was included as shown both for regulating pressure and also as a safety precaution against over pressurising the equipment. The exhaust valve limit was 1200 p.s.i. or 80 bar.

The gas inlet/outlet valve from the gas cylinder was of the type supplied by Air Products Ltd. which differed from the conventional 2 bar gas regulator normally used with gas cylinders in that it allowed full bottle pressure to be achieved. This was connected to the chamber by a length of flexible high pressure copper tubing.

The pressure cell and most of the associated pipework was enclosed in a shielded box of $^{1}/_{4}$" thick aluminium alloy as a safety precaution against explosion. The box was always sealed using ½" steel bolts before pressure was introduced into the chamber.

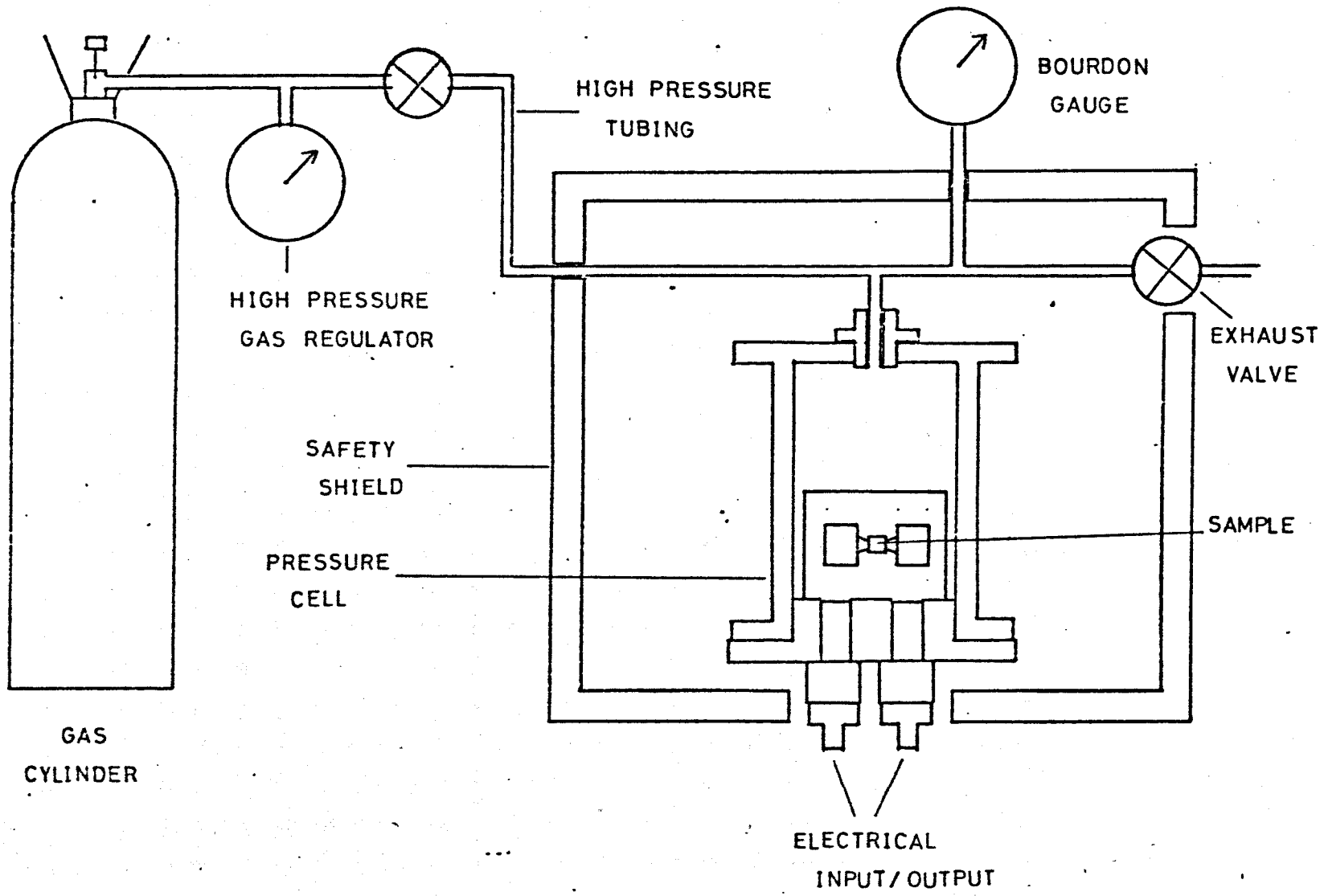

fig. 5.5

THE HYDROSTATIC PRESSURE CELL

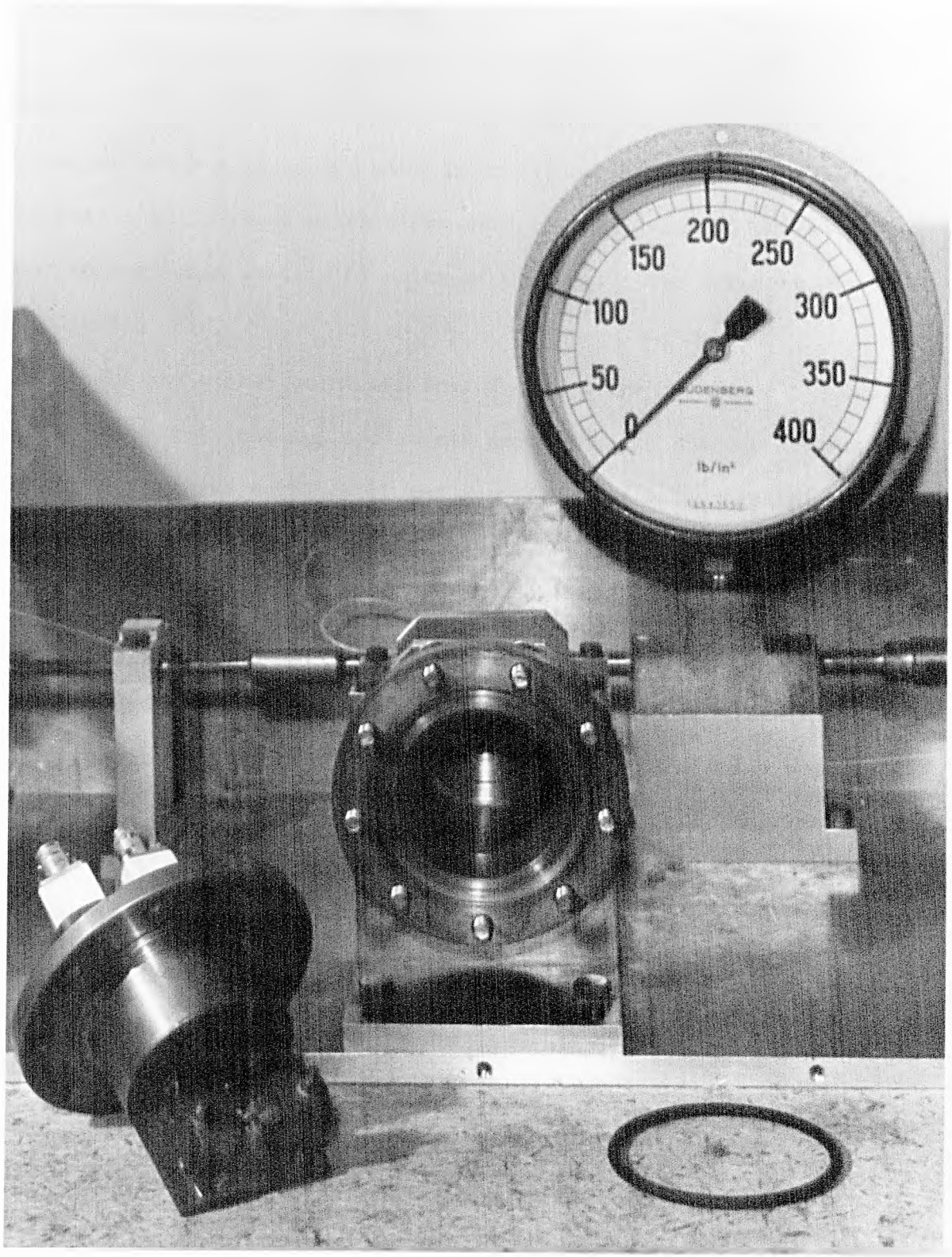

PLATE V

5.2.2 Uniaxial Pressure Apparatus

A uniaxial pressure apparatus was also supplied by Southampton University. This allowed uniaxial stresses of up to 100 kg/cm^2 to be applied by using a lever arm with 5:1 ratio connected on one side to a stainless steel pushrod which compressed the specimen and on the other side, to suspended weights in units of 0.25 kg. The apparatus is shown in fig. 5.6.

A ball and socket joint was introduced at the bottom of the push rod to ensure that the applied stress was normal to the surface of the specimen. The two surfaces of the specimen were made parallel by lapping to within 5^o. By this technique any deviation between the direction of motion of the push rod and the normal to the specimen plate was compensated for.

The push rod was constrained to move vertically by three tufnel rings along the length. Tufnel was used because of its low coefficient of friction with stainless steel [1]. Frictional forces acting against the applied stress were thereby minimised.

The specimen plate was made to specifications at this University. It consisted of a plate of 1" thick duralumin alloy to support the specimen under forces of up to 100 kg.wt. It contained two movable electrical probes mounted in insulating tufnel on sliding spring loaded duralumin supports. The probes were of 2 mm diameter brass rod of about 4 mm length connected to the input/output ports in the headpiece by copper wire running the whole length of the apparatus. The specimen was placed on a raised platform in the centre of the specimen plate with transducers bonded on.

It was found that because of the size of specimens (3 mm height x 6 mm diameter) the usual 6 mm diameter transducers could not be used since they would interfere with the application of stress by the push rod,

THE UNIAXIAL PRESS

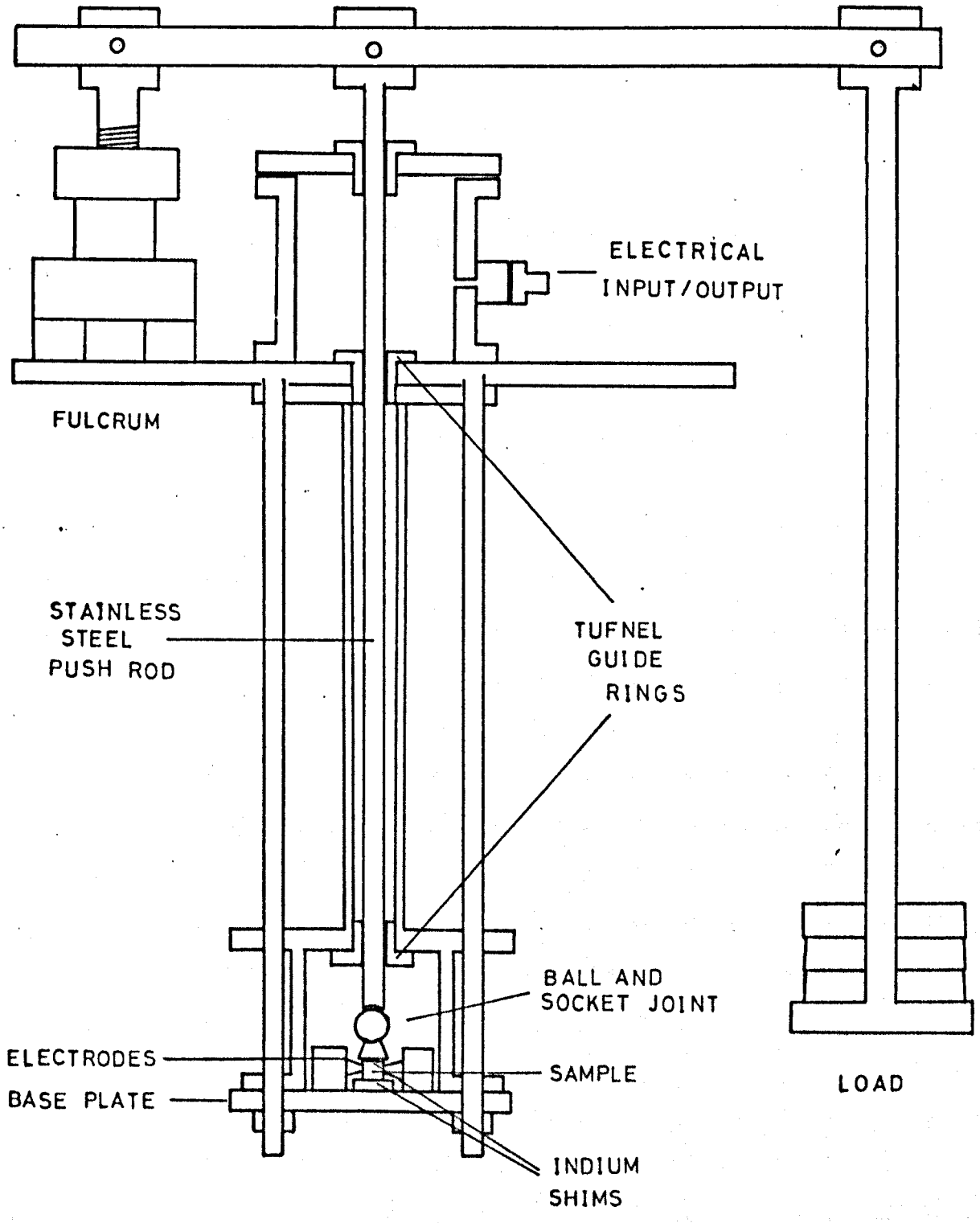

fig. 5.6

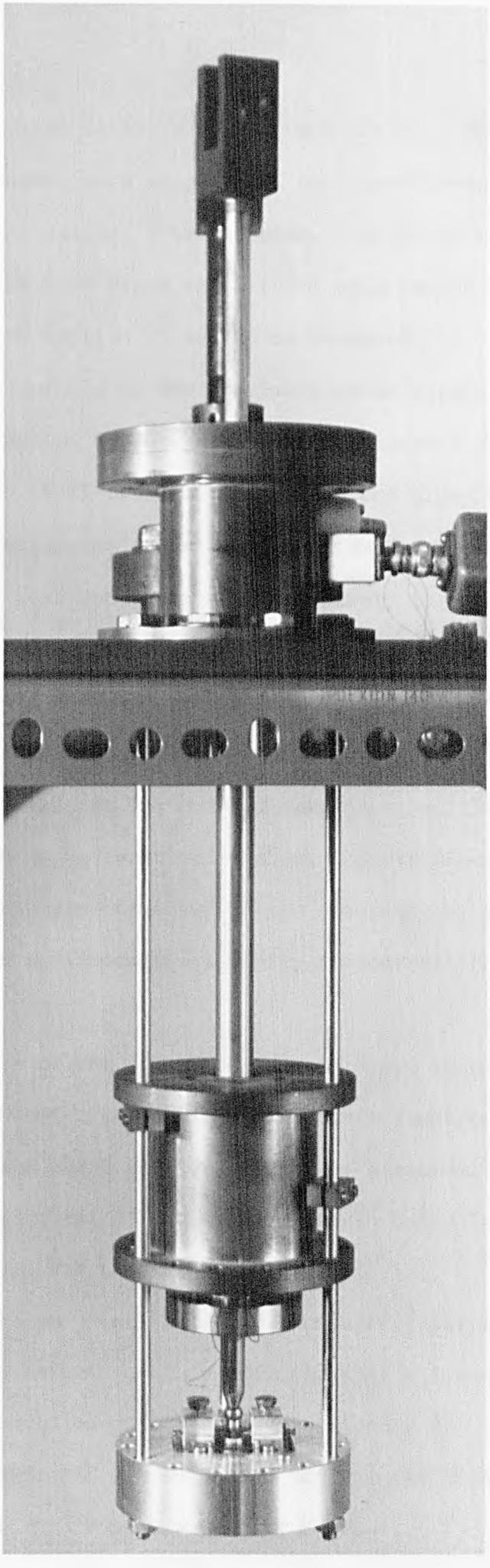

PLATE VI

or at best be shorted to earth on the base plate. Therefore special miniature transducers were supplied to our specifications by Gooch and Housego Ltd. which were of 2 mm diameter. These were not fouled by either push rod or base plate and allowed measurement of acoustic velocity under the applied stress to be measured.

The strains induced in the specimens under stress were measured by strain gauges supplied by Welwyn Strain Measurements Ltd.* The type of gauge used was SK-09-015EH-120. These were also useful for calibrating the apparatus since despite attempts to minimise frictional forces along the push rod these would be likely to occur at least to some extent.

The base plate was held in position by three symmetrically placed stainless steel rods and secured by three nuts. The specimen chamber was closed by a brass can which could mate into position on the base plate and could be moved vertically along the stainless steel support rods. The chamber was connected to the headpiece by a length of 30 cm of ⅛" thin walled stainless steel tubing through which all lead wires passed.

The headpiece of the apparatus contained two tufnel rings to position the push rod (see fig. 5.6) and three input/output ports, two for the sing around which had b.n.c. sockets attached, mounted on P.T.F.E. support blocks and a third for allowing strain gauge leads and thermocouple leads to be passed into the sample space.

The lever bar had small holes drilled vertically into each bearing to allow it to be oiled, thereby ensuring that all parts moved freely. A counterweight could be attached to the opposite end of the lever (not shown) to compensate for the weight of the arm and thus allow all measurements to start from zero applied stress.

---

* Welwyn Strain Measurements Ltd., Armstrong Road, Basingstoke, Hants.

5.2.3 High Hydrostatic Pressure Equipment

High hydrostatic pressures up to 5 kbar were obtained using the S.R.C. high pressure facility at Standard Telecommunications Ltd. (I.T.T.) of Harlow. The apparatus is shown schematically in fig. 5.7. The pressure medium in this case was castor oil in a high pressure cell and compressed by a stainless steel piston. Input and output leads were connected via high pressure sealed lead-throughs in the piston. A high pressure manganin-copper 'O' ring was used to seal the chamber.

5.3 Specimen Preparation

5.3.1 Crystal Growth

The crystals were grown by workers at other universities* or by Metals Research Ltd. The low purity Erbium and Terbium crystals from Metals Research were 98-99% pure, while the Gadolinium and high purity Terbium were 99.9% pure and were grown using the solid state electro-transport method. The resistance ratio for the Gadolinium was also supplied ($\rho_{273}/\rho_{4.2} = 250$). Crystals were in the form of cylinders of about 2 - 3 mm length and 5 - 6 mm diameter. The axis parallel to the direction of the unique axis of the cylinder was specified in all cases, and in most one other axis was marked in the plane of the cylinder.

5.3.2 X-Ray Diffraction

In order to determine the orientation of crystals whose crystallographic directions had not been marked, Laue back reflection photographs were taken using a 50 kV X-Ray set in the Physics Department. The photographs were then compared with known patterns for hexagonal crystals to find the orientation. Alignment of the axes could be made to within $\pm 1^{\circ}$ by this method.

---

* Department of Materials Science, University of Birmingham, Bristol Road, Birmingham B15 2TT.

THE HIGH HYDROSTATIC PRESSURE CELL

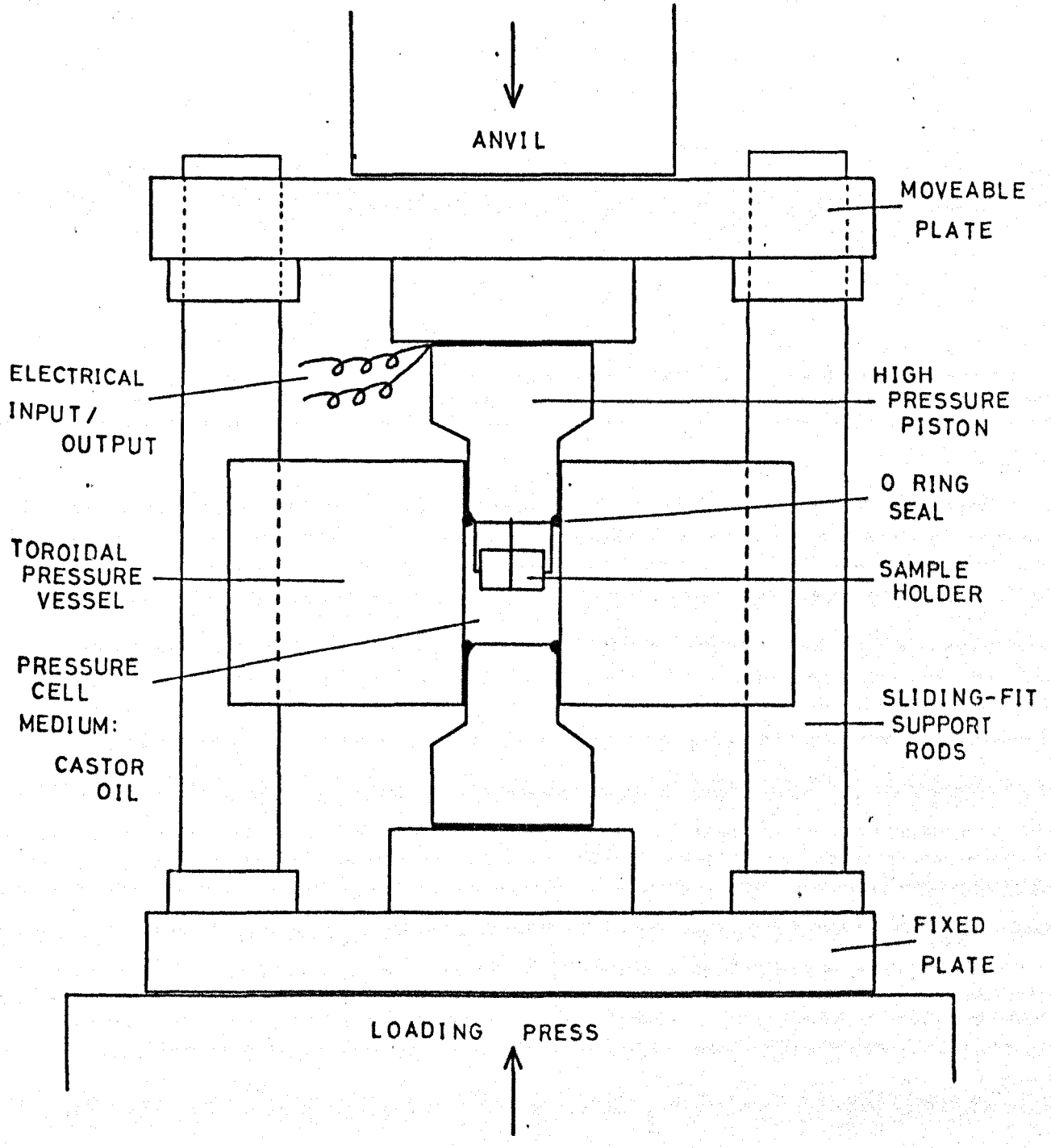

fig. 5.7

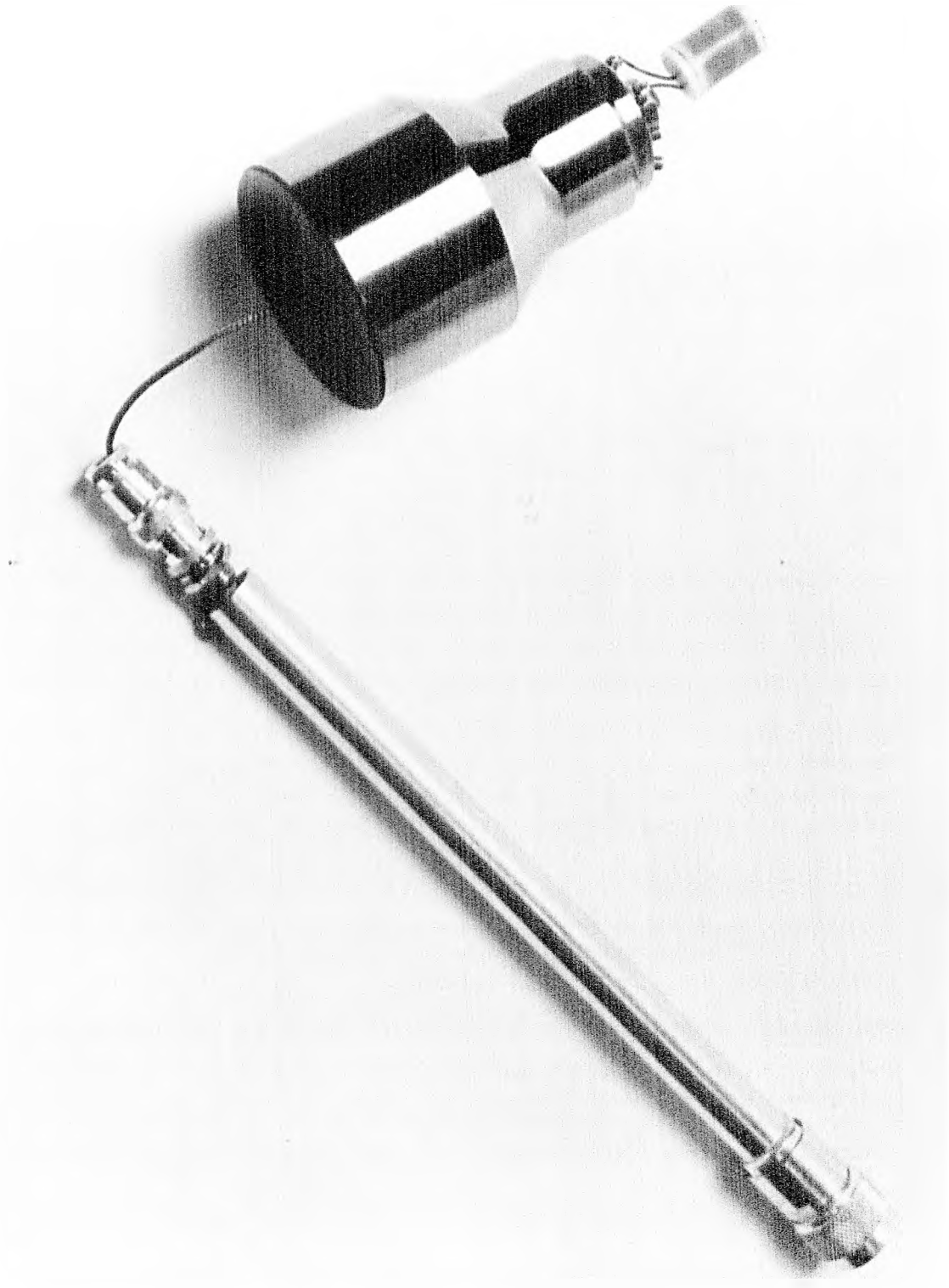

PLATE VIII

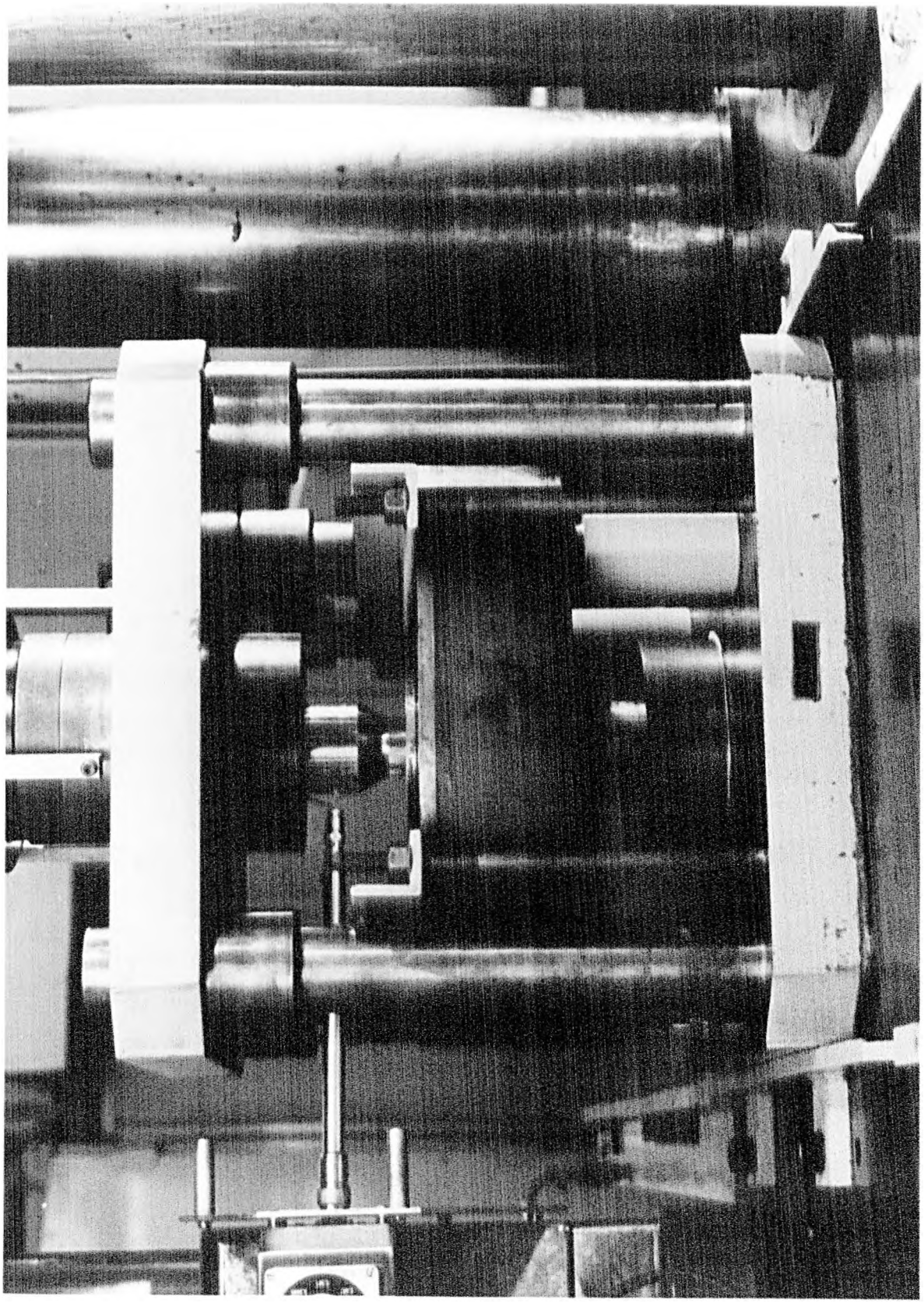

PLATE VII

5.3.3 Spark Machining

When further modification of the crystals was necessary either planing more surfaces for the application of stress or in the one case when a crystal had actually to be cut from a boule the spark machining facilities at the University of Birmingham were used.

This method was chosen since at present it is the best technique for cutting a crystal without damaging it (e.g. by introduction of dislocations) more than is necessary. The machine used was an SMD made by Metals Research Ltd. The planing is achieved by spark discharges between a brass disc rotating in a horizontal plane and the specimen both of which are immersed in a bath of paraffin. This discharge voltage varies up to $\sim$ 250 volts and this causes abrasion of small particles of the solid from the surface. By this method two surfaces of a crystal may be planed flat and parallel to within $\pm$ 1 micron.

5.3.4 Diamond Saw Cutting

In the instances when polycrystalline specimens were used, for example in the preliminary testing of the uniaxial stress apparatus, there was no need to try to eliminate dislocation damage. For these the cutting of faces in the specimens was achieved by using a circular diamond saw manufactured by Metals Research Ltd. to cut two parallel surfaces which were then lapped and polished.

5.3.5 Lapping, Polishing and Etching

Lapping and polishing of crystals was on a hand lapping machine using abrasives and diamond polishing pastes supplied by Engis Ltd. Thickness and parallelism could be checked using a slip gauge.

To remove oxide layers which formed on the surfaces of crystals an etching solution of 50% glacial acetic acid and 50% nitric acid was recommended. Etching was for 30 - 60 seconds at room temperature. To prevent or minimise the formation of oxide layers the purer specimens were stored under vacuum in glass tubes with greased ground glass joints. Other specimens were stored in a desiccator containing self indicating silica gel as a drying agent, which also reduced the rate of contamination.

5.3.6 Transducers and Bonding Materials

The most frequently used type of transducer in this work was piezoelectric quartz in the form of thin discs of diameter 6 mm with opposite faces coated with gold foil electrodes. These were supplied by Gooch and Housego Ltd. and had a resonant frequency of 15 MHz. The transducers were specified as shear or longitudinal wave generators depending on the axis of the quartz crystal which is perpendicular to the plane of the surface. The shear wave transducers had the direction of displacement marked. In this work quartz or CdS transducers were used, although a large number of piezoelectric materials are now available commercially.

In order to generate acoustic waves in a solid a large energy transfer between transducer and specimen is needed. This can not be achieved over a solid-air interface and consequently a material bonding medium between transducer and specimen is needed. The requirements of a good bonding medium have been reported elsewhere [2].

Some bonding materials which were tried were

(i) Nonaq Stopcock Grease
(ii) Dow Corning Silicone Liquid DC200
(iii) Dow Corning Resin 276-V9
(iv) Araldite Epoxy Resin
(v) Rapid Araldite Epoxy Resin
(vi) Phenyl Benzoate
(vii) Vacuum greases and oils.

The Nonaq grease was useful for longitudinal waves for temperatures down to about 140°K. Below this temperature the bond was liable to break due to differential thermal expansion between the specimen and transducer. It was not found satisfactory for shear waves.

The Dow Corning fluids and resins were found useful for temperatures below room temperature and down to about 200°K. The resin needed to be heated to reduce its viscosity before it could be used to bond the transducer.

Phenyl Benzoate was recommended for use with shear waves when both the Nonaq and Dow Corning resins proved unsuitable. Unfortunately this material was impracticable due to the fact that the sing around requires two transducers to be accurately aligned both with respect to a particular crystallographic direction and with each other. The alignment was found to be very difficult to achieve without either the phenyl benzoate crystallising or the alignment being disturbed before the bond was made.

The Araldite epoxy resins were found to be.by far the best bonding materials in the present work. They could be used for both shear and longitudinal waves, and for temperatures down to 4.2°K without bond breakage. The Rapid Araldite was more convenient since it set forming a bond within about 15 minutes, whereas the other required up to 24 hours to cure. The only disadvantage with araldite resins is when the transducer needs to be removed. For this overnight soaking in chloroform is recommended.

Vacuum greases and oils were used only intermittently for bonds at room temperature.

5.4 Temperature, Pressure and Magnetic Field

5.4.1 Temperature Measurement

Temperature measurement was made mainly using thermocouples although instances did occur when platinum resistance thermometers were used, particularly in calibrating the thermocouples, and a mercury in glass thermometer was used to obtain some fixed points above 273°K notably the boiling point of water.

For measurements of temperatures down to 77°K, the liquid nitrogen point, a copper v. constantan thermocouple was used and for temperatures between 4.2°K and 77°K a gold/iron v. chromel thermocouple was preferred. The reference junctions were maintained at 273°K in a mixture of ice and water in a dewar vessel. The other junction was embedded in the body of the sample holder as close to the specimen as possible.

5.4.2 Thermocouple Calibration

Two types of calibration were used for the thermocouples. The simpler method was due to White [3,p133] and depends on fitting a curve of the form,

$$E(T) = AT^3 + BT^2 + CT + D \qquad \ldots.5.1$$

where E(T) is the emf. of the thermocouple at temperature T and A,B,C,D are the coefficients of the polynomial. The coefficient D is the residual emf. when both junctions are at the same temperature and was found by placing both junctions in the ice-water mix. The term was found to be less than ± 1μV and therefore considered negligible.

The calibration therefore resolved into fitting the polynomial

$$E(T) = AT^3 + BT^2 + CT \qquad \ldots.5.2$$

which may be found by measuring the emf. at three fixed points other than 273°K and solving the three simultaneous equations exactly for A, B and C. The values of temperature found using this calibration at

values lying within the range defined by the three calibration points should not be in error (according to White) by more than 2μV representing about ± 0.1 - 0.2 °K. This estimation would seem to be rather optimistic when compared with the second calibration method. Readings outside the range defined by the three calibration points and 273°K are not valid. It should be borne in mind that the quoted error in temperatures represents the error in temperature of the thermocouple junction as measured by the calibration. The error in temperature of the specimen is larger than this and is at best only within ±0.5°K with the methods used here.

The second calibration method depends on the accurate determination of temperature using a platinum resistance thermometer. Measurements were taken of thermocouple emf. against voltage across a platinum resistance thermometer of nominal (i.e. at 273°K) resistance 100Ω using a constant current source of 100μA. From the calculated value of the Z function (see 5.4.3) at each point, the value of temperature was read from tables of Z against temperature [3,p115]. Interpolation between tabulated values was made where necessary as described in 5.4.3.

A table of values of thermocouple emf. against temperature could then be made and a polynomial curve fit of the form,

$$E(T) = AT^5 + BT^4 + CT^3 + DT^2 + GT + K \qquad \ldots.5.3$$

could be made from the data using a least squares method.

The method [4] of obtaining the temperatures from Z values which are intermediate between values available in tables is outlined in 5.4.3 and given in detail in the appendix.

In both methods the data was handled by computer and the programs will be found in the appendix. Tables of values of thermocouple emf. against temperature taken from the polynomial approximations were printed out at intervals of 0.2°K.

That the second method was more accurate can not be doubted. An assessment of the relative performances of the two methods confirmed this. However, the simplicity of the first method and the fact that the maximum discrepancies between the two methods corresponded to temperature of less than $1^{o}K$ when errors of at least $0.5^{o}K$ in specimen temperatures were expected meant that in practice it was preferred.

5.4.3 Platinum Resistance Thermometer

A platinum resistance thermometer of nominal resistance 100Ω was used to calibrate the thermocouples. The resistance of the thermometer was measured at $273^{o}K$ and at the helium point $4.2^{o}K$. The resistance R_T at any subsequent temperature was used to calculate the value of the Z function

$$Z = \frac{R_T - R_{4.2}}{R_{273} - R_{4.2}} \qquad \ldots.5.4$$

Tables of values of Z against temperature are available [eg.3,p115] and any necessary interpolation was made by using polynomial approximations over four regions bounded by $23^{o}K$, $47^{o}K$ and $150^{o}K$. The Z function varies differently with temperature over these four regions hence four separate approximations were made giving four independent polynomials, one for use with interpolation in each of the regions. Again computer programs were used to ease the calculation. A graph of Z against T obtained by this method is shown in appendix 6.

5.4.4 Temperature Control

The temperature of the specimen was controlled by application of an emf. to the heater coil on the specimen holder. The heater was controlled by a commercial temperature controller type 3010 MkII supplied by Thor Cryogenics Ltd. The emf. of the thermocouple was compared to a preset value determined by the experimenter. Any positive difference

was amplified and the amplified emf. used to supply the heater, while any negative difference was ignored. By this method if the temperature registered by the sensing thermocouple was below the preset value the applied emf. to the heater raised the temperature. If the temperature exceeded the preset level the heater was automatically set to zero.

A maximum of 40 Watts was supplied to a 150Ω chromel resistance coil wound on the sample holder. Separate thermocouples were used for temperature measurement on a D.V.M. and for the temperature controller. The D.V.M. used was a Hewlett Packard 3490A multimeter with a sensitivity of 1μV. The temperature of the specimens was measured to an accuracy of ± 0.5^{o}K, although temperatures below 15^{o}K were expected to be in more serious error due to the inaccuracy of the platinum resistance calibration below this temperature.

5.4.5 Magnetic Field and its Measurement

An eleven inch commercial electromagnet was used to apply magnetic fields of up to 2.5T to the specimens. The current coils of the magnet were supplied by a Mullard Precision Current Controller type MS4113, which could be operated either manually or by an automatic electronic sweep unit MS4115. The magnet was water cooled using a closed circuit water cooling system to minimise corrosion of the cooling pipes.

The magnetic field attainable by the electromagnet could be varied by adjusting the gap between the pole pieces. The field was measured using a Scalamp Fluxmeter search coil available from W. G. Pye & Co. Ltd. This consisted in one case of 100 turns for measuring fields less than 0.7T and of 10 turns for measuring larger fields. The calibration was plotted as a function of coil current.

5.4.6 Measurement of Deformation using Strain Gauges

In order to measure the deformation of the specimens under uniaxial stress strain gauges available from Welwyn Strain Measurements were used. The gauges depend on the variation of resistance with strain of a karma alloy grid embedded in a glass fibre reinforced epoxy resin backing material. The gauge type found most suitable was Gauge SK-09-015EH-120 which had overall physical dimensions of about 3 mm x 2 mm.

5.4.7 Strain Gauge Preparation Technique

The bonding of strain gauges onto the surface of a specimen requires a detailed technique of abrading and degreasing the surface and careful bonding. These may be found in the Micromeasurements Bulletin B-129 (May 1976) concerning cleaning and Micromeasurements Bulletin B-130-3 (May 1974) concerning bonding. The adhesive used was M-Bond 610 an epoxy resin which must be stored at sub-zero temperature for preservation. The specimen and bond were annealed at 200^{o}C for two hours to allow the bond to 'cure'.

5.4.8 Measurement of Resistance using a Bridge Network

In order to measure accurately the change in resistance of the gauge the Wheatstone bridge network shown in fig. 5.8 was constructed. The gauge and dummy are remote being connected to the main circuit by a length of screened three core flex encased in the usual plastic sleeve with an additional thick P.V.C. cable sleeve to reduce any thermal variation in the resistance of the leads. By keeping the leads to the gauge and dummy together in this way, the effect of any thermal variation in resistance of the leads which does occur, despite the precautions, will be minimised since the same change in resistance will occur in both arms of the bridge.

CIRCUIT DIAGRAM FOR THE STRAIN GAUGE BRIDGE

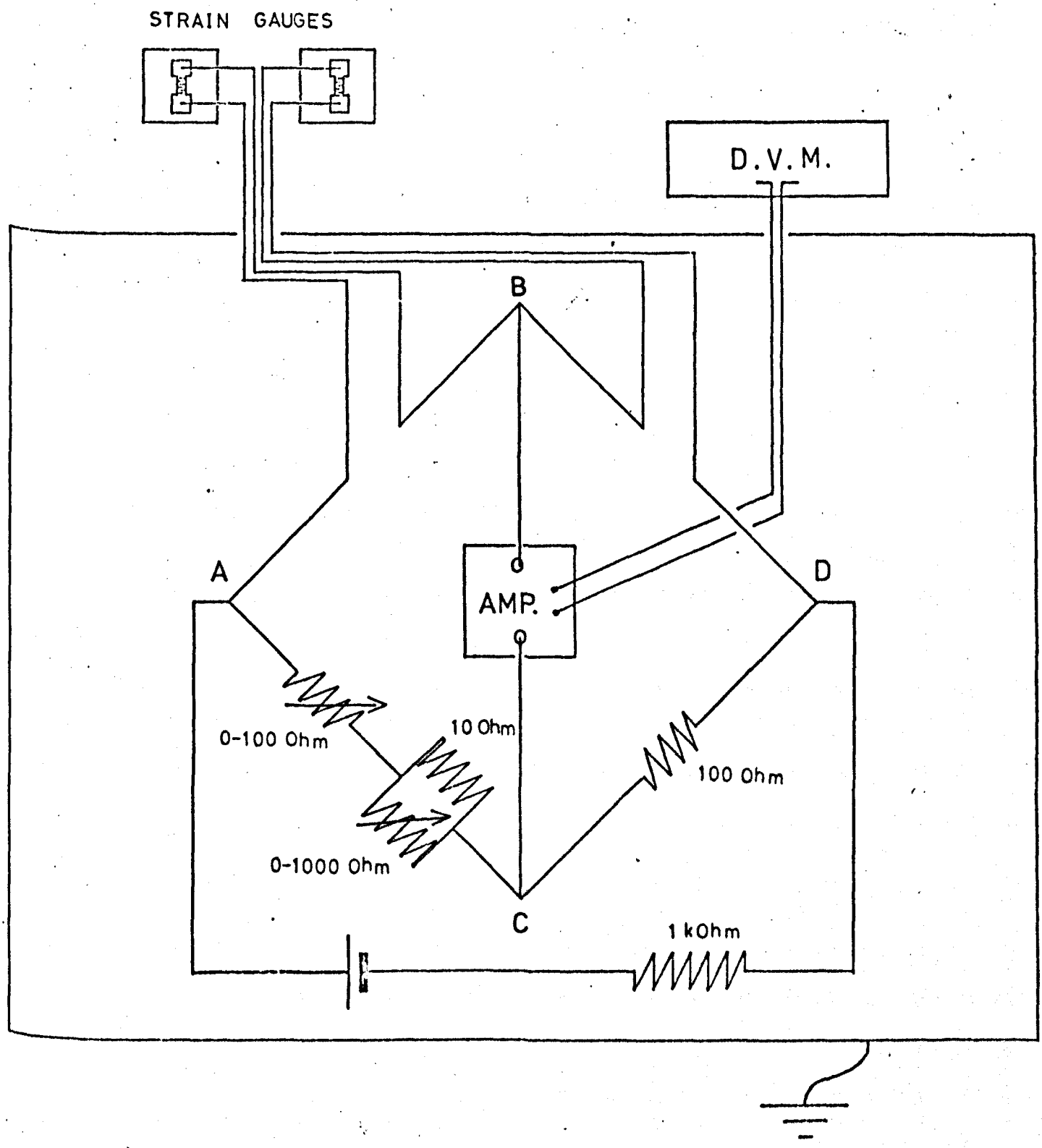

fig. 5.8

The dummy is placed as close to the gauge as possible and bonded onto a similar material to compensate for any changes in resistance due to thermal expansion. By this method it was expected that the only variation in resistance detected by the bridge is due to strain in the specimen.

The strain gauge resistance under zero strain is 120Ω ± 0.6%. The gauge factor G is defined as the fractional change in resistance per unit strain,

$$G = \frac{1}{R} \frac{dR}{ds} \qquad \ldots.5.5$$

where ds is the strain, i.e. $ds = d\ell/\ell$. For the gauges used G = 2.05 ± 2.0% at 75°F room temperature.

5.4.9 Measurement of Strain

If the change in voltage across the points B and C (see fig. 5.8) from the balanced position is ΔV due to a change in resistance of the gauge dR_g/R_g, then

$$\Delta V = k \cdot \frac{dR_g}{R_g} \qquad \ldots.5.6$$

where k is a constant. The voltage change is thus proportional to the fractional change in resistance. The bridge may be calibrated by making changes in the coarse resistor on the arm AC of dR_{AC} and measuring the corresponding voltage change across AB, ΔV_{AB}

$$\Delta V_{AB} = k. \frac{dR_{AC}}{R_{AC}} \qquad \ldots.5.7$$

and in this case both ΔV_{AB} and dR_{AC}/R_{AC} are known, which allows k to be found.

When the bridge is in operation this value of k may be used in the equation 5.6 to give the change in resistance of the strain gauge. By

definition $dR_g/R_g = G.d\ell/\ell$ from equation 5.5 and hence

$$ds = \frac{1}{k.G} \Delta V \qquad ....5.8$$

5.4.10 Voltage Amplification

In order to increase the out-of-balance voltage, ΔV, an ANCOM 15C-3a amplifier with a gain of x1000 was used. The sensitivity of the bridge network was ± 0.1mV after amplification, which meant that changes in voltage across BC down to 0.1μV before amplification could be detected. Changes in R_{AC} of 0.1Ω gave changes in voltage ΔV_{BC} of typically 15mV after amplification. Consequently, changes in resistance down to ± 0.001Ω could be measured giving a limit of sensitivity of about 0.15 mV. This meant that measurement of strain down to a limit of 0.5×10^{-5} or 5 μ.strain was possible with the existing bridge network.

5.4.11 Interference and Stabilisation of the Bridge Network

The strain gauge leads were found to be picking up r.f. signals from the sing around leads which were unscreened inside the uniaxial pressure apparatus. Due to the small size of the strain gauge and its associated leads it was impractical to consider screening. Instead it was found that if the sing around was switched off (i.e. left in 'sing around mode' without supplying the initial pulse) while the strain measurements were made the results were satisfactory.

Capacitors of 0.47μF (ceramic) were placed across the inputs from the gauge and dummy leads to eliminate any stray r.f. pick up that did occur. A similar capacitor was placed across the output from the amplifier. All leads outside the screened box were shielded. The bridge with these modifications was found to be stable to ± 0.02 mV compared with the previous ± 0.1 mV.

5.5 Irradiation of Specimens

5.5.1 Problems Associated with the Measurement of Elastic Constants under Stress

Uniaxial stresses large enough to produce measurable changes in the transit time of ultrasound through single crystals are also likely to cause movement of dislocations inside the solid. The dislocation mobility changes the observed velocity of sound in the crystal and affects the measured elastic constants and their stress derivatives. The mechanism of this process is described in the appendix.

The contribution of these dislocations to the elastic moduli may be linear or non linear. It was hoped originally that the linear variation of elastic constant with stress, the third order constant, could be extracted from non linear effects due to dislocations by making polynomial fits to the data and removing the non linear terms. This was found to be unsuccessful, and later it was realised that the technique had already been attempted [6] with the same result. The fact that the dislocation contribution may be linear makes it difficult to distinguish between lattice anharmonicity and the dislocation effects.

There are two possible solutions to the problem. One is to use small uniaxial stresses which do not give rise to significant dislocation mobility, in conjunction with a method of measuring very small changes in elastic constant. Another method is to use some way of pinning the dislocations to prevent their movement contributing to the elastic constant. The first method is not feasible at present and previous work has been concentrated on methods of pinning.

5.5.2 Pinning of Dislocations

The problem of dislocation effects has been discussed by Truell et al [7]. The most successful methods to date have been neutron or gamma irradiation of the specimen or the use of prestressing techniques. Hiki and Granato [8] showed that the apparent elastic range (i.e. when stress is proportional to strain) can be extended by prestressing. They also observed in the untreated specimens deviations from linearity in the graph of elastic constant against stress in the initial parts of each measurement; that is for low stresses on a decreasing stress run. This was similar to observations made in the present work.

5.5.3 Criterion for Elimination of Dislocation Contribution

Salama and Alers [9] were able to show that a criterion for determining whether dislocations effects had been eliminated was when uniaxial and hydrostatic pressure derivatives of the elastic moduli were compatible. Linearity of the graph of elastic modulus against stress was shown to be an insufficient condition for determining the reliability of results because, as mentioned above, the dislocation contribution may be linear or non linear.

5.5.4 Pinning by Irradiation with Gammas or Neutrons

Salama and Alers were also able to show that irradiation with a large flux of gamma or neutrons produced no detectable change in attenuation of ultrasound with stress and gave a linear variation of elastic constant with stress which was in good agreement with hydrostatic pressure measurements. It was concluded that the dislocation effects had been adequately suppressed.

Their gamma irradiation was carried out for 28 hours close to a 4000 Ci Cobalt-60 gamma source at a temperature of 150^{o}C. Neutron irradiation was in the core of a nuclear reactor producing a flux of

1.4×10^{13} neutrons/cm^2.sec for two hours giving a fluence of $\sim 10^{17}$ neutrons/cm^2.

Thomas [6] also used neutron irradiation to suppress dislocation effects in single crystals of aluminium. He found the same criterion for elimination of dislocation contributions as reported by Salama and Alers, although he had tried to eliminate non linear contributions from his data without success. The criterion was satisfied after neutron irradiation. The energy of neutrons reported was 100keV.

In the present work the single crystal specimens of Erbium were irradiated by placing them inside the core of the Universities Research Reactor at Risley Warrington for 24 hours at 120°C giving an integrated flux of about 10^{17} fast neutrons per square centimetre.

CHAPTER 6

The Magnetic Properties of Heavy Rare Earths

6.1 Introduction

6.1.1 Electronic Structure of the Rare Earths

The rare earth elements Lanthanum to Lutetium form a class of materials which, although they have very similar chemical properties, exhibit a variety of different magnetic structures. The magnetic behaviour of these metals can be explained at least qualitatively in terms of two main factors, the exchange and crystal field interactions. Other contributions to the magnetic energy do exist and of these the most important is the magnetoelastic effect.

In a rare earth crystalline solid the outer 5d and $6s^2$ electrons migrate throughout and form the conduction electron band. The 4f shell which is filled during the series, is screened from the outside by the 5s and 5p shells, and is responsible for the magnetic moment of the ions. The electronic structures of these elements is given in fig. 6.1. It can be shown [1] that the 4f electron configuration acted upon by the crystal field and coupled by the exchange interactions gives a reasonably simple explanation of the complex magnetic properties observed throughout the Lanthanide series.

6.1.2 Crystal Structures

The crystal structures of the light rare earths Lanthanum to Europium are mainly double hexagonal close packed (dhcp), while the heavy rare earths Gadolinium to Thulium are hexagonal close packed (hcp). A table of the crystal structures is given in fig. 6.2. The c/a ratios for these crystals vary from 1.591 in Gadolinium to 1.584 in Lutetium passing through a minimum of 1.571 between Holmium and Thulium. This compares with the ideal value of 1.632.

The Outer Electron Configurations of the Rare Earth Atoms $La_{57} - Lu_{71}$

R		R^{3+}	Ionic Radius Å
La	$5s^2.5p^6.5d^1.6s^2$	$5s^2.5p^6$	1.061
Ce	$4f^2.5s^2.5p^6.6s^2$	$4f^1.5s^2.5p^6$	1.034
Pr	$4f^3.5s^2.5p^6.6s^2$	$4f^2.5s^2.5p^6$	1.013
Nd	$4f^4.5s^2.5p^6.6s^2$	$4f^3.5s^2.5p^6$	0.995
Pm	$4f^5.5s^2.5p^6.6s^2$	$4f^4.5s^2.5p^6$	0.979
Sm	$4f^6.5s^2.5p^6.6s^2$	$4f^5.5s^2.5p^6$	0.964
Eu	$4f^7.5s^2.5p^6.6s^2$	$4f^6.5s^2.5p^6$	0.950
Gd	$4f^7.5s^2.5p^6.5d^1.6s^2$	$4f^7.5s^2.5p^6$	0.938
Tb	$4f^9.5s^2.5p^6.6s^2$	$4f^8.5s^2.5p^6$	0.923
Dy	$4f^{10}.5s^2.5p^6.6s^2$	$4f^9.5s^2.5p^6$	0.908
Ho	$4f^{11}.5s^2.5p^6.6s^2$	$4f^{10}.5s^2:5p^6$	0.894
Er	$4f^{12}.5s^2.5p^6.6s^2$	$4f^{11}.5s^2.5p^6$	0.881
Tm	$4f^{13}.5s^2.5p^6.6s^2$	$4f^{12}.5s^2.5p^6$	0.869
Yb	$4f^{14}.5s^2.5p^6.6s^2$	$4f^{13}.5s^2.5p^6$	0.858
Lu	$4f^{14}.5s^2.5p^6.5d^1.6s^2$	$4f^{14}.5s^2.5p^6$	0.848

The inner electron structure remains the same throughout the series

$1s^2.2s^2.2p^6.3s^2.3p^6.3d^{10}.4s^2.4p^6.4d^{10}$

fig. 6.1

Crystallographic Properties of the Rare Earths

	Crystal Structure	Density $g.cm^{-2}$	a Å	c Å	c/a *	Melting Point °C
La	dhcp	6.166	3.772	12.144	1.610	920
Ce	dhcp	6.771	3.673	11.802	1.607	798
Pr	dhcp	6.772	3.672	11.833	1.611	931
Nd	dhcp	7.003	3.659	11.799	1.612	1018
Pm		7.26	3.65	11.65	1.600	
Sm	rhom	7.537	3.626	26.18	1.605	1072
Eu	bcc	5.253	4.580			822
Gd	hcp	7.898	3.634	5.781	1.591	1311
Tb	hcp	8.234	3.604	5.698	1.581	1360
Dy	hcp	8.540	3.593	5.655	1.574	1409
Ho	hcp	8.781	3.578	5.626	1.572	1470
Er	hcp	9.045	3.560	5.595	1.572	1522
Tm	hcp	9.314	3.537	5.558	1.571	1545
Yb	fcc	6.972	5.483			824
Lu	hcp	9.835	3.505	5.553	1.584	1656

* c/a ratios of dhex crystals are given as $c/_{2a}$

fig. 6.2

Removal of the 5d and $6s^2$ electrons into the conduction band leaves a tripositive ionic core located at the lattice sites. The rare earths therefore behave as tripositive ions with highly localised magnetic moments due to the tightly bound 4f electrons. The total moment of each atom is given by application of Hund's rules as shown in the spectroscopic properties in fig. 6.3. The spin orbit coupling is strong giving $J = L - S$ for the light rare earths and $J = L + S$ for the heavy rare earths.

6.1.3 Effects of the Crystal Field on Magnetic Ordering

In the heavy rare earth crystals the crystalline field has an important effect upon the detailed structure of magnetic ordering, however it is still of secondary importance compared with the exchange interaction in these materials, since it is the latter which determines whether or not ordering occurs. In the light rare earths the 4f shells are much larger and the effects of the crystal field are correspondingly greater so that they can affect the existence or otherwise of magnetic ordering.

A phenomenological theory of magnetic ordering in the rare earths has been built up in which the contribution of the conduction electrons to the total magnetic properties is ignored. The behaviour only of a system of localised 4f electrons with associated magnetic moments is considered, with various interacting forces between these.

6.2 The Principal Magnetic Interactions

6.2.1 Contributions to the Magnetic Hamiltonian

The existence of a particular type of magnetic ordering in the rare earths is determined by the minimum magnetic free energy under the given conditions. This magnetic energy may be derived from the total Hamiltonian and has the following main contributing terms

Spectroscopic Properties of the Rare Earth Series La_{57} - Lu_{71}

	L	S	J	λ	$g\sqrt{J(J+1)}$
La	0	0	0	0	0.00
Ce	3	$^1/_2$	$^5/_2$	$^6/_7$	2.56
Pr	5	1	4	$^4/_5$	3.58
Nd	6	$^3/_2$	$^9/_2$	$^8/_{11}$	3.62
Pm	6	2	4	$^3/_5$	2.68
Sm	5	$^5/_2$	$^5/_2$	$^2/_7$	0.84
Eu	3	3	0	-	0.00
Gd	0	$^7/_2$	$^7/_2$	2	7.94
Tb	3	3	6	$^3/_2$	9.70
Dy	5	$^5/_2$	$^{15}/_2$	$^4/_3$	10.60
Ho	6	2	8	$^5/_4$	10.60
Er	6	$^3/_2$	$^{15}/_2$	$^6/_5$	9.60
Tm	5	1	6	$^7/_6$	7.60
Yb	3	$^1/_2$	$^7/_2$	$^8/_7$	4.50
Lu	0	0	0	0	0.00

where g is the gyromagnetic ratio and $\mu_B = g\sqrt{J(J-1)}$ gives the effective magnetic moment of the atom in Bohr magnetons

fig. 6.3

$$H_{mag} = H_{iso.ex} + H_{an.ex} + H_{c.f.} + H_{m.s.} + H_z \quad ....6.1$$

where the first two terms are the exchange energy Hamiltonian , $H_{c.f.}$ is the crystal field term, $H_{m.s.}$ is due to magnetostriction and H_z is the Zeeman energy in an applied magnetic field.

6.2.2 The Exchange Interaction

As explained in section 3.2.3 and in more detail in Appendix 2 the exchange interaction arises directly from the Pauli exclusion principle. A spin moment $\underline{s}_1$ located at $\underline{r}_1$ and a spin moment $\underline{s}_2$ at $\underline{r}_2$ give an exchange energy E_{ex} of

$$E_{ex} = -J(\underline{r}_1 - \underline{r}_2)\, \underline{s}_1 \cdot \underline{s}_2 \quad ....6.2$$

In the rare earths the amount of direct overlap between 4f orbitals on neighbouring lattice sites is negligible, so that exchange between these electrons is small. However, the 4f electrons do overlap with s electrons in the conduction band and the net result of this is an indirect exchange mechanism between the 4f orbitals by means of the direct s-f exchange. The best known model of this indirect exchange is the RKKY model [2,3,4] which has the same general form for the exchange energy between 4f orbitals as in the direct exchange.

6.2.3 The s-f Exchange

The exchange integral between the bound 4f electrons and the free s conduction electrons will have the form of equation A2.10

$$J_{sf}(\underline{k},\underline{k}') = \sum_i \int\int \psi^*(\underline{r}',\underline{k})\ \psi_{4f}(\underline{r}_i) \cdot \frac{e^2}{|\underline{r}_i - \underline{r}'|}\, \psi(r_i k')\psi_{4f}(\underline{r}')d\underline{r} \quad ....6.3$$

// spins

where the ψ are the wave functions for s electrons and ψ_{4f} for the 4f electrons.

This energy favours parallel alignment of the s and 4f electron moments in the rare earths, so that the conduction electron moments add to the ionic 4f moments [5]. In the RKKY theory the exchange interaction is assumed to be isotropic and hence only a function of $|\underline{r}_i - \underline{r}_j|$. In practice it is necessary to include a term due to anisotropic exchange [6,P.19] which is the term $H_{an.ex.}$ obtained in the magnetic Hamiltonian.

6.2.4 The Indirect 4f - 4f Exchange

To a first approximation the indirect 4f - 4f exchange has the same form as the direct exchange which is

$$H_{ex} = \sum_{R_{ij}} J(R_{ij}) \underline{s}_i . \underline{s}_j \qquad \ldots.6.4$$

where $\underline{R}_{ij} = \underline{r}_i - \underline{r}_j$, the vector between the ith and jth electron.

The magnetic moment of the atom $\underline{J}$ is a constant rather than $\underline{s}$ because of strong spin-orbit coupling ($\underline{s} - \underline{L}$). The exchange may therefore be expressed in terms of $\underline{J}$ by projection of $\underline{s}$ into $\underline{J}$, which is $(g-1)\underline{J}$ so that equation 6.4 becomes

$$H_{ex} = -(g-1)^2 \sum_{R_{ij}} J(R_{ij}) . \underline{J}_i . \underline{J}_j \qquad \ldots.6.5$$

The exchange energy is consequently larger in the heavy rare earths than in the light rare earths because $\underline{J}$ is generally greater in the former, as can be seen from the table of spectroscopic properties in fig. 6.3.

6.2.5 The RKKY Model

For the heavy rare earths the mean radius of the tightly bound 4f orbitals is only one tenth of the interatomic spacing. Direct overlap of the wavefunctions is therefore negligible. The exchange interaction between the 4f electrons which is responsible for the production of ordered magnetic states therefore proceeds via a direct 4f - s exchange involving polarisation of the conduction s electrons.

In the RKKY theory [2,3,4] the exchange integral between the s and 4f electrons is assumed to be isotopic and consequently depend only on the distance between the electrons.

$$J_{sf}(\underline{R}_{ij}) = J_{sf}(\underline{r}_i - \underline{r}_j) \quad \ldots.6.6$$

and further it is taken to be constant, say J_o

$$J_{sf} = J_o \quad \ldots.6.7$$

So that the exchange interaction between a conduction s electron $\underline{s}_s$ at $\underline{r}_s$ and a bound f electron $\underline{s}_f$ at $\underline{r}_f$ is

$$E_{sf} = -J_o \, \underline{s}_f \cdot \underline{s}_s \quad \ldots.6.8$$

This will cause polarisation of the conduction electrons, since for example, if J_o is positive then conduction electrons whose moment is parallel to $\underline{s}_f$ will prefer to be close to the ion since this gives a minimum of the exchange energy, while conduction electrons with spins antiparallel will be distant from the ion.

The exchange energy between the 4f electrons then has the same general form as in the direct exchange and results in an expression of the form

$$E_{4f4f} = -\sum_{i,j} J_{4f4f}(\underline{R}_{ij}) \underline{s}_i \cdot \underline{s}_j \quad \ldots.6.9$$

where now the $J_{4f4f}(\underline{R}_{ij})$ and $J(\underline{R}_{ij})$ are not necessarily the same.

The 4f-6s exchange integral for some rare earths has been calculated by Milstein and Robinson [7]. In particular they were interested in its variation with interatomic spacing. Their results indicated that the 4f-6s exchange integral was relatively insensitive to changes in interatomic spacing a result which might be expected in keeping with the assumption of equation 6.7 in the RKKY theory.

6.2.6 The Crystal Field Interaction

The exchange interactions align magnetic moments in certain directions relative to each other. This may cause all moments to be parallel or for nearest neighbours to be antiparallel as in a simple antiferromagnet, or for moments in neighbouring hexagonal planes to be inclined at a fixed angle to one another as in helical antiferromagnetism. The exchange interaction can not however explain why the moments may favour a particular crystallographic direction to any other, for example, the alignment of moments along the c-axis in ferromagnetic Gadolinium between 240°K and 293°K, or alignment in the base plane b axis in ferromagnetic Terbium below 214°K.

In the heavy rare earths the next most important contribution to the magnetic Hamiltonian is that due to the electrostatic crystal field experienced by the 4f electrons. The charges around any ion in a solid will give rise to an electric field at the ion, and in the rare earths the tightly bound 4f electrons which are localised at the ionic sites will experience this field. The 4f electron charge clouds are highly anisotropic and will therefore experience a torque which tends to align their moments along particular crystal directions.

The general form of the potential energy will then be given by [6]

$$V(\underline{r}_i) = \int_{\substack{\text{all}\\ \text{crystal}}} \rho(\underline{R}) \cdot \frac{e}{|\underline{r}_i - \underline{R}|} \, d\underline{R} \qquad \ldots.6.10$$

where $\underline{r}_i$ is the position vector of a particular 4f electron and $\rho(\underline{R})$ is the charge density at the general point $\underline{R}$. If $\rho(R)$ lies entirely outside the ion then the potential $V(\underline{r}_i)$ will be a solution of Laplace's equation as explained in Appendix 5 and consequently this can be expressed as a series solution

$$V(r,\theta,\phi) = \sum_{\ell} \sum_{m} A_{\ell}^{m} \cdot r^{\ell} \cdot Y_{\ell}^{m}(\theta,\phi) \qquad \ldots.6.11$$

and when the symmetry of the hexagonal crystal is taken into account this reduces to the form

$$V(\underline{r}_i) = A_2^0.r^2.Y_2^0(\theta,\phi) + A_4^0.r^4.Y_4^0(\theta,\phi) + A_6^0 r^6 Y(\theta,\phi)$$

$$+ A_6^6.r^6\,[Y_6^6(\theta,\phi) + Y_6^{-6}(\theta,\phi)] \qquad ....6.12$$

where the $Y_\ell^m(\theta,\phi)$ are spherical harmonics. This may be expressed in the form given in the Appendix 5 using Legendre polynomials

$$V(r,\theta,\phi) = K_2^0 P_2^0(\cos\theta) + K_4^0.P_4^0(\cos\theta) + K_6^0.P_6^0(\cos\theta) + K_6^6 \sin^6\theta.\cos 6\phi$$

$$....6.13$$

The expression favoured by the experimentalists may be derived from this by grouping together the powers of $\sin\theta$ and this gives

$$V(r,\theta,\phi) = K_2^1 \sin^2\theta + K_4^1 \sin^4\theta + K_6 \sin^6\theta + K_{66}^1 \sin^6\theta\cos 6\phi$$

$$....6.14$$

measurement of anisotropy using this equation necessarily includes any anisotropic exchange.

6.2.7 Physical Meaning of Terms in the Crystal Field Expansion

The A_ℓ^m terms in equation 6.12 represent the electric field components of the appropriate symmetry in the crystal while the $r^\ell.Y_\ell^m(\theta,\phi)$ are the various multiples of the electron distribution. All matrix elements with $\ell > 6$ are zero for hexagonal symmetry. The A_2^0, A_4^0 and A_6^0 coefficients represent the axial anisotropy in a hexagonal crystal while the A_6^6 represent the anisotropy in the base plane. Since the minimum of the anisotropy potential represents the stable magnetisation direction, negative values of A_2^0, A_4^0 and A_6^0 favour c axis alignment, while positive values favour base plane directions.

The magnetocrystalline anisotropy can be very strong giving energies equivalent to field strengths of 100T and therefore making contributions to the magnetic Hamiltonian approaching the magnitude of the exchange interaction. In heavy rare earths however the exchange interaction is still the dominant effect.

6.2.8 Magnetic Anisotropy in the Heavy Rare Earths

The relative magnitudes of the anisotropy coefficients determines the fine detail of magnetic ordering in the heavy rare earths. The expression for the anisotropy 6.13 and its regrouped form 6.14 were used by Rhyne and Clark [8] in their determination of the anisotropy coefficients of Terbium and Dysprosium. For most of the heavy rare earths the K_2^0 which gives the axial anisotropy corresponding to the A_2^0 potential, is the dominant term. The K_6^6 base plane is about 100 times smaller than K_2^0 while the other terms K_4^0 and K_6^0 are intermediate in value. These last two are important in stabilising the conical magnetic structures in elements such as Erbium and Holmium.

The majority of the magnetic properties of the rare earths can be explained at least qualitatively in terms of these two major contributions to the magnetic energy given by equations 6.5 and 6.13. The crystal field gives a particular contribution to the magnetic Hamiltonian of the 4f electrons due to the presence of a Coulomb field of the neighbouring ions. Therefore the crystal field can not give rise to cooperative magnetic effects such as order-disorder transitions.

6.2.9 Magnetostriction

The final two terms in the magnetic Hamiltonian are the magnetostrictive and Zeeman energies. The magnetostrictive energy consists of two components

$$H_{ms} = H_{me} + H_e \qquad \ldots.6.15$$

where H_e is the elastic energy associated with homogeneous strain components and H_{me} is the magnetoelastic energy which couples the spins to the strains [9].

Work has been done on the magnetostrictive effects in the rare earths [10,11] and on the magnetoelastic effects [12,13] and their relation to the thermal expansion behaviour. According to Bozorth a close

relationship exists between the magnetoelastic effects and the crystal anisotropy.

Greenough [13] suggests that the thermal expansion and Néel temperature of Dysprosium are dependent on the residual internal strain in the specimen.

6.3 Magnetic Ordering in the Rare Earths

6.3.1 Phenomenological Theory

The phenomenological theory of rare earth magnetic ordering involves a distinction being made between the localised magnetic 4f electrons and the outer 5d and $6s^2$ conduction electrons. The magnetic contributions of the outer electrons are ignored in favour of the larger contributions due to the 4f shell. This works excellently for the heavy rare earths Gadolinium, Terbium, Dysprosium, Holmium and Erbium and gives a reasonably good explanation of the properties of the light rare earths. It is however completely unsuitable for some of the more complex magnetic properties of Cerium and Ytterbium.

6.3.2 Effects of the Crystal Field on Ordering

Much of the early work on the theory of rare earth spin structures approached the problem by considering the interactions of the 4f electrons with the crystal field. The crystal field for the hexagonal lattice was determined in its operator form by Elliott and Stevens [14] as

$$V(\underline{r}_i) = A_2^0\langle r^2\rangle\alpha_J O_2^0 + A_4^0\langle r^4\rangle\beta O_4^0 + A_6^0\langle r^6\rangle\gamma_J O_6^0 + A_6^6\langle r^6\rangle\gamma_J O_6^6 \quad \ldots.6.16$$

where the various terms can be seen to correspond to those of equation 6.12. Calculations show that the effects of the crystal field are dominantly through the A_2^0 potential. The sign of the Stevens factor α_J gives the relation of the quadrupole of the 4f electrons to the J direction. The values of the crystal field potentials are $A_2^0 = -300\ cm^{-1}$, $A_4^0 = -60\ cm^{-1}$,

$A_6^0 = 15\ cm^{-1}$ and $A_6^{-6} = -90\ cm^{-1}$ according to Taylor and Darby [5].

In Terbium, Dysprosium and Holmium the calculated α_J are negative and the prediction of crystal field theory consequently tends to align the magnetic moments perpendicular to the c axis, which is in agreement with the known magnetic structures of these elements. In Erbium α_J is positive hence predicting alignment parallel to the c axis. The antiferromagnetic state of Erbium has magnetic moments aligned both parallel and antiparallel to the c axis, in keeping with the A_2^0 potential. However, in the ferromagnetic phase and also in the antiferromagnetic regime between 53° and $20^\circ K$ it has a component in the base plane which orders helically and corresponds to the effect of the A_6^0 potential. The effects of the various terms were given by Taylor and Darby and are reproduced in fig. 6.4.

6.3.3 Effect of the Exchange Interaction

Although the crystal field calculations were able to show whether the magnetic moments would lie along the c axis or in the base plane, and further, through the A_6^6 term which of the base plane axes was preferred, they were unable to explain why the magnetic moments in successive planes should lie parallel or at a fixed angle, the turn angle, to one another. That is, they were unable to explain cooperative phenomena, at least in the heavy rare earths.

The original attempt at using the exchange interaction to explain the magnetic structure of Dysprosium was by Enz [15]. Dysprosium has a helical antiferromagnetic structure with the magnetic moments confined to the basal plane between temperatures of $178^\circ K$ and $85^\circ K$. Below $85^\circ K$ it is ferromagnetic with moments aligned along an a axis.

In the helical antiferromagnetic phase each hexagonal layer or base plane is assumed to be ordered ferromagnetically with the orientation varying from plane to plane. If the exchange interaction between the n th

The Effect of Various Crystal Field Terms on the easy direction of magnetisation. Directions are w.r.t. the c axis except A_6^6 w.r.t. a axis in base plane. Relative magnitudes of the different terms are also given.

	Gd	Tb	Dy	Er
$\alpha_J A_2^0$		$\perp$	$\perp$	//
$\beta_J A_4^0$		//	$\angle$	//
$\gamma_J A_6^0$		//	$\angle$	$\angle$
$\gamma_J A_6^6$		30° to a axis	0° a axis	0° a axis
$2\alpha_J J^2$		0.73	0.71	0.29
$8\beta_J J^4$		1.27	4.48	3.36
$16\gamma_J J^6$		0.84	2.9	5.9

fig. 6.4

and (n+1)th planes is denoted by J_1 and between the n th and (n+2)th by J_2 etc., and if the angle of the arbitrary origin is θ_n, then the total exchange energy of the crystal is obtained by summing equation 6.9 over the whole crystal.

$$E_{ex} = - \sum_m \sum_n J_m . \cos(\theta_{m+n} - \theta_n) . s^2 \qquad ....6.17$$

where the magnitude of s is independent of m and n, and only its direction is dependent on m. If the interlayer turn angle is ω then

$$\theta_{n+m} - \theta_n = m\omega \qquad ....6.18$$

and further, assuming that the energy of each plane is the same, then the total energy will be simply N times the energy of one plane, where N is the number of planes.

$$E_{ex} = -N . s^2 \sum_m J_m . \cos(m\omega) \qquad ....6.19$$

where the summation is now over the number of planes whose interactions are being considered. Considering that interactions from three or more planes away will be negligible this leaves

$$E_{ex} = -N . s^2 (J_o + 2J_1 \cos\omega + 2J_2 \cos 2\omega) \qquad ....6.20$$

Ignoring other contributions, the equilibrium condition will give a minimum value of the exchange energy E_{ex}.

$$\frac{dE_{ex}}{d\omega} = N . s^2 (2J_1 \sin\omega + 4J_2 \sin 2\omega) \qquad ....6.21$$

which will be zero when,

$$0 = 2J_1 \sin\omega + 4J_2 \sin 2\omega \qquad ....6.22$$

The solution of equation 6.22 is when

$$\cos\omega = \frac{-J_1}{4J_2} \qquad ....6.23$$

The helical spin antiferromagnetic structure is therefore stable for those conditions under which $J_1/|J_2| \leq 4$. When J_2 becomes smaller than $J_1/4$ the ferromagnetic structure is formed.

MAGNETIC MOMENT STRUCTURES OF THE HEAVY RARE EARTHS

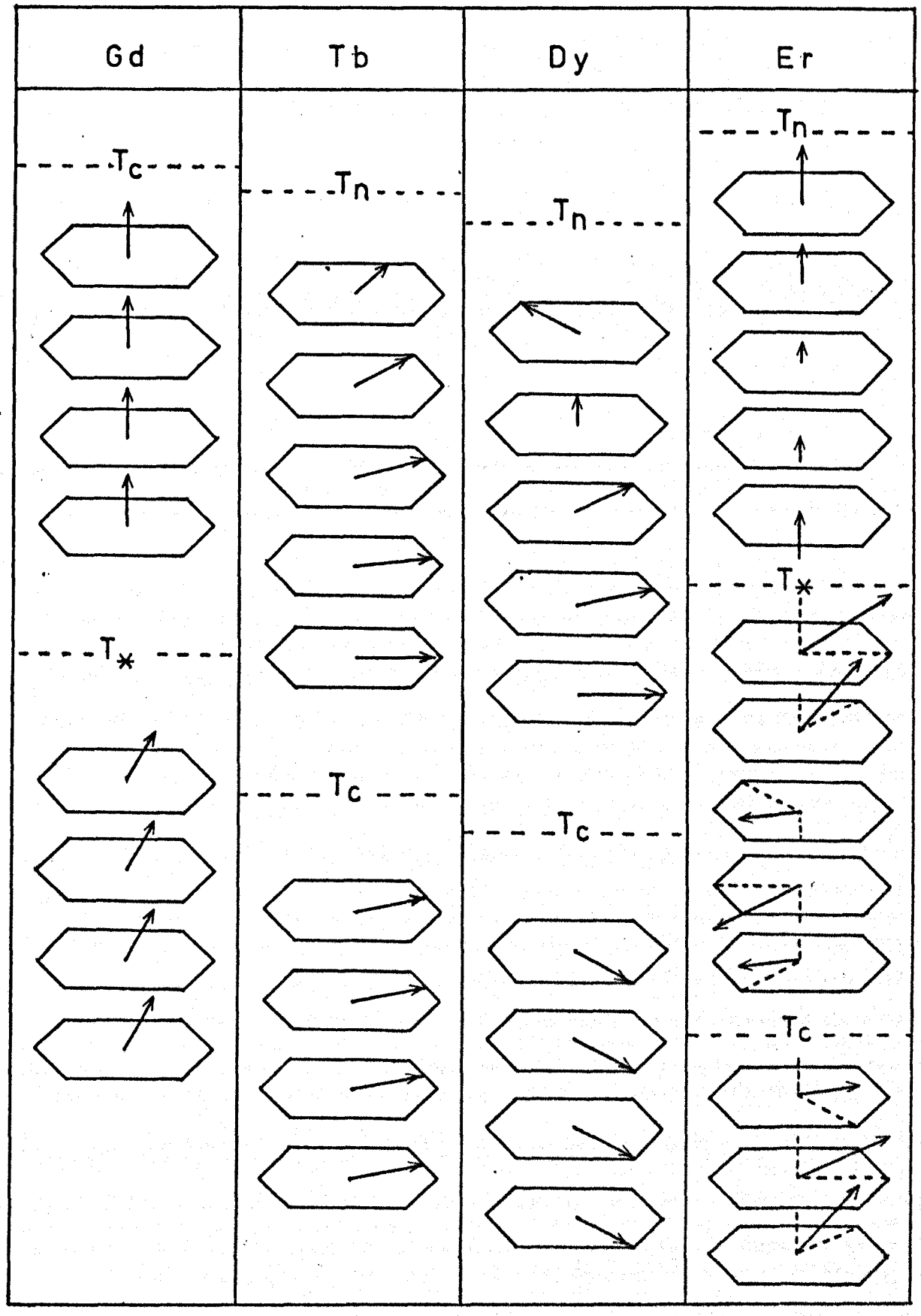

fig. 6.5

6.3.4 Helical Antiferromagnetism

In the antiferromagnetic phases of the heavy rare earths the most commonly occurring order is the helical spin system governed by the conditions described above for Dysprosium. The helical base plane component may also be accompanied by a c axis component which may be constant as in Erbium below 20°K, vary sinusoidally as in Erbium between 53°K and 85°K or vary as a square wave as in the antiphase domain structure in Erbium between 20°K and 53°K. The turn angle ω in the base plane is also temperature dependent, decreasing as the temperature decreases.

Application of a magnetic field in the base plane of this type of structure gives a continuous distortion of the helix until the field strength is sufficient to cause rotation of the spins with components in the reverse direction of the field, into the field direction. This results initially in a fan-type structure, and as the field is increased the fan angle becomes smaller, eventually closing completely to give a ferromagnetic alignment. Recently, however, Crangle [16] has expressed some doubt concerning the existence of the fan state following results which show in one case only an increasingly deformed helix as the field strength is raised.

Landry [17] has given an explanation of the variation in helimagnetic turn angle as a function of interlayer spacing, suggesting that the results are due to the variation of exchange interaction with interatomic spacing. This would appear to be contrary to the view held by Robinson and Milstein [7] for the RKKY interaction.

6.3.5 Ferromagnetic Ordering

The existence of long range periodic spin structures depends on the long range exchange interaction. The exact details of the structure, for example which crystallographic direction the moments point along, is determined by the crystal field anisotropy. As the temperature is reduced

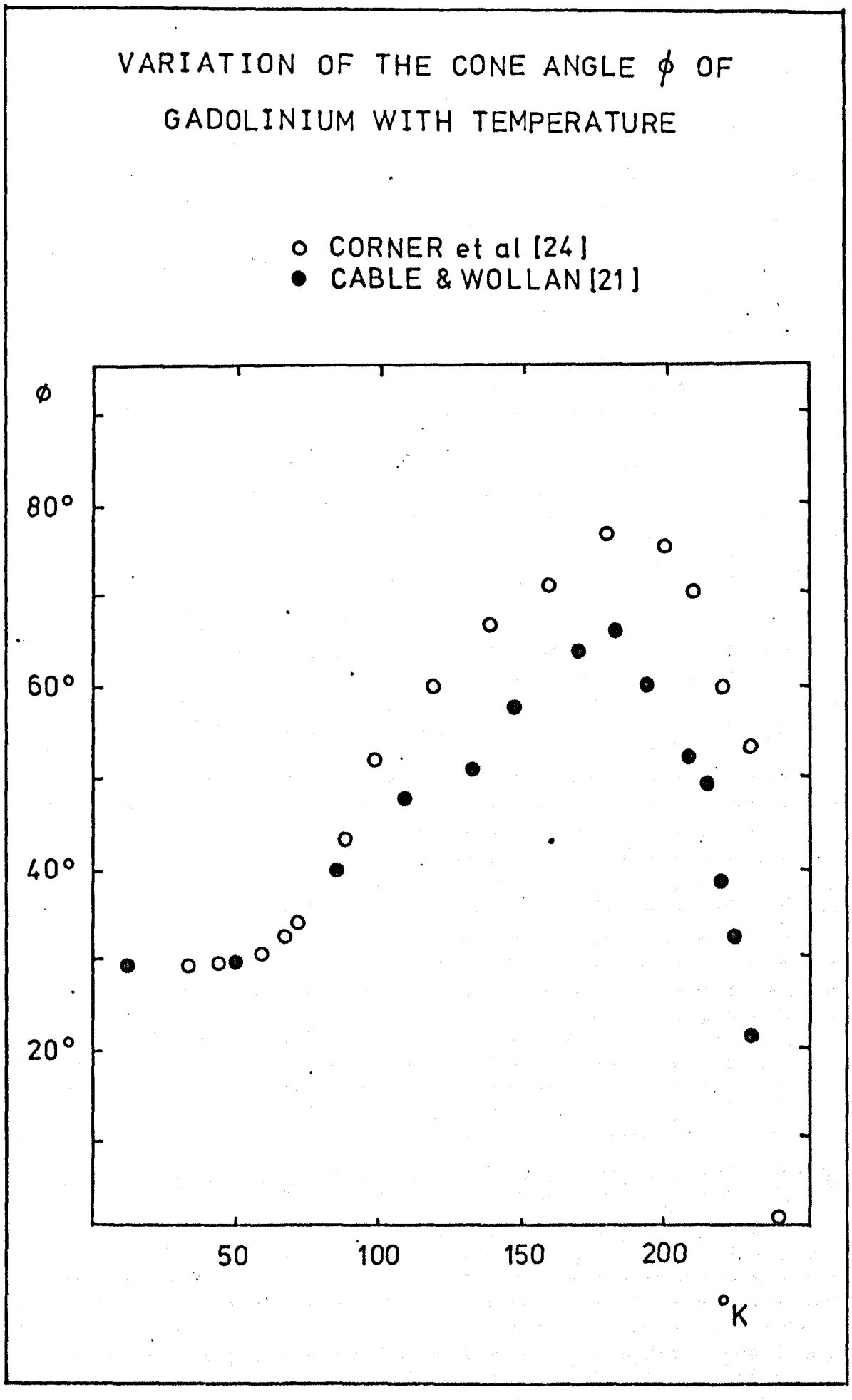
VARIATION OF THE CONE ANGLE ϕ OF
GADOLINIUM WITH TEMPERATURE
CORNER et al [24]
CABLE & WOLLAN [21]
ϕ
80°
60°
40°
20°
50
100
150
200
°K

fig. 6.6

the energies due to the crystal field increase. At low temperatures the crystal anisotropy in the rare earths corresponds typically to a magnetic field of about 10T according to Mackintosh [18]. This results in a reduction of the turn angle in helimagnetic ordering. This effect is therefore largely responsible for the eventual transition from antiferromagnetic to ferromagnetic ordering at the lower transition temperature.

6.3.6 Description of Magnetic Order

The magnetic structures of the heavy rare earths are notable for their long range periodicity along the c axis, which is due mainly to the form of the indirect exchange. The form of ordering may therefore be expressed in terms of two basic structures [18] the helix and the longitudinal wave. In the helix the components of magnetic moments in the basal plane, corresponding to the xy plane of coordinates, may be expressed as

$$J_{x_i} = m.J_{\perp} \cos \underline{Q}.\underline{R}_i \qquad ....6.24$$

$$J_{y_i} = m.J_{\perp} \sin \underline{Q}.\underline{R}_i \qquad ....6.25$$

and in the case of a longitudinal wave the c axis component varies as

$$J_{z_i} = m\, J_{//} \cos \underline{Q}.\underline{R}_i \qquad ....6.26,$$

where in both cases $\underline{R}_i$ is the position vector of the i th plane measured from some arbitrary origin plane and $\underline{Q}$ is the wave vector of the magnetic order which also lies along the z axis. From this values of $\underline{Q}$ may be plotted against temperature for the different rare earth elements. Results from some neutron diffraction measurements of Koehler et al [19] and Dietrich and Als-Nielson [20] are given in fig. 6.7. The wave vector has been converted into an angle which in the case of Dysprosium and Terbium represents the interplanar turn angle ω. For Erbium above $53^{o}K$ in which only a longitudinal wave along the c axis exists the angle represents the phase angle between moments in successive base planes since in this case the term 'turn angle' would be meaningless.

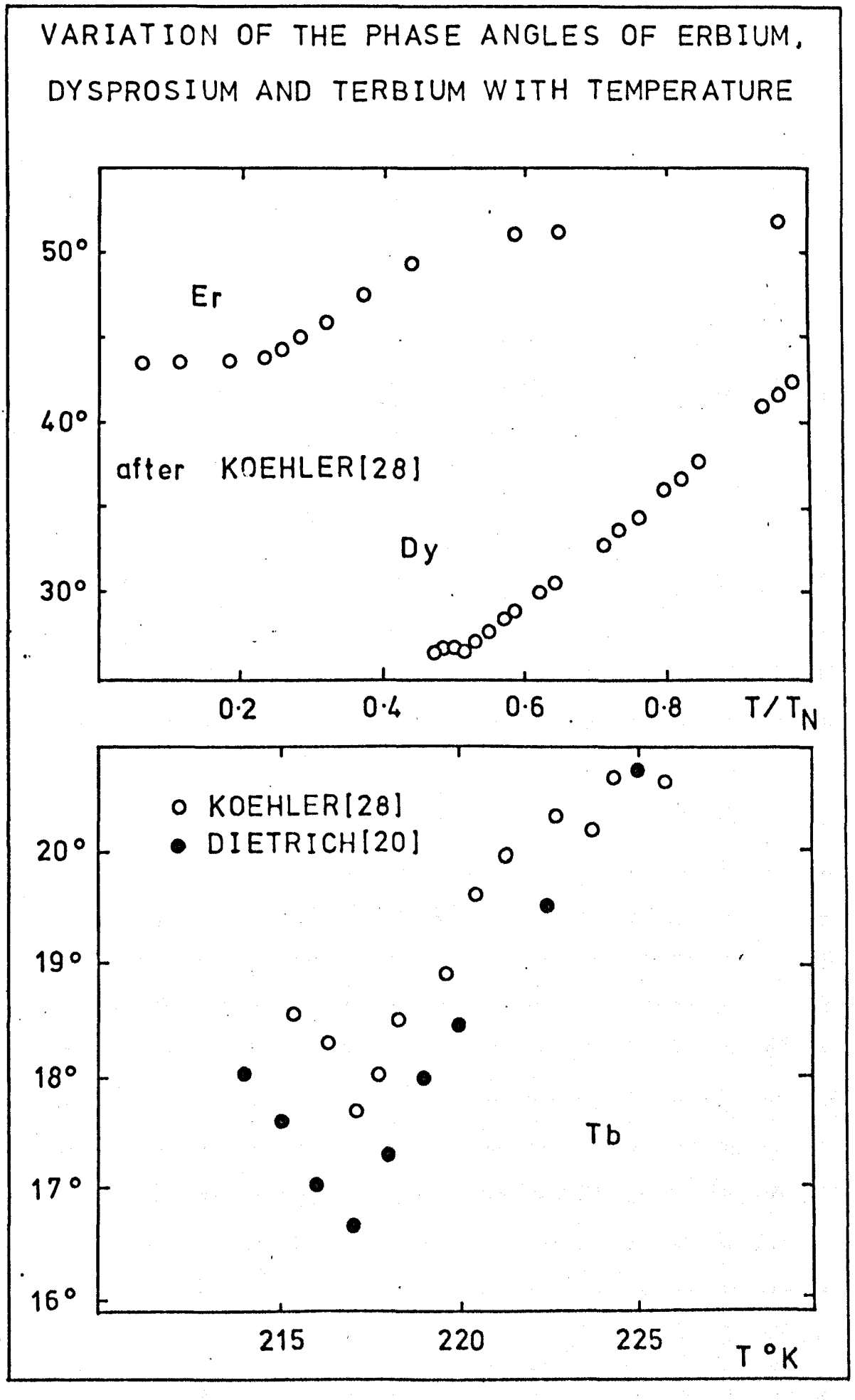
VARIATION OF THE PHASE ANGLES OF ERBIUM, DYSPROSIUM AND TERBIUM WITH TEMPERATURE
50°
40°
30°
Er
after KOEHLER[28]
Dy
0·2
0·4
0·6
0·8
T/T_N
KOEHLER[28]
DIETRICH[20]
20°
19°
18°
17°
16°
Tb
215
220
225
T °K

fig. 6.7

Curie and Néel Temperatures of the Heavy Rare Earths Gd, Tb, Dy and Er

	Gd	Tb	Dy	Er
T_N		225 230	180	85
T_*	225			53
T_C	294	219 214	88	20

Units are ^oK

fig. 6.8

6.3.7 Present State of the Theory

The present state of the phenomenological theory is one in which it has reached a level capable of explaining broadly most of the existing results. The magnetic properties can be explained in terms of the two main interactions, the exchange and crystal field, together with the magnetostrictive coupling. The combination of these three factors and their variation, both from element to element in the Lanthanide series, and in a single element as a function of temperature as for example in the case of Terbium [18] lead to a wide variety of magnetic structures.

Some progress has been made in calculating the exchange integrals from first principles although this has not included anisotropic exchange. Calculations of the crystal field effects are also lacking. On the whole therefore the analytical theory of rare earth magnetism is at a very primitive stage of development.

6.4 Magnetic Structures of the Heavy Rare Earths

6.4.1 Determination of Structure

In order to determine the exact magnetic structures of the rare earths most of the information has been obtained by neutron diffraction and magnetisation measurements on single crystal specimens. From the analysis of data obtained using these two techniques the magnetic configurations shown in fig. 6.5 have been deduced. Early work on neutron diffraction by the heavy rare earths was carried out at Oak Ridge, Tennessee and magnetisation measurements at the Ames Laboratory at Iowa State University.

6.4.2 Variation of Magnetic Structure with Temperature

The magnetic moment structures of the heavy rare earths Gadolinium, Terbium, Dysprosium and Erbium are given in fig. 6.5. As the temperatures of the rare earth paramagnets are reduced a critical

temperature is reached at which the elements adopt one form or another of ordered magnetic structure. These temperatures at which order-disorder transitions occur are marked by discontinuities or anomalies in the electrical, thermal, magnetic and mechanical properties.

All except Gadolinium exhibit an antiferromagnetic state at some point in the temperature range. The antiferromagnetic states of Dysprosium and Terbium are both helical antiferromagnetic with the moments confined to the base plane. Erbium however has an antiferromagnetic phase in the range $53^{\circ}K$ - $85^{\circ}K$ in which the moments are confined to the c axis but vary sinusoidally in both magnitude and direction. Another antiferromagnetic phase of Erbium also occurs with ordering in the base plane.

All except Gadolinium have a lower transition temperature from the antiferromagnetic to ferromagnetic state. Gadolinium itself also has a lower transition at which a component of magnetic moment appears in the base plane inclining the net moment to the c axis so that it lies on the surface of a cone. The magnetic structure however continues to be simple ferromagnet. Terbium and Dysprosium form base plane ferromagnets, while the ferromagnetic transition in Erbium occurs when the component of moment parallel to the c axis orders ferromagnetically while the base plane is still helical, giving it a conical structure.

6.4.3 Gadolinium

Results of previous work on Gadolinium indicate that it is a ferromagnet below its Curie point of $293^{\circ}K$ down to $4.2^{\circ}K$ [21,22], although there had been some speculation, notably by Belov [23] concerning the existence of an antiferromagnetic helical structure between $240^{\circ}K$ and $293^{\circ}K$. It is now well established that in this temperature range the moments lie parallel to the c axis, and that below $240^{\circ}K$ they deviate from this axis by the introduction of a component in the base plane. The maximum

deviation from the c axis occurs at 180°K when the moments lie on a cone of semi-vertical angle 65°. This angle then reduces to a value of about 32° at 60°K and then remains fairly constant down to 4.2°K. The variation of this cone angle as a function of temperature is shown in fig. 6.6, the results being taken from the neutron diffraction work of Cable and Wollan [21] and from the determination of the magnetic easy axis by the magnetisation measurements of Corner, Roe and Taylor [24] and later Corner and Tanner [25]. An antiferromagnetic structure in Gadolinium in the temperature range 240°K - 293°K has been reported under high hydrostatic pressure of 30 k bar by McWhan and Stevens [26].

6.4.4 Terbium

The Néel and Curie temperatures of this element seem to vary rather widely from sample to sample. Terbium undergoes a transition from the paramagnetic to a base plane helical antiferromagnetic structure at a Néel point of 230°K, although some results seem to indicate that this is closer to 225°K. The antiferromagnetic phase exists only over a narrow temperature range of about 10°K, and reported Curie points vary from 214°K - 220°K. Throughout the ordered state the moments are confined to the base plane by large anisotropy fields. Magnetisation measurements at high fields show that the susceptibility along the c axis is fairly constant with applied field, and that the moments are lifted less than 9° out of the base plane by fields of up to 7 Tesla at 4.2°K.

Magnetisation measurements by Hegland et al [27] indicate that the b axis is the easy magnetic direction throughout the antiferromagnetic phase. At about 5°K below the Néel point the transition from antiferro- to ferromagnetic structure begins according to neutron diffraction measurements.

The turn angle in Terbium varies from about 20.5° at T_N through a minimum of about 17° and then rises to about 18.5° at T_C. Results due to the early neutron diffraction work of Koehler et al [28] and later Dietrich

and Als-Nielson [20] are shown in fig. 6.7. The latest neutron diffraction results of Crangle [29] using a recent high purity Terbium specimen do not show the existence of a minimum in the variation of turn angle with temperature, but rather give an almost linear variation over the range.

The helical antiferromagnetic structure can be completely destroyed in Terbium by the application of fields as small as 0.1 - 0.2 Tesla along the easy b axis, which again indicates a rather delicate balance between the anisotropy and exchange forces in this phase of Terbium as mentioned by MacIntosh [18].

At the Curie point the magnetic moments lie along the base plane b axis and this ferromagnetic structure is stable down to 4.2°K.

6.4.5 Dysprosium

Below its Néel temperature of 180°K Dysprosium has a helical magnetic structure similar to Terbium, in which the magnetic moments are again confined to the base plane by large axial anisotropy forces. This antiferromagnetic phase exists over a much wider temperature range than in Terbium, the helix existing down to 90°K when the transition to the ferromagnetic phase begins, terminating at a Curie temperature of between 85°K and 88°K, depending on different purity of the specimens and different methods of determination, when the moments align along the base plane a axis.

The interplanar turn angle varies from 43° at the Néel temperature to 26° at 90°K as shown in fig. 6.7. The critical magnetic field applied in the base plane that is necessary to convert the antiferro- to the ferromagnetic alignment varies linearly from zero at T_C up to 1.1 Tesla at 160°K. Above 135°K the collapse of the antiferromagnetic order is not immediate when the critical field is reached but rather passes through a series of fan states. The easy axis in this case is the base plane a axis, although

some work on the changes in the easy axis during magnetisation have been indicated by Bly, Corner and Taylor [30] and later again by Corner and Welford [31]. In the ferromagnetic state the moments lie along the a axis.

6.4.6 Erbium

Erbium undergoes an order-disorder transition to an antiferromagnetic state at a Néel temperature of 85°K. The 4f quadrupole moment is rotated through 90° compared with Terbium and Dysprosium causing the zero field moments to lie along the c axis between 53°K and 85°K. Over this temperature range the c axis components vary sinusoidally, while no order has been detected in the base plane.

At 53°K another transition occurs in which the base plane components order helically while the c axis components, modified by the anisotropy alter from sinusoidal to an antiphase domain type structure of four moments in one direction followed by four moments in the other. Some authors consider that a higher harmonic appears in the sinusoidal variation causing the variation to become more like a square wave as for example in a Fourier series.

The Curie point of Erbium occurs at about 20°K at which point the c axis moments order ferromagnetically to give a cone of semi vertical angle 30°. This equilibrium represents once again the result of competing anisotropy and exchange forces on the lowest energy state.

The variation of the wave vector of Erbium is given in fig. 6.7. In the temperature range 53°K - 85°K this respresents the phase angle between successive c axis moments, and appears to be constant at 51.5°. Between 53°K and 20°K this represents the interplanar turn angle which decreases from 51.5° at 53°K down to 43.5° at the Curie point of 20°K when the ordering along the c axis becomes ferromagnetic and the turn angle stabilises at 43.5°. The net effect is therefore a conical ferromagnetic structure.

Application of a c axis field to Erbium closes the cone angle in the ferromagnetic state. In the region between 20°K and 53°K this is preceded by a first order transition from the anti aligned cone structure to the pure conical state. This means that the structure is ordered ferromagnetically and that the Curie point has been effectively raised. Application of a base plane magnetic field results in a phenomenon requiring a more complicated explanation. The cone appears to collapse to a fan state lying at an angle to the c axis. This appears as an abrupt change in the base plane component of the magnetic moment at an internal field strength of 1.7T according to Rhyne et al [32]. The a and b axis moments remain isotropic up to an internal field of 4.5 Tesla which marks the collapse of the fan state. At higher fields the a and b axis components become anisotropic with final base plane ferromagnetism not being achieved below 20 Tesla for the b axis direction.

6.5 Bulk Magnetic Properties

These are the macroscopic or average responses of the materials to the sum of all the microsccpic interactions discussed above. The hexagonal crystal structure of the heavy rare earths leads to large anisotropies in the crystal field and in most of the magnetic and elastic properties.

6.5.1 Magnetisation Measurements

The magnetisation measurements on the heavy rare earths Gadolinium, Terbium, Dysprosium and Erbium have been described in detail in section 6.4 on the determination of magnetic structure. The original single crystal magnetisation data on these heavy rare earths was due tc Legvold, Spedding and co-workers at the Iowa State University. The earliest reported measurements for Gadolinium were by Nigh, Legvold and Spedding [33], for Terbium by Hegland, Legvold and Spedding [34], for Dysprosium by Behrendt, Legvold and Spedding [35] and for Erbium by Green, Legvold and Spedding [36].

Other important magnetisation measurements not mentioned in section 6.4 include work on Terbium by Rhyne et al [8] and on Erbium by Rhyne et al [32] again and by Flippen [37].

6.5.2 Determination of Critical Fields

The critical magnetic fields necessary to cause changes in the magnetic ordering from antiferro- to ferromagnetic when applied along the magnetic easy axis have been reported by Coqblin [38] for all the heavy rare earths with the exception of Gadolinium. The results were obtained from magnetisation measurements on single crystal specimens by Feron [39] using applied fields of up to 4T. In most cases internal fields of no greater than 2.5T were sufficient to produce reorientation of magnetic moments.

The Curie points of those heavy rare earths which have an antiferromagnetic phase represent the transition from antiferromagnetic to ferromagnetic alignment. In all cases this transition temperature has been found to be field dependent and approaches the Néel temperature as the field is increased. The critical field is also strongly temperature dependent.

6.5.3 Magnetocrystalline Anisotropy Measurements

As indicated above the early magnetisation measurements on heavy rare earths showed evidence of large crystalline anisotropy. The anisotropy constants as given in equation 6.14 may be determined by magnetisation or torque magnetometer measurements.

The variations of the anisotropy constants of Gadolinium have been measured by Corner et al [24] and were found to be much larger than for other typical hexagonal magnetic materials, for example Cobalt. The principal term, K_2', was found to change sign just below $240^{\circ}K$, corresponding to the movement of moments away from the c axis at the spin reorientation transition.

The anisotropy constants of Terbium and Dysprosium were measured as a function of temperature by Rhyne and Clark [8] and also by Bly, Corner and Taylor [40,41]. No reliable measurement of the anisotropy constants of Erbium appears to have been made because the exchange energy is field dependent and it has so far eluded analysis.

The easy magnetic directions in the rare earths are given in fig. 6.9. In the cases of Terbium and Dysprosium the easy axis lies in the base plane, while for Erbium it is along the c axis. This is in agreement with the contributions of the anisotropy constants as discussed in section 6.3.2 and as shown in fig. 6.4. In the case of Gadolinium the easy direction is variable below the spin reorientation transition.

6.5.4 Magnetostriction Measurements

Values of all the single crystal magnetostriction coefficients of the heavy rare earths are now available [1]. Magnetostrictive strains which are closely related to the crystal anisotropy through the elastic energy have been found to be unusually large in the rare earths.

6.5.5 Anomalous Thermal Expansion Measurements

The observed thermal expansion of rare earths has a very anomalous temperature dependence located close to magnetic transition temperatures. In those rare earths with helical spin structures, such as Dysprosium and Terbium, a large c axis expansion anomaly of exchange origin is observed.

Lattice distortions in the rare earths are sufficiently large to be determined accurately by X-Ray diffraction techniques. Darnell [42,43] has studied the temperature dependence of the a, b and c axes of Gadolinium, Terbium, Dysprosium and Erbium. The results are in good agreement with the bulk thermal expansion data obtained using strain gauges in the paramagnetic and antiferromagnetic regions. Below T_C the average strain observed by a strain gauge is not unique because it depends on the domain structure that the crystal forms. The strain gauge data are therefore not reliable below T_C.

Directions of the Easy Magnetisation Axes for Gd, Tb, Dy, Er

	Gd	Tb	Dy	Er
T_C				
	c	b	a	c
T_*				c
T_N	VARIABLE	b	a	c

fig. 6.9

6.5.6 Specific Heat Measurements

Specific heat measurements have been made on all the rare earths below 300°K, the early work being carried out between 1951 and 1960 by the group at Iowa State University [44,45,46,47]. The results show lambda type anomalies in specific heat at the ordering temperatures. In the helical antiferromagnetic to ferromagnetic transition in Dysprosium a sharp first order anomaly is observed.

6.6 Effects of Pressure on Magnetic Properties

6.6.1 Variation of Magnetic Ordering Temperatures

The variation of the Curie temperature of Gadolinium and the Néel temperatures of Terbium, Dysprosium, Holmium and Erbium have been found as a function of pressure by several groups of workers. Robinson and Milstein [48] monitored the change in susceptibility using Gadolinium as the core of a transformer up to pressures of 40 k bar. Bloch and Pauthenet [49] measured the weak field permeability using their specimens at the centre of two coils to obtain a mutual inductance. McWhan and Stevens [26] used both X-Ray diffraction and A.C. susceptibility measurements similar to Robinson and Milstein. Finally Bartholin and Bloch [50] used magnetisation measurements under pressures of up to 6 k bar.

The transition temperatures were found to decrease with increased pressures in all cases by typically 1°K per k bar. The exact details are given in fig. 6.10. Both T_N and T_C were found to decrease in a linear fashion with pressure. The explanation offered for this is that the exchange energy and crystal field interactions decrease with pressure, and in particular are strongly dependent on the c axis parameter.

One exception tc this rule has been found [48] in which the transition temperature of a Gadolinium-Dysprosium alloy increased with temperature, but for the pure metals all transition temperatures decrease.

6·6·2 Variation of Exchange Interaction with Atomic Separation

The Curie point in Gadolinium or the Neel point in the other heavy rare earths gives some indication of the magnitude of the exchange interaction energy since it is approximately the point at which the exchange energy and thermal random energy are equal. An investigation into the variation of the order-disorder transition temperature with pressure will also yield information on the variation of exchange interaction.

Results by Robinson [48] for pressures up to 20 k bar indicated the decrease of T_C for Gadolinium with pressure, and hence that the free energy of the ferromagnetic state must increase with pressure and hence decrease with interatomic spacing. This would result in the paramagnetic phase being energetically favoured at a lower temperature.

Results due to McWhan and Stevens showed that the exchange interactions, in the form of $T_C/[(g-1)^2 J(J+1)]$, increased smoothly on passing through the series from Gadolinium to Holmium, that is with increasing R/r where R is the interatomic spacing and r is the average radius of the 4f orbital.

6.6.3 Crystallographic Phase Changes with Pressure

Work by McWhan and Stevens up to pressures of 85 k bar showed that high pressure phase changes occurred approximately at Gd 25 k bar, Tb 27 k bar, Dy 52 k bar and Ho 30-40 k bar.

These higher pressure phases had lower critical temperatures than the low pressure phases which is in keeping with the idea that ordered magnetic states have a free energy which increases with pressure. There also appeared to be the same sequence of crystallographic structure occurring for all the heavy rare earths, these being hcp → Sm type → dhcp → fcc as the pressure increased.

Variation of Magnetic Phase Transition Temperatures of single crystal Gd, Tb, Dy and Er as a Function of Hydrostatic Pressure

	Gd	Tb	Dy	Er
$\frac{dT_N}{dP}$		-0.84	-0.41	-0.26
$\frac{dT_*}{dP}$	-4.9			-1.3
$\frac{dT_C}{dP}$	-1.4	-1.24	-1.27	-0.8

Units of $\frac{dT}{dP}$ are $^{o}K/kbar$

fig. 6.10

6.6.4 Other Properties

Bloch and Pauthenet measured the spontaneous and saturation magnetisations of the heavy rare earths Gd, Tb, Dy, Ho. Measurement of saturation moments for Gd and Dy at 77°K were consistent with the variation of conduction electron polarisation, however the Terbium results were completely different and indicated that the application of high pressures induces electrons to transfer from the 4f shell to the conduction band. Spontaneous magnetisation of specimens was found to decrease by typically 0.1% per k bar for the heavy rare earths.

Neutron diffraction work on Terbium and Holmium [51] showed that the turn angle in the helical antiferromagnetic state varies with pressures up to 5 k bar. This has also been predicted theoretically. Results for Dy [50] indicated the same.

CHAPTER 7

Elastic Properties of the Heavy Rare Earths

7.1 Variation of Elastic Properties with Temperature

7.1.1 Elastic Constants of Polycrystalline Rare Earths

The low temperature elastic properties of polycrystalline specimens of the heavy rare earths were measured by Rosen [1] in 1968, over the range 4.2 - 300°K. The results, giving the variation in longitudinal and transverse sound velocity in Gadolinium, Terbium, Dysprosium, Holmium and Erbium, showed anomalies corresponding to the location of magnetic phase transitions in the materials.

This work was followed by the complete set of adiabatic second order elastic constants of Dysprosium by Klimker and Rosen [2] in 1970. In this later paper the compressional constants C_{11} and C_{33} and the cross coupling coefficients C_{12}, C_{13} were found to give sharp minima in the vicinity of the Neel temperature T_N and the Curie temperature T_C. In contrast the shear moduli C_{44} and C_{66}, although giving anomalies at T_C, were found to be little affected at T_N.

7.1.2 Elastic Constants of Single Crystal Specimens

Early measurements of the adiabatic second order elastic constants (SOEC) of single crystal Dysprosium over the temperature range 298 - 900°K, and single crystal Erbium over 60° - 300°K were made in 1967 by Fisher and Dever [3]. Their primary objective was however to show a correlation between the shear anisotropy ratio C_{44}/C_{66} and the existence of a martensitic hcp → bcc crystallographic phase transformation. This is incidental to the present work although their measurements appear to be the first complete set of single crystal SOEC of any of the heavy rare earths.

Moran and Lüthi [4] investigated the changes in longitudinal acoustic velocity along the c axis (C_{33}) for single crystal Gadolinium, Terbium, Dysprosium and Holmium at temperatures down to 77°K again showing anomalies in elastic constant close to the magnetic transitions. The existence of a critical external applied magnetic field of 1.2T along the a axis of Dysprosium at 167°K was shown from the elastic constant and similar behaviour in Gadolinium and Terbium was indicated.

The SOEC of single crystal Terbium were reported by Salama et al [5] over the range 77 - 300°K, the behaviour of C_{11} showing an unusual maximum at T_C = 221°K. The authors concluded that the separation of the Curie and Néel points of only 8°K may cause some overlap of the magneto-elastic effects of the paramagnetic to antiferromagnetic and a.f. to f. transitions. The behaviour of the elastic constants in the region of the phase transitions in Terbium was also investigated by Jensen [6].

7.1.3 Systematic Investigation of the SOEC of Single Crystal Heavy Rare Earths

The variation of the five SOEC of single crystal Dysprosium and Holmium with temperature over the range 4.2 - 360°K was reported by Palmer and Lee [7] and of Gadolinium, Terbium and Erbium by Palmer et al [8] over the same range. Measurements were made in fields of zero and 2.5T applied along the easy axis where possible. The moduli showed marked anomalies again in accordance with Klimker and Rosen [2].

Differences in the moduli in zero and 2.5T fields of Dysprosium, Holmium and Terbium were considered to be due to domain wall rotation effects since the field caused, as far as possible, magnetic saturation and converted the crystals into single domain ferromagnets. This change in the elastic moduli, termed the Δc effect, was considered to be analogous to the ΔE effect in polycrystalline magnetic materials. The theory behind this ΔE effect has been discussed by Bozorth [9]. Briefly, if a

polycrystalline magnetic material is subjected to stress the observed strain will have two component contributions. One is the normal elastic strain of the material while the other is due to the reorientation of domains caused by the applied stress. The value of the Young's Modulus, defined as the ratio of stress to strain, will therefore appear to be less than would be expected in a non-magnetic solid. The ΔE effect is thus always positive. However, in the heavy rare earths the large magnetostrictive strains can allow the 'Δc' effect to be either positive or negative as explained by Palmer and Lee [7]. The ΔE effect was found to be greater in annealed crystals by Köster [10] who therefore considered that the effect decreased with internal strain.

For Erbium and Gadolinium it was considered by Palmer et al [8] that the field strength of 2.5T would not be sufficient to convert the crystal into a single domain ferromagnet, and hence that the observed difference between the elastic constants in zero and 2.5T applied fields would not be the total 'Δc' effect. The magnetic fields were applied along the magnetic easy axes as given in fig. 6.10 whenever this was orthogonal to the direction of propagation of the acoustic waves. In the case of Gadolinium the field was aligned parallel to the c axis where possible, although the easy axis in this case varies over the temperature range $4.2^{\circ}K - 240^{\circ}K$ as indicated by Corner et al [11].

Magnetic remanance was observed in the elastic constants of Holmium at $4.2^{\circ}K$. That is after application and removal of a magnetic field of 2.5T along the easy axis, the elastic moduli did not recover their original zero field values. It was found necessary to heat the specimen above its Curie point and recool before the original value was regained.

In the case of Erbium the elastic moduli were found to be significantly lower than the results reported by Fisher and Dever [3] by

a factor of up to 4% for C_{13} at 300°K, which could not be attributed to experimental error. Results of the single crystal elastic moduli of the heavy rare earths Gd, Dy, Er and Tb of various workers are summarised in figs. 7.1 and 7.2.

7.2.1 Variation of Elastic Moduli under Constant Applied Field

The variation of the five SOEC of single crystal Erbium under constant external applied magnetic fields of up to 3.9T has been investigated by du Plessis [12], although their isothermal magnetic dependences were not studied. The temperature range covered was from 10°K - 300°K. In the case of C_{33} the application of a magnetic field led to extreme softening of the modulus near 53°K instead of restoring it to that expected for a non-magnetic material.

The temperature variation of the two moduli C_{33} and C_{44} for Gadolinium over the range 77°K - 330°K was reported by Long et al [13]. They also measured the behaviour close to the spin reorientation transition at 225°K in constant applied magnetic fields of up to 0.8T. The work was based on the behaviour of this spin reorientation anomaly under different fields. The anomaly was found to disappear completely in fields greater than about 0.5T. Theoretical interpretation of the results was given by Levinson and Shtrickman [14].

7.2.2 Critical Fields from Location of Magnetoelastic Anomalies

Moran and Lüthi [15,16] showed in a series of experiments on Gadolinium, Terbium and Dysprosium that the critical change in sound velocity near the Néel temperature obeys the relation $\Delta v/v \alpha \omega_o \ln\varepsilon$ where ε is the reduced temperature $(T - T_N)/T_N$ and ω is the angular frequency of the acoustic vibrations. The anomaly was found to be independent of the frequency for the three values 30MHz, 50MHz and 70MHz used. The existence of such anomalies has already been noted as the ΔE or Δc effect.

Comparison of the results of single crystal SOEC of Gadolinium and Terbium from Various Workers

Gadolinium

	Temp ^{o}K	Palmer [8]	Long [15]	Moran [4]
C_{33}	4.2 77 300	7.90 7.80 7.12	 7.8 7.3	 7.2 6.6
C_{11}	4.2 77 300	7.68 7.59 6.78		
C_{44}	4.2 77 300	2.38 2.35 2.08		
C_{12}	4.2 77 300	- - 2.56		
C_{13}	4.2 77 300	1.91 1.93 2.07		

Units are 10^{10} $N.m^{-2}$

Terbium

	Temp ^{o}K	Palmer [8]	Salama [5]
C_{33}	4.2 77 300	8.24 8.18 7.44	 7.98 7.22^{5}
C_{11}	4.2 77 300	- 5.89 6.92	- 6.56 6.79
C_{44}	4.2 77 300	2.52 2.49 2.18	- 2.39 2.14
C_{12}	4.2 150 300	- - 2.50	- 1.85 2.43
C_{13}	4.2 150 300	- - 2.18	- 1.99 2.30

Units are 10^{10} $N.m^{-2}$

Fig. 7.1

Comparison of the results of single crystal SOEC of Erbium and Dysprosium from Various Workers

Erbium

	Temp ^{o}K	Palmer [8]	Fisher [3]	du Plessis [14]
C_{33}	4.2	8.12	-	-
	77	8.51	8.73	8.6
	300	8.45	8.55	8.43
C_{11}	4.2	8.70	-	-
	77	8.81	9.10	8.85
	300	8.37	8.63	8.39
C_{44}	4.2	2.76	-	-
	77	2.90	2.98	2.83
	300	2.75	2.81	2.65
C_{12}	4.2	-	-	-
	77	2.92	3.09	2.90
	300	2.93	3.05	2.93
C_{13}	4.2	2.31	-	-
	77	2.22	2.26	2.34
	300	2.22	2.27	2.42

Units are 10^{10} $N.m^{-2}$

Dysprosium

	Temp ^{o}K	Palmer [7]	Fisher [3]	Rosen [2]
C_{33}	4.2	8.51	-	8.52
	77	8.38	-	8.4
	300	7.81	7.87	7.90
C_{11}	4.2	8.01	-	7.72
	77	-	-	6.80
	300	7.31	7.47	7.07
C_{44}	4.2	2.68	-	2.70
	77	2.61	-	2.65
	300	2.40	2.43	2.48
C_{12}	4.2	-	-	2.50
	77	-	-	1.75
	300	2.53	2.61	2.53
C_{13}	4.2	1.86	-	1.97
	77	-	-	1.99
	300	2.23	2.23	2.08

Units are 10^{10} $N.m^{-2}$

fig. 7.2

The variation of the compressional modulus C_{33} of Dysprosium as a function of both magnetic field and temperature was investigated by Isci [17] who also reported similar properties in the intra-rare earth alloys Gd-40%Y and Ho-50%Tb. Isci and Palmer [18,19] were able to draw conclusions concerning the magnetic phase diagrams of their specimens from the location of minima in the elastic constants associated with magnetic phase transitions. This followed similar conclusions from experiments to locate maxima in ultrasonic attenuation in specimens of rare earths by Treder et al [20,21], and also from magnetisation measurements by Behrendt [22] and Jew and Legvold [23] and from magnetoresistance measurements by Akhavan [24].

7.3.1 Application of Hydrostatic Pressure at Room Temperature

The effects of hydrostatic pressures of up to 5 kbar on single crystal SOEC of Gadolinium, Dysprosium and Erbium in their paramagnetic states at 298°K was reported by Fisher et al [25]. The five SOEC were found to vary linearly with pressure and the derivatives are reproduced in Table 7.3. The size of the pressure derivatives of the adiabatic SOEC indicated according to Fisher that a small ion core model could be used for interpreting the data theoretically. The results could also be useful in testing the validity of the central force Born model, ($\varphi = {}^{-a}/_{r^m} + {}^{b}/_{r^n}$), and calculations along these lines were performed by Ramji Rao [28].

Grüneisen parameters were calculated from the experimental data obtained (see section 2.5.3) and were found to be in poor agreement with those obtained from thermal expansion data. This was explained in terms of the change in ${}^{c}/_{a}$ ratio of the crystals with volume. Calculation of Grüneisen parameters from theoretical lattice potentials by Ramji Rao et al [29,30,31,32] were in good agreement with the corrected data of Fisher.

Hydrostatic Pressure Derivatives of the SOEC of Gadolinium, Dysprosium and Erbium as reported by Fisher et al [25]

	Gd	Dy	Er
C_{11}	3.018 ± 0.02	3.092 ± 0.006	4.768 ± 0.02
C_{33}	5.726 ± 0.05	5.331 ± 0.008	5.448 ± 0.018
C_{44}	0.185 ± 0.012	0.434 ± 0.001	0.949 ± 0.005
C_{66}	0.377 ± 0.002	0.408 ± 0.002	0.853 ± 0.012
C_{12}	2.26 ± 0.02	2.277 ± 0.006	3.062 ± 0.044
C_{13}	3.53 ± 0.05	3.32 ± 0.1	2.16 ± 0.04
K_S	3.320 ± 0.039	3.214 ± 0.054	3.302 ± 0.02
K_T		3.228 ± 0.044	3.256 ± 0.25

fig. 7.3

7.3.2 Application of Hydrostatic Pressure at Low Temperature

The effect of high hydrostatic pressure on the single crystal moduli of Gadolinium over the temperature range 180°K - 340°K was measured by Klimker and Rosen [26]. Isobaric measurements only were made using pressures up to 6 kbar and employing a high hydrostatic pressure cell which was temperature controllable down to the cryogenic region. The authors suggested that it could be used down to 4.2°K at pressure, however no results appear to have been obtained down to such temperatures. The object of the work was to investigate the effect of pressure on the magnetoelastic anomaly at the spin reorientation transition at 225°K and at the Curie point 294°K. Pressure dependence of the transition temperatures from the location of the anomalies were also determined from these measurements and were broadly in agreement with those of other workers as reported by Elliott and shown in fig. 6.11.

7.3.3 Effects of Internal Strain of Transition Temperatures

Greenough et al [27] showed that the existence of internal strain in specimens of 50%Ho-Tb alloy affected the position of the Néel temperature as determined by elastic constant measurements by up to 4°K. After thermal cycling this effect appeared to be irreversible in the particular crystal used.

7.4.1 Theoretical Calculation of Third Order Elastic Constants

The second and third order elastic constants can be calculated theoretically as reported by Srinivasan and Ramji Rao [33,34] using either a central force model or via Keating's approach [35,36]. Attempts to compute the third order elastic constants of the heavy rare earths were made in a series of papers by Ramji Rao and co-workers for Gadolinium [29], Erbium [30], Terbium [31] and Dysprosium [32]. They investigated not only third order elastic constants but also the Grüneisen parameters of

these materials. The method of calculation was based on the Keating approach except in the case of Erbium for which a Born type central force potential was used. This was found to be less accurate than Keating's method when compared with the experimental results of Fisher [25].

From anharmonic parameters yielded by Keating's method the ten TOEC were calculated and using these the hydrostatic pressure derivatives of the five SOEC were found and compared with the experimental results. The calculated TOEC are given in Table 7.4 and the hydrostatic pressure derivatives are compared with the measured values in Table 7.5.

7.4.2 Thermal Expansion and Grüneisen Parameters

The Grüneisen parameters γ may be calculated from a knowledge of the TOEC as outlined by Srinivasan [33]. From these generalised parameters the effective Grüneisen parameters $\bar{\gamma}_{\perp}$ and $\bar{\gamma}_{//}$, perpendicular and parallel to the unique axis, may be found. In the same series of publications Ramji Rao et al [28 et.seq.] calculated the effective Grüneisen parameters for Gd, Tb, Dy, Er as a function of temperature and thereby derived the related thermal expansions. The thermal expansion behaviour of crystals of the hexagonal class had been expounded by Munn [37] and is given in section 2.5.2 where expressions for the derived Grüneisen parameters will be found.

Calculated Third Order Elastic Constants of Gadolinium, Dysprosium, Terbium and Erbium from Ramji Rao et al [28, 29, 30, 31, 32]

	Gd	Dy	Tb	Er
C_{111}	-50.3	-53.2	-48.0	-79.6
C_{112}	-13.3	-16.4	-16.2	-18.7
C_{113}	+0.4	-0.8	-1.1	-5.0
C_{123}	-6.3	-6.9	-5.4	-7.0
C_{133}	-9.7	-12.4	-11.1	-16.7
C_{144}	-3.9	-4.6	-4.3	-5.4
C_{155}	-2.0	-3.1	-2.2	-6.6
C_{222}	-55.1	-62.0	-57.1	-87.8
C_{333}	-76.2	-73.5	-73.7	-74.7
C_{344}	-9.7	-12.4	-11.1	-16.7

Units are 10^{10} $N.m^{-2}$

fig. 7.4

Comparison of Hydrostatic Pressure Derivatives of SOEC of Gadolinium, Dysprosium and Erbium as measured by Fisher [25] and calculated by Rao [28 et seq]

	GADOLINIUM		DYSPROSIUM		ERBIUM	
	FISHER [25]	RAO [29]	FISHER [25]	RAO [32]	FISHER [25]	RAO [28]
C_{11}	3.018	3.019	3.092	3.094	4.768	4.77
C_{33}	5.726	5.726	5.331	5.336	5.448	5.45
C_{44}	0.185	0.183	0.434	0.432	0.949	0.95
C_{66}	0.377	0.379	0.408	0.409	0.853	0.85
C_{12}	2.26	2.261	2.277	2.276	3.062	3.06
C_{13}	3.53	-	3.32	-	2.16	2.00

fig. 7.5

CHAPTER 8

Results (I): Performance of the Sing Around

In this chapter some preliminary results using the new sing around system are presented. As indicated in chapter four there were two possible modes of data output, the repetition rate of the sing around averaged over a period of about a second was displayed on a frequency meter, or the values of individual sing around periods were obtained using a fast sampling mode of about ten milliseconds and the data recovered on punched tape.

The repetition rate of the sing around was used to investigate variations of the SOEC of Gadolinium and Erbium as a function of temperature, the results of which are presented in section 8.2. The fast sampling mode was used to measure the variation of the compressional modulus C_{33} of Terbium as a function of a rapidly swept magnetic field. These results are compared with repetition rate measurements which were taken simultaneously and are given in section 8.3.

8.1 Determination of Absolute Velocity

The absolute values of velocity and hence the actual values of the elastic constants can not be measured very accurately using the sing around technique. Therefore the values of elastic constants have been calculated where possible from absolute velocity determinations on the same specimens by other workers. In cases where this was not possible, for example with new samples, the absolute velocity determination was made using a spike generator to obtain an approximate value of the transit time through the specimen and bond to within ± 0.02μsecs, and then a pulse echo overlap, driven by a frequency synthesizer, used to measure the transit time to within ± 0.001μsecs. This allowed the velocity to be measured to within

about 0.5%. The error in the velocity at points other than the calibration point is then dependent upon the point-to-point accuracy of the equipment used to determine $\Delta v/v$. The values of the elastic constants calculated in this way in the present work are not expected to be in error by more than 2%.

8.2 Measurement of $\Delta v/v$ from Repetition Frequency

The fractional change in acoustic velocity $\Delta v/v$ may be related directly to the fractional change in the repetition frequency $\Delta f/f$ of the sing around. As indicated in section 4.2.3 this instrument gives a precision of about ± 2 parts in 10^6 for $\Delta v/v$. As a demonstration of the sensitivity the behaviour of C_{33} of Gadolinium has been investigated close to its Curie point, T_C, of 293°K.

8.2.1 Variation of C_{33} of Gadolinium close to T_C

The variation of C_{33} of Gadolinium close to T_C has been investigated by several previous workers, the earliest of which appears to be that reported by Long et al [1] using a pulse echo overlap technique. Later measurements on similar purity specimens were made by Moran and Lüthi [2] and by Palmer et al [3]. Finally measurements were carried out on some of the latest high purity Gadolinium by Savage and Palmer [4]. A comparision of the results of these various workers is given in fig. 8.1, showing differences in the quoted values of the elastic constant of up to 7% from specimen to specimen.

In fig. 8.2 the fractional changes in elastic constant $\Delta c/c$ compared with the quoted values at 300°K are plotted against the reduced temperature, $(T-T_C)/T_C$ in each case, for the same results. These show that the depth of the anomaly compared with the value at 300°K is about 4% according to Palmer et al, while according to the other three reports it is about 2.5%. In these cases the temperature control was to within ± 0.1°K.

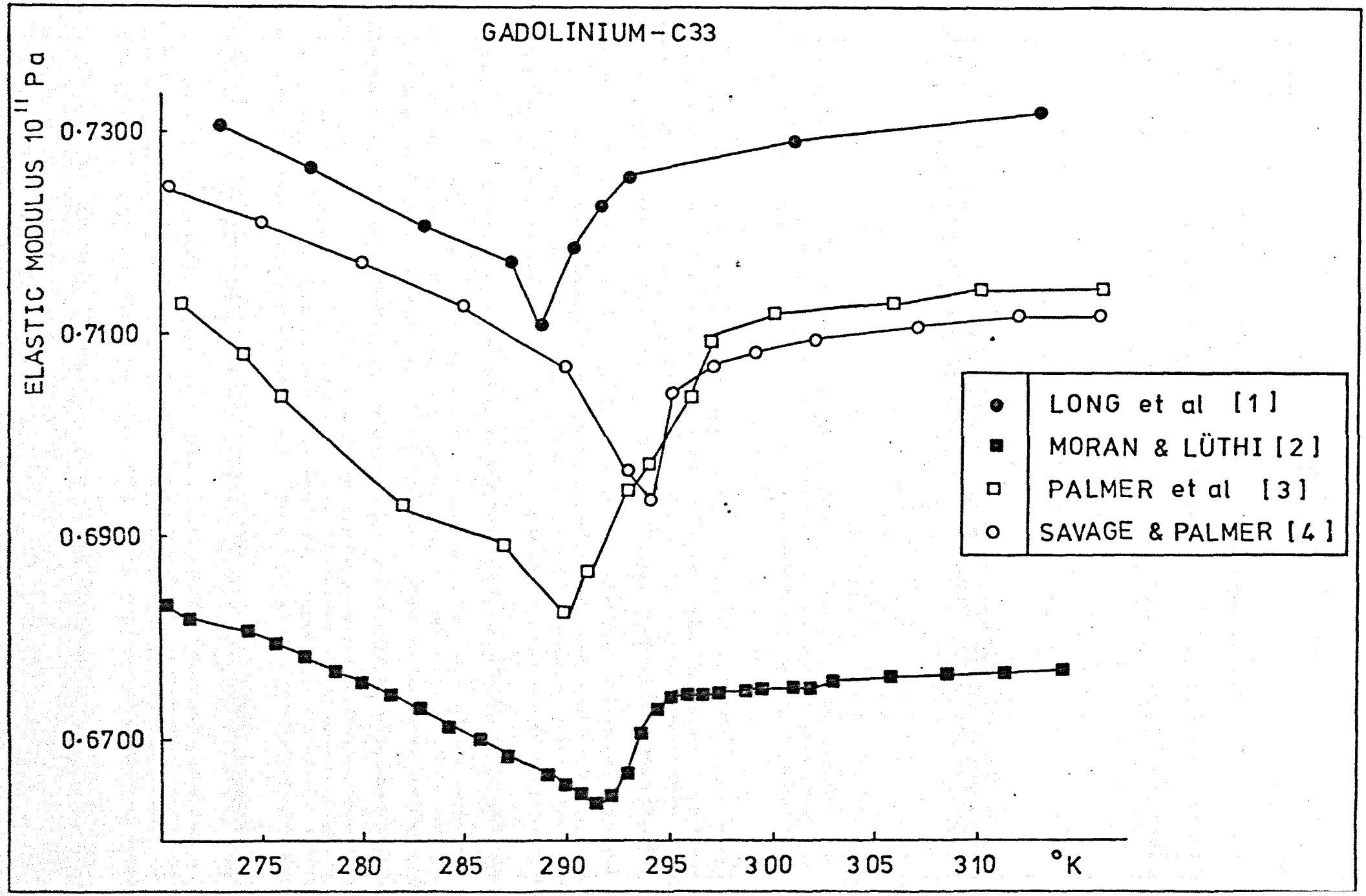
GADOLINIUM – C33
ELASTIC MODULUS 10^{11} Pa
0·7300
0·7100
0·6900
0·6700
275
280
285
290
295
300
305
310
°K
LONG et al [1]
MORAN & LÜTHI [2]
PALMER et al [3]
SAVAGE & PALMER [4]

fig. 81

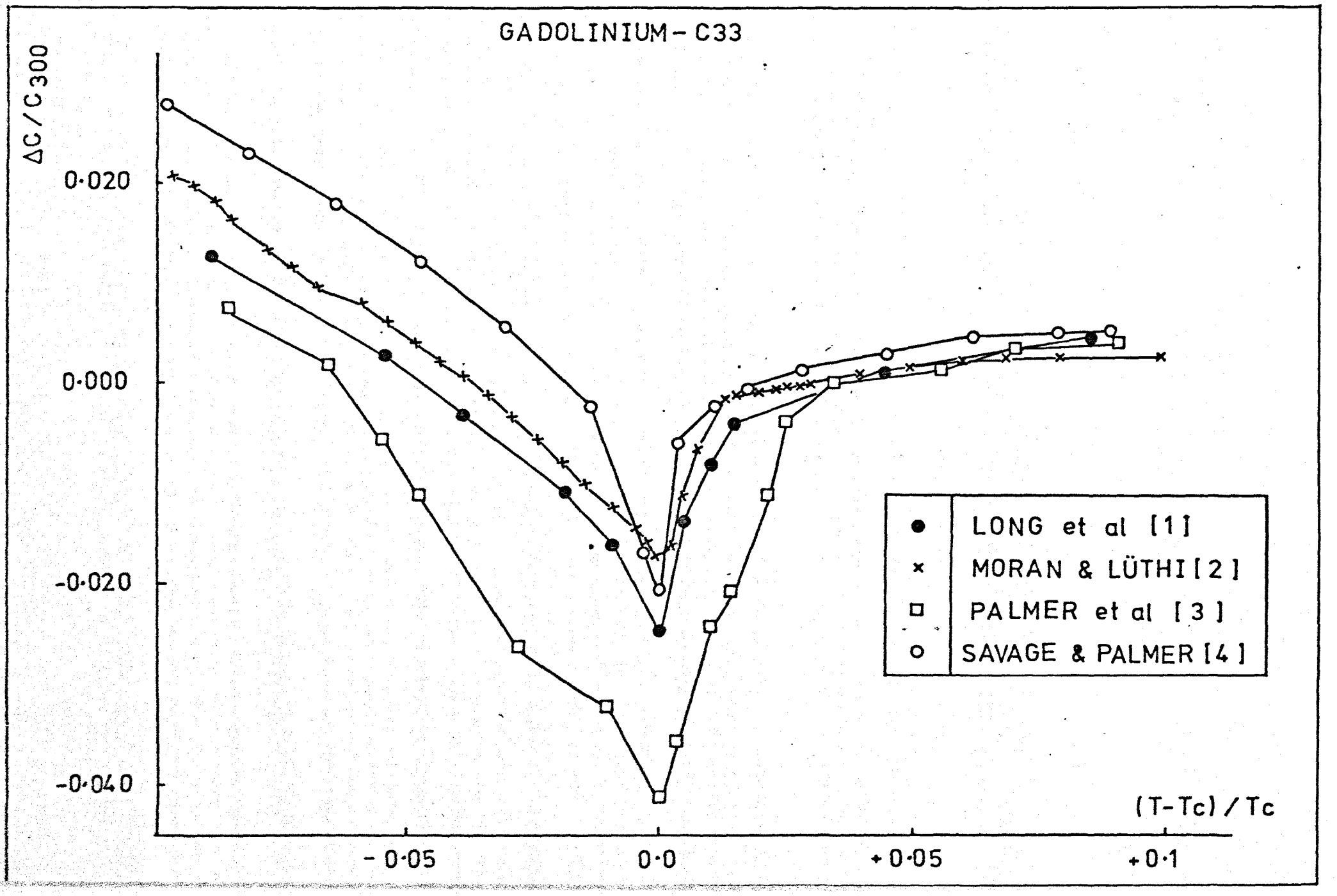
GADOLINIUM - C33
ΔC / C300
0·020
0·000
-0·020
-0·040
- 0·05
0·0
+ 0·05
+ 0·1
(T-Tc) / Tc
LONG et al [1]
MORAN & LÜTHI [2]
PALMER et al [3]
SAVAGE & PALMER [4]

fig. 8.2

In the present work the temperature control was to within ± 1mK with an accuracy of 10mK using a specially designed thermostat made available by the Department of Physics at the University of Southampton. The temperature of the specimen was varied at a rate of $2^{o}K$ per hour using this equipment and the results provided a useful indication of the sensitivity and stability of the electronic circuitry.

The resulting variation of the elastic modulus C_{33} of Gadolinium on either side of its Curie point is shown in fig. 8.3. This may be compared with the variation reported by Savage and Palmer on the same specimen. The elastic constant appears to have reached a certain degree of stability at about $294.5^{o}K$, however results could not be continued much above this due to a failure in the equipment. The depth of the anomaly as shown in the figure again appears to be about 2%.

Each reading represents a difference in temperature of typically 10mK. The change in acoustic velocity $\Delta v/v$ which would arise from such a change in temperature is 3 parts in 10^{5} just below T_{C} and about 2 parts in 10^{4} just above T_{C}. These are both rather greater than the actual resolution of the instrument, however the performance of the equipment over the flat region of the curve close to T_{C} gives some indication of its stability, at least over a period of an hour or so. Here the difference between successive readings was approximately equal to the resolution.

8.2.2 Variation of the SOEC of Erbium with Temperature

The variation of the SOEC of Erbium as a function of temperature has also been investigated by several groups of workers. The first measurements of the single crystal moduli of Erbium were reported by Fisher and Dever [5]. However these results were taken over the range $60 - 300^{o}K$. Rosen et al [6] and Palmer et al [3] both measured the full set of SOEC over the range $4.2 - 300^{o}K$ in zero magnetic field and the latter

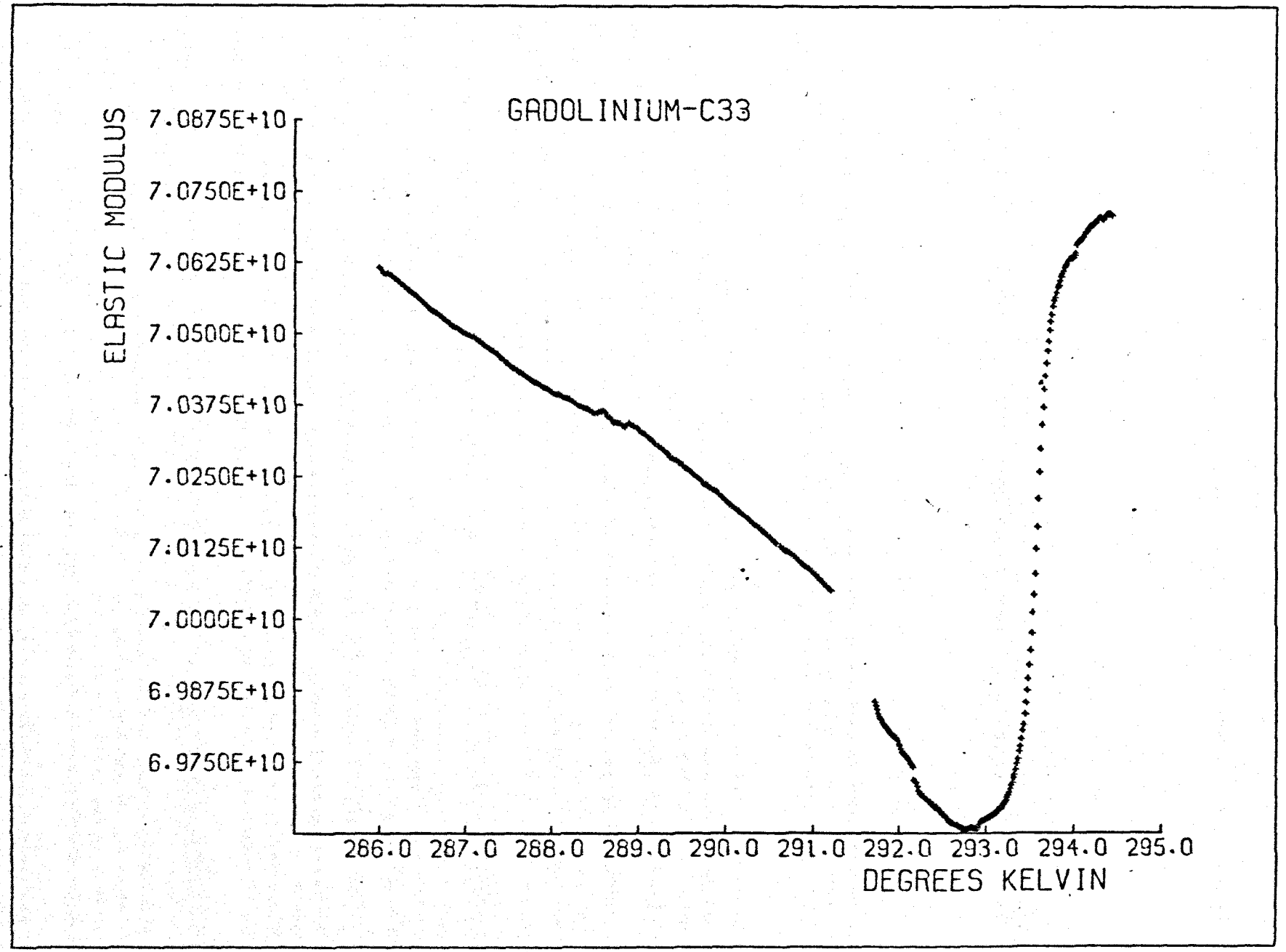
GADOLINIUM-C33
ELASTIC MODULUS
7.0875E+10
7.0750E+10
7.0625E+10
7.0500E+10
7.0375E+10
7.0250E+10
7.0125E+10
7.0000E+10
6.9875E+10
6.9750E+10
286.0 287.0 288.0 289.0 290.0 291.0 292.0 293.0 294.0 295.0
DEGREES KELVIN

fig. 8.3

work also in a constant applied magnetic field of 2.5T. Finally du Plessis [7] investigated the behaviour of the SOEC with temperature under several constant applied magnetic fields of up to 4T. The results of these different investigations are shown.

In fig. 8.4 the variations of C_{33} with temperature over the range 4.2 - 100°K are compared. All workers report rapid changes in the modulus at the phase transition temperatures of 20°K, 53°K and 85°K, giving a characteristic 'step-like' appearance to the modulus. Because of the well-defined location of these changes the values of C_{33} have also been used to compare the transition temperatures in fig. 8.6. The discrepancy in the values of C_{33} between the various samples corresponds to about 1.5% at 10°K and about 1% at 100°K, the results of du Plessis being consistently higher than those of the other two.

The results of the present work on C_{33}, using the same sample as Palmer et al, are given in fig. 8.5. This shows good agreement with the general form of the results of the other workers, although the resolution of the present equipment has allowed far more detail to be shown.

The results of previous work on C_{11} are given in fig. 8.7. Here there is significant disagreement between the results in particular concerning the depth of the anomaly at about 45 - 50°K. The results of du Plessis indicate that the depth of the anomaly is about 12%, while the results of Rosen suggest a value nearer 7%. The results of Palmer et al could not be continued in this region due to excessive attenuation of signal in the sample. Otherwise the discrepancy between the various results does not exceed 2%. The present results for C_{11} are shown in fig. 8.8. Again the main feature is a deep anomaly in the region between 20 - 50°K with a depth of about 6% which is in agreement with the results of Rosen. A sharp increase in the modulus at the Curie point of about 22°K is present

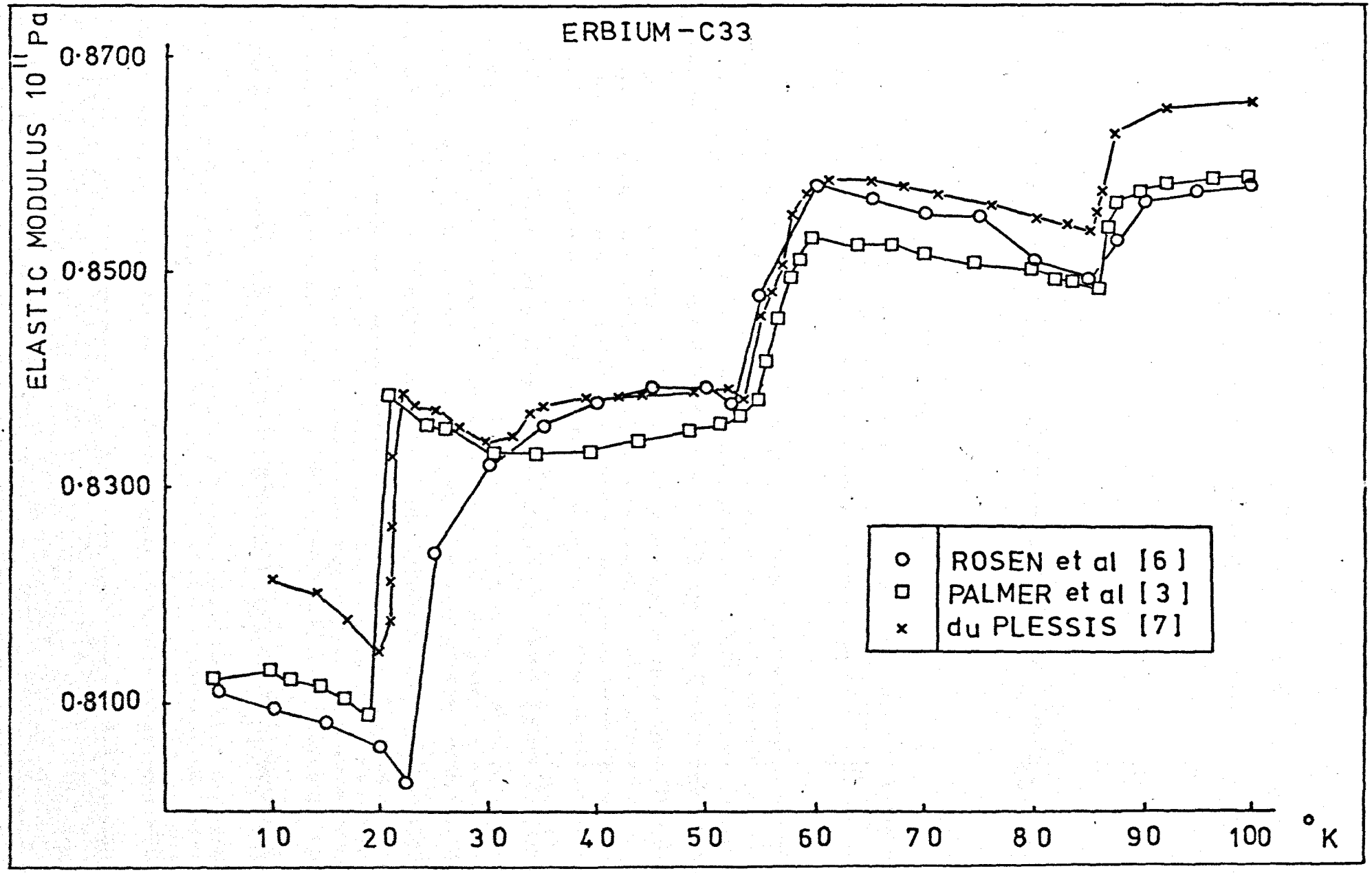
ERBIUM - C33
ELASTIC MODULUS 10^{11} Pa
0·8700
0·8500
0·8300
0·8100
10
20
30
40
50
60
70
80
90
100
°K
ROSEN et al [6]
PALMER et al [3]
du PLESSIS [7]

fig. 8.4

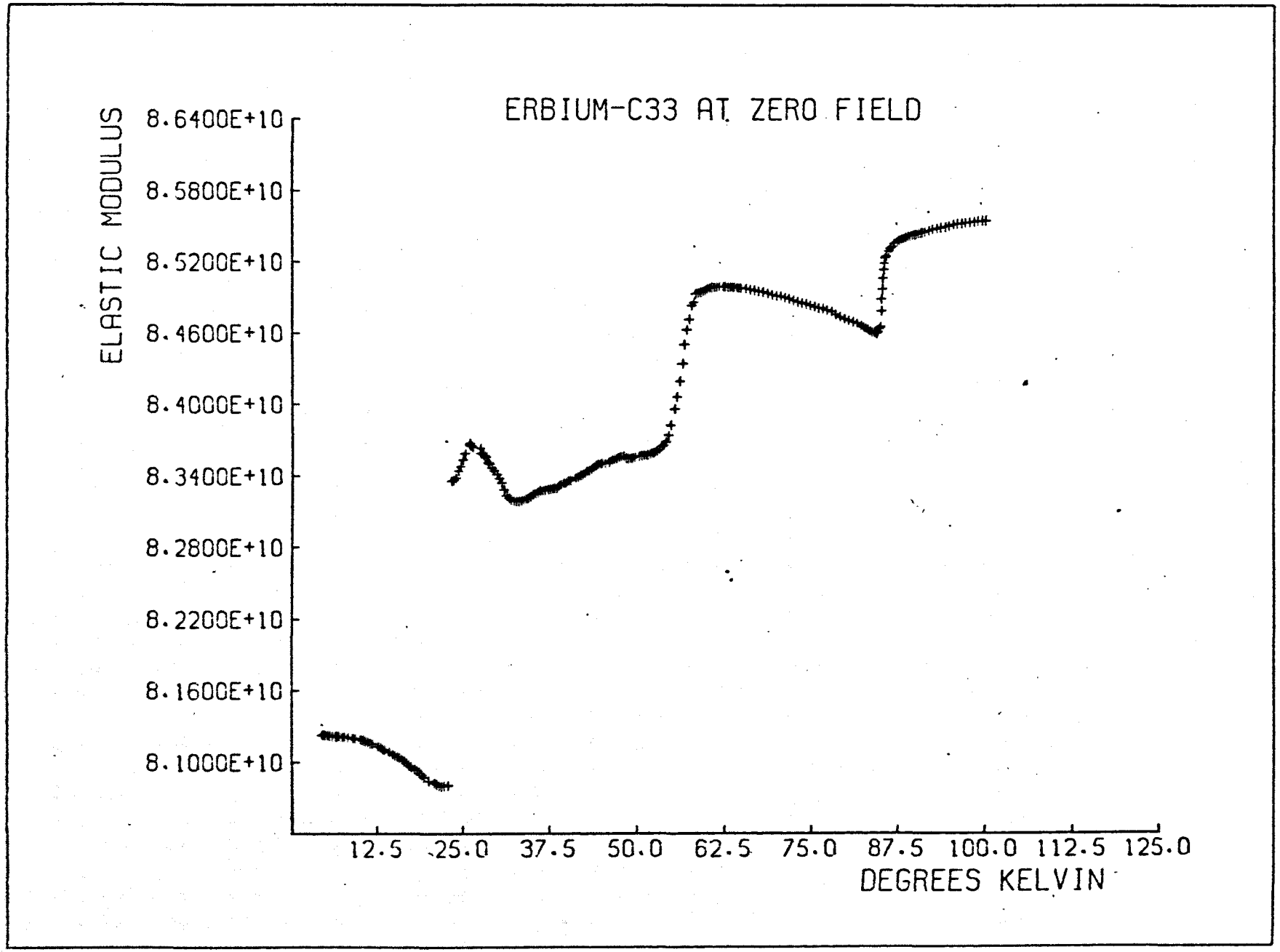
ERBIUM-C33 AT ZERO FIELD
ELASTIC MODULUS
8.6400E+10
8.5800E+10
8.5200E+10
8.4600E+10
8.4000E+10
8.3400E+10
8.2800E+10
8.2200E+10
8.1600E+10
8.1000E+10
12.5
25.0
37.5
50.0
62.5
75.0
87.5
100.0
112.5
125.0
DEGREES KELVIN

fig. 8.5

Comparison of the Transition Temperatures of Erbium according to the various different workers. The results are based on the variations of C_{33} with temperature

	T_C	T^*	T_N
Rosen [6]	22.5	52.5	85
Palmer [3]	19	54.5	85.5
du Plessis [7]	20	53	85
this work	22	54.5	84.5

fig. 8.6

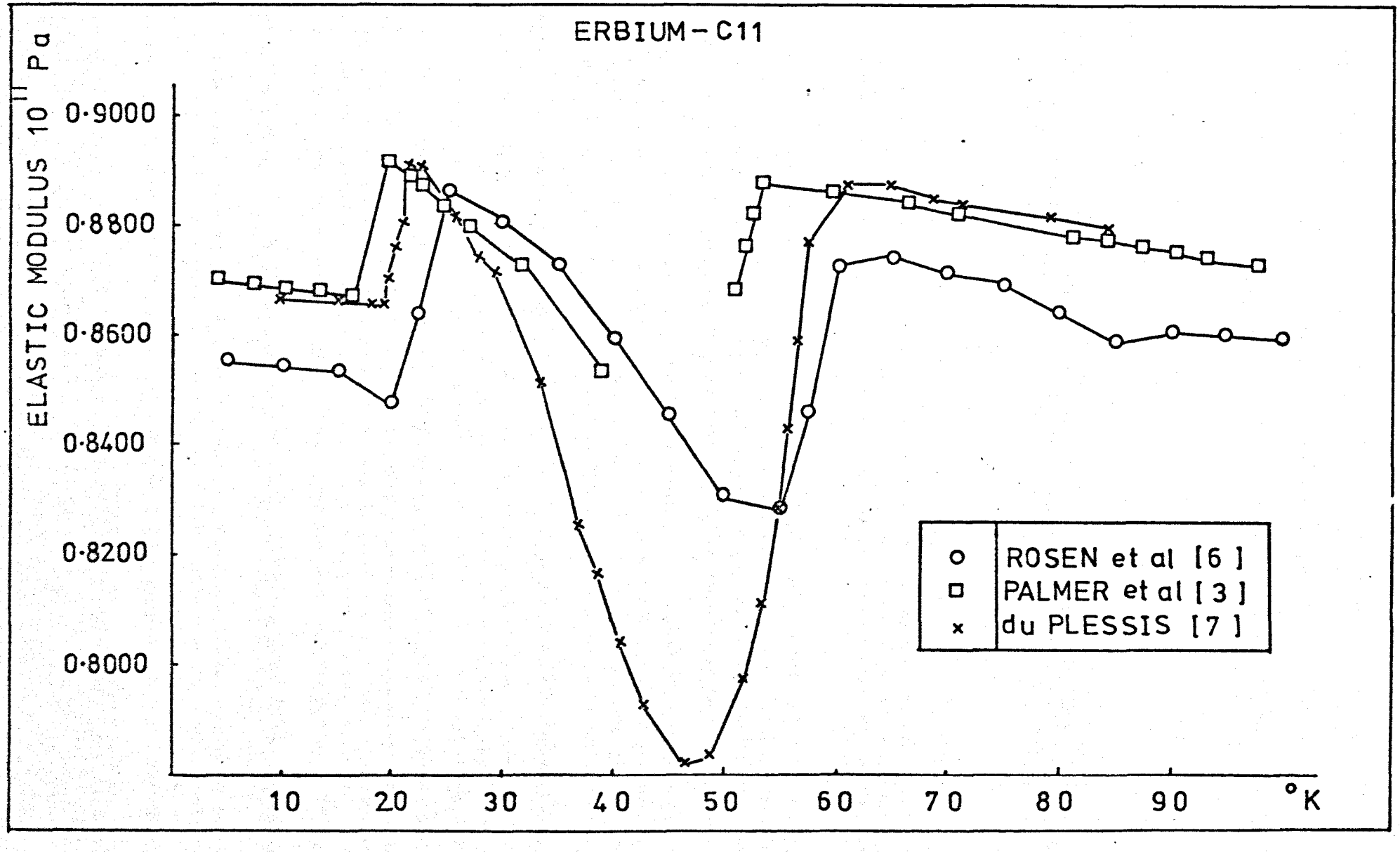
ERBIUM - C11
ELASTIC MODULUS 10^{11} Pa
0·9000
0·8800
0·8600
0·8400
0·8200
0·8000
10
20
30
40
50
60
70
80
90
°K
ROSEN et al [6]
PALMER et al [3]
du PLESSIS [7]

Fig. 8.7

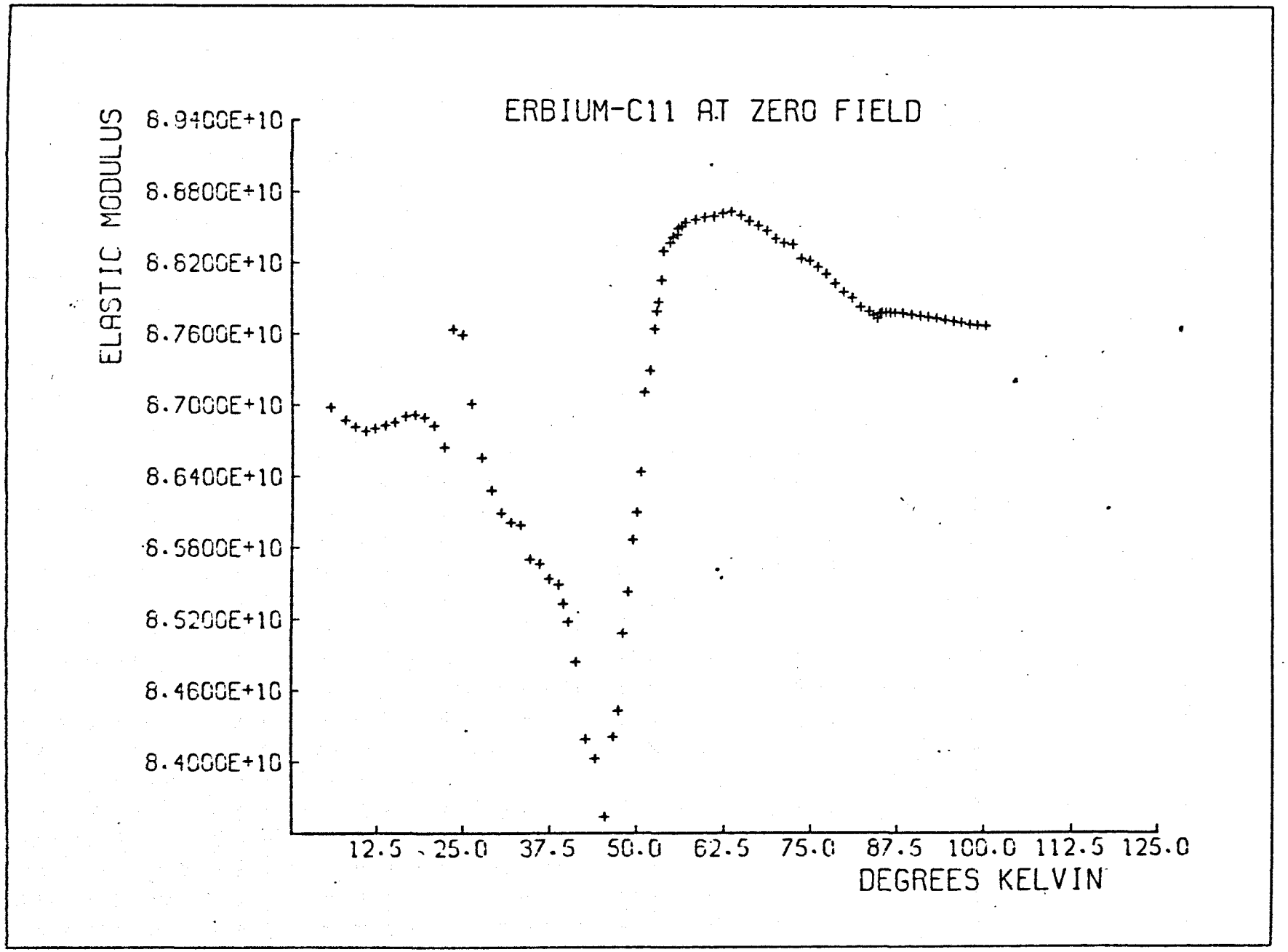
ERBIUM-C11 AT ZERO FIELD
ELASTIC MODULUS
8.9400E+10
8.8800E+10
8.8200E+10
8.7600E+10
8.7000E+10
8.6400E+10
8.5800E+10
8.5200E+10
8.4600E+10
8.4000E+10
12.5
25.0
37.5
50.0
62.5
75.0
87.5
100.0
112.5
125.0
DEGREES KELVIN

fig. 8.8

and also a small anomaly and a definite change in slope at 84.5°K which does not appear in the work of Palmer et al or du Plessis, although the work of Rosen shows this behaviour.

A comparison of the results for C_{44} is given in fig. 8.9. The main features are a sharp change in the modulus at the Curie point followed by a slower increase up to a maximum at a temperature of about 50°K. A change in slope occurs at about 85°K. The maximum discrepancy between the results is about 5% between the values of Rosen et al, and the values of du Plessis. The results of Palmer et al are intermediate.

The behaviour of C_{44} from the present work is given in fig. 8.10 and is in broad agreement with the earlier findings. A small but definite change in slope of the elastic modulus occurs at 56°K close to the phase transition. This was also present in the results of Rosen but is missing from the other reports. The change in slope at the Neel temperature occurs at 86°K.

Finally the results of previous work on C_{66} are given in fig. 8.11. Here the main characteristic is a deep anomaly between 20 - 55°K similar to that observed in C_{11}, and corresponding to the helically ordered base plane magnetic structure with an antiphase domain type of c axis modulation. According to Palmer et al the attenuation below 53°K was too great to allow results to be taken. Rosen et al show an anomaly with a depth of about 12% while du Plessis indicates a deeper anomaly of some 28% reduction in the value of this modulus and again results were not obtained over the whole range because of severe attenuation. None of these results show any abrupt changes in the modulus at either 20°K or 85°K.

The present results for C_{66} are given in fig. 8.12. The characteristic softening of this mode between 25°K and 55°K is again present. Results were not possible over a large region of the temperature

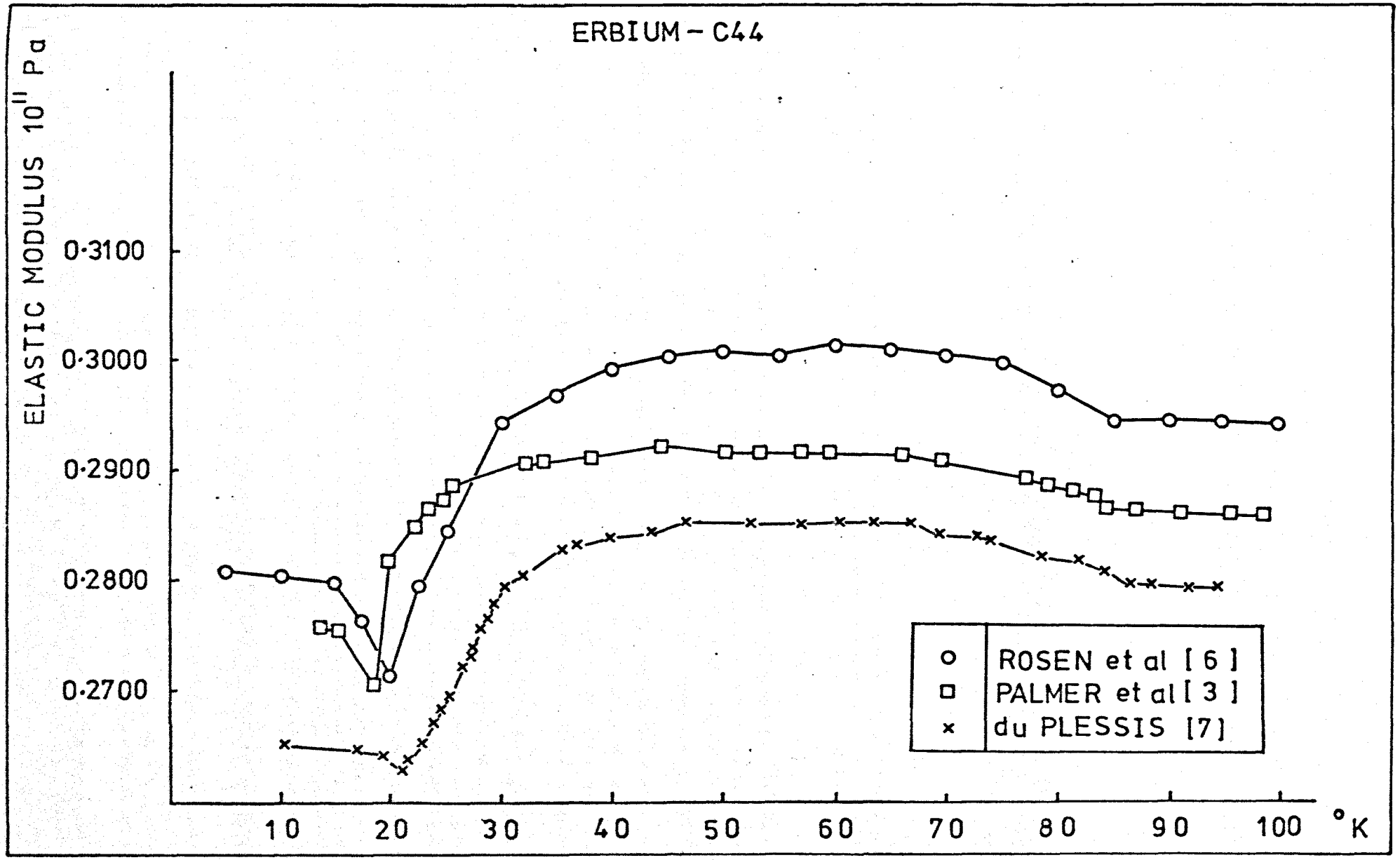
ERBIUM – C44
ELASTIC MODULUS 10^{11} Pa
0·3100
0·3000
0·2900
0·2800
0·2700
10
20
30
40
50
60
70
80
90
100
°K
ROSEN et al [6]
PALMER et al [3]
du PLESSIS [7]

Fig. 8.9

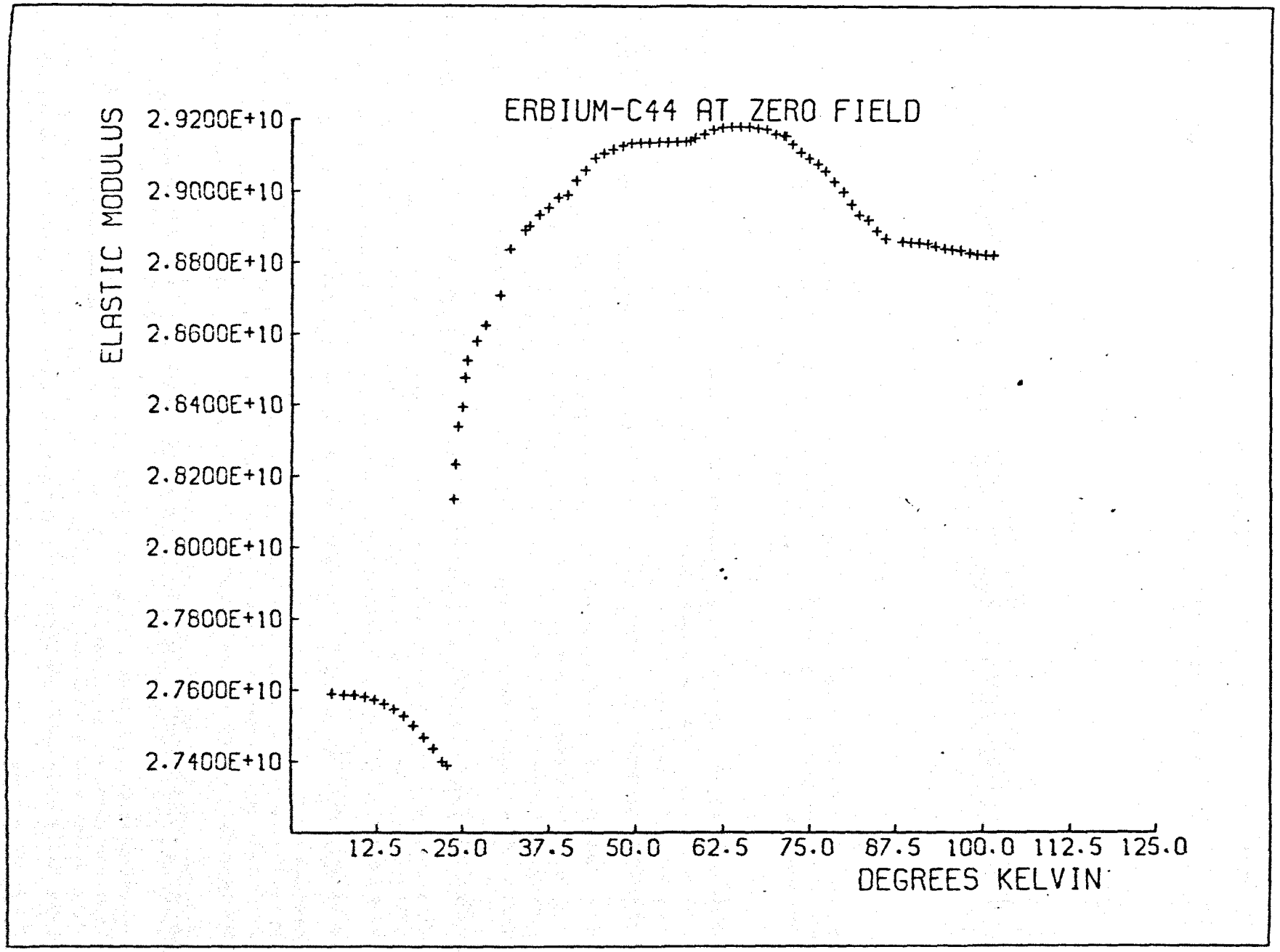
ERBIUM-C44 AT ZERO FIELD
ELASTIC MODULUS
2.9200E+10
2.9000E+10
2.8800E+10
2.8600E+10
2.8400E+10
2.8200E+10
2.8000E+10
2.7800E+10
2.7600E+10
2.7400E+10
12.5
25.0
37.5
50.0
62.5
75.0
87.5
100.0
112.5
125.0
DEGREES KELVIN

fig. 8.10

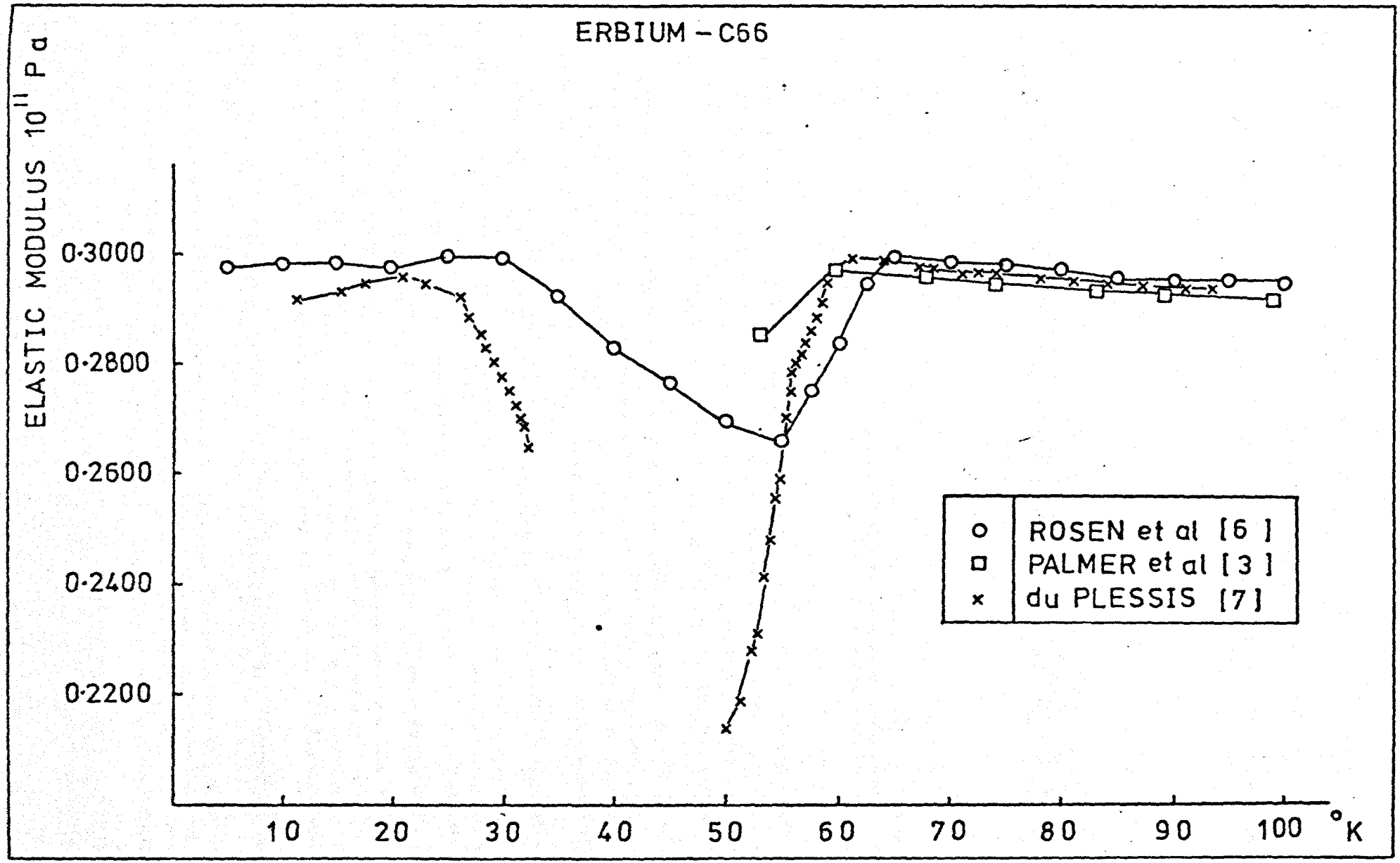
ERBIUM – C66
ELASTIC MODULUS 10^{11} Pa
0·3000
0·2800
0·2600
0·2400
0·2200
10
20
30
40
50
60
70
80
90
100
°K
ROSEN et al [6]
PALMER et al [3]
du PLESSIS [7]

fig. 8.11

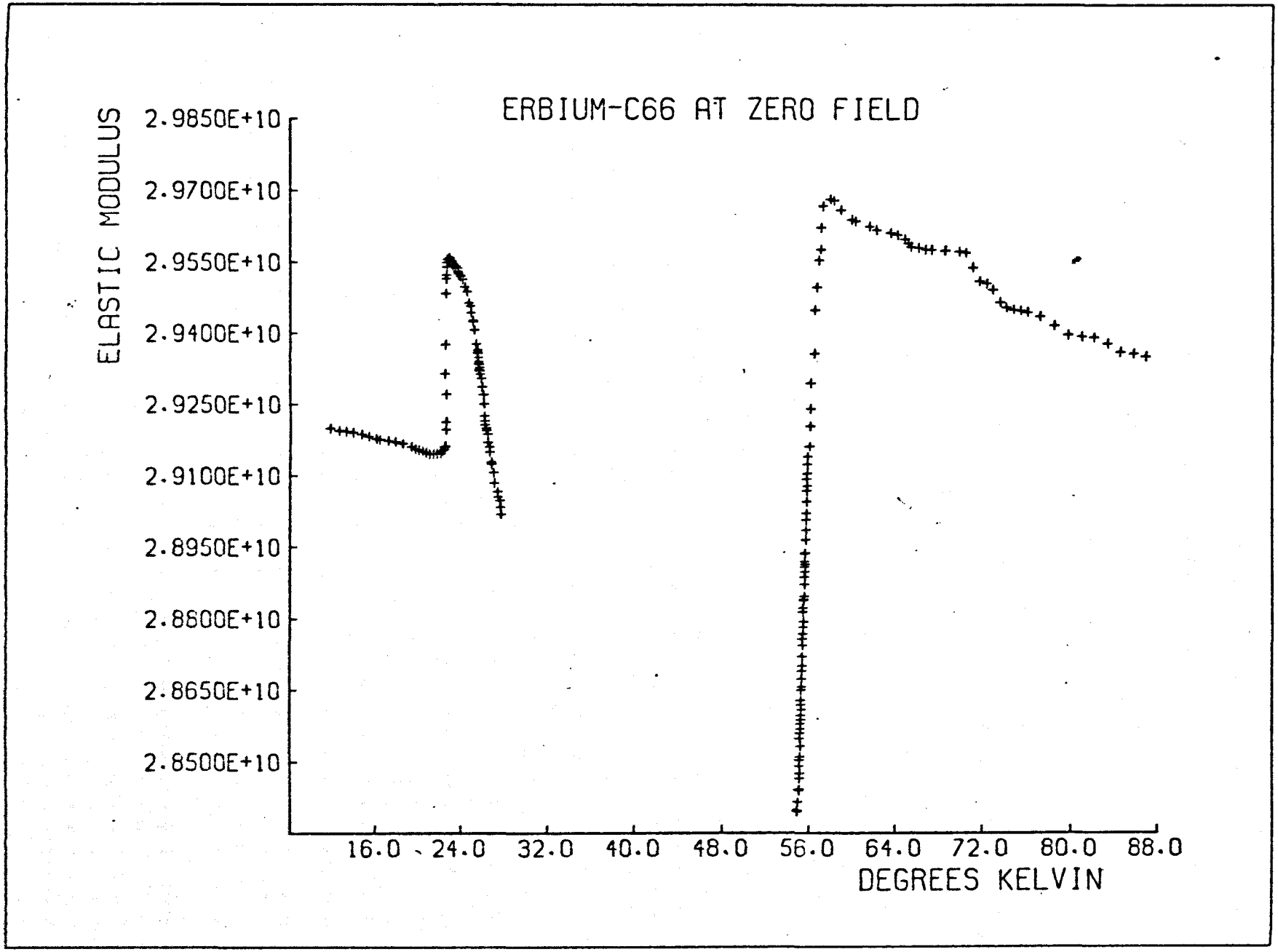
ERBIUM-C66 AT ZERO FIELD
ELASTIC MODULUS
2.9850E+10
2.9700E+10
2.9550E+10
2.9400E+10
2.9250E+10
2.9100E+10
2.8950E+10
2.8800E+10
2.8650E+10
2.8500E+10
16.0
24.0
32.0
40.0
48.0
56.0
64.0
72.0
80.0
88.0
DEGREES KELVIN

fig. 8.12

range. The anomaly here had a depth of 4.5% before readings became impossible due to attenuation and consequently no upper limit can be given to its depth. Another feature not reported in the earlier work was the pronounced increase of C_{66} in the region of T_C of about 1% followed by the already reported anomaly above T_C.

Results for the cross checking measurement $\frac{1}{2}(C_{66} + C_{44})$ are shown in fig. 8.13 giving again a deep anomaly at about 50°K corresponding to the softening of the C_{66} mode. This has a depth of about 10% compared with the value of the modulus at 60°K, and since the value of C_{44} does not vary much between 50°K and 60°K this would indicate that the anomaly in C_{66} which could not be observed because of attenuation would be of a depth of about 20%. Also a change in shape occurs at about 84°K corresponding to the observed change in slope of C_{44}. Those measured results are compared with the calculated values of $\frac{1}{2}(C_{66} + C_{44})$ in fig. 8.14.

8.3 Measurement of Transit Time τ

The transit time τ of acoustic pulses through a specimen of Terbium has been measured, using the internal memory store, as a function of a rapidly swept applied magnetic field. The raw data was converted into a time measurement in microseconds using equation 4.1, viz.

$$\tau_i = 0.128(D + 1) + \frac{t_i + 2}{1000} \qquad \ldots.8.1$$

where D is the digital delay which controls the width of the delay gate and t_i is the coded number from the punched tape.

8.3.1 Variation of C_{33} of Terbium as a Function of Applied Magnetic Field

Some results of transit times of three round trips through a sample of Terbium, Tb(I), have been taken as a function of magnetic field applied along the easy direction of magnetisation, the b axis, in the antiferromagnetic regime. Application of such a field should cause initially a distortion of the helical structure and at higher field strengths, according to Nagamiya

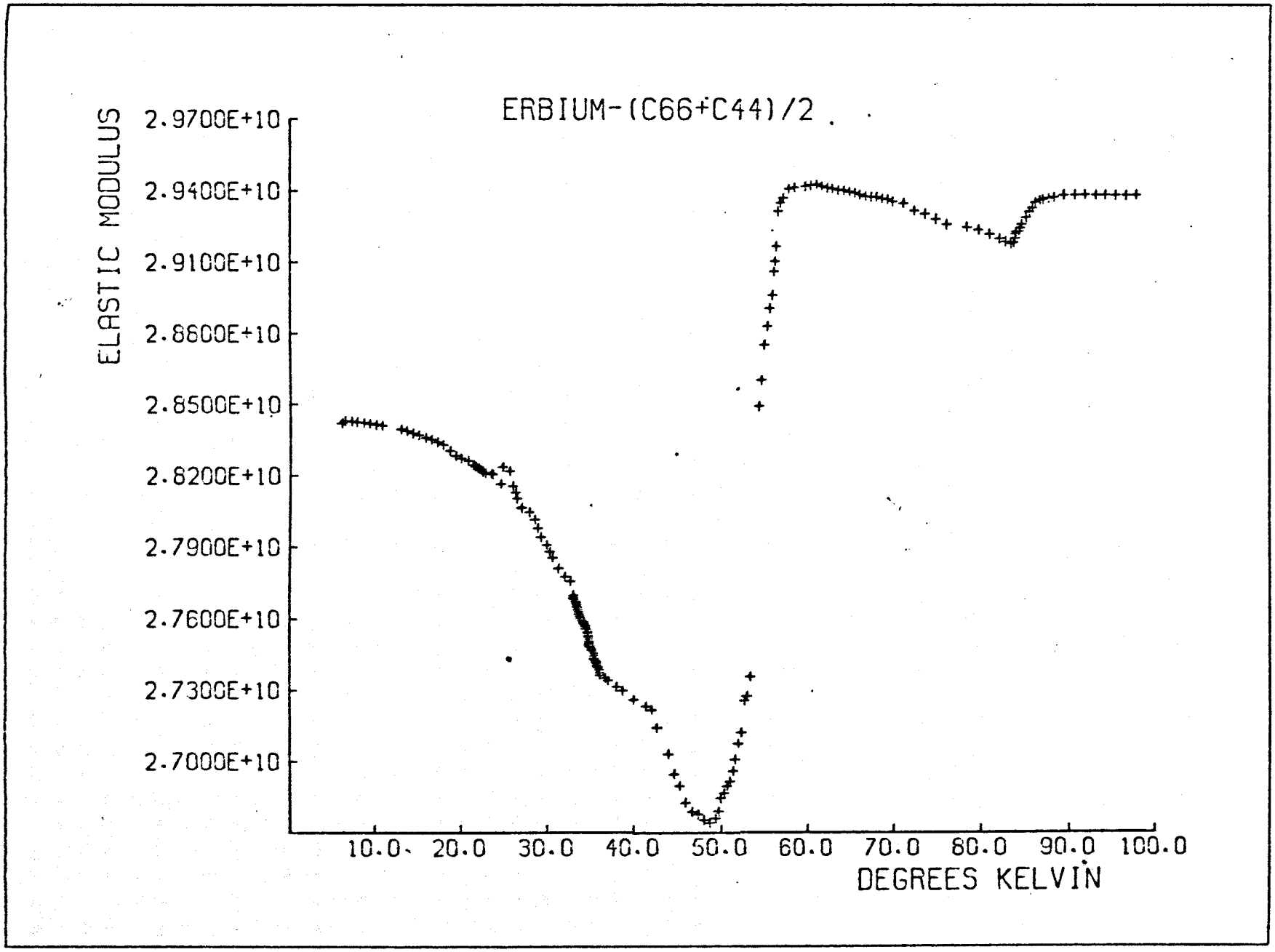
ERBIUM-(C66+C44)/2
ELASTIC MODULUS
2.9700E+10
2.9400E+10
2.9100E+10
2.8600E+10
2.8500E+10
2.8200E+10
2.7900E+10
2.7600E+10
2.7300E+10
2.7000E+10
10.0
20.0
30.0
40.0
50.0
60.0
70.0
80.0
90.0
100.0
DEGREES KELVIN

fig. 8.13

Comparison of values of the mode $\frac{1}{2}(C_{44} + C_{66})$ as measured in fig. 8.15 and as calculated from the corresponding values of C_{44} and C_{66}

Temp°K	Calculated	Measured	Discrepancy
15	0.28365	0.28370	0.176×10^{-3}
20	0.28303	0.28271	0.989×10^{-3}
25	0.28926	0.28231	0.240×10^{-1}
55	0.28789	0.28792	0.104×10^{-3}
60	0.29402	0.29422	0.680×10^{-3}
65	0.29387	0.29395	0.272×10^{-3}
70	0.29366	0.29348	0.613×10^{-3}
75	0.29271	0.29282	0.376×10^{-3}
80	0.29196	0.29237	1.404×10^{-3}
85	0.29122	0.29281	5.445×10^{-3}

fig. 8.14

and Kitano [8], a 'fan' state should be produced. (Crangle has recently [9] suggested that in fact no such fan state exists in Terbium). At higher field strengths still the angle of the fan closes and finally the alignment becomes ferromagnetic.

The behaviour of the elastic modulus C_{33} in Terbium follows a similar pattern to that in Dysprosium [10] when subjected to a field. An initial slow decrease, corresponding to the distortion of the helix, is followed by a rapid softening of the modulus when the fan state is formed and then a slow, and in some cases incomplete, recovery as the fan angle closes to form a ferromagnetic alignment.

The present results are shown in figs. 8.15 - 8.21. The transit times from the fast sampling mode have error bars representing the uncertainty of ± 3 nsecs in the timing as discussed in section 4.2.3. Alongside these results the simultaneously measured repetition rate frequencies of the sing around, as monitored on the frequency meter, are given in kiloherz.

As can be seen from the results the maxima in the transit times occur at the same field strengths as the corresponding minima in repetition rate, or velocity. These occur at field strengths of between 0.35 and 0.45 Tesla according to the temperature of the specimen. The actual location of the minima in velocity may be compared with the resulting phase diagram of Tb(I) given in chapter nine, since the minimum velocity will correspond to the minimum value of the elastic constant.

The general shape of the curves of transit time τ against field and repetition rate against field shown in figs. 8.15 - 8.21 are also similar bearing in mind that $\tau \propto {}^{1}/_{f}$. For example the results at 214°K given in fig. 8.15 show the transit time and velocity recovering much of their original value after the maximum/minimum, whereas at 226.5°K which is just into the paramagnetic region, the behaviour is less field dependent after the maximum/minimum with the velocity and transit time not recovering their original values.

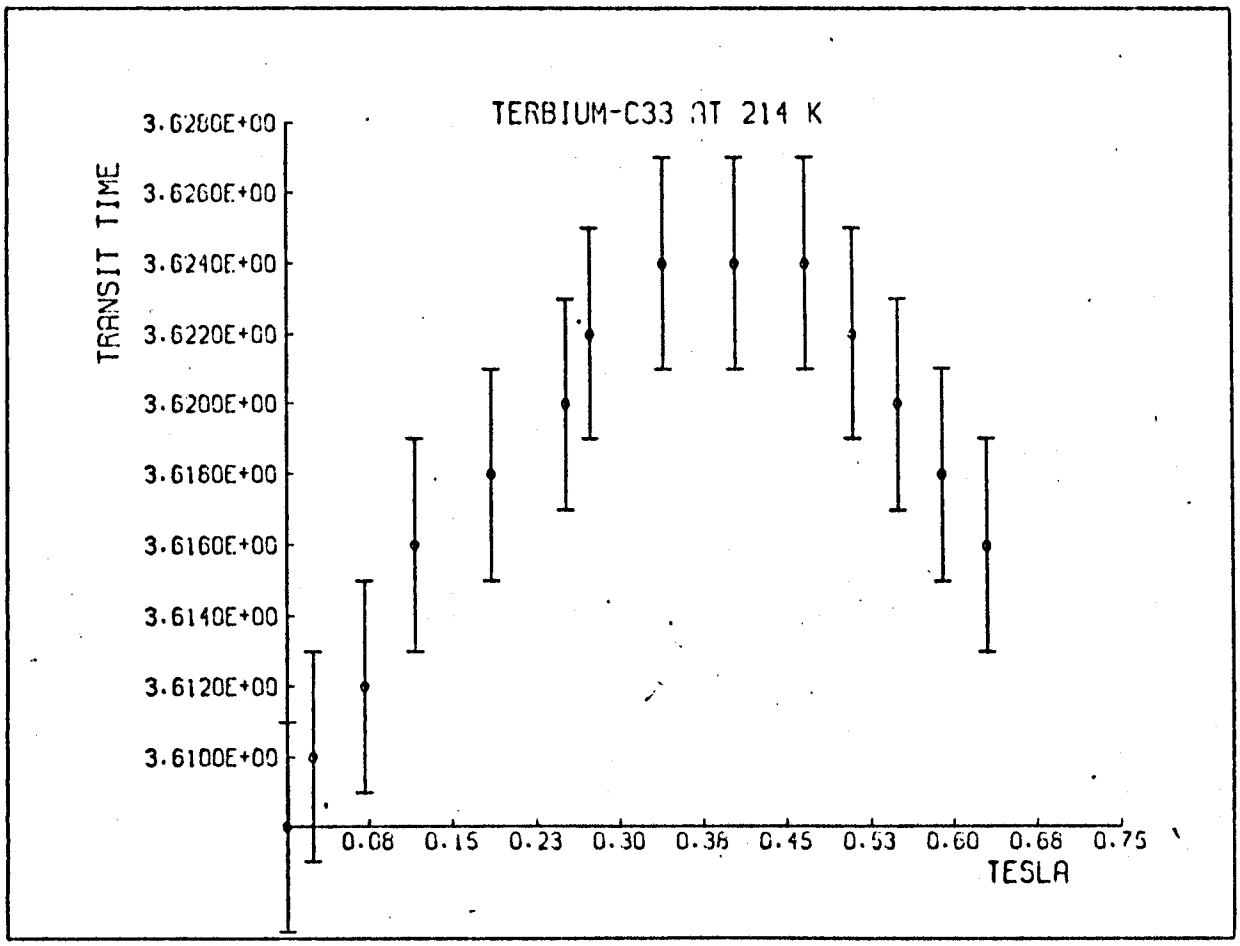
TERBIUM-C33 AT 214 K
TRANSIT TIME
3.6280E+00
3.6260E+00
3.6240E+00
3.6220E+00
3.6200E+00
3.6180E+00
3.6160E+00
3.6140E+00
3.6120E+00
3.6100E+00
0.08
0.15
0.23
0.30
0.38
0.45
0.53
0.60
0.68
0.75
TESLA

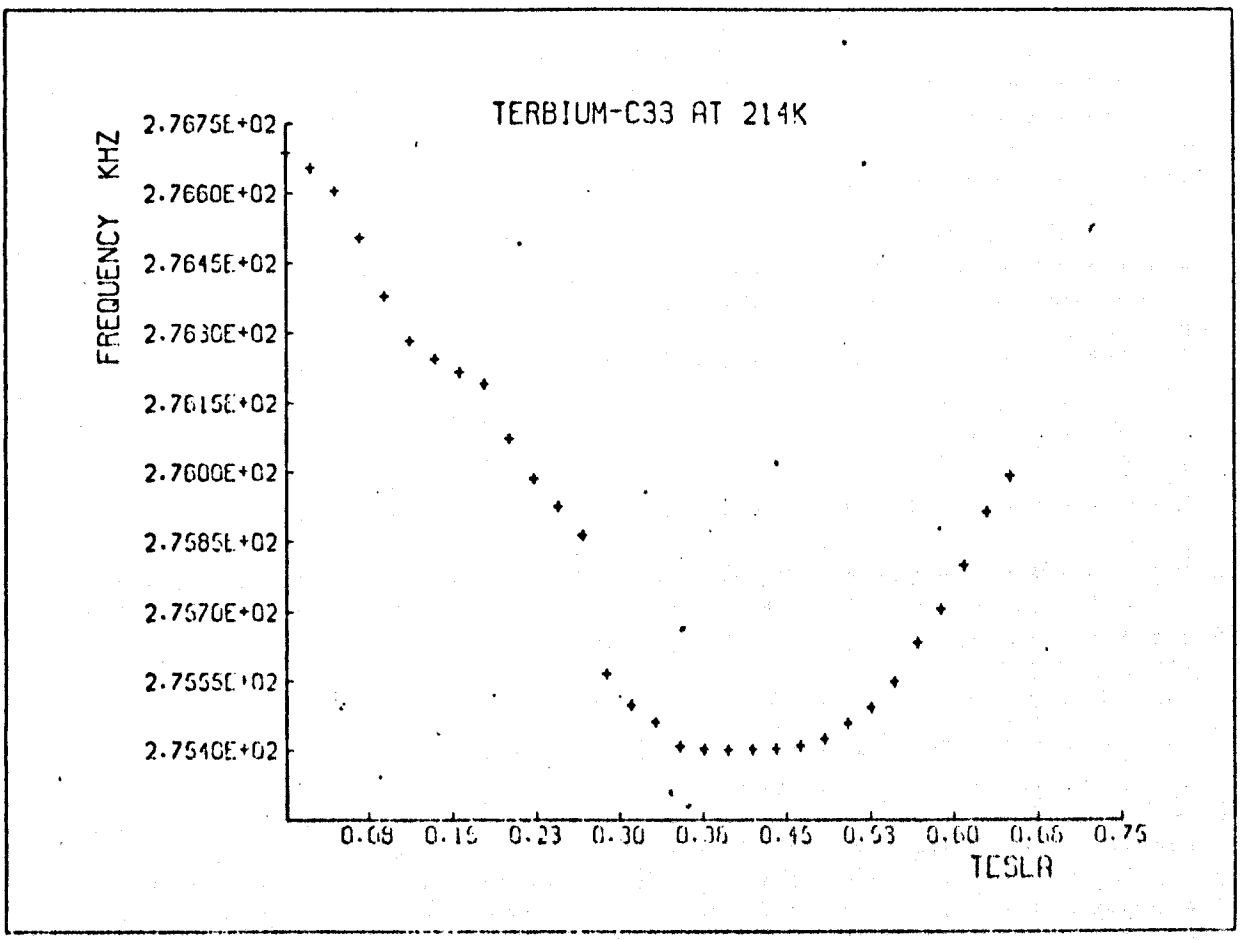
TERBIUM-C33 AT 214K
FREQUENCY KHZ
2.7675E+02
2.7660E+02
2.7645E+02
2.7630E+02
2.7615E+02
2.7600E+02
2.7585E+02
2.7570E+02
2.7555E+02
2.7540E+02
0.08
0.15
0.23
0.30
0.38
0.45
0.53
0.60
0.68
0.75
TESLA

fig. 8.15

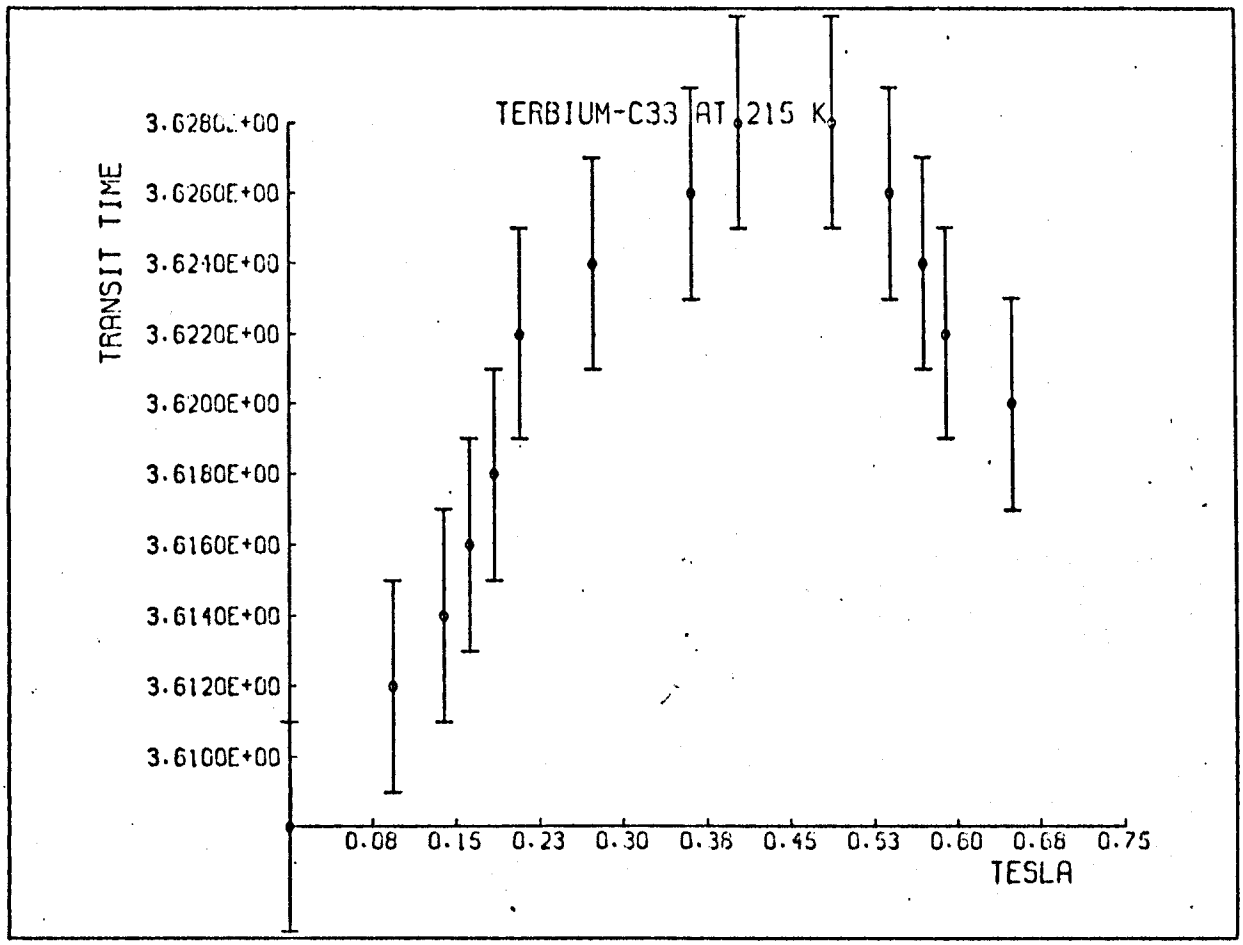
TERBIUM-C33 AT 215 K
TRANSIT TIME
3.6280E+00
3.6260E+00
3.6240E+00
3.6220E+00
3.6200E+00
3.6180E+00
3.6160E+00
3.6140E+00
3.6120E+00
3.6100E+00
0.08
0.15
0.23
0.30
0.38
0.45
0.53
0.60
0.68
0.75
TESLA

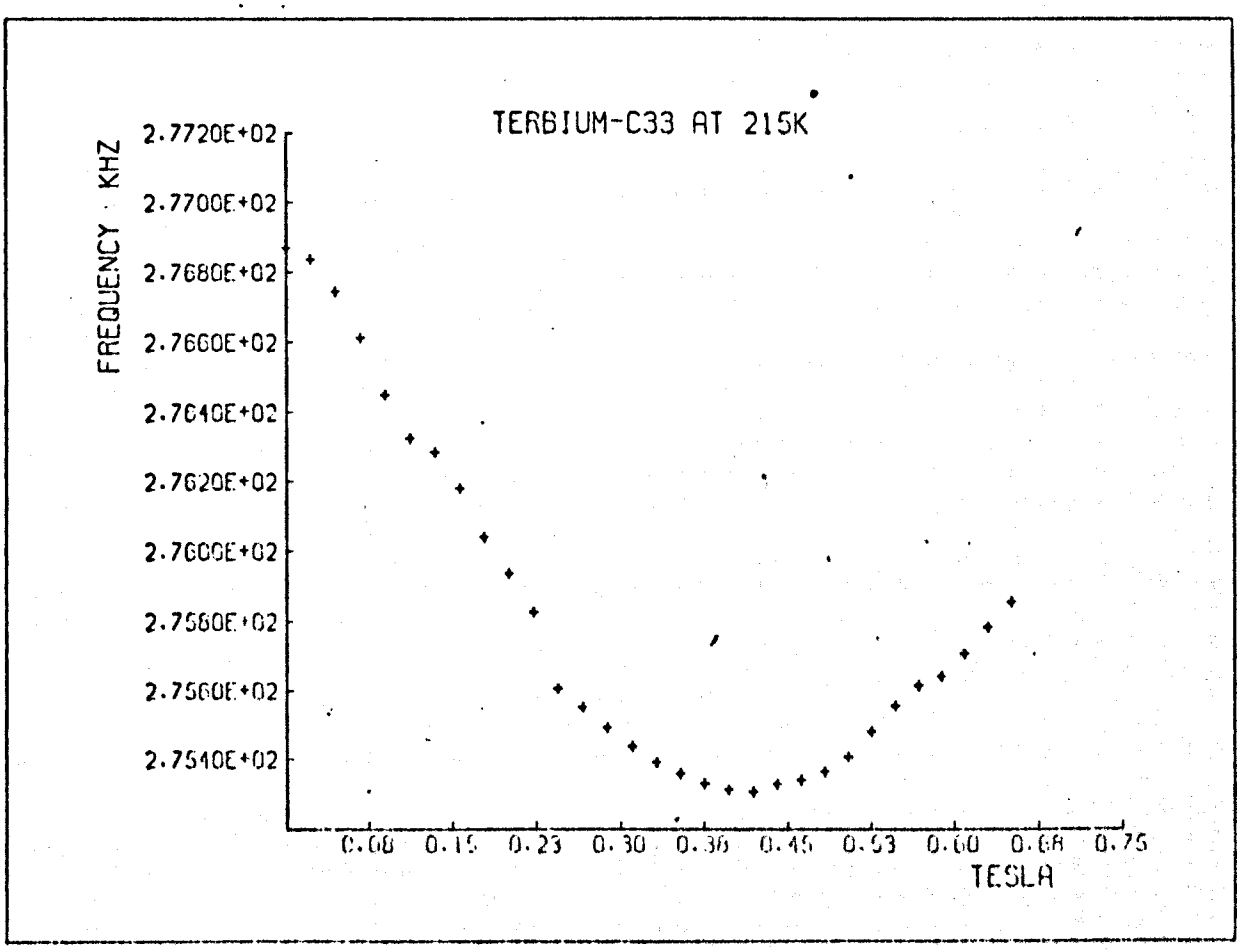
TERBIUM-C33 AT 215K
FREQUENCY - KHZ
2.7720E+02
2.7700E+02
2.7680E+02
2.7660E+02
2.7640E+02
2.7620E+02
2.7600E+02
2.7580E+02
2.7560E+02
2.7540E+02
0.08
0.15
0.23
0.30
0.38
0.45
0.53
0.60
0.68
0.75
TESLA

fig. 8.16

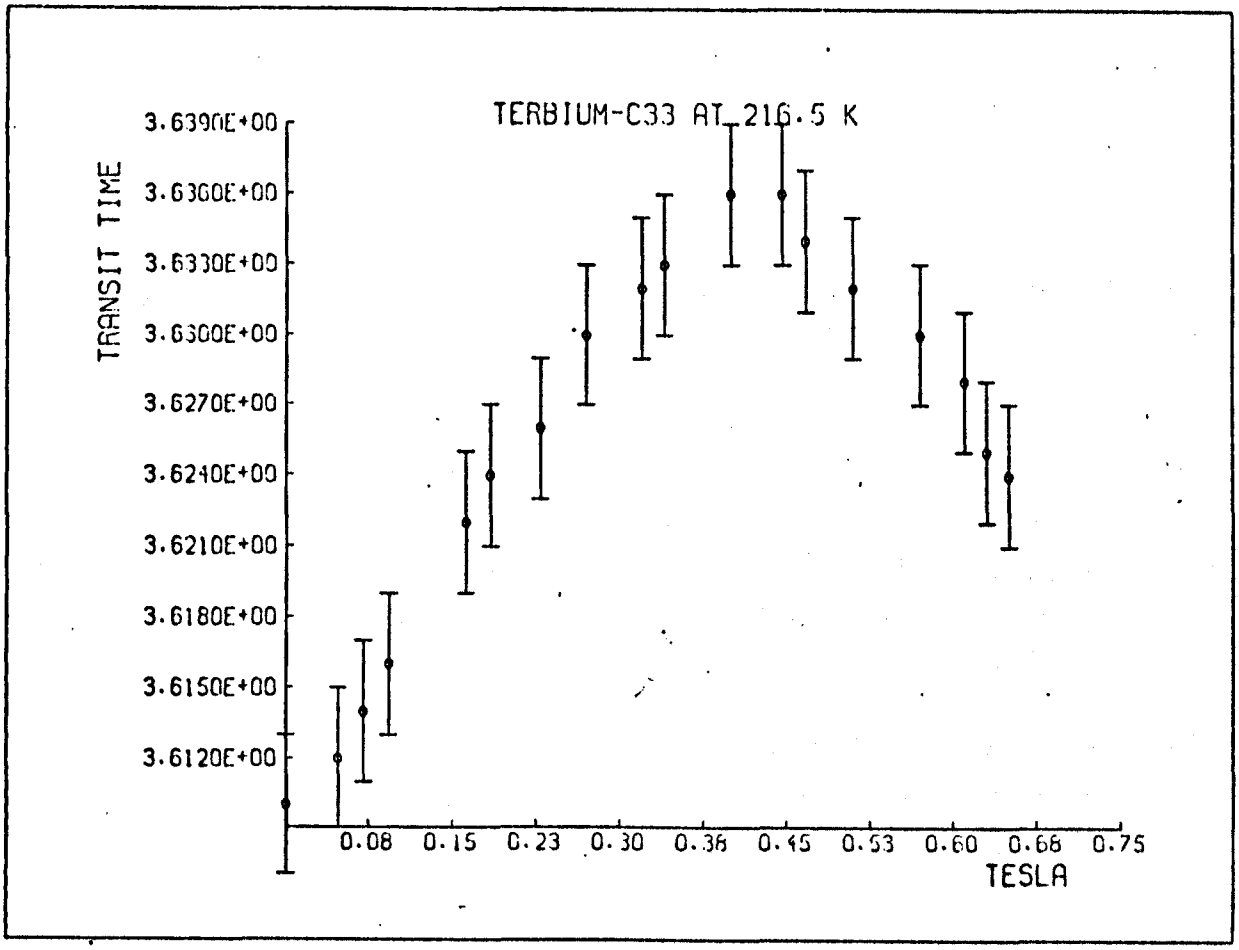
TERBIUM-C33 AT 216.5 K
TRANSIT TIME
3.6390E+00
3.6360E+00
3.6330E+00
3.6300E+00
3.6270E+00
3.6240E+00
3.6210E+00
3.6180E+00
3.6150E+00
3.6120E+00
0.08
0.15
0.23
0.30
0.38
0.45
0.53
0.60
0.68
0.75
TESLA

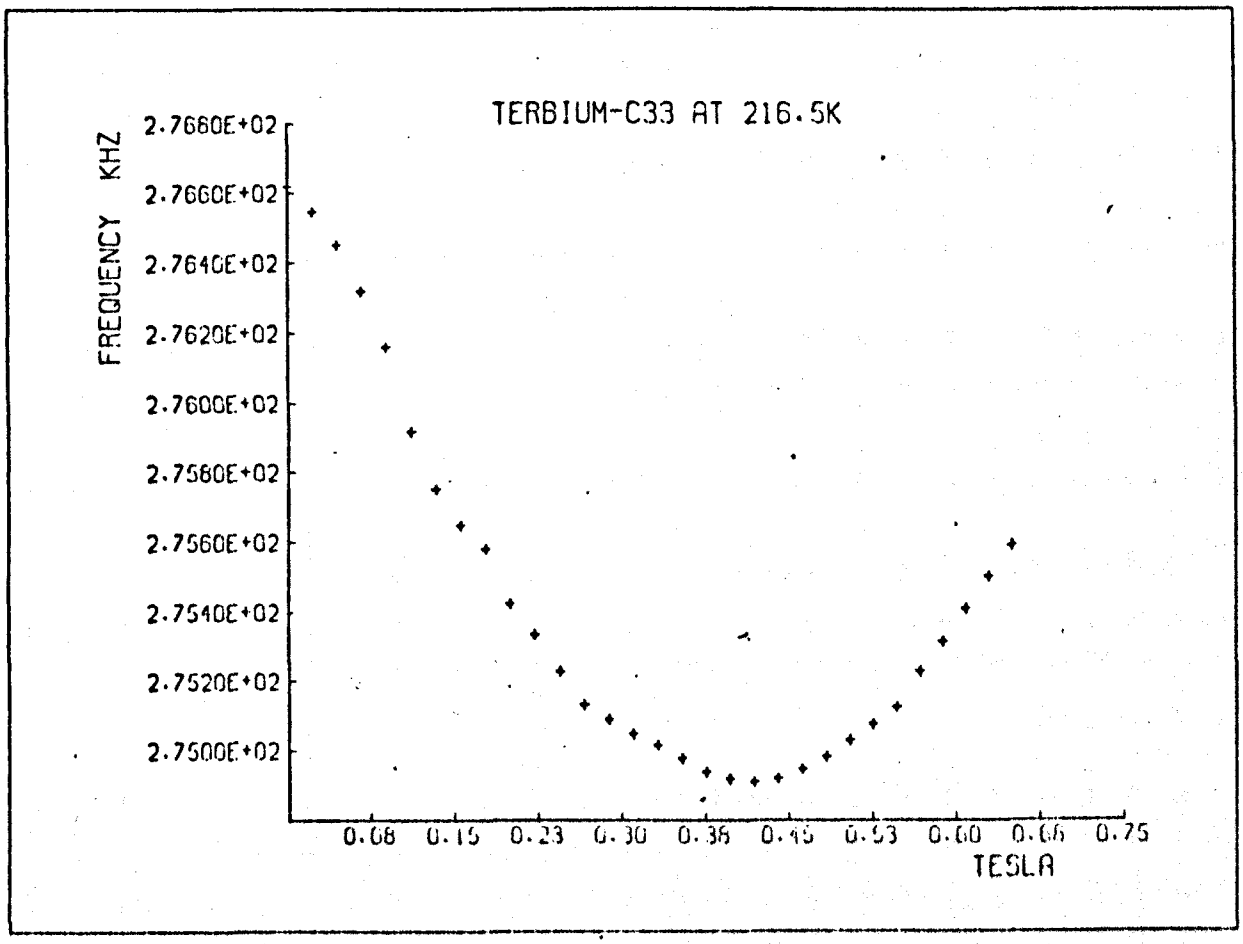
TERBIUM-C33 AT 216.5K
FREQUENCY KHZ
2.7660E+02
2.7660E+02
2.7640E+02
2.7620E+02
2.7600E+02
2.7580E+02
2.7560E+02
2.7540E+02
2.7520E+02
2.7500E+02
0.08
0.15
0.23
0.30
0.38
0.45
0.53
0.60
0.68
0.75
TESLA

fig. 8.17

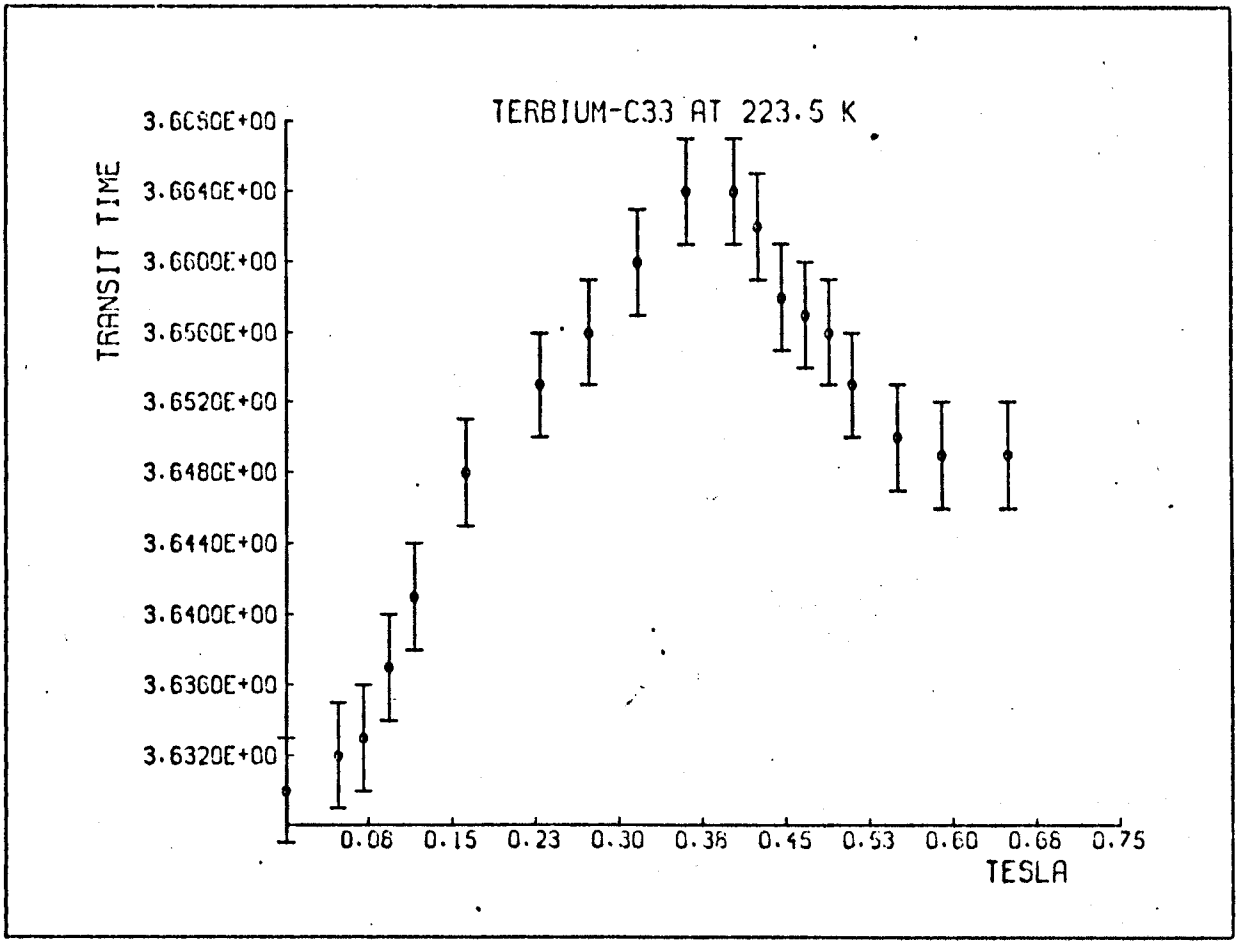
TERBIUM-C33 AT 223.5 K
TRANSIT TIME
3.6680E+00
3.6640E+00
3.6600E+00
3.6560E+00
3.6520E+00
3.6480E+00
3.6440E+00
3.6400E+00
3.6360E+00
3.6320E+00
0.08
0.15
0.23
0.30
0.38
0.45
0.53
0.60
0.68
0.75
TESLA

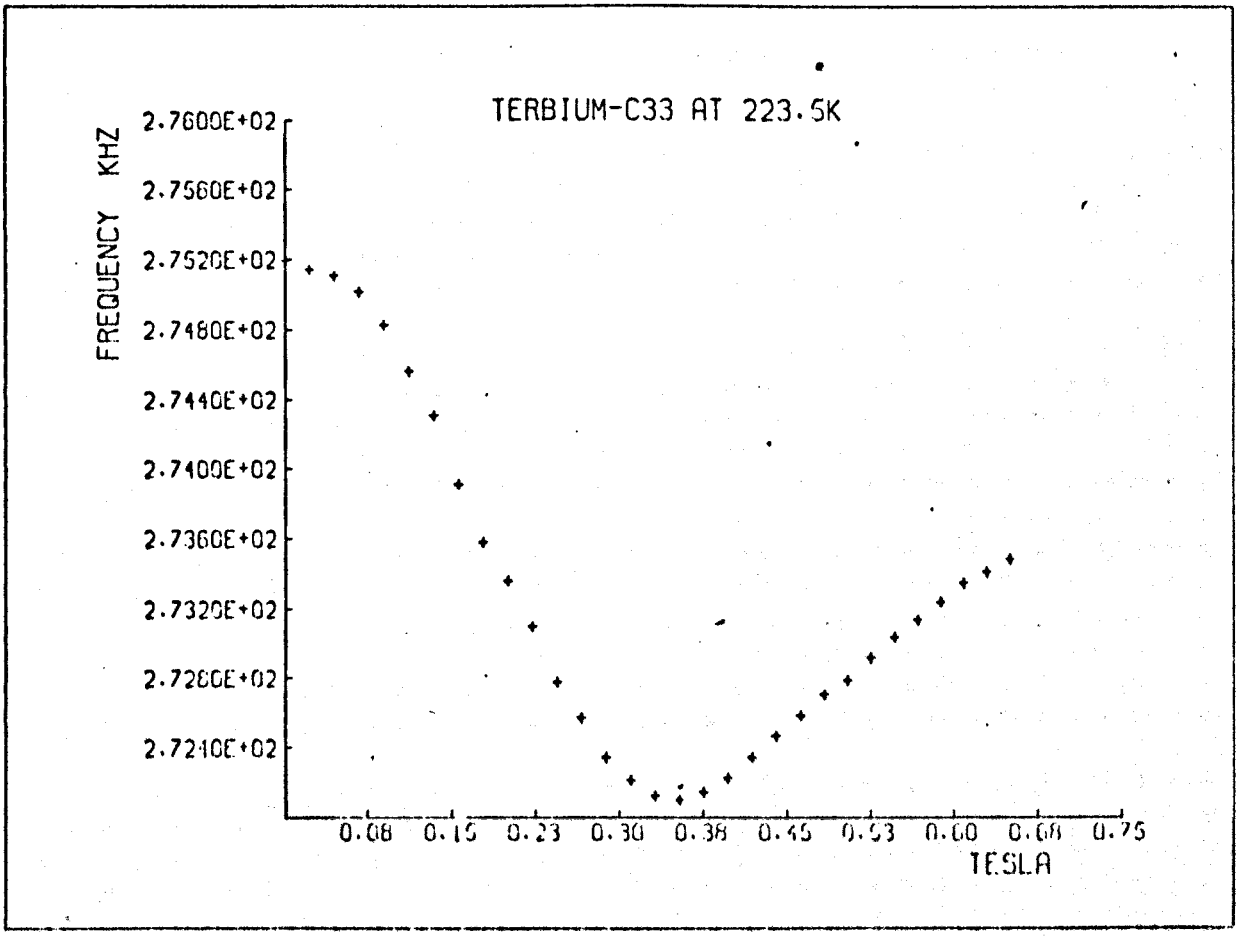
TERBIUM-C33 AT 223.5K
FREQUENCY KHZ
2.7600E+02
2.7560E+02
2.7520E+02
2.7480E+02
2.7440E+02
2.7400E+02
2.7360E+02
2.7320E+02
2.7280E+02
2.7240E+02
0.08
0.15
0.23
0.30
0.38
0.45
0.53
0.60
0.68
0.75
TESLA

fig. 8.18

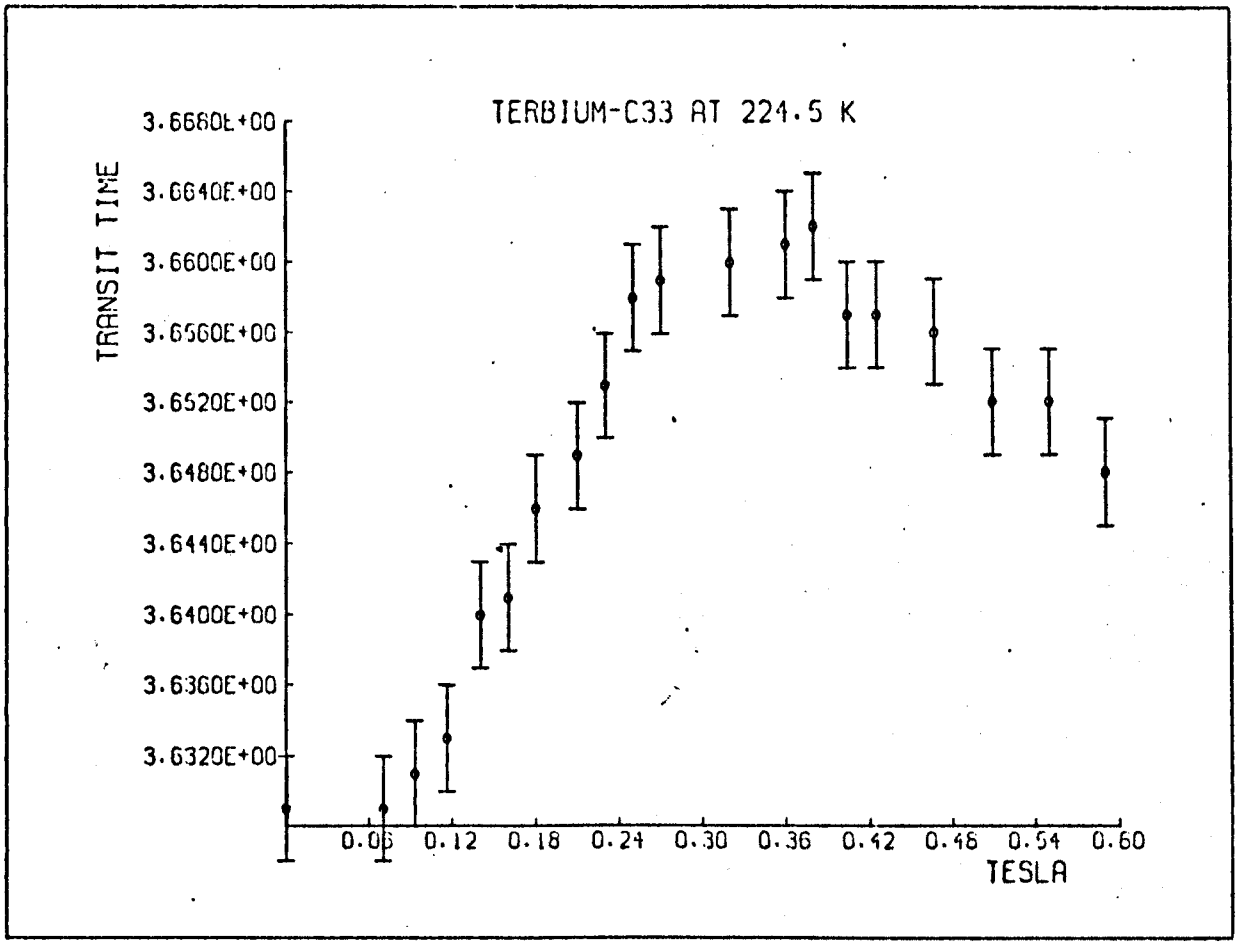
TERBIUM-C33 AT 224.5 K
TRANSIT TIME
3.6680E+00
3.6640E+00
3.6600E+00
3.6560E+00
3.6520E+00
3.6480E+00
3.6440E+00
3.6400E+00
3.6360E+00
3.6320E+00
0.06
0.12
0.18
0.24
0.30
0.36
0.42
0.48
0.54
0.60
TESLA

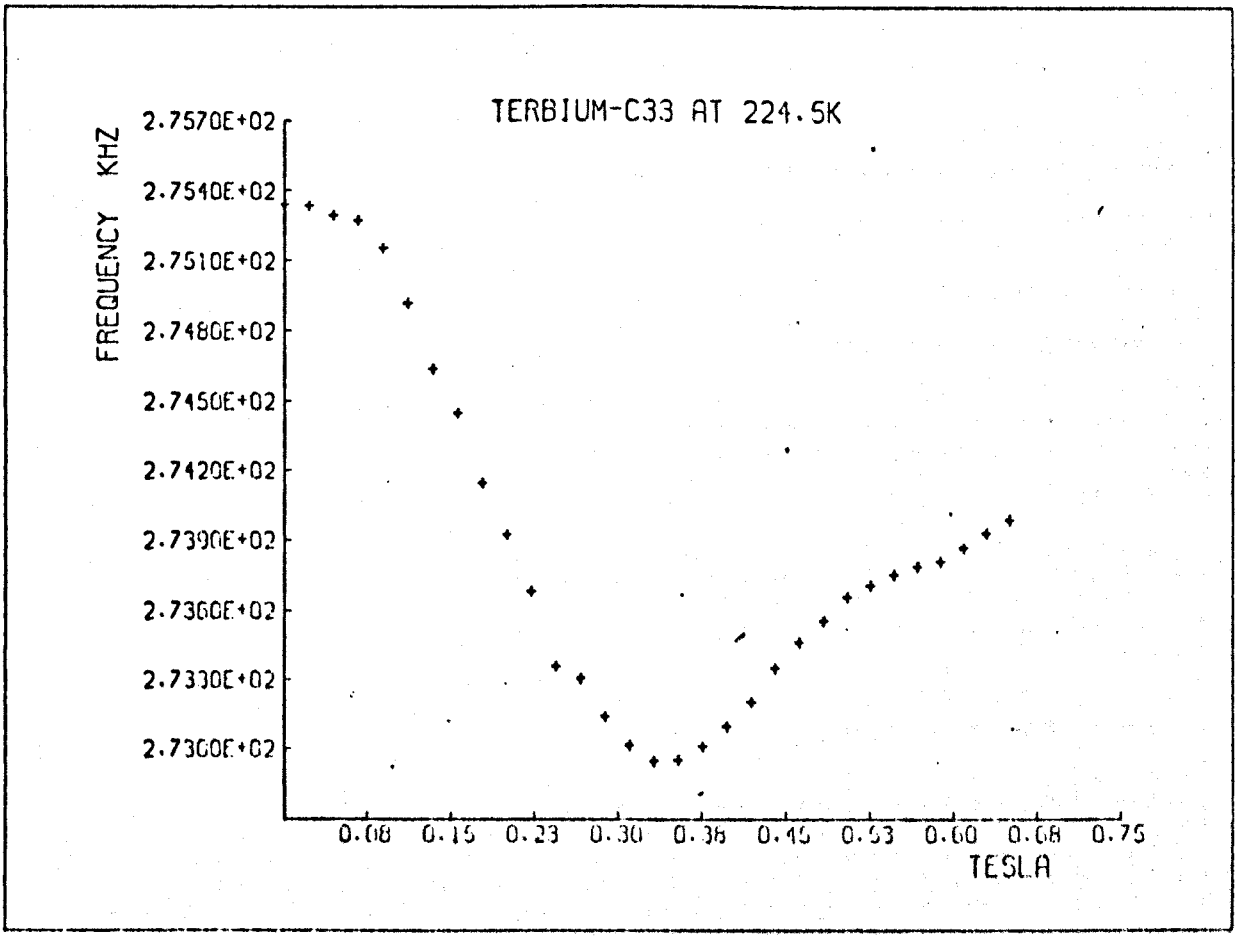
TERBIUM-C33 AT 224.5K
FREQUENCY KHZ
2.7570E+02
2.7540E+02
2.7510E+02
2.7480E+02
2.7450E+02
2.7420E+02
2.7390E+02
2.7360E+02
2.7330E+02
2.7300E+02
0.08
0.15
0.23
0.30
0.38
0.45
0.53
0.60
0.68
0.75
TESLA

fig. 8.19

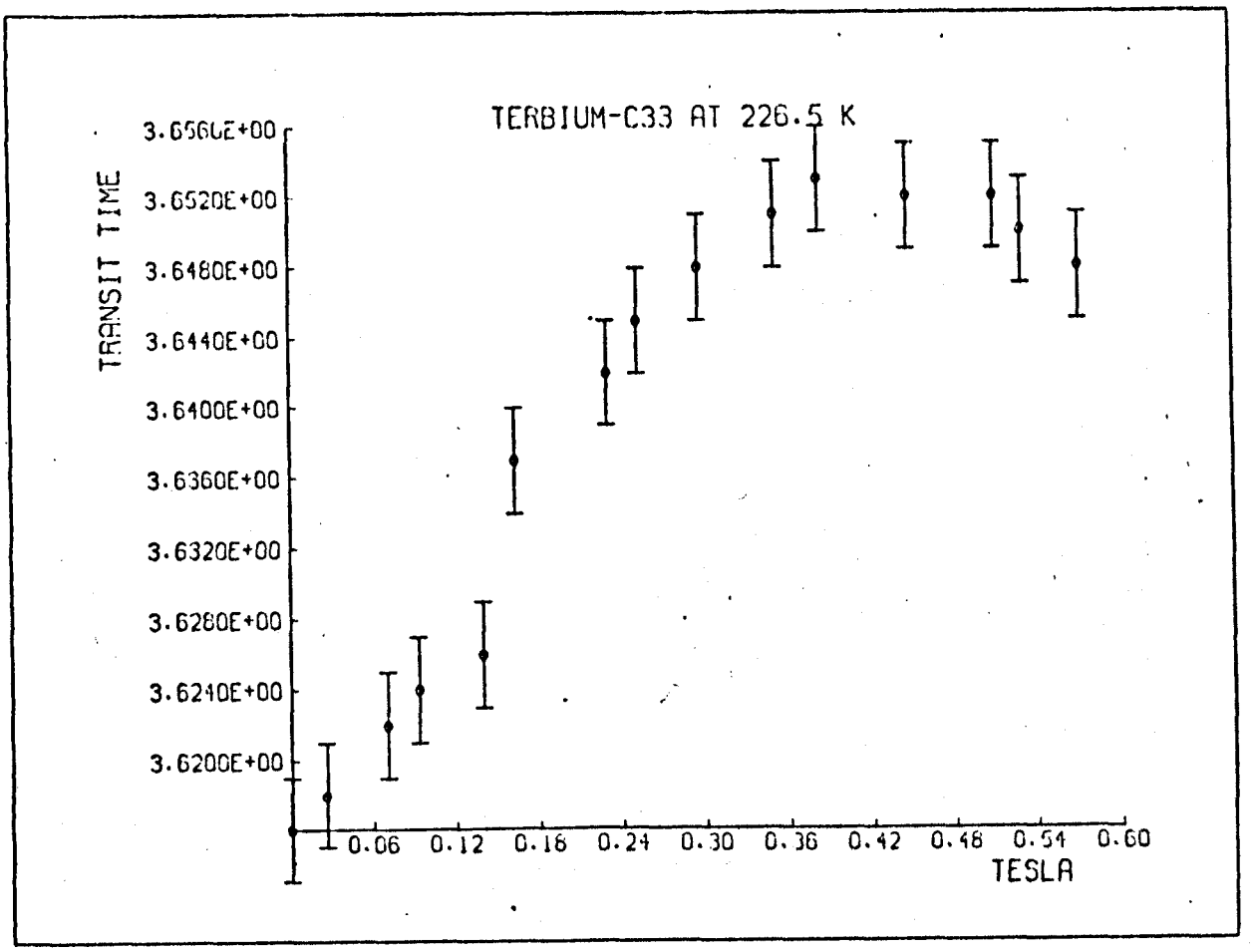
TERBIUM-C33 AT 226.5 K
TRANSIT TIME
3.6560E+00
3.6520E+00
3.6480E+00
3.6440E+00
3.6400E+00
3.6360E+00
3.6320E+00
3.6280E+00
3.6240E+00
3.6200E+00
0.06
0.12
0.18
0.24
0.30
0.36
0.42
0.48
0.54
0.60
TESLA

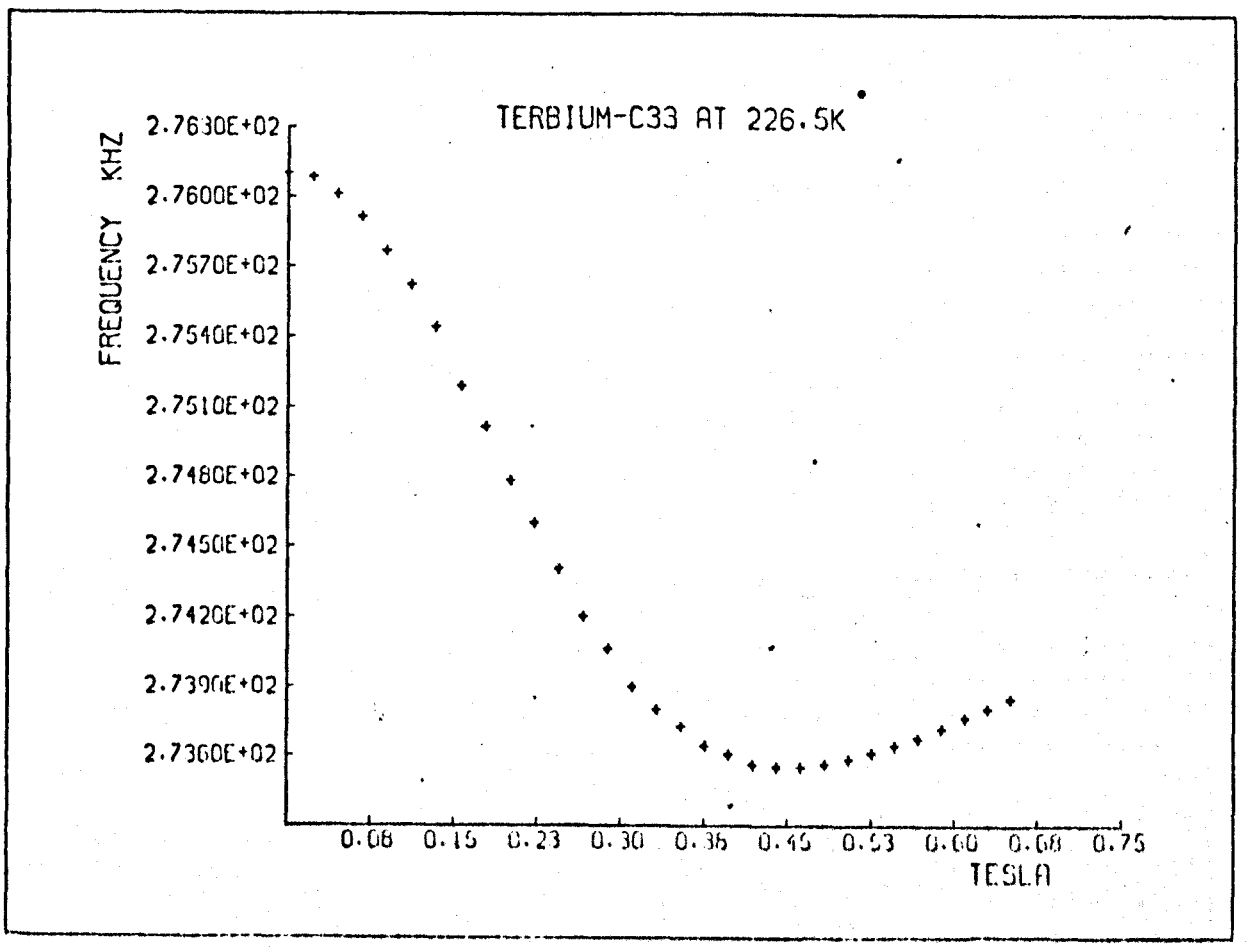
TERBIUM-C33 AT 226.5K
FREQUENCY KHZ
2.7630E+02
2.7600E+02
2.7570E+02
2.7540E+02
2.7510E+02
2.7480E+02
2.7450E+02
2.7420E+02
2.7390E+02
2.7360E+02
0.08
0.15
0.23
0.30
0.38
0.45
0.53
0.60
0.68
0.75
TESLA

fig. 8.20

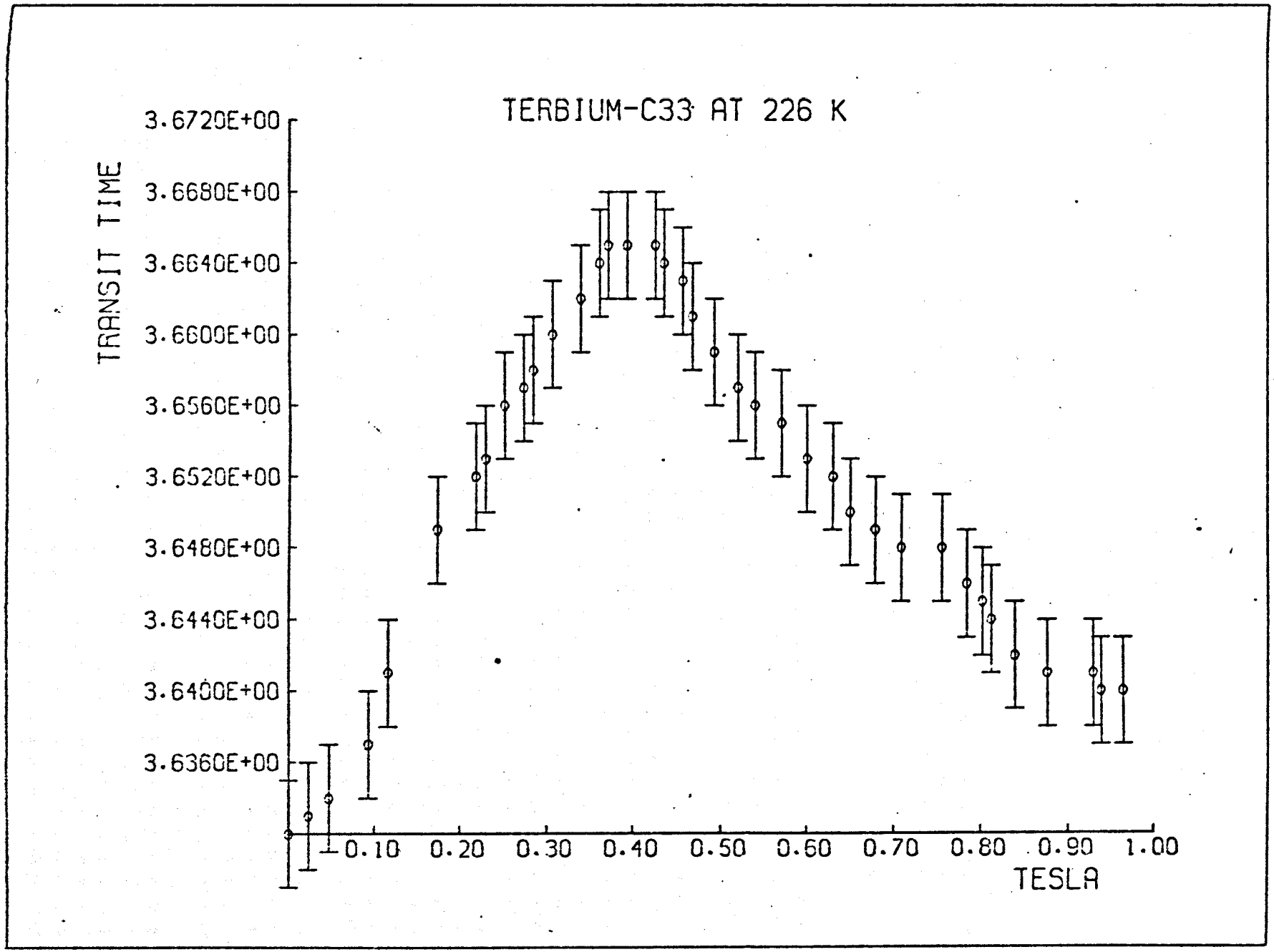
TERBIUM-C33 AT 226 K
TRANSIT TIME
3.6720E+00
3.6680E+00
3.6640E+00
3.6600E+00
3.6560E+00
3.6520E+00
3.6480E+00
3.6440E+00
3.6400E+00
3.6360E+00
0.10
0.20
0.30
0.40
0.50
0.60
0.70
0.80
0.90
1.00
TESLA

fig.8.21

8.3.2 Comparison of Transit Time Measurements with Changes in Velocity as Measured from the Frequency Meter

Comparison of the transit times obtained using the fast sampling mode and the reciprocal of the sing around frequency, which itself corresponds to an averaged transit time, shows good agreement for the results presented. The fractional changes $(\tau_{max} - \tau_o)/\tau_o$ and $(f_o - f_{min})/f_{min}$ between the zero field values f_o, τ_o and the values at the maximum/minimum f_{min}, τ_{max} are shown in fig. 8.22, with the exception of one case, within 10%.

The reciprocal of the repetition rate was taken to be the 'correct' value of the sing around period. Its point-to-point accuracy was nearly two orders of magnitude better than the transit time measurements made in the fast sampling mode. The values of the transit time τ obtained from the fast sampling mode have been compared to the reciprocal of the repetition rate for the zero field values in fig. 8.23. The values of τ will be seen to be correct to within $\pm$ 3 nsecs.

Comparisons of the transit times for the field sweeps at 216.5^{o}K and 225.5^{o}K are shown in figs. 8.24 and 8.25 respectively. Again the results show agreement to within $\pm$ 3 nsecs. The results therefore indicate that the fast sampling mode is operating to its quoted specifications.

Comparison of Changes in Transit Time τ and Changes in Repetition Rate f for C_{33} of Terbium Tb(I) at Various Temperatures in the Antiferromagnetic Region

Temp ^{o}K	Field at which τ_{max} occurs Tesla	$\frac{f_o - f_{min}}{f_{min}}$	$\frac{\tau_{max} - \tau_o}{\tau_o}$
214	0.4	0.00452	0.00443
215	0.4	0.00563	0.00554
216.5	0.4	0.00629	0.00719
223.5	0.35	0.01138	0.00936
224.5	0.35	0.00908	0.00908
226.5	0.4	0.00908	0.01022

fig. 8.22

Results of Sing Around Frequency and its Reciprocal in Microseconds compared with the Transit Time τ measured by the fast sampling mode

Tb(I) - C_{33} in zero applied field			
Temp ^{o}K	Sing Around Frequency f KHz	$1/f$ μsecs	τ μsecs
212	276.448	3.617	3.616
214	276.687	3.614	3.612
215	276.868	3.612	3.612
215.5	276.721	3.614	3.612
216.5	276.618	3.615	3.614
223.5	275.193	3.634	3.634
224.5	275.339	3.632	3.633
225.5	275.716	3.627	3.628
226.5	276.103	3.622	3.620

fig. 8.23

Results of Sing Around Frequency and its Reciprocal in Microseconds compared with the Transit Time τ measured by the fast sampling mode

Tb(I) - C_{33} at 216.5°K			
Applied Field (Tesla)	Sing Around Frequency KHz	$1/f$ μsecs	τ μsecs
0.00	276.618	3.615	3.614
0.045	276.451	3.617	3.616
0.067	273.318	3.619	3.618
0.089	276.160	3.621	3.620
0.156	275.646	3.628	3.626
0.178	275.579	3.629	3.628
0.222	275.333	3.632	3.630
0.266	275.129	3.635	3.634
0.310	275.046	3.636	3.636
0.332	275.014	3.636	3.637
0.397	274.918	3.637	3.640
0.440	274.920	3.637	3.640
0.461	274.947	3.637	3.638
0.504	275.029	3.636	3.636
0.567	275.227	3.633	3.634
0.609	275.409	3.631	3.632
0.630	275.500	3.630	3.629
0.650	275.591	3.629	3.628

fig. 8.24

Results of Sing Around Frequency and its Reciprocal in Microseconds compared with the Transit Time τ measured by the fast sampling mode

Tb(I) - C_{33} at 225.5°K			
Applied Field Tesla	Sing Around Frequency KHz	$1/f$ μsecs	τ μsecs
0.00	275.716	3.627	3.628
0.067	275.522	3.629	3.630
0.089	275.326	3.632	3.632
0.111	275.124	3.635	3.636
0.134	274.992	3.636	3.636
0.156	274.779	3.639	3.638
0.178	274.517	3.643	3.641
0.222	274.094	3.648	3.648
0.244	273.880	3.651	3.649
0.288	273.515	3.656	3.656
0.310	273.372	3.658	3.657
0.354	273.227	3.660	3.658
0.397	273.219	3.660	3.660
0.483	273.405	3.658	3.660
0.525	273.548	3.656	3.660
0.567	273.653	3.654	3.656
0.588	273.685	3.654	3.654
0.650	273.830	3.652	3.652

fig. 8.25

CHAPTER 9

Results (II): Elastic Properties as a Function of Temperature and Magnetic Field

9.1 Introduction

In this chapter results of the variation of the elastic moduli of Gadolinium, Terbium and Erbium as a function of temperature and applied magnetic field are presented. In particular attention has been concentrated on the regions in which the materials undergo phase transitions.

The modulus C_{33} of Gadolinium has been investigated over the range $180 - 300^{\circ}K$ as a function of magnetic field applied in the base plane. The location of field and temperature dependent anomalies has been plotted and critical fields determined from these. Tentative proposals are put forward for the underlying mechanisms behind the elastic behaviour under these conditions. Corrections for demagnetising fields in the sample have been made and a magnetic phase diagram of the material obtained.

Similar work has been performed on Terbium with the field applied along the easy direction, the b axis, over the range $200 - 235^{\circ}K$ with the main interest centred on the behaviour of the antiferromagnetic phase. In Erbium the modulus C_{33} has been studied as a function of field applied along the b axis below $20^{\circ}K$. Above $20^{\circ}K$ the modulus C_{11} has been investigated with the field applied along the easy direction, the c axis.

9.1.1 Previous Elastic Constant Measurements

Previous measurements on the elastic moduli of Gadolinium and Erbium in zero field have been reported in chapter eight. Some measurements of the elastic properties under constant applied magnetic fields have been performed on Gadolinium by Long et al [1], reference to which is made in

fig. 9.11 of section 9.2.3, and on Erbium by du Plessis [2]. Some results on the zero field behaviour of C_{33} of Terbium have been reported by Salama et al [3] and by Palmer et al [4]. Distinct minima in this modulus are seen to occur at the Néel and Curie temperatures. The behaviour of the elastic moduli of Terbium in a constant applied field of 2.5T along the b axis was also reported by Palmer et al.

9.1.2 Determination of Critical Fields

Critical magnetic fields may be found by studying one or more of several magnetically dependent properties of a material, for example magnetisation, magnetoresistance, magnetostriction or specific heat. In Gadolinium critical fields have been found from magnetoresistance measurements by Hiraoka and Suzuki [5] for some temperatures in the range 77 - 400°K although the measurements were not exhaustive. Specific heat and resistivity measurements close to T_C have been made by Simons and Salamon [6] in fields of up to 0.17T. Magnetisation measurements have been carried out by Nigh et al [7] and by Feron [8,9].

In Terbium magnetoresistance measurements in fields of up to 8T over the range 4.2 - 20°K have been made by Singh et al [10] although no measurements of this property over the temperature range of interest in the present work have been reported. Magnetostriction measurements by Belov et al [11] in fields of up to 1.5T for the range 215 - 230°K, have enabled critical fields near the two phase transitions to be obtained. Magnetisation measurements have been made by Hegland et al [12] and by Feron [9,13]. This latter work has also included magnetisation measurements in low fields close to the transition temperatures from which critical fields have been determined over the temperature range of interest in the present work.

In Erbium magnetisation measurements have been made by Green et al [14] and by Feron et al [15]. Also magnetisation work has been performed by Flippen [16] which has yielded critical fields in this material.

Determination of critical fields and magnetic phase diagrams via elastic properties has been made on Dysprosium and the intra rare earth alloys Holmium-50% Terbium and Gadolinium-40% Yttrium by Isci and Palmer [17,18,19], although no such determinations for any of the other rare earths appears to have been reported to date. The present study of the properties of Gadolinium, Terbium and Erbium has attempted to provide knowledge of the behaviour of their elastic properties under applied fields and to deduce from such results the magnetic phase diagrams of the materials. It is also hoped that the results will help to complement the findings of workers using different methods.

9.2 Gadolinium

As mentioned in chapter six Gadolinium orders ferromagnetically below a Curie point of 293.5^{o}K with magnetic moments aligned along the c axis. Between 240^{o}K and 225^{o}K a second transition occurs when the moments rotate away from the c axis and lie along the generators of an easy cone. Evidence for this structure has been obtained independently by the neutron diffraction work of Cable and Wollan [20] and the magnetisation measurements of Corner et al [21,22].

The modulus C_{33} is strongly coupled to the magnetic structure in Gadolinium and distinct minima occur in this mode at the two transition temperatures. The dependence of this modulus upon temperature and magnetic field has been studied in the present work to investigate the behaviour of the elastic properties under these conditions and also to gain some insight into the magnetic structure.

9.2.1 Zero Field Temperature Dependence and Critical Behaviour

The temperature dependence of C_{33} of the Gadolinium specimen used in the present work has already been investigated in zero field by Savage and Palmer [23]. The origin and purity of this sample have been discussed in chapter five. The present measurements over the range 200 - 325°K are shown in fig. 9.1. A deep anomaly occurs at the Curie point and a rather shallower minimum at the spin reorientation temperature. This is in agreement with the findings of Savage and Palmer who reported that the anomaly at the spin reorientation transition in this high purity material is less pronounced than had been reported for much lower purity specimens by earlier workers [1,4,24].

A more detailed investigation of the behaviour close to T_C has also been conducted to enable the critical variation of velocity to be studied. A Curie point of 293.7°K was found by locating the minimum velocity. The variation of acoustic velocity in this region has been compared with the relation recommended by Moran et al [25,26] for critical changes in velocity

$$\frac{\Delta v}{v} \quad \alpha \quad \ell n \varepsilon \qquad \ldots.9.1$$

where ε is the reduced temperature $(T-T_C)/T_C$ and $\Delta v/v$ is the fractional change in velocity. This is shown in fig. 9.2 together with a plot of the expression

$$\ell n \frac{\Delta v}{v} \quad \alpha \quad \beta \ell n \varepsilon \qquad \ldots.9.2$$

which derives from

$$\frac{\Delta v}{v} = k \varepsilon^{\beta} \qquad \ldots.9.3$$

where β is the critical exponent and k is a constant. Comparison of the graphs shows that 9.1 only applies to the data over a limited region. Reference to a similar comparison made by Moran and Lüthi [25] shows that the derivation from the relation 9.1 only occurred very close to T_C, for

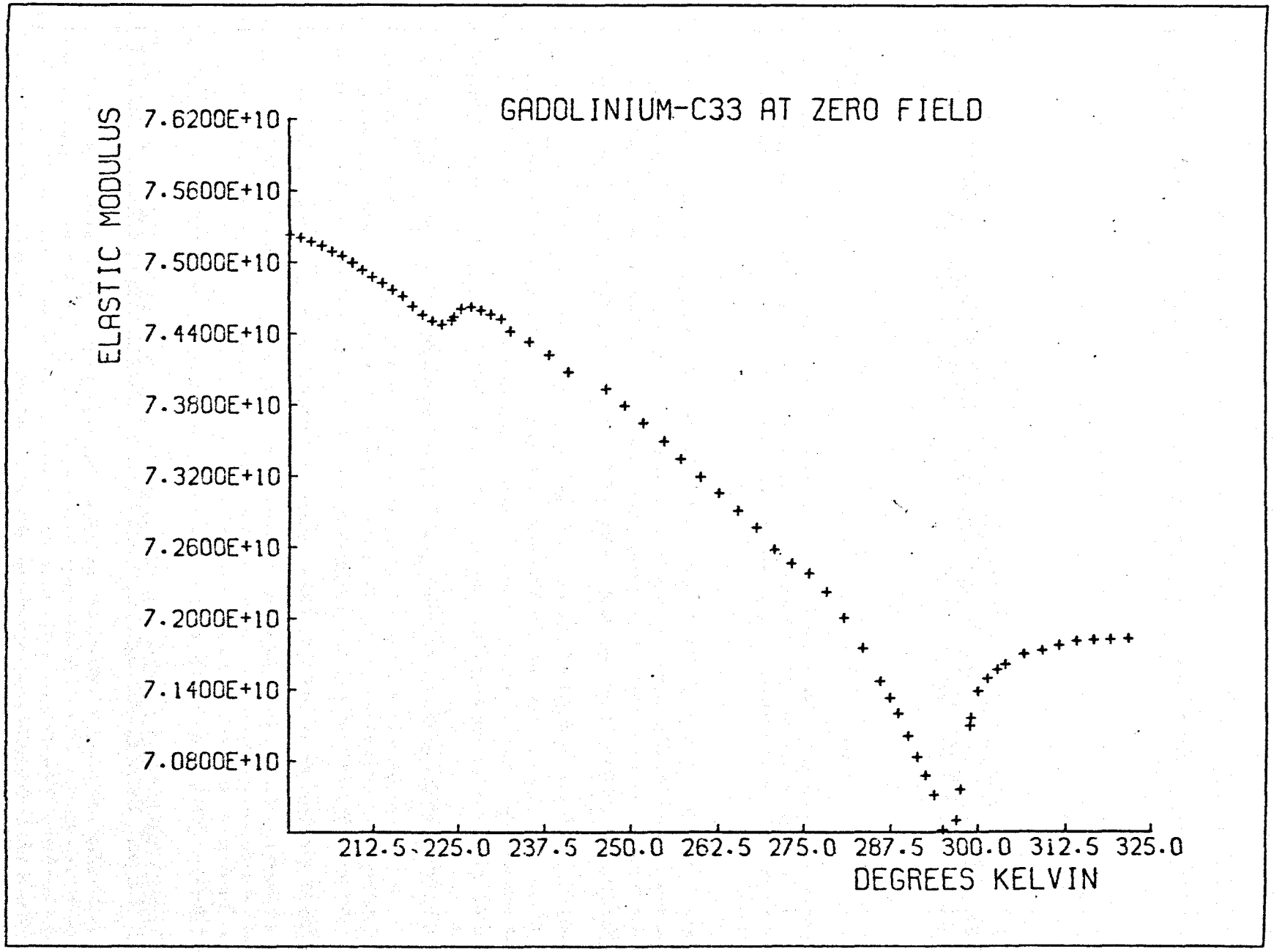
GADOLINIUM-C33 AT ZERO FIELD
ELASTIC MODULUS
7.6200E+10
7.5600E+10
7.5000E+10
7.4400E+10
7.3800E+10
7.3200E+10
7.2600E+10
7.2000E+10
7.1400E+10
7.0800E+10
212.5 225.0 237.5 250.0 262.5 275.0 287.5 300.0 312.5 325.0
DEGREES KELVIN

fig. 9.1

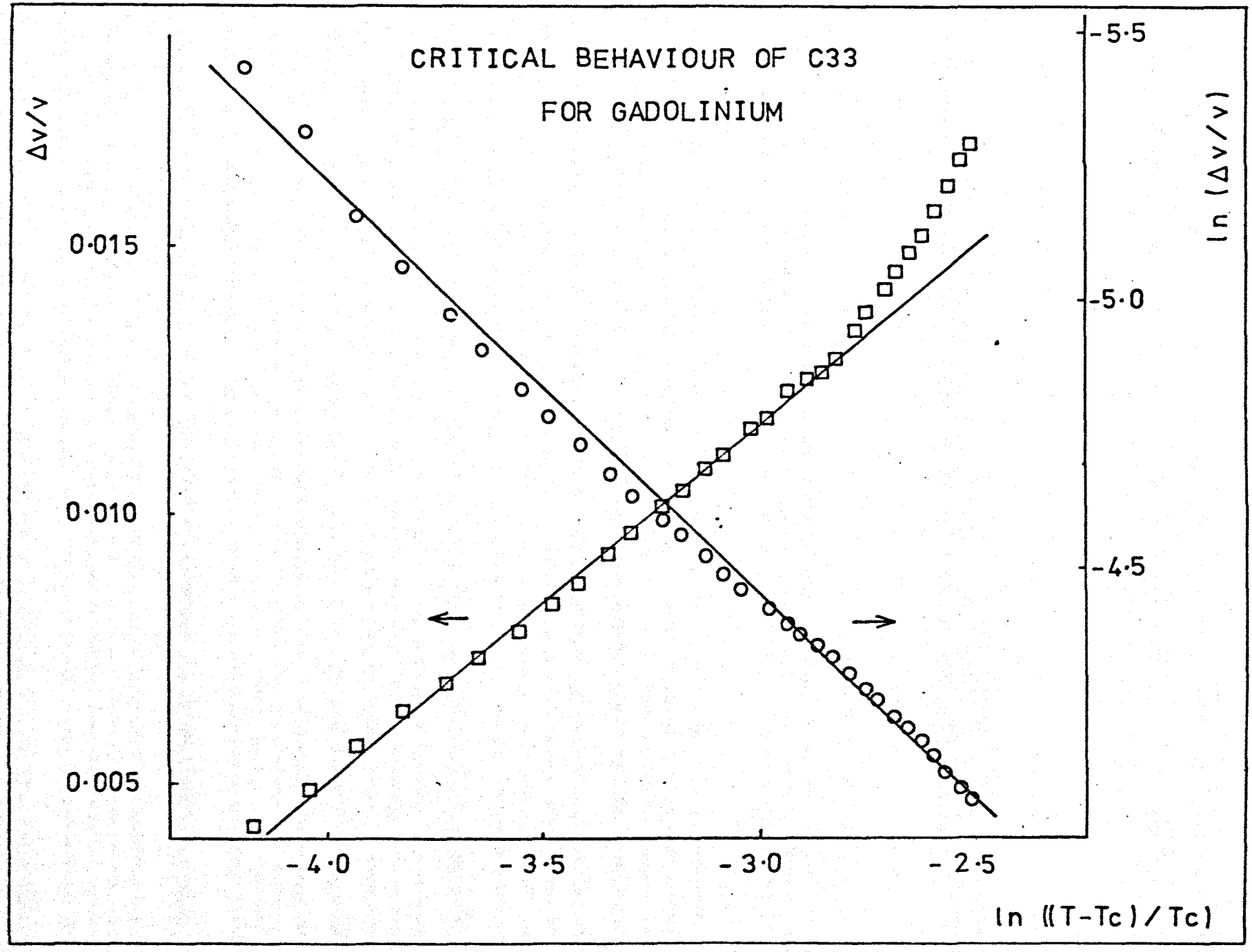
CRITICAL BEHAVIOUR OF C33
FOR GADOLINIUM
Δv/v
0·015
0·010
0·005
-5·5
-5·0
-4·5
ln (Δv/v)
-4·0
-3·5
-3·0
-2·5
ln ((T-Tc)/Tc)

fig. 9.2

$\ell n\varepsilon < -5.0$, which was an expected limitation since $\ell n\varepsilon$ tends rapidly towards $-\infty$ as ε decreases. Such deviations are therefore not due to an injudicious choice of T_c. However the present results for Gadolinium show that the relation does not seem to hold very well for $\ell n\varepsilon > -2.5$ either which is surprising since the reported results for Dysprosium hold to the relation for values of $\ell n\varepsilon$ up to about -1. Reported results on Gadolinium [26] show that the linearity of the relation holds for Gadolinium for $\ell n\varepsilon > -2.5$ as far as $\ell n\varepsilon = -1$ which is outside the range of the results quoted here. It may be concluded that the relation 9.1 does not hold for the high purity specimen of Gadolinium used in the present investigations further than $\ell n\varepsilon = -2.5$ from the Curie point, or closer than $\ell n\varepsilon = -4.25$.

The relation 9.2 is also shown plotted in fig. 9.2, using the right hand ordinates, to enable a comparison to be made. This gives a much closer agreement with the true behaviour of Gadolinium close to its Curie point, and from this a critical exponent of $\beta = 0.82$ has been extracted.

The results presented are for the ferromagnetic phase of Gadolinium, The variation of velocity in the paramagnetic region does not appear to follow either relation. Robinson and Lanchester [40] have observed similarly unsual behaviour in the critical specific heat and thermal expansion of Gadolinium in the paramagnetic phase.

9.2.2 Field Dependence of the Modulus close to T_{SR}

At temperatures well below the spin reorientation region the elastic modulus is almost field independent for applied field strengths of up to 0.4T in the base plane. At a field of between 0.45 - 0.5T a small maximum occurs as shown in fig. 9.3. This is followed by an equally shallow minimum before the modulus rises towards saturation above 0.6T.

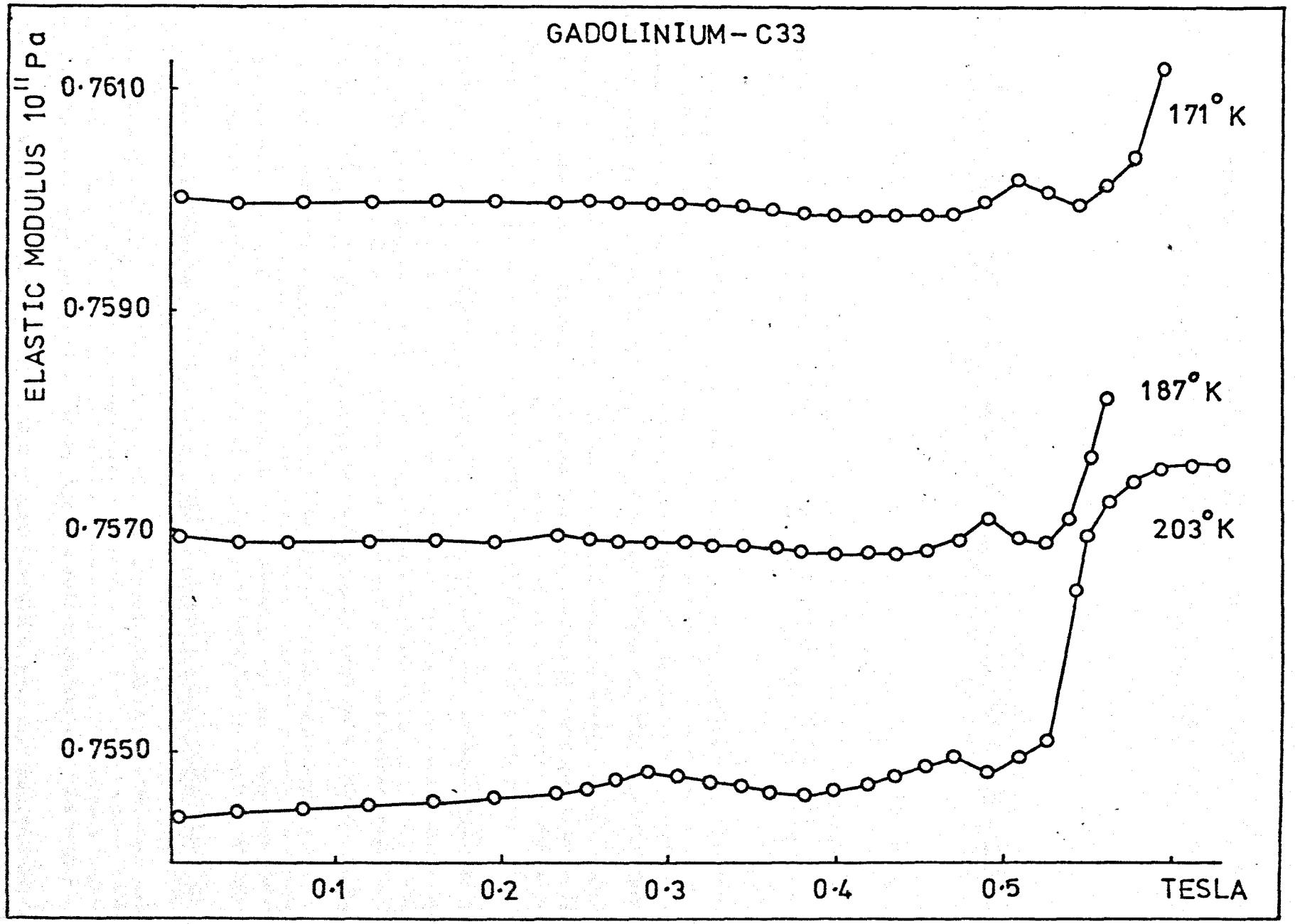
GADOLINIUM – C33
ELASTIC MODULUS 10^{11} Pa
0·7610
0·7590
0·7570
0·7550
171° K
187° K
203° K
0·1
0·2
0·3
0·4
0·5
TESLA

Fig. 9.3

As the temperature is raised the location of the maximum moves at first slowly towards lower field strengths and also grows in size as can be seen from fig. 9.4. At 214°K the maximum occurs at a field strength of about 0.4T, but above this temperature it moves rapidly to lower fields and increases in magnitude very quickly at temperatures above 220°K. Above 226°K it has moved to zero field and completely swamped the previous low field behaviour.

The location of the minimum remains close to 0.5T throughout this temperature range and it becomes more pronounced as the low field maximum gains in strength. Above 225°K the minimum appears as the most noticeable feature, as for example at 229°K as shown in fig. 9.6. Above this temperature the location of the minimum moves very slowly to lower field strengths.

The low field values of the elastic constant above 226°K show behaviour characteristic of the low field maximum below T_{SR}. At higher temperatures, fig. 9.7, the behaviour is similar to that at 229°K except that the value of the elastic constant at higher fields ($>$ 0.6T) decreases more rapidly than the zero field value.

9.2.3 Field Dependence of the Modulus close to T_C

The sharp minimum in C_{33} as a function of field occurring at about 0.38T for a temperature of 257°K becomes gradually less well defined as the temperature is increased, fig. 9.8, although for all temperatures up to its ordering point of 293.5°K the value of C_{33} recovers much of its original zero field value for fields greater than about 0.6T. As T_C is approached the location of the minimum gradually moves to lower fields, from 0.4T at 252°K to about 0.2T at 293°K.

Above T_C, in fig. 9.10 the behaviour is rather different. A minimum value of the elastic constant still exists but the softening occurs very soon after the field is applied, for example at 296°K noticeable

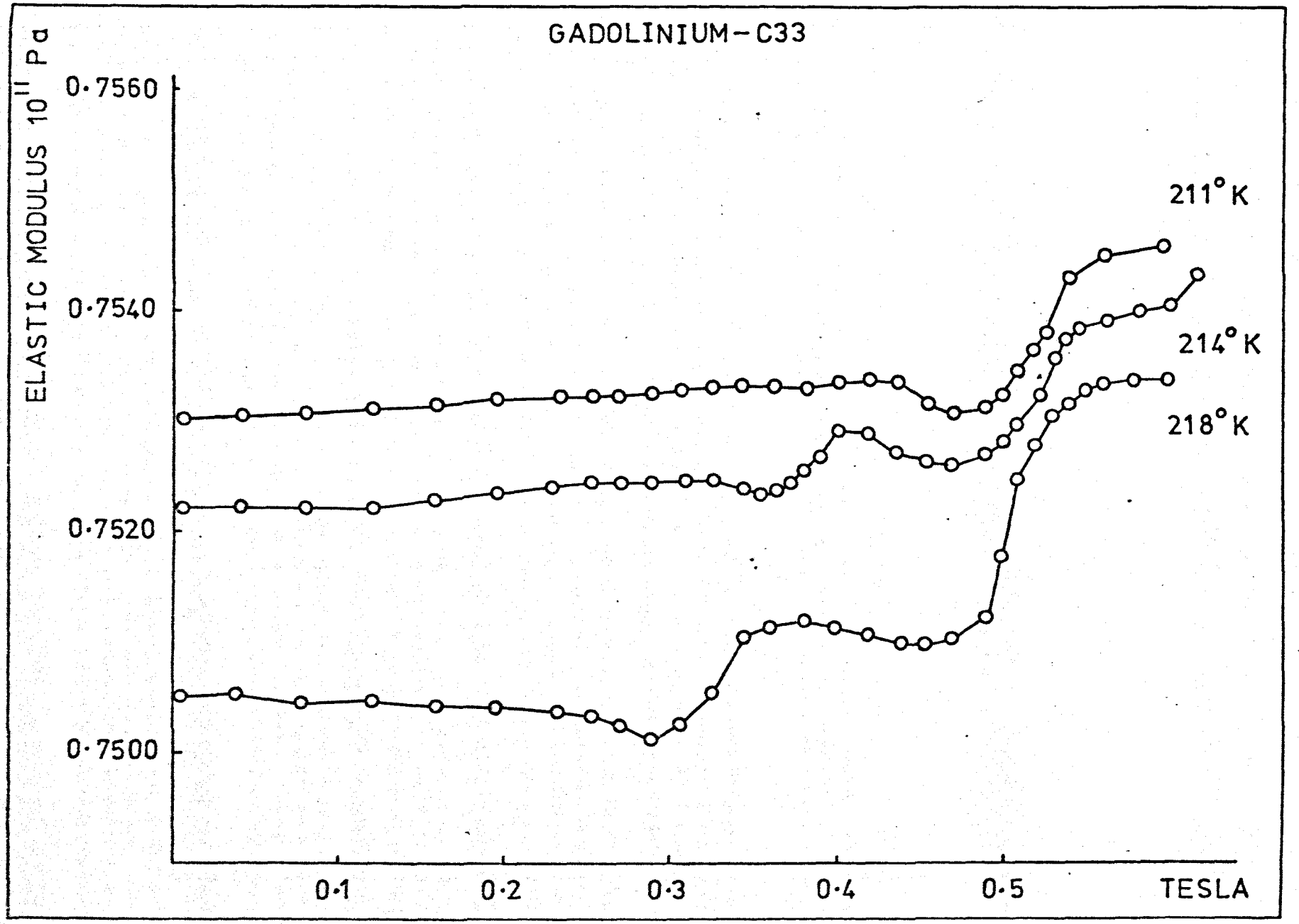
GADOLINIUM – C33
ELASTIC MODULUS 10^{11} Pa
0·7560
0·7540
0·7520
0·7500
211° K
214° K
218° K
0·1
0·2
0·3
0·4
0·5
TESLA

Fig. 9.4

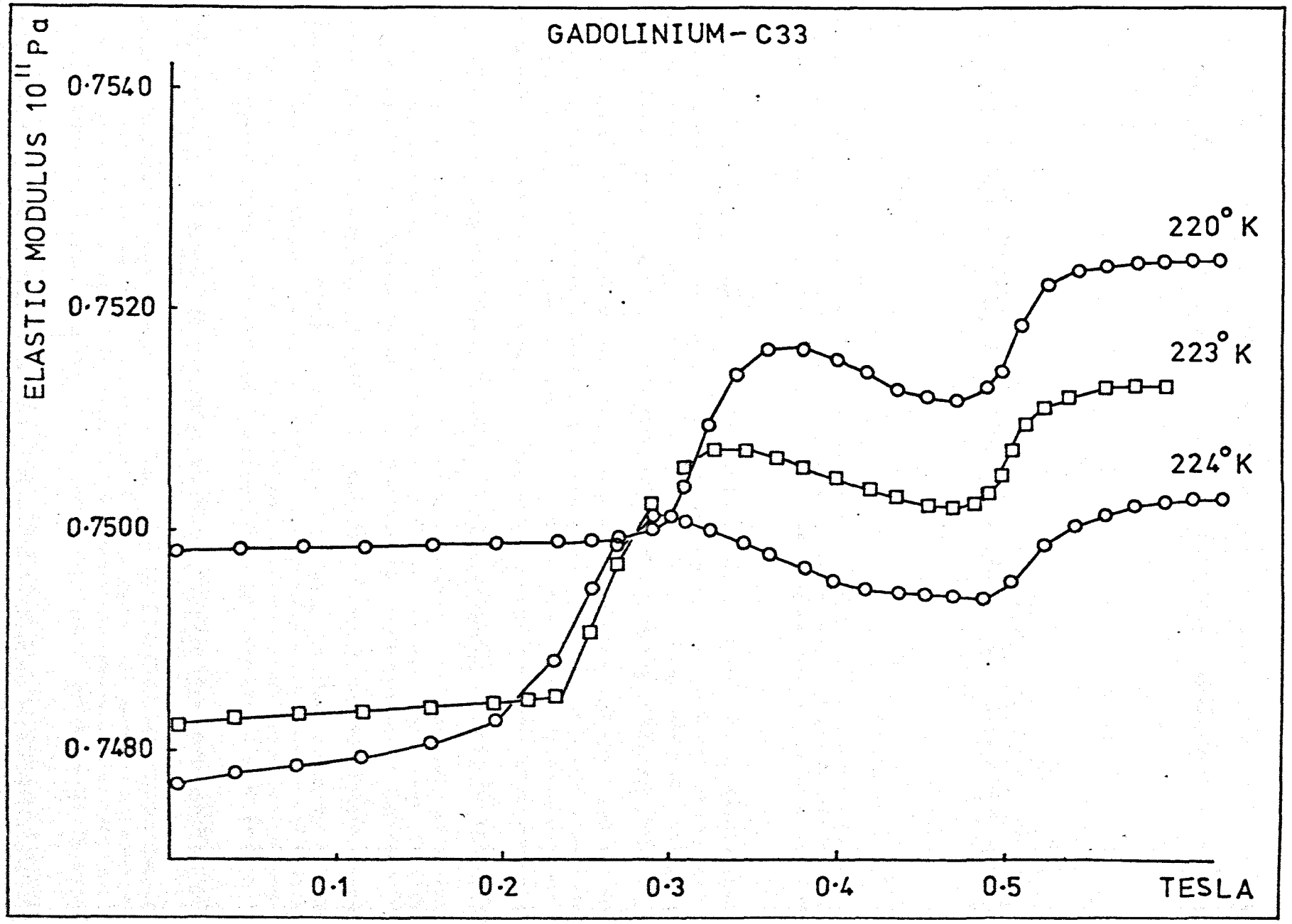
GADOLINIUM – C33
ELASTIC MODULUS 10^{11} Pa
0·7540
0·7520
0·7500
0·7480
220° K
223° K
224° K
0·1
0·2
0·3
0·4
0·5
TESLA

fig. 9.5

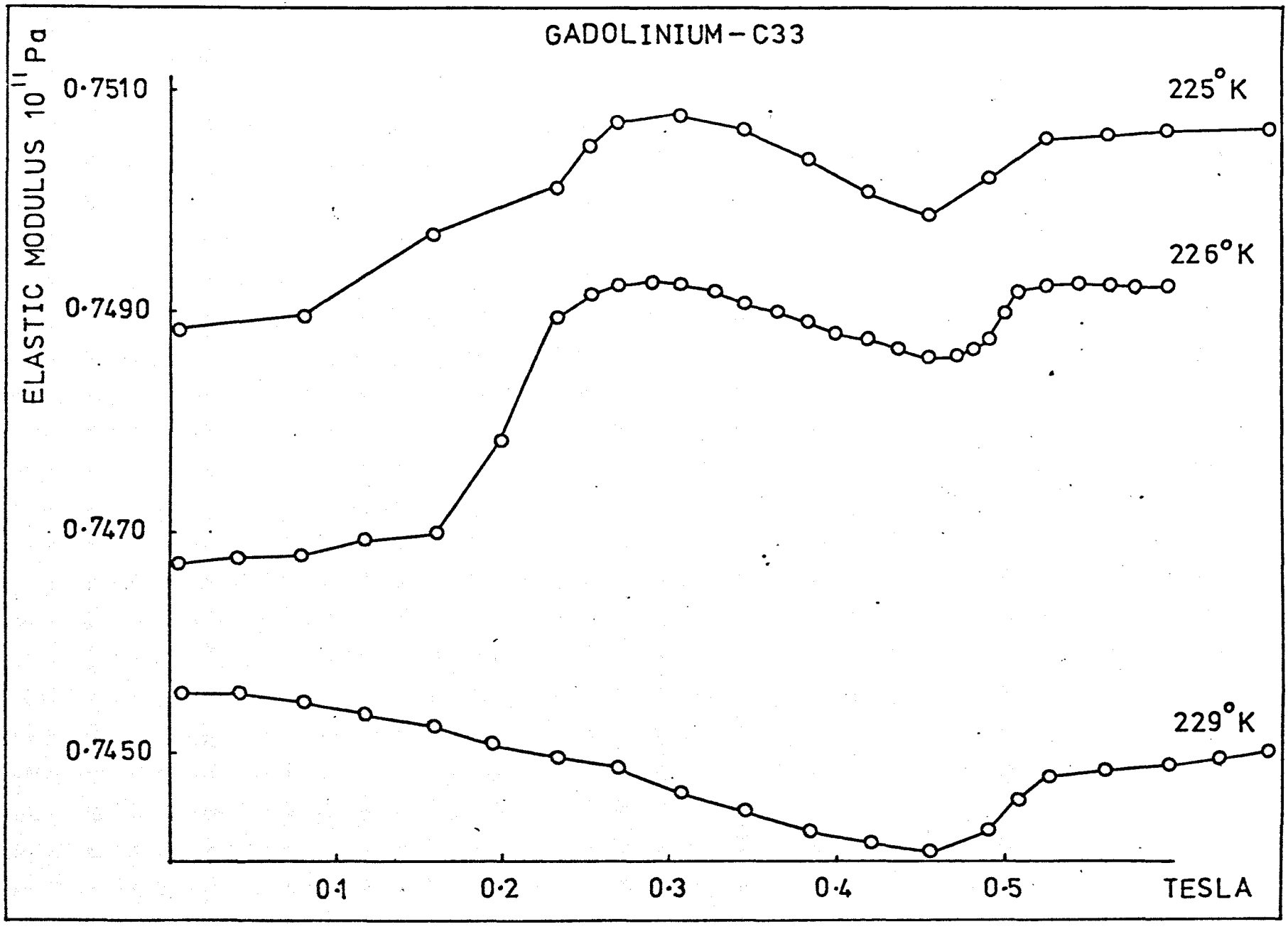
GADOLINIUM – C33
ELASTIC MODULUS 10^{11} Pa
0·7510
0·7490
0·7470
0·7450
225°K
226°K
229°K
0·1
0·2
0·3
0·4
0·5
TESLA

fig. 9.6

ELASTIC MODULUS 10^{11} Pa
0·7460
0·7440
0·7420
0·7400
0·1
0·2
0·3
0·4
0·5
TESLA
GADOLINIUM–C33
232° K
238° K
241° K

fig. 9.7

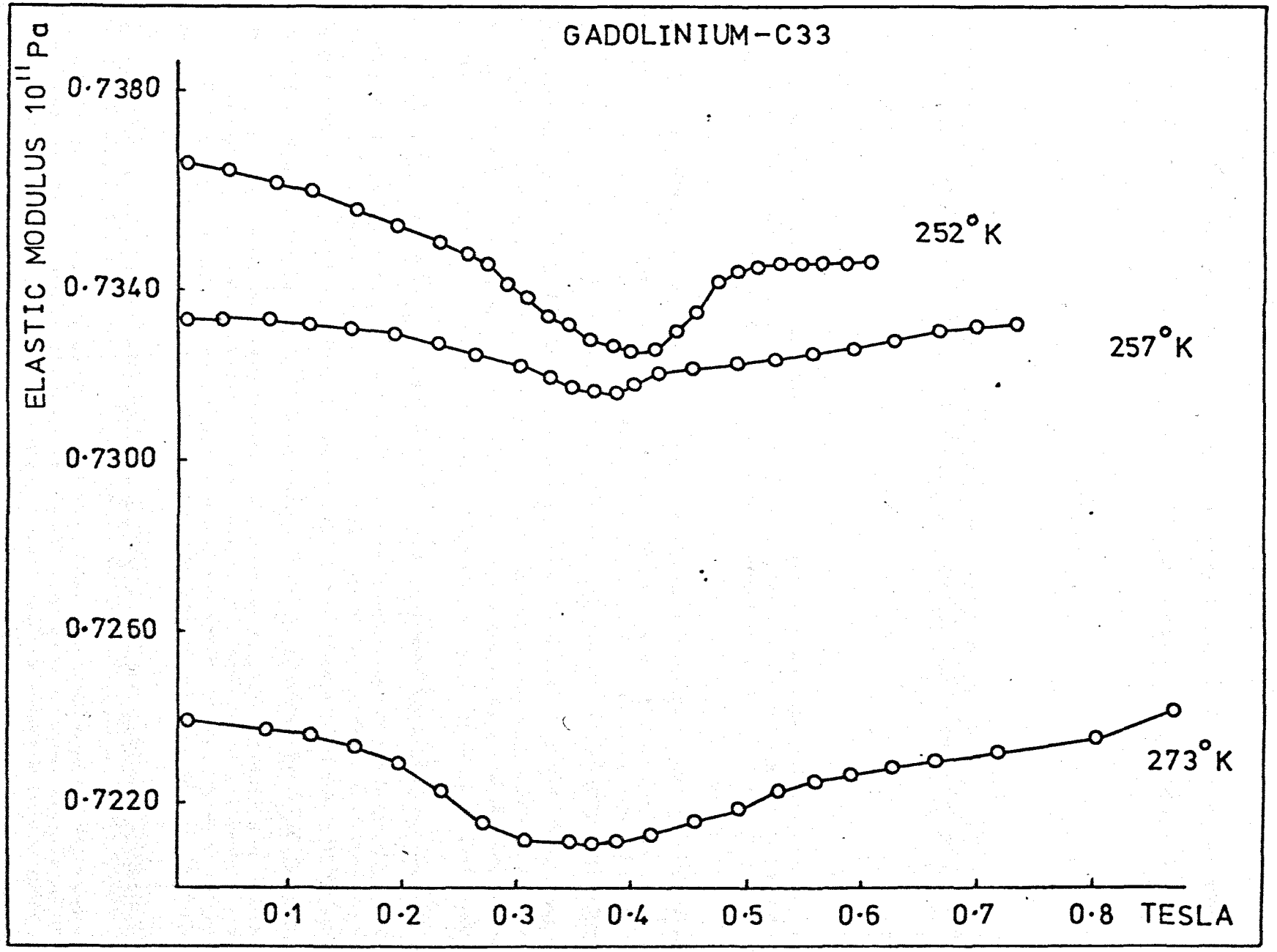
GADOLINIUM-C33
ELASTIC MODULUS 10^{11} Pa
0·7380
0·7340
0·7300
0·7260
0·7220
252°K
257°K
273°K
0·1
0·2
0·3
0·4
0·5
0·6
0·7
0·8
TESLA

fig. 9.8

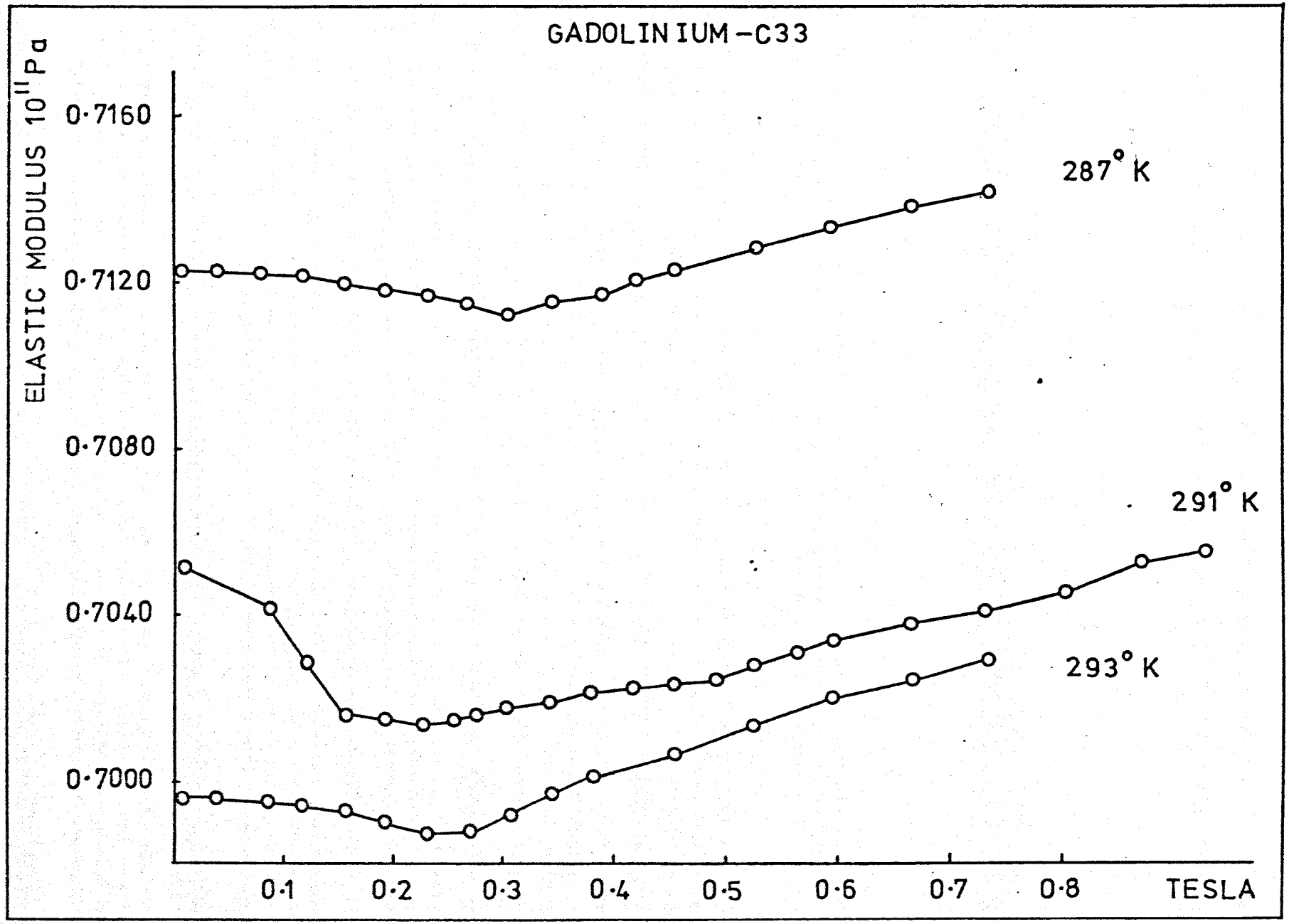
GADOLINIUM – C33
ELASTIC MODULUS 10^{11} Pa
0·7160
0·7120
0·7080
0·7040
0·7000
287° K
291° K
293° K
0·1
0·2
0·3
0·4
0·5
0·6
0·7
0·8
TESLA

fig. 9.9

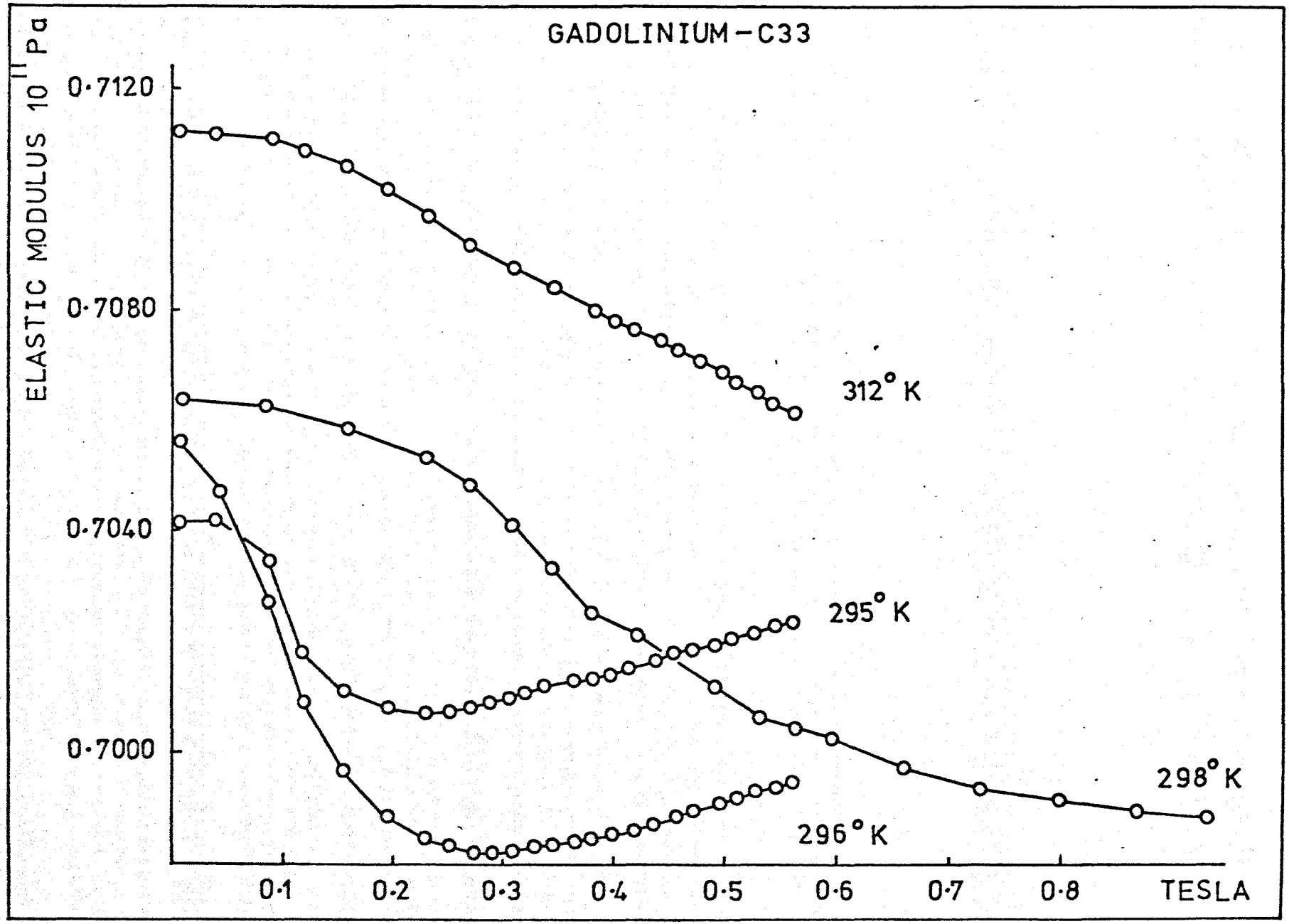
GADOLINIUM – C33
ELASTIC MODULUS 10^{11} Pa
0·7120
0·7080
0·7040
0·7000
312° K
295° K
298° K
296° K
0·1
0·2
0·3
0·4
0·5
0·6
0·7
0·8
TESLA

fig. 9.10

changes in the modulus have occurred at fields below 0.05T. When the broad minimum has been reached the modulus becomes much less field dependent and does not recover to its zero field value for the field strengths used. Further into the paramagnetic region the minimum shifts to higher fields, occurring at about 1T at 298°K.

9.2.4 Temperature Dependence of the Modulus in Constant Applied Fields close to T_{SR}

The temperature dependence of C_{33} in constant applied fields of up to 0.8T in the base plane of Gadolinium has already been investigated some years ago by Long et al [1] on a low purity specimen. These results are shown in fig. 9.11 and attention is drawn to the reported depth of the zero field anomaly.

Results of the present investigations are shown in fig. 9.12 et seq. The location of the minimum in zero field is at 225°K and as the field is increased the minimum moves, at first slowly to lower temperatures. At a field strength of 0.27T the minimum occurs at 207°K, at 0.38T it occurs at 201°K both of which are in agreement with the work of Long. At higher fields of 0.56T and above no minimum was observed above 180°K. The results of Long in fact suggest that the deep zero field anomaly had disappeared in fields greater than 0.5T and that a change in slope occurred at 175°K which probably corresponded to the location of the transition. Present results indicate that the initially shallow anomaly had disappeared for fields greater than about 0.4T.

9.2.5 Temperature Dependence of the Modulus in Constant Applied Fields close to T_C

The anomaly at the Curie point shown in fig. 9.16 appears to be very weakly field dependent and possibly field independent. For fields up to a strength of 0.74T in fig. 9.17 the location has shifted by less than one degree Kelvin. The most notable effect in this region was that the anomaly became less well defined as the field increased. Comparison of

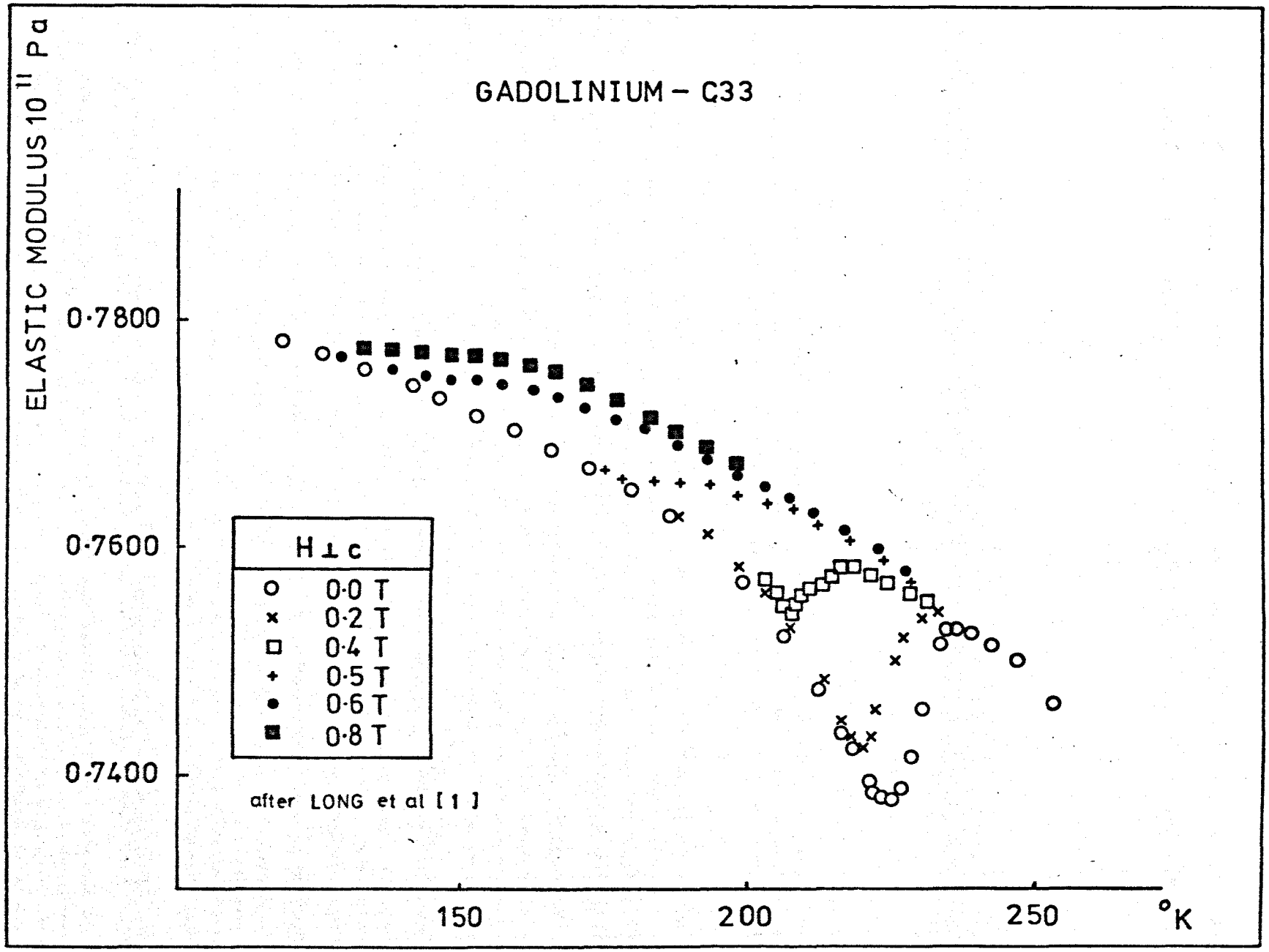
GADOLINIUM – C33
ELASTIC MODULUS 10^{11} Pa
0·7800
0·7600
0·7400
150
200
250
°K
H ⊥ c
0·0 T
0·2 T
0·4 T
0·5 T
0·6 T
0·8 T
after LONG et al [1]

fig. 9.11

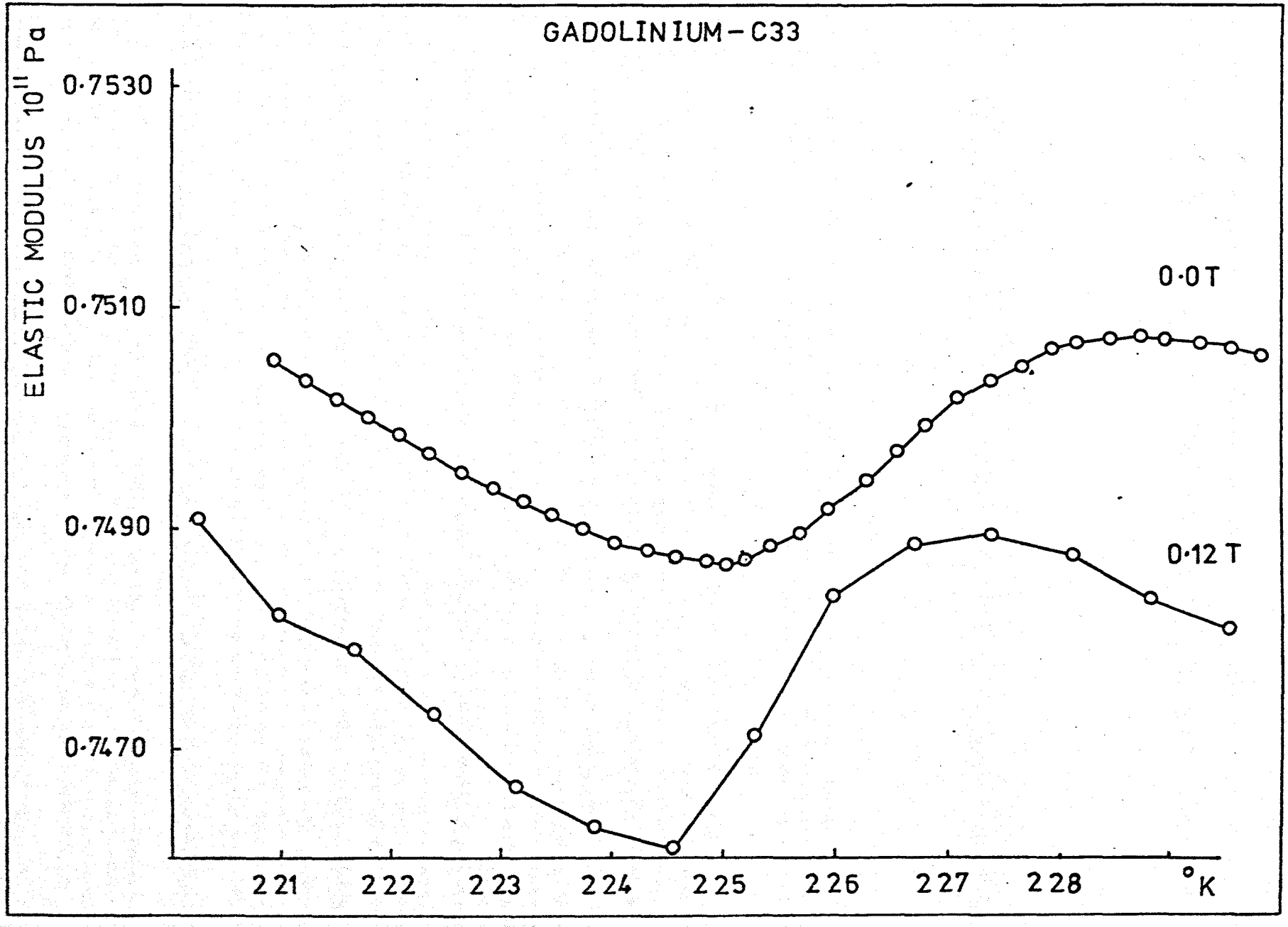
GADOLINIUM – C33
ELASTIC MODULUS 10^{11} Pa
0·7530
0·7510
0·7490
0·7470
0·0 T
0·12 T
2 21
2 22
2 23
2 24
2 25
2 26
2 27
2 28
°K

fig. 9.12

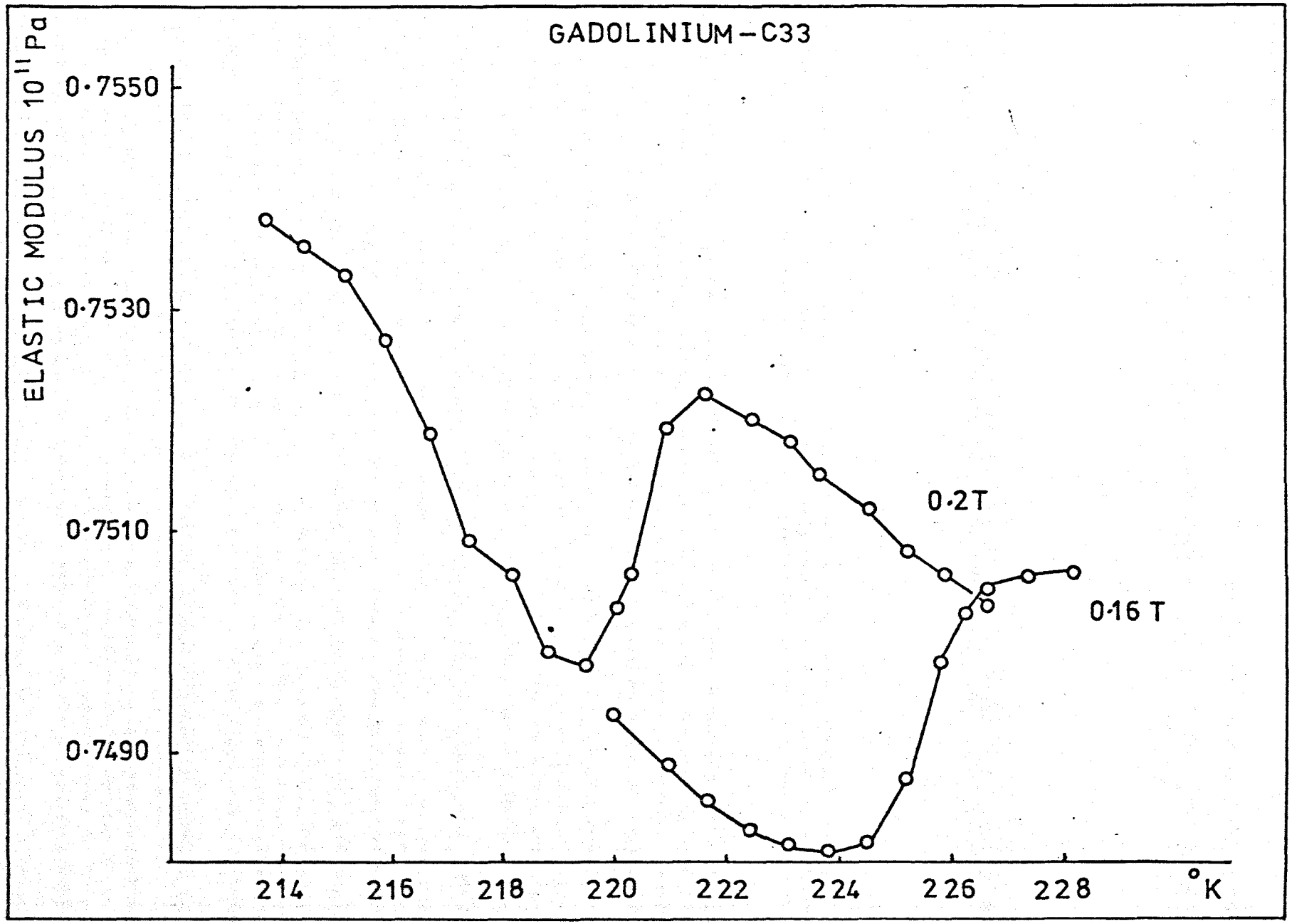
GADOLINIUM – C33
ELASTIC MODULUS 10^{11} Pa
0·7550
0·7530
0·7510
0·7490
0·2T
0·16 T
214
216
218
220
222
224
226
228
°K

fig. 9.13

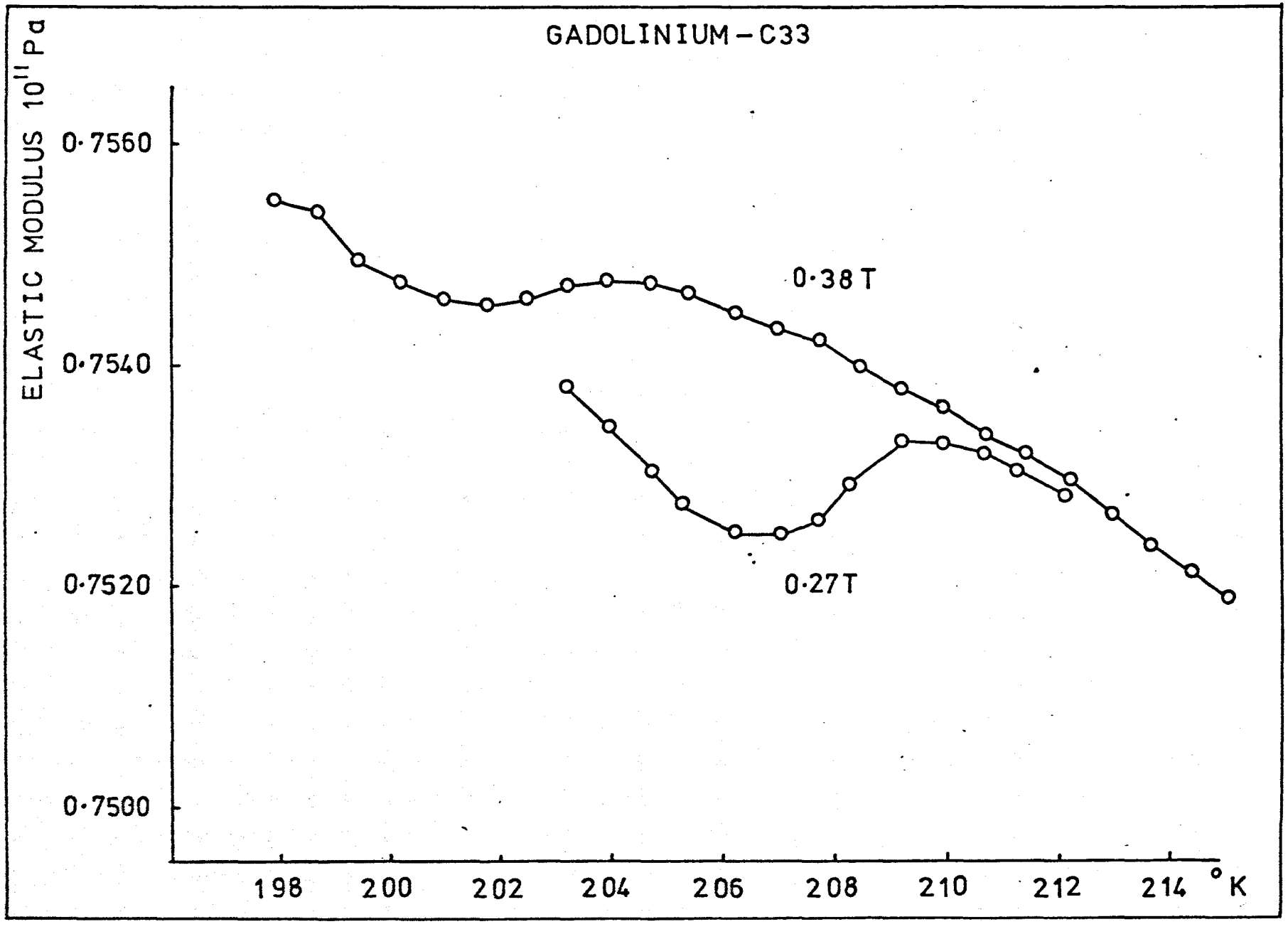
GADOLINIUM – C33
ELASTIC MODULUS 10^{11} Pa
0·7560
0·7540
0·7520
0·7500
0·38 T
0·27 T
198
200
202
204
206
208
210
212
214
°K

fig. 9.14

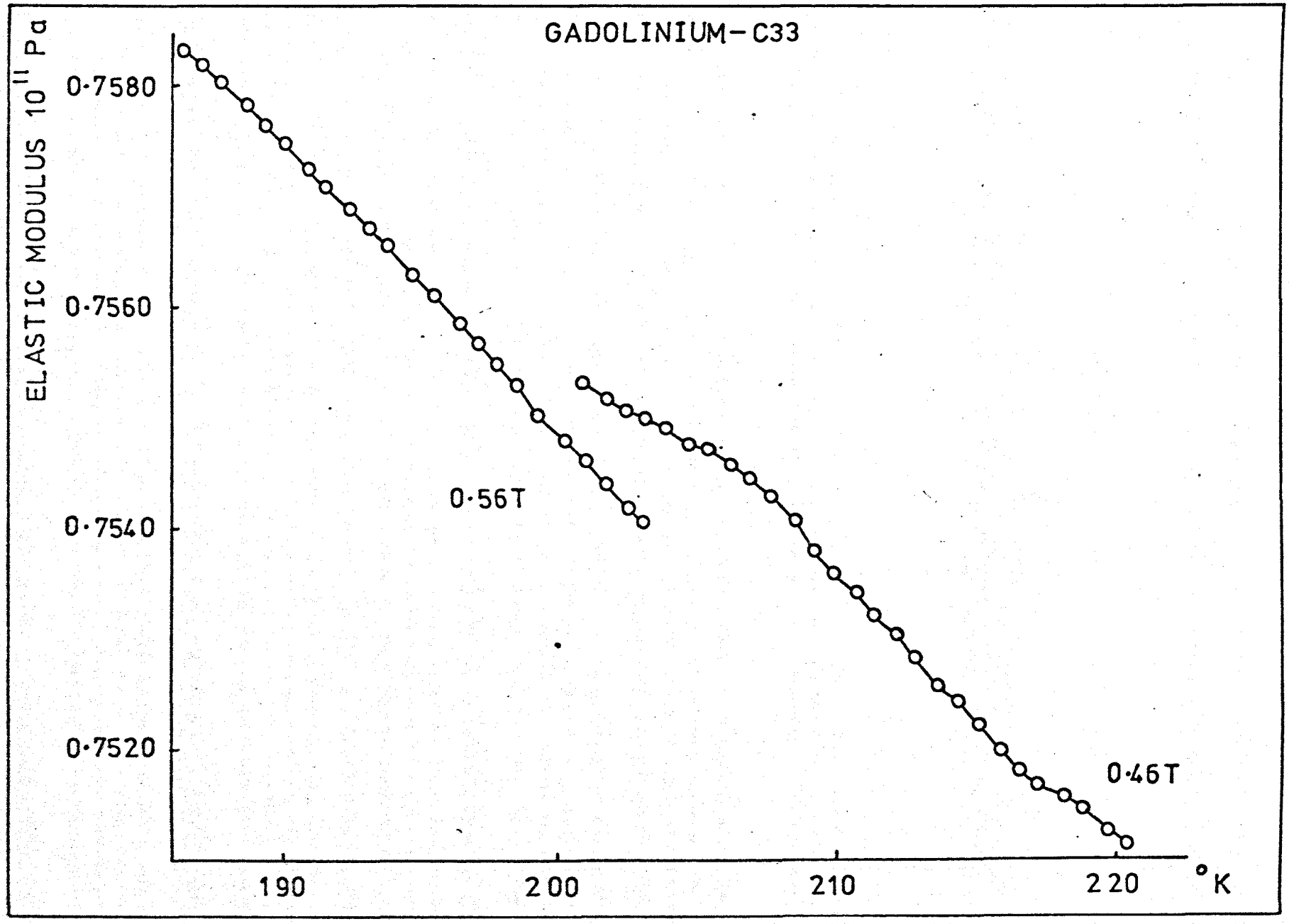
GADOLINIUM – C33
ELASTIC MODULUS 10^{11} Pa
0·7580
0·7560
0·7540
0·7520
0·56T
0·46T
190
200
210
220
°K

fig. 9.15

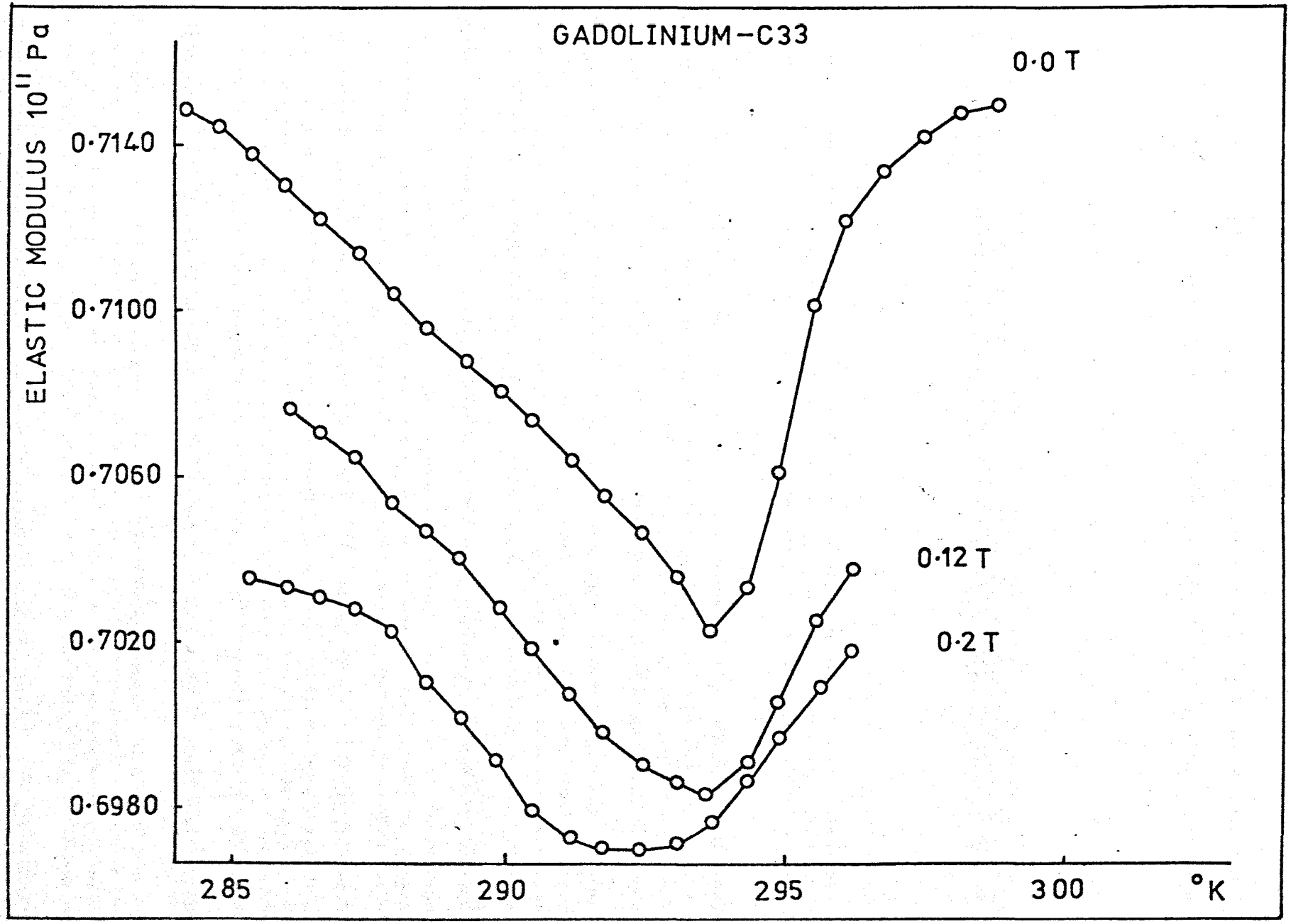
GADOLINIUM–C33
ELASTIC MODULUS 10^{11} Pa
0·7140
0·7100
0·7060
0·7020
0·6980
0·0 T
0·12 T
0·2 T
285
290
295
300
°K

Fig. 9.16

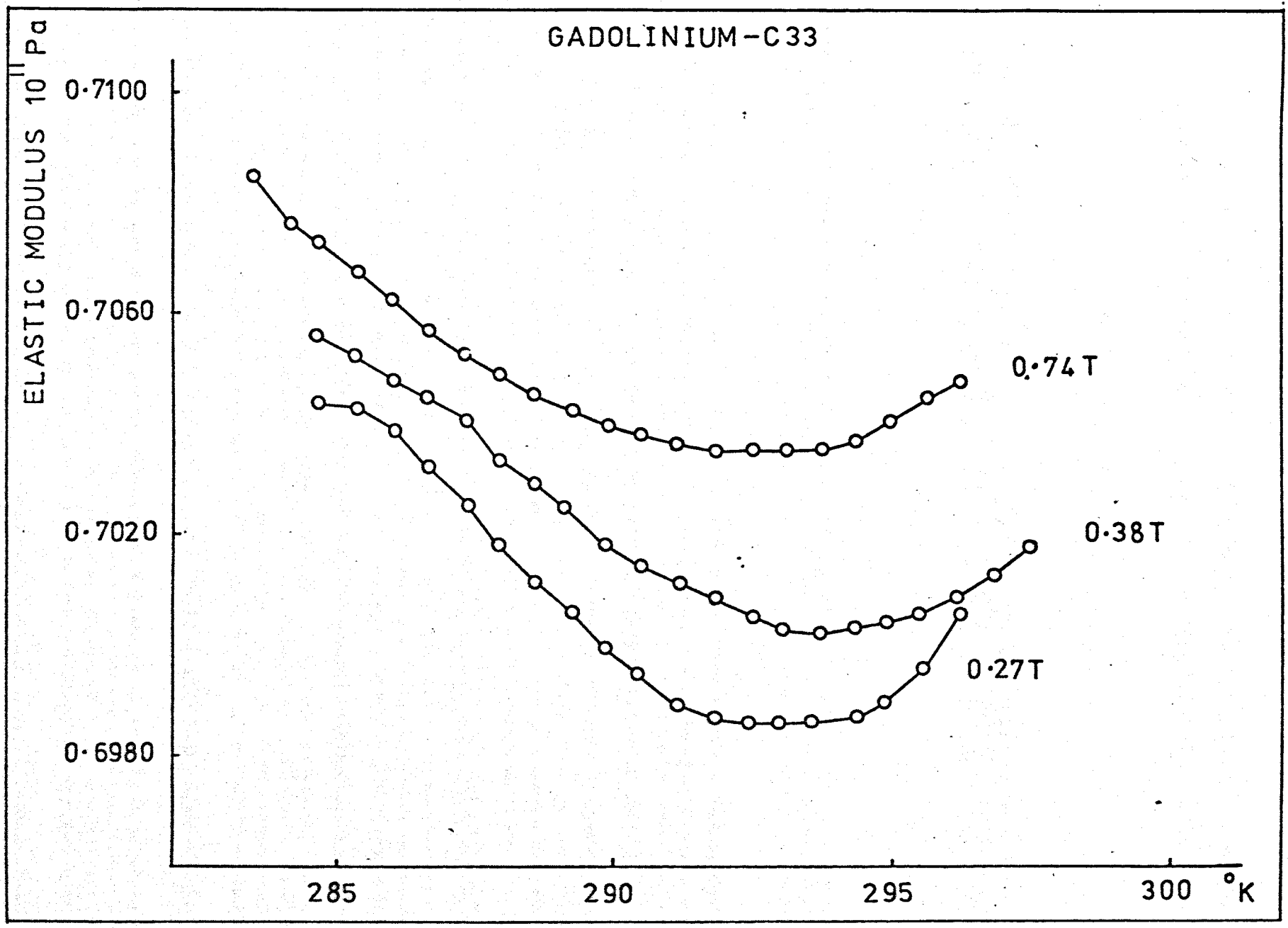
GADOLINIUM-C33
ELASTIC MODULUS 10^{11} Pa
0·7100
0·7060
0·7020
0·6980
0·74 T
0·38 T
0·27 T
285
290
295
300
°K

Fig. 9.17

the sharp zero field minimum in fig. 9.16 with the very broad minima exhibited at higher fields in fig. 9.17 shows that the transition from ferromagnetism to paramagnetism becomes broad and indistinct at high fields.

9.2.6 Interpretation of Results and Phase Diagrams

The phase diagram of this sample of Gadolinium as a function of temperature and applied magnetic field is given in fig. 9.18. The Curie and Spin reorientation temperatures have been taken to correspond to the minima in the elastic modulus similar to those observed at zero field. At fields greater than 0.3T the spin reorientation temperature can be seen to be strongly field dependent.

From the isothermal measurements in the range 225 - 293^{o}K the location of the minimum of the modulus as a function of field has been taken to indicate the existence of a critical field (H_c). Above H_c the moments lie in the base plane, (phase III, using Feron's terminology [8]) and below the moments are all aligned at an angle θ to the c axis, phase II. In zero field the moments lie along the c axis ($\theta = 0$).

At temperatures below the spin reorientation point T_{SR}, the rapidly rising part of the peak observed in the isothermal field sweeps has been taken to mark the transition between the phase below T_{SR}, phase I, and that above, phase II. The minimum has been taken to correspond to the same transition between phases II and III as the minimum which occurs for temperatures above T_{SR}. This phase boundary appears to be very weakly temperature dependent in this region.

9.2.7 Magnetic Structure in the Three Phases

From the phase diagram of Gadolinium tentative proposals are made for the magnetic behaviour in each of the phases. In phase I it is known from previous work [20,21,22] that in zero field the moments lie at

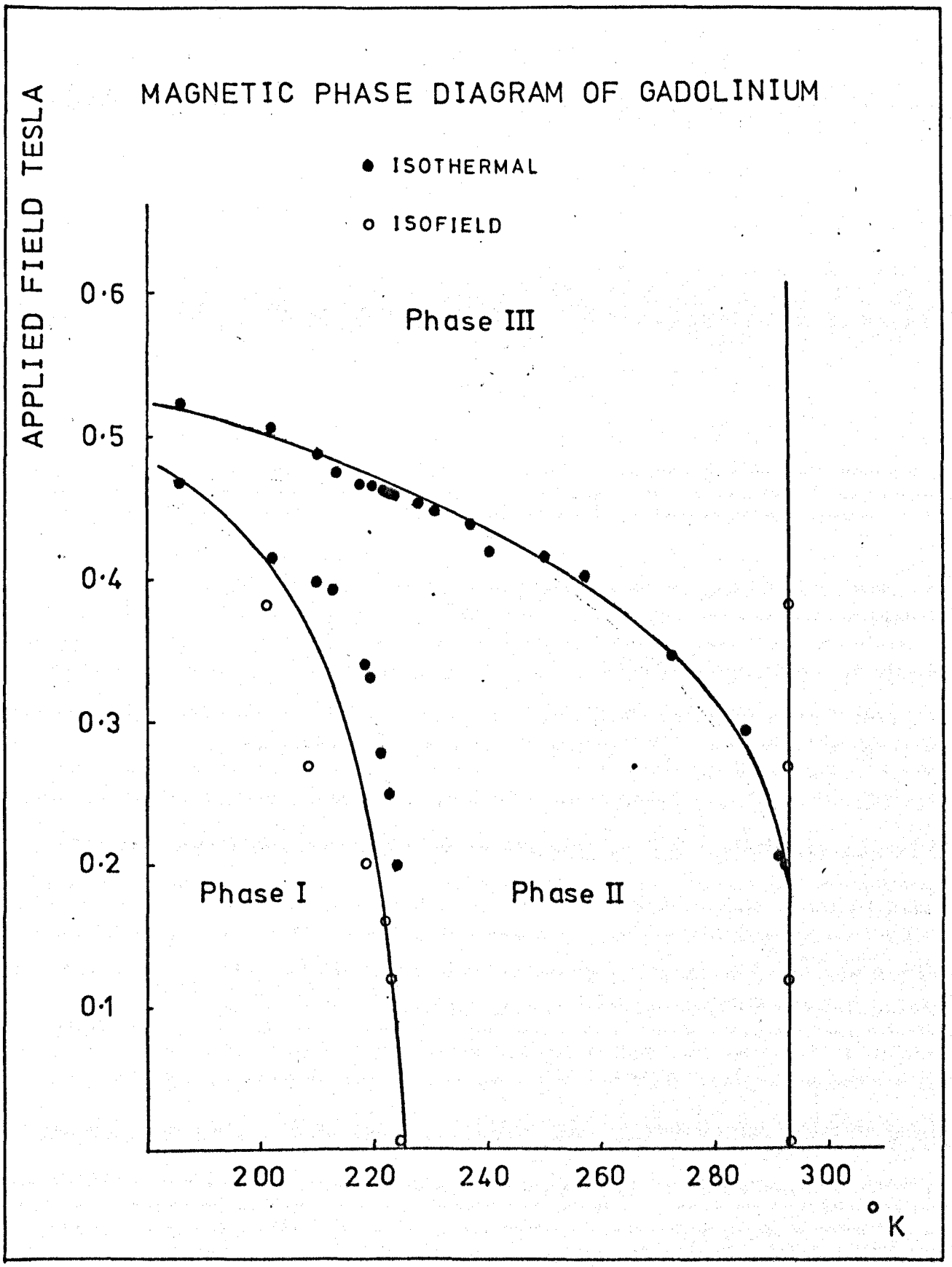
MAGNETIC PHASE DIAGRAM OF GADOLINIUM
ISOTHERMAL
ISOFIELD
APPLIED FIELD TESLA
0·6
0·5
0·4
0·3
0·2
0·1
Phase III
Phase I
Phase II
200
220
240
260
280
300
°K

fig. 9.18

an angle θ inclined to the c axis which varies with temperature. The moments therefore lie on the surface of an easy cone, with the axis of the cone along the c axis of the crystal. All moments in a particular domain are parallel. Referring this to polar angles in fig. 9.19 at any particular temperature the angle is the same for all domains while the angle ϕ varies from domain to domain.

Upon application of a low field it is thought that some domain wall movement occurs so that those domains with components aligned favourably, parallel to the field, grow at the expense of unfavourably oriented domains [27]. Another possibility is that application of the magnetic field causes some distortion of the conical structure so that the axis of the cone no longer lies along the c axis but starts to move into the field direction. The magnetic moments, although remaining in a conical structure will then exhibit various angles θ' to the c axis from domain to domain. In general the θ' would then be larger for those domains aligned with components parallel to the field, as shown in fig. 9.19.

At higher field strengths a domain reorientation would be likely to occur in either of these two cases, corresponding to a bulk rotation of the direction of moments in unfavourably aligned domains. This would mark the phase boundary between phases I and II, since after the rotation all domains would have the same values of θ and ϕ. The first phase boundary below T_{SR} is therefore thought to correspond to a 'sweeping out' of domain in the conical ferromagnetic structure.

At higher fields still the moments are thought to collapse into the base plane which characterises the boundary between phases II and III. This transition is the only one to occur at temperatures above T_{SR}. In phase II at zero field the moments lie along the c axis but as the base plane field is increased the moments move away to lie at an angle θ to the c axis, with a component parallel to the field in all domains.

POSSIBLE MAGNETIC MOMENT STRUCTURES OF GADOLINIUM

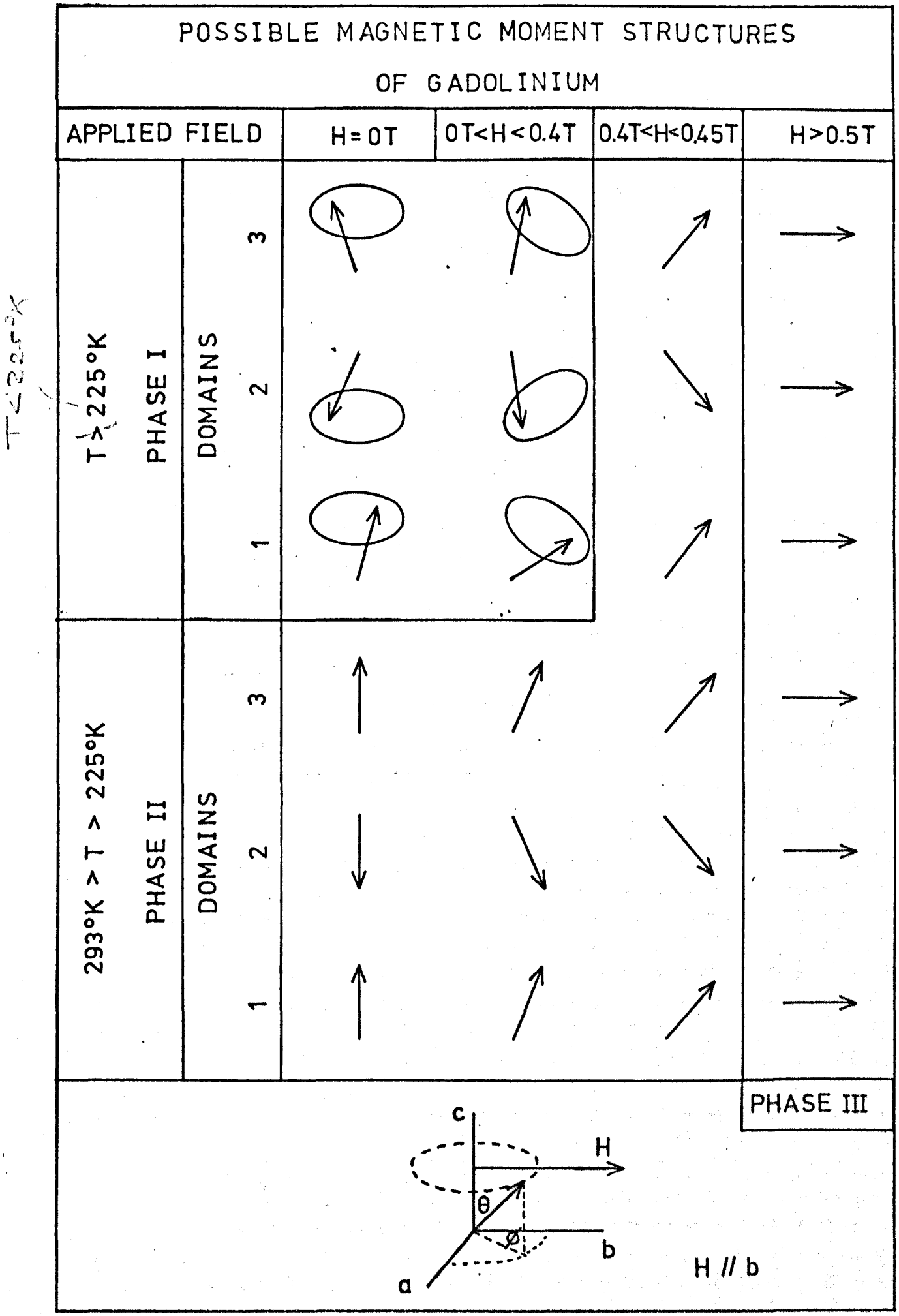

fig. 9.19

9.2.8 Demagnetising Field Corrections

In order to calculate the demagnetising field inside the specimen results for the demagnetising factors N given by Osborne [28] and by Bozorth [29] for the generalised spheroid were employed. The sample was then compared with the spheroid whose shape it most closely resembled and the demagnetising factor for this spheroid used. The sample was in the form of a cylinder of axial length 2.5mm and diameter 3.5 mm.

The demagnetising factor of this particular Gadolinium sample was found to be N = 3.52. The internal magnetic field could then be calculated from

$$H_i = H_a - N.J.\rho \qquad \ldots.9.4$$

where H_i is the internal field and H_a the applied field both measured, in this case in Oersteds, J is the magnetisation in emu./g and ρ is the density in g/cm^3 *. The magnetisation measurements of Nigh et al [7] were used to calculate the magnetisation as a function of applied field for various internal fields for a sample with N = 3.52. A plot of internal against applied field was then made for this sample and is shown in fig. 9.20.

The phase boundaries obtained in fig. 9.19 were then replotted as a function of internal magnetic field and the final phase diagram is shown in fig. 9.21. The critical field for the transition from phase I to phase II, below $225^{o}K$ is seen to be much reduced at about 0.0075T over the temperature independent portion of the curve. The critical field from phase II to phase III is by contrast reduced less at higher temperatures, and appears to increase almost linearly with temperature over most of the

---

* c.g.s. units have been resorted to because previous data of magnetisation and demagnetising factors were in c.g.s.

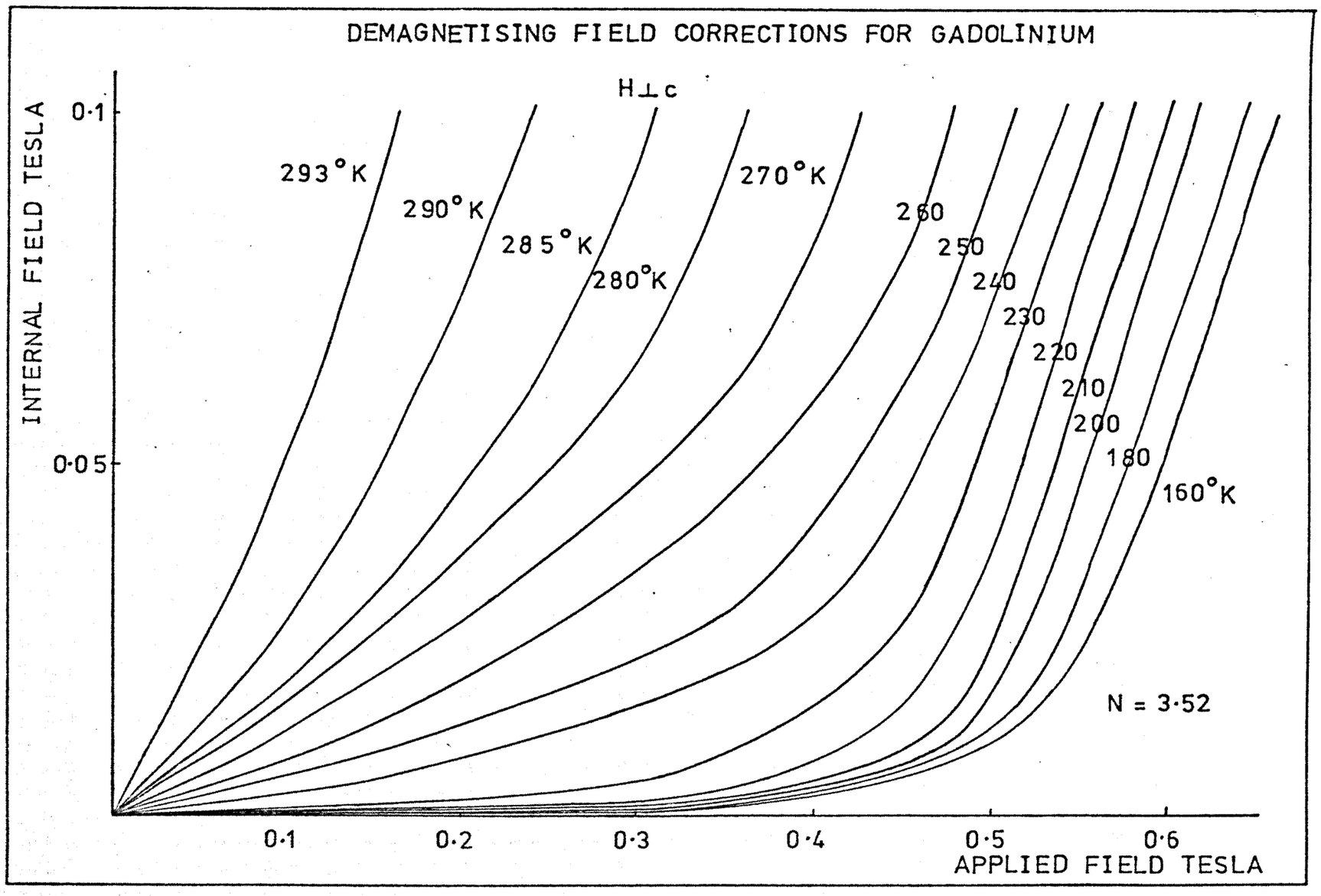
DEMAGNETISING FIELD CORRECTIONS FOR GADOLINIUM
H⊥c
INTERNAL FIELD TESLA
0·1
0·05
293°K
290°K
285°K
280°K
270°K
260
250
240
230
220
210
200
180
160°K
N = 3·52
0·1
0·2
0·3
0·4
0·5
0·6
APPLIED FIELD TESLA

fig. 9.20

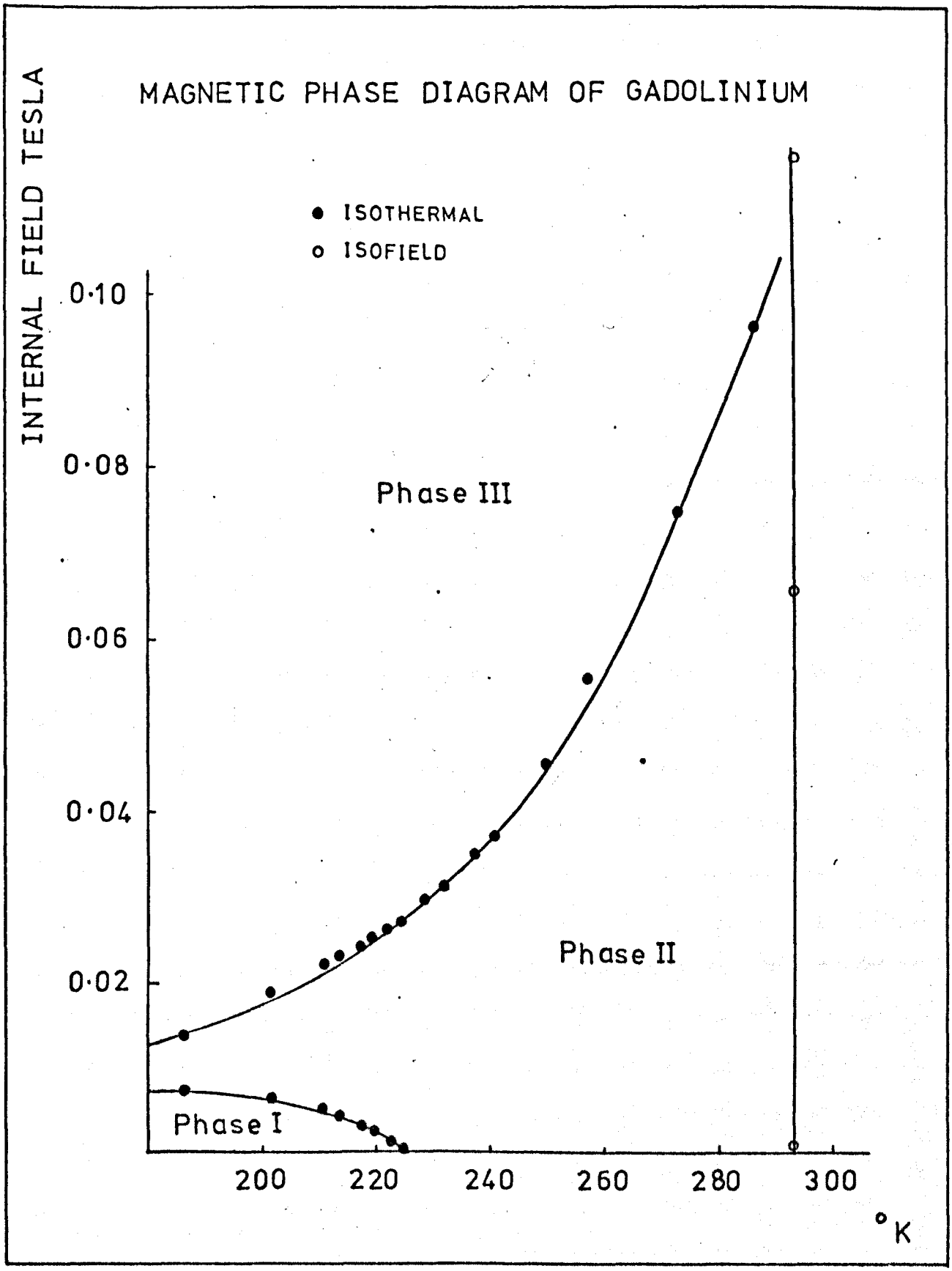
MAGNETIC PHASE DIAGRAM OF GADOLINIUM
INTERNAL FIELD TESLA
ISOTHERMAL
ISOFIELD
0·10
0·08
0·06
0·04
0·02
Phase III
Phase II
Phase I
200
220
240
260
280
300
°K

fig. 9.21

range. For temperatures just below T_C the results were not detailed enough to show whether the critical internal magnetic field showed a decrease, similar to that observed in Dysprosium [30,31,32]. Certainly the critical applied magnetic field showed such a decrease. However, after transforming to internal field, the results were not conclusive. A critical applied field of below 0.18T at 290°K would indicate a decrease in the critical internal field.

9.3 Terbium

Measurements of the variation of the compressional modulus C_{33} have been made on two samples of Terbium. One sample, Tb(I), was obtained from Metals Research Ltd., and had been grown by float zoning techniques. The final purity of this specimen was expected to be of the order of 99%. The other sample, Tb(II), was a high purity specimen which had been grown by the solid state electrotransport method at the Department of Materials Science at the University of Birmingham and was expected to have a purity of 99.9% proof against all impurities. Results on a third specimen which were reported recently [33] have not been included here.

The variation of the elastic modulus as a function of temperature and applied field along the easy b axis has been investigated in the temperature range 200 - 235°K which includes the whole of the antiferromagnetic phase. The two samples exhibited different Curie and Néel temperatures, but the critical fields in the antiferromagnetic phase were found to vary in a similar fashion although they were numerically different.

9.3.1 Zero Field Temperature Dependence of the Modulus of Tb(I)

The zero field temperature dependence of C_{33} of Terbium has been studied by several previous workers including Salama et al and Palmer et al the results of which are shown in fig. 9.22. Work on this modulus has also been performed by Jensen [34]. However in this case the behaviour

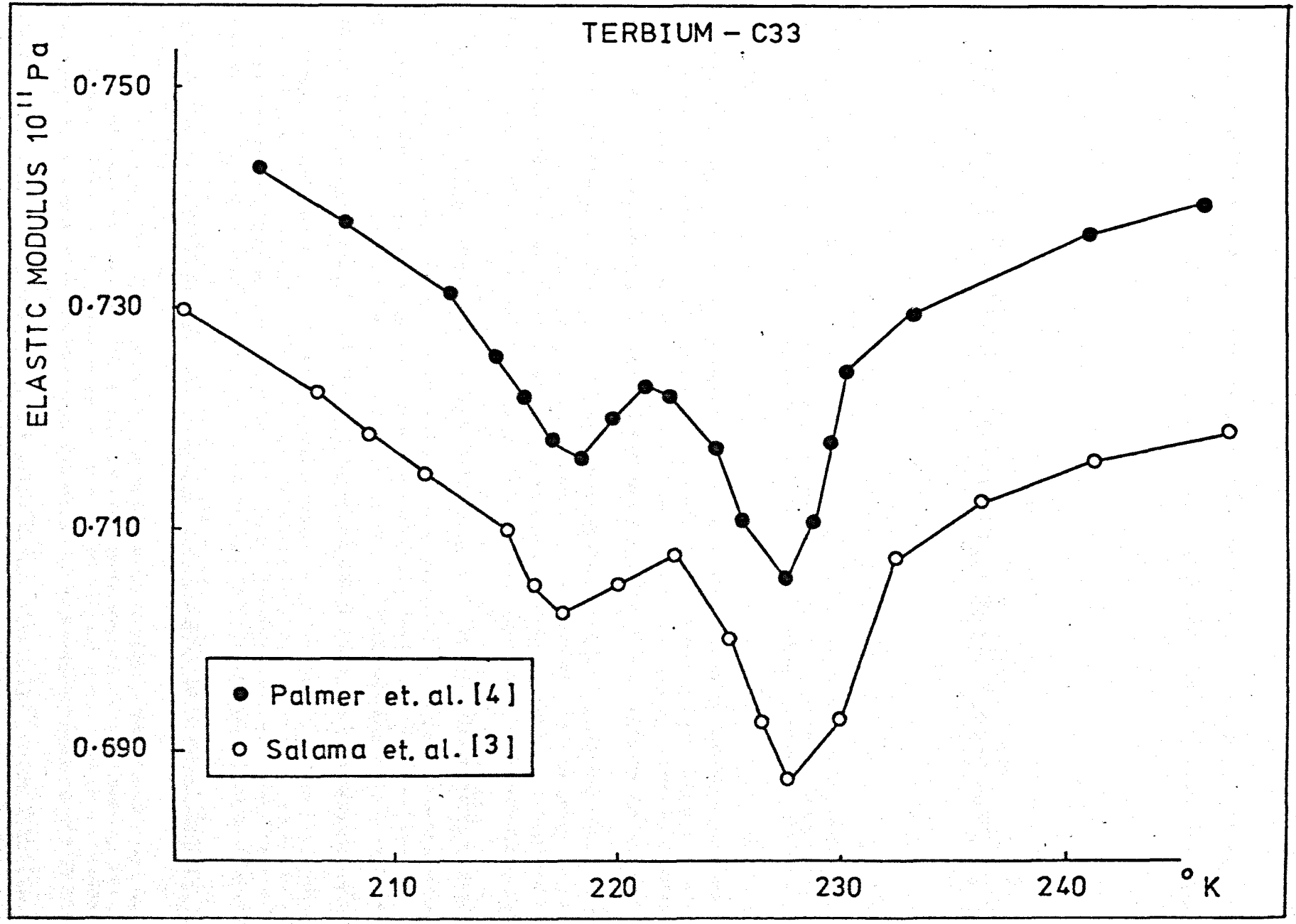
TERBIUM – C33
ELASTIC MODULUS 10^{11} Pa
0·750
0·730
0·710
0·690
210
220
230
240
° K
Palmer et. al. [4]
Salama et. al. [3]

fig. 9.22

was unusual in that it seemed to indicate two Néel points. This was attributed to two 'domains' in the crystal. It is likely that the sample consisted of two crystallites each of which ordered at a different temperature.

Results of the present investigation into the elastic modulus of Terbium under zero field are shown in fig. 9.23. The two runs represent temperature increasing and decreasing. Hysteresis was observed in the Curie point, which is a first order transition, so that when the temperature was increasing from the ferromagnetic phase T_C occurred at 219°K, while when decreasing from the antiferromagnetic phase it occurred at 214°K. The hysteresis does not always seem to occur, since at least one instance occurred when T_C was at 214°K during warming; however, such an observation as hysteresis may help to explain the diverse values of reported Curie temperatures for Terbium.

9.3.2 Field Dependence of the Modulus for Tb(I)

In the ferromagnetic region at 212°K application of a field along the b axis causes a decrease in the modulus resulting in a small but quite definite minimum at a field of 0.38T as shown in fig. 9.24. As the temperature is raised the depth of the minimum decreases faster than the decrease in the zero field value of the elastic modulus. On entering the antiferromagnetic phase at 214°K the nature of the minimum changes and it becomes much broader. Also the appearance of a shoulder is evident at 214°K, although it is less prominent at higher temperatures.

The shoulder occurs at field strengths of 0.15 - 0.2T throughout the antiferromagnetic regime.

As the temperature is raised in the antiferromagnetic phase the minimum becomes lower. The field at which the minimum occurs also decreases slowly as a function of temperature from 0.42T at 213°K to 0.35 at 225°K. At higher fields the modulus recovers most of its zero

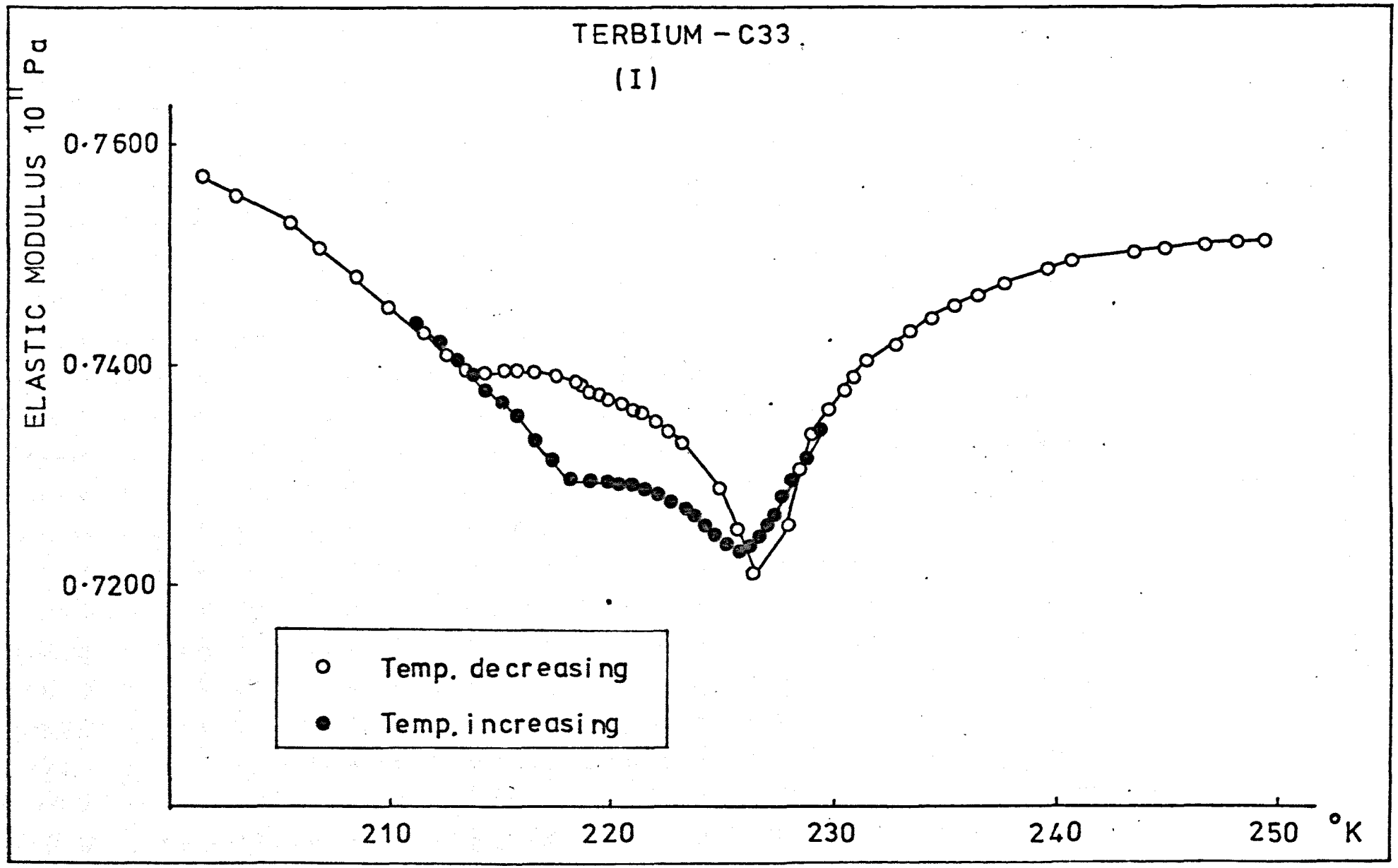
TERBIUM – C33
(I)
ELASTIC MODULUS 10^{11} Pa
0·7600
0·7400
0·7200
Temp. decreasing
Temp. increasing
210
220
230
240
250
°K

fig. 9.23

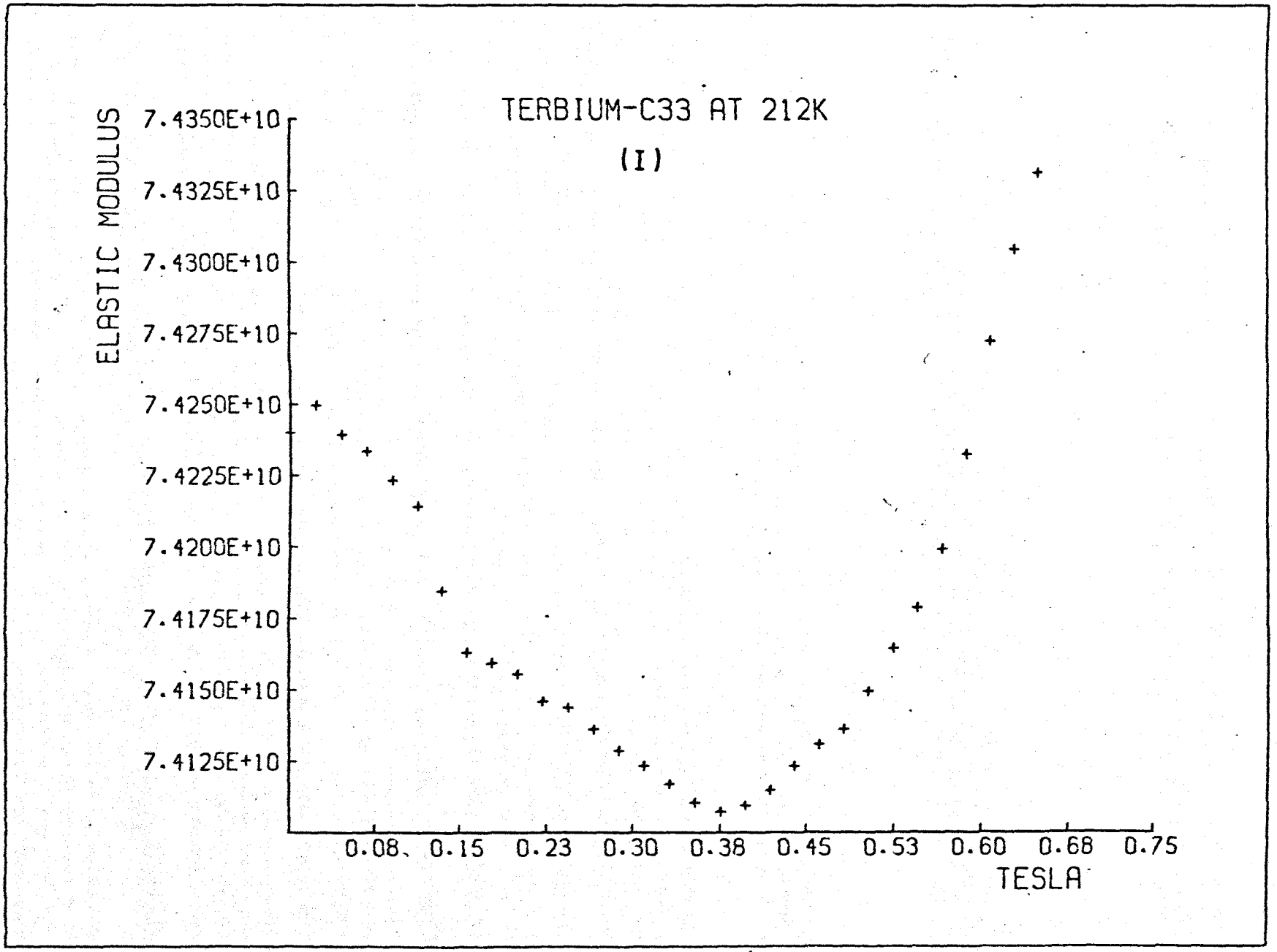
TERBIUM-C33 AT 212K
(I)
ELASTIC MODULUS
7.4350E+10
7.4325E+10
7.4300E+10
7.4275E+10
7.4250E+10
7.4225E+10
7.4200E+10
7.4175E+10
7.4150E+10
7.4125E+10
0.08
0.15
0.23
0.30
0.38
0.45
0.53
0.60
0.68
0.75
TESLA

fig. 9.24

field value, although no indication of saturation is observed in the field strengths used.

Above the Neel temperature the behaviour is somewhat different. The minimum still exists; however, it moves to higher field strengths as the temperature increases. The high field behaviour is much less field dependent than below the Néel point, similar in this respect to the observations of paramagnetic Gadolinium.

9.3.3 Temperature Dependence of the Modulus in Constant Applied Fields for Tb(I)

The temperature dependence under constant applied fields of up to 0.35T resembles the zero field behaviour in figs. 9.30 and 9.31. The Néel point at the minimum does not seem to vary much with field while the Curie point at the shoulder of the curve is weakly field dependent. However above 0.35T the behaviour is entirely different with a minimum occurring where the Curie point would be expected (fig. 9.33). It is thought that this represents the transition from a ferromagnetic alignment to either a fan state, if such a state exists, or else to a badly distorted helical structure in which there exist large ferromagnetic regions which have grown from domain walls aligned parallel to the field direction.

9.3.4 Zero Field Temperature Dependence of the Modulus of Tb(II)

The variation of the elastic modulus of the high purity specimen of Terbium, Tb(II), as a function of temperature is shown in fig. 9.35. This differs from the observed behaviour in the other sample, Tb(I), in several respects. The Néel temperature characterised by the deeper of the two anomalies occurs at 230°K instead of 226°K, while the Curie temperature is at 220°K. Further the behaviour at the Curie point also exhibits a minimum instead of just a change in slope.

TERBIUM-C33
(I)
ELASTIC MODULUS 10^{11} Pa
0·7450
0·7400
0·7350
0·7320
0·1
0·2
0·3
0·4
0·5
0·6
0·7
TESLA
212°K
213°K
214°K

fig. 9.25

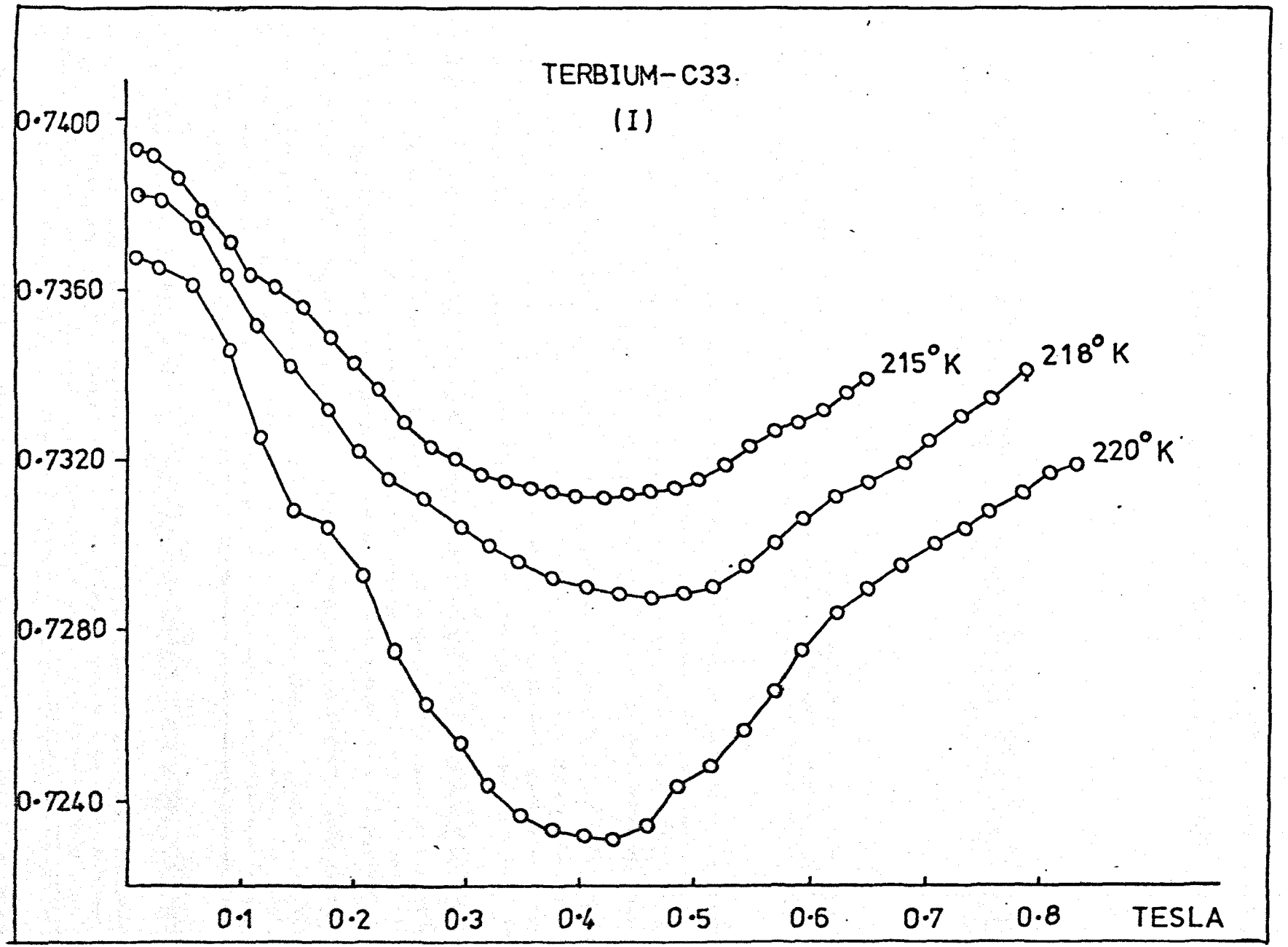
TERBIUM-C33.
(I)
0·7400
0·7360
0·7320
0·7280
0·7240
215°K
218°K
220°K
0·1
0·2
0·3
0·4
0·5
0·6
0·7
0·8
TESLA

fig. 9.26

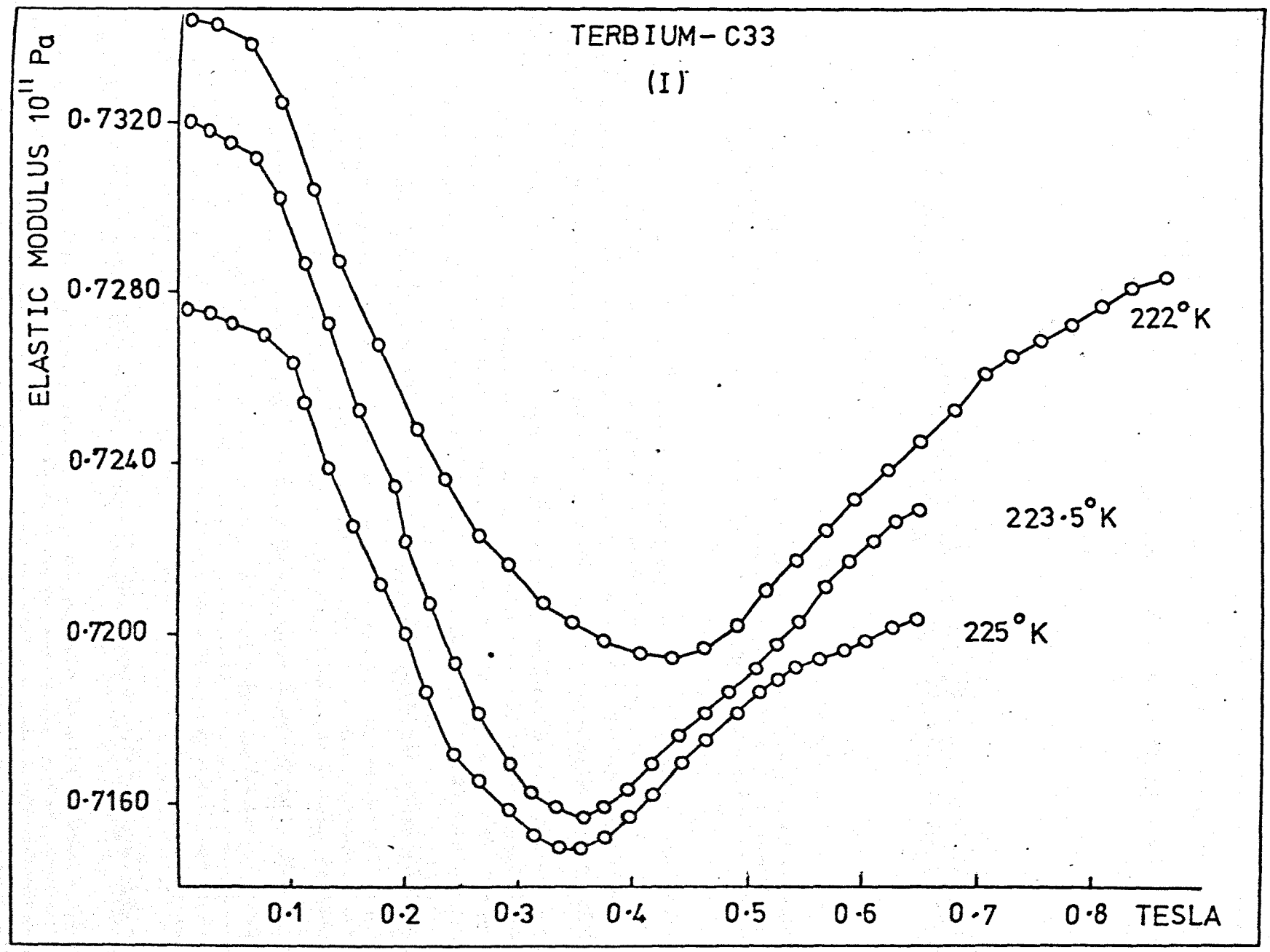
TERBIUM-C33
(I)
ELASTIC MODULUS 10^{11} Pa
0·7320
0·7280
0·7240
0·7200
0·7160
222°K
223·5°K
225°K
0·1
0·2
0·3
0·4
0·5
0·6
0·7
0·8
TESLA

fig. 9.27

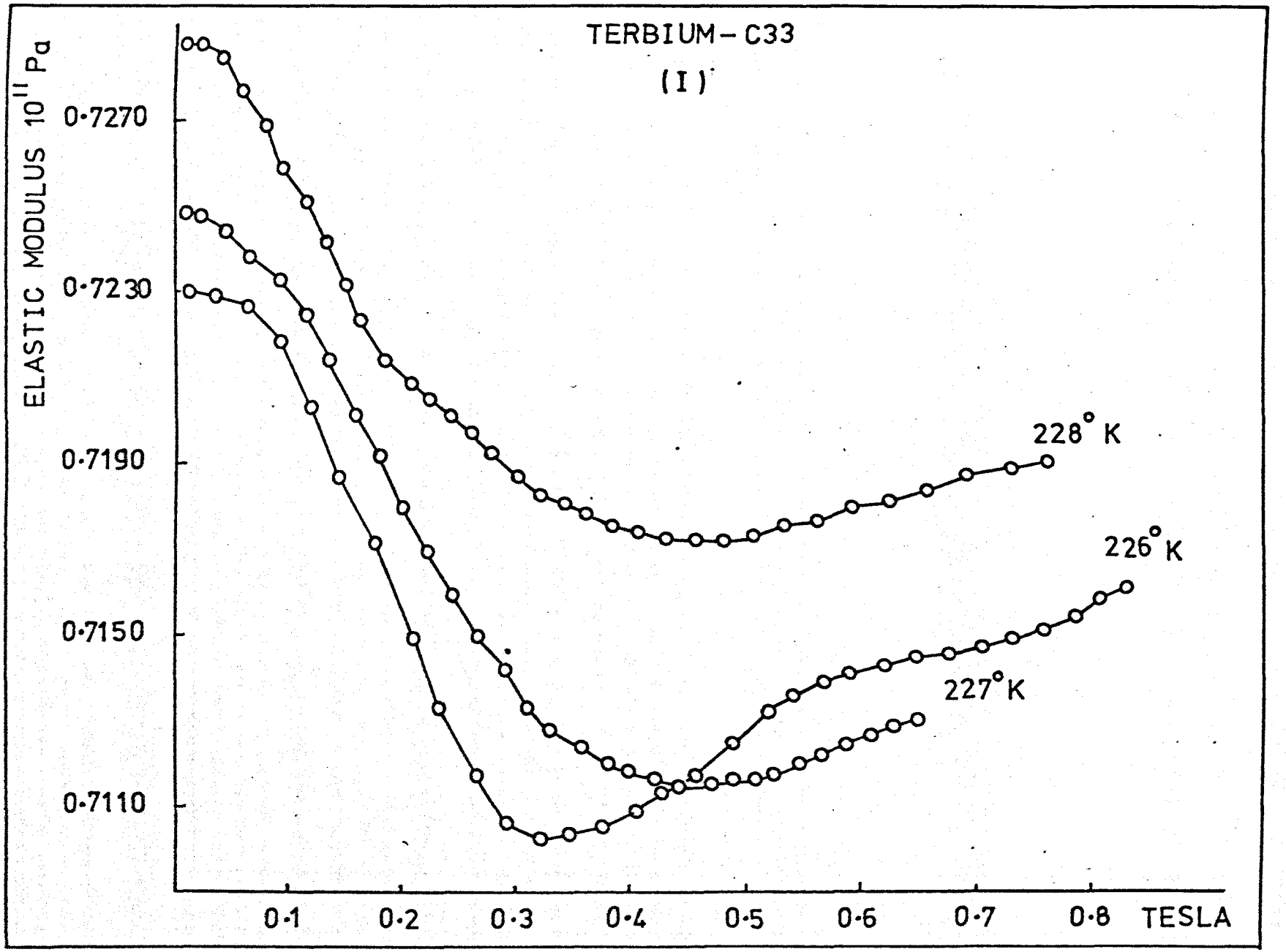
TERBIUM – C33
(I)
ELASTIC MODULUS 10^{11} Pa
0·7270
0·7230
0·7190
0·7150
0·7110
228° K
226° K
227° K
0·1
0·2
0·3
0·4
0·5
0·6
0·7
0·8
TESLA

fig. 9.28

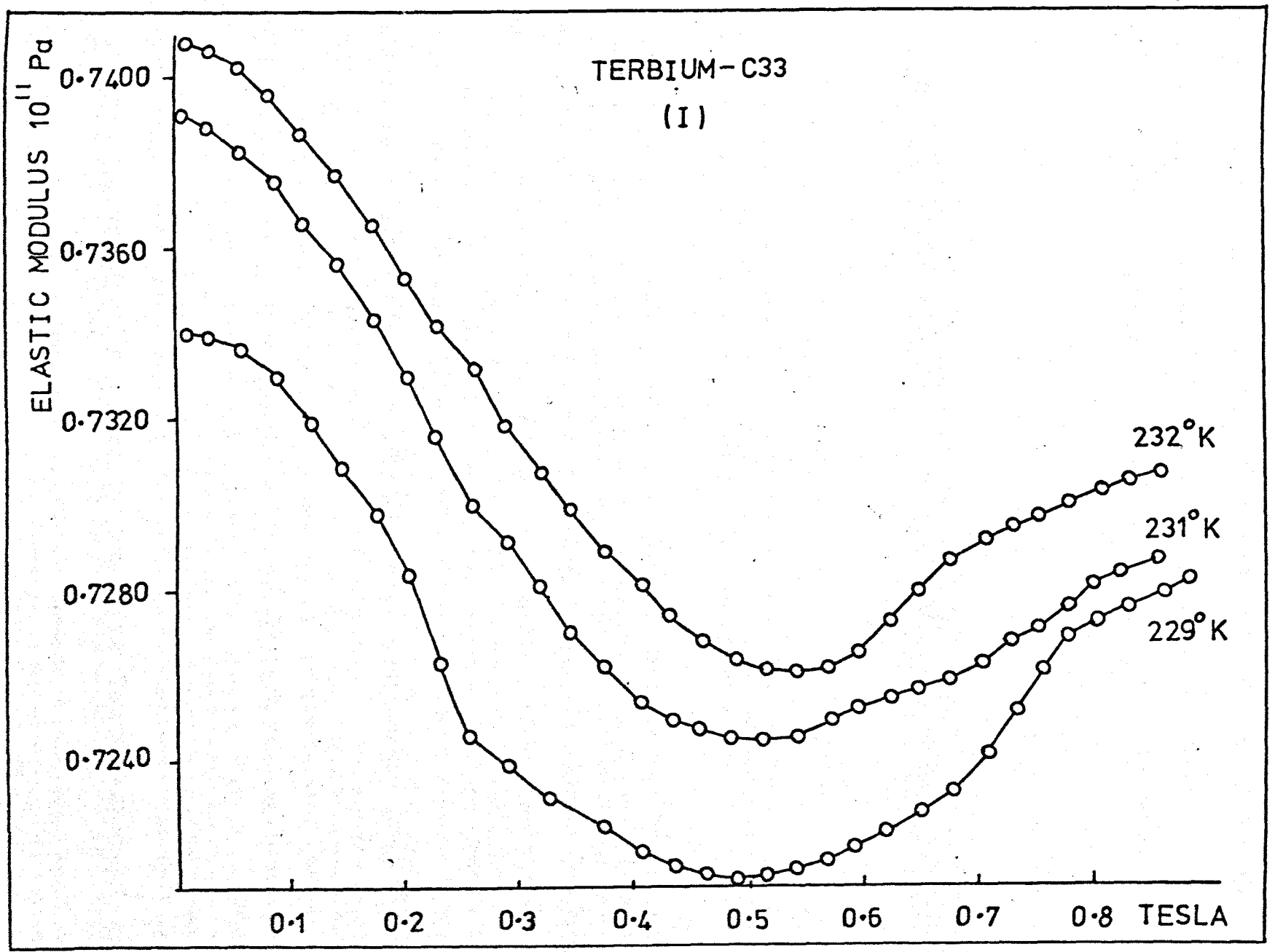
TERBIUM - C33
(I)
ELASTIC MODULUS 10^{11} Pa
0·7400
0·7360
0·7320
0·7280
0·7240
232°K
231°K
229°K
0·1
0·2
0·3
0·4
0·5
0·6
0·7
0·8
TESLA

fig. 9.29

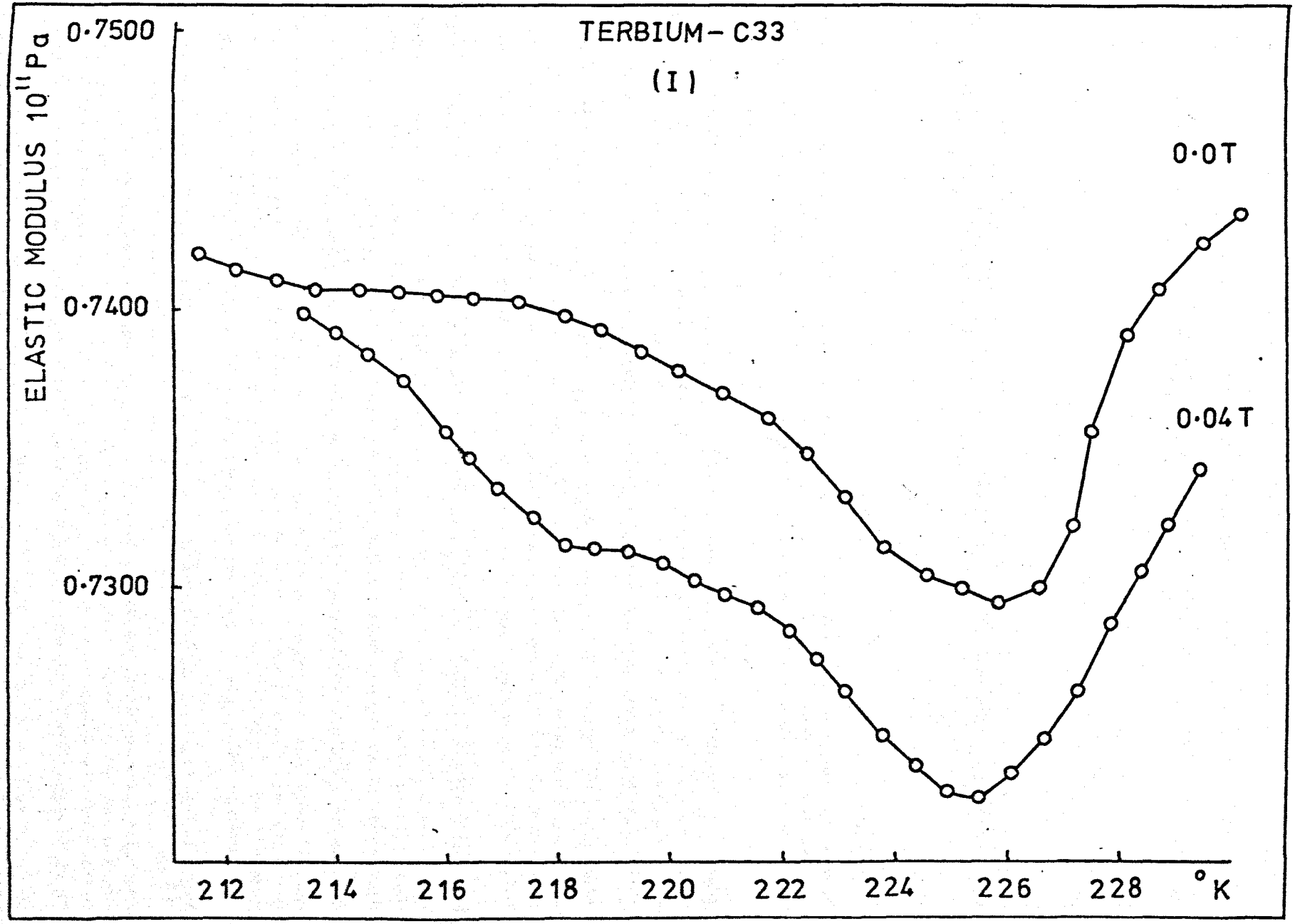
TERBIUM – C33
(I)
ELASTIC MODULUS 10^{11} Pa
0·7500
0·7400
0·7300
0·0T
0·04T
212
214
216
218
220
222
224
226
228
°K

fig. 9.30

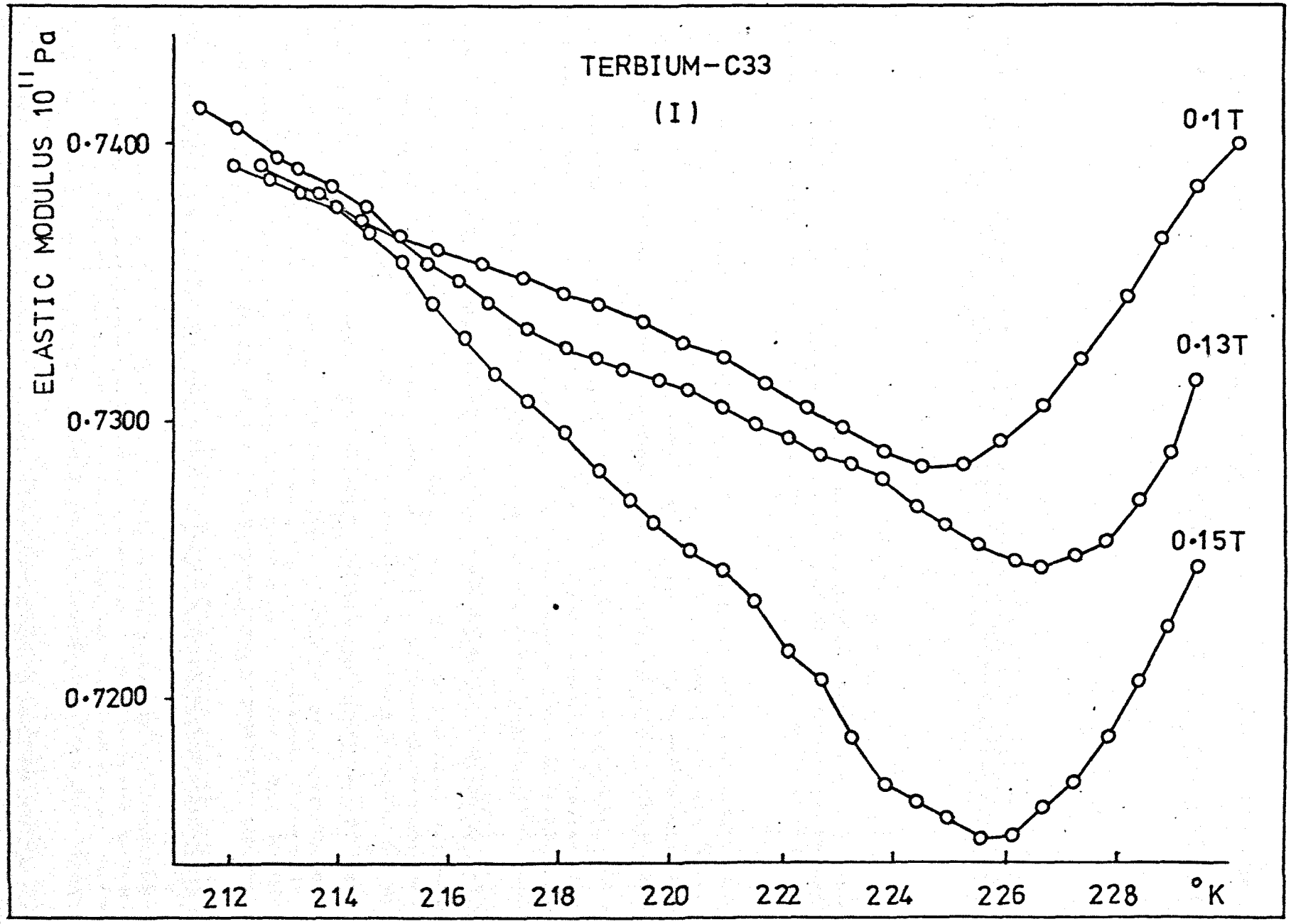
TERBIUM-C33
(I)
ELASTIC MODULUS 10^{11} Pa
0·7400
0·7300
0·7200
0·1T
0·13T
0·15T
212
214
216
218
220
222
224
226
228
°K

Fig. 9.31

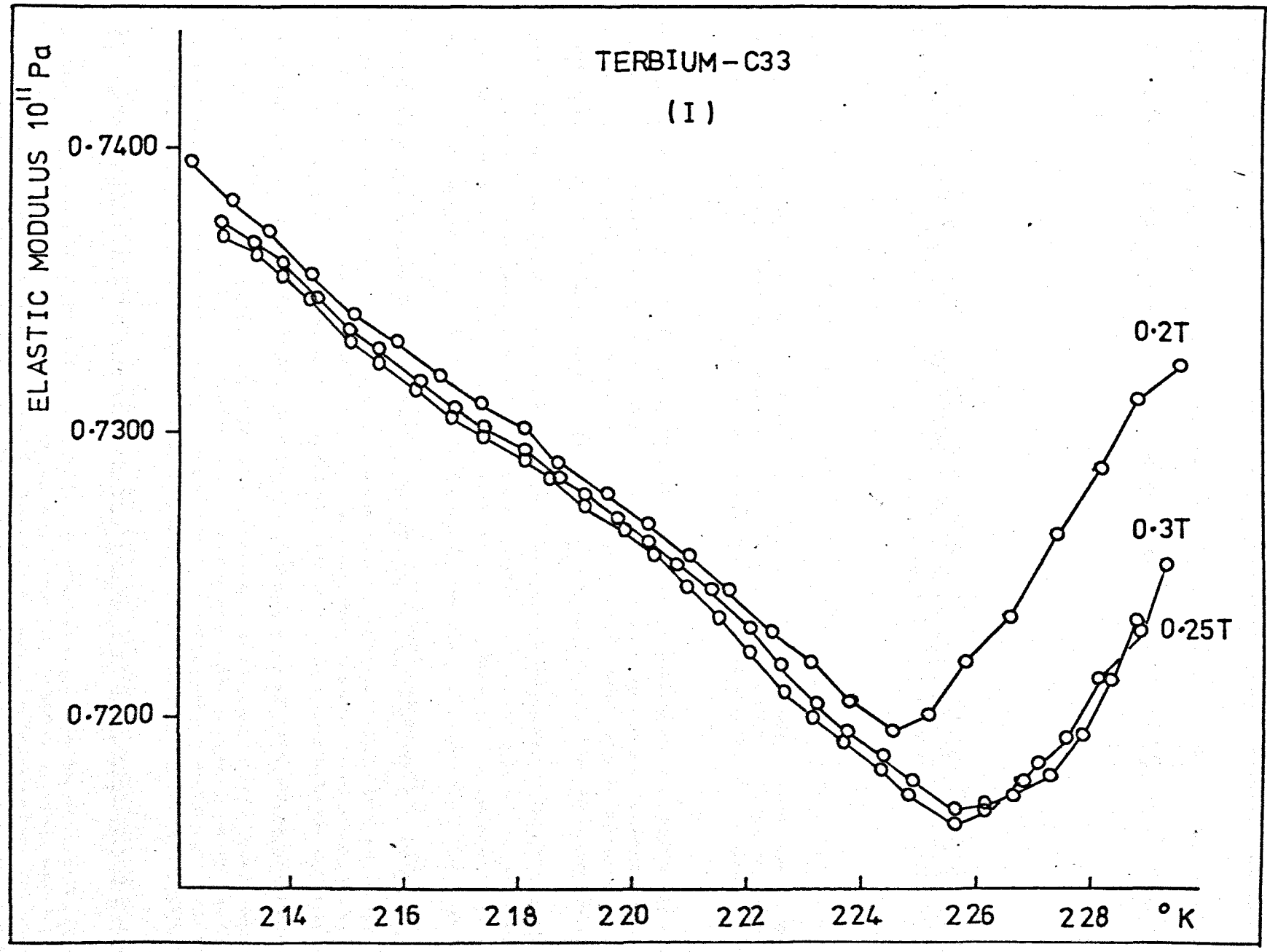
TERBIUM – C33
(I)
ELASTIC MODULUS 10^{11} Pa
0·7400
0·7300
0·7200
0·2T
0·3T
0·25T
2 14
2 16
2 18
2 20
2 22
2 24
2 26
2 28
°K

fig. 9.32

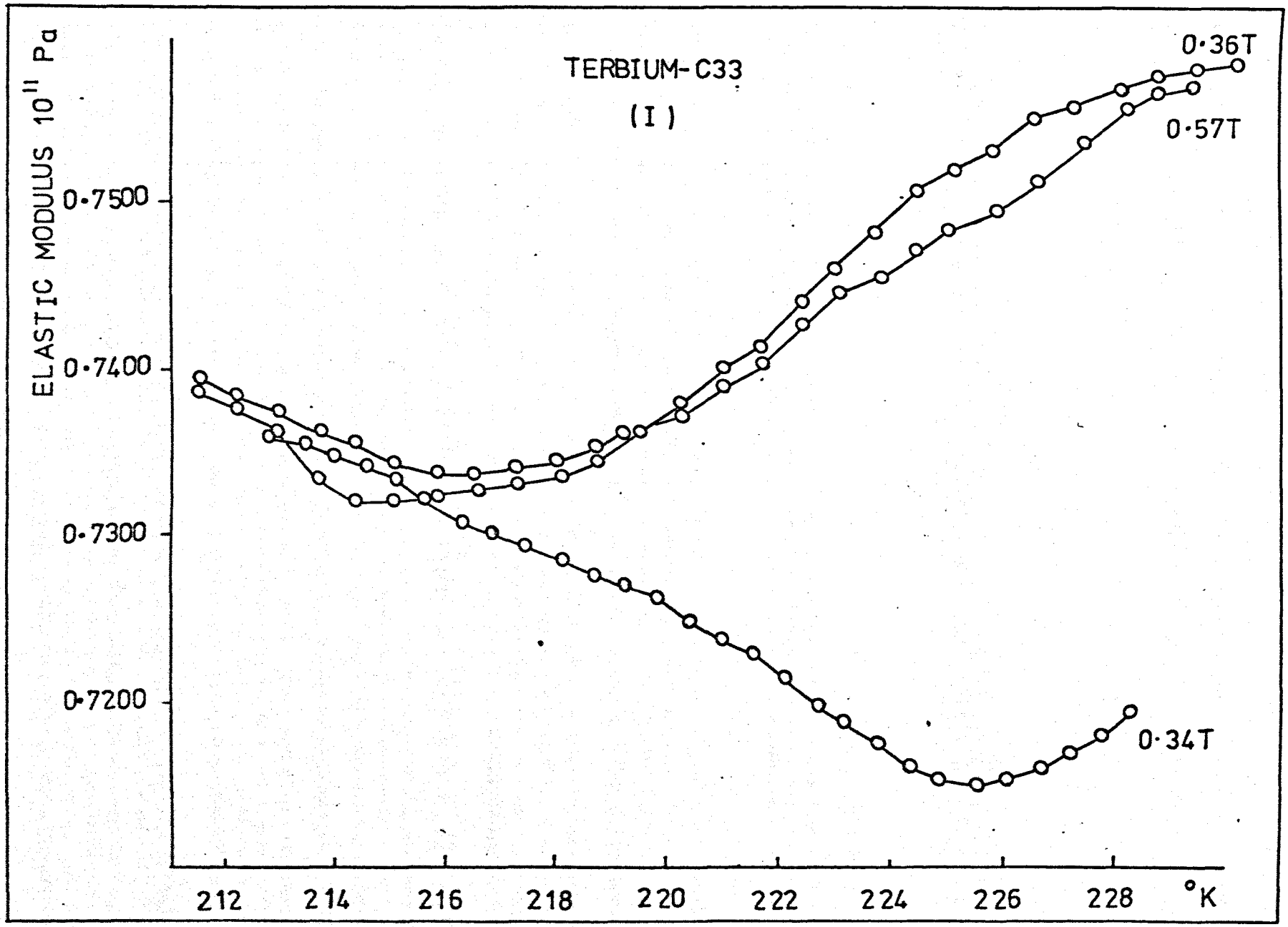
TERBIUM-C33
(I)
ELASTIC MODULUS 10^{11} Pa
0·7500
0·7400
0·7300
0·7200
212
214
216
218
220
222
224
226
228
°K
0·36T
0·57T
0·34T

fig. 9.33

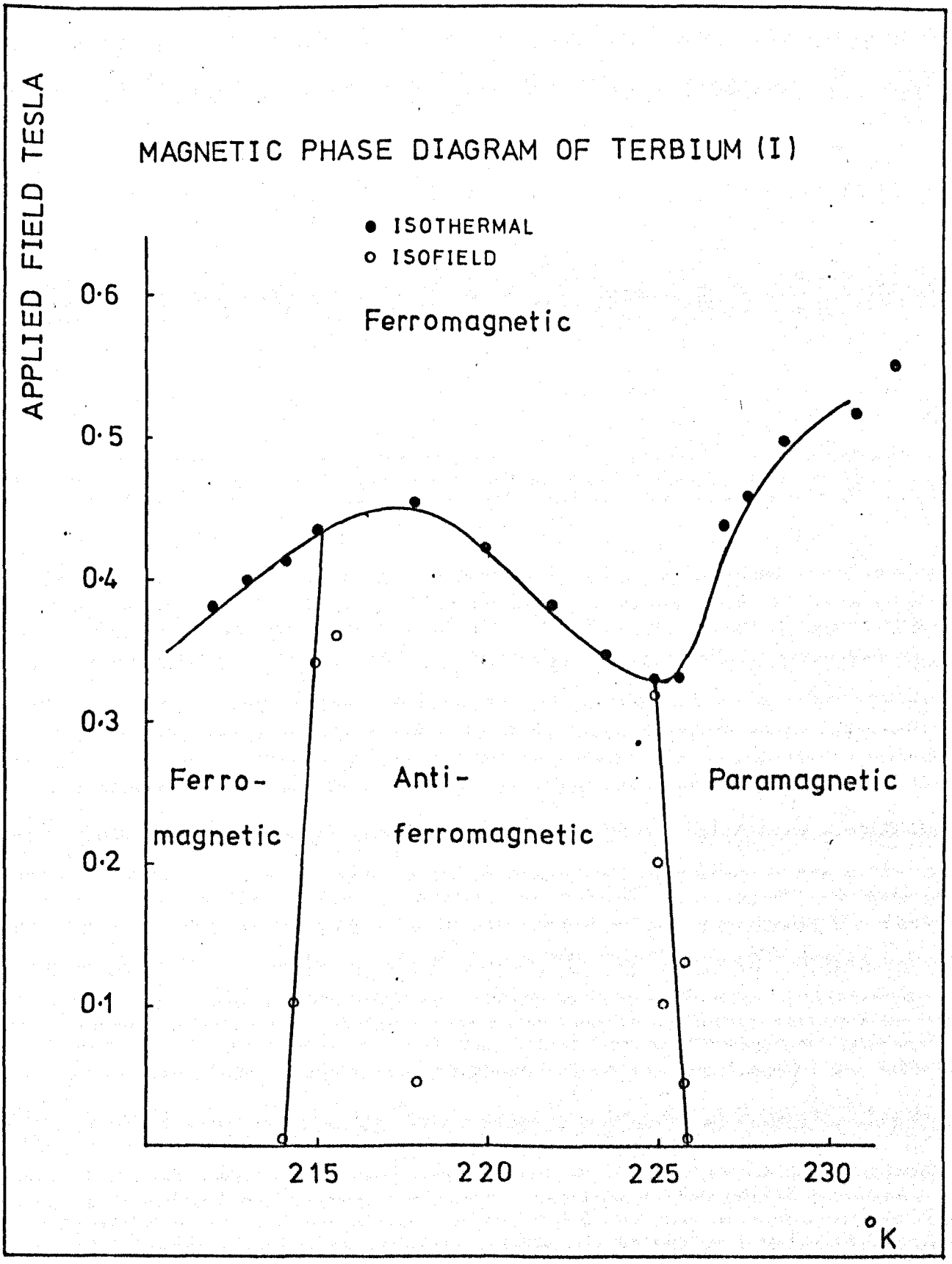
MAGNETIC PHASE DIAGRAM OF TERBIUM (I)
APPLIED FIELD TESLA
ISOTHERMAL
ISOFIELD
Ferromagnetic
Ferro-
magnetic
Anti-
ferromagnetic
Paramagnetic
0·6
0·5
0·4
0·3
0·2
0·1
215
220
225
230
°K

fig. 9.34

9.3.5 Field Dependence of the Modulus of Tb(II)

In the ferromagnetic region the variation of elastic modulus with field shows a minimum between 0.15 and 0.2T, the existence of which can be clearly seen in fig. 9.36. Similar behaviour is shown in fig. 9.38 where the minimum is seen to become broader. In this region, despite the existence of the minimum the elastic modulus is only weakly field dependent.

Above the Curie point a sharp minimum appears at fields decreasing from about 0.44T at 221°K to 0.38T at 226°K. The depth of the minimum in the elastic constant decreases with temperature until the Néel point is reached. Above T_N the familiar paramagnetic field dependence is again in evidence, with the elastic constant not recovering significantly after passing through the minimum.

9.3.6 Temperature Dependence of the Modulus in Constant Applied Fields for Tb(II)

The temperature dependence of the modulus for various constant applied magnetic fields is shown in figs. 9.42 and 9.43. At 0.1T the variation is similar to that at zero field; however, the depth of the minimum at T_C is shallower. The behaviour at 0.2T shows the same Néel temperature but it has two shoulders occurring at 226°K and 220°K.

At higher fields the Curie point minimum has disappeared and the shoulder at 220°K becomes progressively less well defined as the field increases. The Néel point remains the same in all of those cases but the minimum here becomes broader as the field is increased.

9.3.7 Interpretation of Results and Phase Diagrams

The phase diagrams of the two specimens of Terbium are shown in figs. 9.34 and 9.44. The main difference between the two is in the location of the Curie point which in Tb(I) occurs at 214°K, while in Tb(II) it is at 220°K.

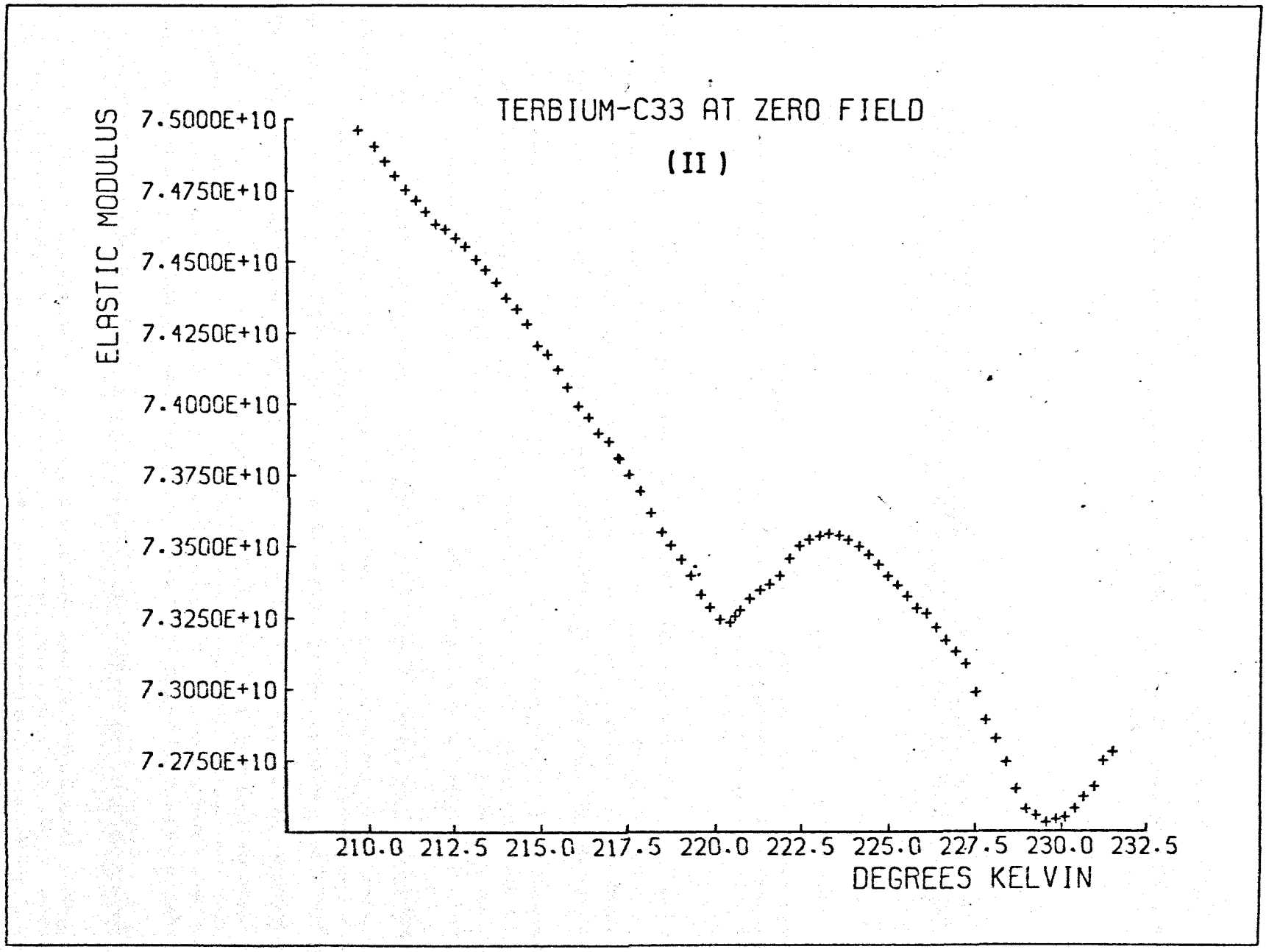
TERBIUM-C33 AT ZERO FIELD
(II)
ELASTIC MODULUS
7.5000E+10
7.4750E+10
7.4500E+10
7.4250E+10
7.4000E+10
7.3750E+10
7.3500E+10
7.3250E+10
7.3000E+10
7.2750E+10
210.0 212.5 215.0 217.5 220.0 222.5 225.0 227.5 230.0 232.5
DEGREES KELVIN

fig. 9.35

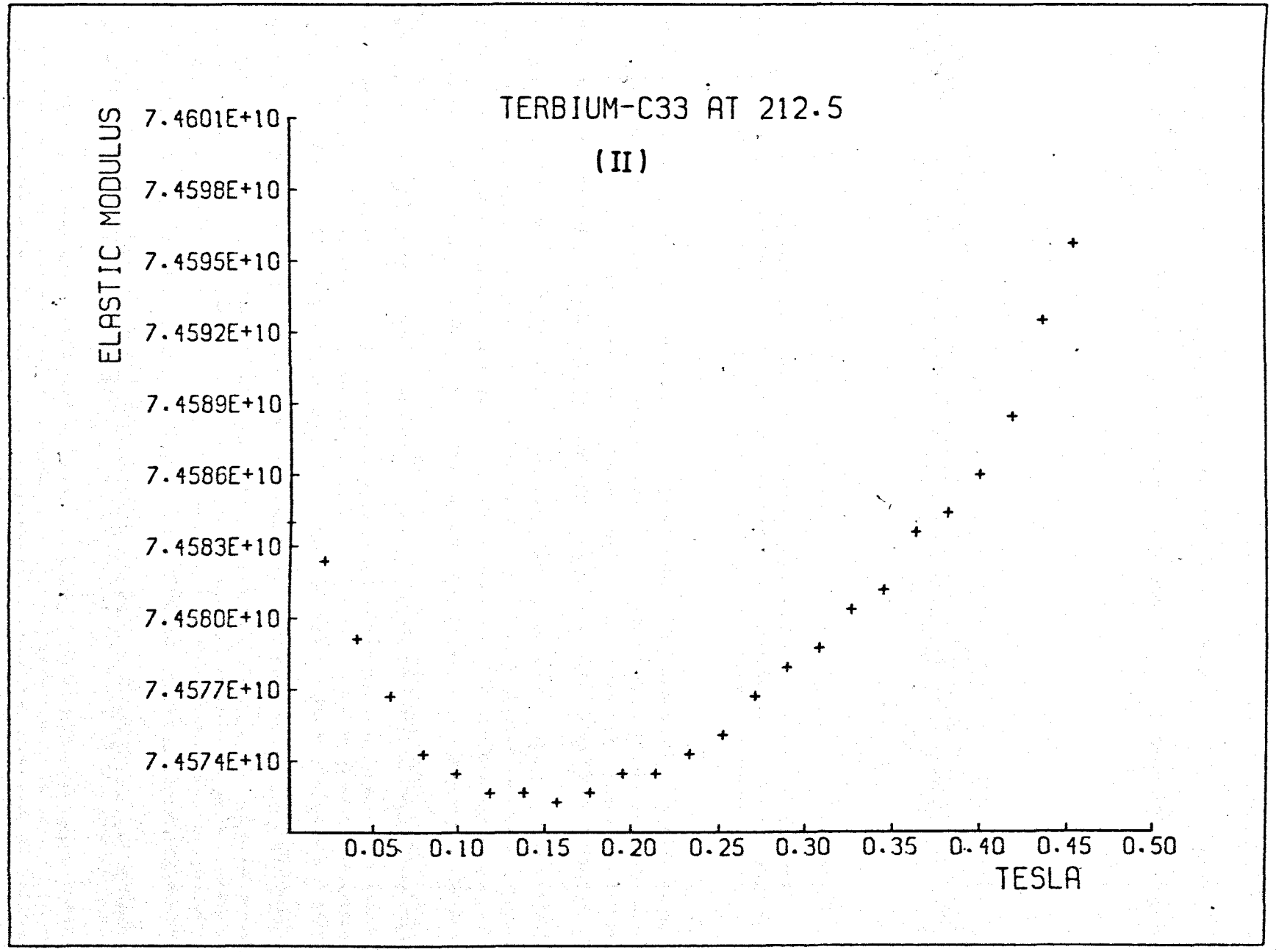
TERBIUM-C33 AT 212.5
(II)
ELASTIC MODULUS
7.4601E+10
7.4598E+10
7.4595E+10
7.4592E+10
7.4589E+10
7.4586E+10
7.4583E+10
7.4580E+10
7.4577E+10
7.4574E+10
0.05
0.10
0.15
0.20
0.25
0.30
0.35
0.40
0.45
0.50
TESLA

fig. 9.36

ELASTIC MODULUS 10^{11} Pa
0·7454
0·7442
0·7430
0·7418
212·5° K
215° K
TERBIUM - C33
(II)
0·1
0·2
0·3
0·4
0·5
TESLA

fig. 9.37

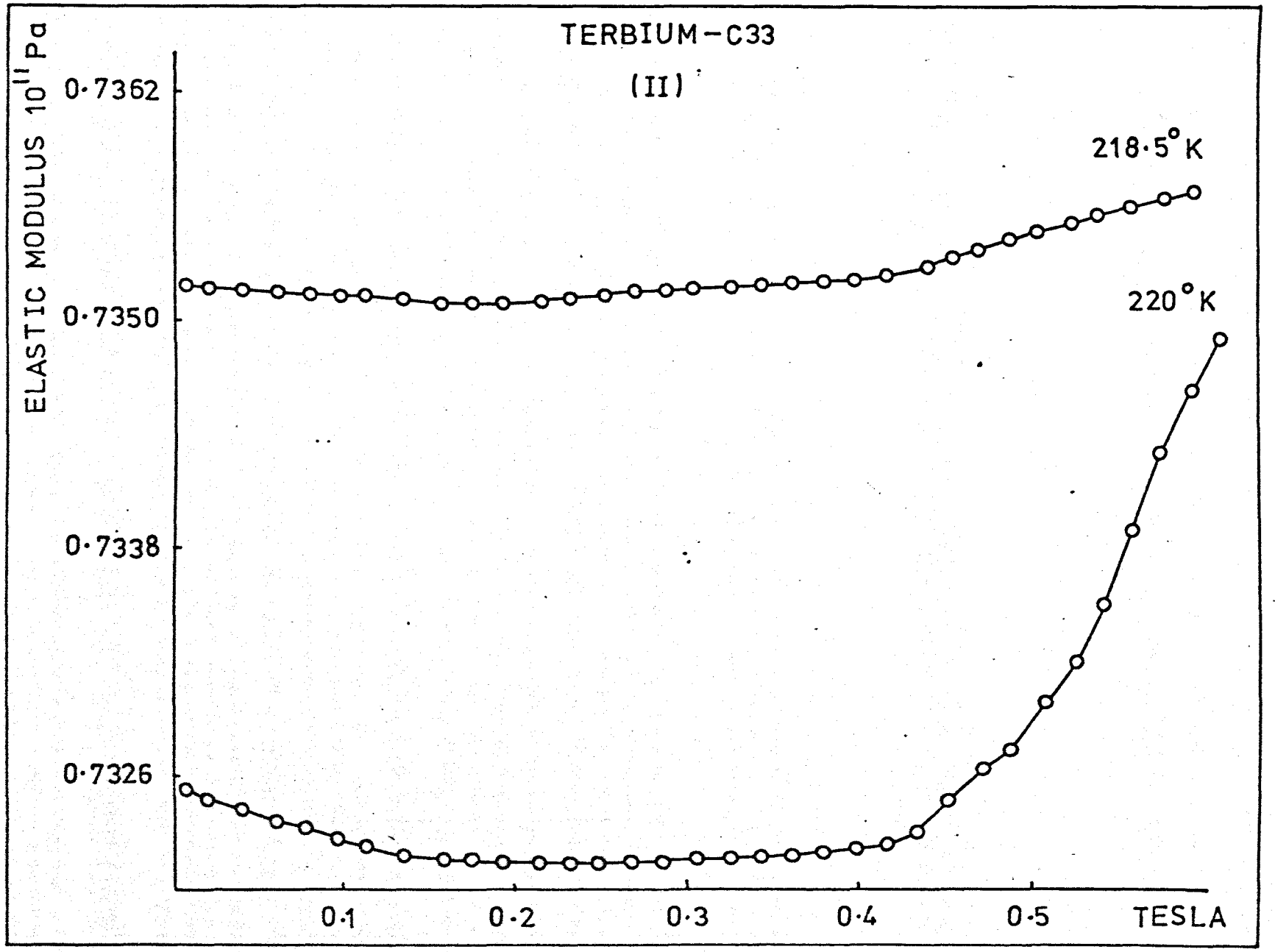
TERBIUM – C33
(II)
ELASTIC MODULUS 10^{11} Pa
0·7362
0·7350
0·7338
0·7326
218·5° K
220° K
0·1
0·2
0·3
0·4
0·5
TESLA

fig. 9.38

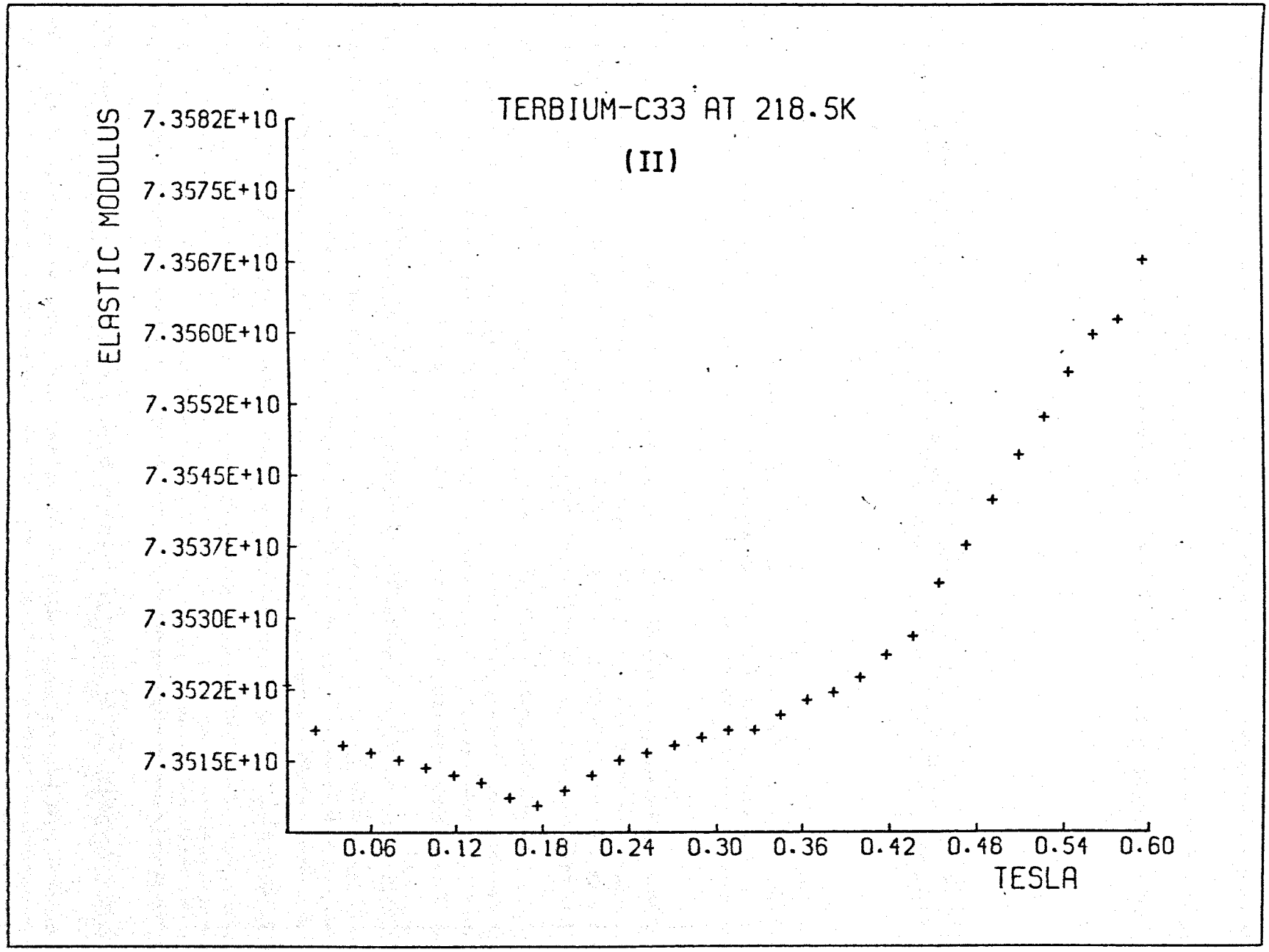
TERBIUM-C33 AT 218.5K
(II)
ELASTIC MODULUS
7.3582E+10
7.3575E+10
7.3567E+10
7.3560E+10
7.3552E+10
7.3545E+10
7.3537E+10
7.3530E+10
7.3522E+10
7.3515E+10
0.06
0.12
0.18
0.24
0.30
0.36
0.42
0.48
0.54
0.60
TESLA

fig.9.39

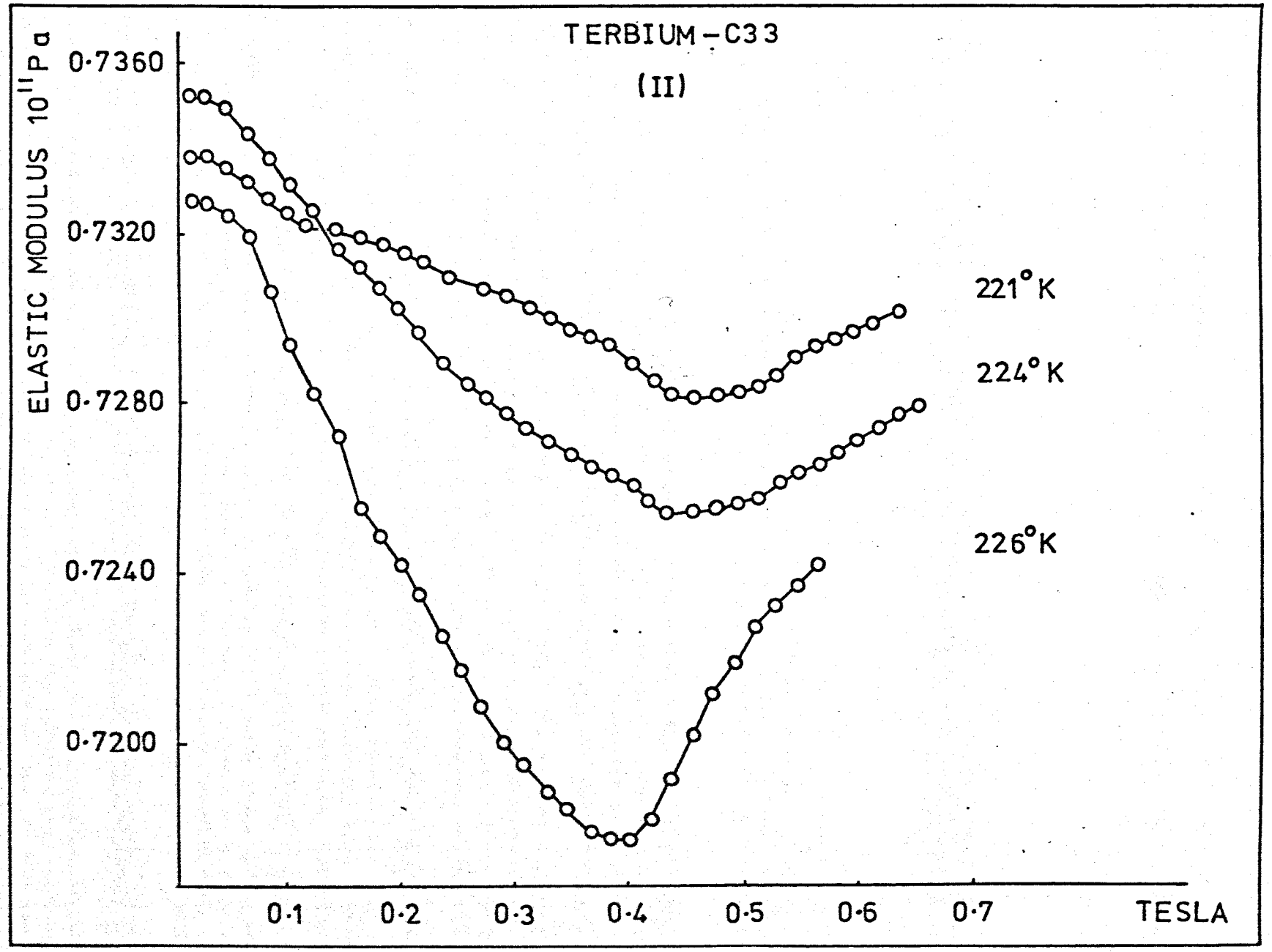
TERBIUM – C33
(II)
ELASTIC MODULUS 10^{11} Pa
0·7360
0·7320
0·7280
0·7240
0·7200
221° K
224° K
226° K
0·1
0·2
0·3
0·4
0·5
0·6
0·7
TESLA

fig. 9.40

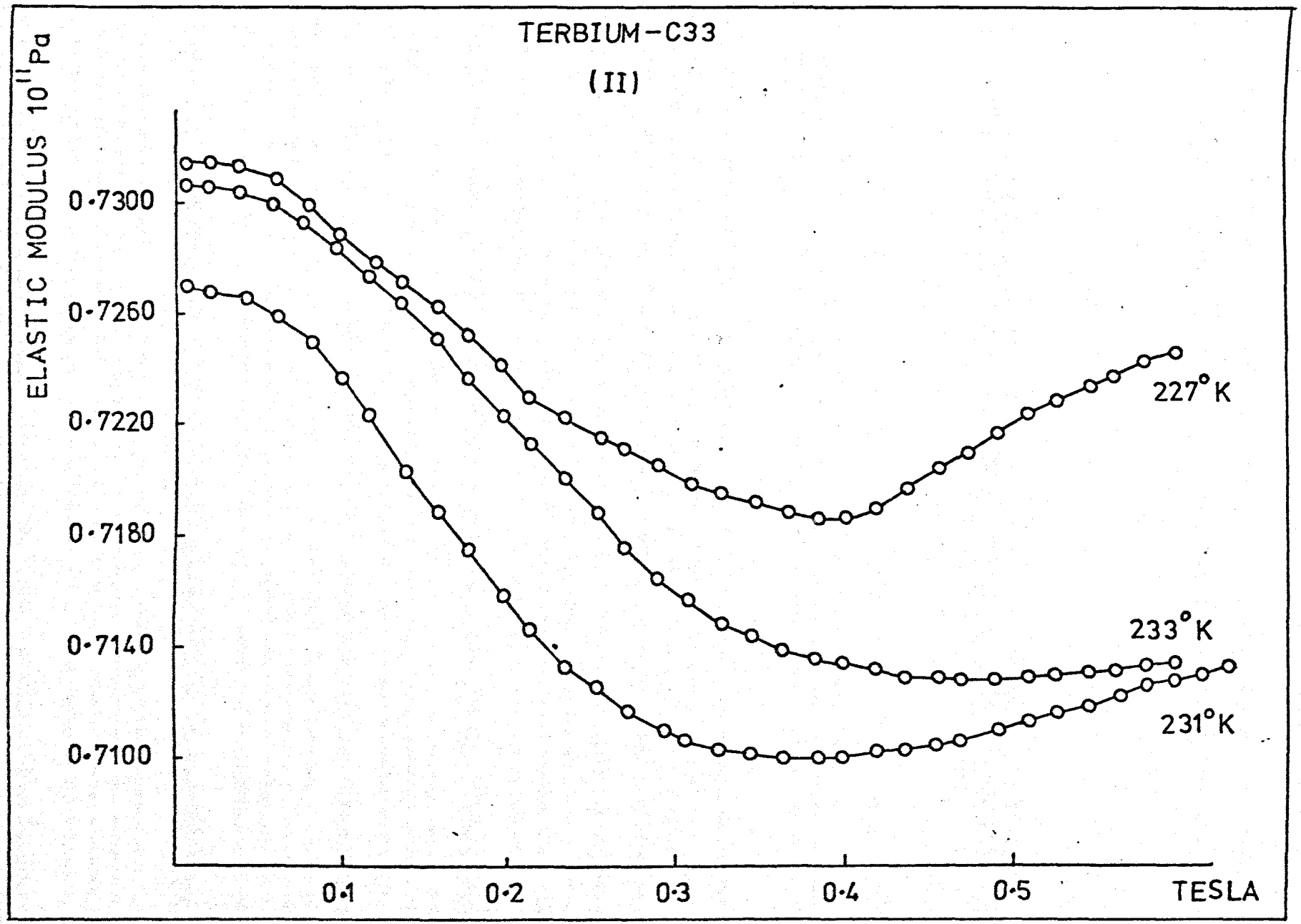
TERBIUM-C33
(II)
ELASTIC MODULUS 10^{11}Pa
0·7300
0·7260
0·7220
0·7180
0·7140
0·7100
227°K
233°K
231°K
0·1
0·2
0·3
0·4
0·5
TESLA

Fig. 9.41

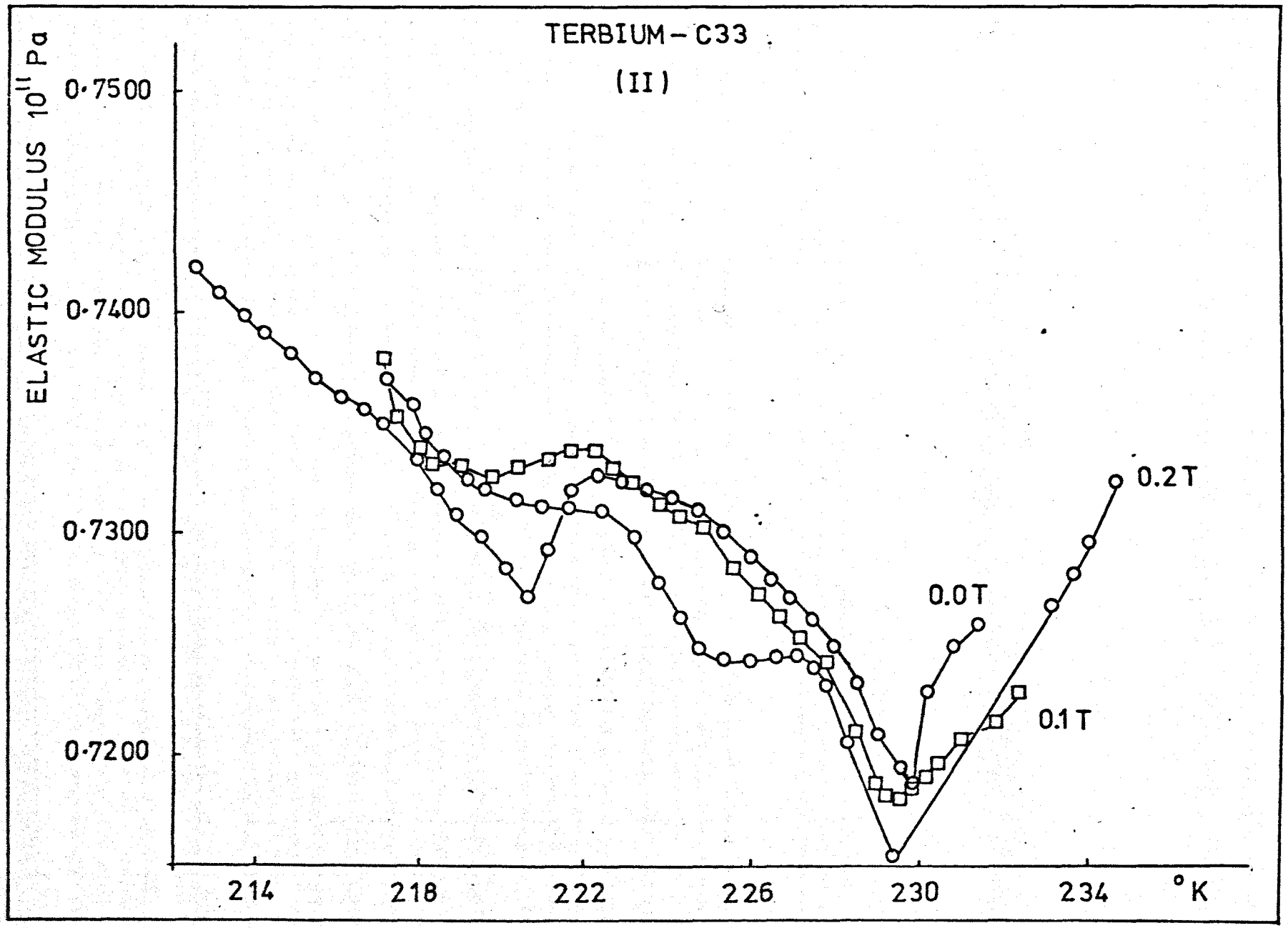
TERBIUM – C33
(II)
ELASTIC MODULUS 10^{11} Pa
0·7500
0·7400
0·7300
0·7200
214
218
222
226
230
234
°K
0.0T
0.1T
0.2T

Fig. 9.42

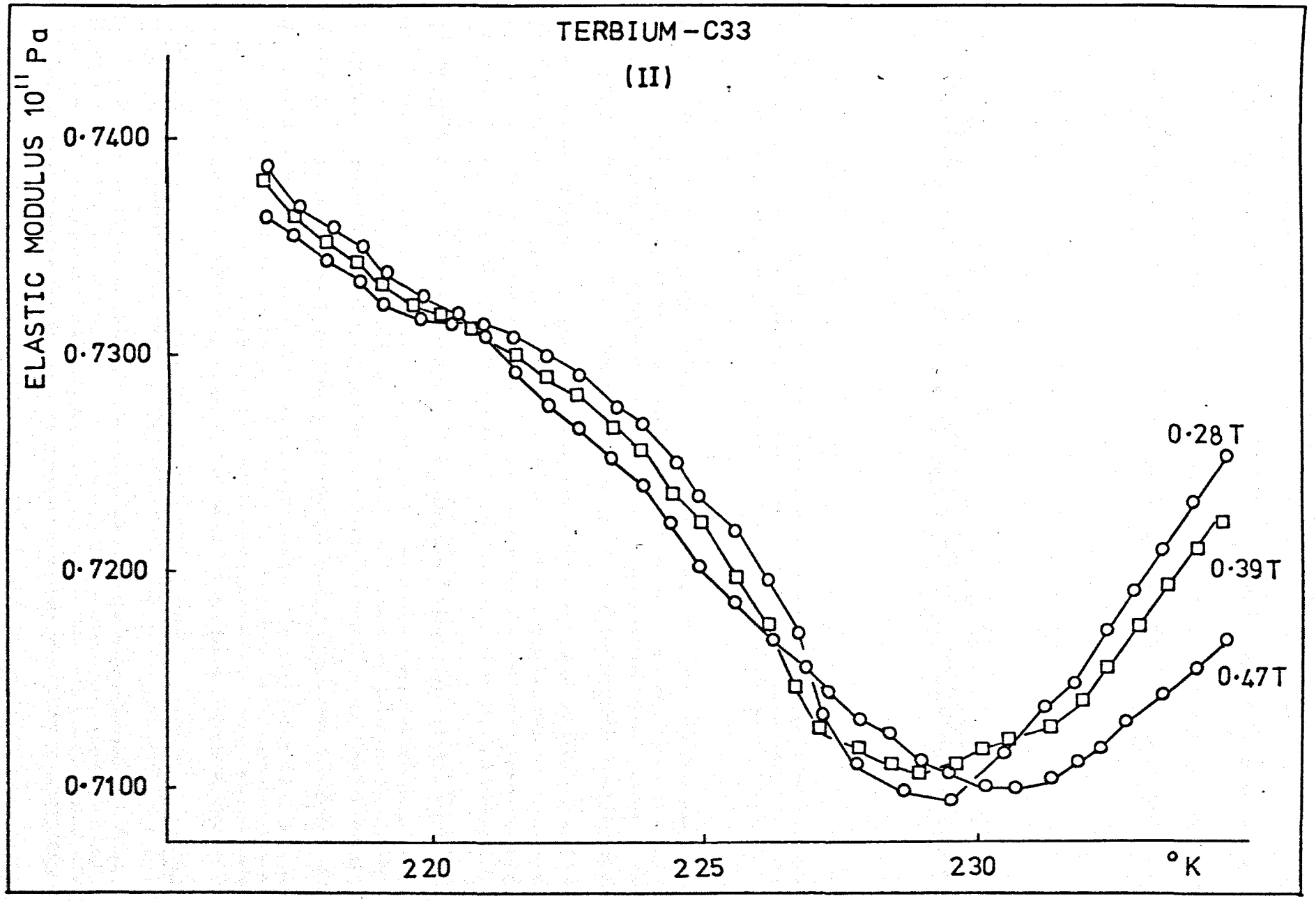
TERBIUM - C33
(II)
ELASTIC MODULUS 10^{11} Pa
0·7400
0·7300
0·7200
0·7100
220
225
230
°K
0·28 T
0·39 T
0·47 T

Fig. 9.43

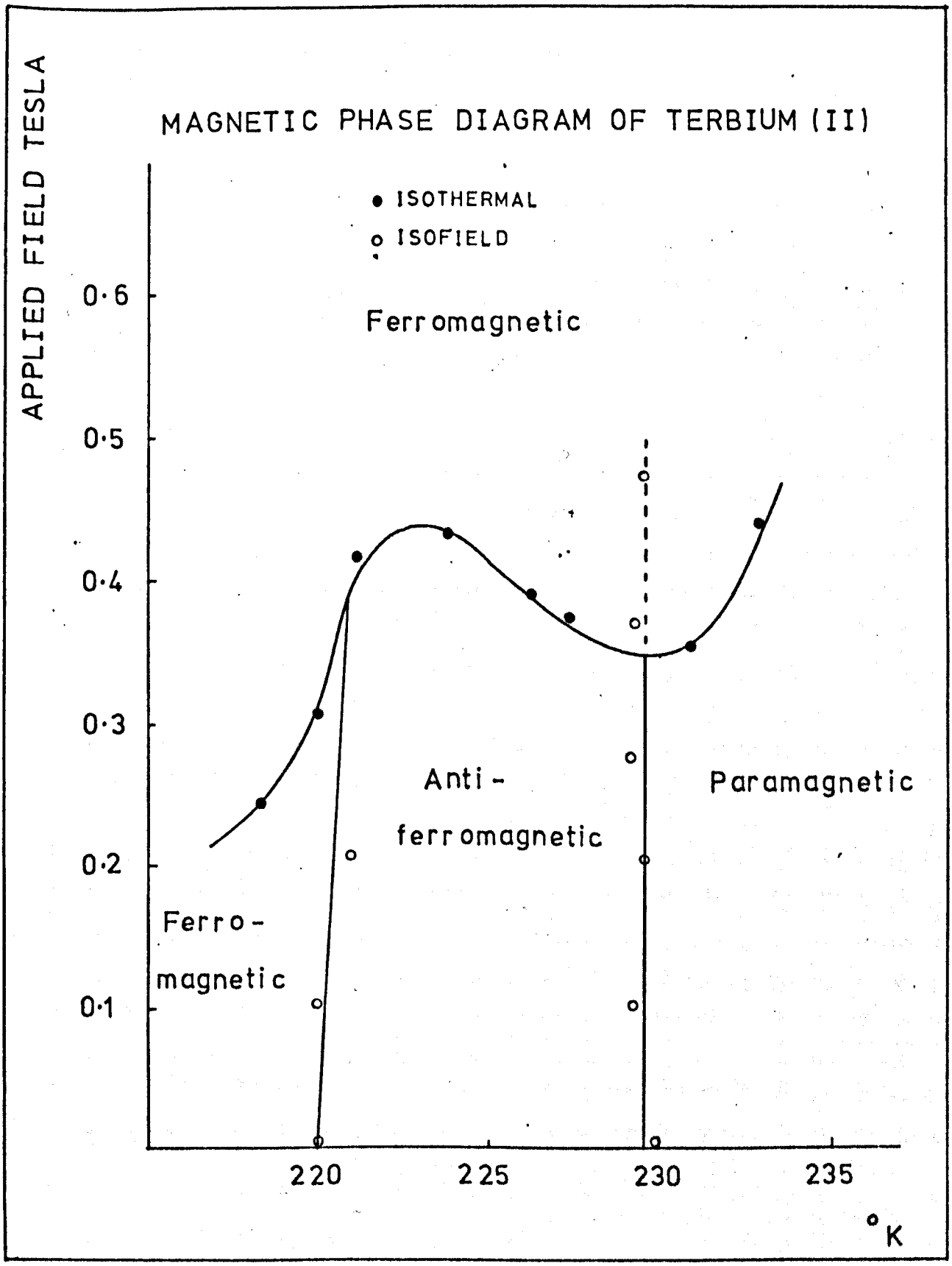
MAGNETIC PHASE DIAGRAM OF TERBIUM (II)
APPLIED FIELD TESLA
ISOTHERMAL
ISOFIELD
Ferromagnetic
Anti-
ferromagnetic
Paramagnetic
Ferro-
magnetic
0·6
0·5
0·4
0·3
0·2
0·1
220
225
230
235
°K

fig. 9.44

Application of a weak field along the b axis in ferromagnetic Terbium is likely to cause a growth of domains with moments oriented favourably, that is along the b axis lying parallel to the field, and a decline of those domains with components against the field. This will result in small wall movements. At higher fields there will be a 'sweeping out' of domains aligned unfavourably either by bulk rotation of magnetic moments or by irreversible domain wall movement. The result is that a single domain crystal is formed at high fields. It is thoughtthat the critical field at which the production of the singledomain is formed corresponds to the minimum of the elastic constant as a function of field. Such effects occur at a field strength of 0.35 - 0.4T in Tb(I) and at a lower field of 0.15 - 0.3T in Tb(II), depending on the temperature of the sample. This may be expected since the less pure sample would be likely to contain more pinning sites for domain walls, resulting in a higher critical field.

In the antiferromagnetic phase the application of a base plane field to the helical magnetic structure should cause distortion of the helix at low fields. According to Nagamiya and Kitano [35,36] at higher fields the moments aligned with components antiparallel to the field rotate and form a fan state at a critical field. However, Crangle [37] has found no evidence of a fan state in either Dysprosium or Terbium and suggests that the critical field corresponds to the point at which there is a rapid growth of regions with moments aligned parallel to the field, for example favourably aligned domain walls between helical domains in the antiferromagnetic phase. It is thought that the critical field corresponds to the location of the minimum in the elastic constant and that at higher fields one of the two possible structures discussed above exists. The recovery of the modulus at higher fields corresponds then to the saturation of the magnetisation caused by either the closing

of the fan angle or the complete destruction of the distorted helix in favour of a ferromagnetic alignment. Until the matter of the existence of a fan state is resolved it is not possible to make a definitive statement concerning the nature of the magnetic structure at higher fields. Publication of neutron diffraction data by Crangle [38] is anticipated and would give further insight into this problem.

Application of a base plane magnetic field to the paramagnetic phase of Terbium causes a rotation of the initially randomly oriented moments into the field direction. There appears to be a minimum in the elastic modulus at a certain field strength which increases with temperature. Above this field the sample has appreciable short range order, Maekawa [41] has in fact classified it as ferromagnetic, although it is strictly paramagnetic. The transition from ferromagnetic to paramagnetic at high fields shows no evidence of an anomaly.

9.3.8 Demagnetising Field Corrections

The demagnetising factors for Terbium were found in a similar way to that indicated for Gadolinium. The factors were found to be N = 5.15 for Tb(I) which was a cuboid of dimensions 3mm x 3mm x 5.5 mm and N = 4.02 for Tb(II) which was a cylinder of height 4.5mm and diameter 5mm. From the magnetisation data of Hegland et al [12] and particularly the low field magnetisation data of Feron [9] the variation of applied magnetic field with temperature for various internal magnetic fields was found for samples with the given demagnetising factors. The dependence of applied field upon internal field for various temperatures, as shown in figs. 9.45 and 9.47, were then plotted for the two samples. Conversions from applied to internal magnetic fields were made and the phase diagrams as a function of temperature and internal field were plotted as shown in figs. 9.46 and 9.48.

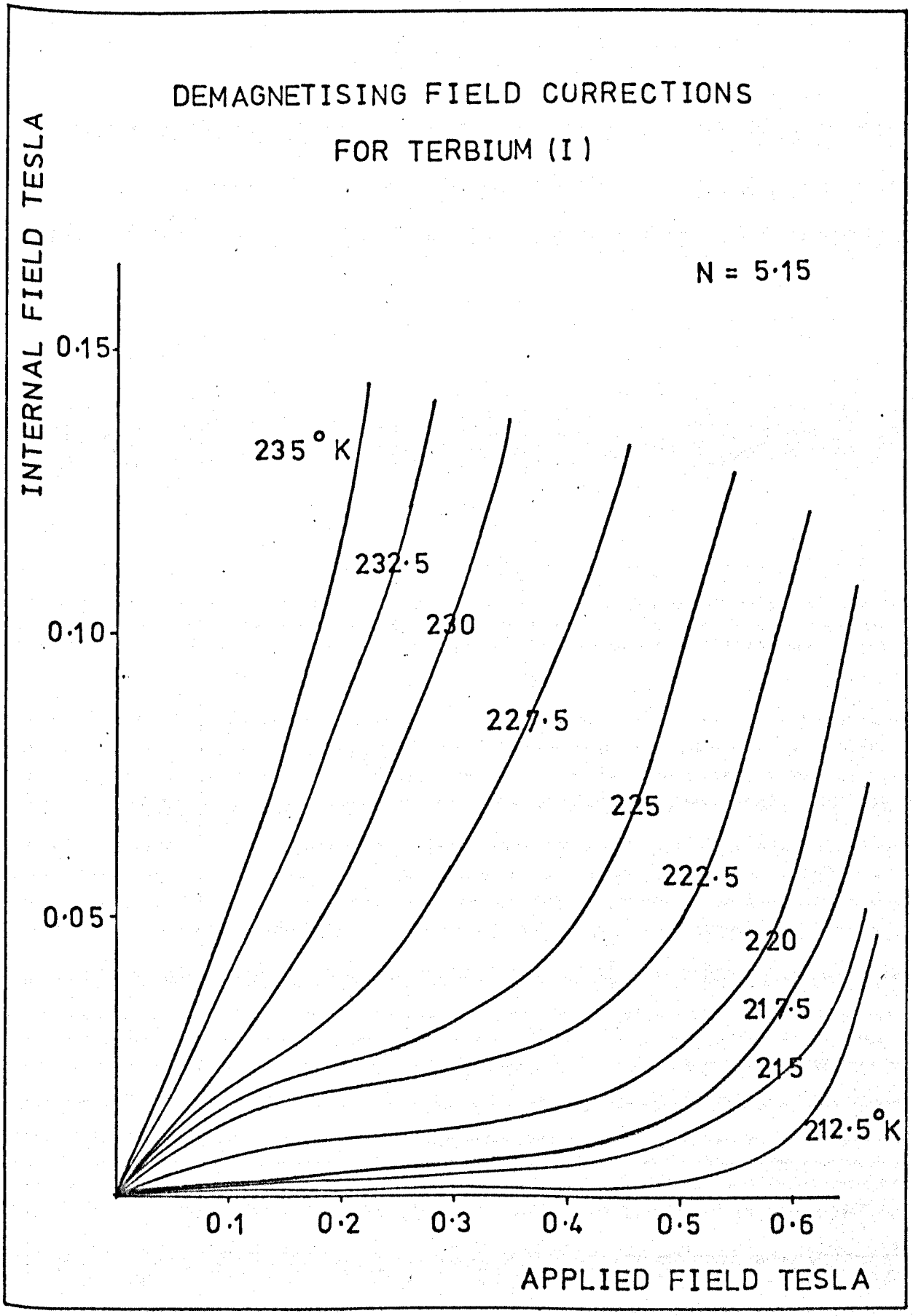
DEMAGNETISING FIELD CORRECTIONS
FOR TERBIUM (I)
N = 5·15
INTERNAL FIELD TESLA
0·15
0·10
0·05
235° K
232·5
230
227·5
225
222·5
220
217·5
215
212·5°K
0·1
0·2
0·3
0·4
0·5
0·6
APPLIED FIELD TESLA

fig. 9.45

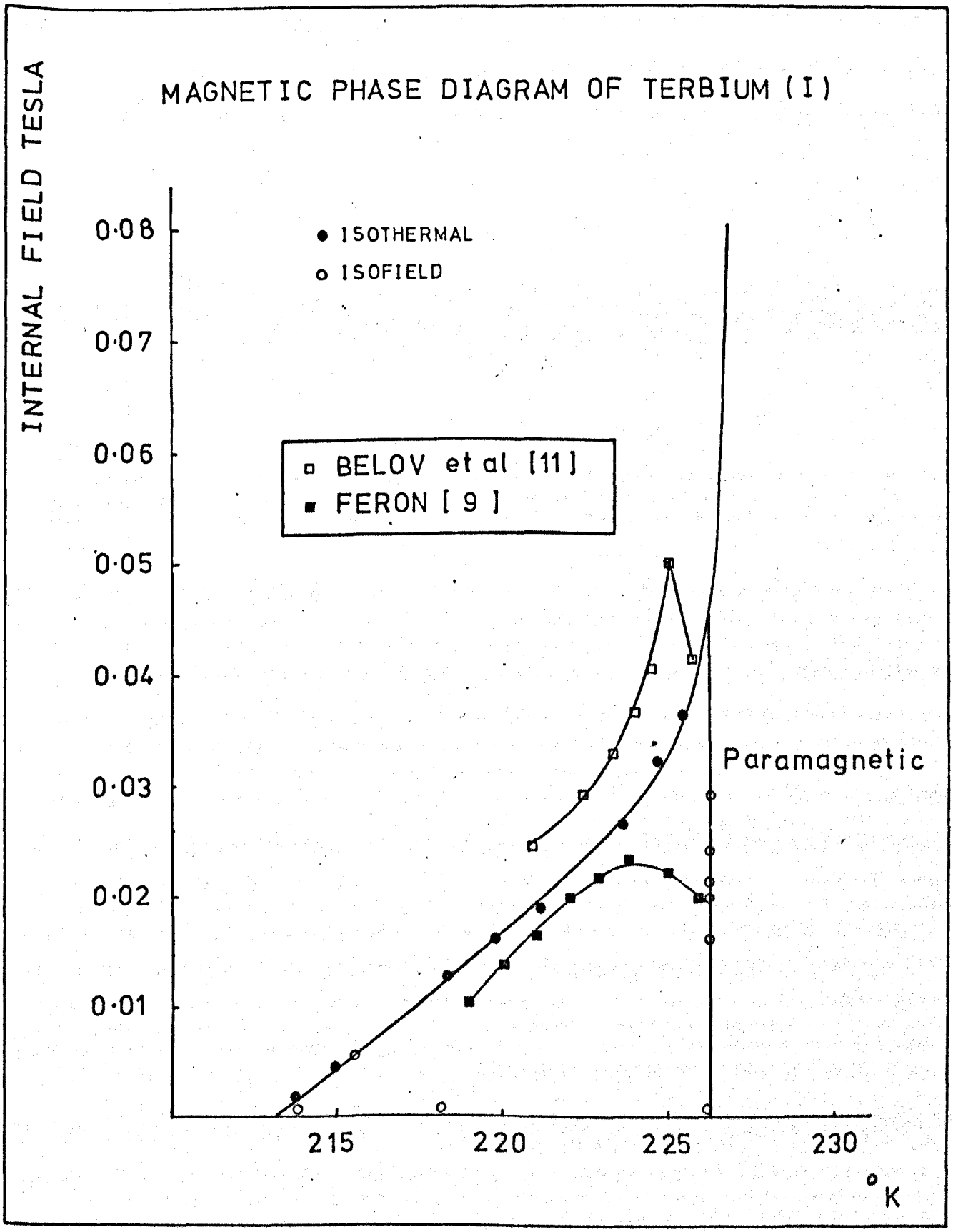
MAGNETIC PHASE DIAGRAM OF TERBIUM (I)
INTERNAL FIELD TESLA
0·08
0·07
0·06
0·05
0·04
0·03
0·02
0·01
● ISOTHERMAL
○ ISOFIELD
□ BELOV et al [11]
■ FERON [9]
Paramagnetic
215
220
225
230
°K

fig. 9.46

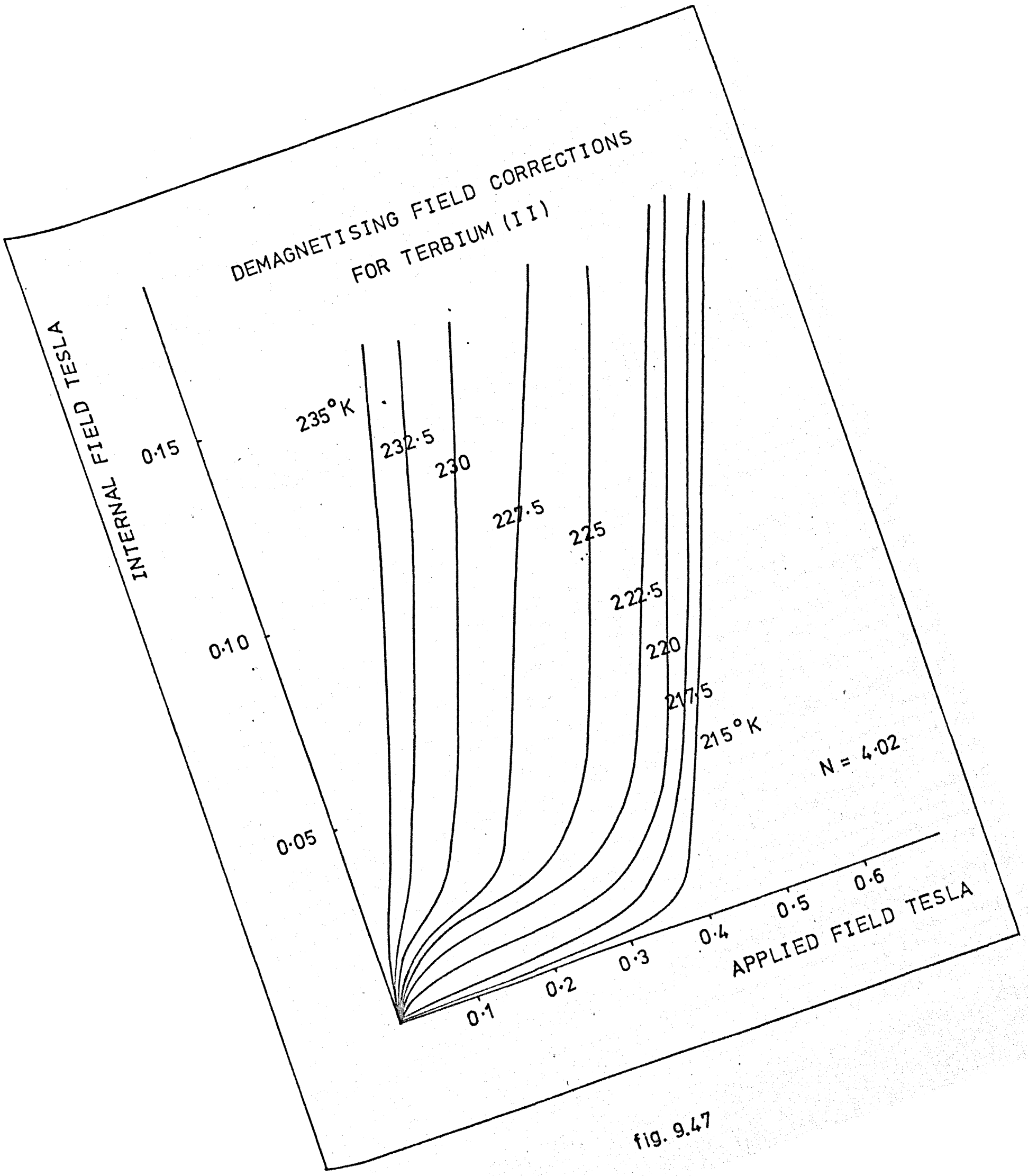
DEMAGNETISING FIELD CORRECTIONS
FOR TERBIUM (II)
INTERNAL FIELD TESLA
0·15
0·10
0·05
235°K
232·5
230
227·5
225
222·5
220
217·5
215°K
N = 4·02
0·1
0·2
0·3
0·4
0·5
0·6
APPLIED FIELD TESLA

fig. 9.47

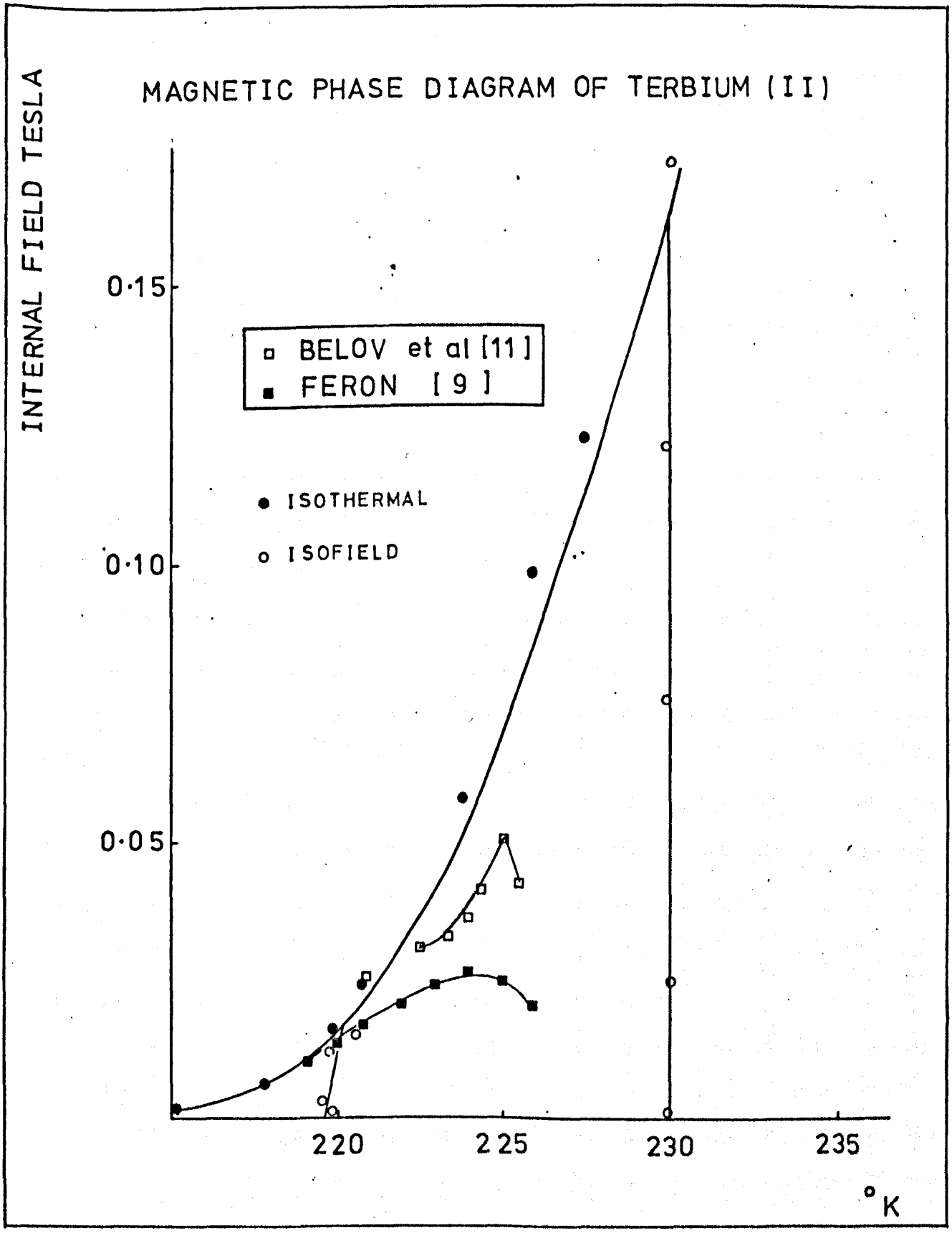
MAGNETIC PHASE DIAGRAM OF TERBIUM (II)
INTERNAL FIELD TESLA
0·15
0·10
0·05
BELOV et al [11]
FERON [9]
ISOTHERMAL
ISOFIELD
220
225
230
235
°K

fig. 9.48

Both phase diagrams show that the critical internal field in antiferromagnetic Terbium is typically $\sim 10^{-2}$T which is much smaller than the critical fields reported for Dysprosium [17,30,31,32]. However the results are broadly in agreement with the critical fields of Terbium reported by Feron [39] from magnetisation measurements and by Belov [11] from magnetostriction measurements. The present results, however, show the critical field decreasing to zero within experimental error, close to the Curie point. The features of the critical field curve are otherwise qualitatively similar to Dysprosium.

9.4 Erbium

Erbium orders antiferromagnetically with a c axis modulated structure below its Néel point of 85°K. A further transition occurs at about 53°K below which ordering in the base plane occurs. The Curie point is at 20°K below which the c axis components order ferromagnetically. These structures are discussed in more detail in chapter six.

The moduli C_{33} and C_{11} have been studied as a function of applied field here. Because of the arrangement of the apparatus it was only possible to measure acoustic velocities in directions at right angles to the field. Therefore when the direction of applied field was changed from the b axis to the c axis the modulus was changed from C_{33} to C_{11}. Behaviour of the moduli as a function of temperature in zero field has been given in chapter eight. The samples used were the same ones as in Palmer et al [4] and are expected to be about 98% pure at the very worst. Results on the temperature dependence of the moduli in constant applied fields up to 4T have already been published by du Plessis [2].

9.4.1 Field Dependence of C_{33} below 20°K

The variation of C_{33} with a magnetic field applied along the b axis for several temperatures below 20°K is shown in fig. 9.49. The behaviour

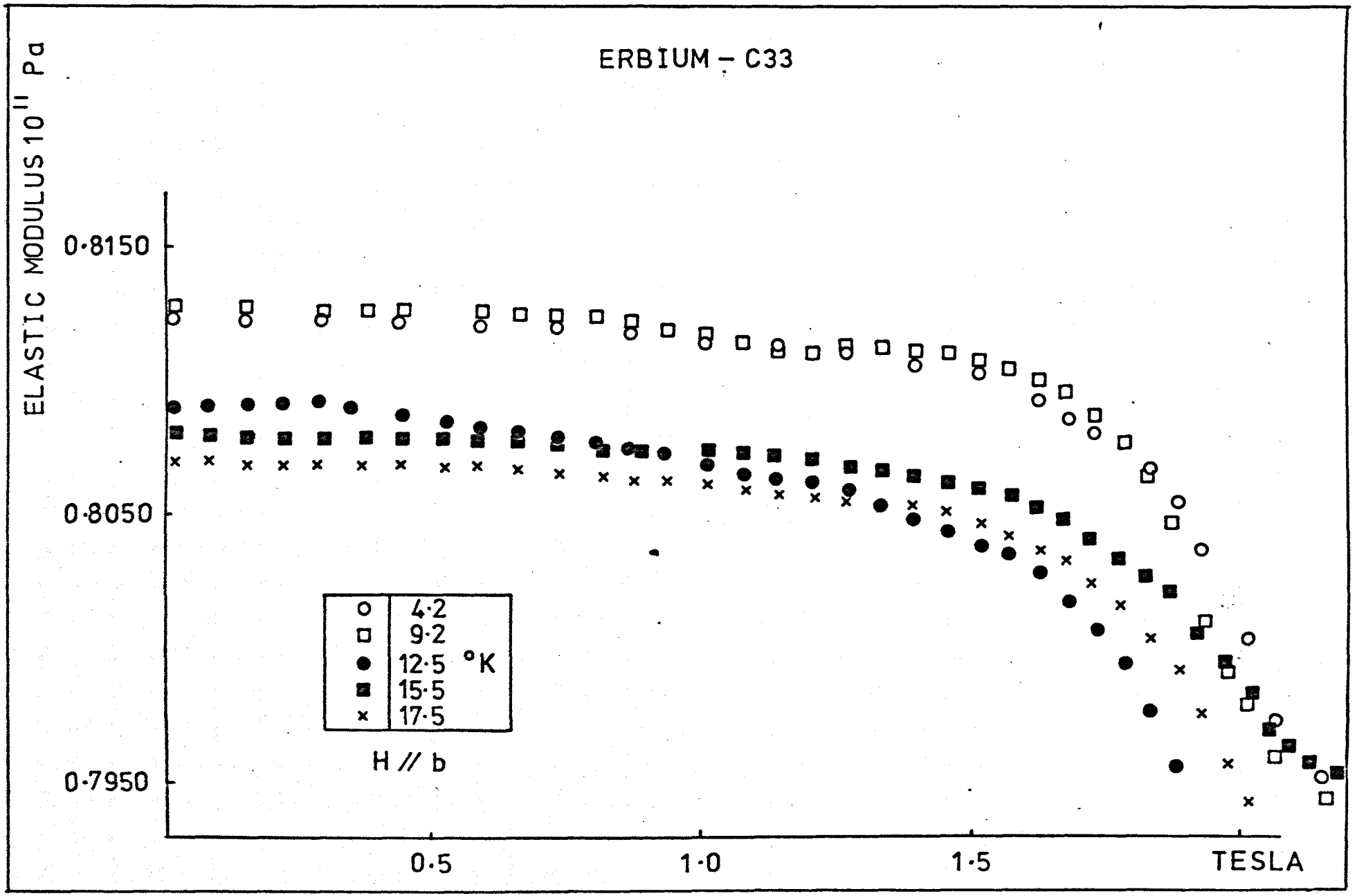
ERBIUM – C33
ELASTIC MODULUS 10^{11} Pa
0·8150
0·8050
0·7950
0·5
1·0
1·5
TESLA
4·2
9·2
12·5 °K
15·5
17·5
H // b

fig. 9.7.6.1

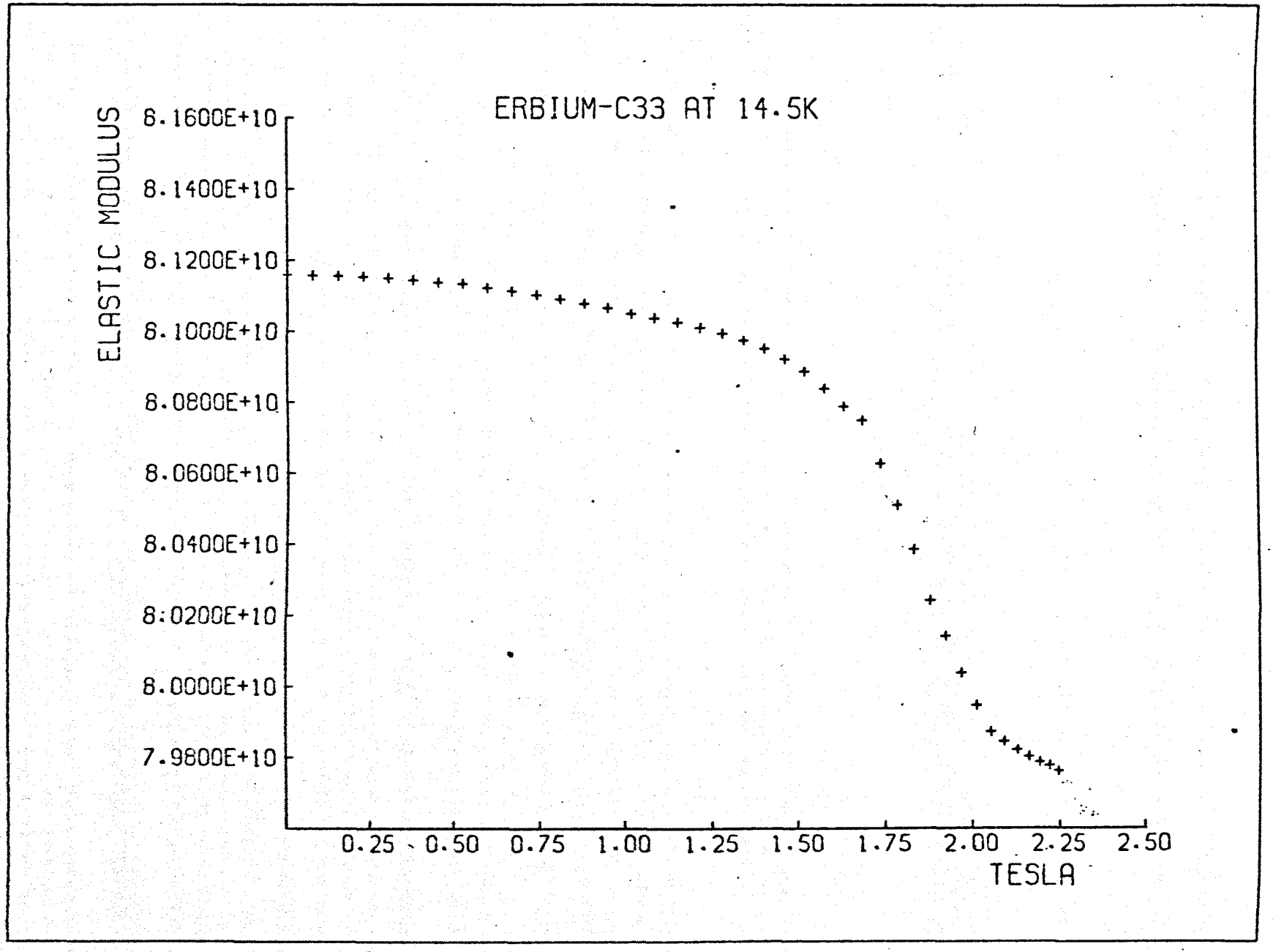
ERBIUM-C33 AT 14.5K
ELASTIC MODULUS
8.1600E+10
8.1400E+10
8.1200E+10
8.1000E+10
8.0800E+10
8.0600E+10
8.0400E+10
8.0200E+10
8.0000E+10
7.9800E+10
0.25
0.50
0.75
1.00
1.25
1.50
1.75
2.00
2.25
2.50
TESLA

fig. 9.50

at all of these temperatures is very similar. For fields of up to about 1.5T the modulus is almost field independent. It then undergoes a fairly rapid decrease resulting in a 2% reduction in the value of the elastic constant. The modulus then levels off at its lower value. A more detailed example is given in fig. 9.50. The critical field was taken as the middle of the rapidly changing part of the curve giving a value of H_c = 1.85T. This critical field appears to be almost temperature independent.

9.4.2 Field Dependence of C_{11} in the Range 20 - 100°K

Above 20°K the variation of C_{11} with a c axis field has been studied. At 20°K the behaviour is similar to that shown by C_{33} below 20°K. The modulus is almost field independent at low fields and then decreases at fields greater than 1.5T. At higher temperatures, fig. 9.51, the high field behaviour shows an increase instead of a decrease in elastic constant. It seems likely therefore that the sample was still ferromagnetic at 20°K and that the Curie point lies somewhere between 20 and 24°K. (See for example the results in chapter eight). Also a shallow minimum occurs at a field of 1.0T for temperatures just above T_c.

As the temperature is increased further, fig. 9.52, the behaviour is more uniform showing an initial field independence at low fields, followed by a rapid rise which appears to reach saturation for fields greater than about 1.5T. This behaviour continues up to 50°K in fig. 9.53, then at 55°K, close to the transition temperature, the zero field value of the elastic modulus increases, becoming almost equal to the high field values of elastic modulus below 55°K. The elastic properties therefore appear to be only weakly field dependent. However, fig. 9.54 shows that the modulus is in fact still increasing with field, although it no longer appears to saturate at high fields.

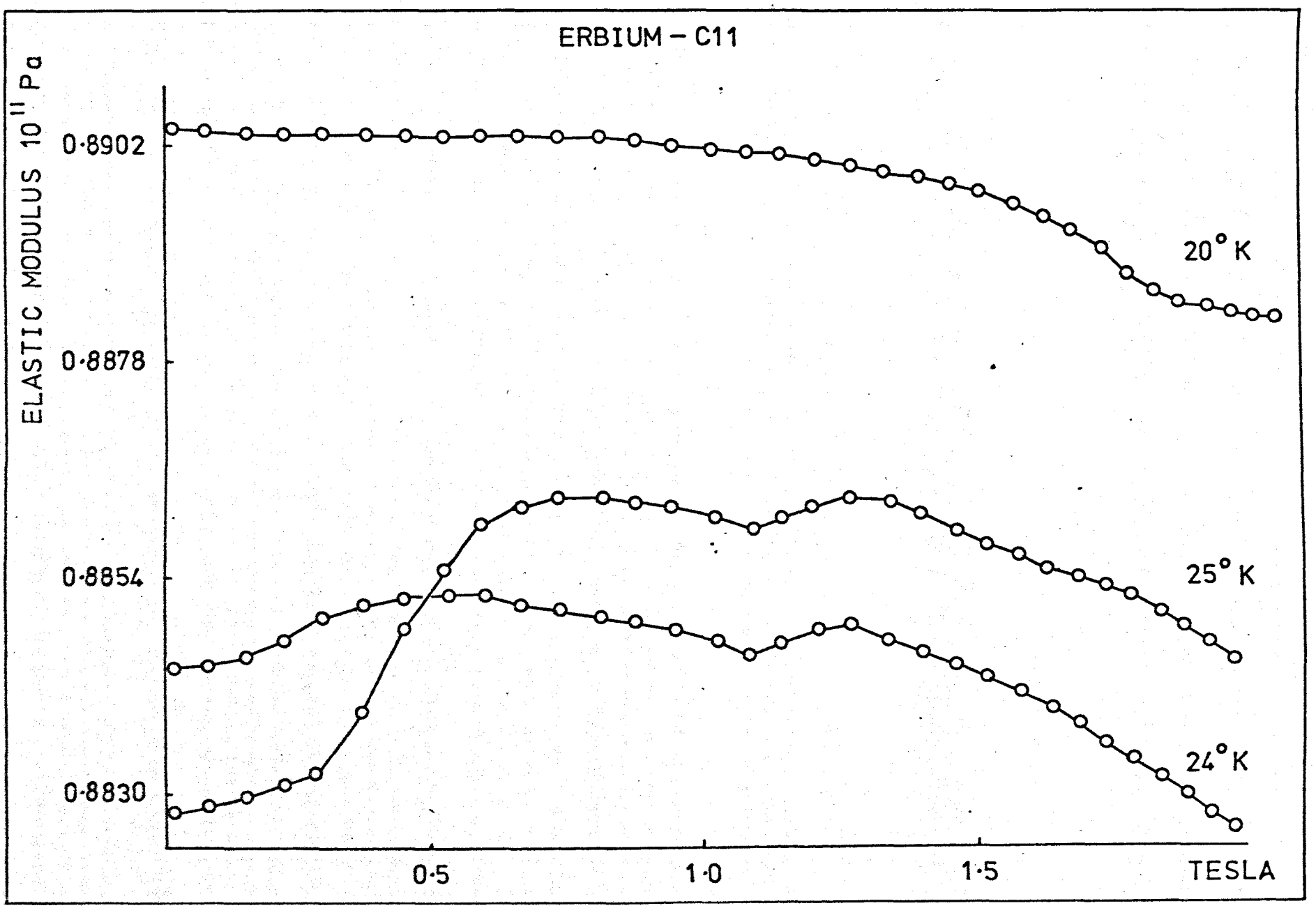
ERBIUM – C11
ELASTIC MODULUS 10^{11} Pa
0·8902
0·8878
0·8854
0·8830
20° K
25° K
24° K
0·5
1·0
1·5
TESLA

fig. 9.51

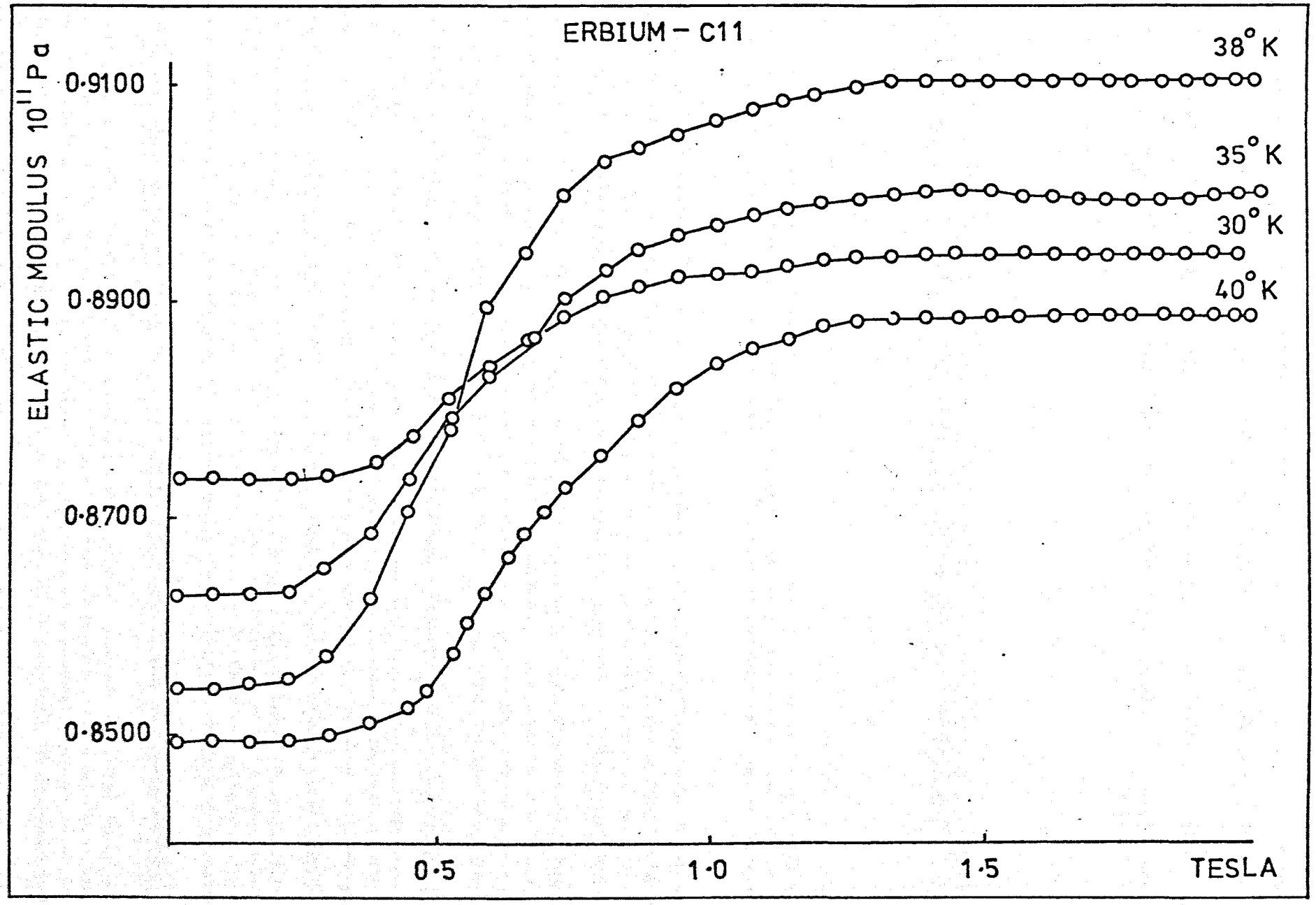
ERBIUM – C11
ELASTIC MODULUS 10^{11} Pa
0·9100
0·8900
0·8700
0·8500
0·5
1·0
1·5
TESLA
38° K
35° K
30° K
40° K

fig. 9.52

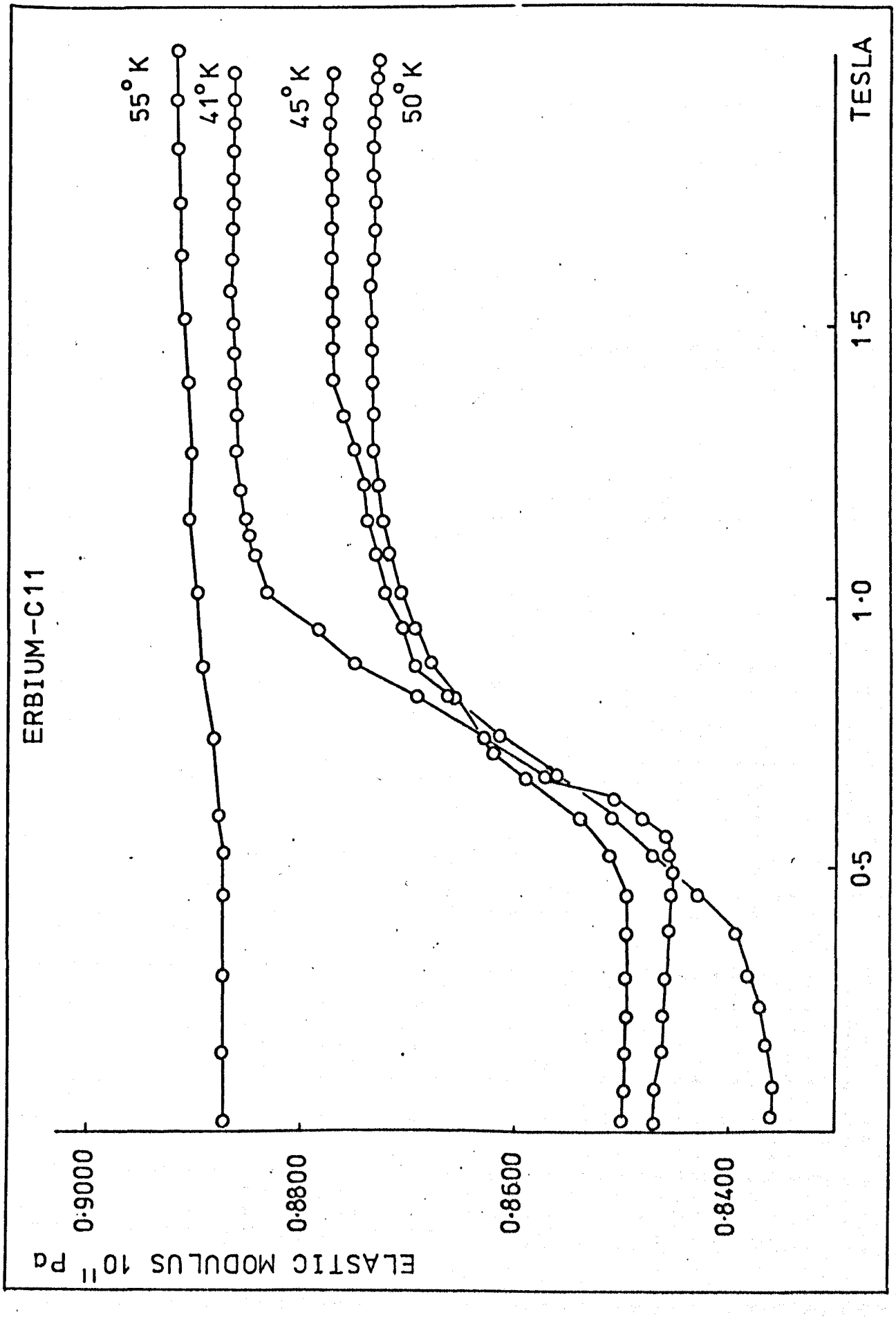
ERBIUM-C11
ELASTIC MODULUS 10^{11} Pa
0·9000
0·8800
0·8600
0·8400
0·5
1·0
1·5
TESLA
55°K
41°K
45°K
50°K

fig. 9.53

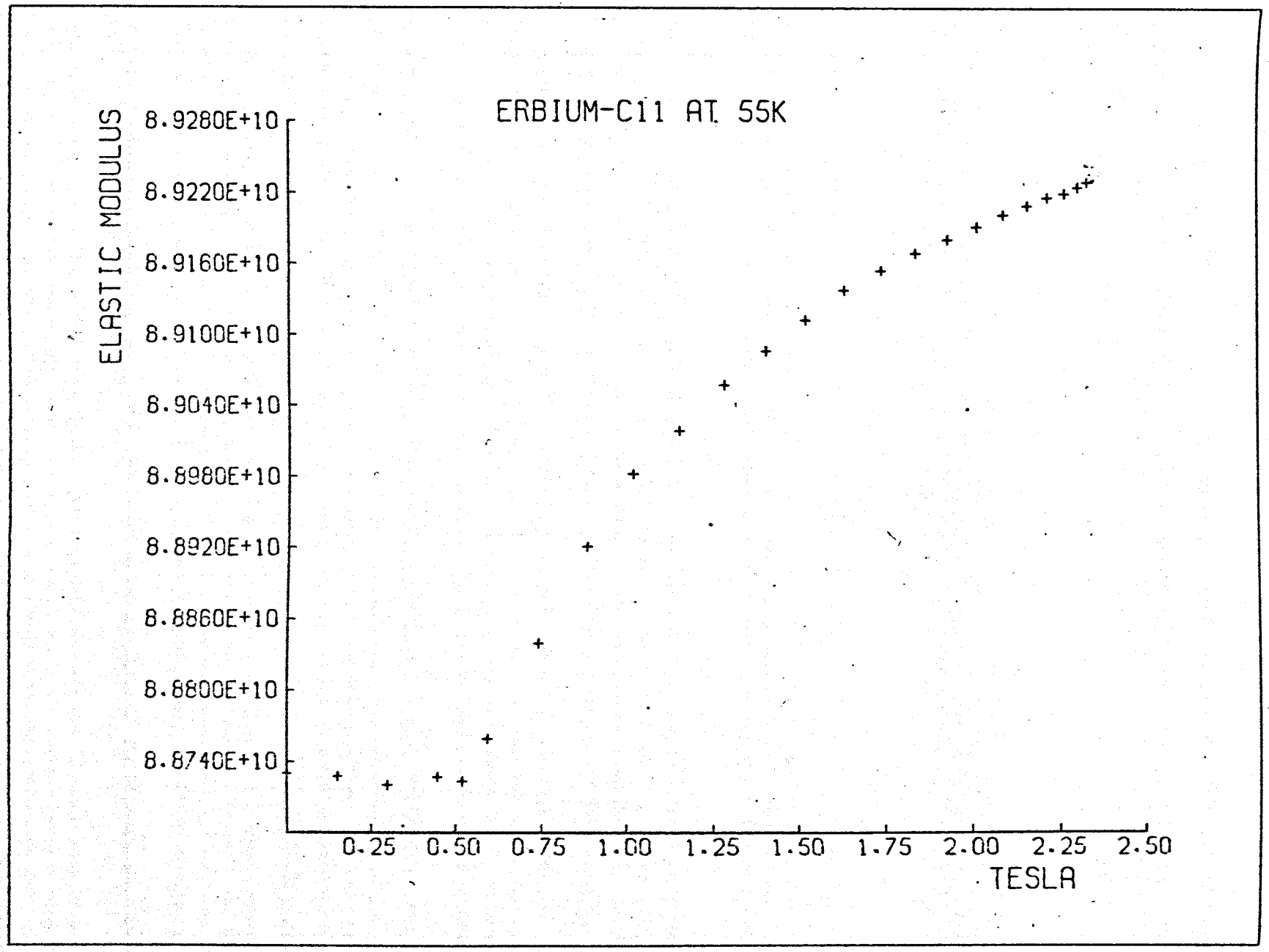
ERBIUM-C11 AT 55K
ELASTIC MODULUS
8.9280E+10
8.9220E+10
8.9160E+10
8.9100E+10
8.9040E+10
8.8980E+10
8.8920E+10
8.8860E+10
8.8800E+10
8.8740E+10
0.25
0.50
0.75
1.00
1.25
1.50
1.75
2.00
2.25
2.50
TESLA

fig. 9.54

ELASTIC MODULUS 10^{11} Pa
0·8869
0·8860
0·8851
0·8842
0·5
1·0
1·5
TESLA
57° K
59° K
61° K
65° K
ERBIUM – C 11

fig. 9.55

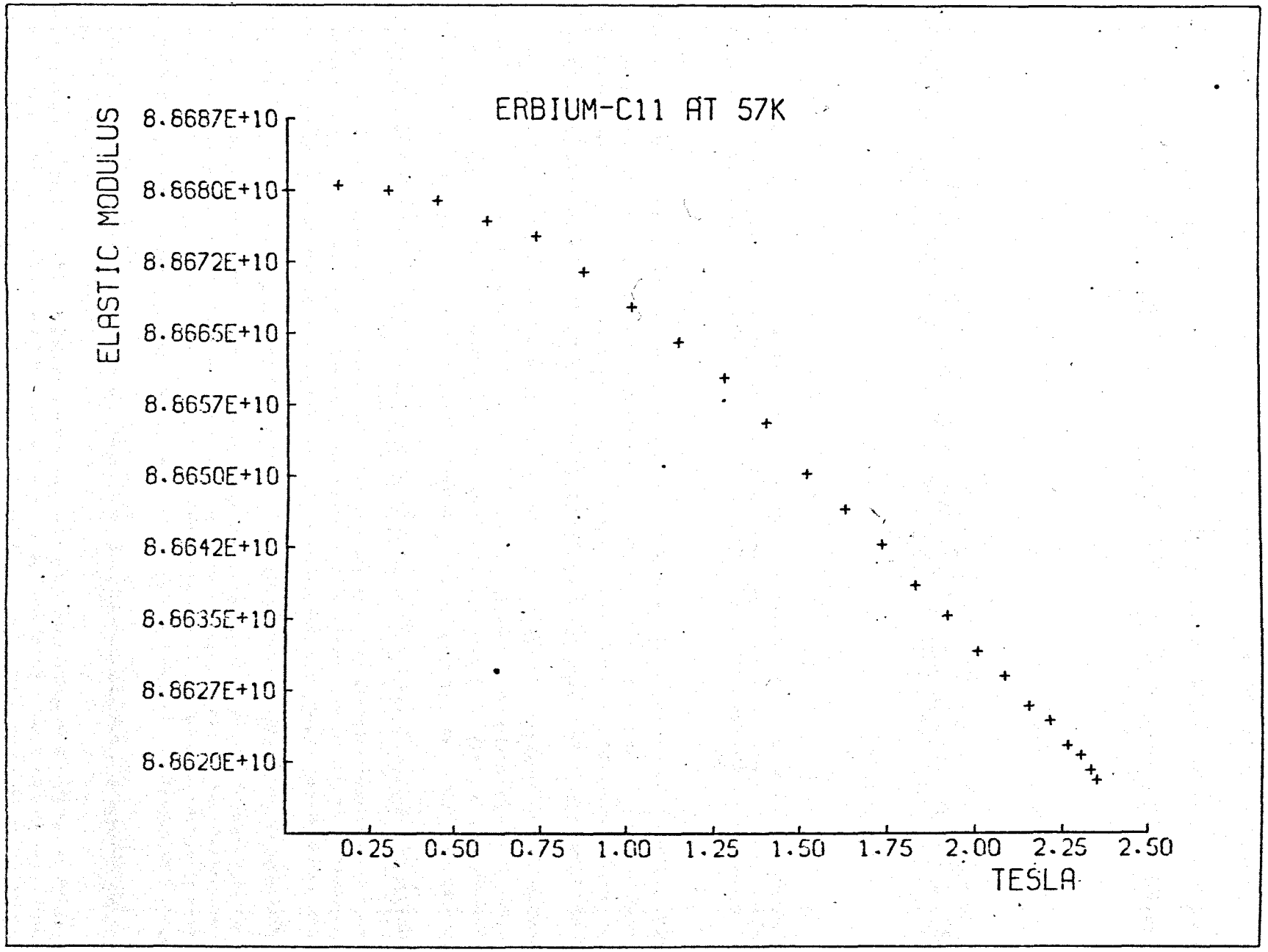
ERBIUM-C11 AT 57K
ELASTIC MODULUS
8.8687E+10
8.8680E+10
8.8672E+10
8.8665E+10
8.8657E+10
8.8650E+10
8.8642E+10
8.8635E+10
8.8627E+10
8.8620E+10
0.25
0.50
0.75
1.00
1.25
1.50
1.75
2.00
2.25
2.50
TESLA

fig. 9.56

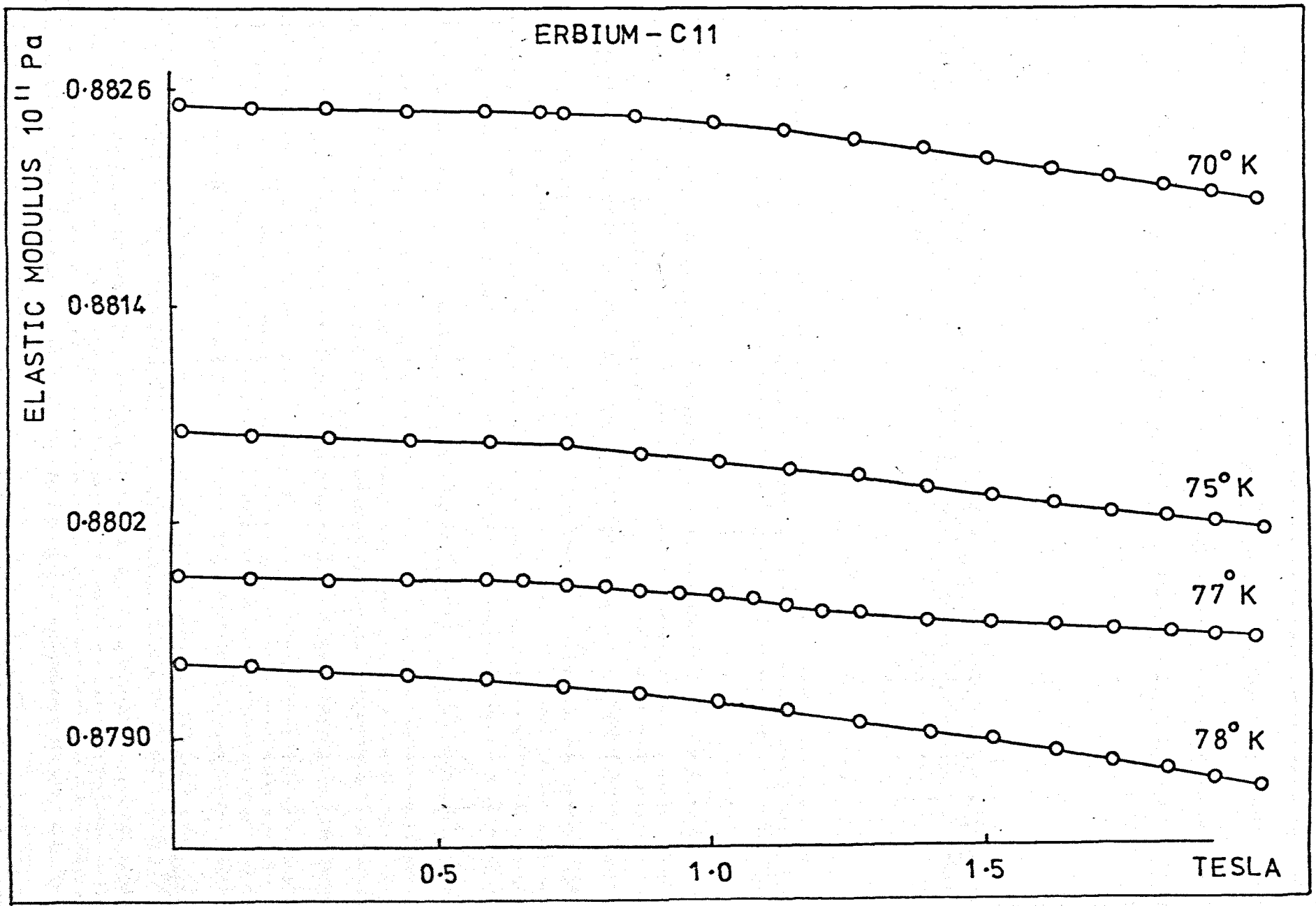
ERBIUM – C11
ELASTIC MODULUS 10^{11} Pa
0·8826
0·8814
0·8802
0·8790
70° K
75° K
77° K
78° K
0·5
1·0
1·5
TESLA

Fig. 9.57

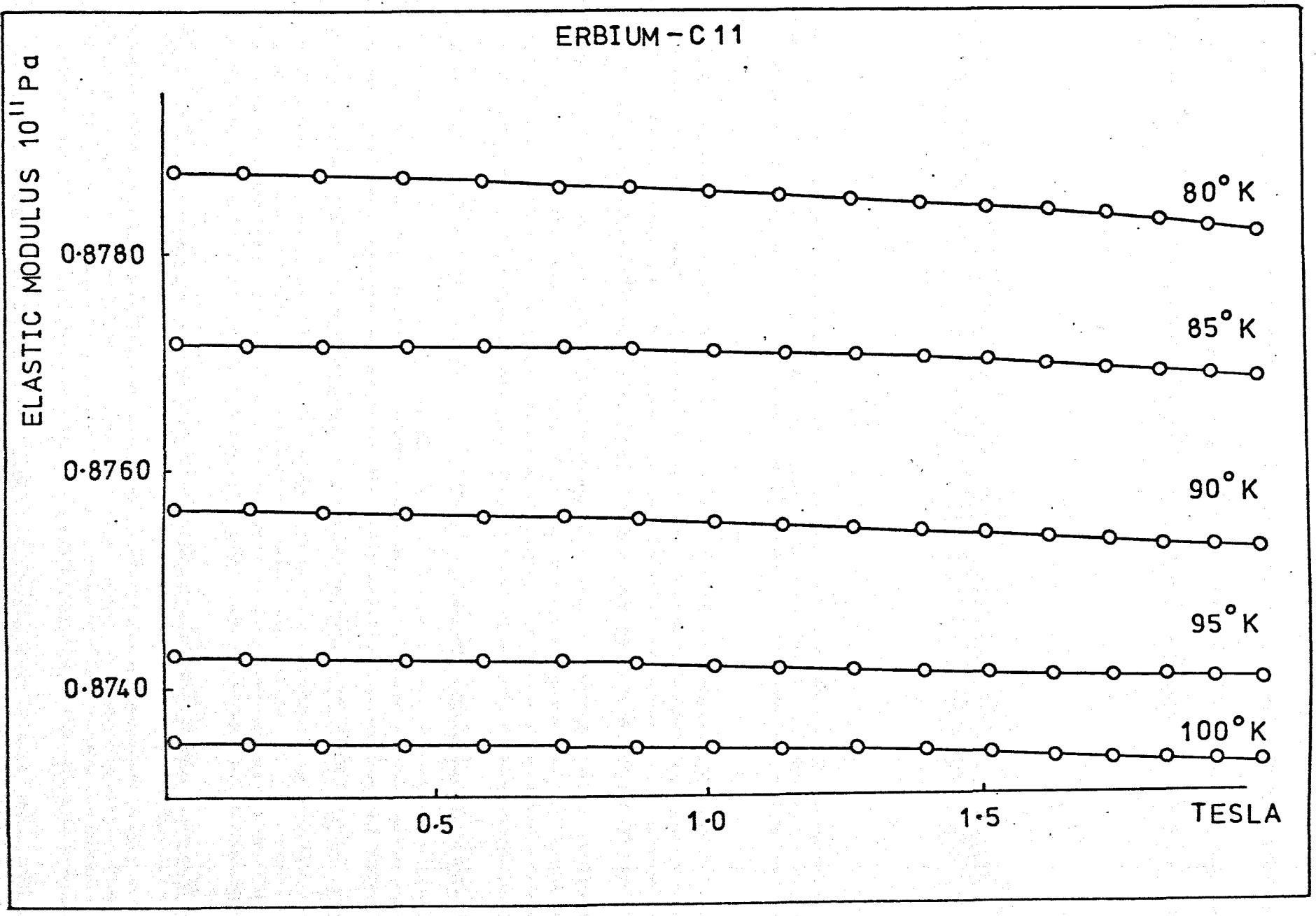
ERBIUM - C 11
ELASTIC MODULUS 10^{11} Pa
0·8780
0·8760
0·8740
80° K
85° K
90° K
95° K
100° K
0·5
1·0
1·5
TESLA

fig. 9.58

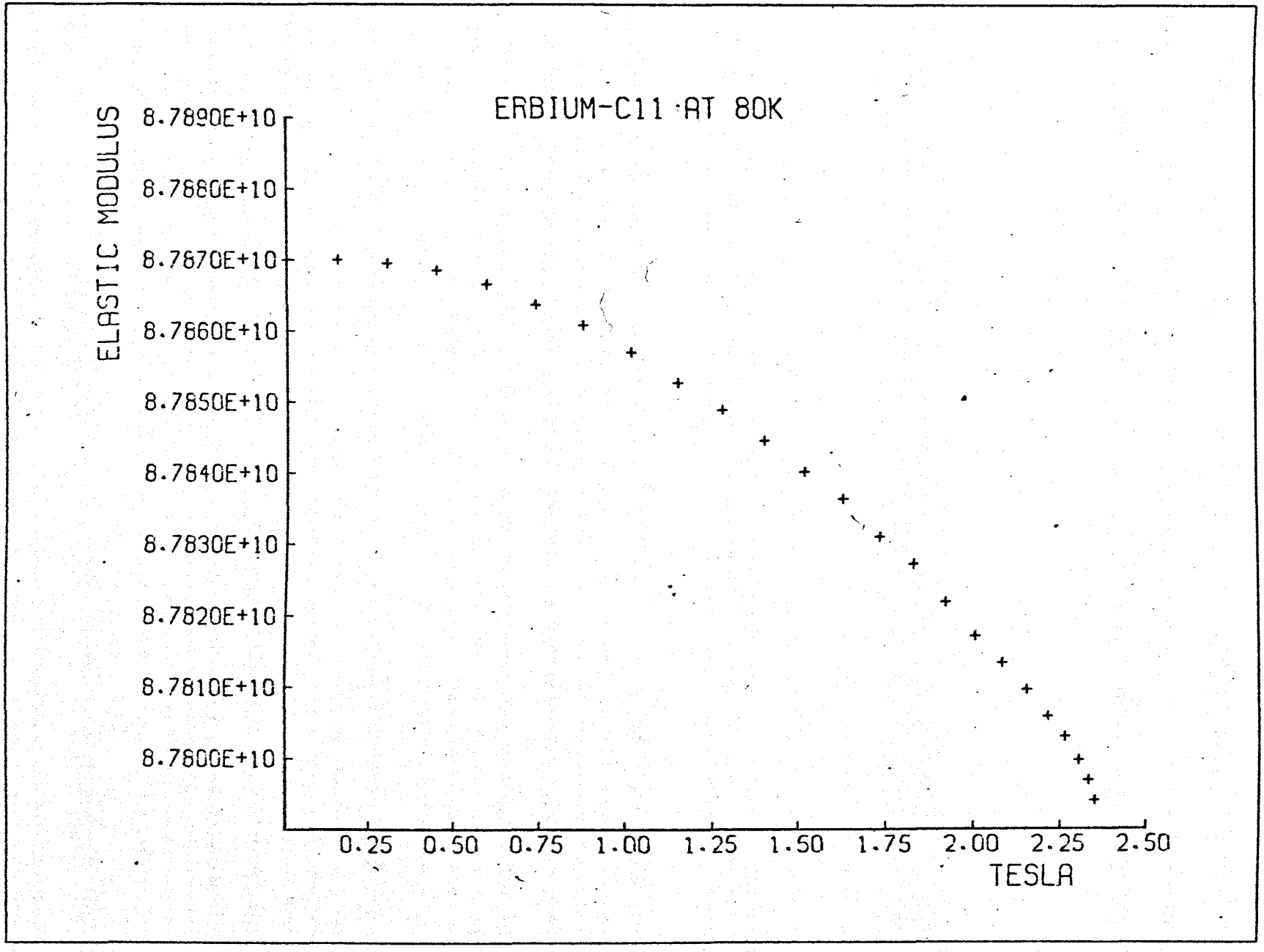
ERBIUM-C11 AT 80K
ELASTIC MODULUS
8.7890E+10
8.7880E+10
8.7870E+10
8.7860E+10
8.7850E+10
8.7840E+10
8.7830E+10
8.7820E+10
8.7810E+10
8.7800E+10
0.25
0.50
0.75
1.00
1.25
1.50
1.75
2.00
2.25
2.50
TESLA

fig. 9.59

Above the transition temperature the modulus is much less field dependent and in fact decreases slightly with field as shown in fig. 9.56. Further increase in the temperature shows similar behaviour. Fig. 9.59 shows that although the decrease with field is slight it is still clearly detectable at 80°K.

9.4.3 Interpretation of Results

The behaviour of C_{33} below the Curie point shows a rapid decrease at a field strength of 1.85T. This is considered to be the critical field at which either the helical structure collapses into a fan state, or at which a rapid growth of favourably oriented domain walls occurs, causing a destruction of the base plane helix in either case. Demagnetising field calculations using the magnetisation data of Feron et al [15] indicate that this applied field corresponds to an internal field of 1.72T at 20°K. This result is in agreement with the published results of the critical b axis field of Erbium below 20°K by Feron [39] and Flippen [16] both of whom indicate that the critical field is temperature independent in this region.

The critical field above 20°K has been taken as that corresponding to the rapidly rising portion of the curve. Demagnetising field corrections have been made, fig. 9.61, and the critical internal magnetic field plotted as a function of temperature in fig. 9.62 where the results are compared to the findings of other workers using magnetisation measurements.

The two samples were approximately cuboids with dimensions 4.5 mm x 5.0 mm x 2.2 mm for the measurements of C_{33}, and 5.5 mm x 3.5 mm x 2.2 mm for the measurements of C_{11}.

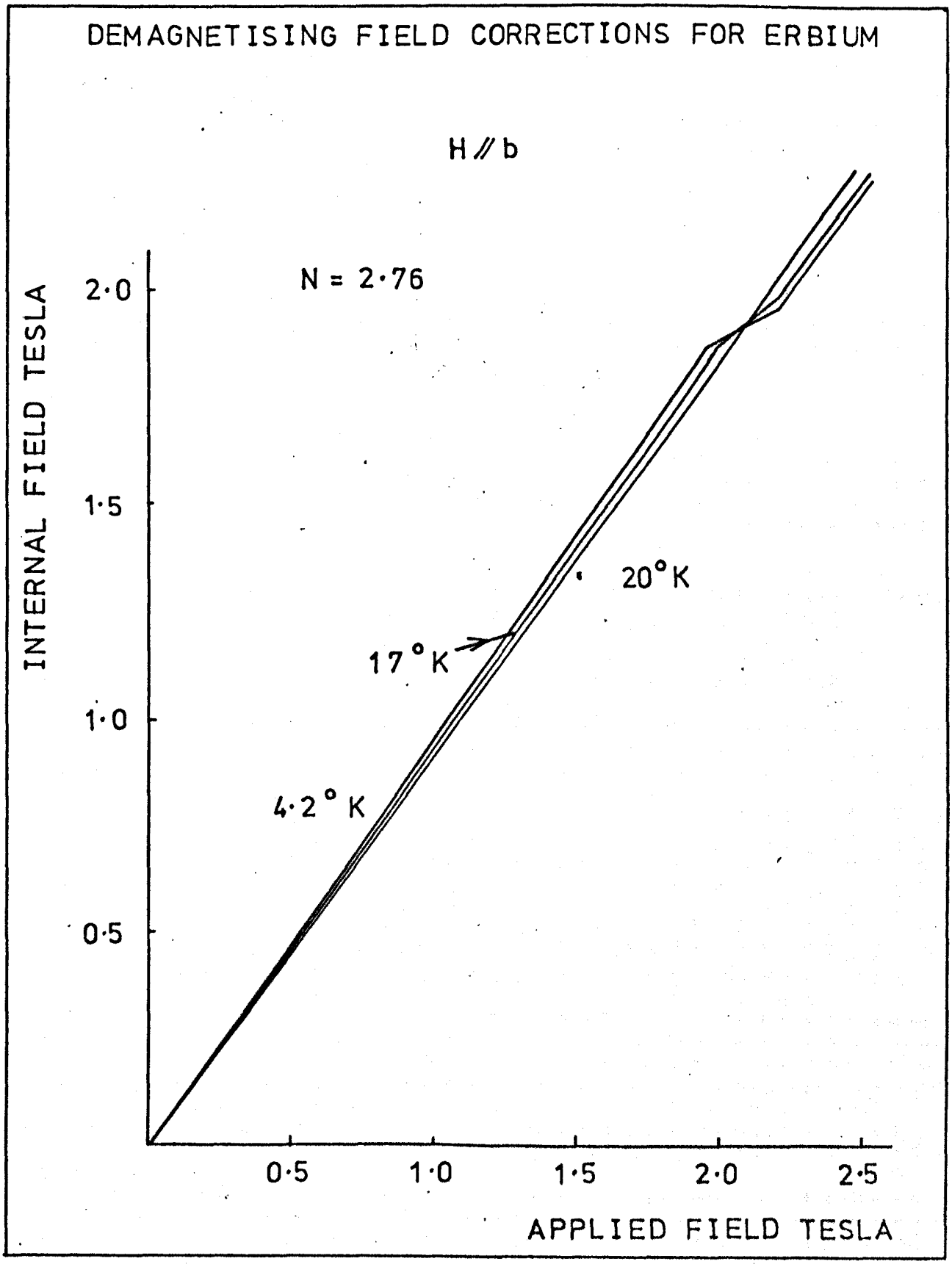
DEMAGNETISING FIELD CORRECTIONS FOR ERBIUM
H // b
N = 2·76
INTERNAL FIELD TESLA
2·0
1·5
1·0
0·5
20°K
17°K
4·2°K
0·5
1·0
1·5
2·0
2·5
APPLIED FIELD TESLA

fig. 9.60

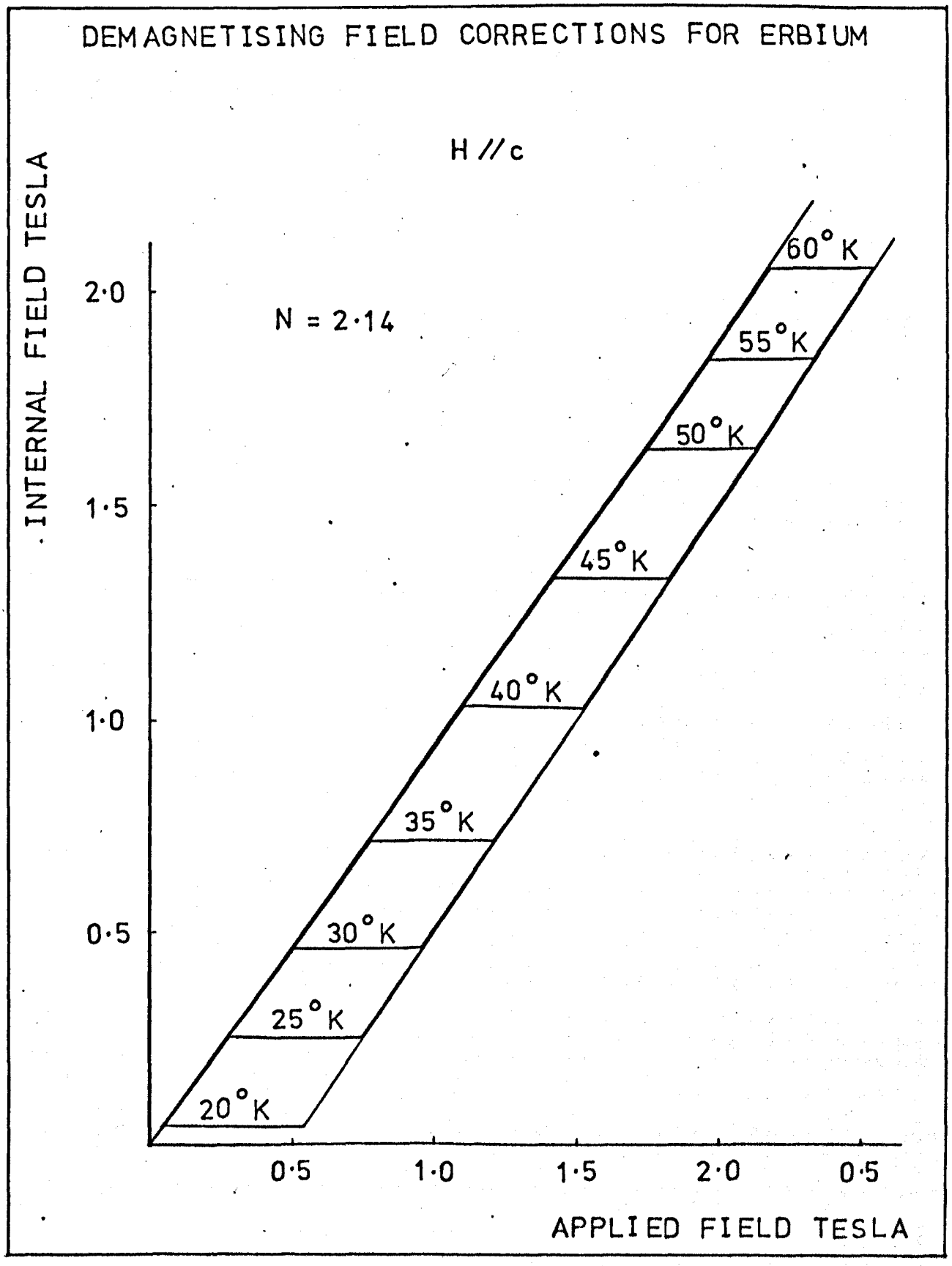
DEMAGNETISING FIELD CORRECTIONS FOR ERBIUM
H // c
INTERNAL FIELD TESLA
N = 2·14
60° K
55° K
50° K
45° K
40° K
35° K
30° K
25° K
20° K
2·0
1·5
1·0
0·5
0·5
1·0
1·5
2·0
0·5
APPLIED FIELD TESLA

fig. 9.61

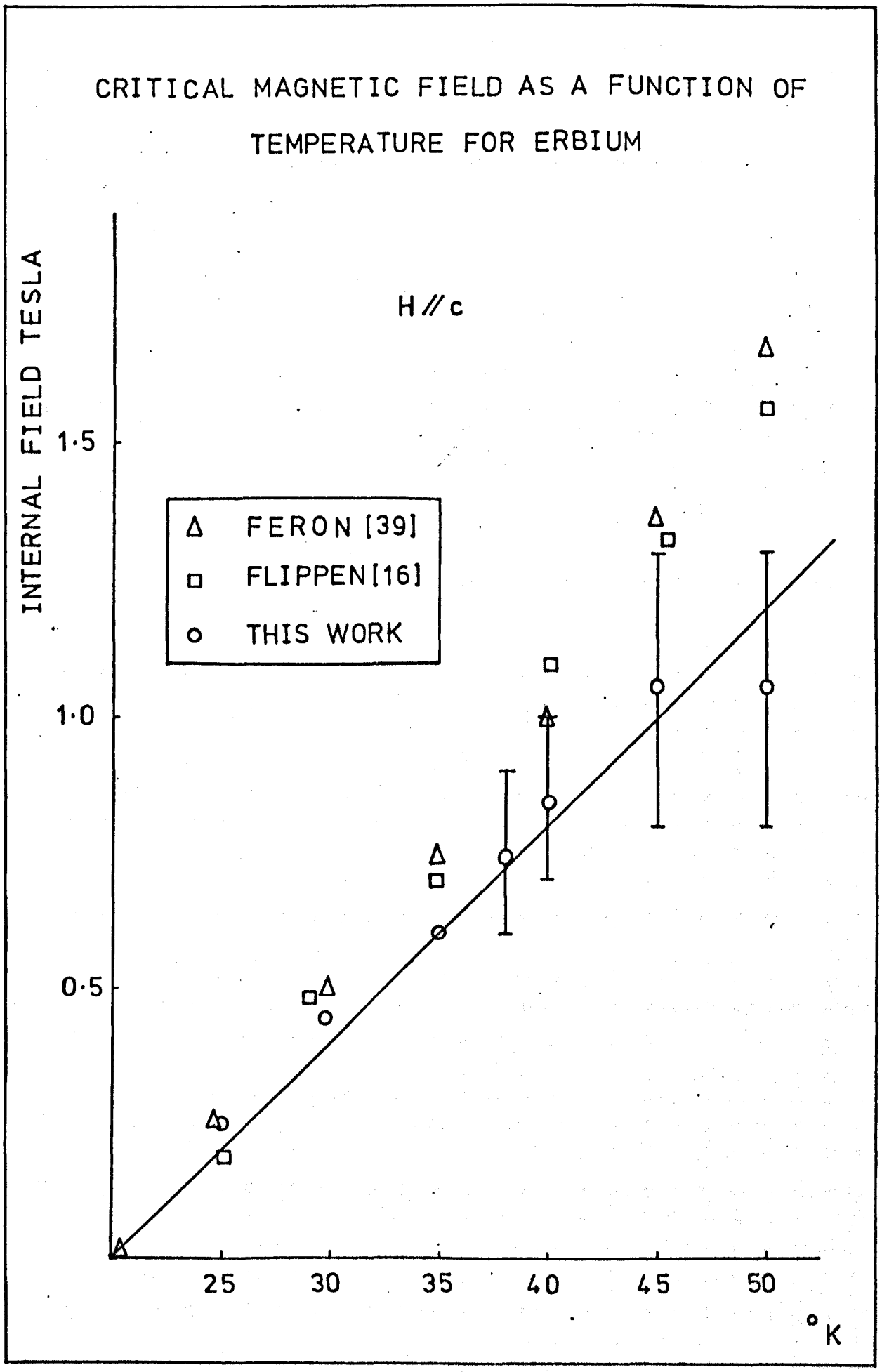
CRITICAL MAGNETIC FIELD AS A FUNCTION OF TEMPERATURE FOR ERBIUM
INTERNAL FIELD TESLA
H // c
1·5
1·0
0·5
FERON [39]
FLIPPEN [16]
THIS WORK
25
30
35
40
45
50
°K

fig. 9.62

9.5 Summary of Results

Results of the variation of C_{33} of Gadolinium with temperature over the range 180-300°K and magnetic fields over the range 0 - 0.9 T have been presented. The behaviour as a function of field below 225°K showed the existence of three magnetic phases, while above 225°K only two phases appeared to be present. Demagnetising field corrections have been made and a final phase diagram of the specimen suggested.

Results on two specimens of Terbium of different purity are reported. The two samples appeared to have different Curie points, and hysteresis in the Curie point of one of the specimens was found, although such an effect was not investigated in the other. Magnetic phase diagrams of the two samples in the temperature region around the antiferromagnetic phase have been constructed and are in agreement with published results of earlier workers.

An investigation of the magnetoelastic behaviour of Erbium using the modulus C_{33} below 20°K showed field independence at low magnetic fields. A critical internal magnetic field of 1.72T was found to be almost temperature independent in this region. The behaviour of C_{11} with a c axis magnetic field in the range 20 - 100°K has also been reported. The results show markedly different behaviour of the modulus above and below 55°K. Critical fields have been deduced with some difficulty from the results and after demagnetising field corrections the results have been shown and compared with those of other workers. Although the agreement is not entirely satisfactory, particularly at higher temperatures, the variation of critical field with temperature up to 50°K is qualitatively in agreement with earlier findings. At higher temperatures the required critical magnetic field could not be achieved with the electromagnet used in the present investigations.

CHAPTER 10

Results (III): Elastic Properties as a Function of Pressure

10.1 Introduction

In this chapter the effects of hydrostatic pressure on the elastic moduli of Erbium, Dysprosium and Terbium are reported. High hydrostatic pressures of up to 500 MPa (5 k bars) were employed using the S.R.C. High Pressure Facility at S.T.L. Ltd. of Harlow*. Details of the equipment have been given in chapter five. Also the behaviour of the second order elastic moduli of Erbium under uniaxial pressures applied along certain crystallographic directions have been investigated, and from these results and the hydrostatic pressure derivatives a complete set of third order elastic constants of Erbium has been calculated.

10.1.1 Previous Measurements of Third Order Elastic Constants

As mentioned in chapter seven there has not yet been a determination of the third order elastic moduli of any of the rare earths from experimental measurements reported to date. Some theoretical work on the TOEC on the heavy rare earths has been conducted by Ramji Rao et al [1] and these have been discussed in chapter seven.

The most notable experimental work on the effects of pressure on the elastic properties of the rare earths has been that of Fisher et al [2] who investigated the hydrostatic pressure derivatives of the SOEC of Gadolinium, Erbium and Dysprosium with pressures up to 300 MPa (3 k bar)† at 298°K.

---

* Standard Telecommunication Laboratories (ITT) Ltd., London Road, Harlow, Essex.

† Private communication indicates that the measurements were up to 3 k bar not 5 k bar as reported in [2]

10.1.2 Measurements of Third Order Elastic Constants of Other Hexagonal Materials

Some measurements of the third order elastic moduli of other hexagonal materials have been made by Swartz and Elbaum [3] for Zinc, and by Naimon [4] for Magnesium. The techniques for determination of single crystal third order elastic moduli are fairly well established [5,6,7,8] in particular the need for pinning of dislocations to suppress mobility during uniaxial stress measurements. Some methods of achieving this have been discussed in chapter five.

10.2 Calculation of Grüneisen Parameters from Hydrostatic Pressure Derivatives

10.2.1 Calculation of Compliances s_{ij} and Compressibilities β_i

The relations between the elastic moduli c_{ij} and the compliances s_{ij} for a hexagonal material are given in fig. 10.1. From these the values of the compliances given in fig. 10.2 have been calculated using data from Palmer et al [9,10].

The volume compressibility of a hexagonal crystal is related to the compliances by

$$\beta_v = 2s_{11} + s_{33} + 2(s_{12} + 2s_{13}) \qquad \ldots.10.1$$

The general expression for the linear compressibilities of a hexagonal crystal is, according to Nye [11].

$$\beta = (s_{11} + s_{12} + s_{13})(\ell_1^2 + \ell_2^2 + \ell_3^2) + (s_{33} + s_{13} - s_{11} - s_{12})\ell_3^2 \qquad \ldots.10.2$$

where the ℓ_i's are the direction cosines along the three principal axes. When resolved into component linear compressibilities parallel and perpendicular to the unique axis, this gives

$$\beta_{//} = 2s_{13} + s_{33} \qquad \ldots.10.3$$

$$\beta_{\perp} = s_{11} + s_{12} + s_{13} \qquad \ldots.10.4$$

The compressibilities are given in fig. 10.3.

Relationship between the Compliances S_{ij} and Elastic Moduli C_{ij} for Hexagonal Crystals

$$S_{12} = \frac{-C_{13}}{C_o}$$

$$S_{33} = \frac{C_{11} + C_{12}}{C_o}$$

$$S_{44} = \frac{1}{C_{44}}$$

$$S_{66} = \frac{1}{C_{66}}$$

$$S_{11} = \frac{1}{2}\left(\frac{C_{33}}{C_o} + \frac{1}{C_{11} - C_{12}}\right)$$

$$S_{12} = \frac{1}{2}\left(\frac{C_{33}}{C_o} - \frac{1}{C_{11} - C_{12}}\right)$$

where

$$C_o = C_{33}(C_{11} + C_{12}) - 2C_{13}^2$$

fig. 10.1

Values of the Compliances S_{ij} of Erbium, Terbium and Dysprosium.

Units are $10^{-11}.Pa^{-1}$

S_{ij}	Er	Dy	Tb
S_{13}	-0.2587	-0.3341	-0.3546
S_{33}	1.3186	1.4720	1.5503
S_{44}	3.6245	4.1667	4.5850
S_{66}	3.6643	4.1754	4.4903
S_{11}	1.4088	1.6262	1.7335
S_{12}	-0.4234	-0.4614	-0.5116

Values calculated from room temperature elastic constants given by Palmer and Lee [9] and Palmer et al [10]

fig. 10.2

Linear and Volume Compressibilities as Calculated from the Compliances S_{ij}

Units are $10^{-11}.Pa^{-1}$ for β's and 10^{11} Pa for K's

	Er	Dy	Tb
β_V	2.255	2.465	2.576
$\beta_{//}$	0.801	0.804	0.841
$\beta_{\perp}$	0.727	0.831	0.867
$\frac{\beta_{//} - \beta_{\perp}}{\beta_V}$	0.033	-0.011	-0.010
K_T	0.444	0.406	0.388
K_S	0.455	0.411	0.405

fig. 10.3

10.2.2 Method of Calculation of Grüneisen Parameters

The method of calculation of the Grüneisen parameters from the pressure derivative of the elastic moduli of a hexagonal single crystal has been discussed in chapter two. The equation 2.105 is utilised, viz.

$$\gamma_P(q) = \frac{\beta_\ell(q)}{\beta_V} - \frac{1}{2} + \frac{1}{2}\frac{1}{\beta_V C_P(q)} \cdot \frac{\partial C_P(q)}{\partial P} \qquad \ldots.10.5$$

where $\gamma_P(q)$ is the mode Grüneisen parameter associated with acoustic vibrations propagated along the q direction with polarisation along the P direction. $\beta_\ell(q)$ is the relevant linear compressibility and β the volume compressibility. $C_P(q)$ is the elastic constant and $\frac{\partial C_P(q)}{\partial P}$ its pressure derivative.

The final terms on the right hand side of the equation may be replaced by a single expression, π_{ij}, following Fisher [2], so that,

$$\gamma_P(q) = \frac{\beta_P(q)}{\beta_V} - \frac{1}{2}(1 + \pi_{ij}) \qquad \ldots.10.6$$

where

$$\pi_{ij} = \frac{\partial \ell n c_{ij}}{\partial \ell n\, V} \qquad \ldots.10.7$$

$$= -\frac{1}{C_{ij} \cdot \beta_V}\frac{\partial C_{ij}}{\partial P} \qquad \ldots.10.8$$

Values of the π_{ij} calculated from the measured values of $\frac{\partial C_{ij}}{\partial P}$ in fig. 10.12 are listed in fig. 10.13 together with Fisher's results for Erbium and Dysprosium.

10.2.3 Hydrostatic Pressure Derivatives

The results of the hydrostatic pressure variations of the different second order elastic moduli of Erbium are shown in figs. 10.4 - 10.7. Pressures up to 500 MPa have been employed. The results seem to show some deviations from linearity in particular the

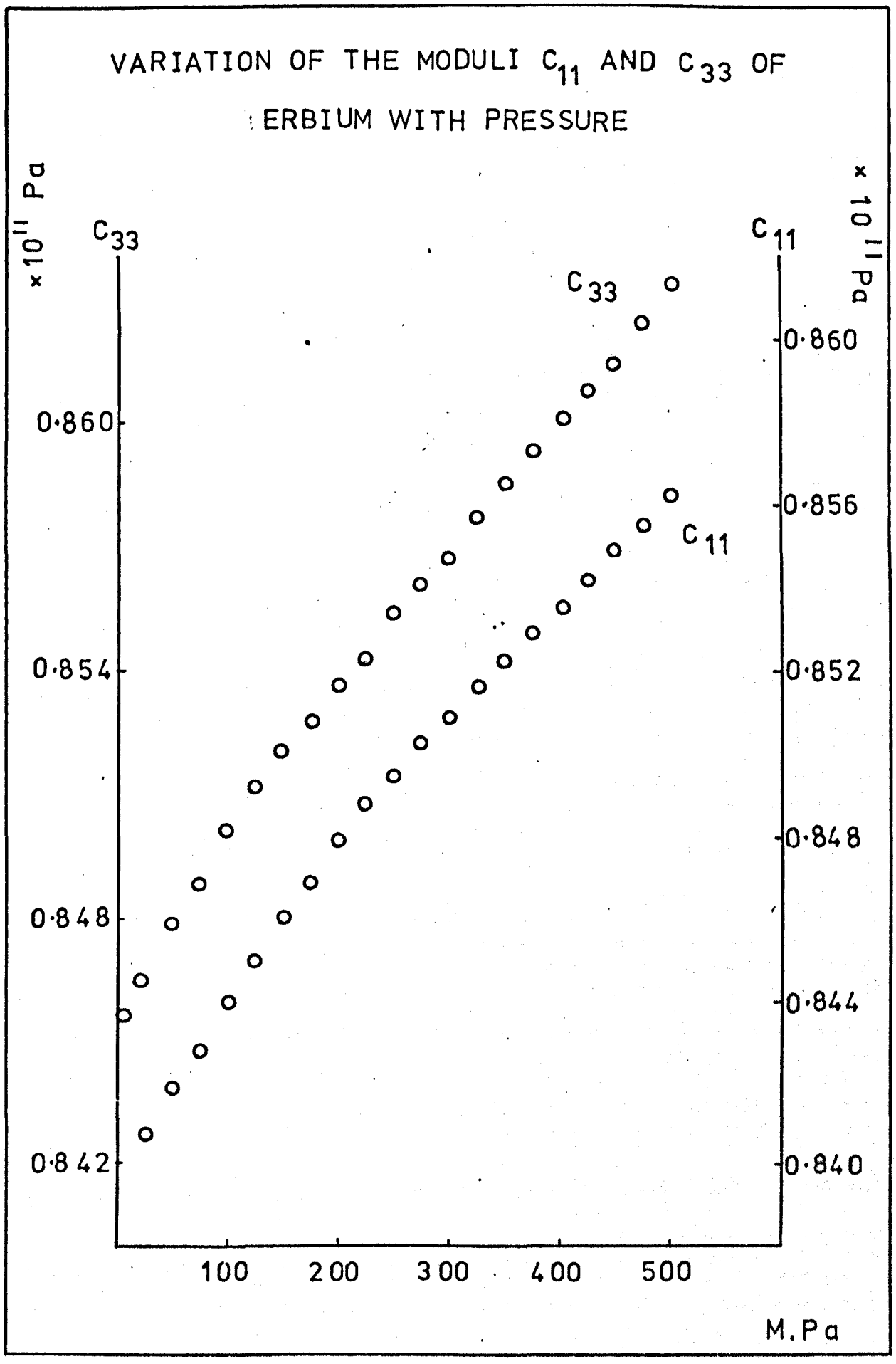
VARIATION OF THE MODULI C_{11} AND C_{33} OF ERBIUM WITH PRESSURE
C_{33}
$\times 10^{11}$ Pa
C_{11}
$\times 10^{11}$ Pa
C_{33}
C_{11}
0·860
0·854
0·848
0·842
0·860
0·856
0·852
0·848
0·844
0·840
100
200
300
400
500
M.Pa

fig.10.4

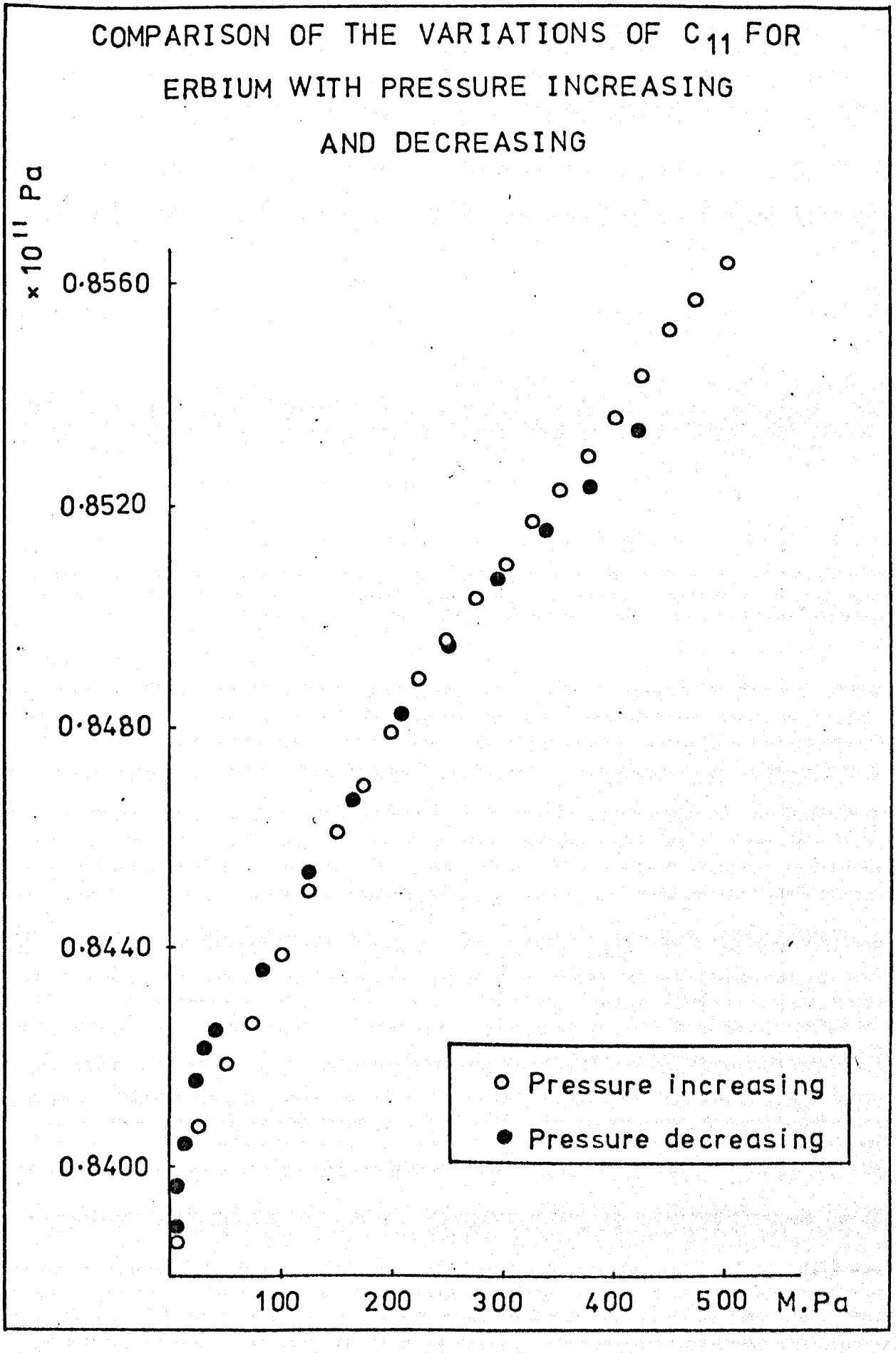
COMPARISON OF THE VARIATIONS OF C_{11} FOR ERBIUM WITH PRESSURE INCREASING AND DECREASING
$\times 10^{11}$ Pa
0·8560
0·8520
0·8480
0·8440
0·8400
100
200
300
400
500
M.Pa
Pressure increasing
Pressure decreasing

fig.10.5

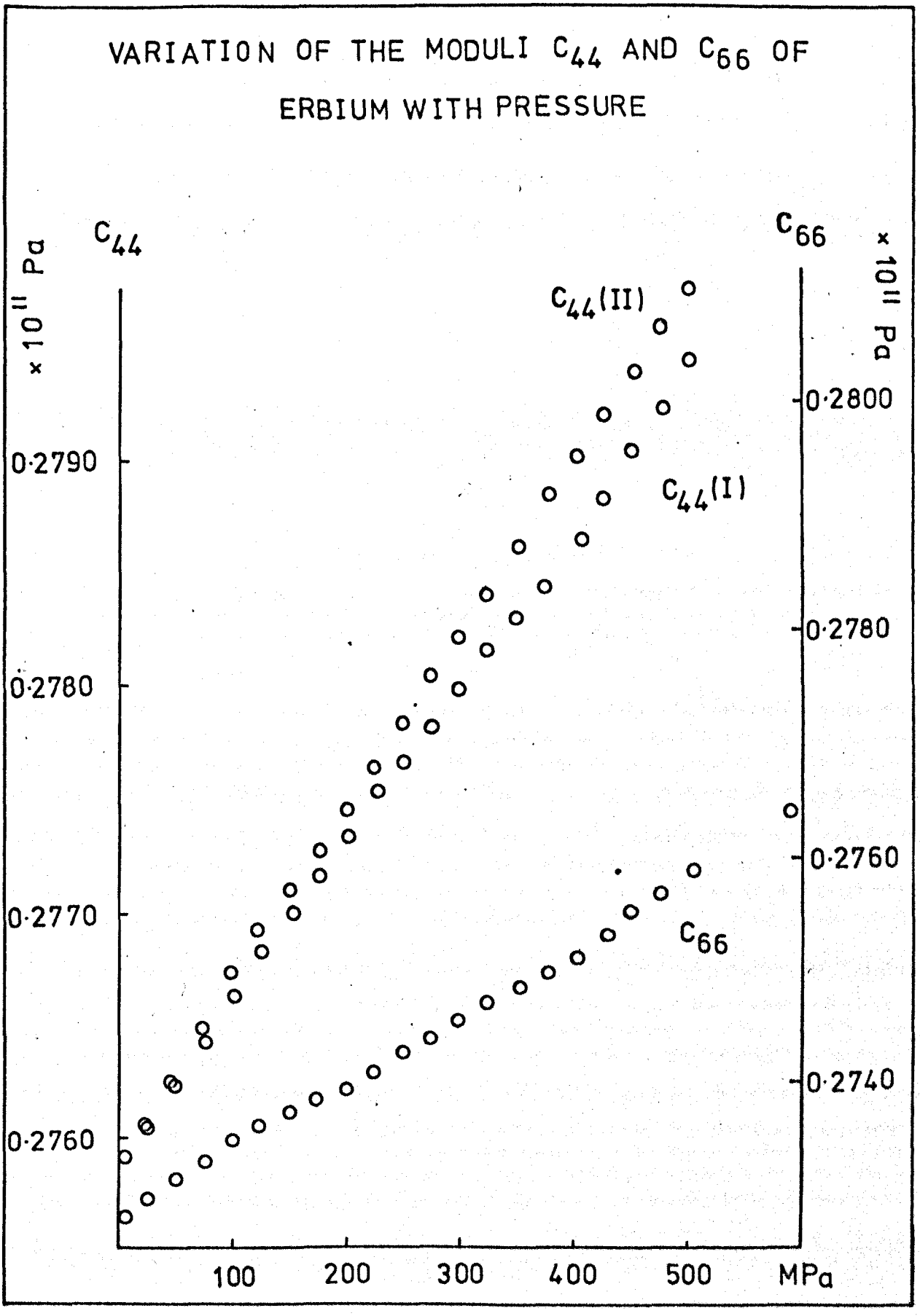
VARIATION OF THE MODULI C_{44} AND C_{66} OF ERBIUM WITH PRESSURE
C_{44}
$\times 10^{11}$ Pa
C_{66}
$\times 10^{11}$ Pa
C_{44}(II)
C_{44}(I)
C_{66}
0·2790
0·2780
0·2770
0·2760
0·2800
0·2780
0·2760
0·2740
100
200
300
400
500
MPa

fig.10.6

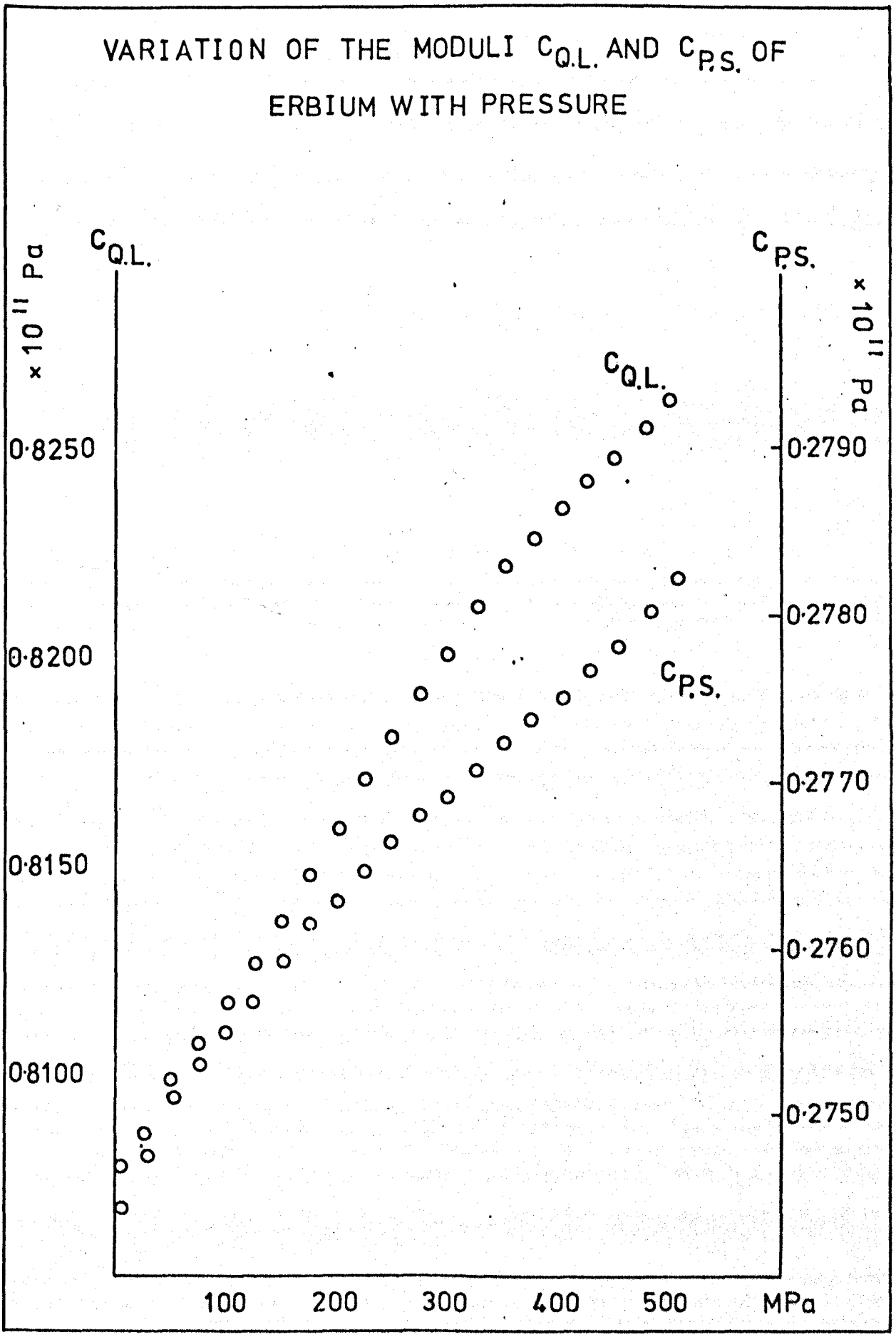
VARIATION OF THE MODULI $C_{Q.L.}$ AND $C_{P.S.}$ OF ERBIUM WITH PRESSURE
$C_{Q.L.}$
$\times 10^{11}$ Pa
0·8250
0·8200
0·8150
0·8100
$C_{P.S.}$
$\times 10^{11}$ Pa
0·2790
0·2780
0·2770
0·2760
0·2750
100
200
300
400
500
MPa

fig.10.7

slopes at low pressure are in some cases noticeably larger than the slopes at higher pressures. The derivative obtained at low pressures (< 50 MPa) from fig. 10.5 is approximately 13.0 which compares favourably with the results of $\frac{\partial C_{11}}{\partial P}$ of Erbium in appendix seven where the low pressure derivatives were markedly larger. Despite this the behaviour under increasing and decreasing pressures appears to be fairly reproducible as evidenced by fig. 10.5.

The temperature variation of the sample throughout the measurements was monitored using a chromel-alumel thermocouple. The change in temperature upon application of pressure, which was typically increased in steps of 25 MPa ($\sim$ 0.25 k bar) was found to be less than 0.25^{o}K. A period of 15 - 20 mins was allowed after each increase in pressure to enable the temperature to return to its equilibrium value. Over the whole range of the measurements the temperature variation was found to drift by less than 1^{o}K (typically it was $\sim$ 0.5^{o}K). Each experimental run took between six and eight hours.

The results of the measurements on Dysprosium and Terbium under similar conditions are presented in figs. 10.8 - 10.11 and the pressure derivatives obtained in figs. 10.12 are the arithmetic means of the increasing and decreasing pressure derivatives which were obtained by a least squares computer fitting procedure. These have been compared with the reported results of Fisher.

From the pressure derivatives the values of the π_{ij}'s given by equation 10.4 have been calculated for each mode of the three specimens and in the cases of Erbium and Dysprosium have been compared with those obtained by Fisher.

The various mode Grüneisen parameters $\gamma_p(q)$ have been calculated from the results using the method indicated, and the average Grüneisen parameters $\Gamma_{//}$, $\Gamma_{\perp}$ and Γ derived from them (fig. 10.14).

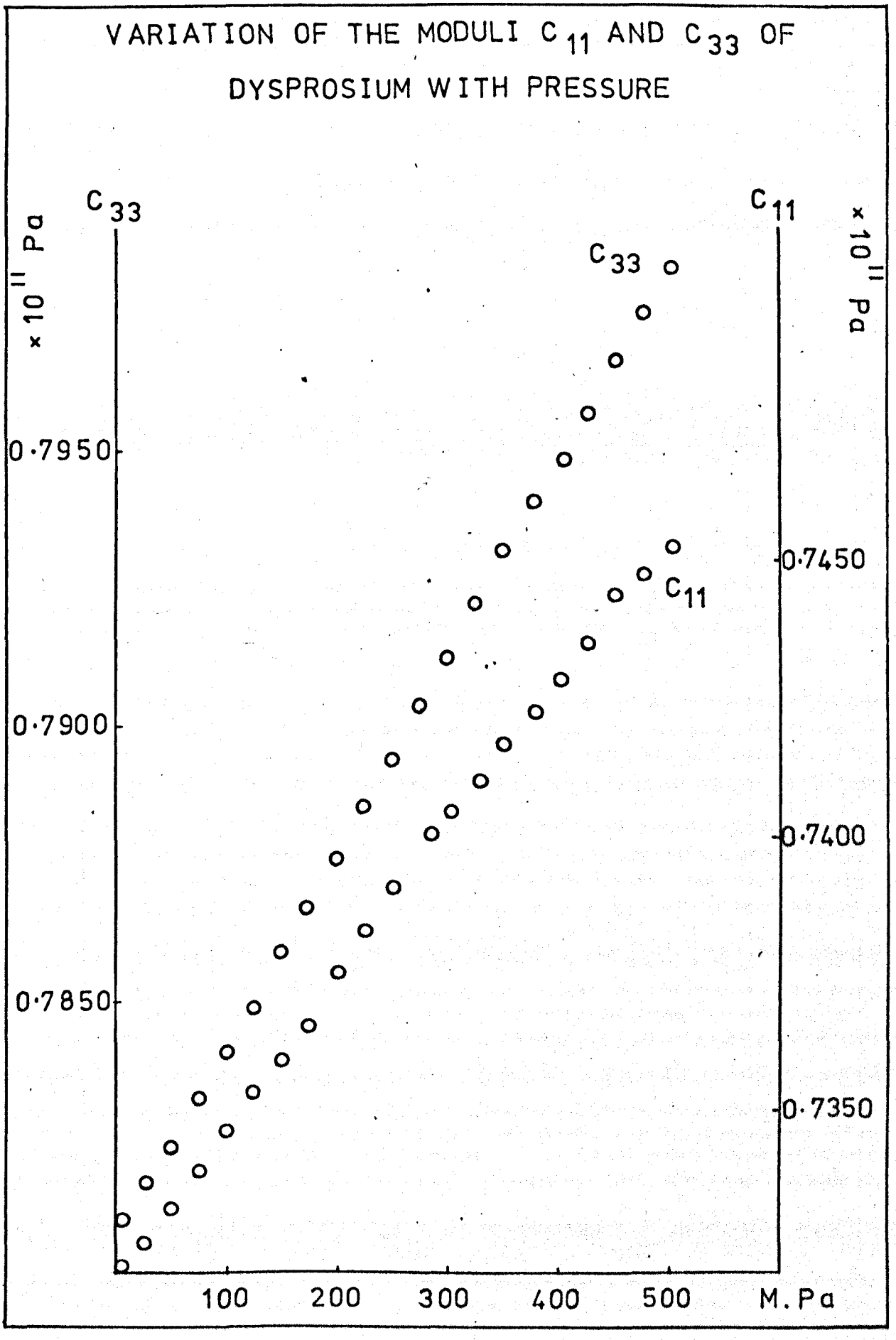
VARIATION OF THE MODULI C_{11} AND C_{33} OF DYSPROSIUM WITH PRESSURE
C_{33}
$\times 10^{11}$ Pa
0·7950
0·7900
0·7850
C_{11}
$\times 10^{11}$ Pa
0·7450
0·7400
0·7350
100
200
300
400
500
M.Pa

fig.10.8

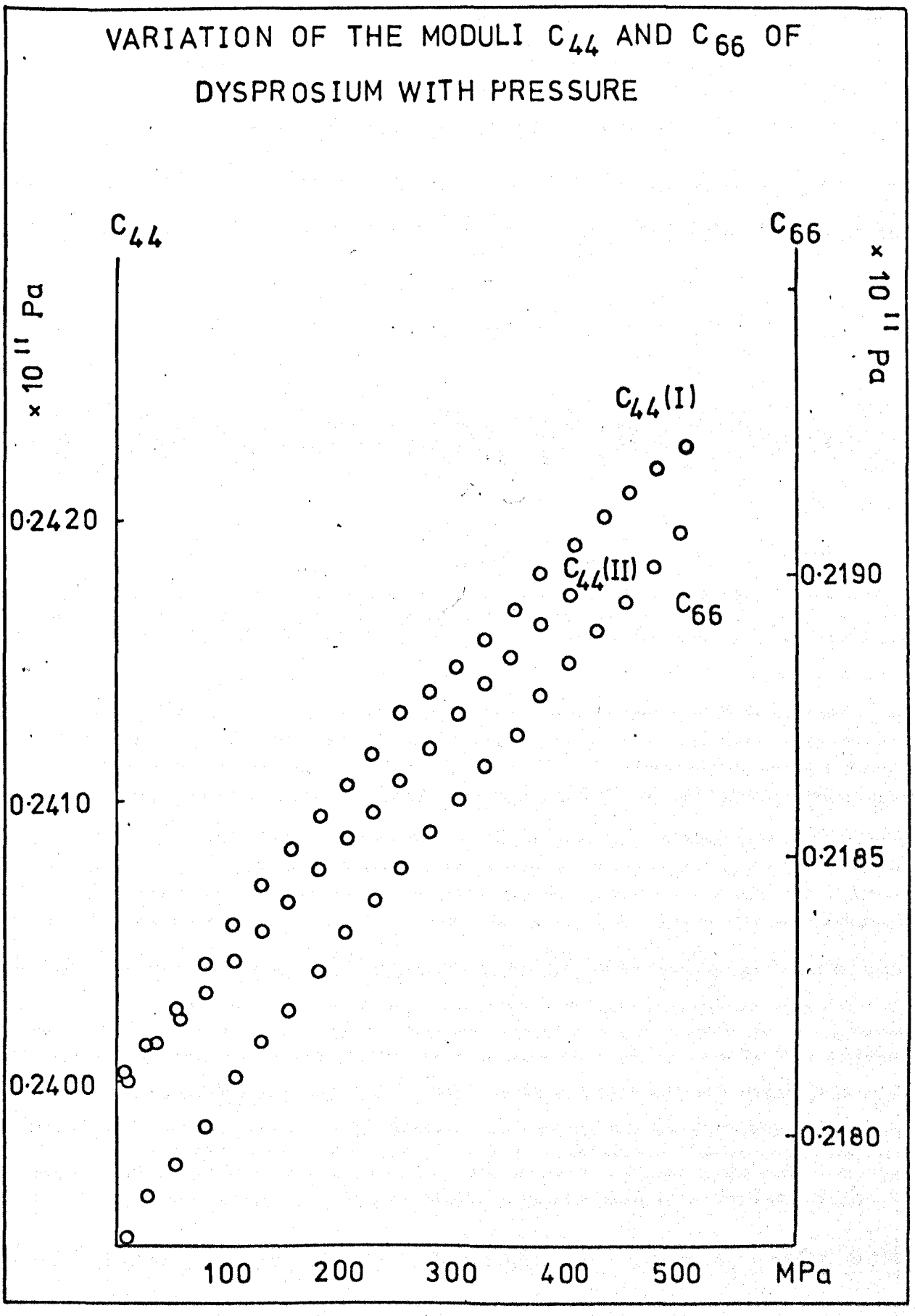
VARIATION OF THE MODULI C_{44} AND C_{66} OF DYSPROSIUM WITH PRESSURE
C_{44}
C_{66}
$\times 10^{11}$ Pa
$\times 10^{11}$ Pa
C_{44}(I)
C_{44}(II)
C_{66}
0·2420
0·2410
0·2400
0·2190
0·2185
0·2180
100
200
300
400
500
MPa

fig.10.9

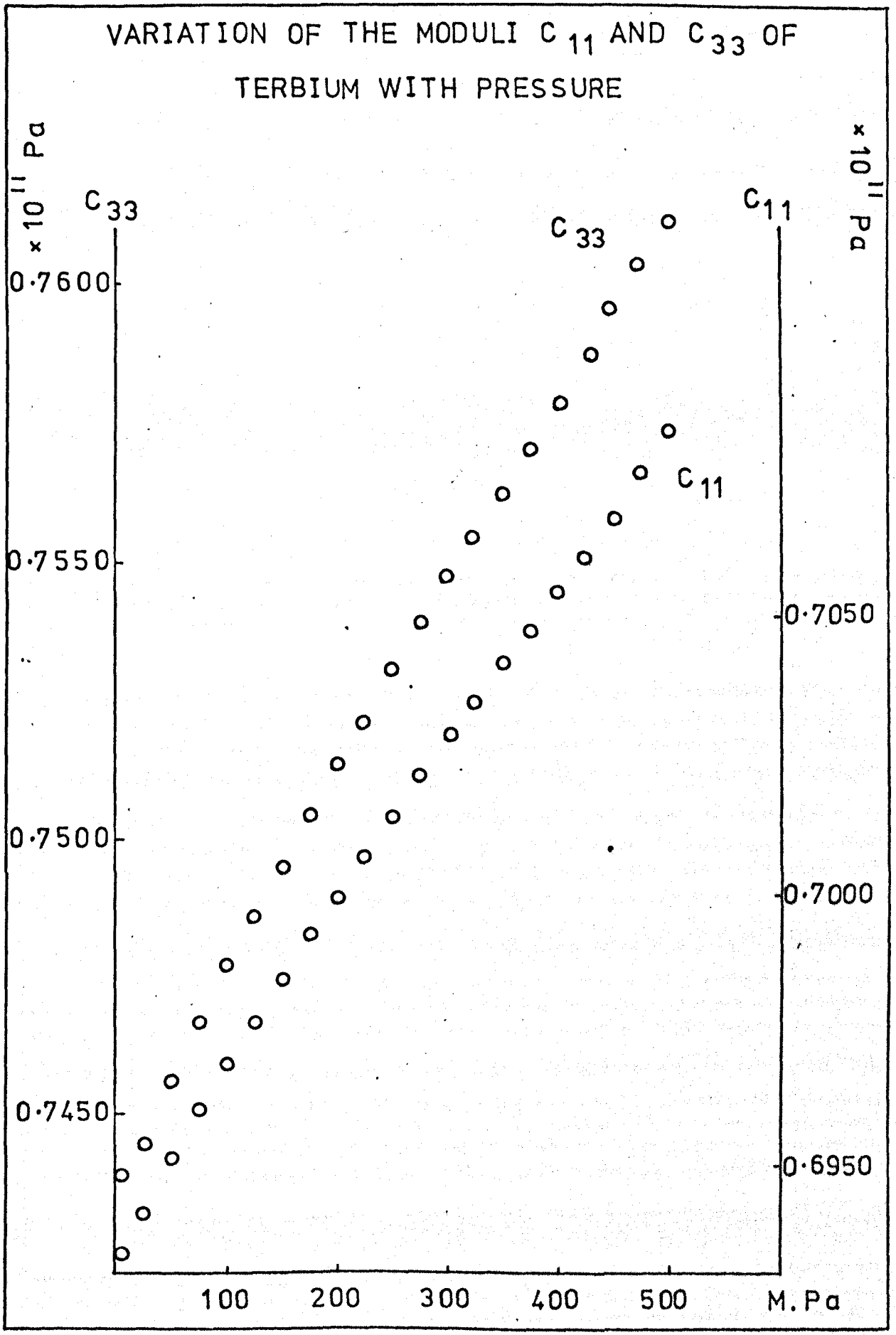
VARIATION OF THE MODULI C 11 AND C 33 OF TERBIUM WITH PRESSURE
C 33
× 10 11 Pa
0·7600
0·7550
0·7500
0·7450
C 11
× 10 11 Pa
0·7050
0·7000
0·6950
100
200
300
400
500
M. Pa

fig.10.10

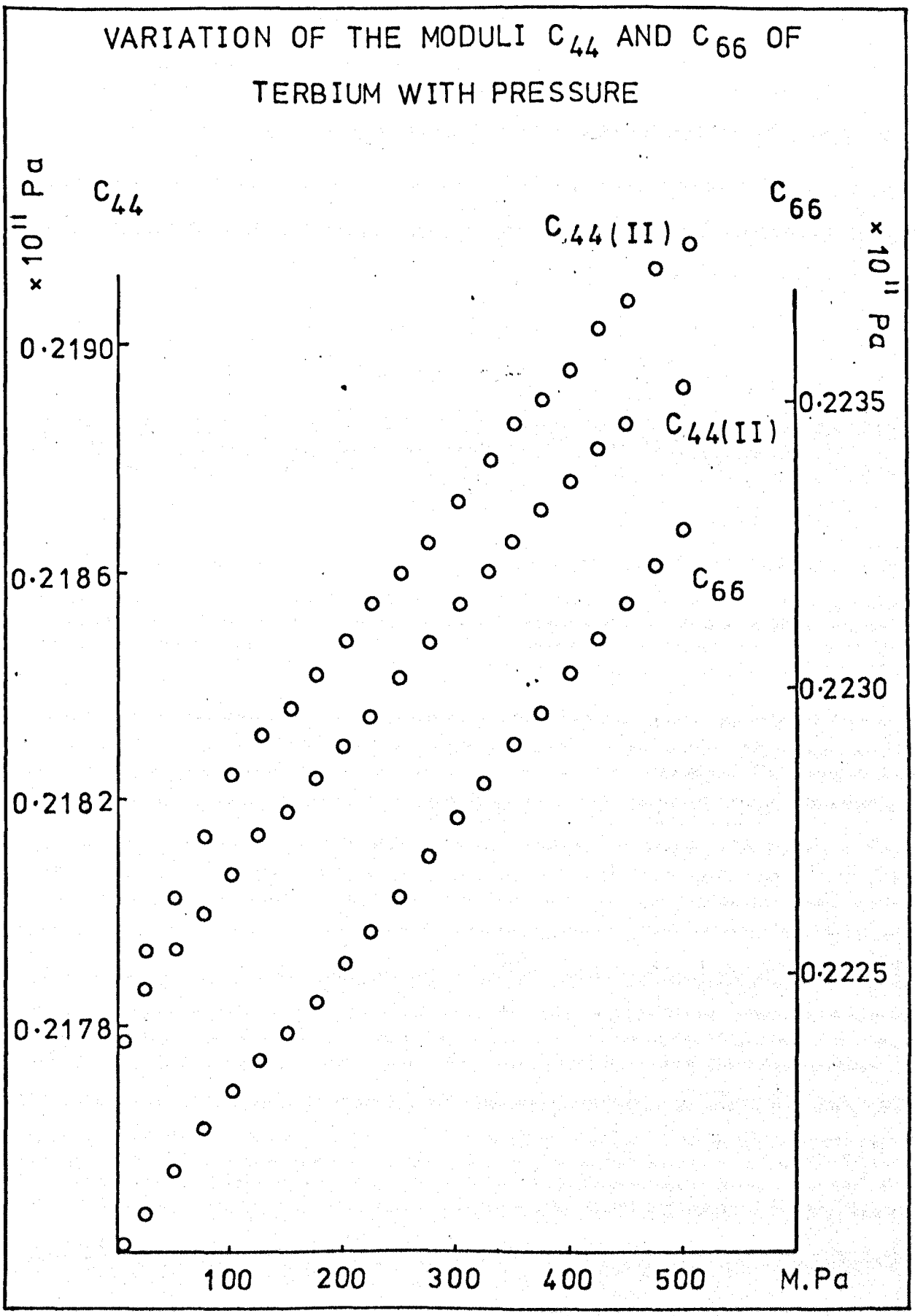
VARIATION OF THE MODULI C_{44} AND C_{66} OF TERBIUM WITH PRESSURE
C_{44}
$\times 10^{11}$ Pa
0·2190
0·2186
0·2182
0·2178
$C_{44(II)}$
C_{66}
C_{66}
$\times 10^{11}$ Pa
0·2235
0·2230
0·2225
100
200
300
400
500
M.Pa

fig.10.11

10.2.4 Discussion of Results

The measurements of the variation of elastic moduli with hydrostatic pressures up to 500 MPa (5 k bars) presented here indicate that there are some deviations from linearity. In particular the derivatives at high pressures ar smaller than those at low pressures. This can not be attributed entirely to a temperature change in the sample, since a variation of $1^{o}K$ over the whole range of the measurements would case a variation in $\frac{\Delta C}{C}$ for C_{33} of Erbium for example of 5.9×10^{-5} whereas the actual variation $\frac{\Delta C}{C}$ caused by such a change in pressure is 2.07×10^{-2} for the same modulus (fig. 10.4). Therefore temperature dependence could only account for a very small part of this deviation.

The temperature variation of the moduli could therefore not be the cause of the discrepancy between the present results and those of Fisher, the only other notable work. In fact, taking again as an example the compressional moduli of Erbium in fig. 10.4, the slopes of the graphs at pressures up to 200 MPa (2 k bars), using a straight line fit to the data by eye, yield pressure derivatives of 4.8 for C_{33} and 4.5 for C_{11} which are in good agreement with Fisher's results.

Recent results by Gerlich and Kennedy [12] on the variation of elastic moduli of polycrystalline copper with hydrostatic pressures up to 2000 MPa have also shown non-linearities, beginning at pressures of 600 MPa. The change in slope $(\frac{dC}{dP})$ was found to be from 1.8 at the lower pressures to 0.9 at the higher pressures, a factor of exactly two. Similar deviations from linearity in the rare earths might be expected to occur at lower pressures simply because the second order elastic moduli are smaller than copper ($\sim 0.8 \times 10^{11}$ Pa compared with 1.7×10^{11} Pa).

Hydrostatic Pressure Derivatives of the Elastic Moduli of Erbium, Dysprosium and Terbium

	Erbium		Dysprosium		Terbium
	This work	Fisher [2]	This work	Fisher [2]	This work
$\frac{\partial C_{33}}{\partial P}$	3.20±0.28	5.448±0.018	3.58 ±0.01	5.331±0.008	3.31±0.22
$\frac{\partial C_{11}}{\partial P}$	3.31±0.05	4.768±0.020	2.50 ±0.30	3.092±0.006	2.48±0.66
$\frac{\partial C_{44}(I)}{\partial P}$	0.72±0.04	0.949±0.005	0.49 ±0.04	0.434±0.001	0.25±0.03
$\frac{\partial C_{44}(II)}{\partial P}$	0.77±0.01	0.949±0.005	0.50 ±0.15	0.434±0.001	0.23±0.03
$\frac{\partial C_{66}}{\partial P}$	0.67±0.09	0.853±0.012	0.245±0.01	0.408±0.002	0.27±0.03
$\frac{\partial C_{P.S.}}{\partial P}$	0.69±0.05	-	-	-	-
$\frac{\partial C_{Q.L.}}{\partial P}$	3.22±0.91	-	-	-	-

Errors quoted are externally consistent [16]

fig. 10.12

Comparison of the Calculated Values of π_{ij}

	Erbium		Dysprosium		Terbium
	This work	Fisher [2]	This work	Fisher [2]	This work
π_{33}	-1.68±0.15	-2.89±0.04	-1.86±0.06	-2.78±0.03	-1.73±0.11
π_{11}	-1.75±0.03	-2.51±0.03	-1.39±0.17	-1.70±0.02	-1.39±0.37
π_{44}(I)	-1.16±0.06	-1.54±0.02	-0.83±0.07	-0.73±0.01	-0.45±0.05
π_{44}(II)	-1.24±0.02	-	-0.85±0.25	-	-0.41±0.05
π_{66}	-1.09±0.15	-1.39±0.03	-0.42±0.02	-0.69±0.01	-0.47±0.05

fig. 10.13

Calculated Values of the Grüneisen Parameters

$\gamma_p(q)$	γ_{ij}	Er	Dy	Tb
$\gamma_c(c)$	γ_{33}	0.695±0.08	0.756±0.03	0.692±0.06
$\gamma_a(c)$	$\gamma_{44}(I)$	0.435±0.03	0.241±0.04	0.052±0.03
$\gamma_a(a)$	γ_{11}	0.697±0.02	0.532±0.08	0.532±0.19
$\gamma_b(a)$	γ_{66}	0.367±0.08	0.047±0.01	0.072±0.03
$\gamma_c(a)$	$\gamma_{44}(II)$	0.442±0.01	0.262±0.12	0.042±0.03
$\Gamma_{\|\|}$	$\frac{1}{3}(\gamma_{33} + 2\gamma_{44}(I))$	0.522±0.05	0.413±0.04	0.265±0.04
$\Gamma_\perp$	$\frac{1}{3}(\gamma_{11} + \gamma_{66} + \gamma_{44}(II))$	0.502±0.04	0.280±0.07	0.215±0.08
Γ	$\frac{1}{3}(\Gamma_{\|\|} + 2\Gamma_\perp)$	0.509±0.04	0.324±0.06	0.232±0.07

fig. 10.14

10.3 Uniaxial Pressure Derivatives and TOEC

10.3.1 Methods of Determination of TOEC

Previous methods of determination of the third order elastic constants of hexagonal single crystals have involved a combination of uniaxial and hydrostatic pressure measurements on the second order constants. The hydrostatic pressures in the measurements of Swartz and Elbaum [3] and Naimon [4] were applied by using a gas pressure cell connected to a cylinder of nitrogen gas. This method was also used for some of the results obtained in the present work, which however are not presented in this chapter. A pressure limit of 5 MPa (50 $kg.cm^{-2}$) was found to be sufficient to allow determination of the pressure derivatives in this work and also in that of Swartz and Elbaum.

Methods of application of uniaxial stress fall broadly into three categories, the hydraulic press used by Swartz and Elbaum, the mechanical system operated by a screw press and calibrated by a proving ring as employed by Brammer [13], and the mechanical lever system used by Salama and Alers [6], Sarma and Reddy [8] and Hames [14]. The lever system was also used in the present work to apply uniaxial stress.

10.3.2 Method of Calculation

The method of calculation of the third order elastic constants from pressure derivaties of various modes of a hexagonal crystal have been given by Brugger [15]. A set of at least four hydrostatic pressure derivatives and at least six linearly independent uniaxial derivatives are needed to calculate the ten TOEC. The measurements used in the present determination have been summarised in fig. 10.15.

The hydrostatic pressure derivatives may be expressed by an equation of the form,

$$-\frac{\partial(\rho_o V^2)}{\partial P} = 1 + 2(\rho_o V^2)F' + G \qquad \ldots.10.9$$

Stress Derivatives required to Calculate the Third Order Elastic Constants of a Hexagonal Crystal

after Brugger [15]

No.		Propagation Direction	Polarisation Direction	Stress	Elastic Modulus
1	$M_0\alpha L$	c	c	hydro	C_{33}
2	$M_0\alpha T_2$	c	b	hydro	C_{44}
3	$M_0\gamma T_2$	b	a	hydro	C_{66}
4	$M_0\gamma L$	b	b	hydro	C_{11}
5	$M_2\alpha L$	c	c	b	C_{33}
6	$M_2\gamma L$	a	a	b	C_{11}
7	$M_3\gamma L$	b	b	c	C_{11}
8	$M_2\gamma T_2$	a	b	b	C_{66}
9	$M_2\gamma T_3$	a	c	b	C_{44}
10	$M_2\alpha T_2$	c	b	b	C_{44}

fig. 10.15

and the uniaxial derivatives by

$$-\frac{\partial(\rho_o V^2)}{\partial P} = 2(\rho_o V^2)F' + G \qquad \ldots.10.10$$

These have been further simplified to an equation of the form,

$$-\frac{\partial(\rho_o V^2)}{\partial P} = F + G \qquad \ldots.10.11$$

where the values of the terms F and G, expressed in products of the compliances and elastic constants are given for the various cases in fig. 10.16. From these ten simultaneous equations the various TOEC, C_{ijk} can be extracted when the pressure derivatives are known.

10.3.3 Results of Uniaxial Pressure Derivatives

Some preliminary uniaxial pressure measurements of the elastic moduli of Erbium have been made and the results are given in fig. 10.17. The results are just sufficient to allow the third order constants to be calculated.

These results should only be considered preliminary on several counts. The actual changes in elastic constant were so small that they were only just detectable above the fluctuations in the sing around frequency, and the results were obtained by averaging several experimental runs. Further, no cross checking measurements have been made, simply because these would only be useful to calculate whether the uniaxial measurements were consistent with previous hydrostatic pressure derivatives. As seen in section 10.2.3, the values of the hydrostatic derivatives have not been finally resolved yet. Doubt has been raised concerning the uniformity of the applied uniaxial stress and although efforts have been made to correct this the possibility remains as a source of error. Finally, although attempts were made to thermally isolate the system, it was not temperature controlled and therefore thermal fluctuations remain a further possible source of error.

Relations between the various pressure derivatives and the TOEC, C_{ijk}

$$\frac{\partial}{\partial P}(\rho V^2) = F + G$$

No.		F	G
1	$M_O \alpha L$	$1 + 2(2S_{13} + S_{33})C_{33}$	$2(S_{11} + S_{12} + S_{13})C_{133} + (2S_{13} + S_{33})C_{333}$
2	$M_O \alpha T_2$	$1 + 2(S_{11} + S_{12} + S_{13})C_{44}$	$(S_{11} + S_{12} + S_{13})(C_{144} + C_{155}) + (2S_{13} + S_{33})C_{344}$
3	$M_O \gamma T_2$	$1 + 2(S_{11} + S_{12} + S_{13})C_{66}$	$\frac{1}{2}(S_{11} + S_{12} + S_{13})(C_{222} - C_{112}) + \frac{1}{2}(2S_{13} + S_{33})(C_{113} - C_{123})$
4	$M_O \gamma L$	$1 + 2(S_{11} + S_{12} + S_{13})C_{11}$	$(S_{11} + S_{12} + S_{13})(C_{111} + C_{112}) + (2S_{13} + S_{33})C_{113}$
5	$M_2 \alpha L$	$2S_{13} \cdot C_{33}$	$(S_{11} + S_{12})C_{133} + S_{13}C_{333}$
6	$M_2 \gamma L$	$2S_{12} \cdot C_{11}$	$S_{12}C_{111} + S_{11}C_{112} + S_{13}C_{113}$
7	$M_3 \gamma L$	$2S_{13} \cdot C_{11}$	$S_{13}(C_{111} + C_{112}) + S_{33}C_{113}$
8	$M_2 \gamma T_2$	$2S_{11} \cdot C_{66}$	$\frac{1}{2}(S_{11} - S_{12})C_{111} - \frac{1}{4}(S_{11} + S_{12})C_{112} + \frac{1}{2}S_{13}(C_{113} - C_{123}) - \frac{1}{4}(S_{11} - 3S_{12})C_{222}$
9	$M_2 \gamma T_3$	$2S_{13} \cdot C_{44}$	$S_{11}C_{144} + S_{12}C_{155} + S_{13}C_{344}$
10	$M_2 \gamma T_2$	$2S_{11} \cdot C_{44}$	$S_{12}C_{144} + S_{11}C_{155} + S_{13}C_{344}$

fig. 10.16

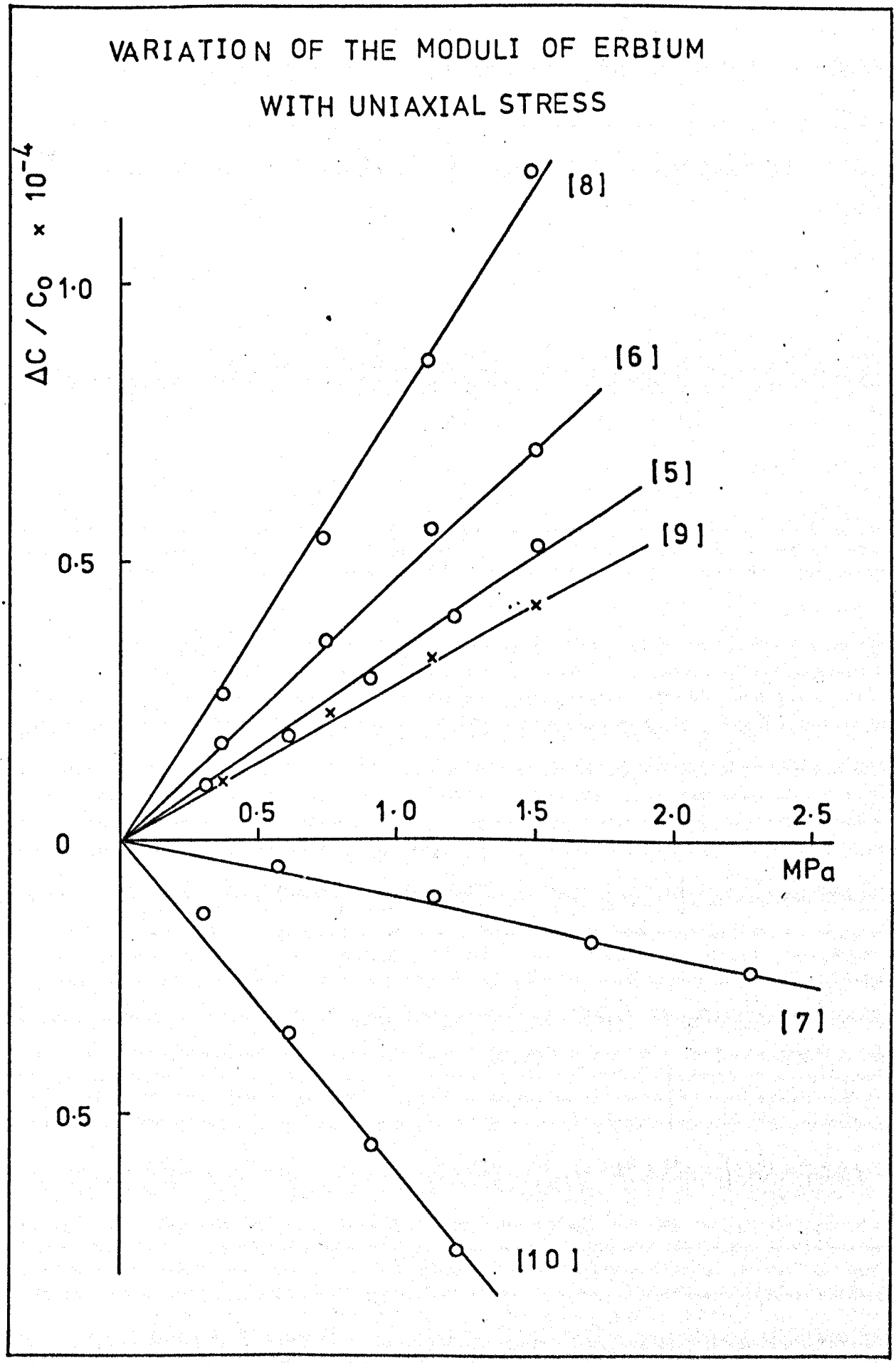
VARIATION OF THE MODULI OF ERBIUM
WITH UNIAXIAL STRESS
ΔC / C0 × 10^-4
1·0
0·5
0
0·5
0·5
1·0
1·5
2·0
2·5
MPa
[8]
[6]
[5]
[9]
[7]
[10]

fig.10.17

The contributions of dislocation mobility to inherent stress provided another problem; however, irradiation by neutrons, as discussed in chapter five, was thought to have suppressed this. The behaviour of the uniaxial derivatives before irradiation were clearly non linear. After irradiation stresses of up to only 3 MPa were applied in order to cause as little dislocation motion as possible, and the derivatives were then linear as far as could be discerned.

10.3.4 Calculation of TOEC from Results

The results of the uniaxial pressure derivatives are given in fig. 10.18. Using the numerical values given in fig. 10.19 and grouping together the two equations involving C_{133} and C_{333}, the three equations involving C_{144}, C_{155} and C_{344} and the five equations involving C_{113}, C_{123}, C_{222}, C_{112} and C_{111}, this leaves three matrix equations whose solution gives the ten TOEC

$$\begin{pmatrix} 1.45 & 0.80 \\ 0.99 & -0.26 \end{pmatrix} \begin{pmatrix} C_{133} \\ C_{333} \end{pmatrix} = \begin{pmatrix} -5.55 \\ -2.59 \end{pmatrix} \quad \ldots.10.12$$

$$\begin{pmatrix} 0.73 & 0.73 & 0.80 \\ 1.41 & -0.42 & -0.26 \\ -0.42 & 1.41 & -0.26 \end{pmatrix} \begin{pmatrix} C_{144} \\ C_{155} \\ C_{344} \end{pmatrix} = \begin{pmatrix} -2.12 \\ -0.63 \\ +0.99 \end{pmatrix} \quad \ldots.10.13$$

$$\begin{pmatrix} 0.40 & -0.40 & 0.36 & -0.36 & 0 \\ 0.80 & 0 & 0 & 0.73 & 0.73 \\ -0.26 & 0 & 0 & 1.41 & -0.42 \\ 1.32 & 0 & 0 & -0.26 & -0.26 \\ -0.13 & -0.13 & -0.67 & -0.25 & +0.92 \end{pmatrix} \begin{pmatrix} C_{113} \\ C_{123} \\ C_{222} \\ C_{112} \\ C_{111} \end{pmatrix} = \begin{pmatrix} -2.08 \\ -5.53 \\ -3.11 \\ 1.49 \\ -2.93 \end{pmatrix} \quad \ldots.10.14$$

From these equations the values of the third order elastic constants given in fig. 10.20 have been found.

Coefficients of the Various Terms given in fig. 10.16 as calculated from the SOEC

units are 10^{11} Pa

No.	See fig. 10.15	C_{133}	C_{333}	C_{144}	C_{155}	C_{344}	C_{113}	C_{123}	C_{222}	C_{112}	C_{111}	Constant Term	$-\frac{\partial C_{ij}}{\partial P}$
1	$M_0\alpha L$	1.45	0.80									2.35	= - 3.20±0.28
2	$M_0\alpha T_2$			0.73	0.73	0.80						1.40	= - 0.72±0.04
3	$M_0\gamma T_2$						0.40	-0.40	0.36	-0.36		1.41	= - 0.67±0.09
4	$M_0\gamma L$						0.80			0.73	0.73	2.22	= - 3.31±0.05
5	$M_2\alpha L$	0.99	-0.26									-0.44	= - 3.03±0.61
6	$M_2\gamma L$						-0.26			1.41	-0.42	-0.71	= - 3.82±0.76
7	$M_3\gamma L$						1.32			-0.26	-0.26	-0.43	= +1.06±0.42
8	$M_2\gamma T_2$						-0.13	-0.13	-0.67	-0.25	0.92	0.79	= - 2.14±0.27
9	$M_2\gamma T_3$			1.41	-0.42	-0.26						-0.14	= - 0.77±0.21
10	$M_2\alpha T_2$			-0.42	1.41	-0.26						0.78	= +1.77±0.35

equations read horizontally, e.g. $1.45C_{133} + 0.80C_{333} + 2.35 = -3.20$

fig. 10.18

Uniaxial Pressure Derivatives of Erbium

Mode	Elastic Modulus	$\frac{dc_{ij}}{dP}$
$M_2{}^{\alpha}L$	C_{33}	3.03 ± 0.61
$M_2{}^{\gamma}L$	C_{11}	3.82 ± 0.76
$M_3{}^{\gamma}L$	C_{11}	-1.06 ± 0.42
$M_2{}^{\gamma}T_2$	C_{66}	2.14 ± 0.27
$M_2{}^{\gamma}T_3$	C_{44}	0.77 ± 0.21
$M_2{}^{\alpha}T_2$	C_{44}	-1.77 ± 0.35

fig. 10.19

Values of TOEC of Erbium

C_{ijk}	This Work	Ramji Rao [1]
C_{133}	-3.01 ± 0.33	-1.96
C_{333}	-1.49 ± 0.11	-7.83
C_{144}	-0.79 ± 0.07	-0.49
C_{155}	0.095 ± 0.09	-0.49
C_{344}	-2.02 ± 0.03	-1.96
C_{113}	-0.299 ± 0.02	-0.38
C_{123}	7.11 ± 0.02	-0.60
C_{222}	-0.95 ± 0.06	-9.1
C_{112}	-3.41 ± 0.10	-2.57
C_{111}	-3.84 ± 0.08	-7.47

units are 10^{11} Pa

fig. 10.20

Agreement with the calculations of Ramji Rao is fair with only the moduli C_{333}, C_{123} and C_{222} showing significant discrepancy.

10.4 Summary of Results and Discussion

Some results of the effects of hydrostatic pressures up to 500 MPa (5 k bar) on the elastic moduli of Erbium, Dysrposium and Terbium have been presented. The results show deviations from linearity which do not seem to be due to temperature variations. The derivatives obtained by making a least squares straight line fit to all the data points are significantly smaller than those reported by Fisher for Erbium and Dysprosium, although the derivaties over the lower parts of the range give farily good agreement in at least one case taken as an example. The measurements on Terbium are believed to be the first determination of the pressure derivatives of this material.

Grüneisen parameters have been calculated from the data and again disagree with the Fisher calculations. Further both sets of calculations disagree with the Grüneisen parameter obtained from thermal expansion data, being in both cases too small. However if there are higher order contributions to the pressure derivative then this would help to explain the disagreement. The results of the non linear behaviour of $^{dc}/_{dp}$ have been compared to similar findings on copper by Gerlich.

Some preliminary measurements of the uniaxial pressure derivatives of Erbium have been made and from these the full set of third order elastic constants calculated. The results are in surprisingly good agreement with the calculations of Ramji Rao.

CHAPTER 11

Conclusions

11.1 Summary of Results

In this work some modifications to a new ultrasonic sing around system have been reported and the performance of the final instrument investigated by measuring the variation of the second order elastic moduli of Gadolinium, Erbium and Terbium. The results were compared where possible with previous measurements of elastic moduli of these materials and the system was found to be operating to its quoted specifications.

The initial results on C_{33} of Gadolinium close to its Curie point of $T_C = 293.5^{o}K$ gave considerably more details of the critical behaviour than had previously been achieved. The measurements of the elastic moduli of Erbium over the range $4.2 - 100^{o}K$ gave once again much finer detail than the earlier results. The variation of the moduli were nevertheless broadly in agreement with earlier results.

The behaviour of C_{33} of Terbium as a function of magnetic field applied along the b axis has also been investigated. The results obtained from the internal memory store agreed with the repetition frequency to within the quoted error of $\pm$ 3nsecs. although the loss of resolution experienced with this mode of output was rather limiting. The general form of the field dependence was rather as expected and similar in some respects to that of Dysprosium under similar conditions.

A detailed study of the variation of the elastic moduli of Gadolinium, Terbium and Erbium with magnetic field and temperature has been made and from the results the magnetic phase diagrams of Gadolinium and Terbium have been constructed. The results for the variation of the spin reorientation temperature of Gadolinium in constant applied field in the base plane compare with earlier published work. The results for Terbium have yielded the

variation of the critical field with temperature and agreement with earlier published work is good.

The results for Erbium gave a critical b axis field which was almost temperature independent below 20°K. The critical c axis field above 20°K was qualitatively in agreement with earlier work, although the present results indicated that it did not increase quite so rapidly with temperature.

Dependence of the elastic moduli of Erbium, Dysprosium and Terbium with hydrostatic pressures up to 4.5 MPa showed serious discrepancies with earlier published results for pressures up to 300 MPa. Later results with pressures up to 500 MPa showed that deviations from linear pressure dependence occurred. In particular the pressure derivaties of elastic constants decreased with increased pressure. These changes in the pressure derivative could not be attributed to temperature variations in the sample as had been suggested initially.

The derivatives obtained in the present work for pressure ranges covered by the previous work, 300 MPa, were in reasonable agreement with the published results. It would appear from this that the pressure derivatives of the elastic moduli are not constant over the range 0 - 500 MPa as had previously been suggested.

Finally some preliminary measurements of the dependences of various elastic moduli of Erbium with uniaxial stresses along selected crystallographic directions have been made. From these a complete set of third order elastic constants has been obtained, although no cross-checking measurements have been made to test the self-consistency of the results.

11.2 Future Work

The loss of resolution when measurements were made using the internal memory store were found to be severely limiting in some cases. It would therefore be useful to try to improve the accuracy of this mode, particularly since the improved speed of measurement would be useful for measuring changes

in elastic constants in pulsed magnetic fields where the sampling rate of even a second or so would be too long. Work is being conducted in this department to improve the accuracy from ± 3nsecs to ± 1.5 nsecs by using a 500 MHz oscillator as a clock instead of the 250 MHz oscillator. However, an improvement of at least an order of magnitude would be ultimately desirable.

Concerning the behaviour of Gadolinium under applied field some results of field dependence of the elastic moduli below 180^{o}K would be useful in order to ascertain whether two or three phases exist there, in particular whether phase II exists right down to 4.2^{o}K. Current opinion is that probably it does not.

The results of the pressure dependences of the elastic moduli seem to have uncovered more problems than they have solved. The low pressure derivatives, with pressures up to 4.5 MPa, and the high pressure derivatives, up to 500 MPa, gave initial disagreement. Further investigation showed that both appeared to be non linear in a way that could be consistent, however the pressure changes using the 500 MPa press could not be adjusted in small enough steps to allow the low pressure derivative to be measured accurately. Despite this an attempt to estimate the low pressure derivative from high pressure measurements was made and the results were encouraging. Plans have since been made to have the elastic constants measured over the intermediate range 0 - 100 MPa so that the problem may be resolved.

Results of the uniaxial pressure variation of the moduli of Erbium were only preliminary and in fact further measurements along these lines should be made before a definitive statement of the TOEC of Erbium can be made. The TOEC of all of the remaining rare earths have yet to be determined and therefore further progress in this direction is needed.

Appendix 1 Data Analysis

The data output from the sing around may be in either of two forms. The sing around frequency may be read directly from the frequency meter, or the delay time between the opening of the electronic gate and the detection of the next echo may be obtained on paper tape. In order to simplify the data analysis two computer programs have been written to calculate the elastic constants from the raw data.

Data Output on Paper Tape: Program 1

The form of the data input for this program consisted of the initial value of the controlled parameter, for example a thermocouple emf. or a coil current for the electromagnet, the increment in this parameter between readings and the digital delay or gate delay as read directly from the preset switches on the sing-around. This last reading may be converted to a delay time in microseconds as indicated in section 4.8. The format of the data used was

V ΔV D

t_1

t_2

.

.

.

t_{113}

-100.0

****

where V was the initial value of the parameter, ΔV the increment between successive readings and D the digital delay. The "-100.0" was simply a terminating character.

The program then calculated the sing around period τ_i for each of the t_i in the data as governed by the equation 4.1

$$\tau_i = (D+1).0.128 + \frac{t_i + 2}{1000} \quad \mu\text{secs.} \qquad \text{A1.1}$$

and then produced a graph of τ_i against the corresponding temperature T_i or magnetic field B_i which was found from the values of V_i given by

$$V_i = V + (i-1).\Delta V \qquad \text{A1.2}$$

by using a calibrating subroutine.

Corrections were then made to the calculated periods τ_i in the following way. Since the frequency of the acoustic waves was 15MHz the time intervals between corresponding points of successive cycles was the reciprocal of this, i.e. 0.067μsecs. Starting from i = 2 if the difference between two successive periods τ_{i-1} and τ_i was greater than 0.066μsecs., then a function Δ_i, which was initially set to zero, was incremented according to

$$\Delta_i = \Delta_{i-1} \pm 0.0667 \quad \mu\text{secs.} \qquad \text{A1.3}$$

whenever a likely change in the triggering cycle was observed. The sign of the increment was determined by the relative magnitude of the two functions

$$\varepsilon_i^+ = |\tau_i - \tau_{i-1} + 0.0667| \qquad \text{A1.4}$$

$$\varepsilon_i^- = |\tau_i - \tau_{i-1} - 0.0667| \qquad \text{A1.5}$$

If ε^+ were smaller then the positive sign was used and vice versa. A new set of corrected periods τ_i' was then calculated by

$$\tau_i' = \tau_i + \Delta_i \qquad \text{A1.6}$$

and from this the sing around frequency calculated from

$$f_i = \frac{1}{\tau_i'} \qquad \text{A1.7}$$

The square of sing around frequency was proportional to the elastic modulus, and the elastic moduli as a function of the controlled parameter were computed by finding one frequency f_i for which the elastic constant was known to have a particular value C_o. For example, in the magnetic field sweeps the elastic modulus at zero field was often known. The

coefficient of proportionality k was then given by

$$k = \frac{C_o}{f_i^2} \qquad \text{A1.8}$$

and the other results were then scaled by multiplying by k, to give a series of elastic constants against the controlled variable of temperature or magnetic field.

The data output was then in the form of a graph of elastic modulus against the controlled variable using the Computer Centre graph plotter.

Data Output from the Frequency Meter: Program 2

The form of data input for this program consisted of tabulated values of the variable parameter V and the sing around frequency f arranged in corresponding pairs in the format shown below

V_1	f_1
V_2	f_2
.	.
.	.
.	.
V_n	f_n
100.0	-100.0
****	

where again the "-100.0" is a terminating character. The program then plotted a graph of this raw data on the line printer to show its general form. The program then corrected the data in the event of any changes in triggering point which would manifest themselves as abrupt breaks in the graph.

In order to achieve this the moving average of the slope of the curve was recorded, taking the last four data points into consideration. That is, at the ith point it defined a slope function S_i as

$$S_i = \frac{|f_{i-1} - f_{i-2}| + |f_{i-2} - f_{i-3}|}{|V_{i-1} - V_{i-3}|} \qquad \text{A1.9}$$

and then calculated the slope between the current (i th point) and the (i-1)th point.

$$D_i = \frac{|f_i - f_{i-1}|}{|V_i - V_{i-1}|} \qquad \text{A1.10}$$

If $D_i < 5.Si$ then no action was taken and the program moved on to the next operation which involved a check of the change in direction of slope. However, if $D_i \geq 5.Si$ or there was found to be a change in direction of slope between S_i and D_i then a correction was made as outlined below. The factor 5 was determined empirically.

If a correction was to be made to the i th data point in conjunction with the conditions given above, then a function δ was incremented such that δ_i was set initially to zero and when a correction was required,

$$\delta_i = P_i.S_i.(V_i - V_{i-1}) \qquad \text{A1.11}$$

where p_i was simply the direction of the slope S_i given by

$$P_i = \frac{f_{i-1} - f_{i-3}}{|f_{i-1} - f_{i-3}|} \qquad \text{A1.12}$$

and consequently P_i was either ± 1.

After all the δ_i had been evaluated the corrections were made to the data by defining a new function Δ_i such that

$$\Delta_i = \Delta_{i-1} + \delta_i \qquad \text{A1.13}$$

The new function Δ_i could then be added to the values of frequency f_i to give the corrected frequency f_i'

$$f_i' = f_i + \Delta_i \qquad \text{A1.14}$$

When the program had completed its run a new set of corrected frequencies f_i' were obtained and again the f_i^2 were calculated. Using the same procedure as the other program a parameter V_i for which the elastic constant was known to be C_o was found as the other values of f_i^2 scaled accordingly to give values of elastic constants.

The final form of output was then a graph of elastic constant against the controlled variable, either temperature or magnetic field, using the Computer Centre graph plotter.

Generation Function g

The generation function g_i was introduced later to show where corrections had been made to the data. The values of g_i were defined by

$$g_1 = 0 \qquad \text{A1.15}$$

$$g_i = g_{i-1} \quad \text{for } \delta_i = 0 \qquad \text{A1.16}$$

$$g_i = g_{i-1} + 1 \quad \text{for } \delta_i \neq 0 \qquad \text{A1.17}$$

so that each time the frequency is corrected the value of the generation function g increases by one. This was used to identify the corrections. These occurred typically about once every 30 - 50 data points, although this was naturally dependent on how rapidly and how drastically the attenuation changed.

Appendix 2 Origins of the Exchange Interaction

Simultaneously and independently Dirac [1] and Heisenberg [2] explained ferromagnetism using quantum mechanics shortly after Pauli had discovered his exclusion principle. The exchange interaction was discovered as a consequence of this exclusion principle and the physical overlap of the wave functions of the electrons concerned. This additional energy term appeared to have no classical analogue.

The exclusion principle was found to keep electrons with parallel spins apart and thereby reduce the Coulomb repulsion interaction. The difference in energy between the parallel and antiparallel spin configurations of two electrons was called the exchange energy, although this was favourable to ferromagnetism only under certain circumstances.

Heitler-London Approximation for the Wave Functions of Two Electrons in a Hydrogen Molecule

This model will be invoked since the result is useful in obtaining the wave functions of two electrons on neighbouring atoms. In this approximation electron repulsion is considered to be significant in affecting the motions of the electrons so that they will spend most of the time at opposite ends of the molecule. The system will therefore resemble two separated hydrogen atoms. The wavefunctions of the two electrons may then be approximated by using one electron functions, each of which is localised at one of the nuclei. Let these two functions be ψ_a and ψ_b localised at nuclei a and b respectively.

The symmetrical and antisymmetrical wave functions are therefore:

$$\psi_S(r_1,r_2) = \phi_a(r_1)\phi_b(r_2) + \phi_a(r_2)\phi_b(r_1) \qquad \ldots.A2.1$$

$$\psi_A(r_1,r_2) = \phi_a(r_1)\phi_b(r_2) - \phi_a(r_2)\phi_b(r_1) \qquad \ldots.A2.2$$

so that $\phi_a(r_i)$ represents the separate wave function of the first electron at nucleus a and $\phi_b(r_2)$ represents the wave function of the second electron at nucleus b. $\phi_b(r_1)$ and $\phi_a(r_2)$ are the wavefunctions when electrons are exchanged between the nuclei.

Evaluation of the Total Energy

The total energy E of the electrons may then be obtained by

$$E = \iint \psi^*.H.\ \psi\, dV_1\, dV_2 \qquad \ldots.A2.3.$$

where the wavefunction ψ is given by either of the forms A2.1 or A2.2. The sign distinguishes corresponding singlet and triplet states.

The total Hamiltonian for this particular system may be split into its constituent terms

$$H = H_1 + H_2 + H_{1,2} \qquad \ldots.A2.4$$

where H_1 is the energy of the first electron in the absence of the second, and is therefore dependent only on r_1, and H_2 is the energy of the second electron in the absence of the first. The term $H_{1,2}$ is the energy due to interaction of the electrons, which was incidentally neglected in obtaining the approximate wavefunctions.

The evaluation of the energy integral A2.3 may then be obtained as follows, where normalisation factors have been ignored.

$$E = \iint (\phi_a^*(r_1)\phi_b^*(r_2) \pm \phi_a(r_2)\phi_b(r_1))H.(\phi_a(r_1)\phi_b(r_2) \pm \phi_a(r_2)\phi_b(r_1)) \times dV_1\, dV_2 \qquad \ldots.A2.5$$

$$= \iint \phi_a^*(r_1)\phi_b^*(r_2)H.\phi_a(r_1)\phi_b(r_2)\, dV_1\, dV_2$$

$$+ \iint \phi_a^*(r_2)\phi_b^*(r_1)H.\phi_a(r_2)\phi_b(r_1)\, dV_1\, dV_2$$

$$\pm \iint \phi_a^*(r_1)\phi_b^*(r_2)H.\phi_a(r_2)\phi_b(r_1)\, dV_1\, dV_2$$

$$\pm \iint \phi_a^*(r_2)\phi_b^*(r_1)H.\phi_a(r_1)\phi_b(r_2)\, dV_1\, dV_2 \qquad \ldots.A2.6$$

and recalling that ψ^* and H are symmetrical or antisymmetrical in r_1 and r_2, yields,

$$E = 2\iint \phi_a^*(r_1)\phi_b^*(r_2) H . \phi_a(r_1)\phi_b(r_2)\, dV_1\, dV_2 \pm 2\iint \phi_a^*(r_1)\phi_b^*(r_2) H . \phi_a(r_2)\phi_b(r_1)\, dV_1\, dV_2 \quad \ldots\ldots A2.7$$

Separation of the operator H into its constituent terms as indicated in equation A2.4 gives

$$\frac{E_1}{1+\alpha^2} = 2\iint \phi_a^*(r_1)\phi_b^*(r_2) H_1 \phi_a(r_1)\phi_b(r_2)\, dV_1\, dV_2 \quad \ldots\ldots A2.8$$

$$\frac{E_2}{1+\alpha^2} = 2\iint \phi_a^*(r_1)\phi_b^*(r_2) H_2 \phi_a(r_1)\phi_b(r_2)\, dV_1\, dV_2 \quad \ldots\ldots A2.9$$

where E_1 and E_2 are the unperturbed energies of the electrons in their states $_a(r_1)$ and $_2(r_2)$ without any interaction. The factor α^2 is the exchange integral.

$$\alpha^2 E_1 = 2\iint \phi_a^*(r_1)\phi_b^*(r_2) H_1 \phi_a(r_2)\phi_b(r_1)\, dV_1\, dV_2 \quad \ldots\ldots A2.10$$

$$\alpha^2 E_2 = 2\iint \phi_a^*(r_1)\phi_b^*(r_2) H_2 \phi_a(r_2)\phi_b(r_1)\, dV_1\, dV_2 \quad \ldots\ldots A2.11$$

Therefore the sum of these terms gives simply the unperturbed (i.e. no interacting) energy of the two electrons $E_1 + E_2$. This still leaves two extra terms in the total energy, which will be denoted by Q and J.

$$Q = \iint \phi_a^*(r_1)\phi_b^*(r_2) H_{1,2} \phi_a(r_1)\phi_b(r_2)\, dV_1\, dV_2 \quad \ldots\ldots A2.12$$

$$\pm J = \pm \iint \phi_a^*(r_1)\phi_b^*(r_2) H_{1,2} \phi_a(r_2)\phi_b(r_1)\, dV_1\, dV_2 \quad \ldots\ldots A2.13$$

So that the full expression for the energy of the system is

$$E_{tot} = E_1 + E_2 + 2(Q \pm J) \quad \ldots\ldots A2.14$$

where the terms E_1 and E_2 are the energy of the system when the two electrons are not interacting, for example if one nucleus and its electron were at infinity. Q and J are due to the interaction component H_{12} of the Hamiltonian and may therefore be called the interaction energy terms. Q may be interpreted as a Coulomb electrostatic interaction between the electrons. However it is the J term which is particularly interesting.

J is known as the exchange integral and appears because the Pauli principle requires a correlation between the quantum numbers defining the electrons. It owes its existence therefore to the fact that the wave functions of the two electrons have the form given in equations A2.1 and A2.2. The nature of this interaction is therefore electrostatic and not a magnetic dipole type of interaction. The exchange integral is thus responsible for regulating the spin configurations of electrons in atoms, molecules and on a larger scale throughout a solid.

Appendix 3 Magnetic Phase Transitions and Catastrophe Theory

Thermodynamic Equilibrium

In thermodynamics the state of a system is defined by the parameters temperature T, pressure P, volume V, and entropy S. Additional parameters of magnetic field H and magnetisation M are also sometimes used. These may be classified according to the conditions under which an experiment is conducted, into those parameters which may be controlled by the experimenter, the control space, and those parameters which specify the behaviour of the system, and are necessary together with the control parameters to specify the state of the system. These may be termed the behaviour or state space.

For example it often happens that the temperature and pressure of a system are varied in order to produce changes in volume. In this case the control space is the two dimensional space of P,T and the state space is the one dimensional space of V. In order to obtain the equilibrium conditions in this case the Gibbs free energy is found and a minimum obtained with respect to the state variables.

Catastrophe Theory

In catastrophe theory a theorem exists which appears to be analogous to the description of the specification of state of a thermodynamic system. This is the main theorem of catastrophe theory and is stated in a simplified form here:

Theorem:

If C is a control space and Z is a state space let ϕ be a smooth function on Z parametricised by C. Then M the set of stationary values of ϕ with respect to the state variables is a smooth surface in C x Z. The only singularities of the projection of M onto C are elementary catastrophes *(see* [7] *for definition)*.

This means that for elementary catastrophes there exists a smooth potential function ϕ such that the equilibrium conditions of the system are given by

$$\frac{\partial \phi}{\partial y_i} = 0 \qquad i = 1, 2, \ldots \qquad \text{A3.1}$$

where the y_i belong to Z.

Elementary Catastrophes and their Classification

Each of the catastrophes has a particular model and a general formula for the potential function ϕ exists for each type. The formulae are given in the table below although the signs of the coefficients here are arbitrary. In each case the a,b,c,d are parameters for the control space C and x for the state space Z

	dim Z	dim C	ϕ
Field	1	1	$\frac{1}{3}x^3 - ax$
Cusp	1	2	$\frac{1}{4}x^4 - ax - \frac{1}{2}bx^2$
Swallowtail	1	3	$\frac{1}{5}x^5 - ax - \frac{1}{2}bx^2 - \frac{1}{3}cx^3$
Butterfly	1	4	$\frac{1}{6}x^6 - ax - \frac{1}{2}bx^2 - \frac{1}{3}cx^3 - \frac{1}{4}dx^4$

Only those catastrophes with one dimensional state spaces Z have been included since these are the only ones with which the present work is concerned.

The Cusp Catastrophe

In the case when Z is one dimensional and C is two dimensional the set M of stationary values of ϕ gives a surface of the form shown below. This is called the cusp catastrophe and is particularly easy to visualise.

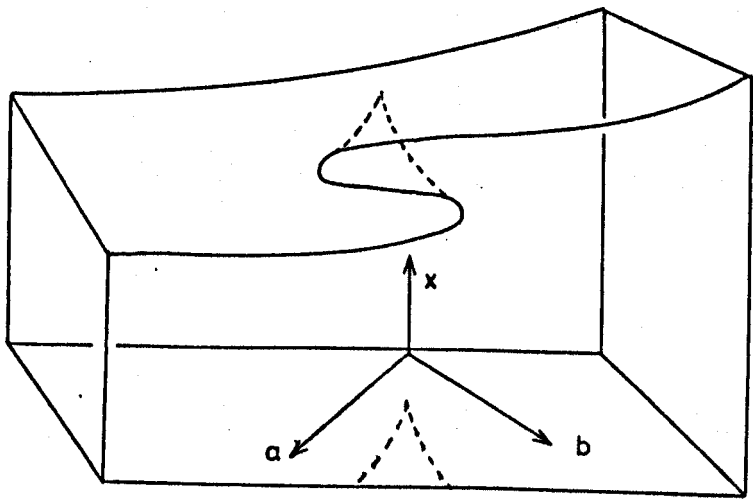

The projection of the fold onto the control space C gives the Riemann-Hugoniot cusp which is the reason for the alternative name of this case, the Riemann-Hugoniot catastrophe. The potential function ϕ has the form,

$$\phi = \frac{1}{4}x^4 - ax - \frac{1}{2}bx^2 \qquad \text{A3.2}$$

therefore the surface, governed by $\frac{\partial \phi}{\partial x} = 0$ is,

$$x^3 = bx + a \qquad \text{A3.3}$$

and differentiating again with respect to x to obtain the cusp points gives on elimination of x the projection of the fold onto the plane a b

$$27a^2 = 4b^3 \qquad \text{A3.4}$$

the Riemann-Hugoniot cusp.

Relevance to the Real Situation

In practical situations two parameters are often varied to give particular states of a system and the resulting phase diagram is a projection of a particular behaviour parameter onto the control plane.

In the present work this has been obtained by finding the magnetic state of a solid as a function of temperature and magnetic field. It therefore appears that this particular form of elementary catastrophe has important applications.

It has been shown in chapter 3 that the general form of the potential function for second order phase transitions with an ordering parameter η may be given by equation 3.50

$$\phi = \phi_o \pm A\eta^2 + C\eta^4 \qquad \ldots.3.50$$

and by application of a magnetic field to prevent symmetry changes the form of the potential is

$$\phi = \phi_o \pm A\eta^2 \pm \alpha\eta + C\eta^4 \qquad \ldots.3.51$$

Hence by application of Thom's theorem the equation 3.51 will generate a surface M in the space $C(T,H) \wedge Z(\eta)$ which has the general form of the cusp catastrophe. The equilibrium surface in this case being given by

$$\left(\frac{\partial\phi}{\partial\eta}\right)_{T,H} = 0 \qquad A3.5$$

Note here than η as defined by 3.43 is closely related to the entropy. In fact

$$S = k\,\ell n\left({}^{N}C_{P+N}\right) \qquad A3.6$$

where k is Boltzmann's constant and ${}^{n}C_{r}$ is the number of ways of selecting r states from a total number of n states.

It might also be expected that the coefficient α is proportional to the applied magnetic field H, and A to the difference between Curie temperature and the observed temperature of the system (i.e. $T_C - T$).

General Form of the Gibbs Function in the Two Cases

(i) When $\alpha = 0$, i.e. zero magnetic field

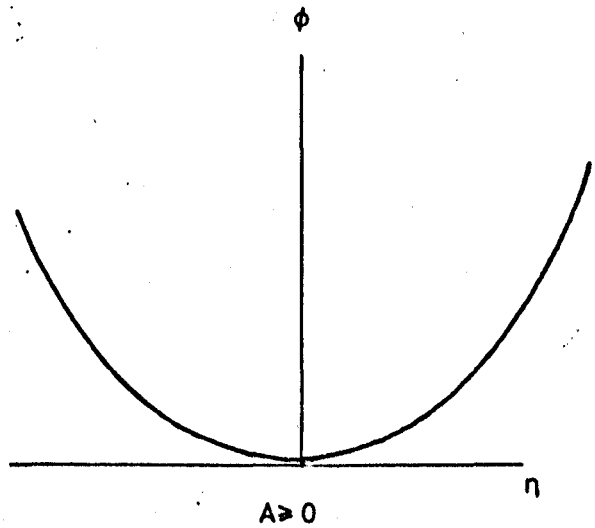

$A \geq 0$

$\phi = C\eta^4 + A\eta^2$

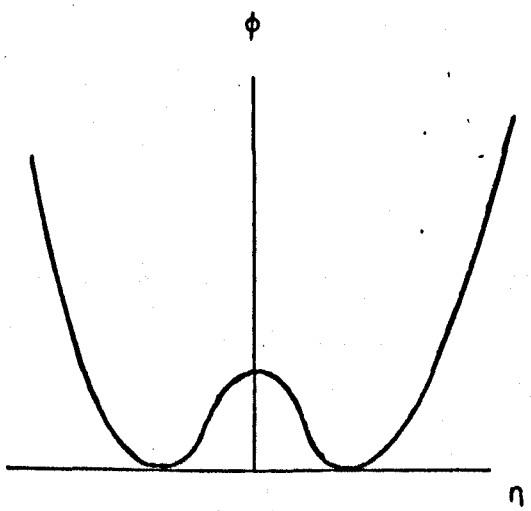

$A < 0$

$\phi = C\eta^4 - A\eta^2$

(ii) When α is non zero

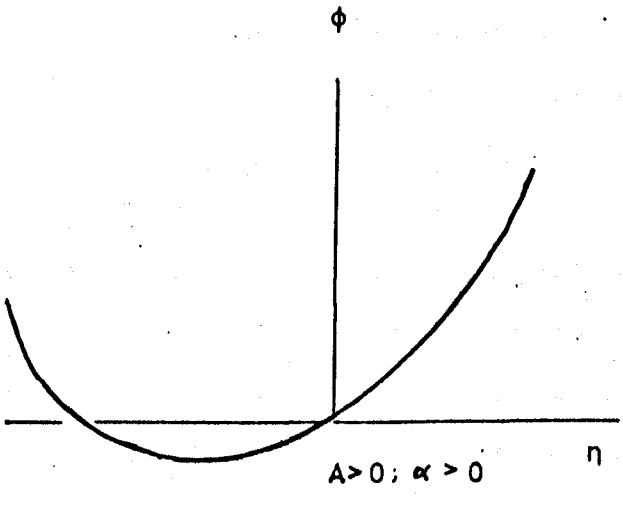

$A > 0 ; \alpha > 0$

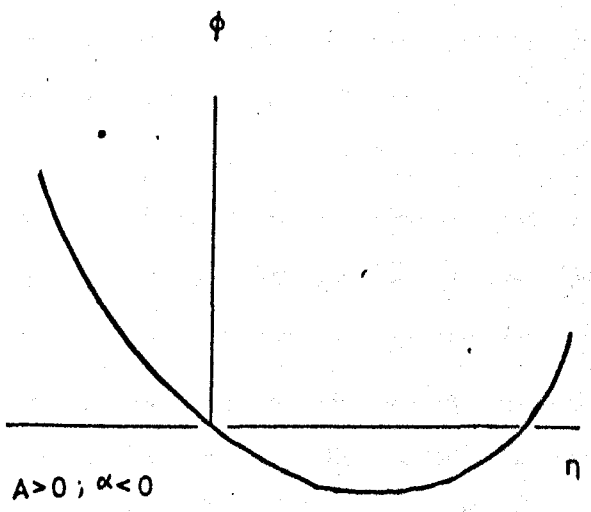

$A > 0 ; \alpha < 0$

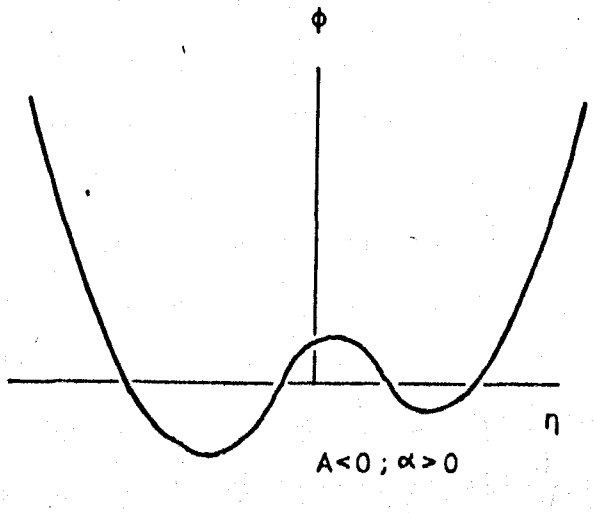

$A < 0 ; \alpha > 0$

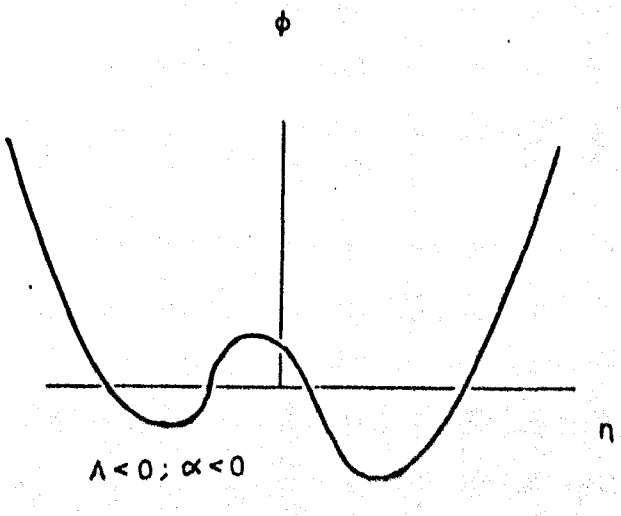

$A < 0 ; \alpha < 0$

The magnetic Gibbs potential function has the form

$$dG = -S.dT + V.dP - M.dH \qquad \text{A3.7}$$

and hence the equilibrium states are given by

$$\left(\frac{\partial G}{\partial V}\right)_{T,H} = \left(\frac{\partial G}{\partial S}\right)_{P,H} = \left(\frac{\partial G}{\partial M}\right)_{T,P} = 0 \qquad \text{A3.8}$$

In order that the behaviour of the system follow that of a Riemann-Hugoniot catastrophe there can be only two control parameters. Otherwise it is necessary to invoke one of the elementary catastrophes of higher dimension. In the particular cases of the present work the two control parameters were T and H.

$$dG = -S.dT - M.dH \qquad \text{A3.9}$$

The case of the general polynomial expansion for the Gibbs function then yields the forms shown in the diagrams above, depending solely on the coefficients α of magnetic field and A of temperature.

In those cases where $A \geq 0$ this corresponds to $T - T_C \geq 0$ and the system is paramagnetic. In those cases where $A < 0$ it is ferromagnetic.

Form of the Riemann-Hugoniot Surface for a Ferromagnet

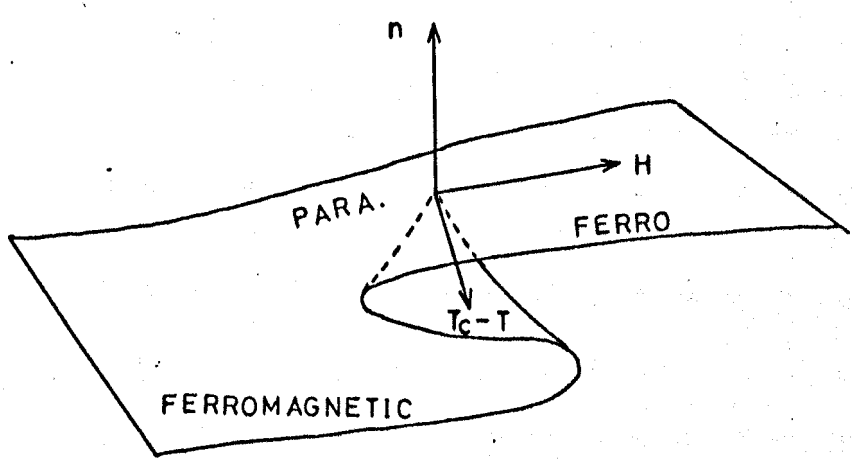

At the critical point of the transition $T_C - T = 0$, $H = 0$, $\eta = 0$. For $\eta = 0$ there is no net magnetic moment and for $\eta > 0$ there is net magnetic moment parallel to the field H.

$T_C - T$ is the splitting factor in Zeeman's definition [2,P19] while H is the normal factor.

Ferromagnetic to Paramagnetic Phase Transition

There can still be a ferromagnetic to paramagnetic phase transition in which there is no change of symmetry [1,P432]. This still constitutes an order-disorder transition. Consider for example a ferromagnet aligned antiparallel to a weak magnetic field. The field is maintained constant but the temperature is raised slowly.

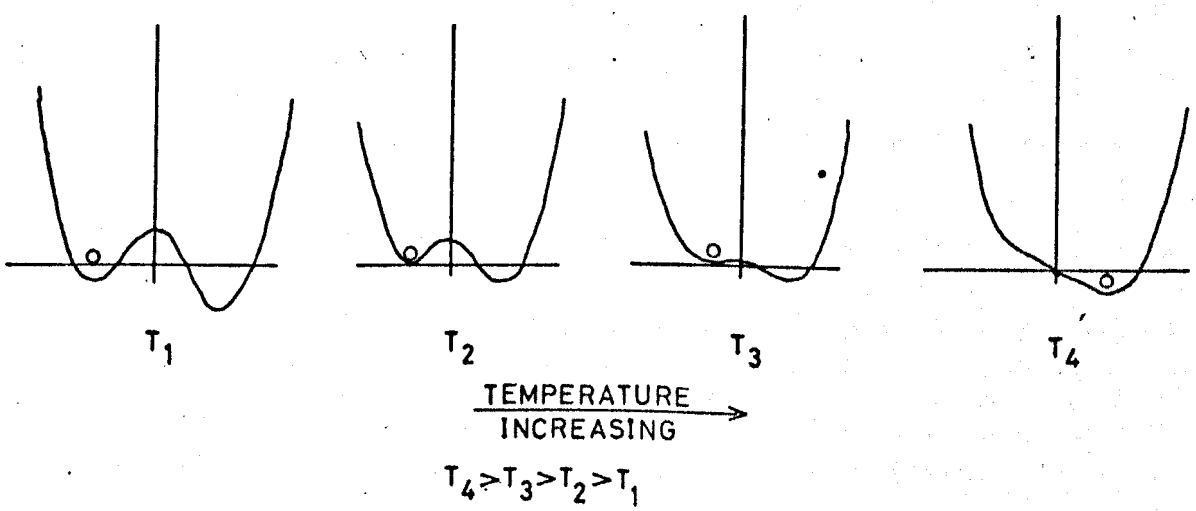

Transitions involving change of Symmetry

Transitions involving change of symmetry have to proceed in general via a second order phase change, for example the ferromagnetic paramagnetic transition in zero field.

The symmetry of the lower symmetry state usually modifies itself until it equals the symmetry of the higher symmetry state [e.g. Landau(1)] and hence such transitions are continuous, and do not exhibit hysteresis or metastable states.

Order-Disorder Transitions

It has been shown above that an order-disorder transition can occur without change of symmetry, for example the ferromagnetic to paramagnetic phase transition in a weak magnetic field. In those cases where $\alpha \neq 0$ this implies a discontinuous change in the ordering parameter η and hence in the entropy S to which it is related.

If as the temperature rises the degree of ordering vanishes by a discontinuous jump from some finite value to another value then the transition will be first order. If the degree of ordering vanishes continuously then it is a second order transition.

Critical and Isolated Points of a Second Order Transition

The potential ϕ given by equation 3.51 seems to give the simplest example of an isolated point of a second order transition. When $\alpha = 0$ the transition is second order and when $\alpha \neq 0$ it is first order. In the case of the control space being P,T instead of T,H then the transition can remain second order throughout since by the symmetry argument given in section 3.4.9 the coefficient α would be limited to zero over the whole control space.

It has been shown by Landau [1] and later by Schulman [4] that in order that a line representing second order transitions be able to reach a critical point and become a locus of first order transitions the dimensions of the control space need to be increased. Since it represents the boundary between phases of different symmetries a second order phase transition curve in the control space can not simply stop at a point.

For the investigation of such a point it has been shown by Landau [1] and confirmed by Schulman [4] on the basis of catastrophes, that such a

system requires a four dimensional control space, i.e. the "butterfly" catastrophe, rather than the "swallowtail" catastrophe which is the next in dimensionality after the "cusp" catastrophe. The potential is in this case

$$\phi = \phi_o \pm \alpha\eta \pm A\eta^2 \pm B\eta^3 \pm C\eta^4 + G\eta^6 \qquad \text{A3.10}$$

where the inclusion of the term $B\eta^3$ is allowed by Landau and this therefore forms the general equation of the potential for the butterfly catastrophe.

The locus of second order phase transitions requires

$$A_i = 0; \quad B_i = 0; \quad C > 0; \quad \alpha = 0 \qquad \text{A3.11}$$

At the tricritical point we must have C = 0 since otherwise this remains a second order transition in a neighbourhood of the point.

General Thermodynamic Behaviour of an Antiferromagnet

In the case of a magnetic material which exhibits both antiferro- and ferromagnetic phases below the ordering temperature, there will be a second order phase transition from paramagnetic to antiferromagnetic as the temperature is reduced through the Néel point T_N. Also application of a magnetic field to the antiferromagnetic phase will produce a ferromagnetic alignment at sufficient high field intensities. Further reduction of temperature in the antiferromagnetic phase will cause a transition to ferromagnetic ordering below the Curie point T_C.

At points in parameter space at which a second order transition changes to a first order transition it is called the critical point of the phase transition. In order to investigate such a transition Landau [P.452] again uses a polynomial expression for the Gibbs function of the form

$$\phi = \phi_o + A\eta + B\eta^2 + C\eta^4 + D\eta^6 \qquad \text{A3.12}$$

where A is the applied field, and on the locus of second order transitions B = 0, C > 0. At the critical point at which the second order transition ends C = 0, D > 0.

This expression for the Gibbs potential may be compared with Zeeman's expression [2p31] for the potential function of the butterfly catastrophe

$$\phi = x^6 - ax - bx^2 - cx^3 - dx^4 \qquad \text{A3.13}$$

where the constant c has been set to zero. Solving this potential function to give the phase transitions in (η, T, B) space where $b = T - T_N$ and $a = H$ gives the solution surfaces in (a,b,x) space in the mathematical model for various values of the parameters d. The two of interest here may be found in Zeeman [P.31] for $c = 0$ and either $d < 0$ or $d > 0$.

For $d < 0$ this again gives the solution surface of an isotropic ferromagnet.

For $d > 0$ this gives a new solution surface for the isotropic antiferromagnet.

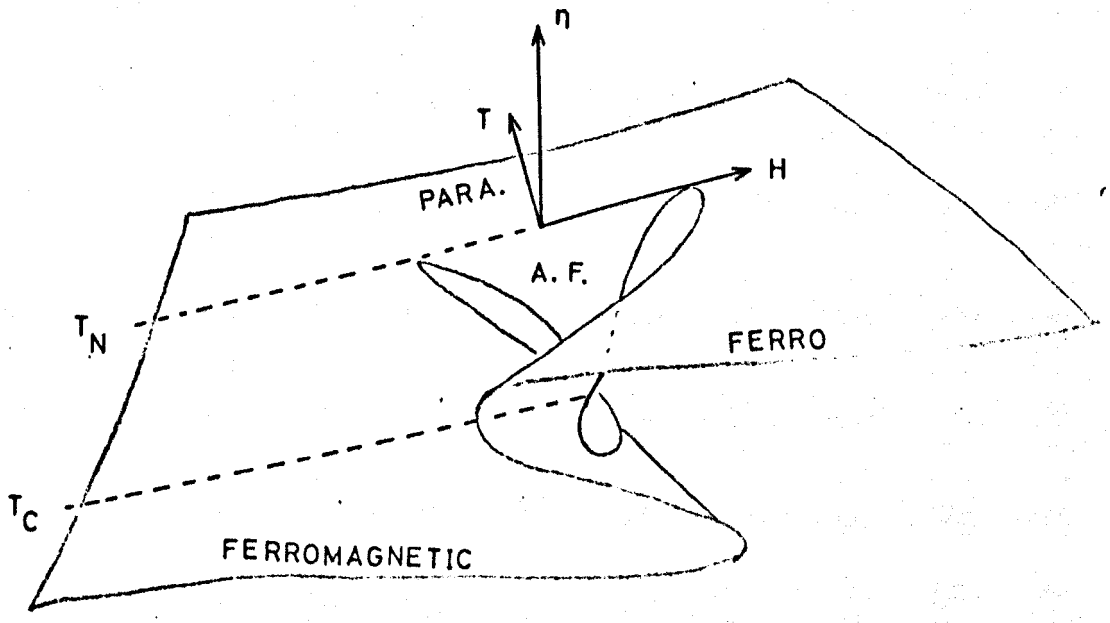

Appendix 4 The Contribution of Dislocation Mobility to the Elastic Properties of a Crystal

In studying the elastic properties of crystals under an applied stress, and in particular in the present work measuring the third order elastic constants, contributions to the elastic moduli due to the motion of dislocations (line defects) occur unless precautions are taken to minimise or eliminate the motion. It appears that the motion of these dislocations is the main cause of the defect contribution to the observed elastic moduli.

Classification and Observation

The dislocations in crystals may be divided into two broad categories, the edge dislocations and the screw dislocations [8,P21-25] depending on the relative orientation of the Burgers vector $\underline{b}$ and the dislocation line vector $\underline{\ell}$. In a screw dislocation $\underline{b}$ and $\underline{\ell}$ are parallel and in an edge dislocation they are perpendicular. In real dislocations the behaviour is generally a mixture of the two basic types in which $\underline{b}$ lies at some finite angle to $\underline{\ell}$. The dislocation may then be resolved into components parallel and perpendicular to $\underline{b}$ and treated as a combination of the resulting screw and edge components.

Dislocations lines can end at the surface of a crystal or at a grain boundary but can never finish at a point inside the crystal. Therefore they form closed loops either upon themselves or by branching into other dislocations.

The existence of these line defects has been confirmed by surface methods, e.g. by preferential etching, by X-Ray diffraction methods and by transmission electron microscopy.

Movement of Dislocations

Two types of motion of a dislocation are possible, glide and climb. Glide occurs in the plane defined by $\underline{b} \wedge \underline{\ell}$ and climb occurs in the direction

normal to this plane. Movements of dislocations through the vector $\underline{b}$ in the glide plane require only a small rearrangement of atomic bonds near the dislocation and the energy is therefore less than would be required to deform a perfect crystal in the same way.

General Case of Slip

In the general case of slip the boundary separating the slipped and unslipped regions is curved, that is the dislocation line is curved (see fig. A4.1). The Burgers vector however remains constant along the length of the dislocation line.

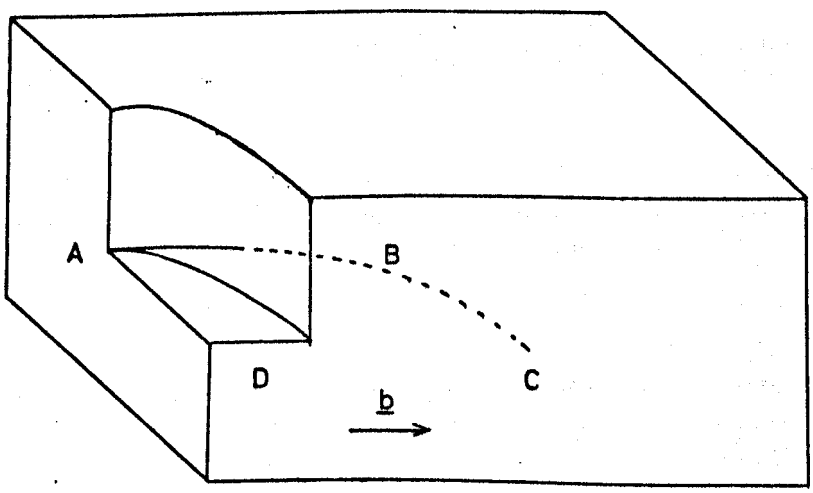

fig. A4.1

The curve ABC represents the dislocation line and $\underline{b}$ is the Burgers vector of the dislocation. At the point C the dislocation is normal to the vector $\underline{b}$ and hence is pure edge dislocation. At A the dislocation line is parallel to $\underline{b}$ and is thus pure screw dislocation. The remainder of the curve ABC has mixed edge and screw dislocation characteristics. Resolution of the line vector $\underline{\ell}$ at any point into components parallel and perpendicular to $\underline{b}$ will allow analysis.

Critical Stress and Stress Field

There is a critical stress, dependent on the properties of the particular solid under investigation which represents the onset of plastic deformation required to set the dislocations moving.

The displacement of a lattice required to produce a dislocation results in an elastic stress field being created round the dislocation. As the dislocation moves so the stress field moves through the solid [5,P72]. The dislocations therefore move as if there were an effective force acting upon them. Consider for example a dislocation moving in a slip plane under a uniform stress σ. If an element $d\ell$ of the dislocation line moves through a distance dx then the work done will be

$$dW = d\ell.dx.\ \sigma.b \qquad \text{A4.1}$$

and consequently the force per unit length of the dislocation $^{dF}/_{d\ell}$ is

$$\frac{dF}{d\ell} = \sigma.b \qquad \text{A4.2}$$

If the dislocation is in the form of a closed loop then, since $\underline{b}$ is constant at all points around the loop, under an applied stress the dislocation moves parallel or antiparallel to $\underline{b}$. This causes the loop of the dislocation to expand or contract accordingly.

Bowing of Dislocation Lines under Stress: Frank-Read Sources

When a crystal already contains a dislocation network and is plastically deformed one method by which its dislocations multiply is by a Frank-Read source as shown in fig. A4.2.

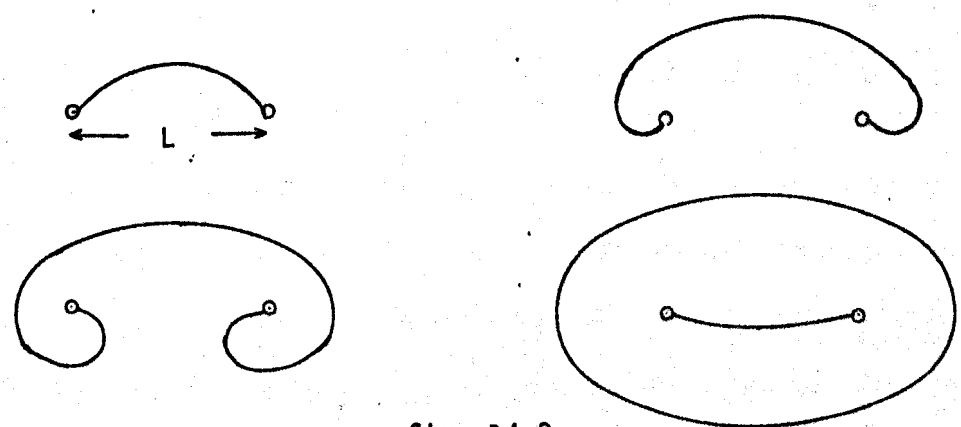

fig. A4.2

As the stress increases the radius of curvature of the dislocation line R is given by

$$R.\sigma = C.\underline{b} \qquad \text{A4.3}$$

where σ is the applied stress, C is the shear modulus and $\underline{b}$ the Burgers vector. (See for example [4,P62]). When R reaches the value $L/2$ the bulge will continue to expand without further increase of stress and eventually a complete glissile loop detaches itself and the process can repeat itself.

Dislocation Contribution to Elastic Moduli

In a perfect crystal if σ is the applied stress, u the strain and c the corresponding elastic modulus then

$$\sigma = C.u \qquad \text{A4.4}$$

In a real crystal however a contribution u_d to the shear strain must be added due to the bowing of the dislocation lines under stress as described above

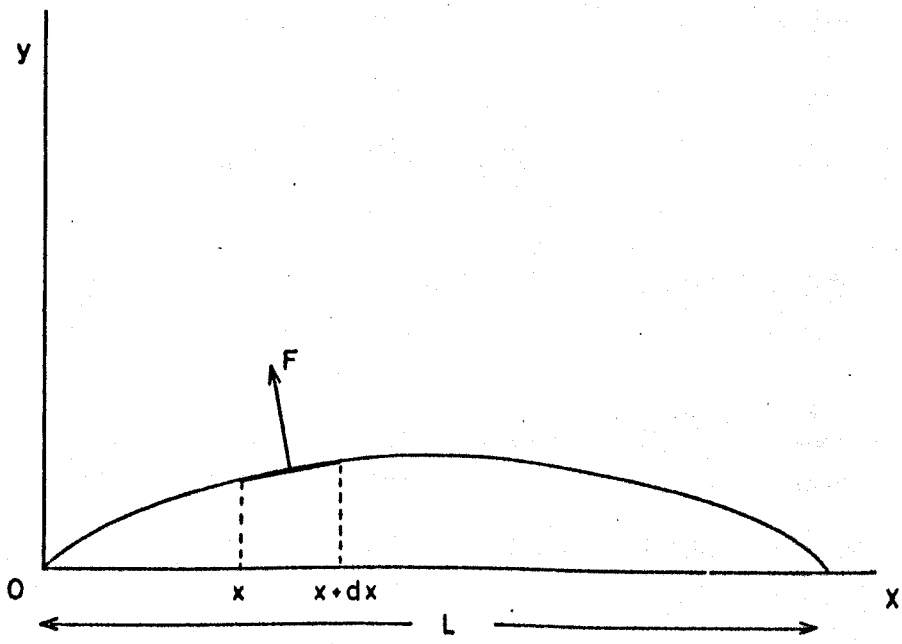

fig. A4.3

Considering the case of the bowed dislocation as shown in fig. A4.3 where $x_A y$ is the plane of the dislocation, the initial dislocation length is L along the x axis. This is displaced to the arc shown. The force F on an element of arc of length ds is given by integration of $\frac{dF}{d\ell}$ given in equation A4.2

$$F = \sigma.b.ds \qquad \text{A4.5}$$

which for small displacements will be perpendicular to Ox. There will also be a resultant restoring force due to the tension in the line T. $\frac{d^2y}{dx^2}.dx$.

Therefore equating these forces under equilibrium,

$$\sigma.b.ds = T \cdot \frac{d^2y}{dx^2} \cdot dx. \qquad \text{A4.6}$$

and for small displacements $ds \simeq dx$.

$$\sigma.b = T \cdot \frac{d^2y}{dx^2} \qquad \text{A4.7}$$

It can also be shown [eg. 4,P57] that $T \simeq C.b^2$ where C is the appropriate shear modulus. So that if k is a constant of order unity this gives

$$\frac{d^2y}{dx^2} = \frac{k.\sigma}{b.C} \qquad \text{A4.8}$$

using the boundary conditions $y=0 \quad x=0,1$ and solving this equation gives

$$y = \frac{k.\sigma}{2.b.C} x(1-x) \qquad \text{A4.9}$$

The area swept out by this segment therefore gives the shear strain due to the dislocation

$$\Delta u_d = \frac{k.\sigma.\ell^3}{12\,G} \qquad \text{A4.10}$$

and summing over all the dislocations present will give the total contribution to the strain by the dislocations in the solid

$$u_d = \frac{\sigma}{C} \int_0^\infty \frac{k.\ell^3}{12} N(\ell)d\ell \qquad \text{A4.11}$$

where $N(\ell)$ is the number of dislocation segments of length ℓ per unit volume of the crystal. If D represents the value of the integral then this gives

$$u_d = \frac{\sigma}{C} \cdot D \qquad \text{A4.12}$$

and adding this to the ideal strain from the equation A4.4

$$u_{tot} = \sigma\left(\frac{1+D}{C}\right) \qquad \text{A4.13}$$

and consequently an effective modulus of elasticity C_{eff} may be defined such that $u_{tot} = \sigma/C_{eff}$

$$C_{eff} = \frac{C}{1+D} \qquad \text{A4.14}$$

the value of the effective or observed modulus of elasticity and its proximity to the value for the perfect crystal depend on the value of the integral D

$$D = \int_0^\infty \frac{k.\ell^3}{12} N(\ell)d\ell \qquad \text{A4.15}$$

Expressions for $N(\ell)$ given by Thompson [4] give rise to the following solutions:

(i) For well annealed crystals

$$C_{eff} = \frac{C}{1 + \frac{k\rho\ell_o^2}{12}} \qquad \text{A4.16}$$

(ii) For random defects, e.g. by radiation damage

$$C_{eff} = \frac{C}{1 + \frac{k\rho\ell_o^2}{2}} \qquad \text{A4.17}$$

where ρ is the dislocation density and ℓ_o is the segment length of dislocation. It should be remarked here that subjecting a solid to radiation damage decreases the segment length ℓ_o of the dislocations and thus the value of C_{eff} in an irradiated crystal may be closer to C than in an unirradiated crystal.

Pinning of Dislocations

Using fast neutrons from the core of a nuclear reactor direct collisions can produce recoils of up to 10^5eV. Thermal neutrons (energy

0.02eV, have insufficient energy to displace atoms in direct collisions and their contribution is mainly through nuclear reactions of the (n,γ) type. These reactions produce small groups of vacancy-interstitial pairs.

Changes in elastic modulus show a tendency to saturate with increasing dose rate, for example the work on copper by Holmes [10] from which fig. A4.4 is taken.

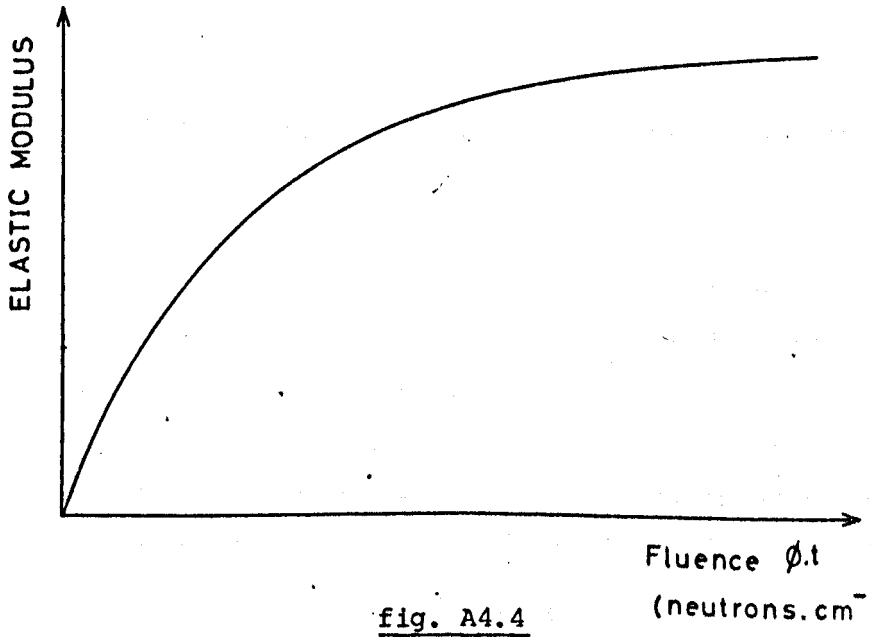

fig. A4.4

This shows the trend in values of the Young's Modulus of copper as a function of exposure $\phi.t$ at 25°C.

Dislocation pinning causes a change in the length of the dislocation ℓ_o in equation A4.17. The segment length is inversely proportional to the number of pinning points n which is given by

$$n = n_o(1 + \gamma\phi t) \qquad \text{A4.18}$$

where n_o is the number of pinning points before irradiation and γ is the efficiency of producing point defects. Since $\ell_o \alpha {}^1/_n$ these values may be substituted into equation A4.17 to give

$$\frac{C_{eff}(\phi.t) - C}{C_{eff}(0) - C} = \frac{1}{(1 + \gamma\phi.t)^2} \qquad \text{A4.19}$$

where $C_{eff}(\phi t)$ is the observed modulus after irradiation and $C_{eff}(0)$ before irradiation. This last equation has been experimentally verified

by Thompson and Paré [9] showing that as $\phi.t$ is increased the value of C_{eff} approaches the value C for the perfect crystal.

Therefore the effect of dislocation mobility on the elastic constants of single crystals can be significantly reduced or even eliminated by irradiation with a high flux of neutrons of suitable energies.

Appendix 5 The General Form of the Crystal Field Potential

The electrostatic potential experienced by an electron in a solid is determined by the array of charges around it. The charges around any particular lattice site will give rise to an electric field at that point with a symmetry determined by the crystal class. This potential is experienced by the 4f electrons in rare earth crystals and therefore can affect the magnetic behaviour of the crystal.

Gauss's law gives the relation between the flux of an electric field $\underline{E}$ through a closed surface so the charge enclosed by the surface and the form of this law is well known,

$$\int_S \underline{E}.d\underline{a} = \frac{1}{\varepsilon_o} \int_\tau \rho.d\tau \qquad \text{A5.1}$$

where ρ is the charge density and τ is the total volume enclosed by the surface s. By application of the divergence theorem

$$\int_S \underline{E}.d\underline{a} = \int_\tau \nabla.\underline{E}d\tau \qquad \text{A5.2}$$

and hence by combination of A5.1 and A5.2, where both integrals are over the same volume, this yields

$$\nabla.\underline{E} = \frac{\rho}{\varepsilon_o} \qquad \text{A5.3}$$

and by replacing $\underline{E}$ by ∇V this gives Poisson's equation

$$\nabla^2 V = \frac{\rho}{\varepsilon_o} \qquad \text{A5.4}$$

There is no general analytical solution of Poisson's equation [1,P.51] although it may be solved in particular cases.

Three Dimensional Solutions of Laplaces Equation

Many examples of two dimensional solutions of Laplace's equation exist [e.g. 1 P163,2 P223]. In this particular case however a solution of Laplaces equation should be as general as possible and so a solution in spherical polar coordinates in three dimensions has been outlined below.

The Laplace equation for the electric potential in spherical coordinates is, [1.P.32]

$$\frac{1}{r^2}\frac{\partial}{\partial r}\left(r^2\frac{\partial V}{\partial r}\right)+\frac{1}{r^2.\sin\theta}\frac{\partial}{\partial\theta}\left(\sin\theta.\frac{\partial V}{\partial\theta}\right)+\frac{1}{r^2.\sin^2\theta}\frac{\partial^2 V}{\partial\phi^2}=0 \qquad \text{A5.5}$$

Employing methods similar to those used for two dimensional solutions express the potential V as a product of three functions each dependent on only one of the three variables, r,θ,ϕ.

$$V(r,\theta,\phi) = \frac{R(r)}{r}.\Theta(\theta).\Phi(\phi) \qquad \text{A5.6}$$

and substituting this into the Laplace equation gives

$$r^2.\sin^2\theta\left[\frac{1}{R}\frac{d^2R}{dr^2}+\frac{1}{r^2.\sin\theta}\cdot\frac{1}{\Theta}\frac{d}{d\theta}\left(\sin\theta.\frac{d\Theta}{d\theta}\right)\right]+\frac{1}{\Phi}.\frac{d^2\Phi}{d\phi^2}=0 \qquad \text{A5.7}$$

The last term depends only on ϕ while ϕ does not appear anywhere else in the expression. Therefore in order to satisfy the expression for all values of ϕ this term must be constant

$$\frac{1}{\Phi}.\frac{d^2\Phi}{d\phi^2} = -m^2 \qquad \text{A5.8}$$

and for real values of m, $m^2 > 0$ gives the solutions

$$\Phi = A\exp(im\phi)+B\exp(-im\phi) \qquad \text{A5.9}$$

Substituting the value $-m^2$ for the term in ϕ in the equation A5.7

$$\frac{r^2}{R}\frac{d^2R}{dr^2}+\frac{1}{\Theta}.\frac{1}{\sin\theta}.\frac{d}{d\theta}\left(\sin\theta.\frac{d\Theta}{d\theta}\right)-\frac{m^2}{\sin^2\theta}=0 \qquad \text{A5.10}$$

By a similar argument the term in r must also be a constant. Therefore let the value be $\ell(\ell+1)$

$$\frac{d^2R}{dr^2}-\frac{\ell(\ell+1)}{r^2}R=0 \qquad \text{A5.11}$$

$$\frac{1}{\sin\theta}\frac{d}{d\theta}\left(\sin\theta\frac{d\Theta}{d\theta}\right)+\left[\ell(\ell+1)-\frac{m^2}{\sin^2\theta}\right]\Theta=0 \qquad \text{A5.12}$$

which leaves the two above differential equations to solve for R and separately. The general solution to A5.11 is

$$R(r) = Ar^{\ell+1}+Br^{-\ell} \qquad \text{A5.13}$$

To solve the differential equation A5.12 make the substition $x = \cos\theta$ and let $P(x) = \Theta(\cos\theta)$. The resulting differential equation is then,

$$\frac{d}{dx}\left[(1-x^2) \frac{dP}{dx} \right] + \left[\ell(\ell+1) - \frac{m^2}{1-x^2} \right] P = 0 \qquad \text{A5.14}$$

which is a form of Legendre's equation [see 1 P167, 2 P234] for which the solutions are Associated Legendre Polynomials dependent on the values of both m and ℓ

$$\Theta(\theta) = P_\ell^m(\cos\theta) \qquad \text{A5.15}$$

Consequently the most general solution for the three dimensional Laplace equation in spherical coordinates is

$$V(r,\theta,\phi) = \sum_{\ell} \sum_{m \leq \ell} (Ar^{\ell} + Br^{-(\ell+1)}) P_\ell^m(\cos\theta) (C \exp im\phi + D \exp -im\phi) \qquad \text{A5.16}$$

where A,B,C,D are constants and m and ℓ are positive integers, with $m \leq \ell$.

Associated Legendre Polynomials

ℓ	m	P_ℓ^m
0	0	1
1	0	$\cos\theta$
1	1	$\sin\theta$
2	0	$\frac{3}{2}\cos^2\theta - \frac{1}{2}$
2	1	$\sin 2\theta$
2	2	$\cos 2\theta - 1$

When m = 0 these become identical to the Legendre Polynomials.

Form of the Crystal Field

If it is assumed that the 4f electrons do not overlap neighbouring ions in the lattice then the potential experienced by those electrons satisfies Laplaces equation and can be expressed in the form

$$V(\underline{r}) = \sum_{\ell} \sum_{m=-\ell}^{+\ell} A_\ell^m . r^\ell . Y_\ell^m(\theta,\phi) \qquad \text{A5.17}$$

where the A^m depend on the distribution of external charge and the $r^\ell Y_\ell^m(\theta,\phi)$ are the various multipoles of the electron distribution.

Summing over n 4f electrons to obtain the total potential gives V_c

$$V_c = \sum_i V(\underline{r}_i) \qquad \text{A5.18}$$

Restriction on terms in V due to Hexagonal Symmetry

In the case of hexagonal symmetry and in particular in the case of the heavy rare earths the terms in the potential energy of a single electron at (r,θ,ϕ) expanded in spherical harmonics as in equation A5.17 are restricted to give [6]

$$V(\underline{r}) = A_2^0 r^2 Y_2^0(\theta,\phi) + A_4^0 r^4 Y_4^0(\theta,\phi) + A_6^0 r^6 Y_6^0(\theta,\phi) + A_6^6 r^6 \left[Y_6^6(\theta,\phi) + Y_6^{-6}(\theta,\phi) \right] \qquad \text{A5.19}$$

As each harmonic $r^\ell Y_\ell^m(\theta,\phi)$ gives a multipole of the electron distribution they may be expanded out, for example for $\ell=2$, $m=0$

$$r^2 Y_2^0(\theta,\phi) = \frac{1}{2}(3z^2 - r^2) \qquad \text{A5.20}$$

which is the quadrupole moment of the electron charge cloud.

Transformation to Operator Equivalents

In evaluating the terms of the potential V_c between multiplet states $|J,M_J\rangle$ the integration has been found to be most easily achieved by transforming to operator equivalents of the multipole terms [5]. For a particular multiplet the matrix elements of the potential V_c are

proportional to the so called "operator equivalents" obtained by replacing x,y,z in the multipole terms by J_x, J_y and J_z.

For example, again using the V_2^0 term,

$$A_2^0.r^2.Y_2^0(\theta,\phi) = A_2^0.\frac{r^2}{2}.(3\cos^2\theta - 1)$$

$$= A_2^0.\frac{1}{2}.(3z^2 - r^2) \qquad \text{A5.21}$$

and replacing z^2 by J_z^2 and r^2 by $J(J+1)$ this gives,

$$= A_2^0.\frac{1}{2}.\alpha_J\,(3J_z^2 - J(J+1)\langle r^2\rangle$$

where $\langle r^2\rangle$ is the value of r^2 averaged over the 4f wave functions. The multipole term is therefore transformed to

$$3z^2 - r^2 \rightarrow \alpha_J.\langle r^2\rangle.[3J_z^2 - J(J+1)]$$

$$= \alpha_J.\langle r^2\rangle.O_2^0 \qquad \text{A5.22}$$

The values of the other operators O_ℓ^m are given elsewhere [4,5]. The operator equivalent expression for the crystal field Hamiltonian is thus

$$V_c = \sum_\ell \sum_m B_\ell^m.O_\ell^m \qquad \text{A5.23}$$

where the B_ℓ^m are related to the crystal field parameters by

$$B_\ell^m = A_\ell^m \langle r^\ell\rangle.\theta_\ell \qquad \text{A5.24}$$

and $\theta_2 = \alpha_J$, $\theta_4 = \beta_J$, $\theta_6 = \gamma_J$ are constants which have been evaluated [6]. Expanding out the expressions A5.23 for the heavy rare earths gives,

$$V_c = A_2^0\langle r^2\rangle.\alpha_J O_2^0(\underline{J}) + A_4^0\langle r^4\rangle.\beta_J.O_4^0(\underline{J}) + A_6^0\langle r^6\rangle.\gamma_J O_6^0(\underline{J})$$

$$+ A_6^6\langle r^6\rangle.\gamma_J.[O_6^6(\underline{J}) + O_6^{-6}(\underline{J})]$$

These various terms acted upon by the gradient of the electric field in their particular crystallographic directions cause changes in the energy of electrons in different orbitals, which differ with differing ℓ values. Consequently this breaks the degeneracies of electron states in a spherically symmetric potential.

Appendix 6 Calibrations

Calibration of Thermocouples

Two thermocouples were used in the present work, copper v. constantan for temperatures from 273°K to 77°K and gold-(0.03%)iron v. chromel for temperatures between 77°K and 4.2°K. Although a good approximation to the temperature was achieved by using a curve fit of the type mentioned in section 5.5.2 and given by equation 5.2, the exact calibrations were made against a platinum resistance thermometer [1]. This is a practical thermometer whose fractional change in resistance over the range 10.5°K - 273°K on the thermodynamic scale of temperature was agreed by the Consultative Committee on Thermometry 1964 from which the data used for correlating resistance of platinum and the absolute temperature has been taken [2]. This is in the form of the Z function given by

$$Z(T) = \frac{R_{(T)} - R_{4.2}}{R_{273} - R_{4.2}} \qquad \text{A6.1}$$

where $R_{(T)}$ is the resistance at temperature T, $R_{4.2}$ is the resistance at the helium point and R_{273} at the ice point. Tabulated values of Z against T over the range 4.2°K - 273°K are available.

Calculation of T as a function of Z

Since the value of Z can be calculated from measurements it is then necessary to convert the observed values into a temperature T. From the tabulated values of Z function against temperature T polynomial curve fittings of the form

$$T = A + BZ + CZ^2 + DZ^3 + FZ^4 + GZ^5 \qquad \text{A6.2}$$

were made over the four intervals bounded by the temperatures 4.2°K, 23°K, 48°K, 150°K and 273°K and the sets of coefficients A, B, C, D, F and G for each section found. From a knowledge of these the temperature

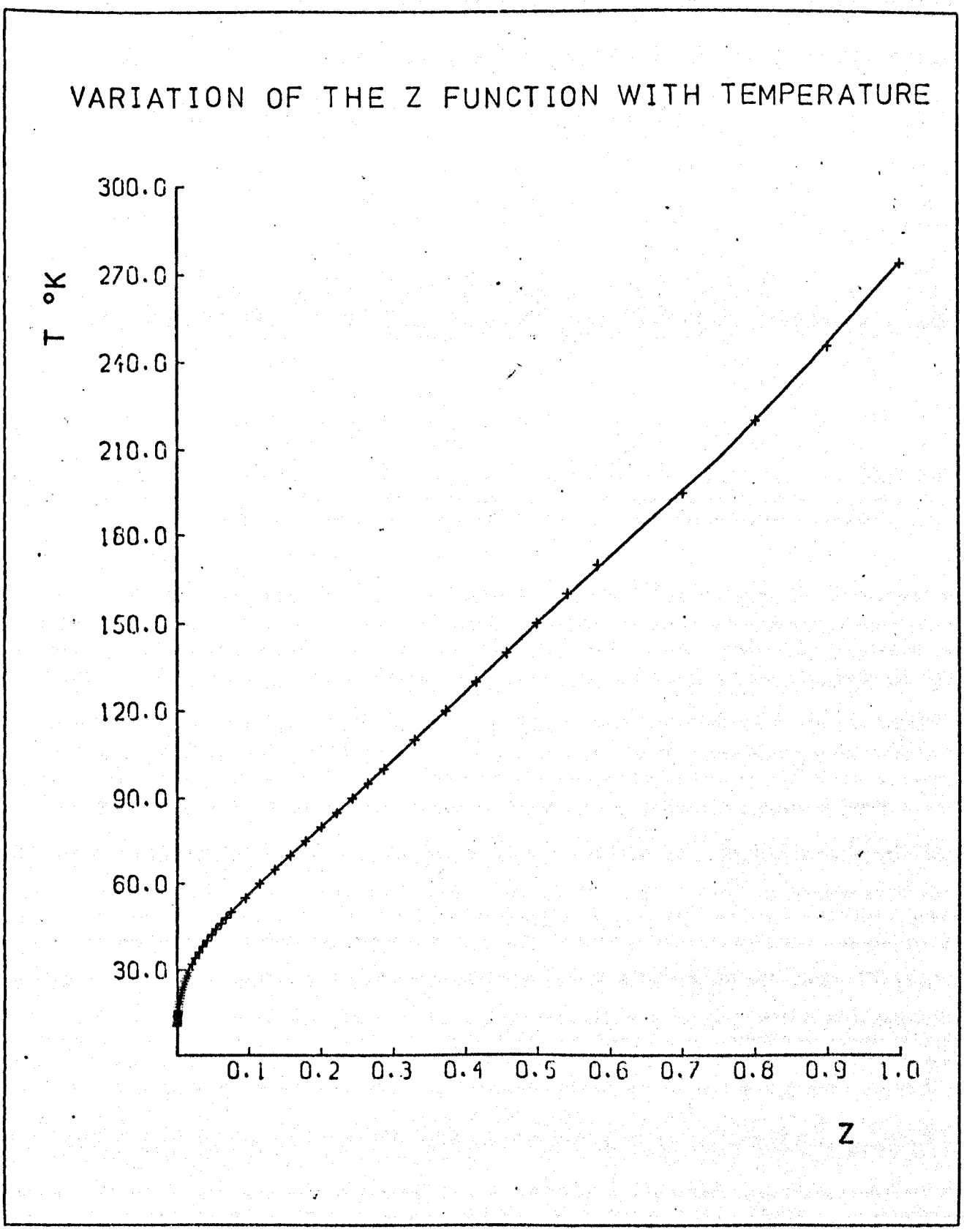
VARIATION OF THE Z FUNCTION WITH TEMPERATURE
T °K
300.0
270.0
240.0
210.0
180.0
150.0
120.0
90.0
60.0
30.0
0.1
0.2
0.3
0.4
0.5
0.6
0.7
0.8
0.9
1.0
Z

fig. A6.1

corresponding to any particular value of Z could be found over the range $4.2^{o}K - 273^{o}K$. A graph of the Z data against temperature is shown in figure A6.1 and the polynomial approximations are given by the curve.

Measurement of Resistance of the Platinum Thermometer

The platinum resistance thermometer and thermocouple were placed close together in the cryostat and readings of thermocouple emf. against resistance of the platinum were taken at predetermined intervals from $4.2^{o}K$ to $273^{o}K$. The circuit used for measurement of resistance is given in fig. A6.2. The voltages V_s across the standard resistor of 100Ω and across the platinum thermometer V_{pt} were made using a potentiometer so that no current was drawn from the circuit. A constant current source of $100\mu A$ was used throughout. The resistance of the platinum was calculated from

$$R_{pt} = \frac{R_s}{V_s} V_{pt} \qquad A6.3$$

From the value of the Z function calculated from each value R_{pt} the temperature was found using the appropriate coefficients from equation A6.2. Tabulatedvalues of thermocouple emf. against temperature were then obtained.

Thermocouple Emf. as a Function of Temperature

The variation of thermocouple emf. as a function of temperature calculated in this way is given for Gold-iron v. chromel in fig. A6.3 and for copper v. constantan in fig. A6.4. The curve fit to the data to give a generating function is given in this case by a polynomial of the form

$$E = A + BT + CT^2 + DT^3 + FT^4 \qquad A6.4$$

over all the data points using a least squares method. This is also compared in both figures with the approximate fit of equation 5.2 using

CIRCUIT DIAGRAM FOR THE DETERMINATION OF RESISTANCE OF THE PLATINUM THERMOMETER

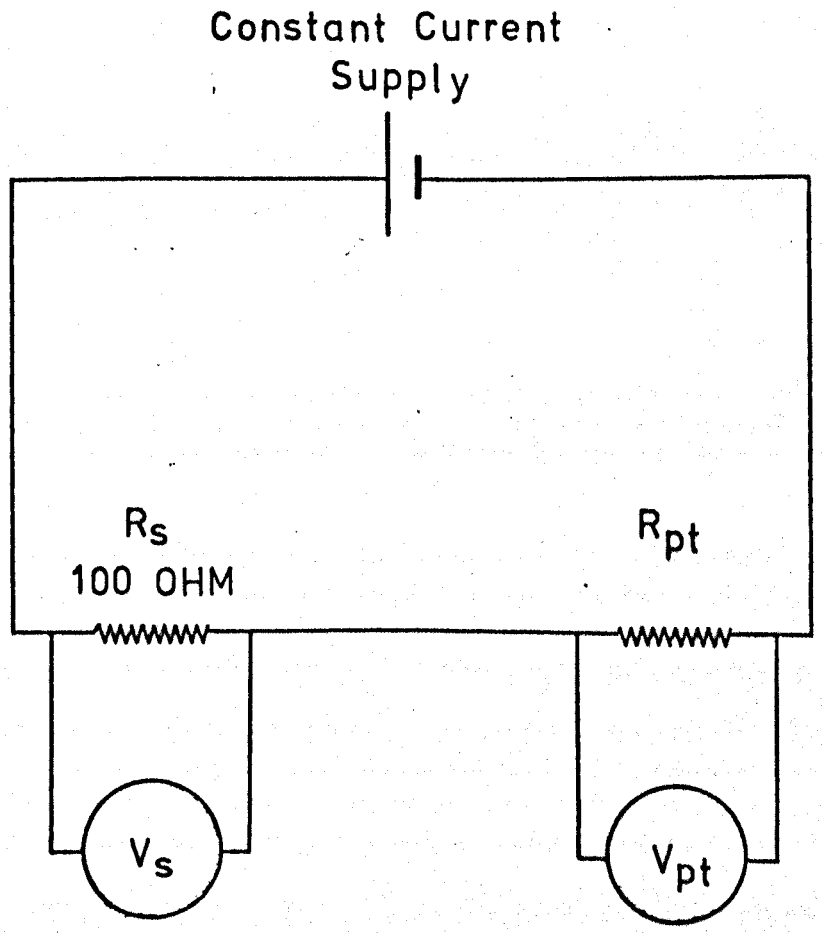

fig. A6.2

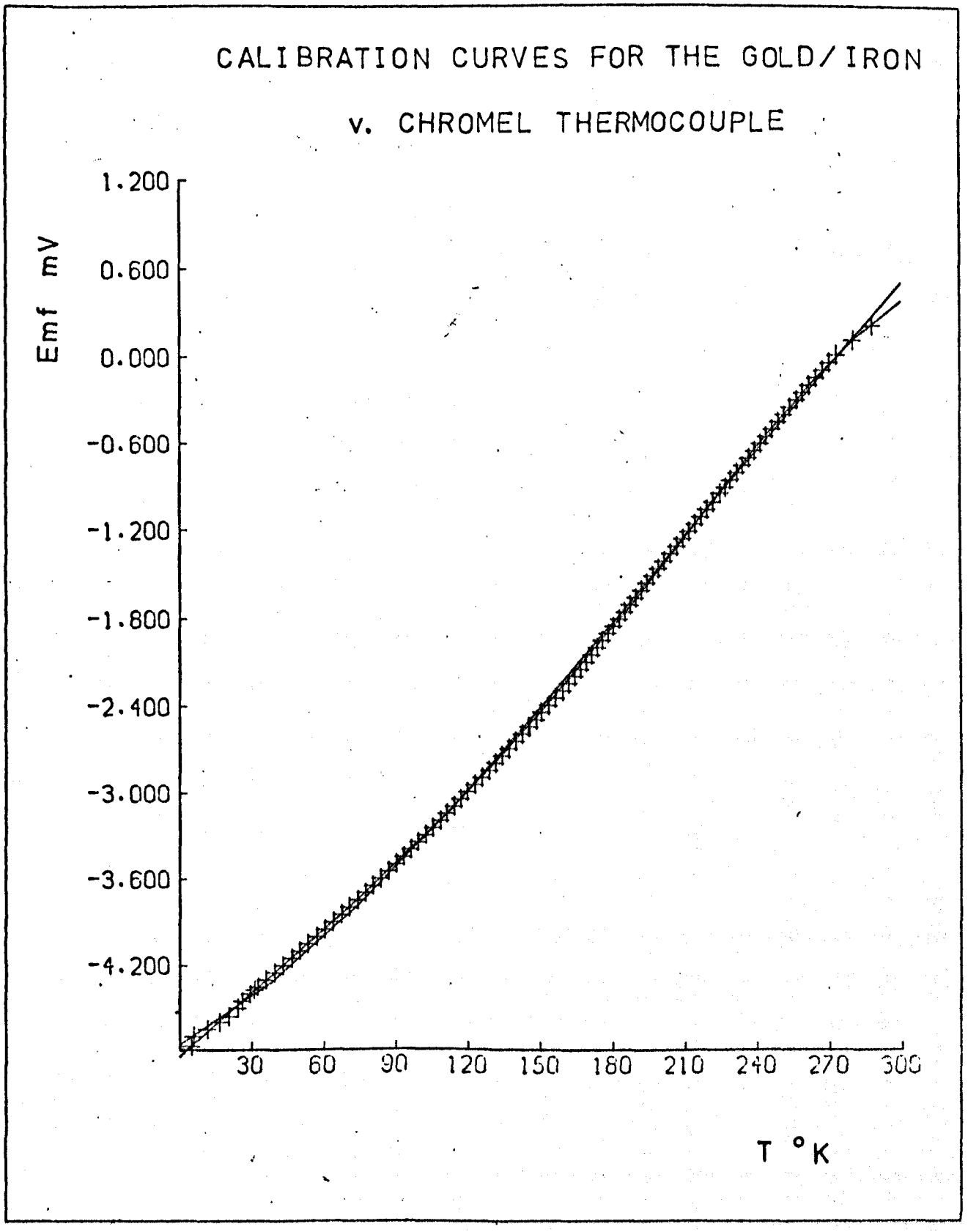
CALIBRATION CURVES FOR THE GOLD/IRON
v. CHROMEL THERMOCOUPLE
Emf mV
1.200
0.600
0.000
-0.600
-1.200
-1.800
-2.400
-3.000
-3.600
-4.200
30
60
90
120
150
180
210
240
270
300
T °K

fig. A6.3

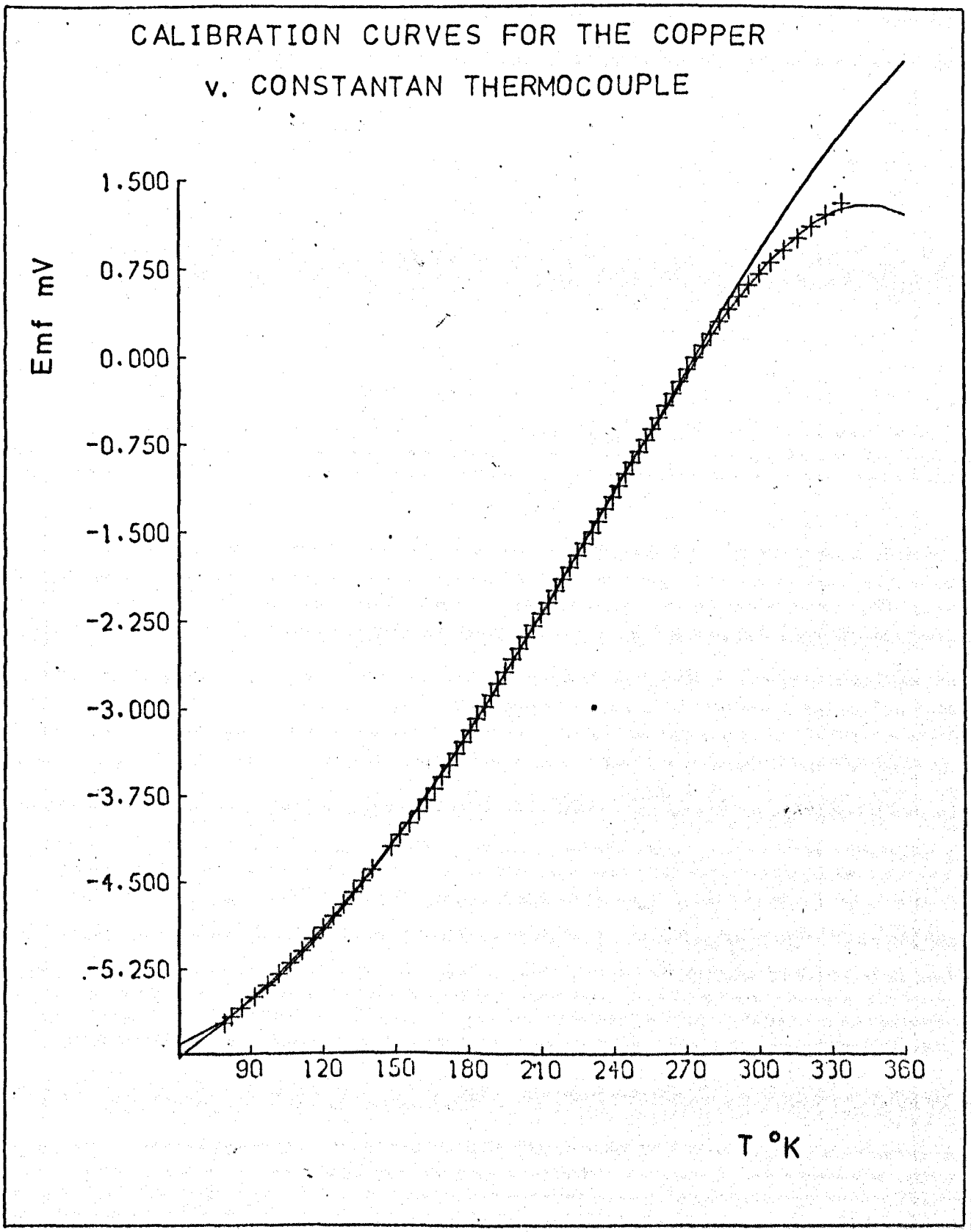
CALIBRATION CURVES FOR THE COPPER
v. CONSTANTAN THERMOCOUPLE
Emf mV
1.500
0.750
0.000
-0.750
-1.500
-2.250
-3.000
-3.750
-4.500
-5.250
90
120
150
180
210
240
270
300
330
360
T °K

fig. A6.4

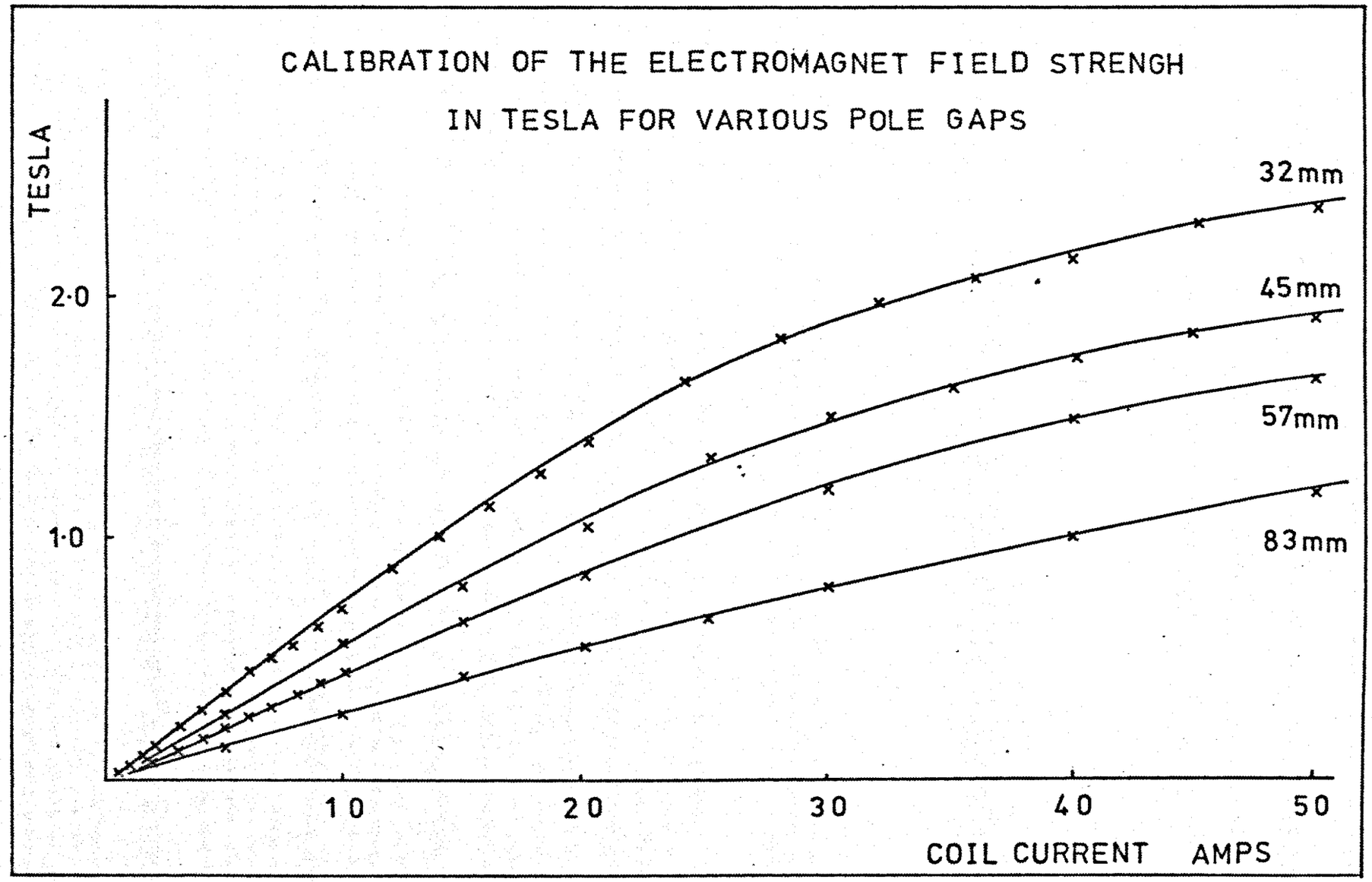
CALIBRATION OF THE ELECTROMAGNET FIELD STRENGH
IN TESLA FOR VARIOUS POLE GAPS
TESLA
2·0
1·0
32mm
45mm
57mm
83mm
10
20
30
40
50
COIL CURRENT AMPS

fig. A6.5

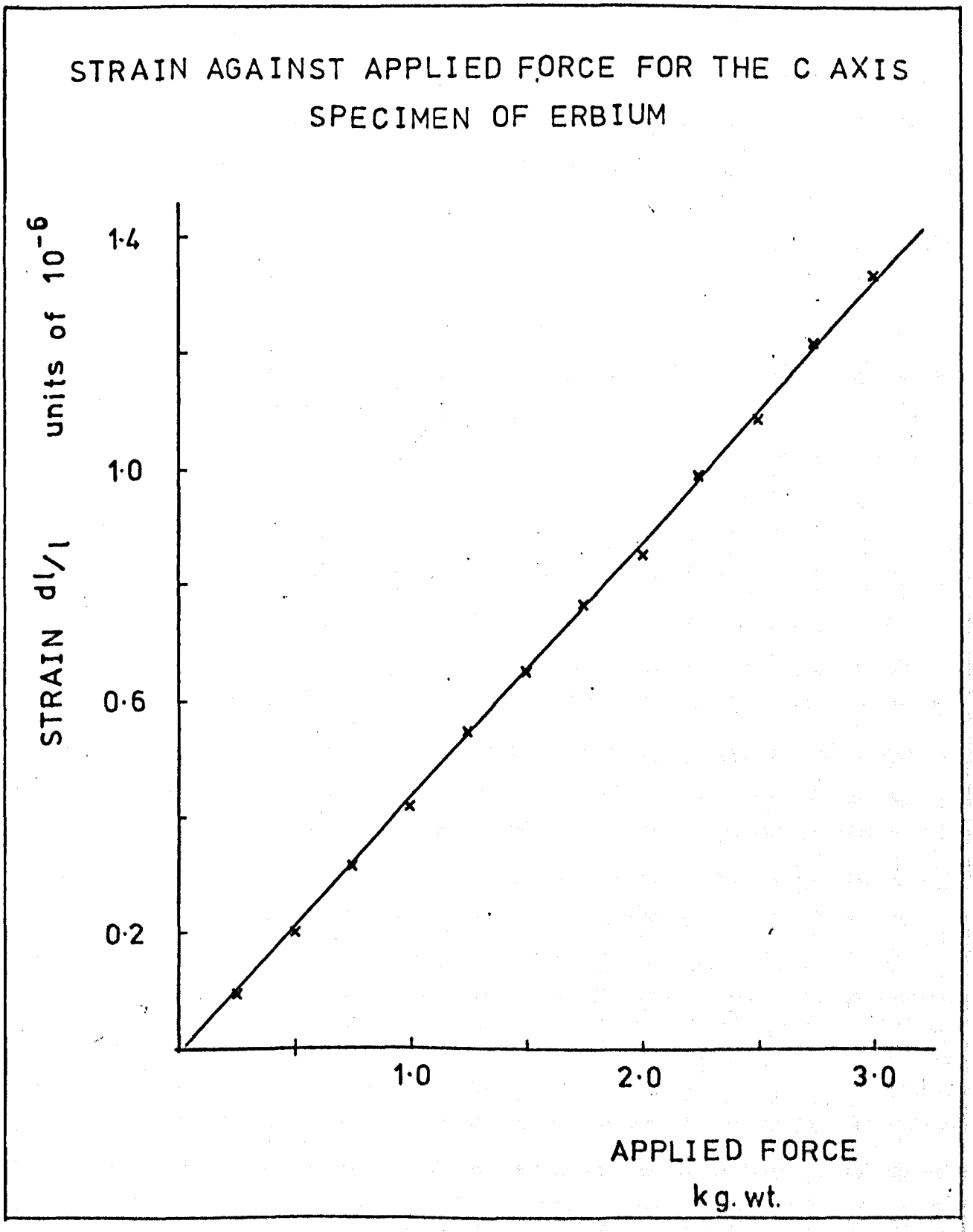
STRAIN AGAINST APPLIED FORCE FOR THE C AXIS SPECIMEN OF ERBIUM
STRAIN dl/l units of 10^{-6}
1·4
1·0
0·6
0·2
1·0
2·0
3·0
APPLIED FORCE
kg. wt.

fig. A6.6

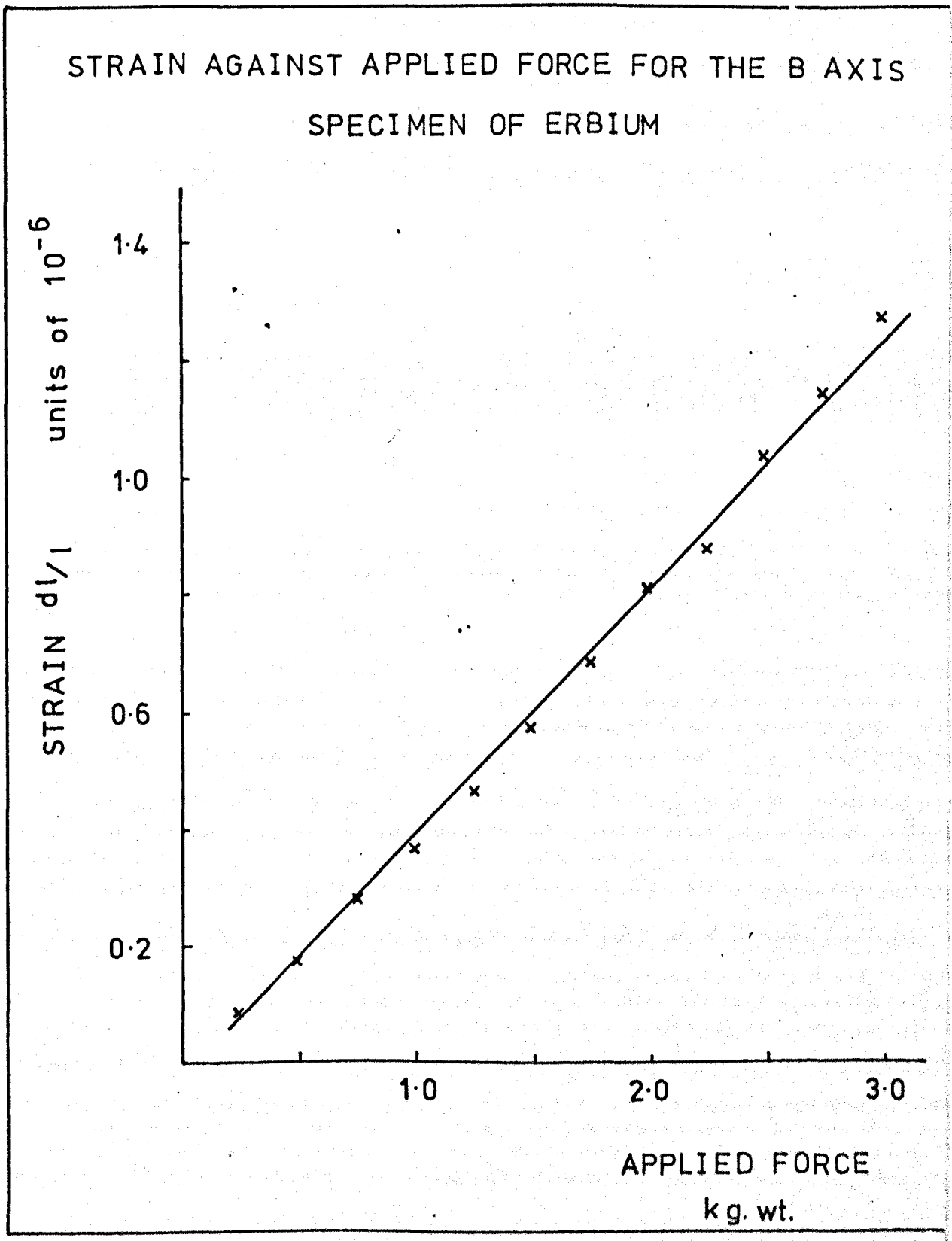
STRAIN AGAINST APPLIED FORCE FOR THE B AXIS
SPECIMEN OF ERBIUM
STRAIN dl/l units of 10⁻⁶
1·4
1·0
0·6
0·2
1·0
2·0
3·0
APPLIED FORCE
kg. wt.

fig. A6.7

four points over the range $4.2^{o}K - 273^{o}K$ so that the relative merits of the two methods can be seen. It will be noticed that once the measurements are outside the range of the approximate calibration they diverge rapidly from the curve. This is particularly clear in fig. A6.4.

Calibration of the Electromagnet

The calibration of the magnetic field in terms of the coil current supplied to the electromagnet was made using a Scalamp Fluxmeter and search coils manufactured by Pye [4]. The fluxmeter was itself calibrated directly in Tesla for the 10 turns.cm^{-2} coil and in 0.1 Tesla for the 100 turns.cm^{-2} second coil. Values of the magnetic field against current for various pole separations are shown in fig. A6.5.

Calibration of the Uniaxial Press

Calibration of the uniaxial pressure equipment was made using strain gauges by the method given in sections 5.5.8 and 5.5.9. The small size of the rare earth specimens made it necessary to use the smallest gauges available, these were SK-09-015EH-120 manufactured by Micromeasurements [5]. The graphs of the strain against applied force in kg.wt. are given along the c axis of Erbium in fig. A6.6 and along the b axis in fig. A6.7.

Appendix 7 Hydrostatic Pressure Derivatives of Erbium, Dysprosium and Terbium with Pressures up to 4.5 MPa

In this appendix some results of the pressure derivatives of the elastic moduli of Erbium, Dysprosium and Terbium with pressures up to 4.5 MPa are presented. These were obtained using a gas pressure cell connected to a cylinder of nitrogen, a technique that has previously been used by several groups of workers including Swartz and Elbaum [1], Naimon [2], Hiki and Granato [3] and Hames [4]. The pressure range of 0 - 4.5 MPa was also typically the same as in the earlier measurements.

Changes in temperature of the cell over the whole range of measurements during these experiments did not exceed 0.02mV on a copper v. constantan thermocouple, which corresponds to $< 0.5^{o}K$. The temperature decreased as the pressure was decreased during the measurements. As the temperature derivative of the elastic constants is negative for all three materials at room temperature, the pressure derivatives so measured would be likely to be smaller than the true value, although the actual recorded results showed values larger than the previously reported derivatives of Fisher et al [5].

The results are presented in figs. A7.1 - A7.8. The calculated pressure derivatives were obtained by averaging the results of typically five experimental runs. The derivatives are shown in fig. A7.9. Grüneisen parameters calculated from these derivates are shown in fig. A7.10.

The results reported here have been shown to be reproducible. Each value of the derivative is the result of averaging several calculated derivatives and the standard deviation has also been indicated. The whole work represents over two hundred separate sets of experimental data all of which show discrepancies from earlier published results and from the high pressure derivatives obtained in chapter ten.

Attempts to isolate any systematic error which could be causing the unexpectedly large values of the pressure derivatives have been unsuccessful, and no reason has yet been found to explain this disagreement with earlier

results. It is conceded however that such a systematic error may have escaped detection.

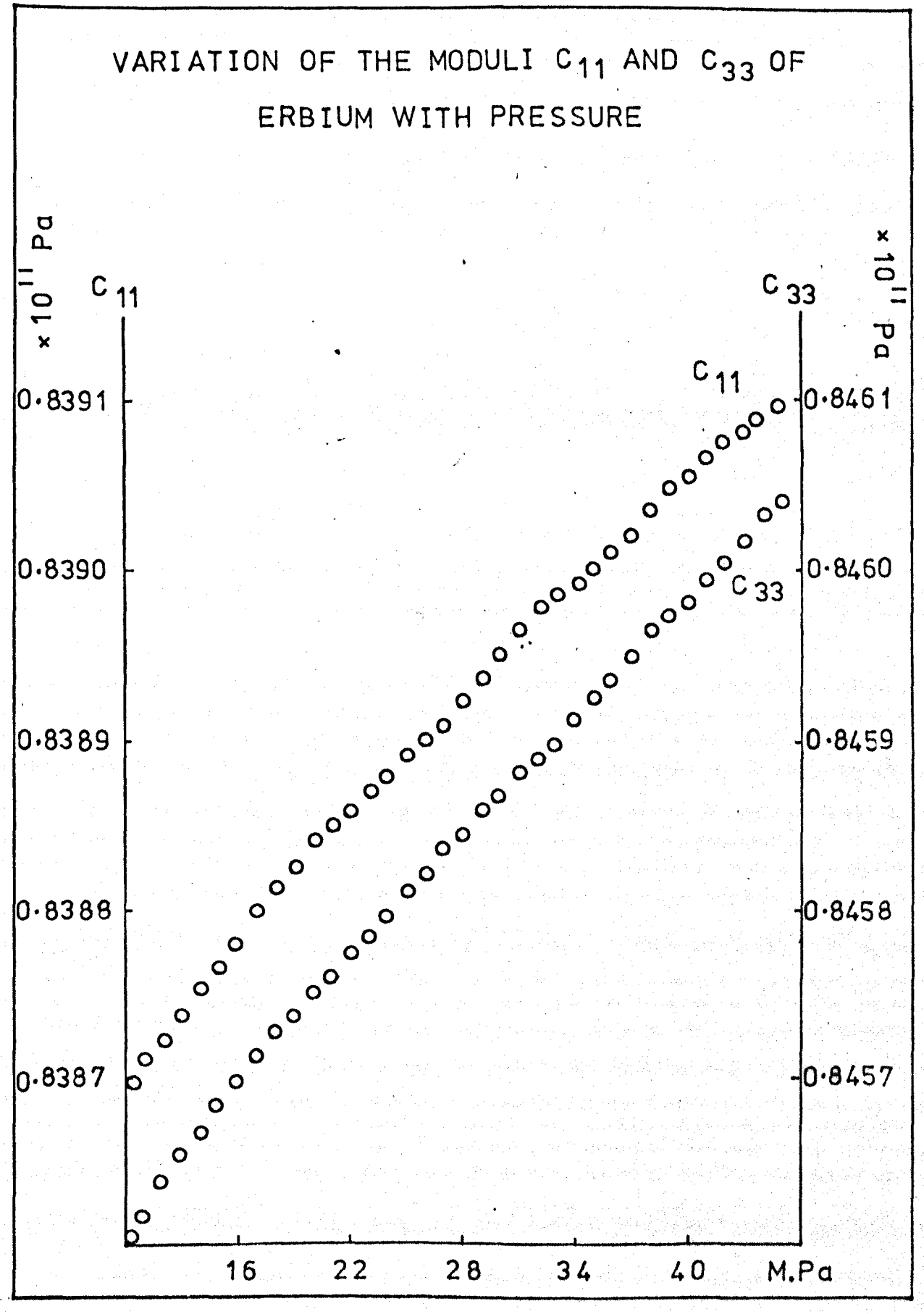
VARIATION OF THE MODULI C_{11} AND C_{33} OF ERBIUM WITH PRESSURE
C_{11}
$\times 10^{11}$ Pa
0·8391
0·8390
0·8389
0·8388
0·8387
C_{33}
$\times 10^{11}$ Pa
0·8461
0·8460
0·8459
0·8458
0·8457
16
22
28
34
40
M.Pa

fig. A 7.1

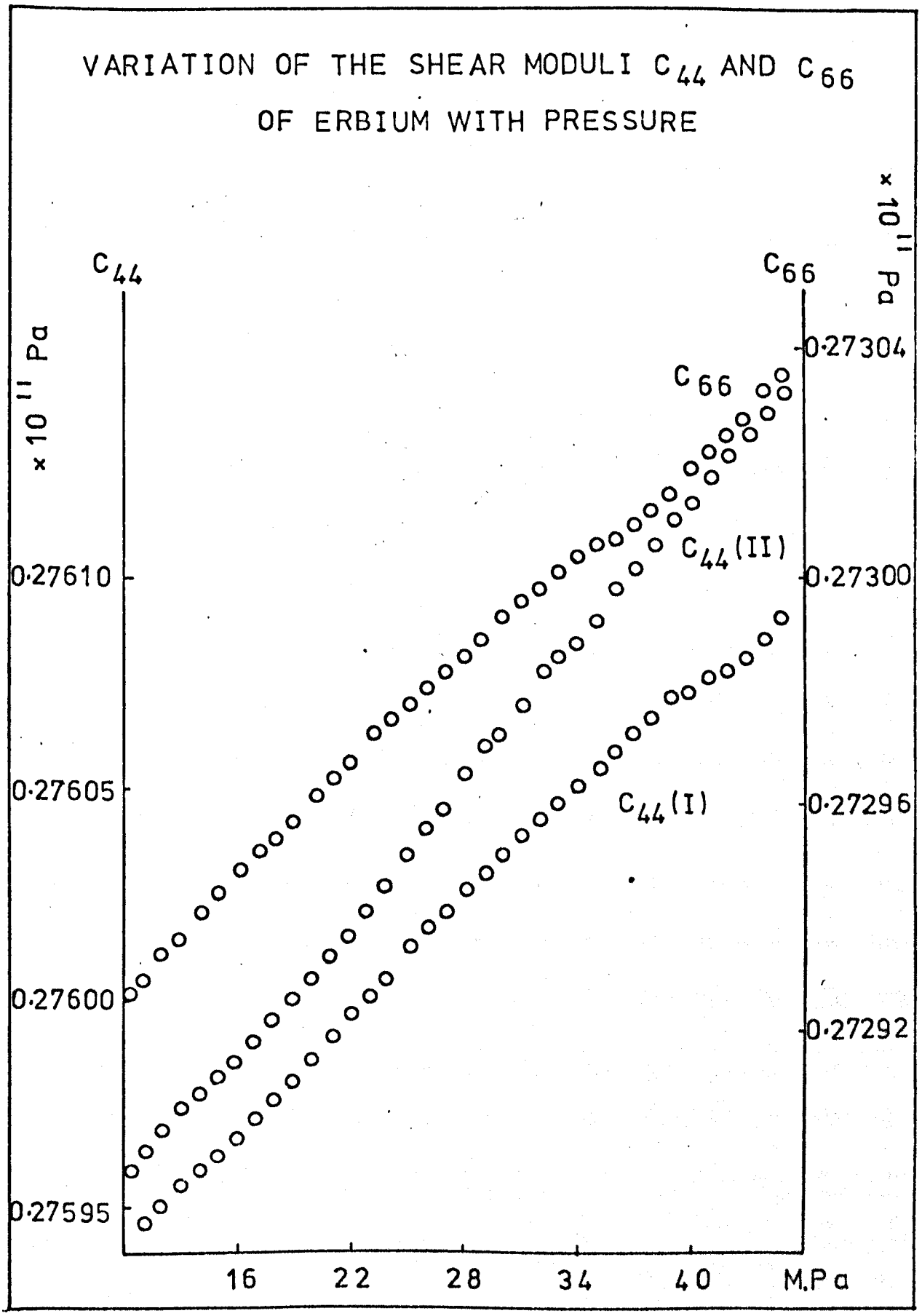
VARIATION OF THE SHEAR MODULI C_{44} AND C_{66} OF ERBIUM WITH PRESSURE
C_{44}
$\times 10^{11}$ Pa
0·27610
0·27605
0·27600
0·27595
C_{66}
$\times 10^{11}$ Pa
0·27304
0·27300
0·27296
0·27292
C_{66}
C_{44}(II)
C_{44}(I)
16
22
28
34
40
M.Pa

fig. A7.2

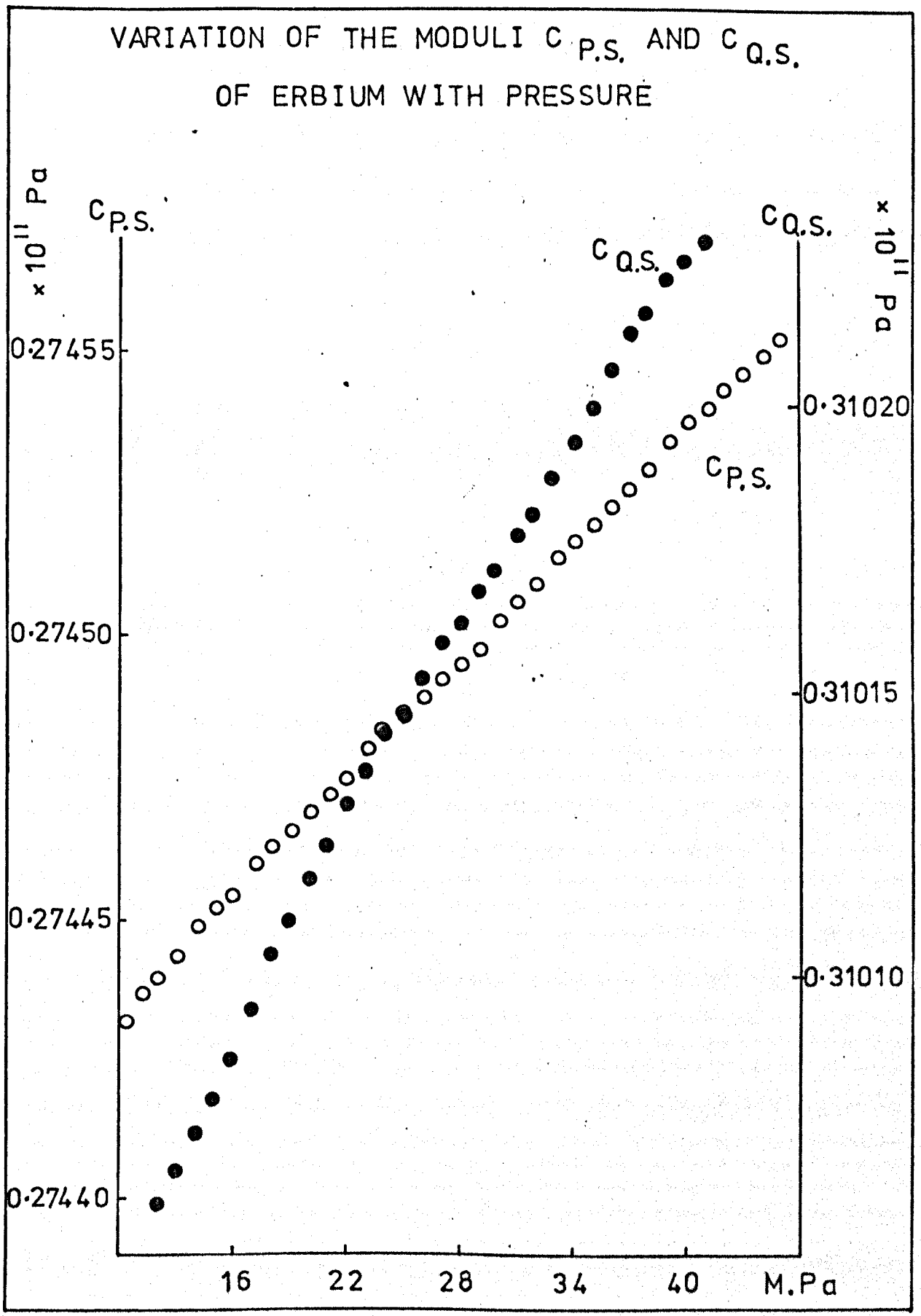
VARIATION OF THE MODULI C P.S. AND C Q.S.
OF ERBIUM WITH PRESSURE
C P.S.
× 10^11 Pa
C Q.S.
C Q.S.
× 10^11 Pa
C P.S.
0·27455
0·27450
0·27445
0·27440
0·31020
0·31015
0·31010
16
22
28
34
40
M.Pa

fig. A7.3

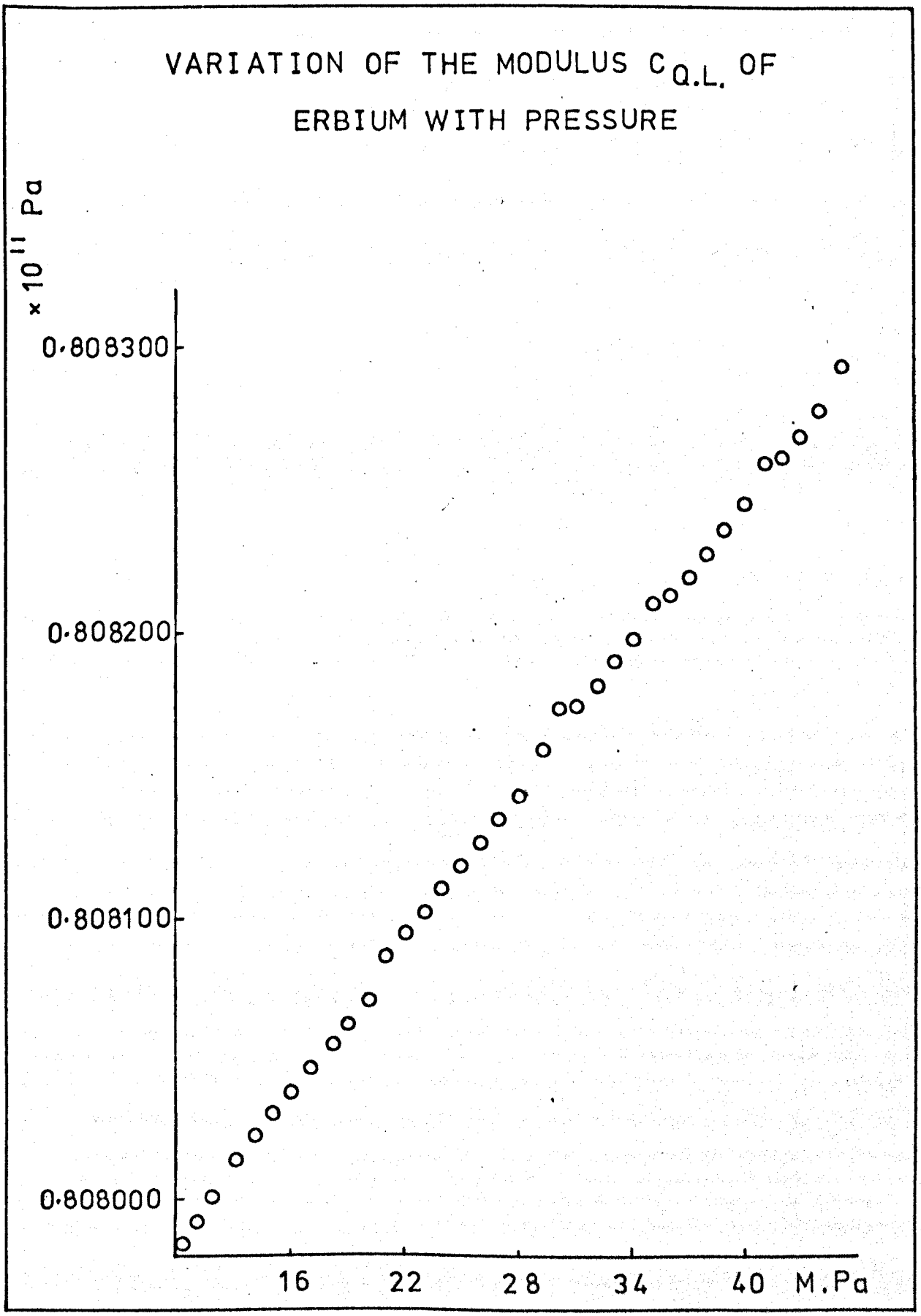
VARIATION OF THE MODULUS $C_{Q.L.}$ OF
ERBIUM WITH PRESSURE
$\times 10^{11}$ Pa
0·808300
0·808200
0·808100
0·808000
16
22
28
34
40
M.Pa

fig. A7.4

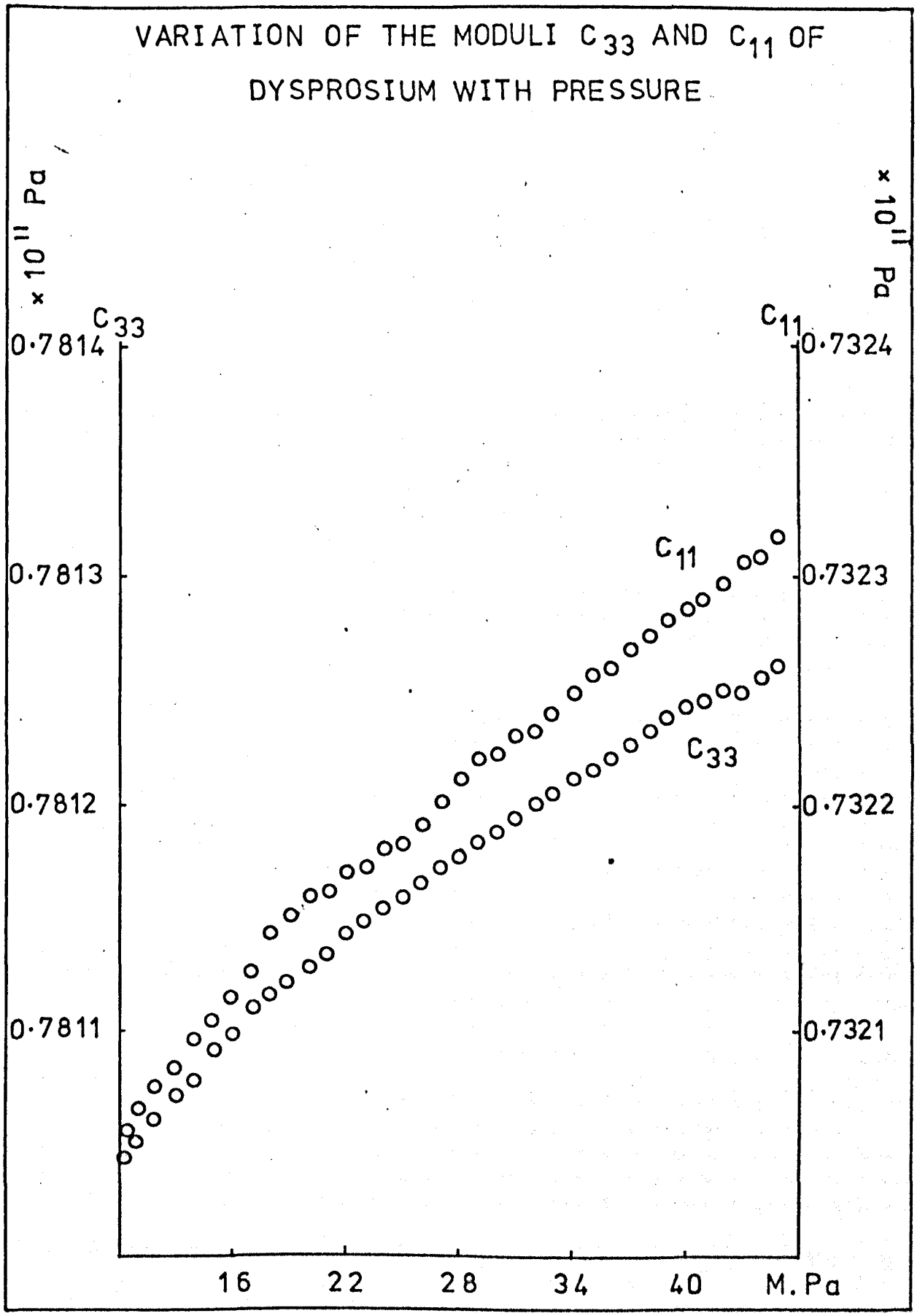
VARIATION OF THE MODULI C_{33} AND C_{11} OF DYSPROSIUM WITH PRESSURE
$\times 10^{11}$ Pa
C_{33}
0·7814
0·7813
0·7812
0·7811
C_{11}
0·7324
0·7323
0·7322
0·7321
$\times 10^{11}$ Pa
16
22
28
34
40
M. Pa

fig. A7.5

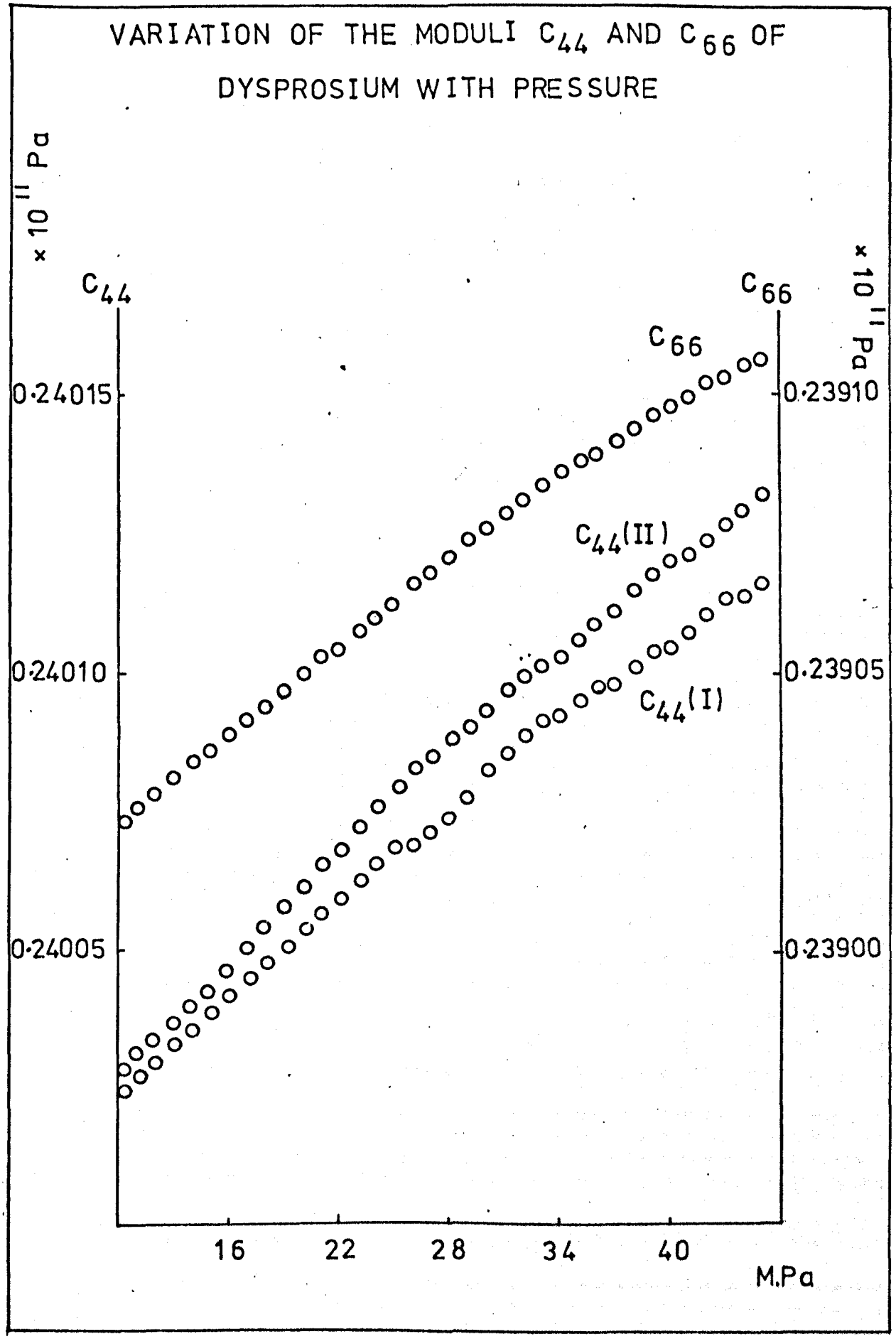
VARIATION OF THE MODULI C_{44} AND C_{66} OF DYSPROSIUM WITH PRESSURE
$\times 10^{11}$ Pa
C_{44}
C_{66}
$\times 10^{11}$ Pa
0·24015
0·24010
0·24005
0·23910
0·23905
0·23900
C_{66}
C_{44}(II)
C_{44}(I)
16
22
28
34
40
M.Pa

fig. A7.6

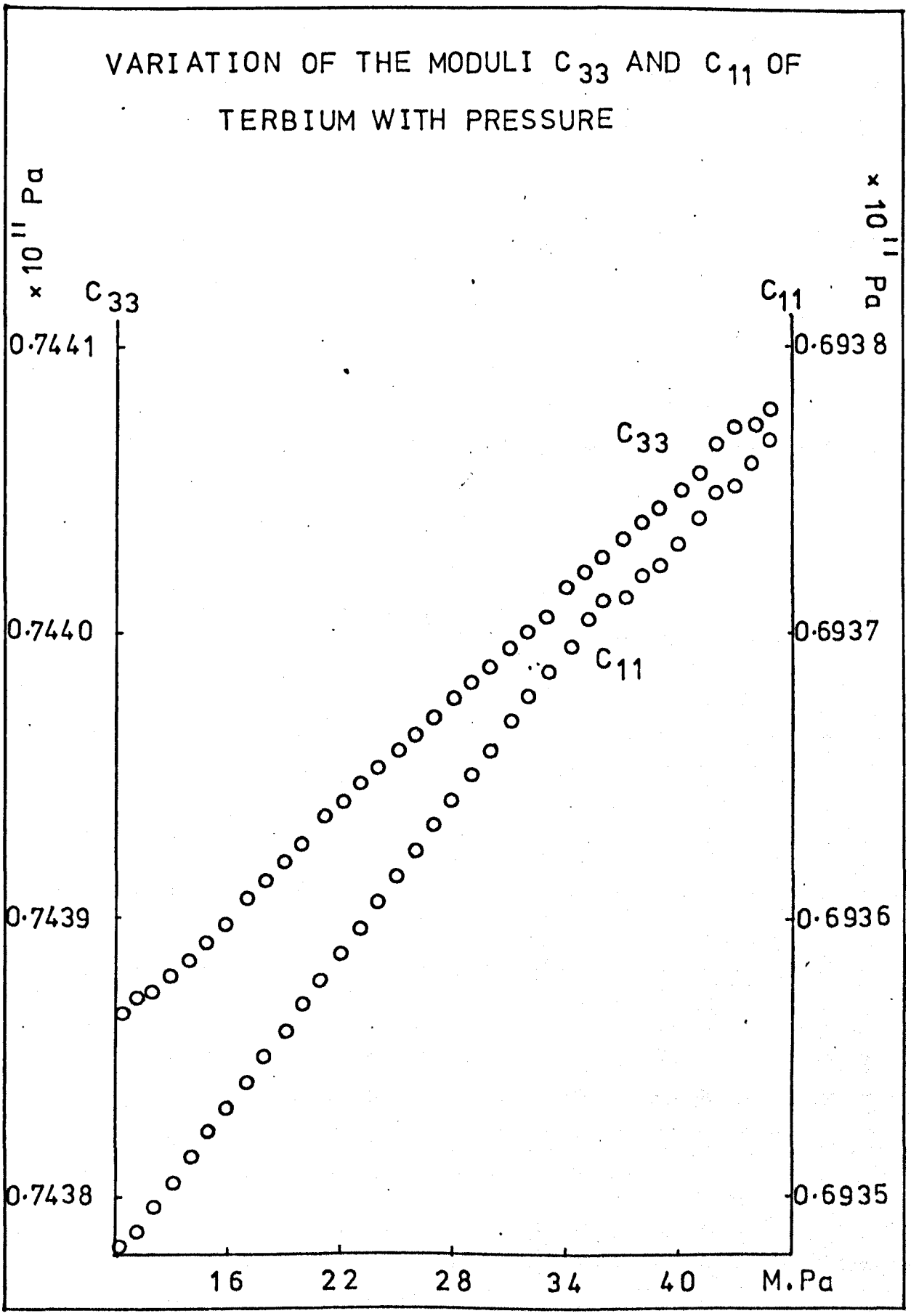
VARIATION OF THE MODULI C_{33} AND C_{11} OF TERBIUM WITH PRESSURE
$\times 10^{11}$ Pa
C_{33}
0·7441
0·7440
0·7439
0·7438
C_{11}
$\times 10^{11}$ Pa
0·6938
0·6937
0·6936
0·6935
16
22
28
34
40
M.Pa

fig. A7.7

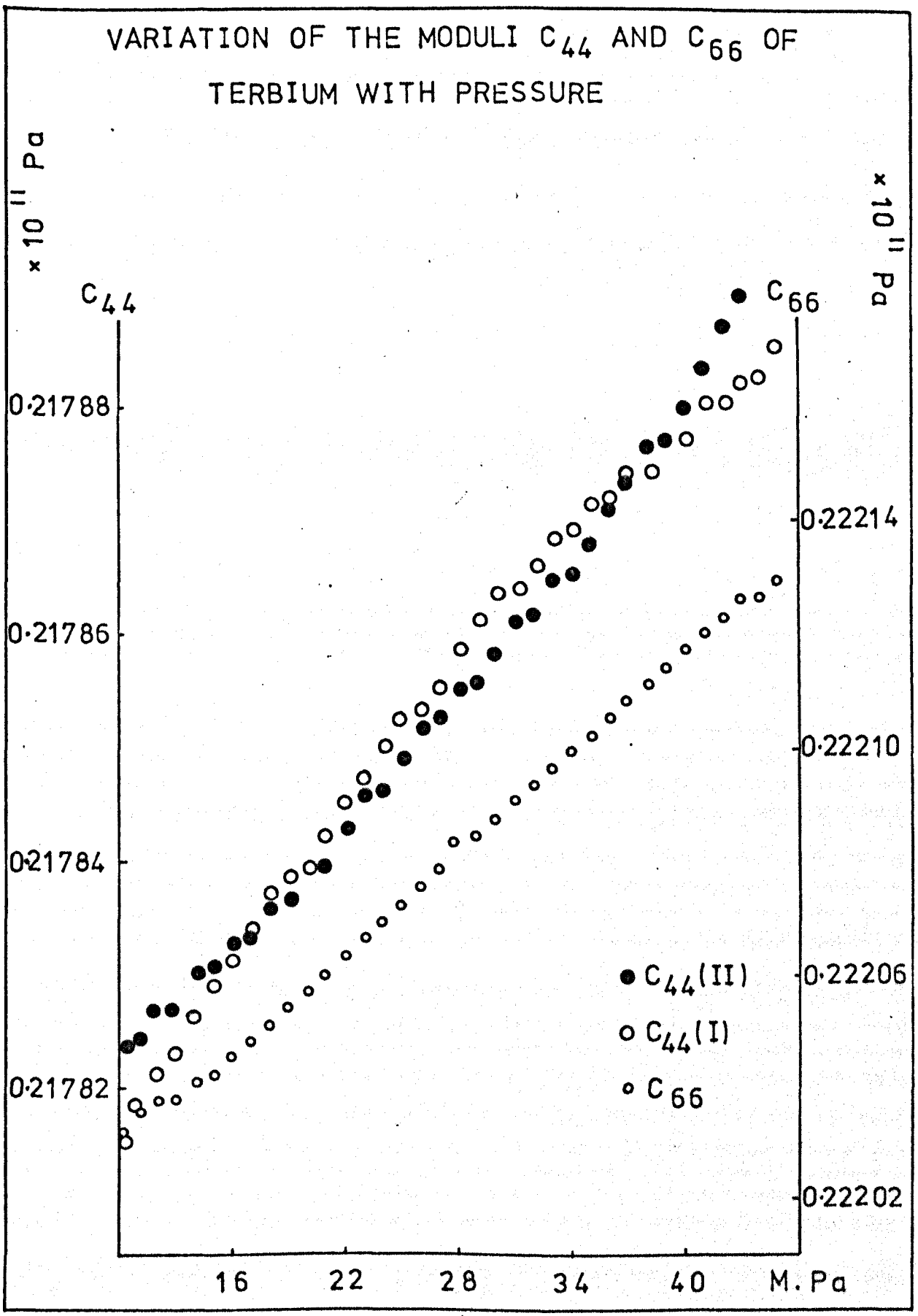
VARIATION OF THE MODULI C_{44} AND C_{66} OF TERBIUM WITH PRESSURE
$\times 10^{11}$ Pa
C_{44}
C_{66}
$\times 10^{11}$ Pa
0·21788
0·21786
0·21784
0·21782
0·22214
0·22210
0·22206
0·22202
C_{44}(II)
C_{44}(I)
C_{66}
16
22
28
34
40
M. Pa

fig. A7.8

Hydrostatic Pressure Derivatives of the Elastic Moduli of Dysprosium, Terbium and Erbium for Pressures up to 4.5M.Pa

	Dy	Tb	Er
$\frac{dC_{33}}{dP}$	6.52 ± 1.24	6.02 ± 0.44	12.10 ± 1.83
$\frac{dC_{11}}{dP}$	6.83 ± 1.02	8.25 ± 1.8	11.54 ± 0.87
$\frac{dC_{44}}{dP}$ (I)	2.64 ± 0.32	1.75 ± 0.22	4.41 ± 0.22
$\frac{dC_{44}}{dP}$ (II)	3.10 ± 0.36	1.97 ± 0.12	4.99 ± 0.83
$\frac{dC_{66}}{dP}$	2.52 ± 0.46	3.02 ± 0.71	3.08 ± 0.63
$\frac{dC_{P.S.}}{dP}$	-	-	3.40 ± 0.11
$\frac{dC_{Q.S.}}{dP}$	-	-	5.67 ± 0.09
$\frac{dC_{Q.L.}}{dP}$	-	-	8.57 ± 1.08

Figure A7.9

Grüneisen Parameters calculated from Pressure Derivatives

up to 4.5M.Pa

$\gamma_p(q)$	γ_{ij}	Er	Dy	Tb
$\gamma_c(c)$	γ_{33}	3.0	1.5	1.4
$\gamma_b(c)$	$\gamma_{44}(I)$	3.4	2.1	1.4
$\gamma_b(b)$	γ_{11}	2.9	1.7	2.2
$\gamma_c(b)$	$\gamma_{44}(II)$	3.8	2.5	1.6
$\gamma_a(b)$	γ_{66}	2.3	2.0	2.5
$\Gamma_{//}$	$(1/3)(\gamma_{33} + 2\gamma_{44}(I))$	3.3	1.9	1.4
$\Gamma_{\perp}$	$(1/3)(\gamma_{11} + \gamma_{66} + \gamma_{44}(II))$	3.0	2.1	2.1
Γ	$(1/3)(\Gamma_{//} + 2\Gamma_{\perp})$	3.1	2.0	1.8

Figure A7.10

Appendix 8 Computer Programs

In this appendix five computer programs are givenwhich have been used to aid data analysis in this work. The first three have been used to analyse data output from the sing around system and convert it into results of elastic constant against a given controlled parameter, for example temperature, pressure or magnetic field. The last two have been used to calibrate thermocouples.

Program 1

This program analyses data obtained from the internal memory store of the sing around system by the method given in appendix 1. Corrections are made to the data if successive readings differ by an interval corresponding to about one cycle of the 15 MHz acoustic vibrations. This would indicate that the trigger point had changed from one cycle to another.

The final data output consists of tabulated values of elastic constant against the controlled parameter, and a graphical representation of the data on the University graph plotter. The subroutines including "GRAPH" and beyond are only responsible for the graphical output. All subroutines before this are concerned with data analysis.

Program 2

This program was used to analyse data obtained from the frequency meter and follows the method outlined in appendix 1. As in the case of program 1 all subroutines including "GRAPH" and beyond are concerned only with the graphical output of results. The first three subroutines deal with the data analysis.

Program 3

This program was used exclusively with pressure measurements when the data was read from the frequency meter. The analysis is similar to program 2 and the outputs both tabulated and graphical are identical.

However, this program contains a subroutine "LINEFIT" which calculates the slope of the data, $^{dC}/_{dP}$, thereby giving the pressure derivatives of elastic constants. More sophisticated programs have been written in which polynomial fits to the data were made in order to detect any fourth-order effects, $^{d^2C}/_{dP^2}$.

Program 4

This program has been used to calibrate a thermocouple against a platinum resistance thermometer. The program calculates the temperature from the resistance of the platinum thermometer by the method outlined in appendix six, and then outputs tabulated and graphical data of thermocouple emf. against temperature. The method used is that recommended by Greenough [1].

Program 5

This program uses the simplified expression given in chapter five relating the emf. of the thermocouple to the temperature. It required four fixed calibration points. The program was originally by Isci [2] utilising the equation of White [3]. A comparison of the two methods of calibration represented by programs 5 and 6 has been given in appendix 6.

PROGRAM 1

```
      MASTER STOREDATA
      REAL INCR,M,K
      COMMON/B1/ANAME,ATYPE,ADATE
      DIMENSION A(100),S(100),M(100),Z(100)
      DIMENSION N(100)
      DIMENSION B(100),K(100),D(100)
      READ(5,1)ANAME,ATYPE,ADATE
1     FORMAT(A8,A2,A8)
      READ(5,15)START,INCR,DELY
15    FORMAT(3F0.0)
      I=1
3     READ(5,5)A(I)
      IF(A(I).EQ.0.0)GOTO 3
10    I=I+1
      READ(5,5)A(I)
5     FORMAT(F0.0)
      IF(A(I).LT.0.0)GOTO 25
      GOTO 10
25    N=I-1
      DO 50 I=1,N
      M(I)=0.0
      D(I)=0.0
      S(I)=A(N+1-I)
      IF(S(I).EQ.0.0)GOTO 50
      M(I)=(DELY+1.0)*0.100+((S(I)*2.0)-1.0)*0.001
      D(I)=1000.0/M(I)
50    CONTINUE
      DO 100 I=1,N
      Z(I)=START+(I-1)*INCR
100   CONTINUE
C
C
C       CALL EITHER THOUPLE OR FIELDCAL
C
C
      CALL FIELDCAL(Z,B,N,M)
      CALL PLOTTER(Z,D,B,N)
C
C       HEADINGS ON NEW PAGE
C
      WRITE(6,30)
30    FORMAT('1',100('*'))
      WRITE(6,31)
31    FORMAT(//,24X,'TAPE DATA',7X,'SING AROUND PERIOD',7X,'FREQUENC
     1',2X,'FIELD')
      WRITE(6,36)
36    FORMAT( 24X,'MICROSECONDS',10X,'  KHZ   ')
      WRITE(6,32)
32    FORMAT('0',17X,21('*'))
C
C     FIRST OUTPUT VARIATION OF FREQUENCY WITH FIELD
C
```

```
      DO 40 L=1,N
35    WRITE(6,37)
37    FORMAT(1H0,17X,'*',4(19X,'*'))
      M(L)=IFIX(S(L))
      WRITE(6,33)M(L),H(L),D(L),B(L)
33    FORMAT(1H0,17X,'*',7X,I4,8X,'*',2(6X,F7.3,6X,'*'),7X,F5.3,7X,
      WRITE(6,37)
      WRITE(6,32)
40    CONTINUE
24    WRITE(6,25)
25    FORMAT( 10X,'RUN FINISHED')
C
C     SECOND OUTPUT GRAPH OF RELATIVE ELASTIC CONSTANT
C     AGAINST TEMPERATURE
C
C
      STOP
      END
      SUBROUTINE FIELDCAL(X,T,N,H)
      COMMON/B1/ANAME,ATYPE,ADATE
      DIMENSION X(100),H(100),T(100)
      DATAB1/0.095/,B2/0.30/,B3/0.65/
      DATAC1/2.0/,C2/7.0/,C3/15.0/
      DELTA=((C1**3)*(C2**2)*C3+(C1**2)*C2*(C3**3)+C1*(C2**2)*(C3**
     1 -C1*(C2**2)*(C3**3)-(C1**2)*(C2**3)*C3-(C1**2)*C2*(C2**2))
      A=(B1*((C2**2)*C3-C2*(C3**2))-B2*((C1**2)*C3-C1*(C3**2))
     1+B3*((C1**2)*C2-C1*(C2**2)))/DELTA
      B=-(B1*((C2**3)*C3-C2*(C3**3))  -B2*((C1**3)*C3-C1*(C3**2))
     1+B3*((C1**3)*C2-C1*(C2**3)))/DELTA
      C=(B1*((C2**3)*(C3**2)-(C2**2)*(C3**3))-B2*((C1**3)*(C2**2)-
     1(C1**2)*(C3**3))+B3*((C1**3)*(C2**2)-(C1**2)*(C2**3)))/DELTA
      DO 1 L=1,N
      T(L)=A*(X(L)**3)+B*(X(L)**2)+C*X(L)
1      CONTINUE
      CALL GRAPH('*',T,H,N,6)
      WRITE(6,300)
300   FORMAT(1H0,38X,'GRAPH OF SING AROUND PERIOD AGAINST FIELD')
      WRITE(6,301)
301   FORMAT(1H0,53X,'RAW DATA')
      WRITE(6,302)ANAME,ATYPE,ADATE
302   FORMAT(1H0,45X,A8,A8,A8)
      WRITE(6,210)
210   FORMAT(1H1,120('*'))
      WRITE(6,211)ANAME,ATYPE,ADATE
211   FORMAT(1H0,45X,'SAMPLE : ',A8,A8,A8)
      WRITE(6,260)
      WRITE(6,214)
214   FORMAT(1H0,16X,'COIL',4X,'MAGNETIC',10X,'OBSERVED',
     113X,'CORRECTED',10X,'FREQUENCY')
      WRITE(6,215)
215   FORMAT(1H0,15X,'CURRENT',11X,'   FIELD   ',11X,'FREQUENCY',10
     1'FREQUENCY',13X,'SQUARED')
```

```
      WRITE(6,220)
  220 FORMAT(//,19X,'I',19X,'E',19X,'F',19X,'CF',19X,'F2',19X,'GEN'
      WRITE(6,260)
  260 FORMAT(//,10X,101('*'))
      RETURN
      END
      SUBROUTINE THCOUPLE(X,T,N,H)
      COMMON/B1/ANAME,ATYPE,ADATE
      DIMENSION V(200),H(100)
      DIMENSION X(200),T(200)
      DATAT1/-196.0/,T2/-100.0/,T3/-50.0/
      DATAV1/-0.00573/,V2/-0.00335/,V3/-0.00181/
      DELVA=((V1**3)*(V2**2)*V3+(V1**2)*V2*(V3**3)+V1*(V2**3)*(V3**
     1 -V1*(V2**2)*(V3**3)-(V1**2)*(V2**3)*V3-(V1**3)*V2*(V2**2))
      A=(T1*((V2**2)*V3-V2*(V3**2))-T2*((V1**2)*V3-V1*(V2**2))
     1+T3*((V1**2)*V2-V1*(V2**2)))/DELVA
      B=-(T1*((V2**3)*V3-V2*(V3**3)) -T2*((V1**3)*V3-V1*(V3**2))
     1+T3*((V1**3)*V2-V1*(V2**3)))/DELVA
      C=(T1*((V2**3)*(V3**2)-(V2**2)*(V3**3))-T2*((V1**3)*(V2**2)-
     1(V1**2)*(V3**3))+T3*((V1**3)*(V2**2)-(V1**2)*(V2**3)))/DELVA
      DO 1 L=1,N
      V(L)=X(L)*0.001
      T(L)=273.0+A*(V(L)**3)+B*(V(L)**2)+C*V(L)
    1  CONTINUE
      CALL GRAPH('*',T,H,N,6)
      WRITE(6,300)
  300 FORMAT(1H0,33X,'GRAPH OF SING AROUND PERIOD AGAINST TEMP')
      WRITE(6,301)
  301 FORMAT(1H0,53X,'RAW DATA')
      WRITE(6,302)ANAME,ATYPE,ADATE
  302 FORMAT(1H0,45X,A8,A8,A3)
      WRITE(6,210)
  210 FORMAT(1H1,100('*'))
      WRITE(6,211)ANAME,ATYPE,ADATE
  211 FORMAT(1H0,45X,'SAMPLE : ',A8,A8,A8)
      WRITE(6,260)
      WRITE(6,214)
  214 FORMAT(1H0,12X,'THERMOCOUPLE',3X,'CORRESPONDING',10X,'CORRECTE
     113X,'CORRECTED',12X,'FREQUENCY')
      WRITE(6,215)
  215 FORMAT(1H0,17X,'EMF',13X,'TEMPERATURE',11X,'FREQUENCY',10X,
     1'FREQUENCY',13X,'SQUARED')
      WRITE(6,220)
  220 FORMAT(//,19X,'V',19X,'T',19X,'F',19X,'CF',19X,'F2',10X,'DEL'
      WRITE(6,260)
  260 FORMAT(//,10X,101('*'))
      RETURN
      END
```

```
      SUBROUTINE PLOTTER(ZZ,DD,T,N)
      COMMON/B1/ANAME,ATYPE,ADATE
C
C     PROGRAM TO CORRECT CHANGES IN SING AROUND FREQUENCY
C     DUE TO TRIGGER POINT JUMPING OR TO DETECTOR BEING
C     RESET.
C
      INTEGER G
      DIMENSION G(120)
      DIMENSION MY(120),MN(120),MAX(120),MIN(120)
      DIMENSION U(120),Z(120)
      DIMENSION T(120),H(120),DIFF(120)
      DIMENSION DD(120),ZZ(120)
      DIMENSION X(120),Y(120)
      G(1)=0
      G(2)=0
      G(3)=0
      J=0
      DO 35 I=1,N
      J=J+1
20    IF(DD(I).NE.0.0)GOTO 30
      J=J+1
      GOTO 20
30    Y(I)=DD(J)
      X(I)=ZZ(J)
      H(I)=1.00/Y(I)
35    CONTINUE
      DO 101 I=1,N
      DIFF(1)=0.0
      IF(I.EQ.1)GOTO 36
      DIFF(I)=ABS(H(I)-H(I-1))
36    IF(DIFF(I).LT.0.0667)GOTO 100
      MY(I)=H(I)+0.0667
      MN(I)=H(I)-0.0667
      MAX(I)=ABS(MY(I)-H(I-1))
      MIN(I)=ABS(MN(I)-H(I-1))
      IF(MAX(I).GT.MIN(I))GOTO99
      H(I)=MY(I)
      GOTO 100
99    H(I)=MN(I)
100   U(I)=1.00/H(I)
101   CONTINUE
      DO 205 K=1,N
      Z(K)=U(K)**2
205   CONTINUE
      DO 250 I=1,N
      WRITE(6,230)
230   FORMAT(1H0,9X,5('*',19X),'*')
      WRITE(6,240) X(I),T(I),Y(I),U(I),Z(I),G(I)
240   FORMAT(1H0,9X,'*',6X,F6.3,7X,'*',4X,F7.3,9X,'*',5X,
     1F7.3,7X,'*',5X,F7.3,7X,'*',6X,F3.0,5X,'*',3X,I2)
      WRITE(6,230)
```

```
      WRITE(6,260)
  260 FORMAT(//,10X,101('*'))
  250 CONTINUE
      CALL GRAPH('*',T,Z,N,6)
      WRITE(6,300)
  300 FORMAT(1H0,38X,'GRAPH OF FREQUENCY SQUARED AGAINST FIELD')
      WRITE(6,301)
  301 FORMAT(1H0,50X,'CORRECTED DATA')
      WRITE(6,302)ANAME,ATYPE,ADATE
  302 FORMAT(1H0,45X,A8,A8,A8)
      RETURN
      END
      SUBROUTINE GRAPH(C,X,Y,N,I)
      DIMENSION X(N),Y(N)
      CALL MNMX(X,N,XMAX,XMIN,10,0)
      CALL MNMX(Y,N,YMAX,YMIN,10,0)
      CALL SCALE IT(XMAX,XMIN,YMAX,YMIN)
      CALL PLOTEM(C,X,Y,N)
      IF(I.GT.0)CALL DUMP IT(I)
      RETURN
      END
      SUBROUTINE MNMX(Y,N,XMAX,XMIN,NDV,INC)
      DIMENSION X(N),A(18)
      DATA A/1.25,1.5,2.,2.5,3.,4.,5.,6.,7.5,8.,10.,12.5/
      DTRNC(Z)=AINT(Z+10000.)-10000.
      IF(INC.GE.1)GOTO 2
      XMAX = X(1)
      XMIN = XMAX
    2 DO 1 IC=1,N
      IF(X(IC).GT.XMAX)XMAX=X(IC)
    1 IF(X(IC).LT.XMIN)XMIN=X(IC)
      PLG=ALOG10((XMAX-XMIN)/NDV)
      EXP=DTRNC(PLG)
      SUX=PLG-EXP
      SUX=10.**SUX
      DO 3 IC=1,18
      IF(SUX.LT.A(IC))GOTO 4
    3 CONTINUE
    4 UX=A(IC)*10.**EXP
      IC=IC+1
      XMX =UX*DTRNC(XMAX/UX+0.9999)
      XMN =UX*DTRNC(XMIN/UX+0.0001)
      IF((XMX-XMN)/UX.GT.NDV+0.1)GOTO 4
      XMIN =XMN
      XMAX = XMN+NDV*UX
      RETURN
      END
      SUBROUTINE SCALE IT(XMX,XMN,YMX,YMN)
      COMMON /ZPLOT/S(663),XMIN,UX,YMAX,UY
      DATA P/'      '/
      XMIN=XMN
      UX =(XMX-XMN)/100.0
```

```
      YMAX = YMX
      UY = (YMX-YMN)/50
      DO 1 IC=1,663
    1 G(IC)=B
      RETURN
      END
      SUBROUTINE PLOTEM(C,X,Y,N)
      DIMENSION X(N),Y(N)
      COMMON /Z96PX/G(663),XMIN,UX,YMAX,UY
      DO 1 IC=1,N
      IX=INT((X(IC)-XMIN)/UX+1.5)
      IF(IX.GT.101)GOTO 1
      IF(IX.LT.1)GOTO 1
      IY=INT((YMAX-Y(IC))/UY+1.5)
      IF(IY.GT.51)GOTO 1
      IF(IY.LT.1)GOTO 1
      CALL COPY(1,G(13*IY-12),IX,C,1)
    1 CONTINUE
      RETURN
      END
      SUBROUTINE LINE(C,X1,Y1,X2,Y2)
      DIMENSION X(10),Y(10)
      COMMON /Z96PX/G(663),XMIN,UX,YMAX,UY
      DX=(X2-X1)/UX
      DY=(Y2-Y1)/UY
      DMAX=AMAX1(ABS(DX),ABS(DY))
      DX=UX*DX/DMAX
      DY=UY*DY/DMAX
      NPT=DMAX-0.5
      X(1)=X1+DX
      Y(1)=Y1+DY
    2 IF(NPT.LT.1)RETURN
      ICE = MIN0(NPT,10)
      DO 1 IC=2,ICE
      X(IC)=X(IC-1)+DX
    1 Y(IC)=Y(IC-1)+DY
      CALL PLOTEM(C,X,Y,ICE)
      NPT = NPT - ICE
      X(1) = X(ICE)+DX
      Y(1) = Y(ICE)+DY
      GO TO 2
      END
      SUBROUTINE DUMP IT(I)
      DIMENSION NS(6)
      COMMON /Z96PX/G(663),XMIN,UX,YMAX,UY
      DO 9 IC=1,6
      NS(IC) = YMIN+20.*UY*(IC-1)
    9 IF(ABS(NS(IC)/UY).LT.0.001)NS(IC)=0.0
      WRITE(I,104)
  104 FORMAT('1'/13X,10('+',9X),'+'/13X,'+',10(9('-'),'+'))
      YAY=YMAX+5.*UY
      JB = 1
```

```
      JE=13
      DO 1 IC=1,10
      YAY=YAY-5.*UY
      IF(ABS(YAY/UY).LT.0.001)YAY=0.0
      WRITE(I,102)YAY,(G(JC),JC=JB,JE)
  102 FORMAT(1X,G10.4,'++',12A8,A5,'++')
      DO 2 KC=1,4
      JB = JE+1
      JE = JE+12
      WRITE(I,101)(G(JC),JC=JB,JE)
  101 FORMAT(12X,'-',12A8,A5,'-')
    2 CONTINUE
      JB=JE+1
    1 JE=JB+12
      YAY=YMAX -50.*UY
      WRITE(I,102)YAY,(G(JC),JC=JB,JE)
      WRITE(I,103)XS
  103 FORMAT(13X,'+',10(9('-'),'+')/13X,10('+',9X),'+'/10X,((G10.4
      RETURN
      END
      FINISH
****
18.40.15←
```

PROGRAM 2

```
      MASTER PLOTTER
C
C     PROGRAM TO CORRECT CHANGES IN SING AROUND FREQUENCY
C     DUE TO TRIGGER POINT JUMPING UP TO DETECTOR BEING
C     RESET.
C
      COMMON/B1/AB(7)
      REAL INC,MOD
      INTEGER G
      DIMENSION INC(500),DIR(500),OBS(500)
      DIMENSION MOD(500)
      DIMENSION G(500),Q(500)
      DIMENSION U(500),Z(500)
      DIMENSION T(500),DEL(500),DIFF(500)
      DIMENSION R(500),S(500),W(500)
      DIMENSION X(500),Y(500)
      I=0
      READ(5,1)AB(1),AB(2),AB(3),AB(4),AB(5),AB(6),AB(7)
1     FORMAT(7A8)
      READ(5,4)POINT,CONST
4     FORMAT(2F0.0)
      CONST=CONST*1.0E 11
5     I=I+1
      READ(5,10) X(I),Y(I)
10    FORMAT(2F0.0)
      IF(Y(I).GT.0.0)GOTO 5
      N=I-1
      WRITE(6,400)
400   FORMAT(1H1,120('*'))
      WRITE(6,401)AB(1),AB(2),AB(3),AB(4),AB(5),AB(6),AB(7)
401   FORMAT(1HO,46X,7A8)
C
C
C      CALL EITHER THCOUPLE OR FIELDCAL
C
C
      CALL THCOUPLE(Y,T,N)
C
C      SET UP ARRAYS TO MONITOR BEHAVIOUR OF DATA
C
      G(1)=0
      G(2)=0
      G(3)=0
      DO 20 I=2,N
      INC(I)=Y(I)-Y(I-1)
      IF(INC(I).EQ.0.0)INC(I)=DIR(I-1)*0.001
      DIR(I)=INC(I)/ABS(INC(I))
      DIR(1)=DIR(2)
      OBS(I)=DIR(I)/DIR(I-1)
20    CONTINUE
      OBS(N+1)=1.0
```

```
      DO 100 I=4,N
      G(I)=0
      U(I)=Y(I)
      A=ABS(Y(I-1)-Y(I-2))
      B=ABS(Y(I-2)-Y(I-3))
      C=A+B
      D=X(I-1)-X(I-3)
      S(I)=ABS(C/D)
      P=Y(I)-Y(I-1)
      Q(I)=X(I)-X(I-1)
      R(I)=ABS(P/Q(I))
      W(I)=5.0*S(I)
100   CONTINUE
C
C      SELECT CONDITIONS UNDER WHICH CORRECTIONS SHOULD
C       BE MADE TO DATA
C
      DO 200 I=4,N
      G(I)=G(I-1)
      IF(OBS(I).GT.0)GO TO 70
      IF(OBS(I+1).GT.0)GOTO 70
      GOTO 71
70    IF(R(I).LE.W(I))GOTO 50
C
C              CORRECTING PROCEDURE FOLLOWS
C
71    J=I
40    A1=(Y(J-1)-Y(J-2))/(X(J-1)-X(J-3))
      IF(A1.NE.0.0)GOTO 60
      J=J-1
      IF(J.LE.3)GOTO 50
      GOTO 40
60    A2=ABS(A1)
      SIGN=A1/A2
      SLOPE=S(I)*SIGN
      DIFF(I)=SLOPE*Q(I)+Y(I-1)-Y(I)
      G(I)=G(I-1)+1
50    CONTINUE
C
C      END OF CORRECTING ROUTINE
C       GO TO 50  BYPASSES CORRECTIONS TO DATA
C
200   CONTINUE
      U(1)=Y(1)
      DEL(1)=0.0
      DO 150 K=2,N
      DEL(K)=DEL(K-1)+DIFF(K)
      U(K)=Y(K)+DEL(K)
150   CONTINUE
      DO 205 K=1,N
      Z(K)=U(K)**2
205   CONTINUE
```

```
290     DO 300 I=1,N
        IF(X(1).NE.POINT)GOTO 300
        COEF=CONST/Z(I)
300     CONTINUE
        DO 350  I=1,N
        MOD(I)=COEF*Z(I)
350     CONTINUE
        WRITE(6,260)
260     FORMAT(//,10X,101('*'))
        DO 250 I=1,N
        WRITE(6,230)
230     FORMAT(1H0,9X,5('*',19X),'*')
        WRITE(6,240) X(I),T(I),Y(I),V(I),MOD(I),G(I)
240     FORMAT(1H0,9X,'*',6X,F6.3,7X,'*',4X,F7.3,8X,'*',5X,
       1F7.3,7X,'*',5X,F7.3,7X,'*',4X,E11.5,4X,'*',3X,I2)
        WRITE(6,230)
        WRITE(6,260)
250     CONTINUE
        CALL GRAPH('*',T,MOD,N,6)
        STOP
        END
        SUBROUTINE THCOUPLE(X,T,N)
        DIMENSION VX(500)
        DIMENSION V(500)
        DIMENSION X(500),T(500)
        REAL K
        DATAT1/-196.0/,T2/-77.2/,T3/-268.9/
        DATAV1/-0.00573/,V2/-0.002741/,V3/-0.006475/
        DELTA=((T1**3)*(T2**2)*T3+(T1**2)*T2*(T3**3)+T1*(T2**2)*(T
       1 -T1*(T2**2)*(T3**3)-(T1**2)*(T2**3)*T3-(T1**3)*T2*(T3**2)
        A=(V1*((T2**2)*T3-T2*(T3**2))-V2*((T1**2)*T3-T1*(T3**2))
       1+V3*((T1**2)*T2-T1*(T2**2)))/DELTA
        B=-(V1*((T2**3)*T3-T2*(T3**3)) -V2*((T1**3)*T3-T1*(T3**3))
       1+V3*((T1**3)*T2-T1*(T2**3)))/DELTA
        C=(V1*((T2**3)*(T3**2)-(T2**2)*(T3**3))-V2*((T1**3)*(T3**2
       1(T1**2)*(T2**3))+V3*((T1**3)*(T2**2)-(T1**2)*(T2**3)))/DEL
        DO 1 L=1,N
        VX(L)=X(L)/1000.0
        K=1.0
        IF(L.EQ.1)TA=20.0
        IF(L.NE.1)TA=T(L-1)
10      V(L)=A*(TA**3)+B*(TA**2)+C*TA
        DV1=VX(L)-V(L)
        IF(ABS(DV1).LT.0.000001)GOTO 20
        SIGNA=DV1/ABS(DV1)
        TA=TA+SIGNA*10.0/K
        V(L)=A*(TA**3)+B*(TA**2)+C*TA
        DV2=VX(L)-V(L)
        SIGNB=DV2/ABS(DV2)
        IF(SIGNB.EQ.SIGNA)GOTO 10
        TA=TA-SIGNA*10.0/K
        K=K*2.0
```

```
      GOTO 10
   20 T(L)=TA+273.0
    1  CONTINUE
      WRITE(6,210)
  210 FORMAT(1H0,120('*'))
      WRITE(6,214)
  214 FORMAT(1H0,19X,'THERMOCOUPLE',8X,'CORRESPONDING',10X,'OBSE
     113X,'CORRECTED',10X,' ELASTIC ')
      WRITE(6,215)
  215 FORMAT(1H0,17X,'EMF',13X,'TEMPERATURE',11X,'FREQUENCY',10X,
     1'FREQUENCY',11X,'CONSTANT')
      WRITE(6,220)
  220 FORMAT(//,19X,'V',19X,'T',19X,'F',19X,'CF',19X,'F2',10X,'C
      RETURN
      END
      SUBROUTINE FIELDCAL(X,T,N)
      DIMENSION X(500),T(500)
      DATAB1/0.57/,B2/1.05/,B3/1.78/
      DATAC1/10.0/,C2/20.0/,C3/40.0/
      DELTA=((C1**3)*(C2**2)*C3+(C1**2)*C2*(C3**3)+C1*(C2**2)*(C3
     1 -C1*(C2**2)*(C3**3)-(C1**2)*(C2**3)*C3-(C1**3)*C2*(C3**2))
      A=(B1*((C2**2)*C3-C2*(C2**2))-B2*((C1**2)*C3-C1*(C3**2))
     1+B3*((C1**2)*C2-C1*(C2**2)))/DELTA
      B=-(B1*((C2**3)*C3-C2*(C3**3)) -B2*((C1**2)*C3-C1*(C2**2))
     1+B3*((C1**3)*C2-C1*(C2**3)))/DELTA
      C=(B1*((C2**3)*(C3**2)-(C2**2)*(C3**3))-B2*((C1**2)*(C3**2)
     1(C1**2)*(C2**3))+B3*((C1**2)*(C2**2)-(C1**2)*(C2**3)))/DELT
      DO 1 L=1,N
      T(L)=A*(X(L)**3)+B*(X(L)**2)+C*X(L)
    1  CONTINUE
      WRITE(6,210)
  210 FORMAT(1H0,120('*'))
      WRITE(6,214)
  214 FORMAT(1H0,16X,'COIL',15X,'MAGNETIC',12X,'OBSERVED',
     113X,'CORRECTED',10X,' ELASTIC ')
      WRITE(6,215)
  215 FORMAT(1H0,15X,'CURRENT',14X,'FIELD',14X,'FREQUENCY',10X,
     1'FREQUENCY',11X,'CONSTANT')
      WRITE(6,220)
  220 FORMAT(//,19X,'I',19X,'B',19X,'F',19X,'CF',19X,'F2',10X,'C
      RETURN
      END
      SUBROUTINE GRAPH(C,X,Y,N,I)
      DIMENSION X(N),Y(N)
      CALL MNMX(X,N,XMAX,XMIN,10,0)
      CALL MNMX(Y,N,YMAX,YMIN,10,0)
      CALL SCALE IT(XMAX,XMIN,XMAX,XMIN)
      CALL PLOTEM(C,X,Y,N)
      IF(I.GT.0)CALL DUMP IT(I)
      CALL DISPLAY(X,Y,N,XMAX,XMIN,YMAX,YMIN)
      RETURN
      END
```

```
      SUBROUTINE MNMX(X,N,XMAX,XMIN,NDV,INC)
      DIMENSION X(N),A(12)
      DATA A/1.25,1.5,2.,2.5,3.,4.,5.,6.,7.5,8.,10.,12.5/
      DTPNC(Z)=AINT(Z+10000.)-10000.
      IF(INC.GE.1)GOTO 2
      XMAX = X(1)
      XMIN = XMAX
    2 DO 1 IC=1,N
      IF(X(IC).GT.XMAX)XMAX=X(IC)
    1 IF(X(IC).LT.XMIN)XMIN=X(IC)
      PLG=ALOG10((XMAX-XMIN)/NDV)
      EXP=DTPNC(PLG)
      SUX=PLG-EXP
      SUX=10.**SUX
      DO 3 IC=1,12
      IF(SUX.LT.A(IC))GOTO 4
    3 CONTINUE
    4 UX=A(IC)*10.**EXP
      IC=IC+1
      XMX =UX*DTPNC(XMAX/UX+0.9999)
      XMN =UX*DTPNC(XMIN/UX+0.0001)
      IF((XMX-XMN)/UX.GT.NDV+0.1)GOTO 4
      XMIN =XMN
      XMAX = XMN+NDV*UX
      RETURN
      END
      SUBROUTINE SCALE IT(XMX,XMN,YMX,YMN)
      COMMON /Z96PX/G(663),XMIN,UX,YMAX,UY
      DATA B/'      '/
      XMIN=XMN
      UX =(XMX-XMN)/100.0
      YMAX = YMX
      UY = (YMX-YMN)/50
      DO 1 IC=1,663
    1 G(IC)=B
      RETURN
      END
      SUBROUTINE PLOTEM(C,X,Y,N)
      DIMENSION X(N),Y(N)
      COMMON /Z96PX/G(663),XMIN,UX,YMAX,UY
      DO 1 IC=1,N
      IX=INT((X(IC)-XMIN)/UX+1.5)
      IF(IX.GT.101)GOTO 1
      IF(IX.LT.1)GOTO 1
      IY=INT((YMAX-Y(IC))/UY+1.5)
      IF(IY.GT.51)GOTO 1
      IF(IY.LT.1)GOTO 1
      CALL COPY(1,C(13*IY-12),IX,G,1)
    1 CONTINUE
      RETURN
      END
```

```
      SUBROUTINE LINE(C,X1,Y1,X2,Y2)
      DIMENSION X(10),Y(10)
      COMMON /Z96PX/G(663),XMIN,UX,YMAX,UY
      DX=(X2-X1)/UX
      DY=(Y2-Y1)/UY
      DMAX=AMAX1(ABS(DX),ABS(DY))
      DX=UX*DX/DMAX
      DY=UY*DY/DMAX
      NPT=DMAX-0.5
      X(1)=X1+DX
      Y(1)=Y1+DY
    2 IF(NPT.LT.1)RETURN
      ICE = MIN0(NPT,10)
      DO 1 IC=2,ICE
      X(IC)=X(IC-1)+DX
    1 Y(IC)=Y(IC-1)+DY
      CALL PLOTEM(C,X,Y,ICE)
      NPT = NPT - ICE
      X(1) = X(ICE)+DX
      Y(1) = Y(ICE)+DY
      GO TO 2
      END
      SUBROUTINE DUMP IT(I)
      DIMENSION HS(6)
      COMMON/E1/AB(7)
      COMMON /Z96PX/G(663),XMIN,UX,YMAX,UY
      DO 9 IC=1,6
      HS(IC) = XMIN+20.*UX*(IC-1)
    9 IF(ABS(HS(IC)/UX).LE.0.001)HS(IC)=0.0
      WRITE(I,100)AB(1),AB(2),AB(3),AB(4),AB(5),AB(6),AB(7)
100   FORMAT(1H1,49X,7A8)
      WRITE(I,104)
  104 FORMAT(1HC/13X,10('+ ',9X),'+ '/13X,'+ ',10(9('- '),'+ '))
      YAY=YMAX+5.*UY
      JB = 1
      JE=13
      DO 1 IC=1,10
      YAY=YAY-5.*UY
      IF(ABS(YAY/UY).LT.0.001)YAY=0.0
      WRITE(I,102)YAY,(G(JC),JC=JB,JE)
  102 FORMAT(1X,G10.4,'++ ',10A8,A5,'++ ')
      DO 2 KC=1,4
      JB = JE+1
      JE = JE+12
      WRITE(I,101)(G(JC),JC=JB,JE)
  101 FORMAT(12X,'- ',10A8,A5,'- ')
    2 CONTINUE
      JB=JE+1
    1 JE=JE+12
      YAY=YMAX -50.*UY
      WRITE(I,102)YAY,(G(JC),JC=JB,JE)
      WRITE(I,103)HS
  103 FORMAT(13X,'+ ',10(9('- '),'+ ')/13X,10('+ ',9X),'+ '/10X,6(G10.4,1
      RETURN
      END
```

```
      SUBROUTINE DISPLAY(X,Y,N,XMAX,XMIN,YMAX,YMIN)
      COMMON/B3/TYPE(2)
      COMMON/B2/ANAME(2)
      COMMON/B1/AB(7)
      DIMENSION X(N),Y(N)
      XSCALE=(XMAX-XMIN)/15.0
      YSCALE=(YMAX-YMIN)/12.5
      XW=(XMAX-XMIN)/10.0
      YW=(YMAX-YMIN)/10.0
      CALL GPSTART(1,24.0,10.0,YSCALE,YSCALE,0)
      CALL GPNEWORIGIN(-XMIN,-YMIN)
      CALL GPAXESNUM(XW,10,0,YW,10,0,4,1,3,0,4,3)
      EKS=XMIN+(XMAX-XMIN)/4.0
      WY=YMAX
      POSX=XMIN+0.66*(XMAX-XMIN)
      POSY=YMIN-YSCALE
      PY=YMIN+0.66*(YMAX-YMIN)
      PX=XMIN-3.0*XSCALE
      CALL GPMOVE(EKS,WY)
      CALL GPTEXT(23,AB(1),1,4,0,0)
      CALL GPMOVE(POSX,POSY)
      CALL GPTEXT(16,ANAME(1),1,4,0,0)
      CALL GPMOVE(PX,PY)
      CALL GPTEXT(16,TYPE(1),1,4,90,0)
      YPS=YMAX+2.0*YSCALE
      YMS=YMIN-2.0*YSCALE
      XPS=XMAX+2.0*YSCALE
      XMS=YMIN-5.0*XSCALE
      CALL GPMOVE(XMS,YMS)
      CALL GPLINE(XPS,YMS)
      CALL GPLINE(XPS,YPS)
      CALL GPLINE(XMS,YPS)
      CALL GPLINE(XMS,YMS)
      DO 50 I=1,N
      CALL GPMOVE(X(I),Y(I))
      CALL GPMARK(0,1)
50    CONTINUE
      CALL GPFINISH
      RETURN
      END
      BLOCK DATA TITLES
      COMMON/B3/TYPE(2)
      COMMON/B2/ANAME(2)
      DATA TYPE/'ELASTIC ','MODULUS '/
      DATA ANAME/'DEGREES ','KELVIN  '/
      END
      FINISH
****
```

PROGRAM 3.

```
      MASTER PLOTTER
C
C     PROGRAM TO CORRECT CHANGES IN SING AROUND FREQUENCY
C     DUE TO TRIGGER POINT JUMPING OR TO DETECTOR BEING
C     RESET.
C
      COMMON/B1/AB(7)
      REAL INC,MOD
      INTEGER G
      DIMENSION O(200)
      DIMENSION A(2),TT(200)
      DIMENSION STR(200),MOD(200)
      DIMENSION AA(200),BB(200)
      DIMENSION INC(200),DIR(200),OBS(200)
      DIMENSION G(200)
      DIMENSION U(200),Z(200)
      DIMENSION T(200),DEL(200),DIFF(200)
      DIMENSION P(200),S(200),W(200)
      DIMENSION X(200),Y(200)
      I=0
      READ(5,1)AB(1),AB(2),AB(3),AB(4),AB(5),AB(6),AB(7)
1      FORMAT(7A3)
      READ(5,4)CONST
4     FORMAT(E0.0)
5     I=I+1
      READ(5,10) X(I),Y(I)
10    FORMAT(2F0.0)
      IF(Y(I).GT.0.0)GOTO 5
      N=I-1
C
C
C     CALL PRESCAL
C
C
      CALL PRESCAL(X,T,N)
C
C      SET UP ARRAYS TO MONITOR BEHAVIOUR OF DATA
C
      G(1)=0
      G(2)=0
      G(3)=0
      DO 20 I=2,N
      INC(I)=Y(I)-Y(I-1)
      IF(INC(I).EQ.0.0)INC(I)=DIR(I-1)*0.001
      DIR(I)=INC(I)/ABS(INC(I))
      DIR(1)=DIR(2)
      OBS(I)=DIR(I)/DIR(I-1)
20    CONTINUE
      DO 100 I=4,N
      G(I)=0
      U(I)=Y(I)
```

```
      BA=ABS(Y(I-1)-Y(I-2))
      B=ABS(Y(I-2)-Y(I-3))
      C=BA+B
      D=X(I-1)-X(I-3)
      S(I)=ABS(C/D)
      P=Y(I)-Y(I-1)
      Q(I)=X(I)-X(I-1)
      R(I)=ABS(P/Q(I))
      W(I)=5.0*S(I)
100   CONTINUE
C
C       SELECT CONDITIONS UNDER WHICH CORRECTIONS SHOULD
C        BE MADE TO DATA
C
      DO 200 I=4,N
      G(I)=G(I-1)
      IF(OBS(I).GT.0)GO TO 70
      IF(OBS(I+1).GT.0)GOTO 70
      GOTO 71
70    IF(R(I).LE.W(I))GOTO 50
C
C                CORRECTING PROCEDURE FOLLOWS
C
71    J=I
40    A1=(Y(J-1)-Y(J-3))/(X(J-1)-X(J-3))
      IF(A1.NE.0.0)GOTO 60
      J=J-1
      IF(J.LE.3)GOTO 50
      GOTO 40
60    A2=ABS(A1)
      SIGN=A1/A2
      SLOPE=S(I)*SIGN
      DIFF(I)=SLOPE*Q(I)+Y(I-1)-Y(I)
      G(I)=G(I-1)+1
50    CONTINUE
C
C       END OF CORRECTING ROUTINE
C        GO TO 50  BYPASSES CORRECTIONS TO DATA
C
200   CONTINUE
      U(1)=Y(1)
      DEL(1)=0.0
      DO 150 K=2,N
      DEL(K)=DEL(K-1)+DIFF(K)
      U(K)=Y(K)+DEL(K)
150   CONTINUE
      DO 205 K=1,N
      Z(K)=U(K)**2
205   CONTINUE
290   DO 300 I=1,N
      IF(X(I).GT.0.0)GOTO 298
      COEF=CONST/Z(I)
```

```
      WRITE(6,299)COEF
  299 FORMAT(1H0,20X,'COEFFICIENT =',E14.7)
      WRITE(6,294)CONST,Z(I)
  294 FORMAT(1H0,25X,E14.7,10X,F10.3)
      GOTO 301
  298 CONTINUE
      IF(I.LT.N)GOTO 300
      CALL LINEFIT(N,A,T,Z)
      COEF=CONST/A(1)
  300 CONTINUE
  301 CONTINUE
      DO 351 I=1,N
      TT(I)=T(I)*1000000.0
  351 CONTINUE
      DO 251 I=1,N
      STR(I)=TT(I)/CONST
      MOD(I)=COEF*Z(I)
  251 CONTINUE
      WRITE(6,260)
  260 FORMAT(//,10X,101('*'))
      DO 250 I=1,N
      WRITE(6,230)
  230 FORMAT(1H0,9X,5('*',19X),'*')
      WRITE(6,240) X(I),T(I),Y(I),U(I),MOD(I),G(I)
  240 FORMAT(1H0,9X,'*',6X,F6.3,7X,'*',4X,F7.3,9X,'*',5X,
     1F7.3,7X,'*',5X,F7.3,7X,'*',4X,E10.6,3X,'*',3X,I3)
      WRITE(6,230)
      WRITE(6,260)
  250 CONTINUE
C     CALL GRAPH('*',T,Y,N,6)
      CALL GRAPH('*',T,MOD,N,6)
C     CALL GRAPH('*',STR,MOD,N,6)
      CALL LINEFIT(N,AA,STR,MOD)
      WRITE(6,390)AB(1),AB(2),AB(3),AB(4),AB(5),AB(6),AB(7)
  390 FORMAT(1H1,///,56X,7A8,///)
      WRITE(6,399)
  399 FORMAT(1H0,40X,40('*'))
      WRITE(6,303)
  303 FORMAT(1H0,40X,'*',11X,'ELASTIC CONSTANTS',10X,'*')
      WRITE(6,301)
      WRITE(6,430)
  430 FORMAT(1H0,40X,'*',7X,'SDEC',9X,'*',7X,'TDEC',7X,'*')
      WRITE(6,302)
  301 FORMAT(1H0,40X,40('*'))
  302 FORMAT(1H0,40X,'*',19X,'*',18X,'*')
      WRITE(6,420)AA(1),AA(2)
  420 FORMAT(1H0,40X,'*',4X,E10.4,5X,'*',4X,E10.4,4X,'*')
      WRITE(6,302)
      WRITE(6,301)
      CALL LINEFIT(N,EE,TT,MOD)
      WRITE(6,409)
  409 FORMAT(////////,41X,40('*'))
```

```
      WRITE(6,305)
  305 FORMAT(1H0,40X,'*',9X,'PRESSURE DERIVATIVES',9X,'*')
      WRITE(6,301)
      WRITE(6,420)
      WRITE(6,302)
      WRITE(6,420)BB(1),BB(2)
      WRITE(6,302)
      WRITE(6,201)
      STOP
      END
      SUBROUTINE PRESCAL(X,T,N)
      DIMENSION X(200),T(200)
      DO 1 L=1,N
      T(L)=X(L)/10.0
    1 CONTINUE
      WRITE(6,210)
  210 FORMAT(1H1,100('*'))
      WRITE(6,214)
  214 FORMAT(1H0,10X,'APPLIED FORCE',7X,'  PRESSURE    ',10X,'OBSERVED
     113X,'CORRECTED',12X,'ELASTIC')
      WRITE(6,215)
  215 FORMAT(1H0,17X,' KG',13X,'MEGA PASCAL',11X,'FREQUENCY',12X,
     1'FREQUENCY',13X,'CONSTANT')
      WRITE(6,220)
  220 FORMAT(//,19X,'W',19X,'P',19X,'F',19X,'CF',19X,'FO',12X,'GEN')
      RETURN
      END
      SUBROUTINE GRAPH(C,X,Y,N,I)
      DIMENSION X(N),Y(N)
      CALL MINMX(X,N,XMAX,XMIN,10,0)
      CALL MINMX(Y,N,YMAX,YMIN,10,0)
      CALL SCALE IT(XMAX,XMIN,XMAX,XMIN)
      CALL PLOTEM(C,X,Y,N)
      IF(I.GT.0)CALL DUMP IT(I)
      CALL DISPLAY(X,Y,N,XMAX,XMIN,YMAX,YMIN)
      RETURN
      END
      SUBROUTINE MINMX(X,N,XMAX,XMIN,NDV,INC)
      DIMENSION X(N),A(12)
      DATA A/1.25,1.5,2.,2.5,3.,4.,5.,6.,7.5,8.,10.,12.5/
      DTRNC(Z)=AINT(Z+10000.)-10000.
      IF(INC.GE.1)GOTO 2
      XMAX = X(1)
      XMIN = XMAX
    2 DO 1 IC=1,N
      IF(X(IC).GT.XMAX)XMAX=X(IC)
    1 IF(X(IC).LT.XMIN)XMIN=X(IC)
      PLG=ALOG10((XMAX-XMIN)/NDV)
      EXP=DTRNC(PLG)
      SUX=PLG-EXP
      SUX=10.**SUX
      DO 3 IC=1,12
      IF(SUX.LT.A(IC))GOTO 4
```

```
    3 CONTINUE
    4 UX=A(IC)*10.**EXP
      IC=IC+1
      XMX =UX*DTPNC(XMAX/UX+0.9999)
      XMN =UX*DTPNC(XMIN/UX+0.0001)
      IF((XMX-XMN)/UX.GT.NDV+0.1)GOTO 4
      XMIN =XMN
      XMAX = XMN+NDV*UX
      RETURN
      END
      SUBROUTINE SCALE IT(XMX,XMN,YMX,YMN)
      COMMON /Z96PX/G(663),XMIN,UX,YMAX,UY
      DATA B/'      '/
      XMIN=XMN
      UX =(XMX-XMN)/100.0
      YMAX = YMX
      UY = (YMX-YMN)/50
      DO 1 IC=1,663
    1 G(IC)=B
      RETURN
      END
      SUBROUTINE PLOTEM(C,X,Y,N)
      DIMENSION X(N),Y(N)
      COMMON /Z96PY/G(663),XMIN,UX,YMAX,UY
      DO 1 IC=1,N
      IX=INT((X(IC)-XMIN)/UX+1.5)
      IF(IX.GT.101)GOTO 1
      IF(IX.LT.1)GOTO 1
      IY=INT((YMAX-Y(IC))/UY+1.5)
      IF(IY.GT.51)GOTO 1
      IF(IY.LT.1)GOTO 1
      CALL COPY(1,G(13*IY-12),IX,C,1)
    1 CONTINUE
      RETURN
      END
      SUBROUTINE LINE(C,X1,Y1,X2,Y2)
      DIMENSION X(10),Y(10)
      COMMON /Z96PX/G(663),XMIN,UX,YMAX,UY
      DX=(X2-X1)/UX
      DY=(Y2-Y1)/UY
      DMAX=AMAX1(ABS(DX),ABS(DY))
      DX=UX*DX/DMAX
      DY=UY*DY/DMAX
      NPT=DMAX-0.5
      X(1)=X1+DX
      Y(1)=Y1+DY
    2 IF(NPT.LT.1)RETURN
      ICE = MIN0(NPT,10)
      DO 1 IC=2,ICE
      X(IC)=X(IC-1)+DX
    1 Y(IC)=Y(IC-1)+DY
      CALL PLOTEM(C,X,Y,ICE)
```

```
      NPT = NPT - ICE
      X(I) = X(ICE)+DX
      Y(I) = Y(ICE)+DY
      GO TO 2
      END
      SUBROUTINE DUMP IT(I)
      DIMENSION HS(6)
      COMMON /Z96PX/G(663),XMIN,UX,YMAX,UY
      DO 9 IC=1,6
      HS(IC) = XMIN+20.*UX*(IC-1)
    9 IF(ABS(HS(IC)/UX).LE.0.001)HS(IC)=0.0
      WRITE(I,104)
  104 FORMAT(1H1/13X,10('+',9X),'+'/13X,'+',10(9('-'),'+'))
      YAY=YMAX+5.*UY
      JB = 1
      JE=13
      DO 1 IC=1,10
      YAY=YAY-5.*UY
      IF(ABS(YAY/UY).LT.0.001)YAY=0.0
      WRITE(I,102)YAY,(G(JC),JC=JB,JE)
  102 FORMAT(1X,G10.4,'++',12A8,A5,'++')
      DO 2 KC=1,4
      JB = JE+1
      JE = JB+12
      WRITE(I,101)(G(JC),JC=JB,JE)
  101 FORMAT(13X,'-',12A8,A5,'-')
    2 CONTINUE
      JB=JE+1
    1 JE=JB+12
      YAY=YMAX -50.*UY
      WRITE(I,102)YAY,(G(JC),JC=JB,JE)
      WRITE(I,103)HS
  103 FORMAT(13X,'+',10(9('-'),'+')/13X,10('+',9X),'+'/10X,6(G10.4,10
      RETURN
      END
      SUBROUTINE LINEFIT(N,A,X,Y)
      DIMENSION A(2),X(200),Y(200)
      SIGX=0.0
      SIGY=0.0
      SIGXY=0.0
      SIGXSQ=0.0
      DO 200 I=1,N
      AN=FLOAT(N)
      SIGXY=SIGXY+X(I)*Y(I)
      SIGX=SIGX+X(I)
      SIGY=SIGY+Y(I)
      SIGXSQ=SIGXSQ+X(I)**2
  200 CONTINUE
      DELTA=AN*SIGXSQ-SIGX**2
      A(1)=(SIGY*SIGXSQ-SIGX*SIGXY)/DELTA
      A(2)=(AN*SIGXY-SIGX*SIGY)/DELTA
      RETURN
      END
```

```
      SUBROUTINE DISPLAY(X,Y,N,XMAX,XMIN,YMAX,YMIN)
      COMMON/B3/TYPE(2)
      COMMON/B2/ANAME(2)
      COMMON/B1/AB(7)
      DIMENSION X(N),Y(N)
      XSCALE=(XMAX-XMIN)/15.0
      YSCALE=(YMAX-YMIN)/15.0
      XW=(XMAX-XMIN)/10.0
      YW=(YMAX-YMIN)/10.0
      CALL GPSTART(1,24.0,10.0,XSCALE,YSCALE,0)
      CALL GPNEWORIGIN(-XMIN,-YMIN)
      CALL GPAXESNUM(XW,10,0,YW,10,0,4,1,3,0,4,3)
      EKS=XMIN+(XMAX-XMIN)/4.0
      WY=YMAX
      POSX=XMIN+0.66*(XMAX-XMIN)
      POSY=YMIN-YSCALE
      PY=YMIN+0.66*(YMAX-YMIN)
      PX=XMIN-3.0*XSCALE
      CALL GPMOVE(EKS,WY)
      CALL GPTEXT(22,AB(1),1,4,0,0)
      CALL GPMOVE(POSX,POSY)
      CALL GPTEXT(16,ANAME(1),1,4,0,0)
      CALL GPMOVE(PX,PY)
      CALL GPTEXT(16,TYPE(1),1,4,90,0)
      DO 50 I=1,N
      CALL GPMOVE(X(I),Y(I))
      CALL GPMARK(0,1)
50    CONTINUE
      CALL GPFINISH
      RETURN
      END
      BLOCK DATA TITLES
      COMMON/B3/TYPE(2)
      COMMON/B2/ANAME(2)
      DATA TYPE/'ELASTIC ','MODULUS '/
      DATA ANAME/'    MEGA',' PASCAL '/
      END
      FINISH
****
```

PROGRAM 4

```
      MASTER THERMOCAL
      COMMON/B1/A(4,11),C(4)
      COMMON/B3/B(4,11)
      COMMON/B4/T1,T2,T3,V1,V2,V3
      DIMENSION ZP(100),ZZ(100),TT(100)
      DIMENSION PP(100),CT(100)
      DIMENSION VS(100),VP(100),E(100)
      DIMENSION T(100),SUM(100),Z(100)
      READ(5,1)C(1),C(2),C(3)
1     FORMAT(3F0.0)
      READ(5,2)NDATA
2     FORMAT(I0)
      DO 15 I=1,NDATA
      READ(5,5)T(I),Z(I)
5     FORMAT(2F0.0)
15    CONTINUE
      M=1
      C(4)=0.0
      CALL ORDER(Z,T,NDATA)
      DO 100 J=1,4
      DO 50 I=M,NDATA
      IF(Z(I).LT.C(J))GOTO 75
      N=N+1
      M=M+1
50    CONTINUE
75    DO 80 I=1,N
      ZZ(I)=Z(M-N-1+I)
      TT(I)=T(M-N-1+I)
80    CONTINUE
      CALL POLYFIT(N,A,ZZ,TT,I,J,K,5)
      N=0
100   CONTINUE
      READ(5,115)PO,PM,PS
115   FORMAT(3F0.0)
      READ(5,120)NUM
120   FORMAT(I0)
      TOT=FLOAT(NUM)
      TOT=TOT/3.0
      M=INT(TOT)
      M2=M*2
      M3=M*3
      DO 130 L=1,NUM
      READ(5,125)VS(L),VP(L),E(L)
125   FORMAT(3F0.0)
      PP(L)=(VP(L)*PS)/VS(L)
130   ZP(L)=(PP(L)-PO)/(PM-PO)
      WRITE(6,190)
190   FORMAT(1H1,80X,81('*'))
      WRITE(6,205)
205   FORMAT(1H0,25X,'PRESSURE',17X,'Z',10X,
     1'TEMPERATURE',14X,'ENE')
      WRITE(6,210)
```

```
210   FORMAT(1H0,20X,81('*'))
      CALL ORDER(ZP,E,NUM)
      CALL ORDER(PP,CT,NUM)
      DO 250 L=1,NUM
      DO 150 J=1,4
      IF(ZP(L).GT.C(J))GOTO 160
150   CONTINUE
160   DO 200 K=1,6
      SUM(L)=SUM(L)+A(J,K)*ZP(L)**(K-1)
      CT(L)=SUM(L)
200   CONTINUE
      WRITE(6,220)PP(L),ZP(L),CT(L),E(L)
220   FORMAT(1H ,20X,4('*',5X,F9.3,5X),'*')
      WRITE(6,230)
230   FORMAT(1H ,20X,81('*'))
250   CONTINUE
      J=1
      T1=CT(M)-273.0
      V1=E(M)
      T2=CT(M2)-273.0
      V2=E(M2)
      T3=CT(M3)-273.0
      V3=E(M3)
      WRITE(6,260)T1,T2,T3
260   FORMAT(1H1,30X,3(F5.2,10X))
      WRITE(6,261)V1,V2,V3
261   FORMAT(1H ,20X,3(F5.3,10X))
      CALL POLYFIT(NUM,E,CT,E,I,J,K,4)
      CALL GRAPH('*',CT,E,NUM,6)
      STOP
      END
      SUBROUTINE ORDER(X,Y,N)
      DIMENSION X(100),Y(100)
      DO 100 J=1,N
      DO 50 I=1,N-1
      IF(X(I+1).LE.X(I))GOTO 50
      PM=X(I)
      X(I)=X(I+1)
      X(I+1)=PM
      PN=Y(I)
      Y(I)=Y(I+1)
      Y(I+1)=PN
50    CONTINUE
100   CONTINUE
      RETURN
      END
      SUBROUTINE POLYFIT(NOPTS,A,X,Y,I,J,L,DEGREE)
      COMMON/BG/DEGPI
C
C   MAIN PROGRAM FOR LEAST SQUARES CURVE FITTING
C    MAX NO DATA POINTS IS 100
C    MAX DEGREE IS 10
```

```
C
      DIMENSION A(4,11),X(100),Y(100),COEF(100)
      INTEGER DEGREE,DEGP1
      DEGP1=DEGREE + 1
      CALL NORMEQ(DEGREE,DEGP1,NOPTS,Y,Y,COEF)
C
C
C     PRINT RESULTS
C
C
      WRITE(6,6)
6     FORMAT(1H1,45X,30('*'))
      WRITE(6,7)
7     FORMAT(1H0,45X,'*',2X,'ORDER          COEFFICIENT',3X,'*')
      WRITE(6,9)
9     FORMAT(1H0,45X,30('*'))
      DO 5 L=1,DEGP1
      K=L-1
      WRITE(6,4)K,COEF(L)
4     FORMAT(1H0,45X,'*',4X,I1,4X,'*',3X,F12.6,3X,'*')
      WRITE(6,8)
8     FORMAT(1H0,45X,30('*'))
      A(J,L)=COEF(L)
5     CONTINUE
      RETURN
      END
      SUBROUTINE NORMEQ(DEGREE,DEGP1,NOPTS,X,Y,COEF)
C
C     ROUTINE TO OBTAIN NORMAL EQUATIONS
C
      INTEGER DEGT2,DEGREE,DEGP1
      DIMENSION POWX(200),X(NOPTS),Y(NOPTS),SUM(11,11),RHS(11)
      DIMENSION COEF(DEGP1)
      DEGT2=DEGREE*2
C
C     COMPUTE SUMS OF POINTS
C
      DO 1 I=1,DEGT2
      POWX(I)=0.0
      DO 1 J=1,NOPTS
1     POWX(I)=POWX(I)+X(J)**I
C
C
C     FROM SUMS OF POWERS COMPUTE THE LHS OF
C     THE EQUATIONS IN THE TWO DIMENSIONAL
C     ARRAY SUM
C
C
      DO 2 I=1,DEGP1
      DO 2 J=1,DEGP1
      K=I+J-2
      IF(K.LE.0)GOTO3
```

```
      SUM(I,J)=POWX(K)
      GOTO 2
3     SUM(I,J)=NOPTS
2     CONTINUE
C
C       SET UP RHS EQUATIONS
C
      RHS(I)=0.0
      DO 4 J=1,NOPTS
4     RHS(I)=RHS(I)+Y(J)
      DO 5 I=2,DEGP1
      RHS(I)=0.0
      DO 5 J=1,NOPTS
5     RHS(I)=RHS(I)+Y(J)*X(J)**(I-1)
C
C
C       CALL SUBROUTINE TO SOLVE THE EQUATIONS
C
      CALL GAUSS(DEGREE,DEGP1,RHS,COEF,SUM)
      RETURN
      END

      SUBROUTINE GAUSS(DEGREE,DEGP1,RHS,COEF,SUM)
C
C
C   THIS SOLVES THE SET OF EQUATIONS
C    SUM(I,J)=RHS(I)
C
C
      INTEGER DEGREE,DEGP1
      DIMENSION RHS(DEGP1),COEF(DEGP1),SUM(11,11)
      DO 10 K=1,DEGREE
      KPLUS1=K+1
      L=K
C
C
C   FIND TERMS OF GREATEST MAGNITUDE
C
C
      DO 11 I=KPLUS1,DEGP1
      IF(ABS(SUM(I,K)).LE.ABS(SUM(L,K)))GOTO 11
      L=I
11    CONTINUE
      IF(L.LE.K)GOTO 12
C
C
C   INTERCHANGE TO OBTAIN ROWS OF DECREASING
C         MAGNITUDE
C
      DO 13 J=K,DEGP1
      TEMP=SUM(K,J)
      SUM(K,J)=SUM(L,J)
```

```
 13     SUM(L,J)=DUMP
        DUMP=RHS(K)
        RHS(K)=RHS(L)
        RHS(L)=DUMP
 12     DO 10 I=KPLUS1,DEGP1
        FACTOR = SUM(I,K)/SUM(K,K)
C
C
C    SET THIS TERM TO ZERO
       SUM(I,K)=0.0
       DO 14 J=KPLUS1,DEGP1
C
C
C
C    COMPUTE OTHER TERMS.
C
C
C
 14     SUM(I,J)=SUM(I,J)-FACTOR*SUM(K,J)
 10     RHS(I)=RHS(I)-FACTOR*RHS(K)
C
C
C    SOLVE SINGLE EQUATION REMAINING
C
C
        COEF(DEGP1)=RHS(DEGP1)/SUM(DEGP1,DEGP1)
        I=DEGREE
 16     IPLUS1=I+1
        TOTAL=0.0
C
C
C    COMPUTE OTHER SOLUTIONS BY SUBSTITUTION
C
C
        DO 15 J=IPLUS1,DEGP1
 15     TOTAL=TOTAL+SUM(I,J)*COEF(J)
C
C
C    RETURN SOLUTIONS IN THE MATRIX COEF
C
C
        COEF(I)=(RHS(I)-TOTAL)/SUM(I,I)
        I=I-1
        IF(I.GT.0)GOTO 16
        RETURN
        END
        SUBROUTINE GRAPH(C,X,Y,N,I)
        DIMENSION X(N),Y(N)
        CALL MNMX(X,N,XMAX,XMIN,10,0)
        CALL MNMX(Y,N,YMAX,YMIN,10,0)
        CALL SCALE IT(XMAX,XMIN,YMAX,YMIN)
        CALL PLOTEM(C,X,Y,N)
```

```
      IF(I.GT.0)CALL DUMP IT(I)
      CALL DISPLAY(X,Y,N,XMAX,XMIN,YMAX,YMIN)
      RETURN
      END
      SUBROUTINE MNMX(X,N,XMAX,XMIN,NDV,INC)
      DIMENSION X(N),A(12)
      DATA A/1.25,1.5,2.,2.5,3.,4.,5.,6.,7.5,8.,10.,12.5/
      DTRNC(Z)=AINT(Z+10000.)-10000.
      IF(INC.GE.1)GOTO 2
      XMAX = X(1)
      XMIN = XMAX
    2 DO 1 IC=1,N
      IF(X(IC).GT.XMAX)XMAX=X(IC)
    1 IF(X(IC).LT.XMIN)XMIN=X(IC)
      RLG=ALOG10((XMAX-XMIN)/NDV)
      EXP=DTRNC(RLG)
      SUX=RLG-EXP
      SUX=10.**SUX
      DO 3 IC=1,12
      IF(SUX.LT.A(IC))GOTO 4
    3 CONTINUE
    4 UX=A(IC)*10.**EXP
      IC=IC+1
      XMX =UX*DTRNC(XMAX/UX+0.9999)
      XMN =UX*DTRNC(XMIN/UX+0.0001)
      IF((XMX-XMN)/UX.GT.NDV+0.1)GOTO 4
      XMIN =XMN
      XMAX = XMN+NDV*UX
      RETURN
      END
      SUBROUTINE SCALE IT(XMX,XMN,YMX,YMN)
      COMMON /Z96PX/G(663),XMIN,UX,YMAX,UY
      DATA B/'      '/
      XMIN=XMN
      UX =(XMX-XMN)/100.0
      YMAX = YMX
      UY = (YMX-YMN)/50
      DO 1 IC=1,663
    1 G(IC)=B
      RETURN
      END
      SUBROUTINE PLOTEM(C,X,Y,N)
      DIMENSION X(N),Y(N)
      COMMON /Z96PY/G(663),YMIN,UX,YMAX,UY
      DO 1 IC=1,N
      IX=INT((X(IC)-XMIN)/UX+1.5)
      IF(IX.GT.101)GOTO 1
      IF(IX.LT.1)GOTO 1
      IY=INT((YMAX-Y(IC))/UY+1.5)
      IF(IY.GT.51)GOTO 1
      IF(IY.LT.1)GOTO 1
      CALL COPY(1,C(13*IY-12),IX,G,1)
    1 CONTINUE
      RETURN
      END
```

```
      SUBROUTINE LINE(C,X1,Y1,X2,Y2)
      DIMENSION X(10),Y(10)
      COMMON /Z96PX/G(663),XMIN,UX,YMAX,UY
      DX=(X2-X1)/UX
      DY=(Y2-Y1)/UY
      DMAX=AMAX1(ABS(DX),ABS(DY))
      DX=UX*DX/DMAX
      DY=UY*DY/DMAX
      NPT=DMAX-0.5
      X(1)=X1+DX
      Y(1)=Y1+DY
    2 IF(NPT.LT.1)RETURN
      ICE = MIN0(NPT,10)
      DO 1 IC=2,ICE
      X(IC)=X(IC-1)+DX
    1 Y(IC)=Y(IC-1)+DY
      CALL PLOTEM(C,X,Y,ICE)
      NPT = NPT - ICE
      X(1) = X(ICE)+DX
      Y(1) = Y(ICE)+DY
      GO TO 2
      END
      SUBROUTINE DUMP IT(I)
      DIMENSION HS(6)
      COMMON /Z96PY/G(663),XMIN,UX,YMAX,UY
      DO 9 IC=1,6
      HS(IC) = YMIN+20.*UY*(IC-1)
    9 IF(ABS(HS(IC)/UY).LE.0.001)HS(IC)=0.0
      WRITE(I,104)
  104 FORMAT(1H1/13X,10('+',9X),'+'/13X,'+',10(9('-'),'+'))
      YAY=YMAX+5.*UY
      JB = 1
      JE=10
      DO 1 IC=1,10
      YAY=YAY-5.*UY
      IF(ABS(YAY/UY).LT.0.001)YAY=0.0
      WRITE(I,102)YAY,(G(JC),JC=JB,JE)
  102 FORMAT(1X,G10.4,'++',10A8,A5,'++')
      DO 2 KC=1,4
      JB = JE+1
      JE = JE+10
      WRITE(I,101)(G(JC),JC=JB,JE)
  101 FORMAT(10X,'-',10A8,A5,'-')
    2 CONTINUE
      JB=JE+1
    1 JE=JB+10
      YAY=YMAX -50.*UY
      WRITE(I,102)YAY,(G(JC),JC=JB,JE)
      WRITE(I,103)HS
  103 FORMAT(13X,'+',10(9('-'),'+')/13X,10('+',9X),'+'/10X,((G10.4,1P
      RETURN
      END
```

```
      SUBROUTINE DISPLAY(X,Y,N,XMAX,XMIN,YMAX,YMIN)
      EXTERNAL G
      EXTERNAL H
      DIMENSION X(N),Y(N)
      XSCALE=(XMAX-XMIN)/12.5
      YSCALE=(YMAX-YMIN)/15.0
      XW=(XMAX-XMIN)/10.0
      YW=(YMAX-YMIN)/10.0
      EPS=YW*0.1
      CALL GPSTART(1,24.0,10.0,XSCALE,YSCALE,0)
      CALL GPNEWORIGIN(-XMIN,-YMIN)
      CALL GPAXESNUM(XW,10,0,YW,10,0,4,1,3,4,3,3)
      YPS=YMAX+3.0*YSCALE
      YMS=YMIN-3.0*YSCALE
      XPS=XMAX+1.0*YSCALE
      XMS=XMIN-3.0*YSCALE
      CALL GPMOVE(XMS,YMS)
      CALL GPLINE(XPS,YMS)
      CALL GPLINE(XPS,YPS)
      CALL GPLINE(XMS,YPS)
      CALL GPLINE(XMS,YMS)
      DO 50 I=1,N
      CALL GPMOVE(X(I),Y(I))
      CALL GPMARK(0,2)
50    CONTINUE
      CALL GPFGRAPH(G,XMIN,XMAX,EPS)
      CALL GPFGRAPH(H,XMIN,XMAX,EPS)
      CALL GPFINISH
      RETURN
      END
      FUNCTION G(X)
      COMMON/B3/B(4,11)/B2/DEGP1
      INTEGER DEGP1
      I=1
      G=B(I,1)+B(I,2)*Y+B(I,3)*Y**2+B(I,4)*Y**3+B(I,5)*Y**4+B(I,6)*Y**
      RETURN
      END
      FUNCTION H(T)
      COMMON/B4/T1,T2,T3,V1,V2,V3
      DELTA=((T1**3)*(T2**2)*T3+(T1**2)*T2*(T2**3)+T1*(T2**3)*(T3**2)
     1 -T1*(T2**2)*(T3**3)-(T1**2)*(T2**3)*T3-(T1**2)*T2*(T3**2))
      A=(V1*((T2**2)*T3-T2*(T3**2))-V2*((T1**2)*T3-T1*(T3**2))
     1+V3*((T1**2)*T2-T1*(T2**2)))/DELTA
      B=-(V1*((T2**3)*T3-T2*(T3**3)) -V2*((T1**3)*T3-T1*(T3**3))
     1+V3*((T1**3)*T2-T1*(T2**3)))/DELTA
      C=(V1*((T2**3)*(T3**2)-(T2**2)*(T3**3))-V2*((T1**3)*(T3**2)-
     1(T1**2)*(T3**3))+V3*((T1**3)*(T2**2)-(T1**2)*(T2**3)))/DELTA
      H=A*(T-273.0)**3+B*(T-273.0)**2+C*(T-273.0)
      RETURN
      END
      FINISH
****
```

PROGRAM 5

```
      MASTER THCOUPLE
C  PROGRAM TO CALIBRATE A THERMOCOUPLE
C  FROM THREE VOLTAGES MEASURED AT CALIBRATION TEMPERATURES
C  CALIBRATION TEMPERATURES ARE 4.2K ,77.3K ,AND WATER AT ROOM TEMP.
C  REFERENCE POINT IS AT 0 DEGREE CETIGRADE
      READ(1,100)T1,T2,T3
100   FORMAT(3F0.0)
      WRITE(2,200)T1,T2,T3
200   FORMAT(' T1=',F6.1/' T2=',F6.1/' T3=',F6.1)
      READ(1,101)V1,V2,V3
101   FORMAT(3F0.0)
      WRITE(2,201)V1,V2,V3
201   FORMAT(' V1=',F9.6/' V2=',F9.6/' V3=',F9.6)
      DELTA=((T1**2)*(T2**2)*T3+(T1**2)*T2*(T3**3)+T1*(T2**3)*(T3**2)
     1 -T1*(T2**2)*(T3**3)-(T1**2)*(T2**3)*T3-(T1**3)*T2*(T3**2))
      A=(V1*((T2**2)*T3-T2*(T3**2))-V2*((T1**2)*T3-T1*(T3**2))
     1+V3*((T1**2)*T2-T1*(T2**2)))/DELTA
      B=-(V1*((T2**3)*T3-T2*(T3**3)) -V2*((T1**3)*T3-T1*(T3**3))
     1+V3*((T1**3)*T2-T1*(T2**3)))/DELTA
      C=(V1*((T2**2)*(T3**3)-(T2**3)*(T3**2))-V2*((T1**3)*(T3**2)-
     1(T1**2)*(T3**3))+V3*((T1**3)*(T2**2)-(T1**2)*(T2**3)))/DELTA
      WRITE(2,202)A,B,C
202   FORMAT(' A=',E12.5/' B=',E12.5/' C=',E12.5)
      WRITE(2,203)
203   FORMAT(1H1,120('*')//,30X,'TEMPERATURE',33X,'VOLTAGE')
205   FORMAT(1H0,120('*'))
      WRITE(6,205)
      WRITE(6,206)
206   FORMAT(//,34X,1HK,33X,1HC,//)
      WRITE(6,205)
      DO 1 I=1,9000,1
      J=I-1
      TE=FLOAT(J)/5.0
      T=TE-273.0
      V=A*(T**3)+B*(T**2)+C*T
      V=V*1000.0
      TK=TE
      TC=T
      WRITE(6,207)
      WRITE(6,204)TK,TC,V
204   FORMAT( 10X,'*',4X,2(F3.1,7X,'*',9X),F10.3,9X,'*')
207   FORMAT( 10X,'*',30X,'*',35X,'*',22X,'*')
1      CONTINUE
      STOP
      END
      FINISH
****
```

Appendix 9 References

Chapter 0

1.	Rosen M.	Phys. Rev.	174	504	1968
2.	Rosen M.	Phys. Rev. B.	1	3748	1970
3.	Fisher E.S. and Dever D.	Trans.Met.Soc.AIME	239	48	1967
4.	Palmer S.B. and Lee E.W.	Proc. Roy. Soc.	A327	519	1972
5.	Palmer S.B., Lee E.W., and Islam M.N.	Proc. Roy. Soc.	A338	341	1974
6.	Papadakis E.P.	C.R.C Critical Review Sol. St. Phys.	3(4)		1973
7.	Holbrook R.D.	J.Acoust.Soc.Am.	20	590	1948
8.	Forgacs R.L.	I.R.E. Trans. Instr.	Dec.	339	1960
9.	Brammer A.J.	Ph.D. Thesis	Exeter Univ.		1967
10.	Fisher E.S. et al	J.Phys.Chm.Sol.	34	687	1973
11.	Brugger K.	J. Appl. Phys.	36	759	1965

Chapter 1

1.	Pierce G.W.	Proc. A.A.A.S.	60	277	1925
2.	Boyle R.W. and Lehmann T.	Phys. Rev.	27	518	1926
3.	Boyle R.W. and Lehmann T.	Trans.Roy.Soc.Can.	21	115	1927
4.	Huntingdon H.B.	Phys. Rev.	72	321	1947
5.	Holbrook R.D.	J. Acoust. Soc. Am.	20	590	1948
6.	Crecraft D.I.	Ultrasonics	117		1968
7.	McSkimin H.J.	J. Acoust. Soc. Am.	37	864	1965
8.	McSkimin H.J.	J. Acoust. Soc. Am.	41	1052	1967
9.	Papadakis E.P.	C.R.C. Crit.Rev.Sol.St. Sci.	3(4)		1973
10.	May J.E.	I.R.E. Nat^{l}.Conv.Rec.	6	134	1958
11.	Williams J. and Lamb J.	J. Acoust. Soc. Am.	30	308	1958
12.	Truell R. et al	Phys. Rev.	105	1723	1957
13.	Myers A. et al	J. Acoust. Soc. Am.	31	161	1959
14.	Forgacs R.L.	I.R.E. Trans. Instr.	Dec	339	1960
15.	Cedrone N.P. and Curran D.R.	J. Acoust. Soc. Am.	26	963	1954
16.	Brammer A.J.	Ph.D. Thesis	Exeter Univ.		1967
17.	Drabble J.R. and Brammer A.J.	Proc.Phys.Soc.Lond.	91	959	1967
18.	Champion K.F.	University Physics	Blackie		p.476

Chapter 2

1.	Landau L.D. and Lifschitz E.M.	Theory of Elasticity	Pergamon		
2.	Kittel C.	Intro. to Sol. St. Physics	Wiley		
3.	Kaplan C.	Phys. Rev.	38	1020	1931
4.	Born M. and Misra R.D.	Proc.Cam.Phil.Soc.	36	466	1940
5.	Hearmon R.F.S.	Acta. Cryst.	6	331	1953
6.	Palmer S.B. and Lee E.W.	Proc. Roy. Soc.	A327	519	1972
7.	Hearmon R.F.S.	Landolt-Bornstein	Vol.1 p.1 and Vol.2 p.1.		
8.	Zemansky M.W.	Heat & Thermodynamics	5th Ed.		1968
9.	Brugger K.	Phys. Rev.	133	A1611	1964
10.	Munn R.W.	Adv. Phys.	18	518	1969
11.	Barron T.H.K. and Munn R.W.	Phil. Mag.	15	85	1967
12.	Elliott R.J. and Gibson A.F.	Intro.Sol.St.Phys.	Macmillan		1974
13.	Collins J.G.	Phil. Mag.	8	323	1963
14.	Sheard F.W.	Phil. Mag.	3	1381	1958
15.	Gerlich D.	J.Phys.Chem.Sol.	30	1638	1969
16.	Fisher E.S. et al	J.Phys.Chem.Sol.	34	687	1973

Chapter 3

1.	Weiss P.	Comptes Rendus	143	1136	1906
2.	Onsager L.	Phys. Rev.	65	117	1944
3.	Greene H.S. and Hurst C.A.	Order-Disorder Phenomena	Interscience		1964
4.	Enz. U.	Physica	26	698	1960
5.	Nicklow R.M. et al	Phys. Rev. Letts.	26	140	1971
6.	Ehrenfest P.	in Zemansky [7]			
7.	Zemansky M.W.	Heat & Thermodynamics	5th Ed.		1968
8.	Landau L.D. and Lifschitz E.M.	Statistical Physics	Pergamon		
9.	Kramers H.A. and Wannier G.H.	Phys. Rev.	60	252	1941
10.	Garland G.W. and Yarnell C.F.	J. Chem. Phys.	44	1112	1966
11.	Garland C.W. and Renand R.	J. Chem. Phys.	44	1120	1966
12.	Lavis D.A. and Bell G.M.	Bull. I.M.A.	13	34	1977
13.	Zeeman E.C.	Catastrophe Theory: Selected Papers			1977

Chapter 4

1.	Whitehead D.G. and Palmer S.B.	IEEE Instr. & Meas.		Sept.	1979
2.	Brammer A.J.	Ph.D. Thesis	Exeter Univ.		1967
3.	Forgacs R.L.	J. Acoust. Soc. Am.	32	1697	1960
4.	Forgacs R.L.	I.R.E. Trans. Instr.	339	Dec.	1960
5.	Papadakis E.P.	C.R.C. Crit.Rev.Sol.St. Sci.	3(4)		1973
6.	McSkimin H.J.	J. Acoust. Soc. Am.	33	606	1961
7.	Truell R. et al	Ultrasonic Meth.Sol.St. Phys.			
8.	McSkimin H.J. and Andreatch P.	J. Acoust. Soc. Am.	41	1052	1967
9.	Heydeman P.	Rev. Sci. Instr.	42	606	1971
10.	Palmer S.B. and Lee E.W.	Proc. Roy. Soc.	A338	341	1974

Chapter 5

1.	Hames T.K.	Ph.D. Thesis	Southampton Univ.		1976
2.	Isci C.	Ph.D. Thesis	Hull Univ.		1977
3.	White G.K.	Exp.Techn.Low.Temp.Phys.	Oxford		1968
4.	Greenough R.D.	Private Communication			
5.	Micromeasurements Ltd.	38905 Chase Rd., Romulus, Michigan, U.S.A.			
6.	Thomas J.F.	Phys. Rev.	175(3)	955	1968
7.	Truell R., Elbaum C. and Chick B.B.	Ultrasonic Tech. in Sol.St.Phys.	Academic		1969
8.	Hiki Y. and Granato A.V.	Phys. Rev.	144(2)	411	1966
9.	Salama K. and Alers G.A.	Phys. Rev.	161(3)	683	1967

Chapter 6

1.	Elliott R.J.	Magnetism Vol.IIA	Ed. Rado & Suhl		1965
2.	Ruderman M.A. and Kittel C.	Phys. Rev.	96	99	1954
3.	Kasuya T.	Prog.Th.Phys.(Jap).	14	45	1956
4.	Yosida K.	Phys. Rev.	106	893	1957
5.	Taylor K.N.R. and Darby M.I.	Physics of Rare Earth Solids	Chapman & Hall		1972
6.	Elliott R.J.	Magn.Props.Rare Earth Mets.	Plenum		1972
7.	Robinson L.B. and Milstein F.	Phys. Rev.	159	466	1967
8.	Rhyne J.J. and Clark A.E.	J. Appl. Phys.	38	1379	1967
9.	Callen E. and Callen H.B.	Phys. Rev.	139	455	1965

Chapter 6 (continued)

10.	Bozorth R.M. and Wakiyama T.	J.Phys.Soc.Jap.	18	97	1963
11.	Moran T.J. and Lüthi B.	J.Phys.Chem.Sol.	31	1735	1970
12.	Southern B.W. and Goodings D.A.	Phys.Rev.B.	7	534	1973
13.	Greenough R.D. and Isci C.	J.Mag.Mag.Mat.	8	43	1978
14.	Elliott R.J. and Stevens K.W.H.	Proc. Roy. Soc.	A218	553	1953
15.	Enz. U.	Physica	26	698	1960
16.	Crangle J.	Private Communication			
17.	Landry P.C.	Phys. Rev.	156	578	1967
18.	MacIntosh A.R.	Physics Today	23	June	1977
19.	Koehler W.C. et al	Rare Earth Research	Gordon & Breach		1963
20.	Dietrich O.W. and Als-Nielsen J.	Phys. Rev.	162	315	1967
21.	Cable J.W. and Wollan E.O.	Phys. Rev.	165	733	1968
22.	Graham C.D.	J. Appl. Phys.	34	1341	1963
23.	Belov K.P. and Pedko A.V.	Sov. Phys. JETP	15	62	1961
24.	Corner W.D., Roe W.C. and Taylor K.N.R.	Proc. Phys. Soc.	80	927	1962
25.	Corner W.D. and Tanner B.	J. Phys. C.	9	627	1976
26.	McWhan D.B. and Stevens A.L.	Phys. Rev.	139	682	1965
27.	Hegland D.E., Legvold S. and Spedding F.H.	Phys. Rev.	131	158	1963
28.	Koehler W.C., Cable J.W., Wollan E.O. and Wilkinson M.K.	J.Phys.Soc.Jap.	17	32	1962
29.	Crangle J.	Proc.Rare Earth Meeting	Birmingham		1979
30.	Bly P.H., Corner W.D. and Taylor K.N.R.	J. Appl. Phys.	40	4787	1969
31.	Corner W.D. and Welford J.	J.Mag.Mag.Mat.	3	212	1976
32.	Rhyne J.J., Foner S., McNiff E.J. & Doclo R.	J. Appl. Phys.	39	892	1968
33.	Nigh H.E., Legvold S. and Spedding F.H.	Phys. Rev.	132	1092	1963
34.	Hegland D.E., Legvold S. and Spedding F.H.	Phys. Rev.	131	158	1963
35.	Behrendt D.R., Legvold S. and Spedding F.H.	Phys. Rev.	109	1544	1958
36.	Green R.W., Legvold S. and Spedding F.H.	Phys. Rev.	122	827	1961
37.	Flippen R.B.	J. Appl. Phys.	35	1047	1964

Chapter 6 (continued)

38.	Coqblin B.	The Electronic Structures of the Rare Earth Metals		Wiley	1977
39.	Feron J.-L.	Ph.D. Thesis			
40.	Bly P.H., Corner W.D. and Taylor K.N.R.	J. Appl. Phys.	39	1336	1968
41.	Bly P.H., Corner W.D. and Taylor K.N.R.	J. Appl. Phys.	40	4787	1969
42.	Darnell F.J.	Phys. Rev.	130	1825	1963
43.	Darnell F.J.	Phys. Rev.	132	1098	1963
44.	Griffel M., Skochdopole R.E. & Spedding F.H.	Phys. Rev.	93	657	1954
45.	Jennings L.D., Stanton R.H. and Spedding F.H.	J. Chem. Phys.	27	909	1957
46.	Griffel M., Skochdopole R.E. & Spedding F.H.	J. Chem. Phys.	25	75	1956
47.	Skochdopole R.E., Griffel M. & Spedding F.H.,	J. Chem. Phys.	23	2258	1955
48.	Robinson L.B. and Milstein F.	Phys. Rev.	134	A187	1964
49.	Bloch D. and Pauthenet R.	Compt. Rendu.	254	1222	1962
50.	Bartholin H. and Bloch D.	J. Phys. Chem. Sol.	29	1063	1968
51.	Umbayaski H., Shirane G., Frazier B.C. & Daniels W.	Phys. Rev.	165	688	1968

Chapter 7

1.	Rosen M.	Phys. Rev.	174	504	1968
2.	Klimker H. and Rosen M.	Phys. Rev. B.	1	3748	1970
3.	Fisher E.S. and Dever D.	Trans.Met.Soc.A.I.M.E.	239	48	1967
4.	Moran T.J. and Lüthi B.	J. Phys. Chem. Sol.	31	1735	1970
5.	Salama K. et al	J. Appl. Phys.	43	3254	1972
6.	Jensen J.	Risø. Rep.	252		1971
7.	Palmer S.B. and Lee E.W.	Proc. Roy. Soc.	A327	519	1972
8.	Palmer S.B. et al	Proc. Roy. Soc.	A338	341	1974
9.	Bozorth R.M.	'Ferromagnetism'			
10.	Köster W.	Z. Metallkunde	35	57	1943
11.	Corner W.D., Roe W.C. and Taylor K.N.R.	Proc.Phys.Soc.Lond.	80	927	1962
12.	du Plessis P.de V.	J.Phys.F.(Met.Phys.)	6	873	1976
13.	Long M.A. et al	Phys. Rev.	178	775	1969
14.	Levinson L.M. and Shtrikman S.	J. Phys. Chem. Sol.	32	981	1971
15.	Moran T.J. and Lüthi B.	Phys. Letts.	29A	665	1969
16.	Lüthi B. et al	J. Phys. Chem. Sol.	31	1741	1970

Chapter 7 (continued)

17.	Isci C.	Ph.D. Thesis	Hull Univ.		1977
18.	Palmer S.B. et al	J.Phys.F.(Met.Phys.)	7	2381	1977
19.	Isci C. and Palmer S.B.	J. Phys. Chem. Sol.	38	1253	1977
20.	Treder R. et al	Phys. Letts.	59A	245	1976
21.	Treder R. et al	J.Mag.Mag.Mat.	5	9	1977
22.	Behrendt D.R. et al	Phys. Rev.	109	1544	1958
23.	Jew T.T. and Legvold S.	U.S. Atomic. En. Comm.	ISP-867	45	1963
24.	Akhavan M.	Phys. Rev.	B8	4258	1973
25.	Fisher E.S. et al	J. Phys. Chem. Sol.	34	687	1973
26.	Klimker H. and Rosen M.	Phys. Rev. B	7	2054	1973
27.	Greenough R.D. et al	Physica	86-88B	61	1977
28.	Ramji Rao R.	Acta. Cryst.	A31	267	1975
29.	Ramji Rao R. and Menon C.S.	J. Phys. Chem. Sol.	35	425	1974
30.	Ramji Rao R. and Menon C.S.	J. Appl. Phys.	44	3892	1973
31.	Ramji Rao R. and Ramanand A.	J. Phys. Chem. Sol.	38	1035	1977
32.	Ramji Rao R. and Menon C.S.	J. Phys. Chem. Sol.	34	1879	1973
33.	Srinivasan R. and Ramji Rao R.	Phys. St. Solidi	29	865	1968
34.	Srinivasan R. and Ramji Rao R.	Phys. St. Solidi	31	K39	1969
35.	Keating P.N.	Phys. Rev.	145	637	1966
36.	Keating P.N.	Phys. Rev.	149	674	1966
37.	Munn R.W.	Proc. Roy. Soc.	18	515	1969

Chapter 8

1.	Long M.A., Wazzan A.R. and Stern R.	Phys. Rev.	178	775	1969
2.	Moran T.J. and Lüthi B.	J. Phys. Chem. Sol.	31	1735	1970
3.	Palmer S.B., Lee E.W. and Islam M.N.	Proc. Roy. Soc.	A338	341	1974
4.	Savage S.J. and Palmer S.B.	Phys. Letts.	60A	358	1977
5.	Fisher E.D. and Dever D.	Trans.Met.Soc.AIME	239	48	1967
6.	Rosen M., Kalir D. and Klimker H.	Phys. Rev.	8	4399	1973
7.	du Plessis P. de V.	J. Phys. F	6	873	1976
8.	Nagamiya T. and Kitano Y.	Prog.Th.Phys.(Jap.)	31	1	1964
9.	Crangle J.	Private Communication			
10.	Isci C. and Palmer S.B.	J.Phys.F.	8	247	1978

Chapter 9

1.	Long M.A., Wazzan A.R. and Stern R.	Phys. Rev.	178	775	1969
2.	du Plessis, P. de V.	J. Phys. F	6	873	1976
3.	Salama K., Brotzen F.R. and Donoho P.L.	J. App. Phys.	43	3254	1972
4.	Palmer S.B., Lee E.W. and Islam M.N.	Proc. Roy. Soc.	A338	341	1974
5.	Hiraoka T. and Suzuki M.	J.Phys.Soc.Jap.	31	1361	1971
6.	Simons D.S. and Salamon M.B.	Phys. Rev. B	10	4680	1974
7.	Nigh H.E., Legvold S. and Spedding F.H.	Phys. Rev.	132	1092	1963
8.	Feron J.-L.	C.R.Acad.Sci.Paris	B-36	549	1969
9.	Feron J.-L.	Ph.D. Thesis	Univ.Grenoble		1969
10.	Singh R.L., Jericho M.H. and Geldart D.J.W.	Phys. Rev. B	13	4949	1976
11.	Belov K.P. et al	Sov. Phys. JETP	34	787	1972
12.	Hegland D.E., Legvold S. and Spedding F.H.	Phys. Rev.	131	158	1963
13.	Feron J.-L.	C.R.Acad.Sci.Paris	B-40	611	1969
14.	Green R.W., Legvold S. and Spedding F.H.	Phys. Rev.	122	827	1961
15.	Feron J.-L., Hug G. and Pauthenet R.	Z.Angew.Physik	30(1)	61	1970
16.	Flippen R.B.	J.App.Phys.	35	1047	1964
17.	Isci C. and Palmer S.B.	J. Phys. F.	8	247	1978
18.	Isci C. and Palmer S.B.	J. Phys. Chem. Sol.	38	1253	1977
19.	Isci C., Palmer S.B., and Hukin D.	J. Phys. F (Met.Phys.)	7	2381	1977
20.	Cable J.W. and Wollan E.O.	Phys. Rev.	165	733	1968
21.	Corner W.D. Roe W.C. and Taylor K.N.R.	Proc.Phys.Soc.Lond.	80	927	1962
22.	Corner W.D. and Tanner B.K.,	J. Phys. C	9	627	1976
23.	Savage S.J. and Palmer S.B.,	Phys. Letts.	60A	358	1977
24.	Moran T.J. and Lüthi B.	J. Phys. Chem. Sol.	31	1735	1970
25.	Moran T.J. and Lüthi B.	Phys. Letts.	29A	665	1969
26.	Lüthi B., Moran T.J. and Pollina R.J.	J. Phys. Chem. Sol.	31	1741	1970
27.	Corner W.D. and Tanner B.K.,	Physics Educ.	11	356	1976
28.	Osborne J.A.	Phys. Rev.	67	351	1945
29.	Bozorth R.M.	'Ferromagnetism'			
30.	Behrendt D.R., Legvold S. and Spedding F.H.	Phys. Rev.	109	1544	1958

Chapter 9 (continued)

31.	Akhavan M. et al	Phys. Rev. B	8	4258	1973
32.	Hudgins A.C. and Pavlovic A.S.	J. Appl. Phys.	36	3628	1965
33.	Palmer S.B. and Jiles D.C.	Journ. de Physique	C5	33	1979
34.	Jensen J.	Danish At.En.Comm.	Risø Report No.		252 1971
35.	Nagamiya T., Nagata K. and Kitano Y.	Prog.Th.Phys.(Jap.)	27	1253	1962
36.	Nagamiya T. and Kitano Y.	Prog.Th.Phys.(Jap.)	31	1	1964
37.	Crangle J.	Private Communication			
38.	Crangle J.	Pre-print			
39.	Feron J.-L.	in The Electronic Structure of Rare Earth Metals, B. Coqblin			1977
40.	Robinson K. and Lanchester P.C.	Private Communication			
41.	Maekawa S., Treder R.A., Tachiki M.	Phys. Rev. B	13	1284	1976

Chapter 10

1.	Ramji Rao R.	See references in last chapter			
2.	Fisher E.S., Manghrani M.H. and Kikuta R.	J. Phys. Chem. Sol.	34	687	1973
3.	Swartz K.D. and Elbaum C.	Phys. Rev. B	1	1512	1970
4.	Naimon E.R.	Phys. Rev. B	4	4291	1971
5.	Hiki Y. and Granato A.V.	Phys. Rev.	144	411	1966
6.	Salama K. and Alers G.A.	Phys. Rev.	161	673	1967
7.	Thomas J.F.	Phys. Rev.	175	955	1968
8.	Sarma V.P.N. and Reddy P.J.	Phys. St. Sol.	10	563	1972
9.	Palmer S.B. and Lee E.W.	Proc. Roy. Soc.	A327	519	1972
10.	Palmer S.B., Lee E.W. and Islam M.N.	Proc. Roy. Soc.	A338	341	1974
11.	Nye J.F.	Physical Properties of Crystals	O.U.P.		1957
12.	Gerlich D. and Kennedy G.C.,	J. Appl. Phys.	50	5038	1979
13.	Brammer A.J.	Ph.D. Thesis	Exeter Univ.		1967
14.	Hames T.K.	Ph.D. Thesis	Southampton Univ.		1976
15.	Brugger K.	J. Appl. Phys.	36	759	1965
16.	Topping J.	Errors of Observation and Their Treatment	Chapman & Hall		1972

Appendix 2

1.	Dirac P.A.M.	Proc. Roy. Soc.	112A	661	1926
2.	Heisenberg W.	Z. Physik	38	441	1926
3.	Schiff L.I.	Quantum Mechanics	McGraw-Hill		1955
4.	Van Vleck J.H.	Electric and Magnetic Susceptibilities	Oxford		1932
5.	Mattis D.C.	The Theory of Magnetism	Harper & Row		1965
6.	Martin D.H.	Magnetism in Solids	Iliffe		1967

Appendix 3

1.	Landau L.D. and Lifschitz E.M.	Statistical Physics			
2.	Zeeman E.C.	Catastrophe Theory			
3.	Lavis D.A. and Bell G.M.	Bull I.M.A.	13	34	1977
4.	Schulman L.	Phys. Rev. B.	7	1960	1973
5.	Schulman L.	Dynamical Systems - Warwick 1974	Springer-Verlag		
6.	Zeeman E.C.	Scientific American	234	Apr(65)	1976
7.	Thom R.	Structural Stability and Morphogenesis			

Appendix 4

1.	Thomas J.F.	Phys. Rev.	175(3)	955	1968
2.	Hiki Y. and Granato A.V.	Phys. Rev.	144(2)	411	1966
3.	Salama K. and Alers G.A.	Phys. Rev.	161(3)	673	1967
4.	Thompson M.W.	Defects and Radiation Damage in Crystals	C.U.P.		1969
5.	Hull D.	Intro. to Dislocations	Pergamon		1965
6.	Weertman J.	Elementary Dislocation Theory	Macmillan		1964
7.	Cottrell A.H.	Theory of Dislocations in Crystals	Blackie		1964
8.	Cottrell A.H.	Dislocation and Plastic Flow	O.U.P.		1952
9.	Thompson D.O. and Paré V.K.	Phys. Acoust. III	Ch.7		1964
10.	Holmes	Interaction of Radiation with Solids			1964

Appendix 5

1.	Lorrain P. and Corson D.R.	Electromagnetic Fields and Waves			
2.	Magid M.	Electromagnetic Fields, Energy and Waves			

Appendix 5 (continued)

3.	Cheston W.B.	Elementary Theory of Electric and Magnetic Fields			
4.	Taylor K.N.R. and Darby M.I.	The Physics of Rare Earth Solids			
5.	Stevens K.W.H.	Proc. Phys. Soc.	A65	209	1952
6.	Elliott R.J. and Stevens K.W.H.	Proc. Roy. Soc.	A219	387	1953
7.	Elliott R.J.	in Magnetism, Ed. Rado & Suhl		Vol.2A	1965

Appendix 6

1.	Research and Engineering Controls Ltd.	Durban Rd., Bognor Regis, Sussex.	
2.	White G.K.	Exp. Tech. in Low Temp. Phys. (2nd Ed.)	p.370
3.	Greenough R.D.	Private Communication	
4.	W.G. Pye & Co. Ltd.,	Cambridge, England.	
5.	Welwyn Strain Measurements,	Armstrong Rd., Basingstoke, Hants.	

Appendix 7

1.	Swartz K.D. and Elbaum C.	Phys. Rev. B	1	1512	1970
2.	Naimon E.R.	Phys. Rev. B	4	4291	1971
3.	Hiki Y. and Granato A.V.	Phys. Rev.	144	411	1966
4.	Hames T.K.	Ph.D. Thesis	Southampton Univ.		1976
5.	Fisher E.S., Manghnani M.H. and Kikuta R.	J. Phys. Chem. Sol.	34	687	1973

Appendix 8

1.	Greenough R.D.	Private Communication		
2.	Isci C.	Private Communication		
3.	White G.K.	Experimental Tech. Low Temp. Phys.	Oxford	1968